AD 013 129

REPORT No. FAA-RD-74-125, II

CORE ENGINE NOISE CONTROL PROGRAM

Volume II - IDENTIFICATION OF NOISE GENERATION AND SUPPRESSION MECHANISMS

K.R. BILWAKESH
W.S. CLAPPER
J.J. EMMERLING
S.B. KAZIN
P.R. KNOTT
D. LATHAM
R.K. MATTA
H. MOROZUMI

AIRCRAFT ENGINE GROUP
GENERAL ELECTRIC COMPANY
CINCINNATI, OHIO 45215

NAFEC
LIBRARY
AUG 5 1975
RECEIVED

FAA WJH Technical Center
00026764

AUGUST 1974

FINAL REPORT

Document is available to the public through the National Technical Information Service, Springfield, Virginia 22151.

Prepared for

U.S. DEPARTMENT OF TRANSPORTATION
FEDERAL AVIATION ADMINISTRATION
Systems Research & Development Service
Washington, D.C. 20590

NOTICE

This document is disseminated under the sponsorship of the Department of Transportation in the interest of information exchange. The United States Government assumes no liability for its contents or use thereof.

Technical Report Documentation Page

1. Report No.	2. Government Accession No.	3. Recipient's Catalog No.
FAA-RD-74-125, II		

4. Title and Subtitle	5. Report Date
Core Engine Noise Control Program Volume II - Identification of Noise Generation and Suppression Mechanisms	August 1974
	6. Performing Organization Code
7. Author(s) S.B. Kazin (Prog. Tech. Dir.), R.K. Matta (Ed), K.R. Bilwakesh, W.S. Clapper, J.J. Emmerling, P.R. Knott, D. Latham, H. Morozumi	8. Performing Organization Report No.
9. Performing Organization Name and Address General Electric Company Aircraft Engine Group Evendale, Ohio 45215	10. Work Unit No. (TRAIS) 36310
	11. Contract or Grant No. DOT-FA72WA-3023
12. Sponsoring Agency Name and Address U.S. Department of Transportation Federal Aviation Administration Systems Research and Development Service Washington, D.C. 20590	13. Type of Report and Period Covered Final July 1972 - April 1974
	14. Sponsoring Agency Code

15. Supplementary Notes Related Documents:
Volume I - Identification of component noise sources, FAA-RD-74-125, I
Volume III - Prediction Methods, FAA-RD-74-125, III

16. Abstract

The mechanisms of noise generation and suppression for the various core engine noise sources in turbofans were defined through a balanced analytical and experimental program. Model, component, and engine tests were used to substantiate the results of the analysis and to determine the basic noise generating parameters. The results were cast in a general form so as to be applicable to a wide variety of cycles, including future technology turbofan engines.

Several suppression concepts were identified through analysis and through logical extension of experience with earlier programs on high velocity jet noise and fan/compressor noise research. The suppression concepts were validated through model and component tests and through evaluation of available engine data.

17. Key Words	18. Distribution Statement
Core Engine Noise, Turbofan Engine Noise, Aircraft Noise Control, Low Noise Technology, Jet Noise, Combustor Noise, Core Noise, Turbine Noise, Tone/Jet Stream Interaction, Obstruction Noise Casing Radiation, Compressor Noise	Document is available to the public through the National Technical Information Service, Springfield, Virginia 22151.

19. Security Classif. (of this report)	20. Security Classif. (of this page)	21. No. of Pages	22. Price
Unclassified	Unclassified	505	

Form DOT F 1700.7 (8-72) Reproduction of completed page authorized

PREFACE

This report describes the work performed under the DOT/FAA Core Engine Noise Control Program (Contract DOT-FA72WA-3023). The objectives of the program were:

- Identification of component noise sources of core engine noise
- Identification of mechanisms associated with core engine noise generation and noise reduction
- Development of techniques for predicting core engine noise in advanced systems for future technology aircraft.

The objectives were accomplished in 4 phases as follows:

Phase I - Analysis of engine and component acoustic data to identify potential sources of core engine noise and classification of the sources into major and minor categories.

Phase II - Identification of the noise generating mechanisms associated with each source through a balanced program of:

- Analytical studies
- Component and model tests
- Acoustic evaluation of data from existing and advanced engine systems.

Phase III - Identification of noise reduction mechanisms for each source through a program with elements similar to phase II.

Phase IV - Development of improved prediction techniques incorporating the results obtained during the preceding two phases.

The work accomplished is reported in three volumes corresponding respectively to the three objectives stated above.

Volume I - Identification of Component Noise Sources.

Volume II - Identification of Noise Generation and Suppression Mechanisms.

Volume III - Prediction Methods.

The ranking of core engine noise sources reported in Vol. I was used to allocate the resources accordingly and to direct the activity in the following phases. This volume documents the results of the analytical and experimental investigations of the noise generation and noise suppression mechanisms conducted in Phases II and III. The information derived from these was then used to determine prediction methods for the various core engine noise sources. This last activity is reported in Volume III.

A visual representation of the overall program and report organization is shown on page iv.

CORE ENGINE NOISE CONTROL PROGRAM
OVERALL REPORT ORGANIZATION

Contract Phase		Contract Documentation
Phase I	Volume I	Identification of Component Noise Sources
Phase II and Phase III	Volume II	Definition of Mechanisms of Noise Generation Definition of Mechanisms of Noise Reduction
Phase IV	Volume III	Development of Prediction Techniques

SUMMARY AND CONCLUSIONS

This volume contains information on the detailed investigation of the source generating mechanisms and suppression of seven core noise sources:

1. Coannular jet noise
2. Combustor noise
3. Turbine noise
4. Interaction noise
5. Obstruction noise
6. Casing radiation
7. Compressor noise.

The coannular jet noise investigation was largely carried out on General Electric's low ambient noise level jet noise facility. A detailed test program was run to determine the effects of the fan flow passing over the high velocity core jet for a range of area ratios (fan nozzle area/core nozzle area), fan jet velocities, and velocity ratios (fan jet/core jet).

Four core suppressors were also run - two lobe suppressors, a hole suppressor and a spoke suppressor. These tests indicated that an 18 lobe, area ratio 2 (annulus area/core flow area) suppressor with a carefully faired (capped) core cowling would produce about 5 PNdB of suppression statically with a core jet velocity of 1600 ft/sec.

A series of tests were conducted to determine the effects of internal turbulence on jet noise generation. These tests indicate increases in noise of up to 7.5 db OASPL when axial turbulence increases from 2% to 20%.

The area of combustion (low frequency core) noise presents a unique measurement problem in the engine system because of its close relation to jet noise in the spectrum. Therefore, it was advantageous to test the combustor as a component at atmospheric pressure. Two combustors were tested. The data from those tests showed a correlation with temperature rise and mass flow as well as exit velocity. The exit geometry was also found to affect the directivity of combustor noise radiation.

A low frequency noise suppressor was also tested. It showed considerable suppression over a wide frequency band.

In the higher frequency range, turbine noise was investigated. Component tests were employed along with an analytical method for the prediction of turbine discrete frequency noise. A single stage high pressure turbine test

indicated no change in noise level with inlet turbulence when the turbine inlet nozzle was choked. A three stage turbine was also tested with and without increased axial spacing between the blade rows. The basic discrete frequency noise data indicated a good correlation with ideal work extraction and blade tip speed. Increased blade row spacing showed reductions in tone levels of 3 db PWL per spacing-to-chord doubling for a spacing increase from 0.29 to 0.89 rotor true chords. The analytic prediction showed good correlation with the actual component noise data.

Interaction noise was found to be related to turbine tone noise generation. The "haystack" phenomenon in the noise spectrum has been attributed to the interaction of a turbine tone with the turbulence in the coannular jets. This process occurs without amplifying the acoustic energy. Thus interaction noise can be reduced by reducing turbine noise or decreasing jet mixing turbulence intensity.

The noise created by obstructions in engine flowpaths was investigated through the use of a free jet laboratory test facility. Both noise and wake survey data were taken for a series of commonly shaped obstructions. All of the noise data acquired was found to correlate with a parameter based on the model chord, span, maximum thickness, and drag coefficient, plus with the incoming velocity. In general, the more streamlined shapes (lowest drag) resulted in the least noise.

Although casing radiation is not a true "source" in that the origin of the acoustic energy is related to other engine components, the characteristics of the casing can play a part in determining the overall engine noise signature. The acoustic impedance of the casing was found to be a function of the casing thickness, critical and ring natural frequencies, and the location of internal struts.

Core compressor noise was examined largely from the point of view of its suppression and overall contribution to the engine noise signature. Generally, the core compressor contributes little to the engine spectrum. What noise does reach the farfield is principally radiated from the engine inlet. The suppression of this noise can be accomplished by using compressor inlet treatment.

Thus, in each of the seven areas cited, the source mechanisms and various means of suppression were examined. This was accomplished through a balanced program of analytical work, component testing, and engine test data analysis.

TABLE OF CONTENTS

Section		Page
1.0	INTRODUCTION	1-1
2.0	JET NOISE	2-1
2.1	Background	2-1
2.2	Unsuppressed Configuration Tests	2-1
2.3	Upstream Turbulence Tests	2-40
2.4	Suppressor Tests	2-63
2.5	Jet Noise in Flight	2-149
3.0	COMBUSTOR NOISE	
3.1	Background	3-1
3.2	Component Tests	3-4
3.3	Suppressor Treatment Selection	3-26
3.4	Suppressed Combustor Tests	3-29
3.5	Summary	3-49
4.0	TURBINE NOISE	
4.1	Background	4-1
4.2	Single Stage (High Pressure) Turbine Tests	4-2
4.3	Three Stage (Low Pressure) Turbine Tests	4-32
4.4	Analytical Prediction of Turbine Discrete Frequency Noise	4-58
5.0	INTERACTION NOISE	
5.1	Background	5-1
5.2	Identification of the Source and Relevant Mechanisms	5-1
5.3	Analysis of the Haystacking Phenomenon	5-11

TABLE OF CONTENTS (Concluded)

Section | Page

5.0 INTERACTION NOISE (Continued)

5.4 Experimental Data on Turbulence Scattering 5-27

5.5 Summary. 5-39

6.0 OBSTRUCTION NOISE

6.1 Background 6-1

6.2 Experimental Work 6-1

6.3 Data Analysis and Results 6-9

6.4 Summary 6-40

7.0 CASING RADIALTION

7.1 Background. 7-1

7.2 Casing Radiation Sources. 7-1

7.3 Reduction of Casing Radiated Noise. 7-5

7.4 Summary 7-16

8.0 COMPRESSOR NOISE

8.1 Background. 8-1

8.2 Analysis of Compressor Noise Propagation Paths. 8-1

8.3 Comparison of Predicted and Measured Compressor Noise 8-8

8.4 Methods of Suppression. 8-8

8.5 Summary 8-15

APPENDICES

A. Nozzle Performance Data. A-1
B. Aero-Acoustic Data Model B-1
C. Suppressor Tests Aero Data C-1
D. Combustor Test Points. D-1
E. Flow Corrections for Probe Measurements. E-1

NOMENCLATURE

A	-	area
A_o	-	incident wave amplitude
A_w	-	axial chord
$A + B$	-	shortest freefield path between source and receiver
AR	-	exhaust nozzle area ratio (fan/core)
a	-	radius of cylinder
$\hat{a}$	-	unit vector
B	-	barometric pressure in inches Hg; also, plate bending stiffness per unit width (Section 7)
BPF	-	blade passing frequency
BPR	-	bypass ratio (fan/core)
b	-	distance between centers of adjacent blade row (Section 4); also, distance propogated through turbulence region (Section 5)
C	-	compressor tone; also, probe frequency response correction (Section 4)
C_b	-	phase speed of bending wave
C_D	-	profile drag coefficient
C_L	-	phase speed of longitudinal wave
C_p	-	coefficient of specific heat at constant pressure
C_x, C_y	-	phase speed of acoustic wave in the direction of the panel edges
CSD_{xy}	-	cross spectral density for x and y
c	-	acoustic velocity; also, semichord (Section 4)
D	-	diameter, normally fan jet diameter; also, straight line distance between source and observer (Section 7)
D_H	-	hydraulic diameter
D_p	-	profile drag
DI	-	directivity index
d	-	diameter, normally core jet diameter
dB	-	decibel
div	-	divergence, $(\nabla\cdot)$ operator

NOMENCLATURE (Continued)

E	-	Young's modulus of elasticity
EGA	-	extra ground attenutation
EPNL	-	effective perceived noise level
e	-	2.71828
F	-	fan tone; also, prediction parameter (Section 3)
f	-	frequency
f/a	-	fuel-air ratio (Section 3)
f_c	-	critical frequency
f_{peak}	-	spectrum peak frequency
f_r	-	ring frequency
f^*	-	modified (Strouhal) frequency, $(f\delta/\bar{U}_o)$
G_m	-	coefficient of unsteady upwash
grad	-	gradient, ∇ operator
$g(\ )$	-	Green's Function
H	-	blade height
Hz	-	Hertz, cycles/second
HP	-	horsepower
h	-	span (Section 6); also, shell plate thickness (Section 7)
I	-	acoustic intensity; also, unit tensor (Section 2)
J	-	Bessel Function of first kind
K	-	Bessel Function of second kind; also, constant (Section 4)
k	-	wave number, $2\pi/\lambda = \omega/c$
kHz	-	kilo-Hertz
k_o	-	wave number of the incident wave
k, k_2, k_3, k_4	-	constants describing wave shape
L	-	length; also, integral scale of turbulence (Section 5)
ℓ	-	chord; also, characteristic length (Section 5)
M	-	Mach number, V/c
M_R	-	relative Mach number, V_{rel}/c
M_t	-	turbulence Mach number

NOMENCLATURE (Continued)

N	-	rpm; also, Fresnel number (Section 7)
N_f	-	design fan rpm
NDP	-	normal diametrical pitch, $\frac{\text{number of gear teeth}}{\text{pitch diameter}}$
NPWL	-	normalized measured OAPWL
n	-	harmonic number; also, number of modes in f, p or s modes (Section 7).
OAPWL	-	overall power level (acoustic), dB re 10^{-13} Watt
OASPL	-	overall sound pressure level, dB re .0002 d/cm^2
P	-	total pressure; also, acoustic power in Watt (Section 2)
P_R	-	pressure ratio
PNL	-	perceived noise level
PWL	-	acoustic power level, dB re 10^{-13} Watt
P/P	-	fan pressure ratio
PWL_N	-	normalized 1/3 octave band PWL
PSD_x	-	power spectral density at x
PSD_y	-	power spectral density at y
p	-	static pressure; also, acoustic pressure (Section 5)
$p_{(measured)}$	-	pressure recorded by acoustic probe
Q	-	heating value of fuel
q	-	dynamic pressure
q_o	-	specific stoichiometric heat of combustion
R	-	pipe radius, turbulence region (Section 5); also, transmission loss through casing material (Section 7)
R_e	-	Reynolds number
R_H	-	Reynolds number based on hydraulic diameter
r	-	position vector; radial coordinate in a polar system (Section 5) axial distance along a duct (Appendix E)
r_{hub}	-	hub radius
$\mathcal{R}$	-	portion of kinetic tensor excluding turbulent stress tensor
S	-	Sears Function
S_n	-	Strouhal number, $\frac{\text{frequency x length}}{\text{velocity}}$

NOMENCLATURE (Continued)

SPL	-	sound pressure level, dB re .0002 d/cm^2
s	-	axial spacing
T	-	total temperature; turbine tone (Section 4); time interval (Section 5); reverberation time (Section 6); also, transmission coefficient (Section 7)
TL	-	transmission loss
t	-	static temperature; pitch (Section 4); time (Section 5); also, thickness (Section 6)
t_e	-	trailing edge thickness of turbine blade
U	-	flow velocity
U_T	-	blade tip speed
u	-	perturbation in velocity due to acoustic wave
u_c	-	maximum velocity defect in viscous wake
u'	-	turbulence velocity vector
V	-	velocity; also, volume (Section 5)
V_a	-	velocity of ambient atmosphere relative to the jet nozzle
V_j	-	absolute jet velocity
V_{rel}	-	relative velocity
VR	-	exhaust velocity ratio (fan/core)
V	-	normal velocity component
$\dot{W}$	-	air flow rate
x	-	axial coordinate
x'	-	$c_2 \left[\frac{b}{c_2 \cos \alpha_1} + \frac{x_2}{c_2} \frac{V_1}{V_2} \right] - .6$, equation (4.4.3-3)
Y	-	wake half width
y	-	normal coordinate
α	-	air angle; air attenuation; also, $k_c \ell_c$, equation (5.3.3-14)
α_m	-	mean angle
$\alpha°$	-	angle of attack
α_1	-	stagger angle of blades
$\alpha(r)$	-	physical lean at radius r
$\tilde{\alpha}$	-	eddy decay parameter

β	-	air angle between rotor and stator blade (Section 4); also, $\frac{h}{[2(3a)^{1/2}\ \ell]}$, equation (7.3-10)
$\beta(r)$	-	$180° - \alpha(r)$
Γ	-	unsteady circulation
γ	-	ratio of specific heats
γ^2	-	coherence function, $(CSD_{xy})^2/(PSD_x)(PSD_y)$
$\gamma(r)$	-	angle between tangent to the vane and the local radial line (Section 4)
γ_p^2	-	partial coherence function
γ_κ	-	$(\kappa_e - \kappa)/\kappa$
γ_ρ	-	$(\rho_e - \rho)/\rho_e$
Δ	-	difference
ΔA	-	incremental area
Δ_s	-	$(\omega - k_i c)$, equation (5.3.3-13)
Δt	-	incremental time
δ	-	density perturbation due to acoustic wave; drop in tone SPL due to "haystacking" (Section 5); also, maximum thickness (Section 6)
ζ_p	-	pressure loss coefficient
η	-	position vector (Section 2); ratio of maximum dynamic pressure defect in wake to freestream dynamic pressure (Section 4); ω_i/ω_c, (Section 5); also, composite plate loss factor (Section 7)
η'	-	ratio of dynamic pressure defect in wake to freestream dynamic pressure
θ	-	angle; also, $\frac{\text{temperature observed}}{\text{reference temperature}}$ (Section 3)
κ	-	compressibility, $1/\rho\ (\partial\rho/\partial p)$
λ	-	wave length; also, second viscosity coefficient (Section 2)
μ	-	Poisson's ratio; also, first viscosity coefficient (Section 2)
μ_s	-	$\frac{\omega}{c}\hat{a}_r - \vec{k}_i$, equation (5.3.3-13)
ν	-	kinematic vicosity; also, resonance frequency (Section 7)
ξ	-	enthalpy loss coefficient

Θ	-	angle factor, $\cos^2\theta \exp\left[-\frac{1}{2}\mu_s^2\ell_c^2 - \frac{1}{2}\left(\frac{\Delta_s}{\omega_c}\right)^2\right]$, equation (5.3.3-15)
π	-	3.14159
ρ	-	density
ρc	-	acoustic impedance
ρ_{isa}	-	density at international standard atmospheric conditions
ρ_m	-	plate mass density
ρ_s	-	plate surface density, ρ_m/t
σ	-	blade row solidity, ℓ/t; also, radiation efficiency (Section 3)
τ	-	viscous stress tensor (Section 2); also, time
$\mathfrak{T}$	-	kinetic tensor, (u u')
ϕ	-	angle; also, equivalence ratio, $\frac{\text{fuel-air ratio}}{\text{stoichiometric fuel-air ratio}}$ (Section 3)
ψ	-	geometric lean (Section 4)
ω	-	circular frequency, $2\pi f$
ω_o	-	circular frequency of incident tone
ω_2	-	reduced frequency, $\frac{\pi c_2}{c_1}\frac{U\sigma_1}{V_1}$
$(\ )_c$	-	correlation value
$(\ )_{core}$	-	primary (core) jet parameter
$(\ )_{cs}$	-	value for circumferential strip modes
$(\ )_e$	-	variation due to turbulence; exit condition; also, eddy condition
$(\ )_f$	-	value for acoustically fast mode
$(\ )_{fan}$	-	secondary (fan) jet parameter
$(\ )_i$	-	incident wave
$(\ )_j$	-	jet parameter
$(\ )_{max}$	-	maximum value
$(\ )_{mean}$	-	mean value
$(\ )_p$	-	value for piston mode
$(\ )_{Ref}$	-	value at reference conditions, reference parameter
$(\ )_s$	-	static conditions; scattered wave (Section 5); also, value for strip mode (Section 7)
$(\ )_T$	-	total conditions
$(\ )_{Tone}$	-	value for tone

NOMENCLATURE (Concluded)

$(\ )_t$	-	transmitted wave
$(\ )_x$	-	component in x-direction
$(\ )_y$	-	component in y-direction
$(\ )_\omega$	-	simple harmonic component
$(\ )_\infty$	-	freestream condition
$(\ )_{1/3OB}$	-	1/3 octave band value
$(\ )_o$	-	reference conditions; also, value within turbulence region (Sections 2 and 5)
$(\ )_1$	-	upstream conditions; also, distance along an upstream blade (Section 4)
$(\ )_2$	-	downstream conditions; also, distance along a downstream blade (Section 4)
$(\ )_{28}$	-	conditions at fan nozzle exit plane
$(\ )_3$	-	conditions entering a combustor
$(\ )_4$	-	conditions at combustor exit
$(\ )_5$	-	conditions at turbine exit
$(\ )_8$	-	conditions at core nozzle exit plane
$\overline{\overline{(\ )}}$	-	tensor
$\widehat{(\ )}$	-	space-averaged value over an arc
$\overline{(\ )}$	-	mean, time averaged value
$(\ )'$	-	time varying component; also, viscous stress tensor
$(\ )^*$	-	normalized quantity
$(\ )$	-	vector
$\langle\ \rangle$	-	time and space-average of mean square quantity
$\|\ \|$	-	magnitude, absolute value

SECTION 1.0

INTRODUCTION

Core engine noise has been assuming increasing significance in bypass engines as fan noise has progressively been brought under control. The major sources of concern were identified in Volume I as:

- Jet
- Combustor
- Turbine and Turbine/Jet Interactions
- Obstructions in the Flowpath.

Two other noise sources of less immediate concern,but which may require attention in a continuing noise reduction program, were identified as:

- Compressor
- Casing Radiation

The above delineation was used to allocate the effort of the Core Engine Noise Control Program.

This volume describes the work performed under Phases II and III of this program; the definition and substantiation of the mechanisms of the noise generation and noise suppression, respectively. These objectives were achieved through a balanced analytical and experimental program, supported by evaluation of a large amount of acoustic data previously obtained on a wide variety of engines. Model and component tests were performed to supplement the analytical work of Phase II in order to establish the basic parameters which control the noise generation.

The facilities utilized for the Phase II tests were also used for Phase III work in order to substantiate the analysis and to extend and validate suppression concepts developed under previous programs. For example, a) suppressor nozzle designs evolved under high velocity single jet programs were tested on the low velocity core jet in a coannular flow configuration, b) a fan noise reduction technique of opening axial spacing between blade rows was applied to turbines, and c) combustor noise suppression was demonstrated using a deep cavity resonator.

The phase 2 and 3 information reported in this volume was used to form the basis for construction of the prediction methods reported in Volume III.

SECTION 2.0

JET NOISE

2.1 BACKGROUND

The high bypass turbofan engine significantly reduced the jet noise problem by transferring the high velocity core jet energy to the low velocity fan stream. Recent advances in fan noise suppression however, have reduced engine noise levels to the point where core jet noise is again a dominant source. Attention has thus been directed toward establishing the acoustic characteristics of high bypass dual flow exhaust systems and toward developing viable suppression techniques.

The experimental investigations related to defining and to understanding the mechanisms of jet noise in dual flow systems must start with a background of basic data applicable to a wide range of engine exhaust systems. Some recent data (References 2.1-1 to 2.1-5) is available for subsonic coaxial jet noise generation, but very little systemic evaluation of jet noise characteristics has been undertaken. Experimental data is particularly needed for relatively large models with hot primary gas flows. The interaction of annular gas flows at different temperatures has not been investigated significantly from the acoustic standpoint.

The approach taken was to utilize a simple baseline dual flow nozzle configuration (such as Figure 2.1-1) and to investigate the effects of secondary to primary area ratio and velocity ratio at one temperature ratio. The same baseline model configuration was used to investigate the effects of flow turbulence intensity on jet noise generation.

2.2 UNSUPPRESSED CONFIGURATION TESTS

2.2.1 Objectives

The objective of the baseline unsuppressed dual flow nozzle evaluation was to investigate and define the secondary to primary area ratio and velocity ratio effects on the acoustic characteristics. The variation of the secondary and primary areas and velocities covered the range of current and proposed turbofan engines. The resulting data provided a prediction technique for the basic noise levels of various engine systems and established the interaction effects of dual flow nozzles.

2.2.2 Test Model Hardware

The core jet baseline nozzle consisted of a contoured convergent nozzle as shown in Figure 2.2.2-1. The exit diameter was 3.56 inches (0.09 m). Four coplanar secondary nozzles were designed to have secondary (fan) flow to primary (core) flow area at ratios of 2,4,6, and 8 (Figure 2.2.2-2). The fan shroud exit diameters and the geometric configuration of the hardware are

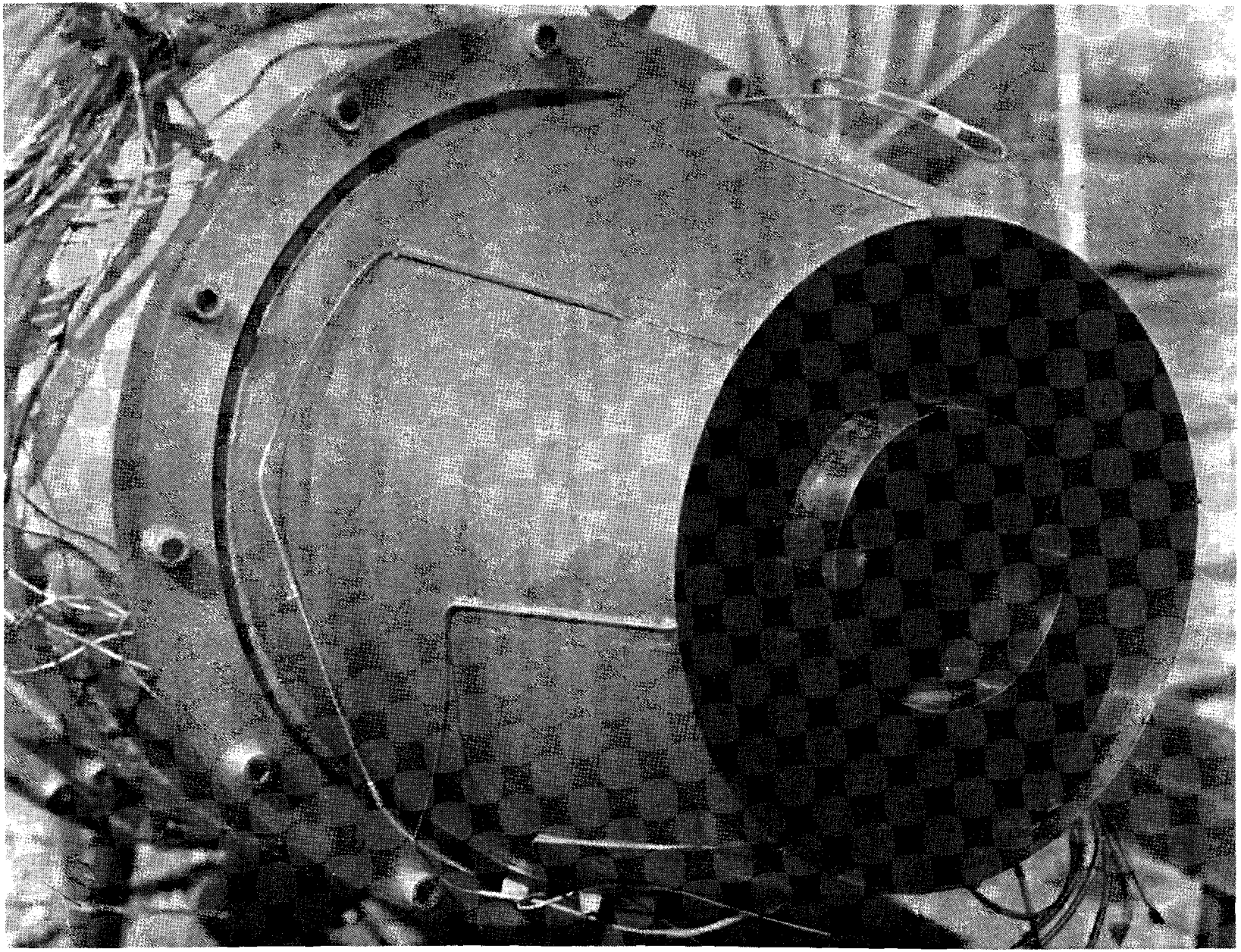

FIGURE 2.1-1 COANNULAR/COPLANAR NOZZLE CONFIGURATION, (SECONDARY-TO-CORE FLOW AREA RATIO = 4)

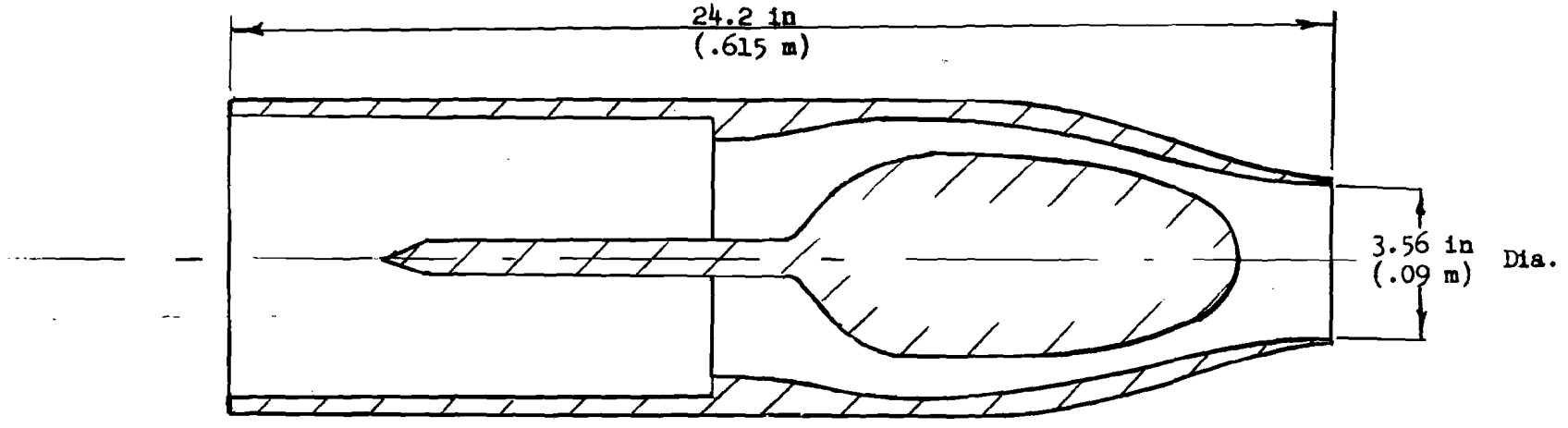

FIGURE 2.2.2 - 1 BASELINE NOZZLE - UNSUPPRESSED COANNULAR TEST

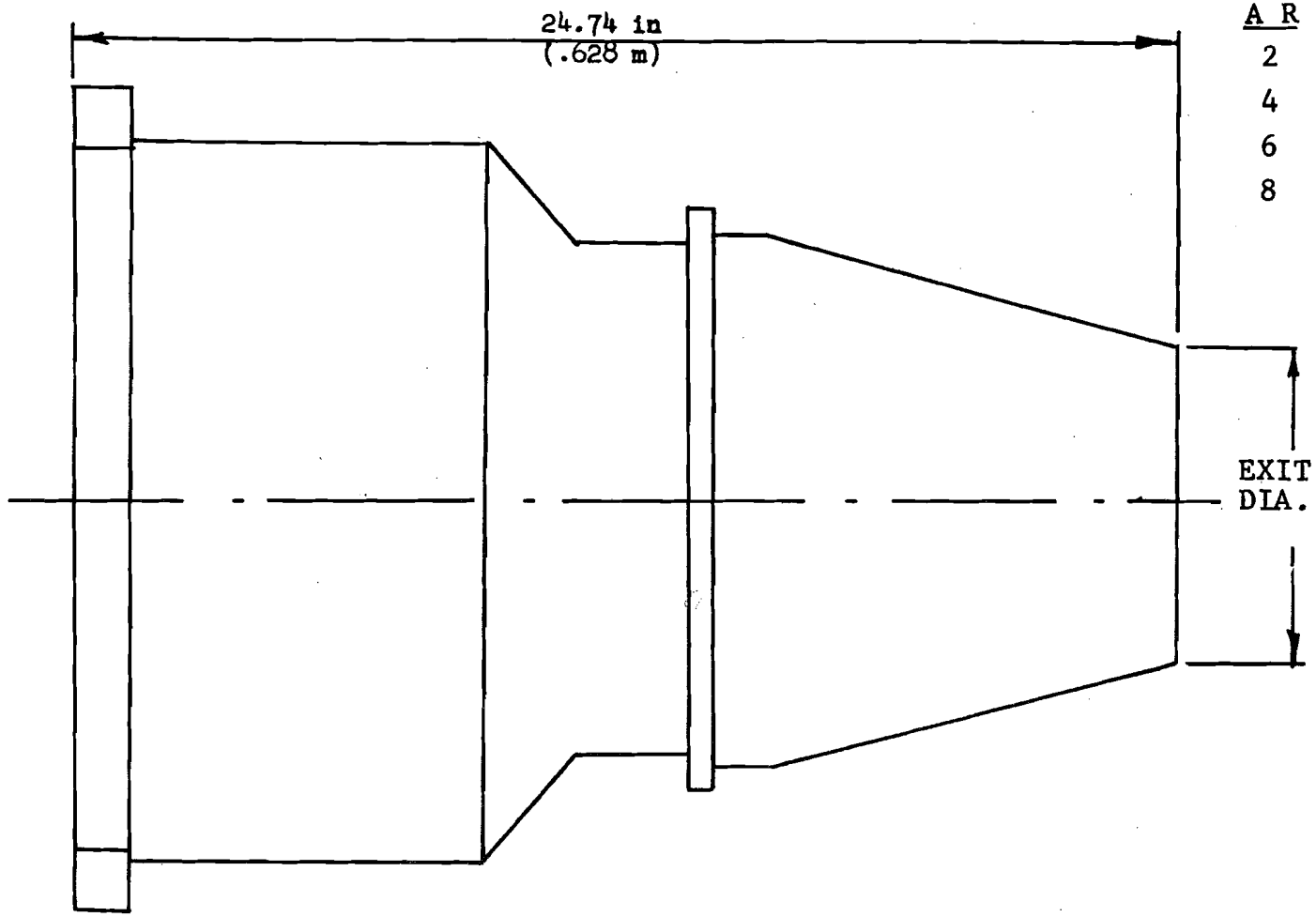

EXIT DIAMETER

A R	INCHES	METERS
2	6.18	.157
4	7.92	.201
6	9.43	.240
8	10.70	.272

FIGURE 2.2.2 - 2 ADAPTER AND SHROUD, UNSUPPRESSED COANNULAR TEST

also shown in the figure. The model hardware provided a family of coplanar, coannular convergent nozzles applicable to current and future aircraft installations as well as a basic reference configuration for dual flow jet noise testing.

2.2.3 Test Facility Description

The models were tested on a dual flow acoustic test facility with capabilities for hot core flow and cold secondary flow. This Jet Engine Noise Outdoor Test Stand (JENOTS) is located at General Electric, Evendale, Ohio (Figure 2.2.3-1). The coannular facility includes an acoustically treated plenum (Figure 2.2.3-2) in which upstream piping, valve, and combustor noise is absorbed. Cold high pressure air is supplied separately to the plenum secondary and primary chambers through air lines from compressors in a nearby building. The core flow is heated in the preburner up to temperatures of 1600° R (890° K) by a combustor using jet fuel (JP4). Hence, the core and fan flow streams are independently controlled and produce clean jet sources at low velocity conditions.

2.2.3.1 Coannular Plenum

The coannular rig is shown schematically in Figure 2.2.3.1-1. Air for the primary and secondary streams is supplied from the Evendale central air supply system through 10 inch (0.254 m) and 16 inch (0.406 m) air lines respectively. The plenum chamber to which the test models were attached served a two-fold purpose: 1) to give the flow a uniform velocity profile, and 2) to eliminate any high frequency system noise through the use of acoustically treated baffles located in the secondary and primary streams.

Flow conditions for the primary and secondary streams were controlled separately with the airflows being measured using an orifice plate system coupled with pressure and thermocouple rakes. Flow conditions at the nozzle exit plane of the models were set through the use of total pressure and total temperature rakes located on the model. The range of conditions under which the facility operates are:

	Minimum	Maximum
Bypass Ratio	0	15
Fan Temperature (° R)	ambient	ambient
Core Temperature (° R)	ambient	1600 (890 K)
Fan Pressure Ratio	1.05	3.5
Core Pressure Ratio	1.05	4.0
Fan Weight Flow (lb/sec)	0	30.0 (13.6 kg/sec)
Core Weight Flow (lb/sec)	0	30.0 (13.6 kg/sec)

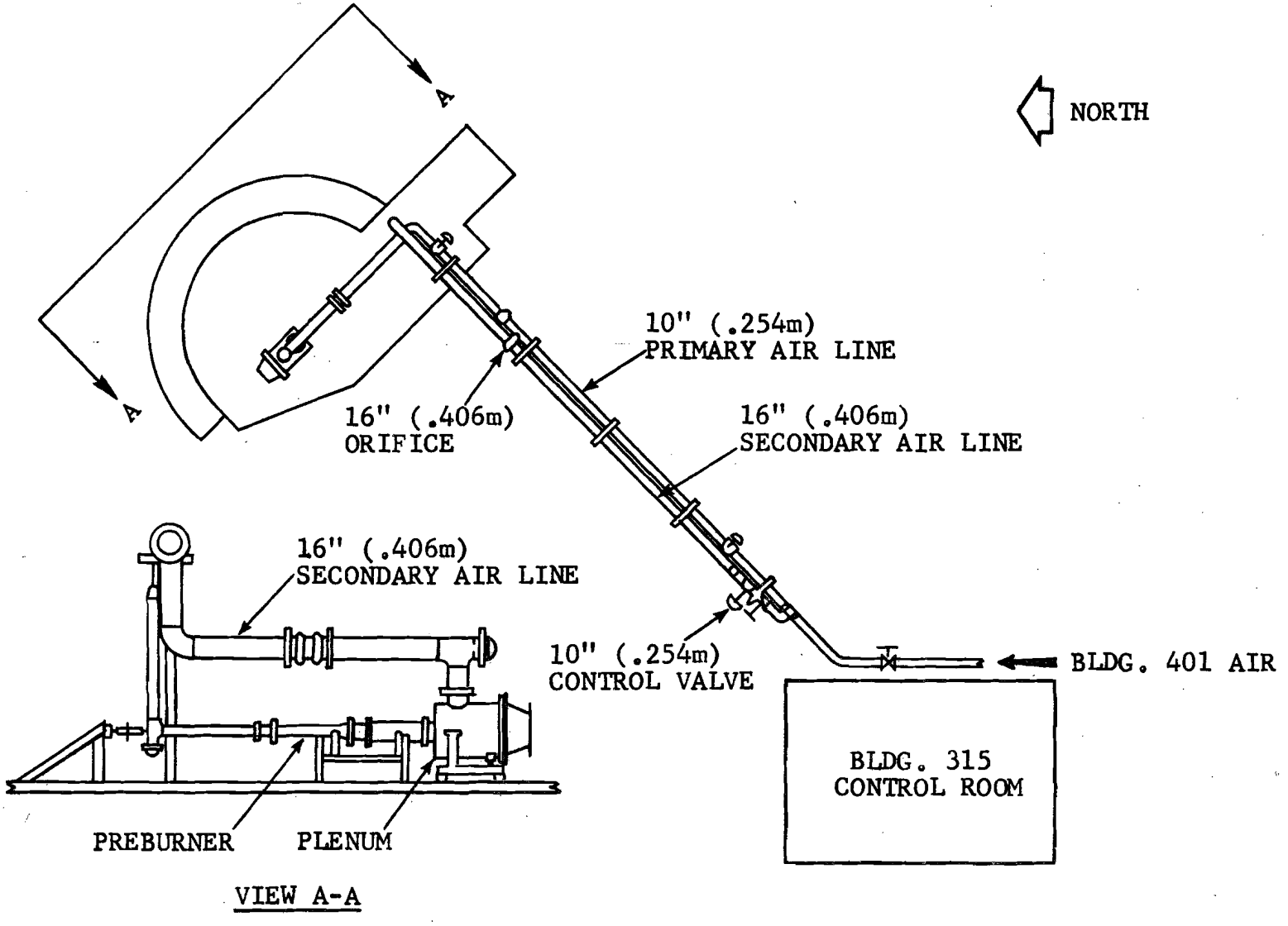

FIGURE 2.2.3 -1 SCHEMATIC OF COANNULAR FLOW JET NOISE FACILITY

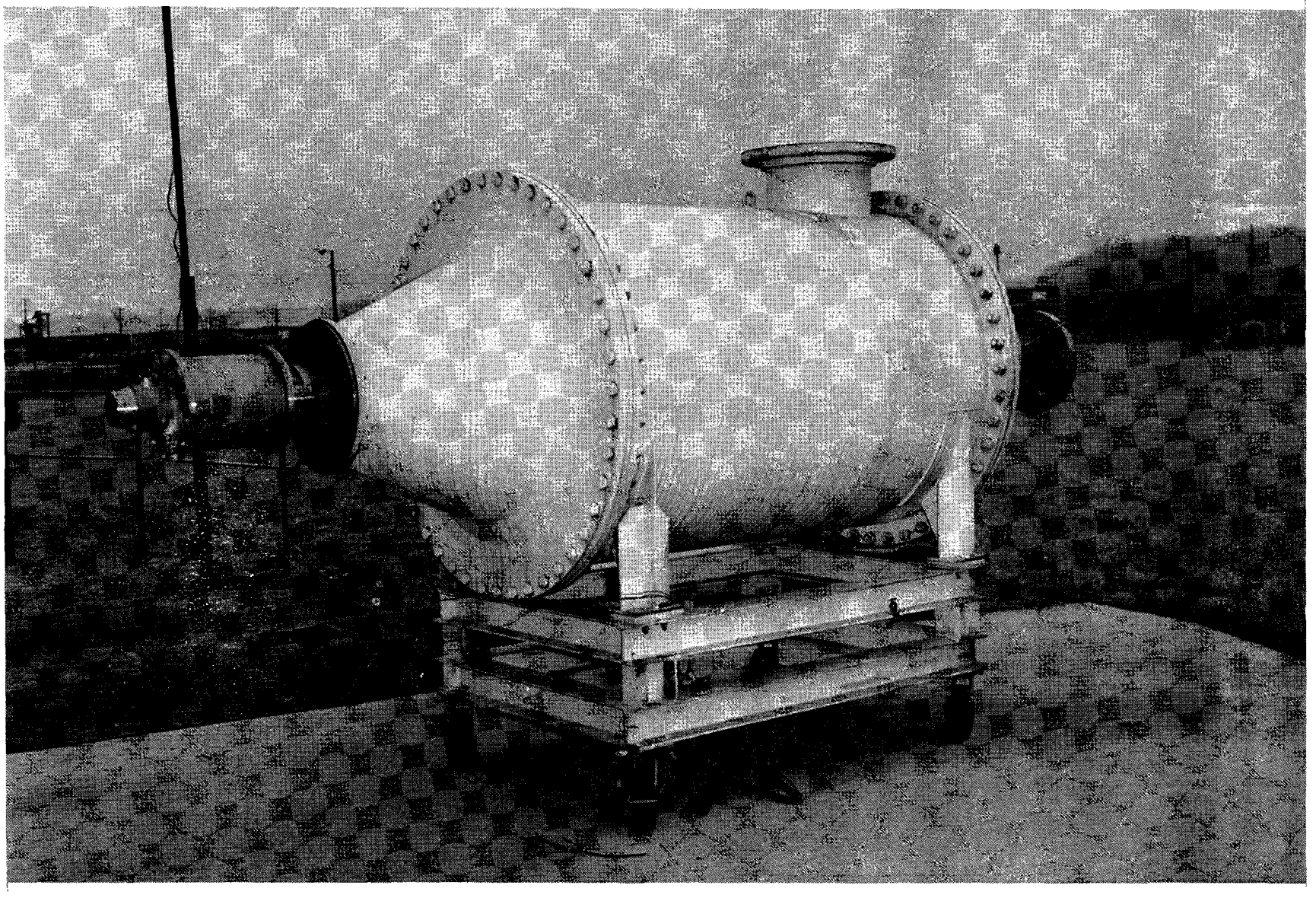

FIGURE 2.2.3-2 ENOTS TREATED PLENUM CHAMBER FOR COANNULAR FACILITY (SECONDARY AIR ENTERS FROM ABOVE)

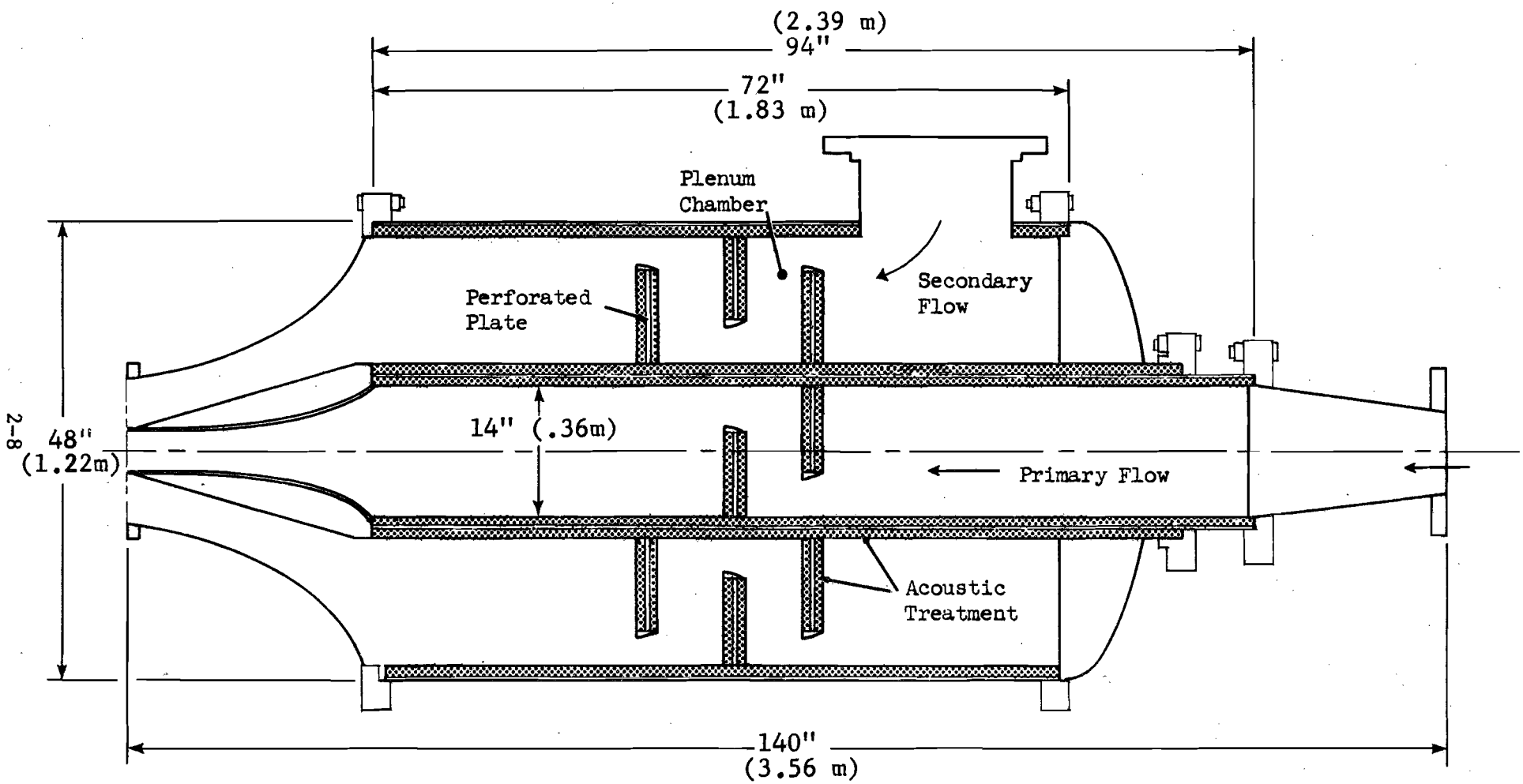

FIGURE 2.2.3.1-1 JENOTS COANNULAR PLENUM CHAMBER

Several precautions have been taken to eliminate extraneous noise (piping noise, etc.) emanating from the facility itself. Where possible, all air supply lines were wrapped with acoustically absorbing material to prevent pipe noise from escaping through the walls of the air supply lines. All elbows in the air supply lines were packed with acoustically absorbing material to minimize the generation of turning noise. To eliminate the high frequency piping noise, the plenum chamber (Figure 2.2.3-2) uses acoustically treated baffles. The low Mach number of the flows over the baffles (0.06 to 0.18) assured the effectiveness of the treatment which gave 25dB suppression for frequencies greater than 1000 Hz.

2.2.3.2 JENOTS Acoustic Arena

The outdoor facility has the nozzle centerline 55 inches (1.4 m) above the ground plane. The ground plane is composed of concrete to a radius of 20 feet (6.1 m) from the nozzle exit and then crushed rock to a 40 foot (12.2 m) radius. A grassy field exists beyond the acoustic arena. All structures present in the facility have been designed to eliminate acoustic reflection interference at the microphone positions.

The outdoor arena is subject to ambient weather conditions. The outside air temperature, barometric pressure, and wet and dry bulb temperatures are recorded throughout a test. The wind speed and wind direction are also recorded. These data are used to correct the sound data to standard day.

No acoustic testing is conducted during rain, snow, or winds over 10 mph.

2.2.3.3 Facility Acoustic Validation

Acoustic farfield data is recorded using a 40 ft (12.2 m) hemispherical arc microphone array consisting of 1/2 inch (0.0127 m) condenser microphones mounted on 16 ft (4.88 m) towers. The towers are positioned at 10° (0.175 rad) intervals to provide data from 20° (0.35 rad) to 160° (2.8 rad) from the inlet axis, see Figure 2.2.3.3-1. The towers are fitted with goose neck adapters for the microphones to insure no reflections from the towers (Figure 2.2.3.3-2).

This microphone array was implemented to minimize the effect of ground reflections on scale model data. By changing the geometry of the facility the loci of the reflection points moved closer to the source, Figure 2.2.3.3-3. This caused the ground reflection pattern to shift to the low frequency range (see Figure 2.2.3.3-4). The effect on the spectra due to the microphone mount is presented in Figure 2.2.2.3-5. Through a combination of these geometrical improvements plus the careful attention paid to reducing extraneous piping and valve noise sources by treating the pipework with lead wrapping and reducing any airborne noise such as combustor rumble by the design of the coannular plenum chamber (see Figure 2.2.3-2) a smooth jet noise spectrum unhampered by ground effects can be obtained. Figure 2.2.3.3-6 shows a narrow band (80 Hz) spectrum of jet noise from a conical nozzle measured on the final facility configuration.

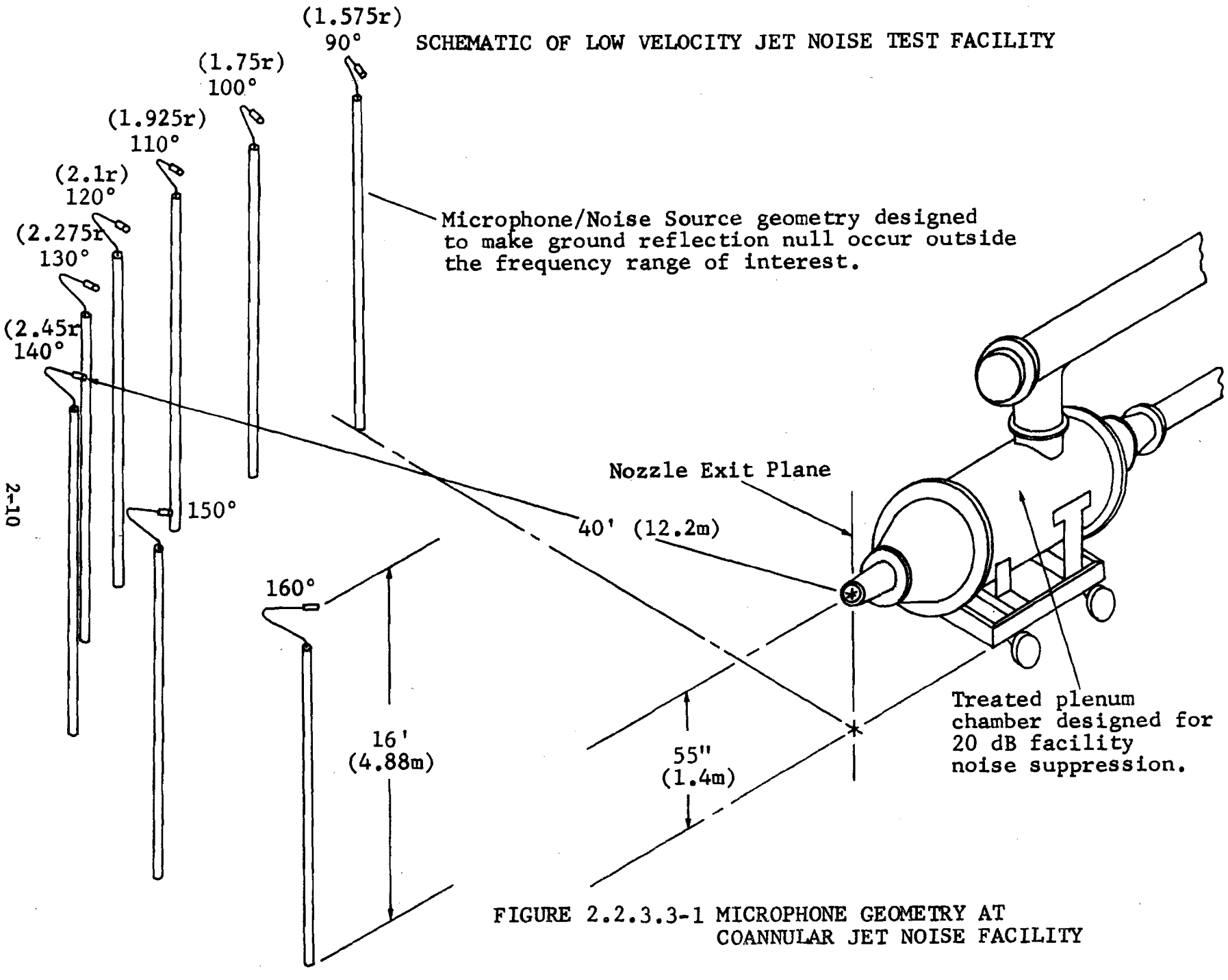

FIGURE 2.2.3.3-1 MICROPHONE GEOMETRY AT COANNULAR JET NOISE FACILITY

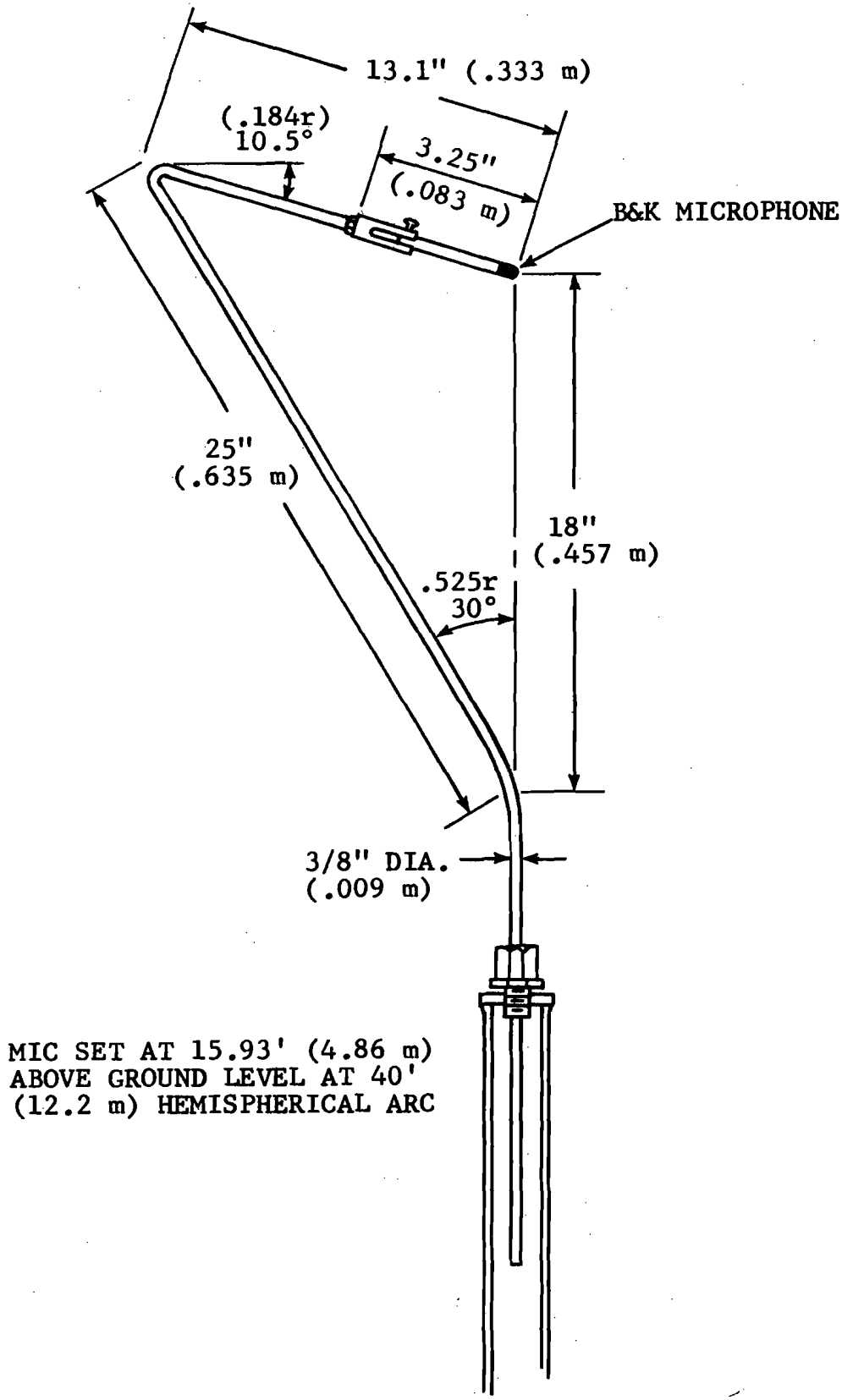

FIGURE 2.2.3.3-2 MICROPHONE GOOSE NECK ADAPTER

PLAN VIEW

80° (1.4 Rad) THROUGH 20° (.35 Rad.), SAME GEOMETRY AS 100° (1.75 Rad.) THROUGH 160° (2.8 Rad.)

OLD MICROPHONE ARRAY

- 40 FT. (12.2 m) ARC
- MICROPHONE HEIGHT = 55" (1.4 m) ABOVE GROUND

NEW MICROPHONE ARRAY

- 40 FT. (12.2 m) HEMISPHERICAL ARC
- MICROPHONE HEIGHT = 15.9 FT. (4.85 m) ABOVE GROUND

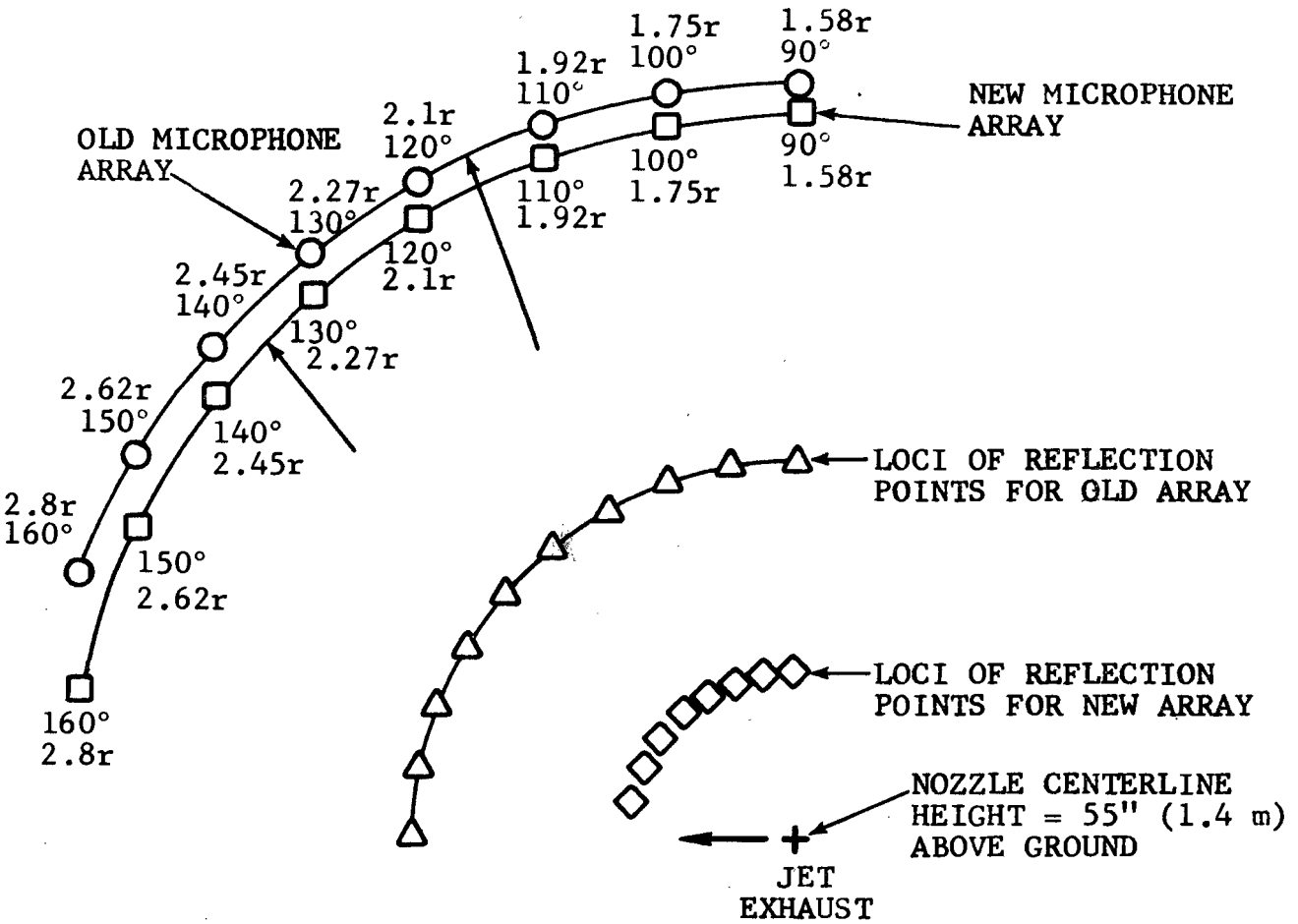

FIGURE 2.2.3.3-3 COMPARISON OF JENOTS OLD AND NEW MICROPHONE ARRAY

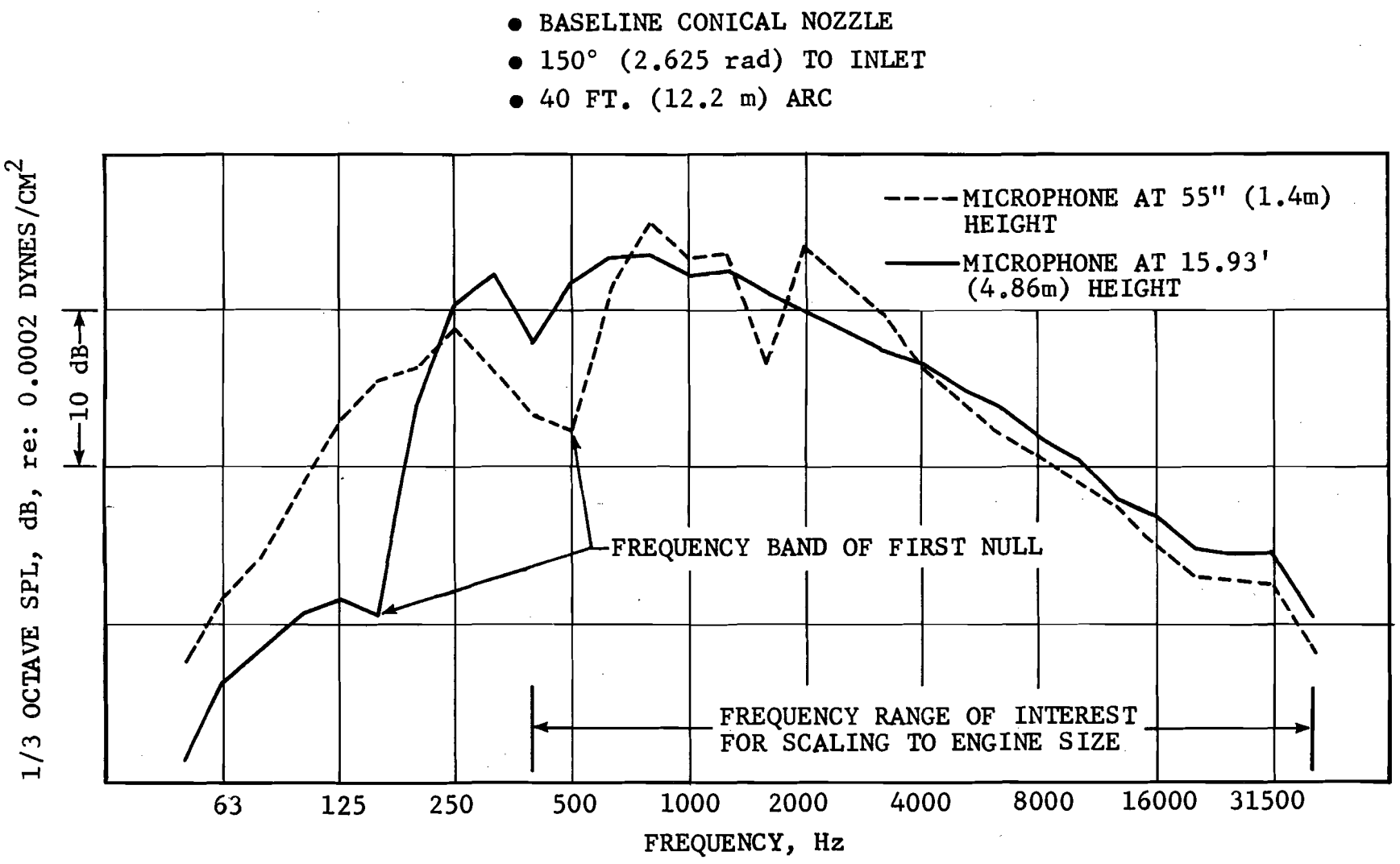

FIGURE 2.2.3.3-4 COMPARISON OF SPECTRA MEASURED WITH OLD AND NEW MICROPHONE ARRAY

- θ_I = 90° (1.575 rad)
- V_j = 1000 FT/SEC (304.8 m/Sec)
- DATA NOT CORRECTED TO A STANDARD DAY
- 40 FT (12.2 m) ARC

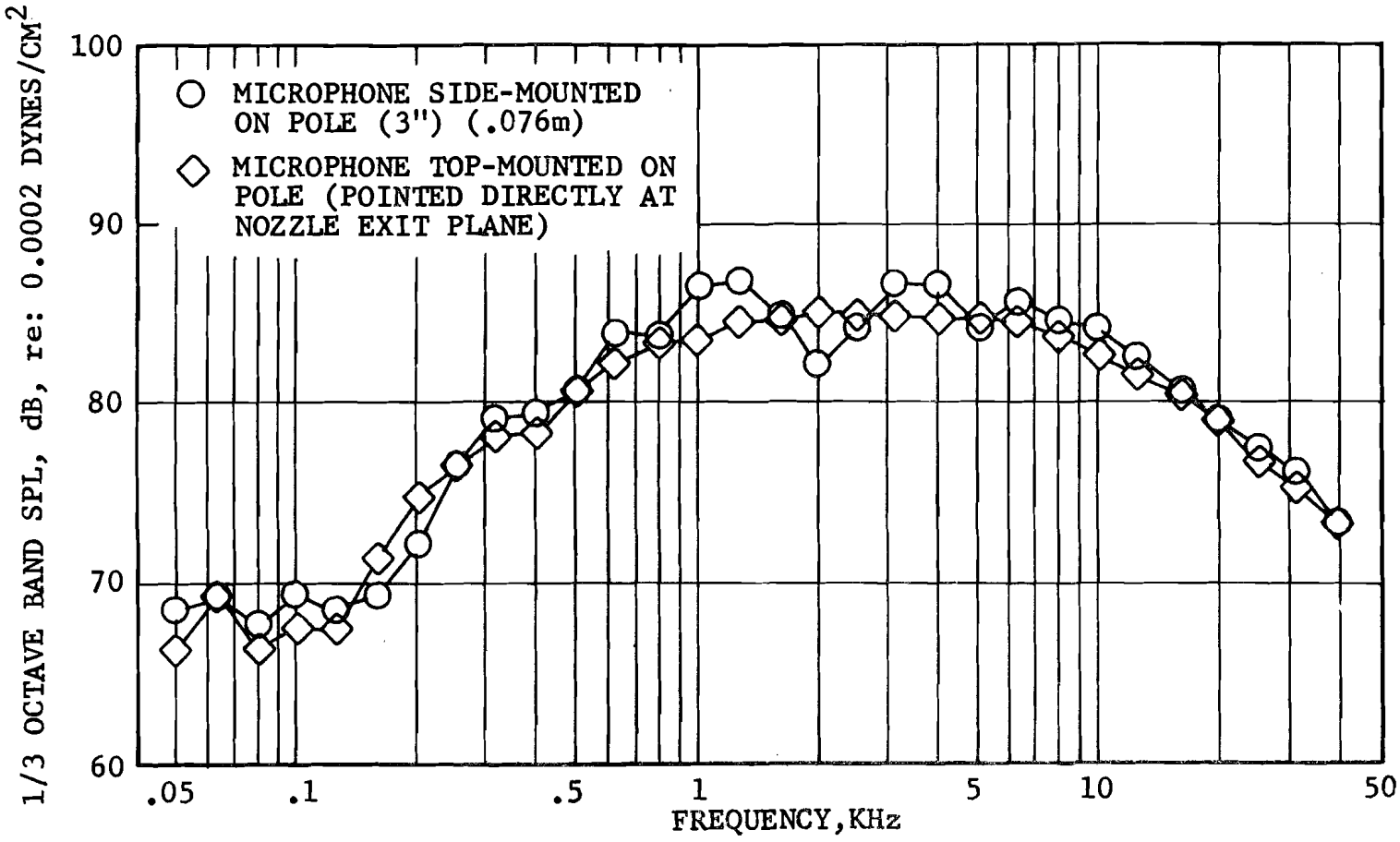

FIGURE 2.2.3.3-5 COMPARISON OF SPECTRA MEASURED WITH OLD AND NEW MICROPHONE MOUNT

- MODEL CONICAL NOZZLE
- 40 FT. (12.2 m) HEMISPHERICAL ARC
- 90° (1.575 rad) TO JET EXHAUST AXIS
- MICROPHONE AT 15.9 FT. (4.85 m) ABOVE GROUND PLANE
- NOZZLE CENTER LINE AT 55" (1.4 m) ABOVE GROUND PLANE
- V_j = 1000 FT/SEC (304.8 m/Sec)
- 80-Hz BANDWIDTH

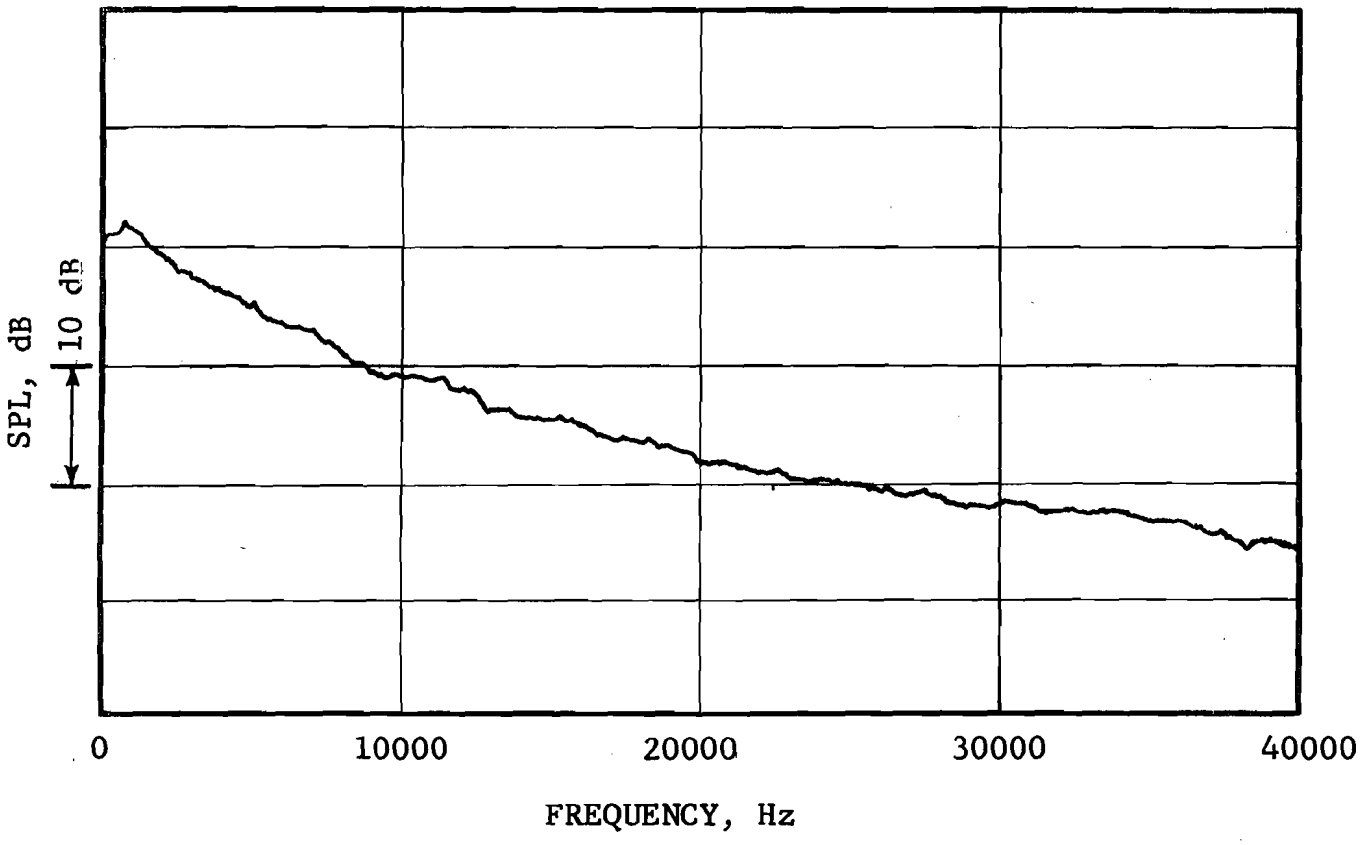

FIGURE 2.2.3.3-6 NARROWBAND ANALYSIS OF JENOTS MEASUREMENT WITH NEW MICROPHONE ARRAY, SHOWING ABSENCE OF GROUND REFLECTIONS.

A comparison between acoustic data (uncorrected for ground reflections) using the microphone array and anechoic chamber acoustic data over a range of jet velocities is given in Figure 2.2.3.3-7. The anechoic chamber data curve was obtained from Reference 2.1-5. The data repeatability is excellent and the agreement over a velocity range of 600 ft/sec (182.9) to 1500 ft/sec (457.2 m/sec) is within 2dB. A spectral comparison between JENOTS and the same anechoic chamber data is shown in Figure 2.2.3.3-8.

The ambient noise levels of the outdoor stand were evaluated to establish the noise floor below which acoustic testing was not practical. Figure 2.2.3.3-9 shows a typical set of spectra for a conical nozzle operating over the velocity range of 400 (121 m/sec) to 1600 ft/sec (488 m/sec). For a jet velocity of 372 ft/sec (112 m/sec), the spectrum at the peak polar OASPL angle is very nearly ambient. The spectrum corresponding to V_j = 582 ft/sec (176 m/sec) is, however, clearly above the ambient range. It is concluded, therefore, that the JENOTS facility provides clean jet noise down to approximately 600 ft/ ft/sec (150 m/sec).

2.2.4 Test Program

The test program was designed to measure the far field noise and nozzle flow data at specified velocity ratios for each area ratio configuration. The fan velocities were set at 400, 600, 800, and 1000 feet per second (221, 182, 242, and 303 m/sec) and the velocity ratios (fan velocity to core velocity) of 1.0, .833, .714, and .625 resulted in the test matrix shown in Table 2.2.4-1.

2.2.5 Test Results

Farfield acoustic data and nozzle flow data were recorded on the baseline conical nozzle and on four coannular, coplanar dual flow nozzles with secondary to primary flow areas of 2, 4, 6, and 8. The detailed test results are included in Appendices C and D. The nozzle jet exit velocities as a function of measured nozzle pressure ratios and temperatures are shown in Appendix A. The acoustic data are summarized as peak values on the 40 foot (12.2 m) arc (along with the pertinent aerodynamic data) in tabular form in Appendix B.

2.2.5.1 Baseline Conical Nozzle Jet Noise

The baseline conical nozzle or core nozzle was evaluated, as a reference, over the entire range of exit velocity conditions. The peak OASPL spectra on the 40 foot (12.2 m) arc are shown in Figure 2.2.3.3-9. Except for the lowest jet exit velocity, the sound power levels are above the ambient background noise level.

Directivities of the conical baseline nozzle over a range of velocities are shown in Figure 2.2.5.1-1. The peak angles occur, as expected, at 140° to 150°. The repeatability of the data is also evident in that minor velocity differences do not change the directivity significantly. Thus, the core nozzle is a typical conical nozzle and provides a good baseline from which to evaluate the effect of dual flow with different secondary flow rates and velocities.

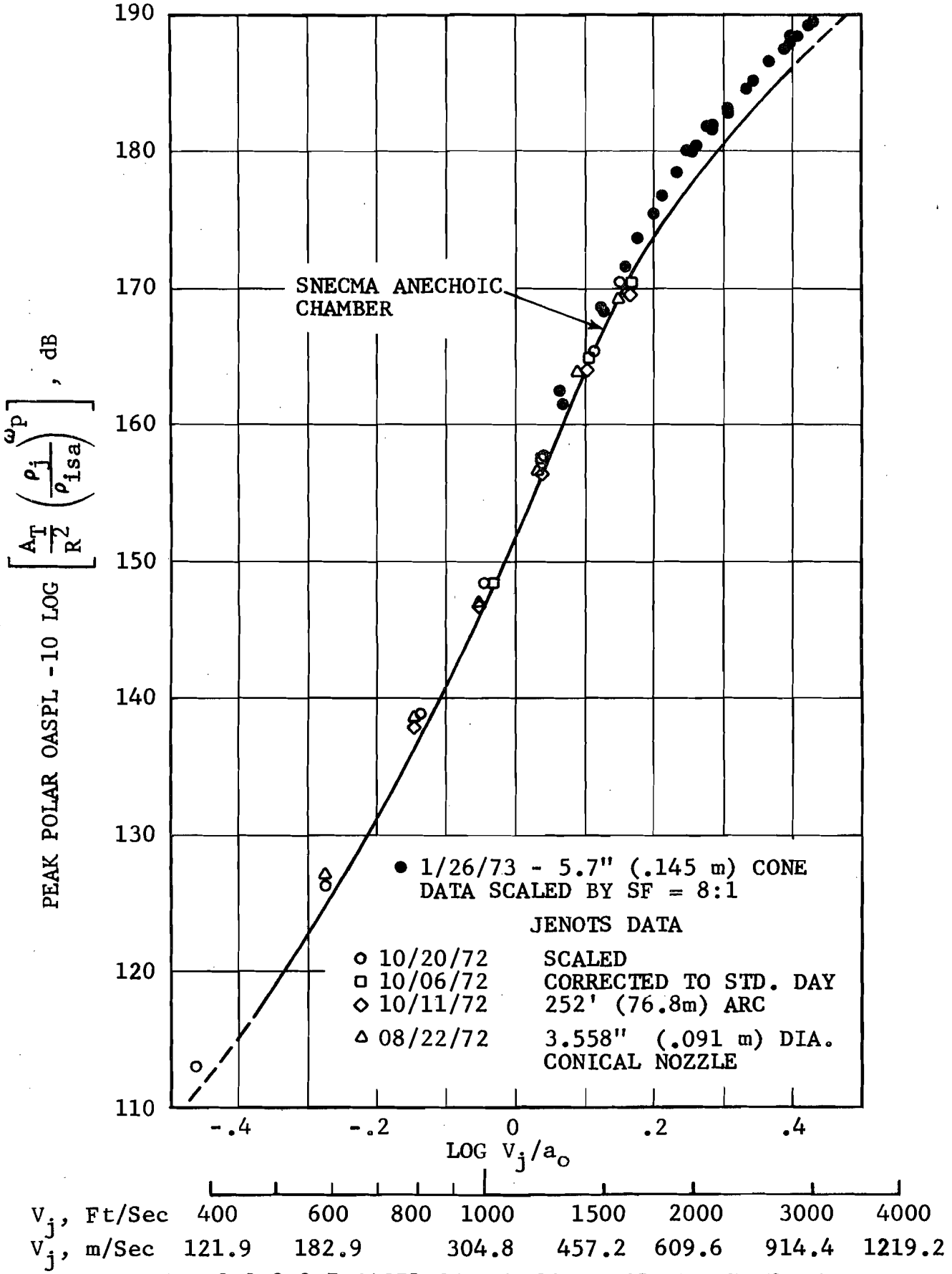

FIGURE 2.2.3.3-7 OASPL COMPARISON BETWEEN JENOTS AND ANECHOIC CHAMBER DATA

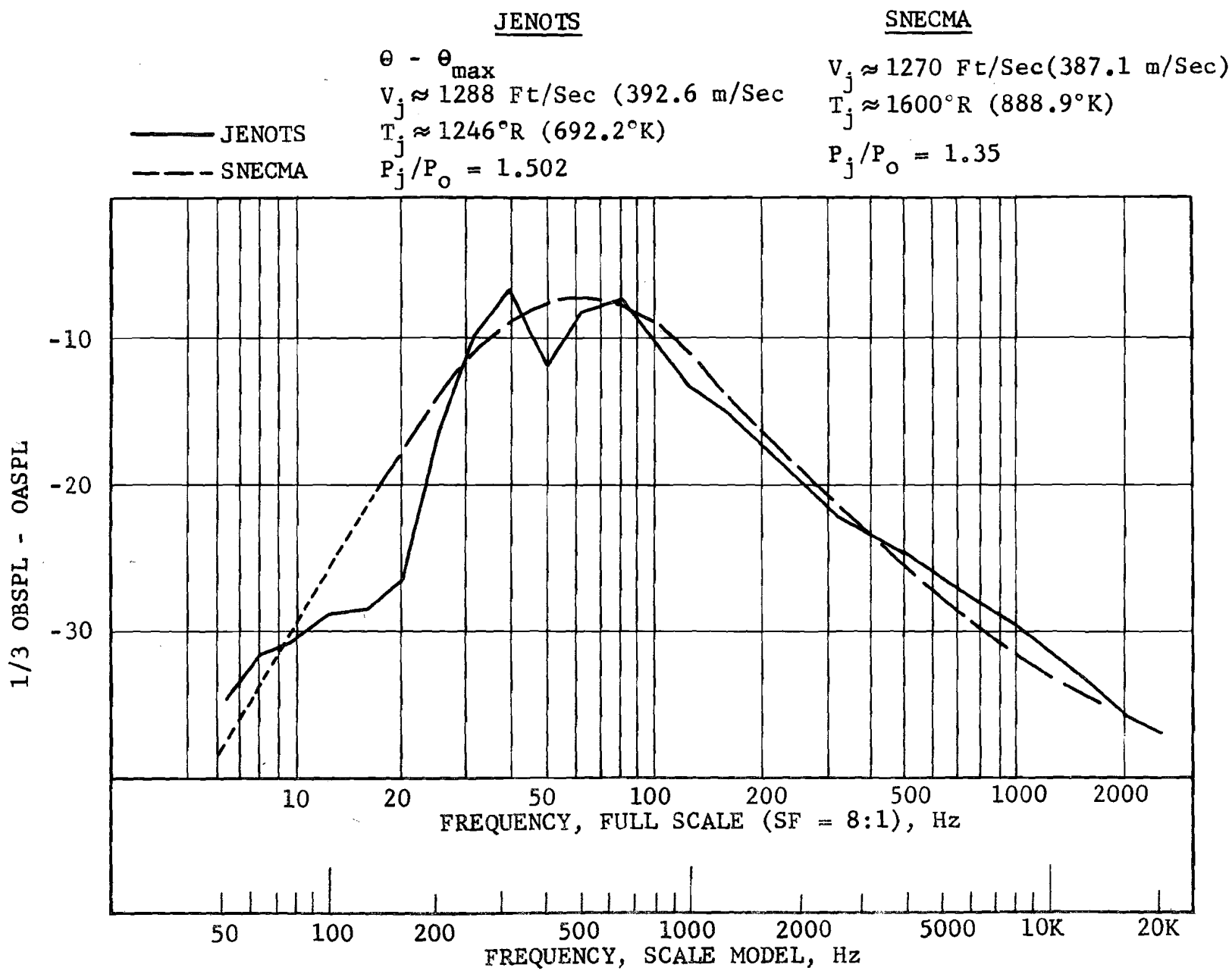

FIGURE 2.2.3.3-8 SPECTRAL COMPARISON BETWEEN JENOTS AND ANECHOIC CHAMBER DATA

- 40 FT. (12.2 m) ARC
- AS-MEASURED DATA CORRECTED TO STANDARD DAY
- 3.558" (.09 m) CONICAL NOZZLE

PT. No.	ANGLE FROM INLET Deg.	Rad.	JET VELOCITY Ft/Sec	m/Sec
○ 1	150	2.625	372	113.4
▷ 2	150	2.625	582	177.4
◺ 3	140	2.45	798	243.2
△ 4	140	2.45	992	302.4
◇ 5	140	2.45	1208	368.2
□ 6	140	2.45	1428	435.3
○ 7	140	2.45	1558	474.9

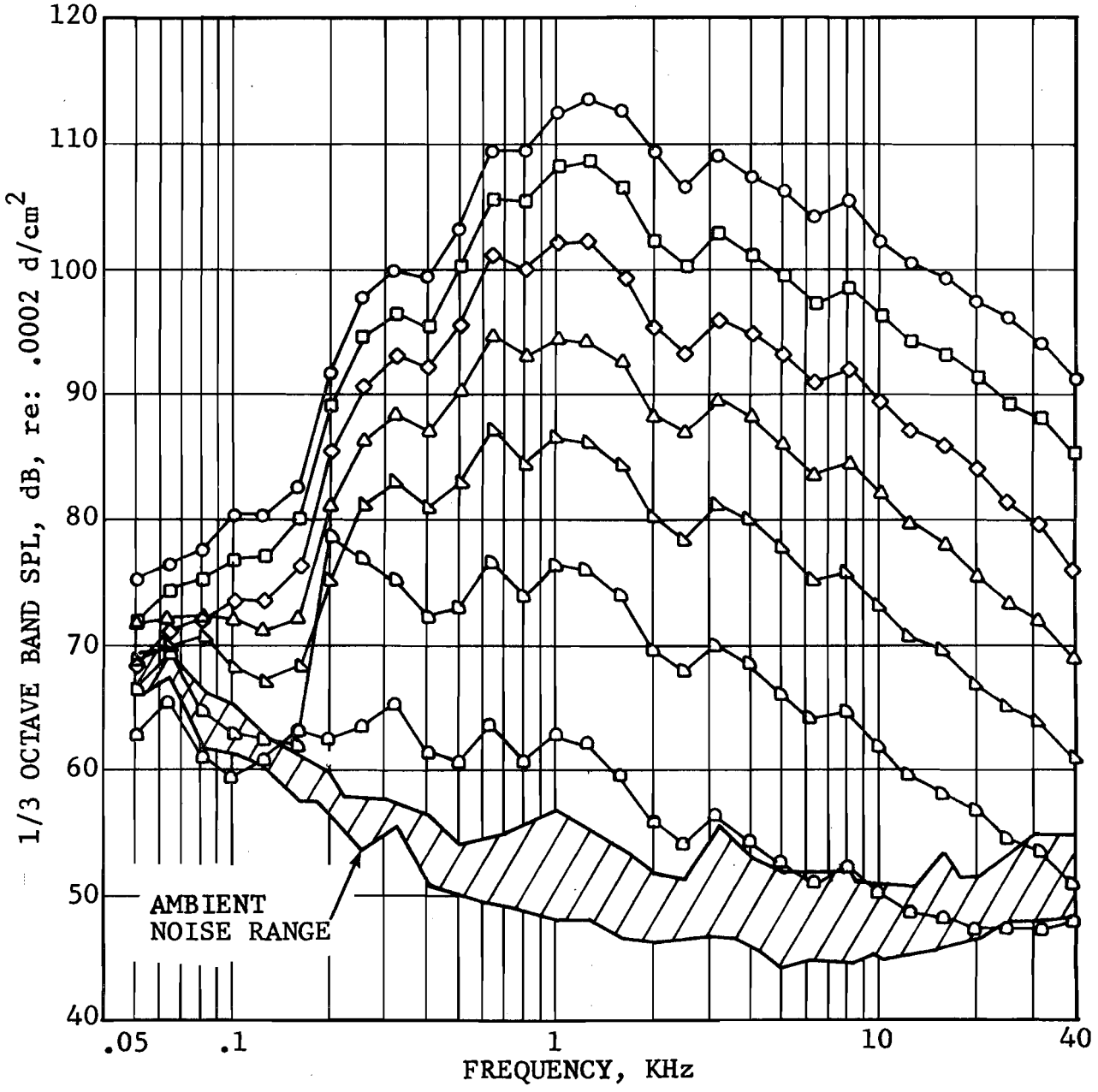

FIGURE 2.2.3.3-9PEAK OASPL SPECTRA FOR CONICAL BASELINE RUN NO. 5

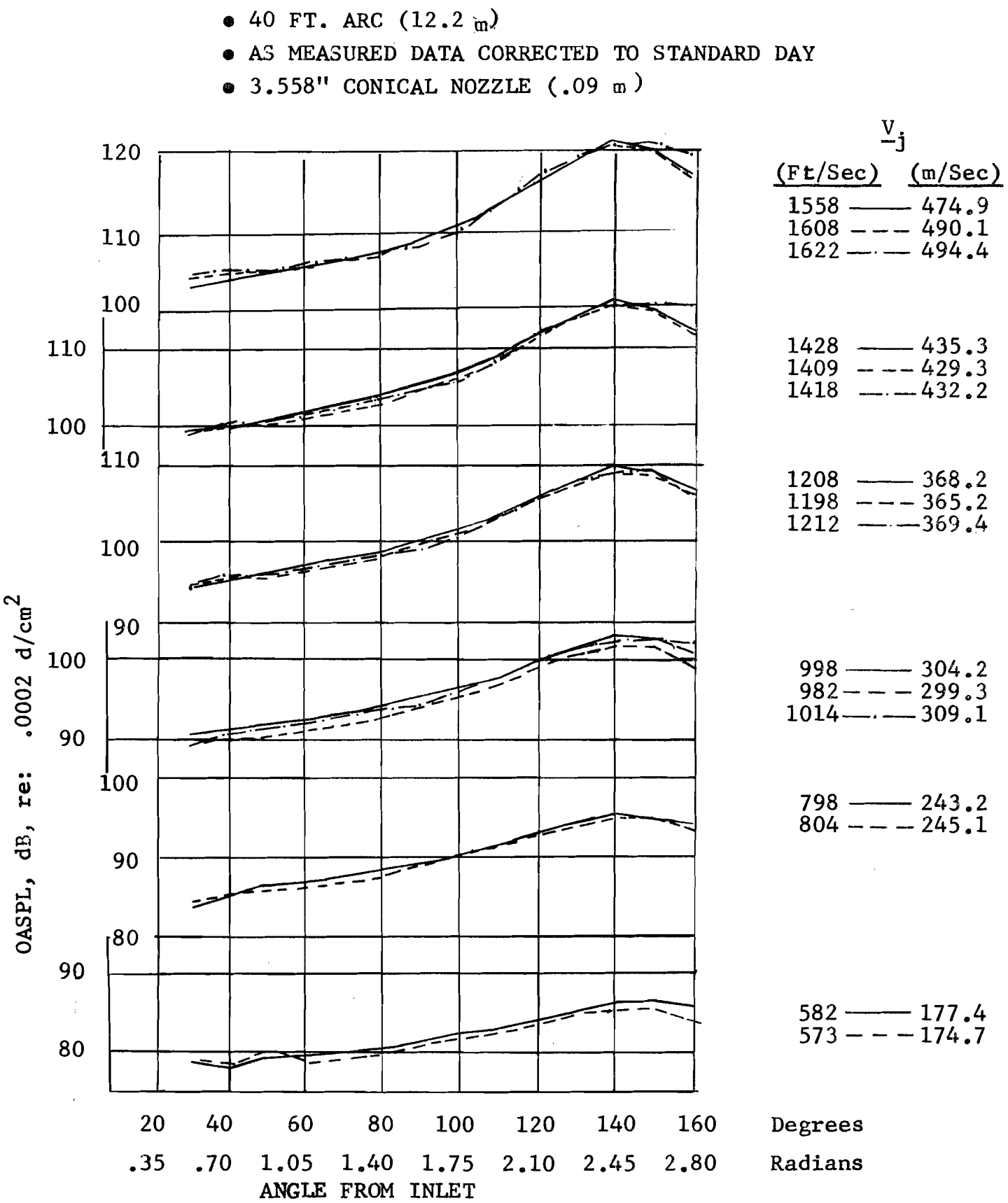

FIGURE 2.2.5.1-1 OASPL VS ACOUSTIC ANGLE FOR CONICAL NOZZLE

2.2.5.2 Dual Flow Nozzle Jet Noise

The effect of secondary flow rate and secondary jet exit velocity (V_{28}) was evaluated by testing the core nozzle with each of the four shrouds and by varying the velocity ratio (secondary/primary) as shown in Table 2.2.4-1. The farfield acoustic results show that secondary flow does indeed suppress the core jet noise below the level of the core jet alone at a given core jet velocity (V_8).

The peak angle OASPL 1/3 octave band spectra for a secondary (fan) exit velocity of 800 ft/sec (244 m/s) for all four dual flow configurations are shown in Figures 2.2.5.2-1 through 2.2.5.2-4 (see Appendix for other data). At area ratio 2, some high frequency suppression occurs with increase in the core jet velocity. At area ratio 4 (Figure 2.2.5.2-2), reductions in core velocity below the fan velocity result in the fan jet dominating the spectra. When the core velocities exceed the fan velocity, the low frequency levels increase, while the high frequency noise levels tend to be suppressed. The trend of high frequency suppression is very apparent at area ratio 6. The area ratio 8 dual flow nozzle shows the low frequency noise levels increasing with core jet velocity, while the high frequency levels initially decrease and then finally increase. Overall, the spectra indicate that the presence of secondary flow tended to reduce the generation of high frequency noise.

The peak OASPL are shown plotted versus velocity for each configuration in Figures 2.2.5.2-5 through 2.2.5.2-8. These summary curves show the suppression effects of secondary flow. At velocity ratios (fan to core) of 1.0, the noise levels are equal to those obtained from a single nozzle flow with the diameter and jet velocity equal to that of the dual flow configuration. The core nozzle, only reference plotted in each of the figures, shows the scope of the $V_{28}/V_8 = 1.0$ locus. As the core velocity increases ($V_{28}/V_8 < 1.0$), the decreased slope of the lines at constant fan velocity indicates that suppression is present. In fact, at $V_{28}/V_8 = 0.625$, the noise level of the combined fan and core flows is less than the noise level of the core flow by itself. The cross-over occurs at $V_{28}/V_8 \cong 0.75$ for the configurations tested. Thus, the effect of secondary flow is such that the core jet noise level can be suppressed below that of a single flow nozzle.

As a point of reference, a comparison was made between the data measured at JENOTS and the data presented in Reference 2.1-3 from Wyle Laboratories. Note that the Wyle Lab data was for cold flow. Figure 2.2.5.2-9 presents plots of OASPL versus angle from the inlet for comparable test conditions for the area ratio of 2. This directivity comparison indicates very good agreement at all angles. The 1/3 octave band spectra at 140° (peak OASPL angle) is shown in Figure 2.2.5.2-10. The JENOTS data is slightly higher at low frequencies and slightly lower at high frequencies. However, the JENOTS data was for hot core flow and was not corrected to free field, which may account for the discrepancies.

Other Wyle Lab data was available for an area ratio of 5 and was compared with the JENOTS data for area ratios of 4 and 6 (see Figures 2.2.5.2-11 and 2.2.5.2-12). The trends are consistent. However, the JENOTS data for the

	PT. No.	ANGLE FROM INLET Deg.	Rad.	CORE VELOCITY Ft/Sec	m/s
△	16	150	2.625	806	246
◇	17	150	2.625	954	291
□	18	150	2.625	1129	344
○	19	150	2.625	1291	394

- AS-MEASURED DATA CORRECTED TO STANDARD DAY
- 40 FT. (12.2 m) ARC

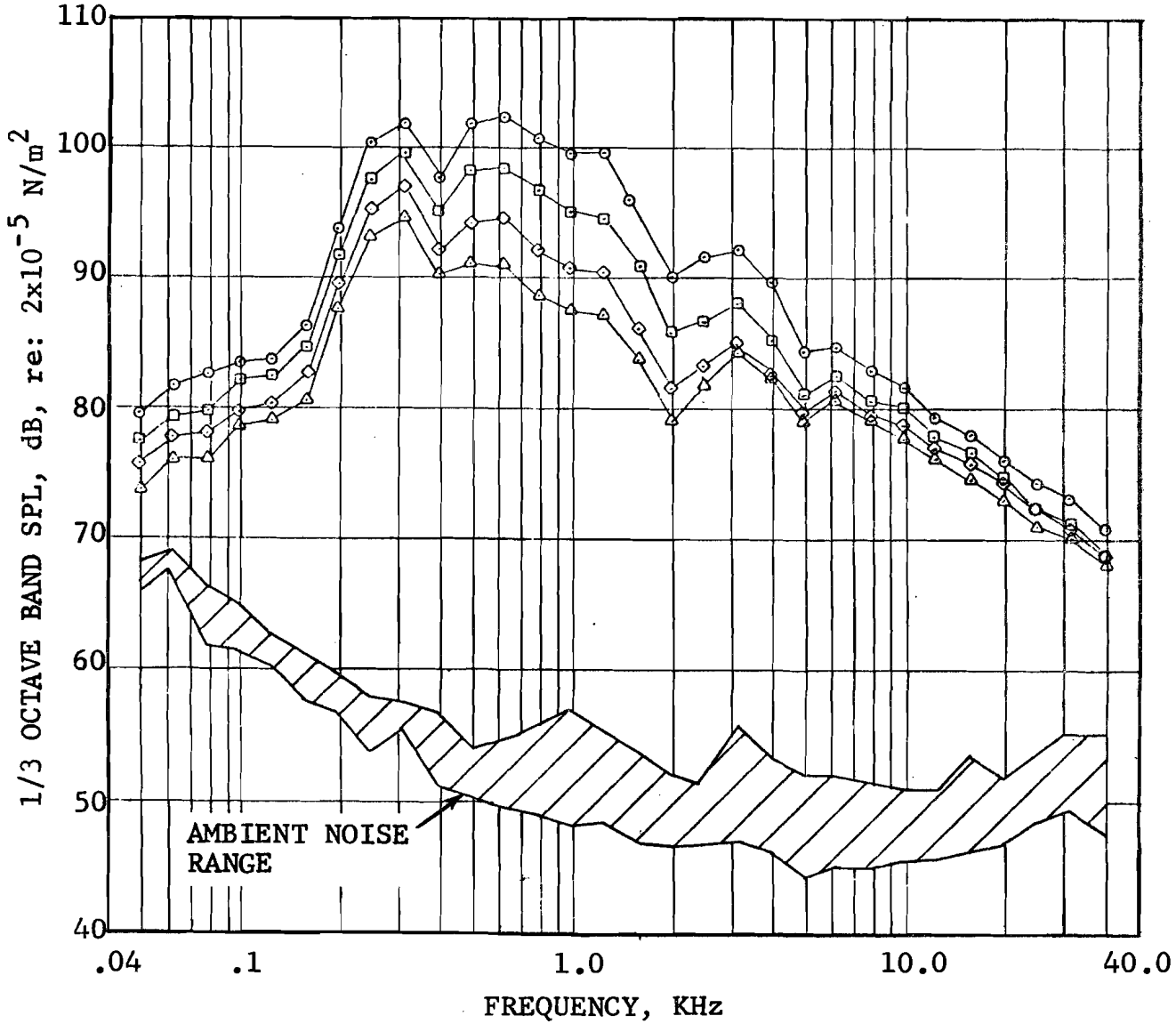

FIGURE 2.2.5.2-1 PEAK OASPL SPECTRA FOR AREA RATIO = 2 MODEL, FAN VELOCITY 800 FT/SEC (244 m/s)

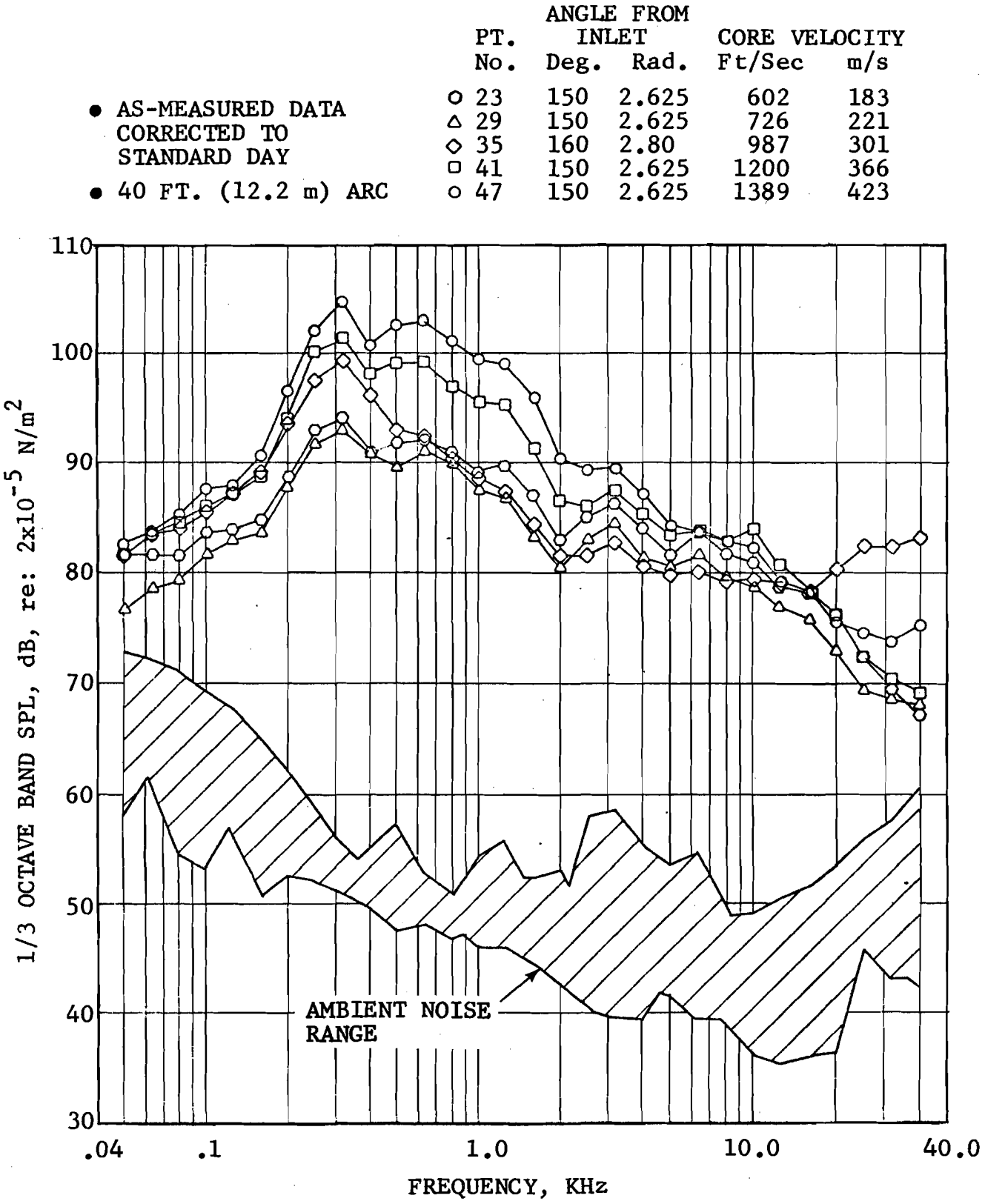

FIGURE 2.2.5.2-2 PEAK OASPL SPECTRA FOR AREA RATIO = 4 MODEL, FAN VELOCITY 800 FT/SEC (244 m/s)

	PT. No.	ANGLE FROM INLET Deg.	Rad.	CORE VELOCITY Ft/Sec	m/s
	◇ 16	150	2.625	820	250
• AS-MEASURED DATA CORRECTED TO STANDARD DAY	△ 17	150	2.625	982	299
	□ 18	150	2.625	1139	347
• 40 FT. (12.2 m) ARC	○ 19	150	2.625	1341	409

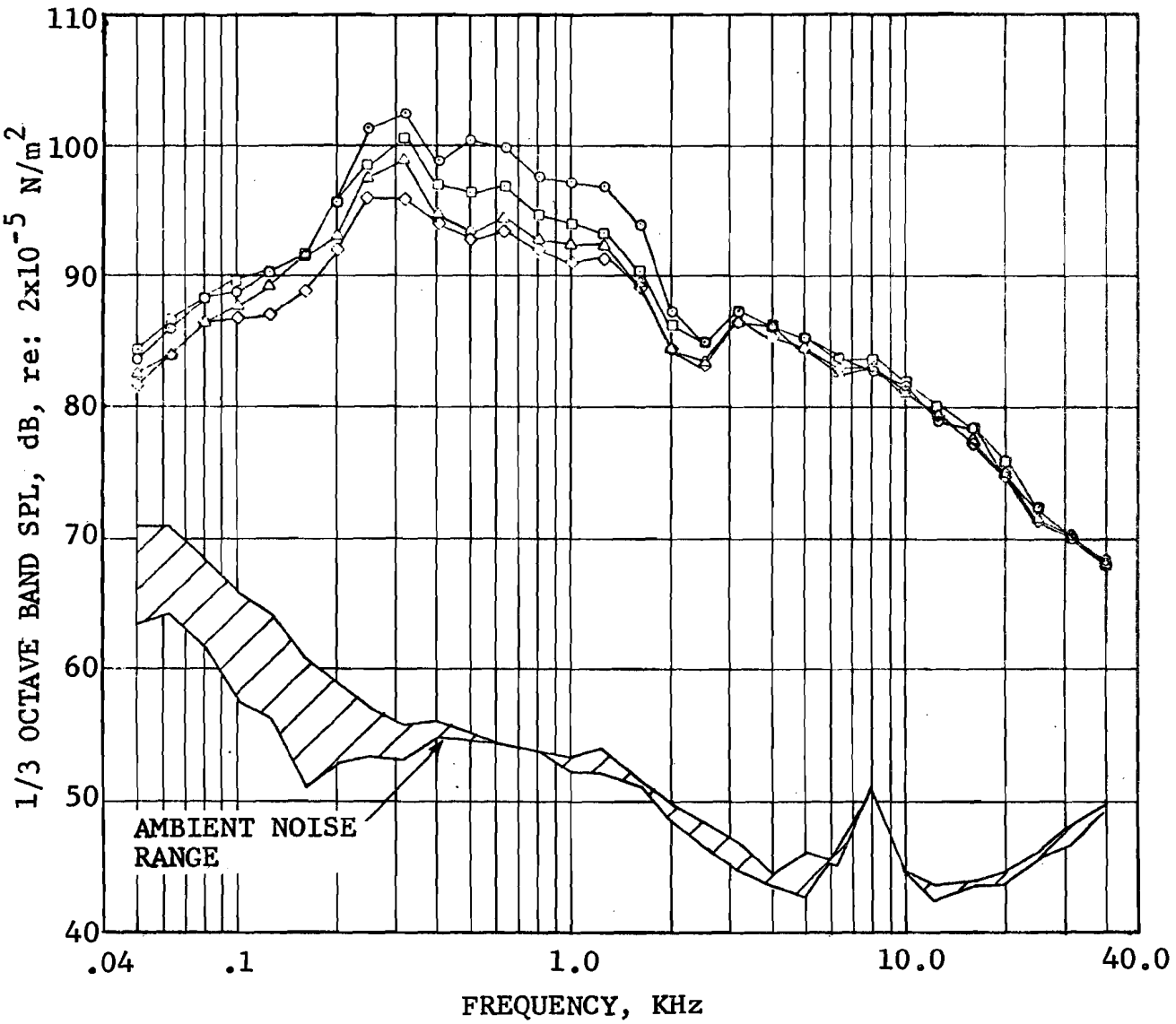

FIGURE 2.2.5.2-3 PEAK OASPL SPECTRA FOR AREA RATIO = 6 MODEL, FAN VELOCITY 800 FT/SEC (244 m/s)

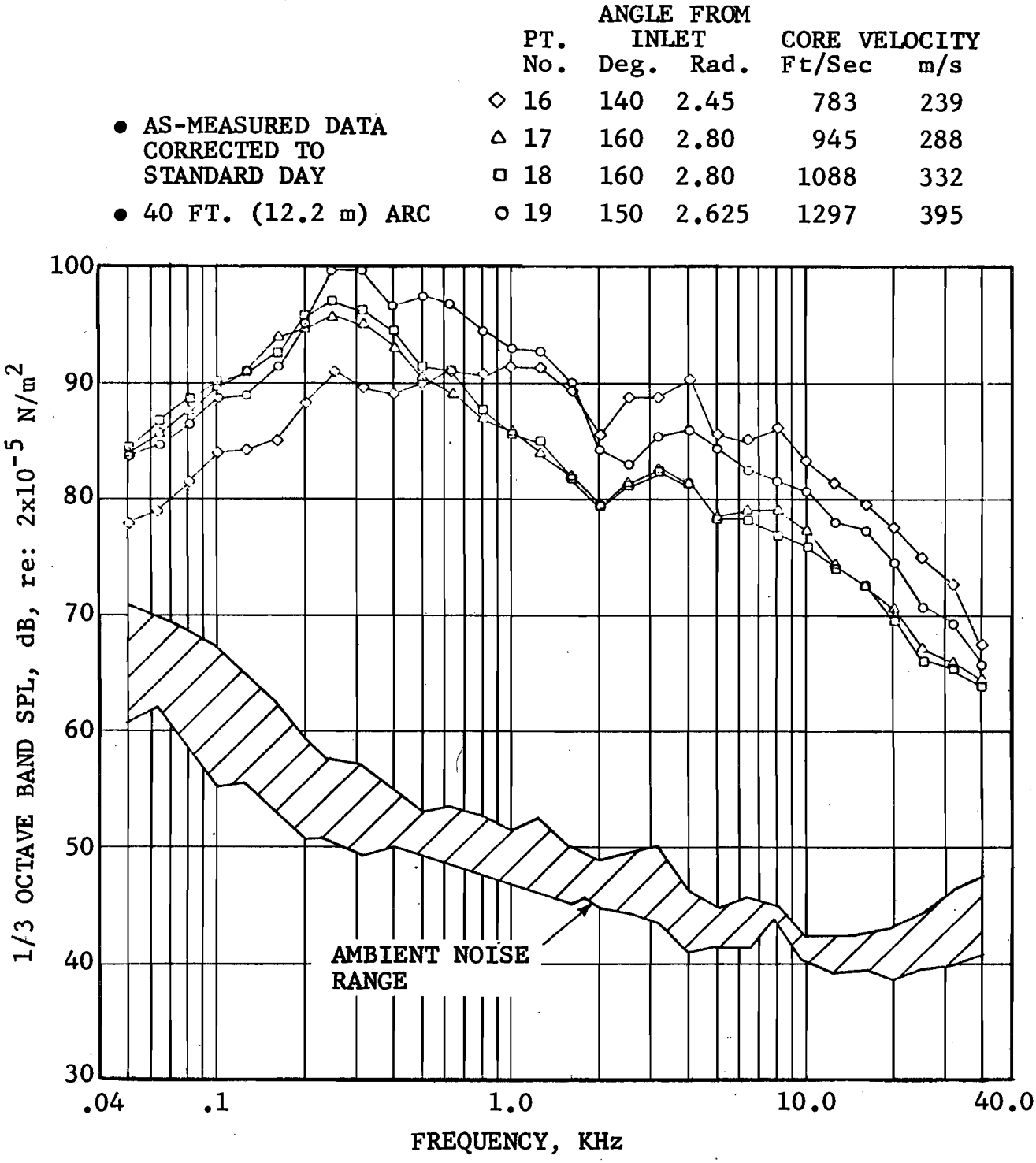

FIGURE 2.2.5.2-4 PEAK OASPL SPECTRA FOR AREA RATIO = 8 MODEL, FAN VELOCITY 800 FT/SEC (244 m/s)

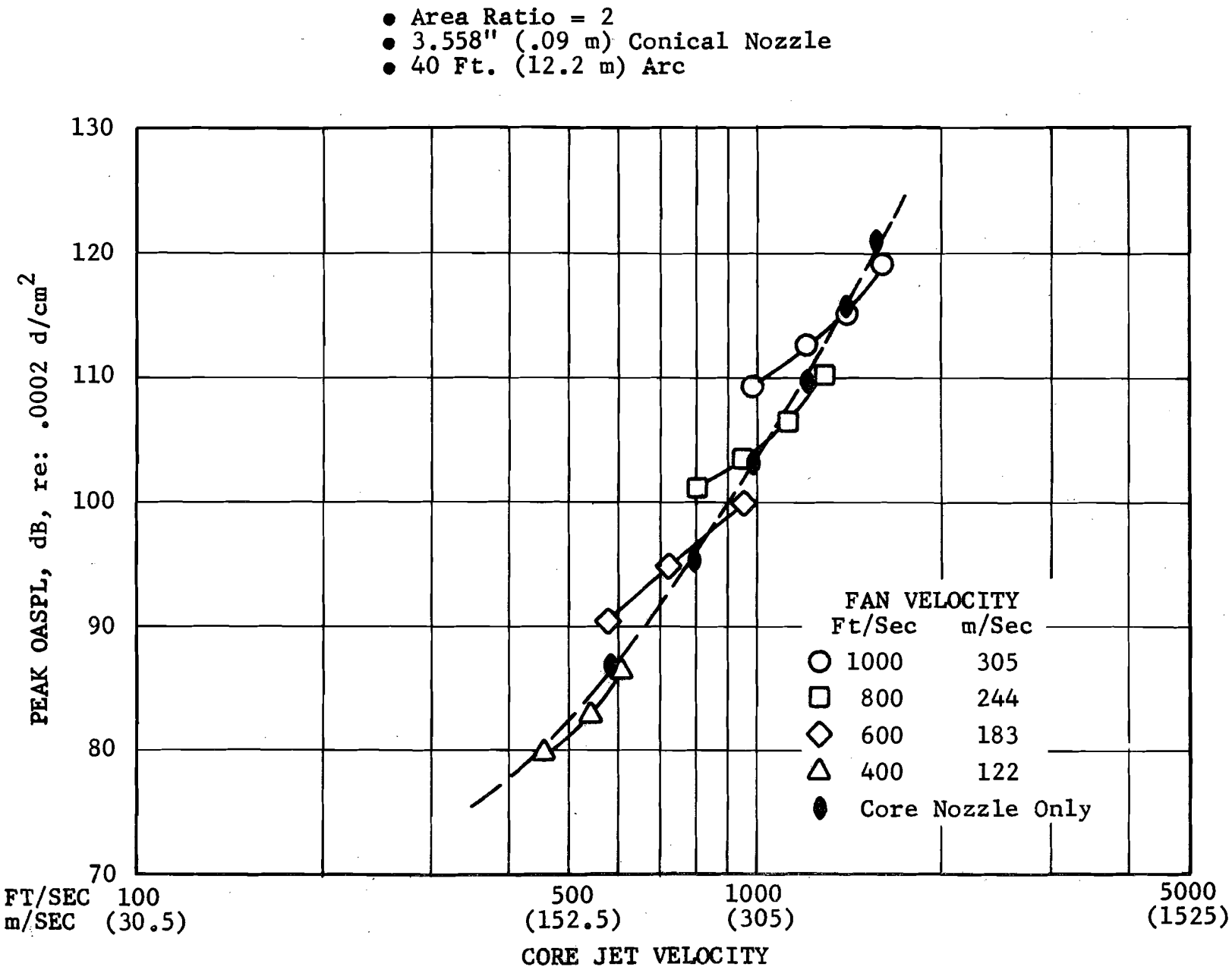

FIGURE 2.2.5.2-5 PEAK OASPL VS CORE JET VELOCITY FOR AREA RATIO = 2

- Area Ratio = 4
- 3.558" (.09 m) Conical Nozzle
- 40 Ft. (12.2 m) Arc

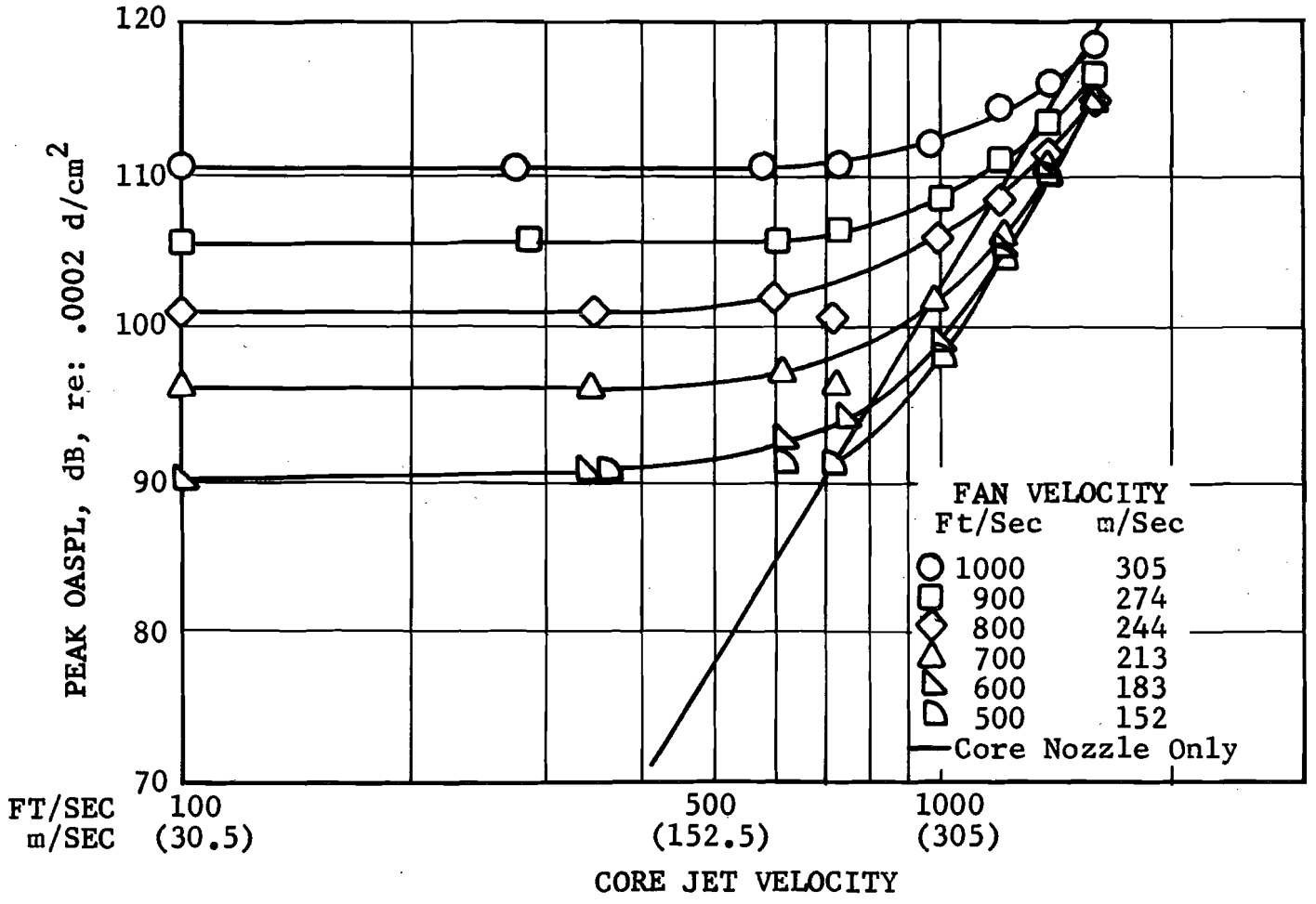

FIGURE 2.2.5.2-6 PEAK OASPL VS CORE JET VELOCITY FOR AREA RATIO = 4

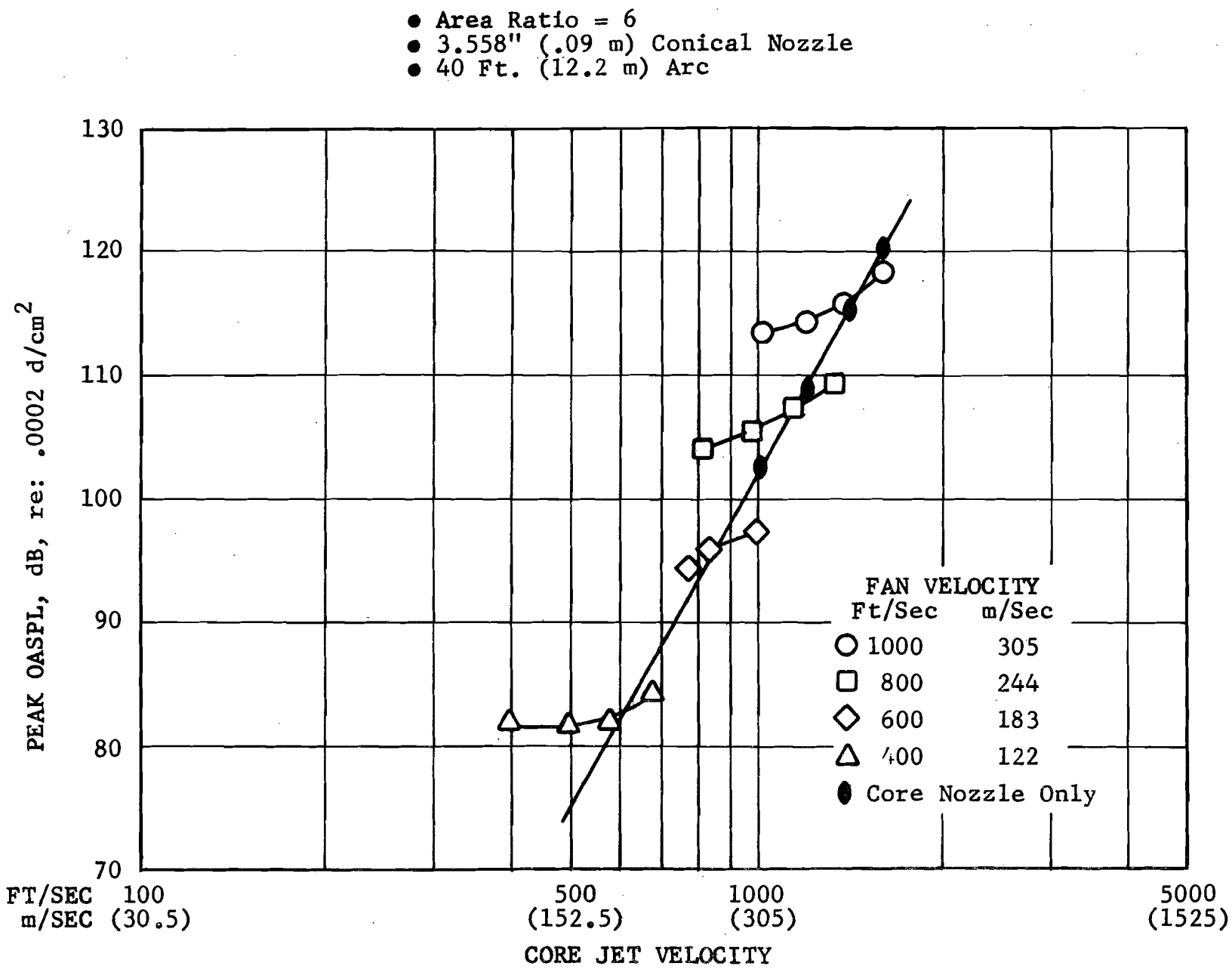

FIGURE 2.2.5.2-7 PEAK OASPL VS CORE JET VELOCITY FOR AREA RATIO = 6

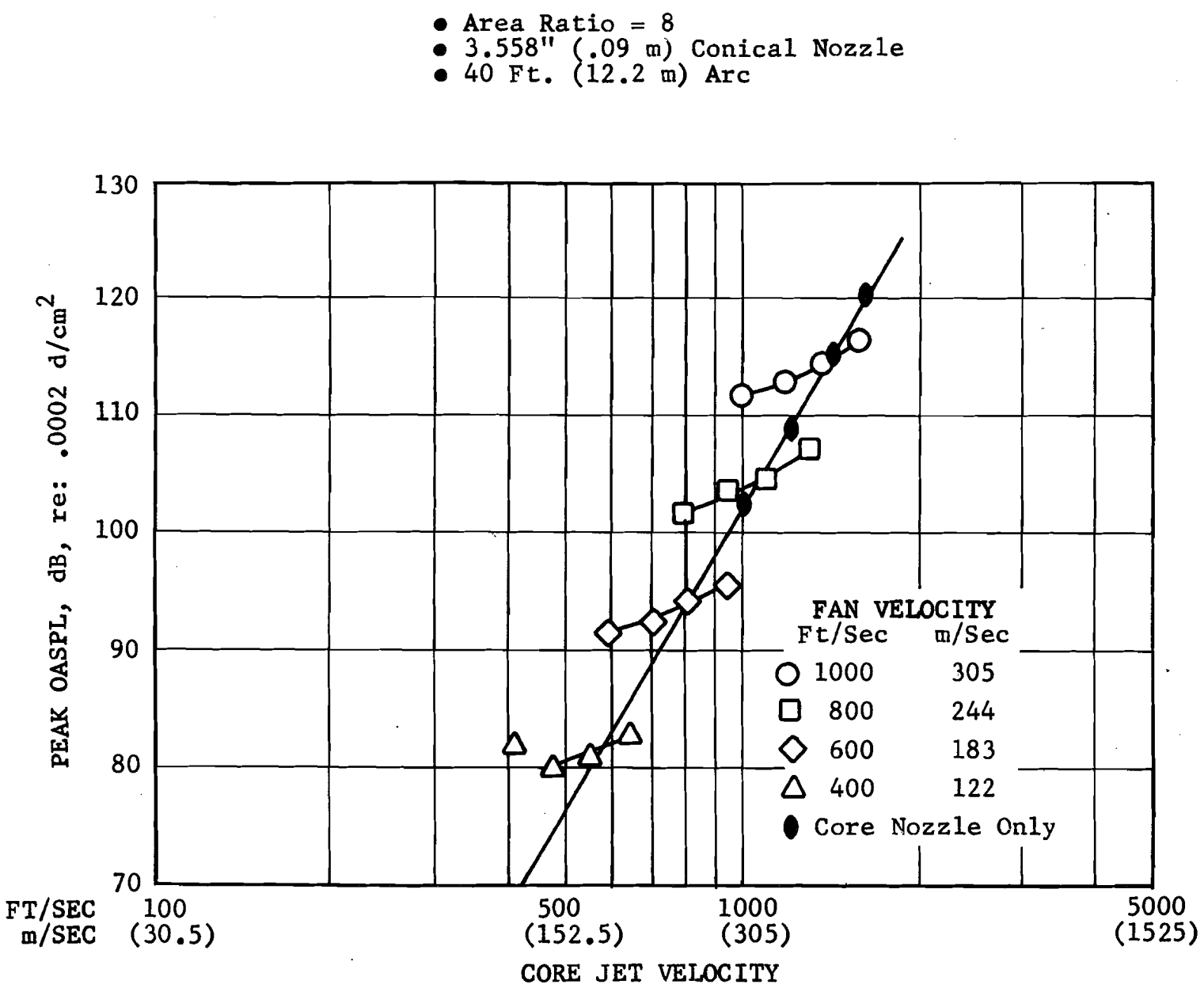

FIGURE 2.2.5.2-8 PEAK OASPL VS CORE JET VELOCITY FOR AREA RATIO = 8

- Scale Model Data
- 50.6 Ft (15.4 m) Arc
- Wyle Lab Data Scaled to Equivalent JENOTS Size

WYLE LAB DATA

Area Ratio = 2

V_{28}/V_8 = .69

V_8 = 1359 Ft/Sec (277 m/Sec)

JENOTS DATA

Area Ratio = 2

V_{28}/V_8 = .69

V_8 = 1407 Ft/Sec (285 m/Sec)

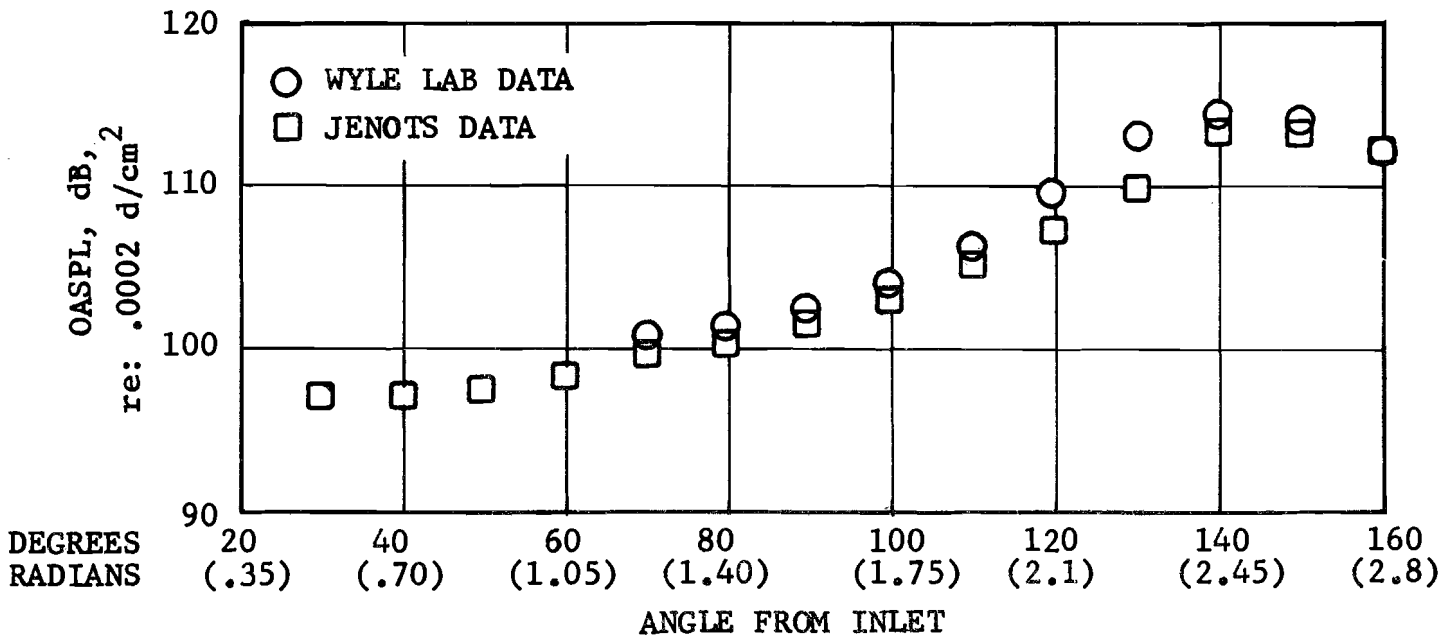

FIGURE 2.2.5.2-9 OASPL DIRECTIVITY COMPARISON BETWEEN JENOTS AND WYLE LAB DATA, AREA RATIO = 2

- Angle From Inlet = 140° (2.45 rad.)
- Scale Model Data
- 50.6 Ft. (15.4 m) Arc
- Wyle Lab data scaled to Equivalent JENOTS Size

WYLE LAB DATA	JENOTS DATA
Area Ratio = 2	Area Ratio = 2
V_{28}/V_8 = .69	V_{28}/V_8 = .69
V_8 = 1359 Ft/Sec (414 m/Sec)	V_8 = 1407 Ft/Sec (429 m/Sec)

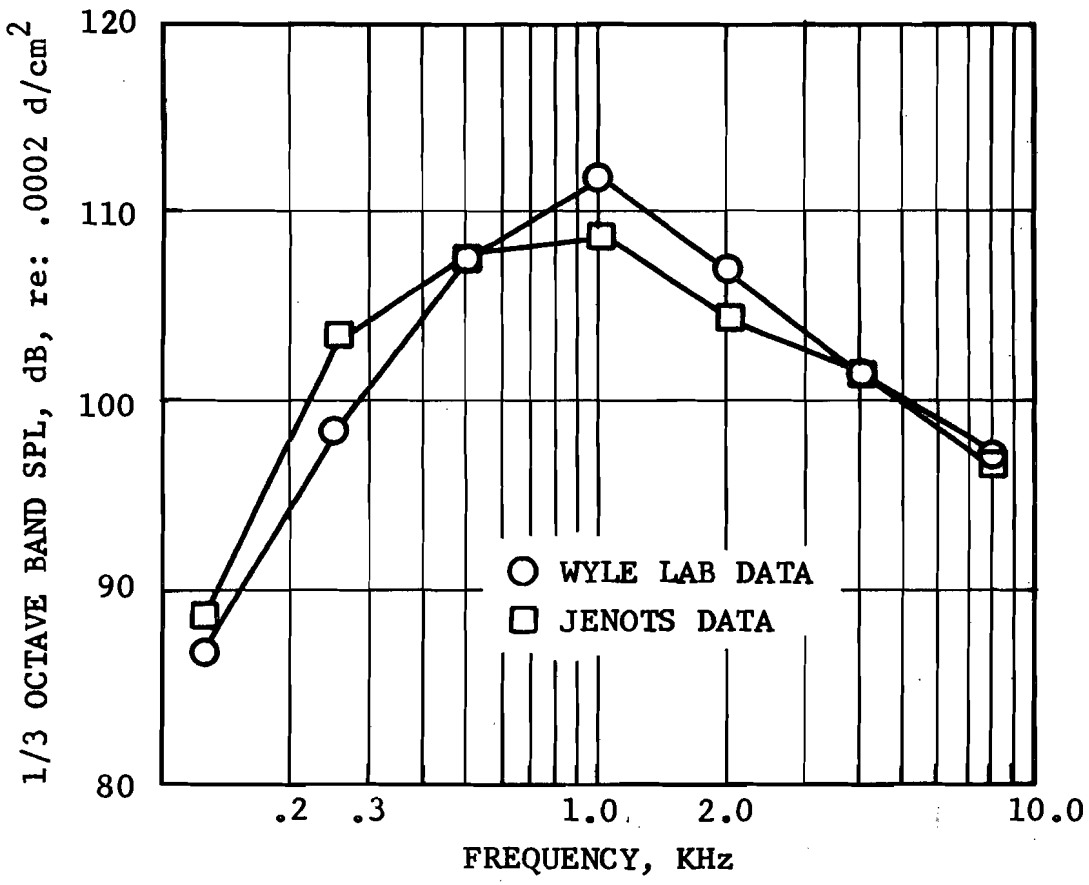

FIGURE 2.2.5.2-10 SPECTRAL COMPARISON BETWEEN JENOTS AND WYLE LAB DATA

- Scale Model Data
- 50.6 Ft. (15.4 m) Arc
- Wyle Lab Data Scaled to Equivalent JENOTS Size

WYLE LAB DATA	JENOTS DATA	JENOTS DATA
Area Ratio = 5	Area Ratio = 4	Area Ratio = 6
V_{28}/V_8 = .693	V_{28}/V_8 = .67	V_{28}/V_8 = .72
V_8 = 1362 Ft/Sec (415 m/Sec)	V_8 = 1381 Ft/Sec (421 m/Sec)	V_8 = 1390 Ft/Sec (424 m/Sec)

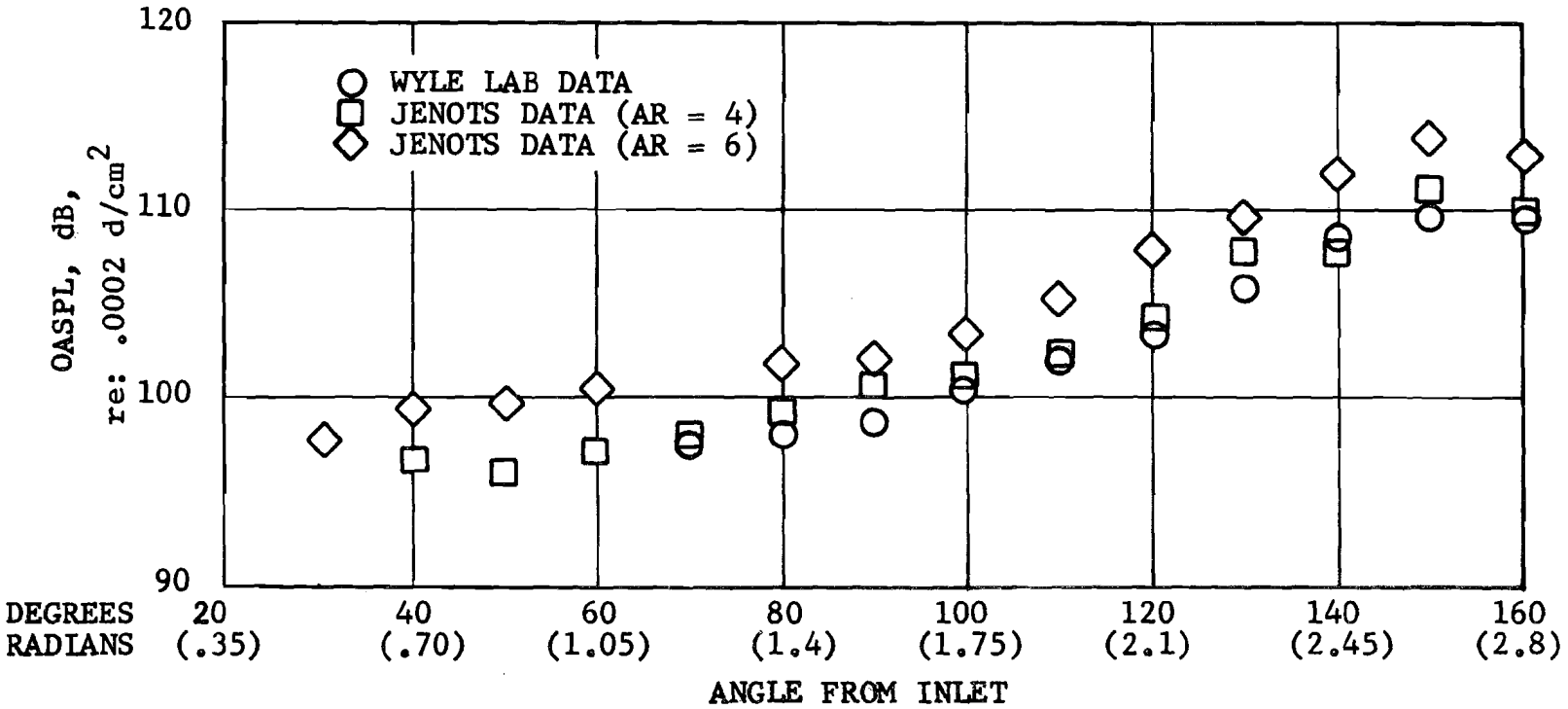

FIGURE 2.2.5.2-11 OASPL DIRECTIVITY COMPARISON BETWEEN JENOTS AND WYLE LAB DATA, AREA RATIOS = 4, 5, AND 6

- Angle From Inlet = 140° (2.45 rad.)
- Scale Model Data
- 50.6 Ft. (15.4 m) Arc
- Wyle Lab Data Scaled to Equivalent JENOTS Size

WYLE LAB DATA

Area Ratio = 5

V_{28}/V_8 = .693

V_8 = 1362 Ft/Sec (415 m/Sec)

JENOTS DATA

Area Ratio = 4

V_{28}/V_8 = .67

V_8 = 1381 Ft/Sec (421 m/Sec)

JENOTS DATA

Area Ratio = 6

V_{28}/V_8 = .72

V_8 = 1390 Ft/Sec (424 m/Sec)

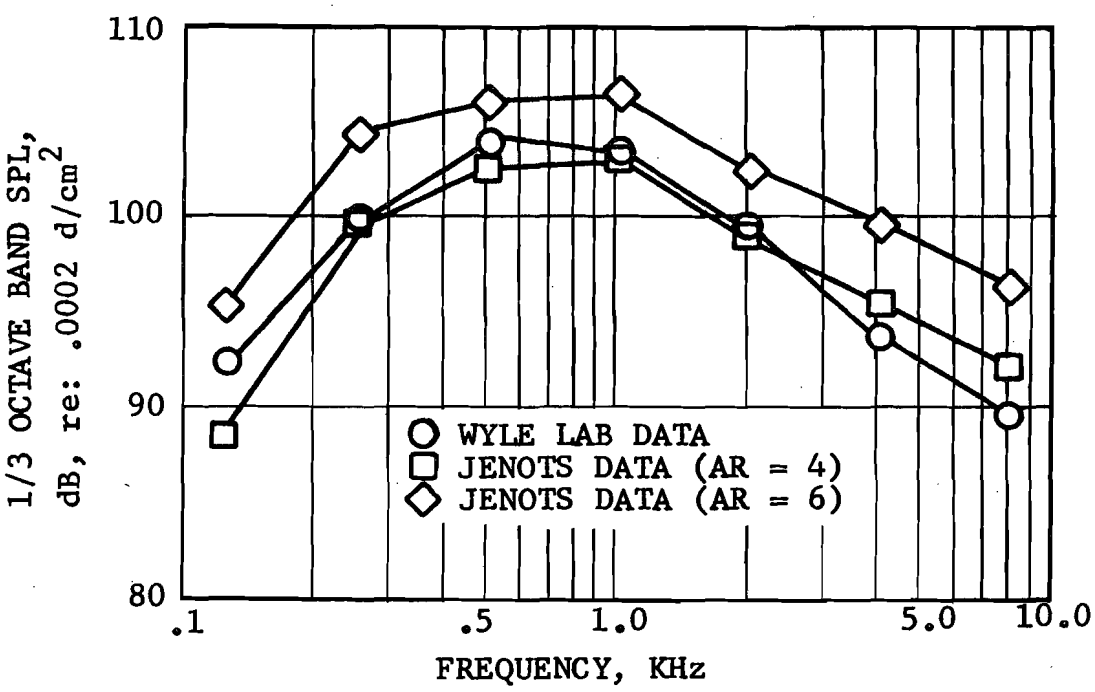

FIGURE 2.2.5.2-12 SPECTRAL COMPARISON BETWEEN JENOTS AND WYLE LAB DATA

area ratio 4 configuration appears slightly high, a possible consequence of the hot core flow. The 1.5 dB difference in OASPL between area ratios of 4 and 6 indicates the effect of increasing area ratio. Figure 2.2.5.2-12 shows good agreement between the three spectra at the 140° angle.

The secondary flow shielding effect suggested by Williams (Reference 2.1-4) results in a suppression parameter which can be represented by OASPL (COAN) - OASPL (Core Only). Williams suggests that for small velocity ratios ($V_{28}/V_8 < 1$), the acoustic output of a coannular nozzle may be represented as $P_1 \sim d^2 (V_8^2 - V_{28}^2)^4$ where d is the core nozzle diameter. For large velocity ratios ($V_{28}/V_8 > 1$), he suggests that $P_2 \sim D^2 \cdot (d^2/D^2\ V_8^2 + (1 - d^2/D^2)\ V_{28}^2)^4$ where D is the diameter of the secondary nozzle. Using the core nozzle as reference ($P_c \sim d^2\ V_8^8$), a set of theoretical curves of OASPL (COAN)-OASPL (CORE) vs. V_{28}/V_8 for various values of d/D can be generated. Figures 2.2.5.2-13 through 2.2.5.2-16 show these curves for area ratios (A_{28}/A_8) of 2, 4, 6 and 8 with the measured data superimposed. Good agreement with Williams' theory is obtained in all cases for the range of V_{28}/V_8 investigated.

The trends suggested in Figures 2.2.5.2-13 through 2.2.5.2-16 indicate that the maximum suppression will occur at velocity ratios (V_{28}/V_8) of approximately 0.5. This trend is supported by the data at area ratio 4.

The results of the dual flow test have demonstrated that core nozzle suppression can be achieved by utilizing an annular secondary flow. The secondary or fan flow from the coannular nozzle modifies the core nozzle alone jet noise characteristics. The overall sound pressure level (OASPL) of the dual flow jet at a specific area ratio decreases with respect to the core jet only OASPL for initial increases in fan flow velocity (from zero). The $OASPL_{dual\ flow}$ reaches a minimum when the velocity ratio V_{28}/V_8 is approximately 0.5. The effect of area ratio (A_{28}/A_8) at this point is to lower the $OASPL_{dual\ flow}$ as the area ratio of each configuration increases. Further increases in secondary flow velocity raise $OASPL_{dual\ flow}$ so that at a velocity ratio V_{28}/V_8 of 0.7 the $OASPL_{dual\ flow} = OASPL_{core\ only}$. Further increases in secondary flow increase the $OASPL_{dual\ flow}$ higher than the levels of core flow alone. This result has been observed by Williams, et al. (Reference 2.1-4) who establishes, through dimensional analysis, the noise output of coannular flow with respect to the core flow noise.

2.2.6 Summary and Conclusions

Experimental investigations have been successfully completed on the jet noise characteristics of coannular nozzles. Large scale models were tested and the core flow was heated to provide an accurate simulation of turbofan engine performance cycles. The data was considered pure jet noise above jet velocities of 500 ft/sec (152 m/sec); also, when scaling techniques are utilized to provide full scale predictions, this information will be free of ground reflection interference. The results of the investigations confirmed the existence of an interaction effect between the fan and core flows and comparison with a theoretical approach tends to support the analysis which relates the interaction in terms of a relative velocity function. Generally, several observations can be made if a fixed core velocity is considered:

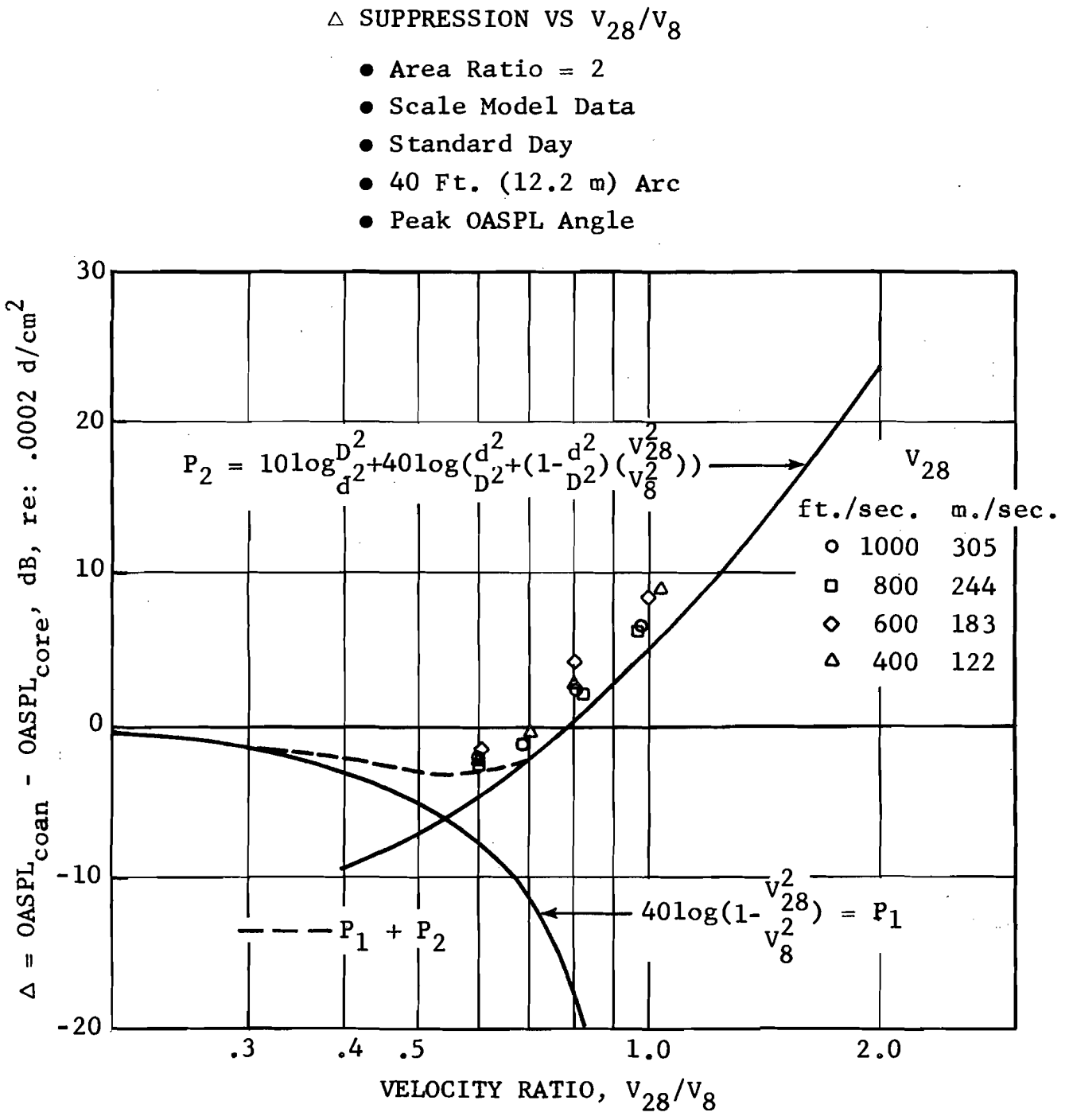

FIGURE 2.2.5.2-13 △ SUPPRESSION VS V_{28}/V_8 FOR AREA RATIO = 2

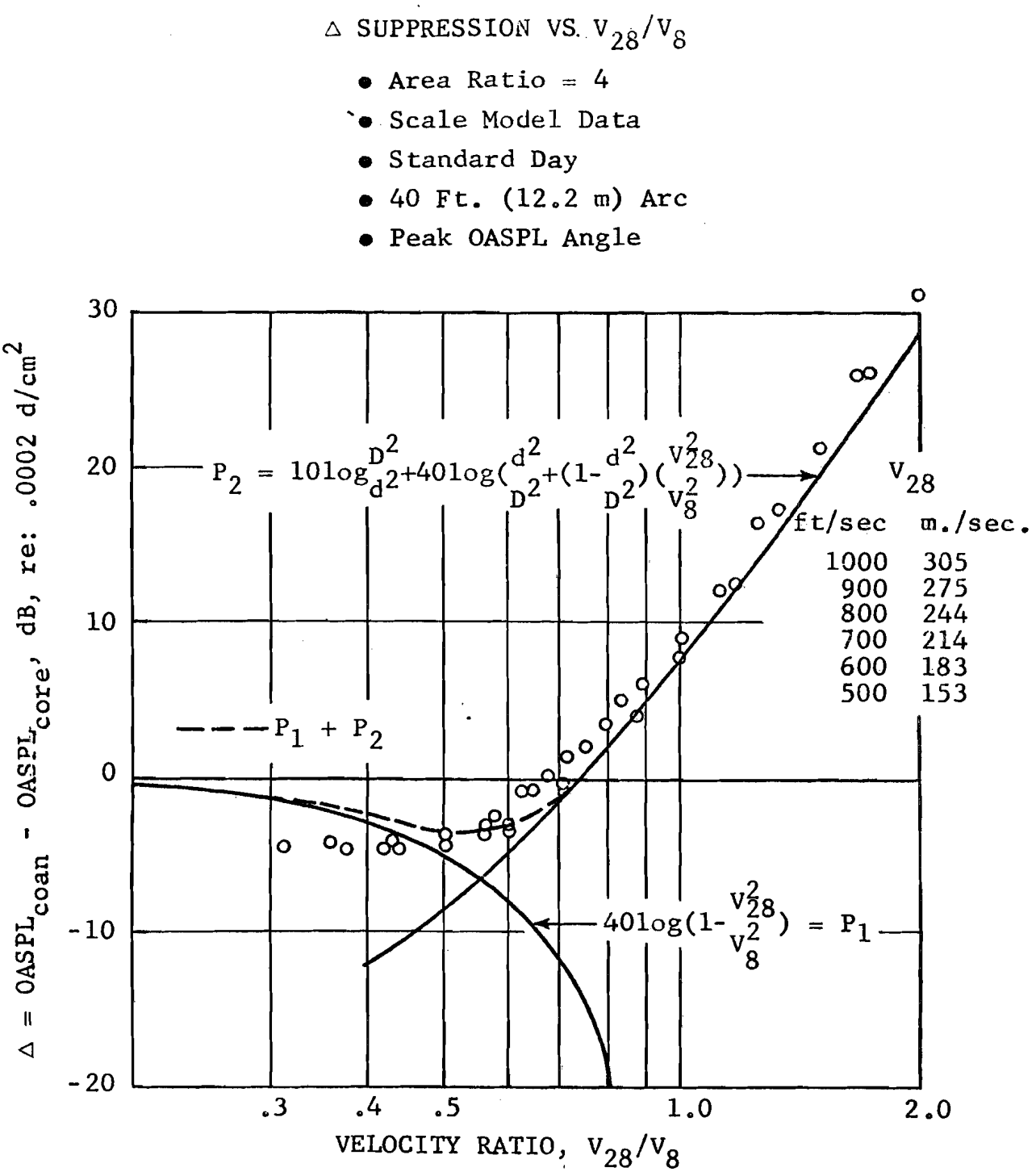

FIGURE 2.2.5.2-14 △ SUPPRESSION VS V_{28}/V_8 FOR AREA RATIO = 4

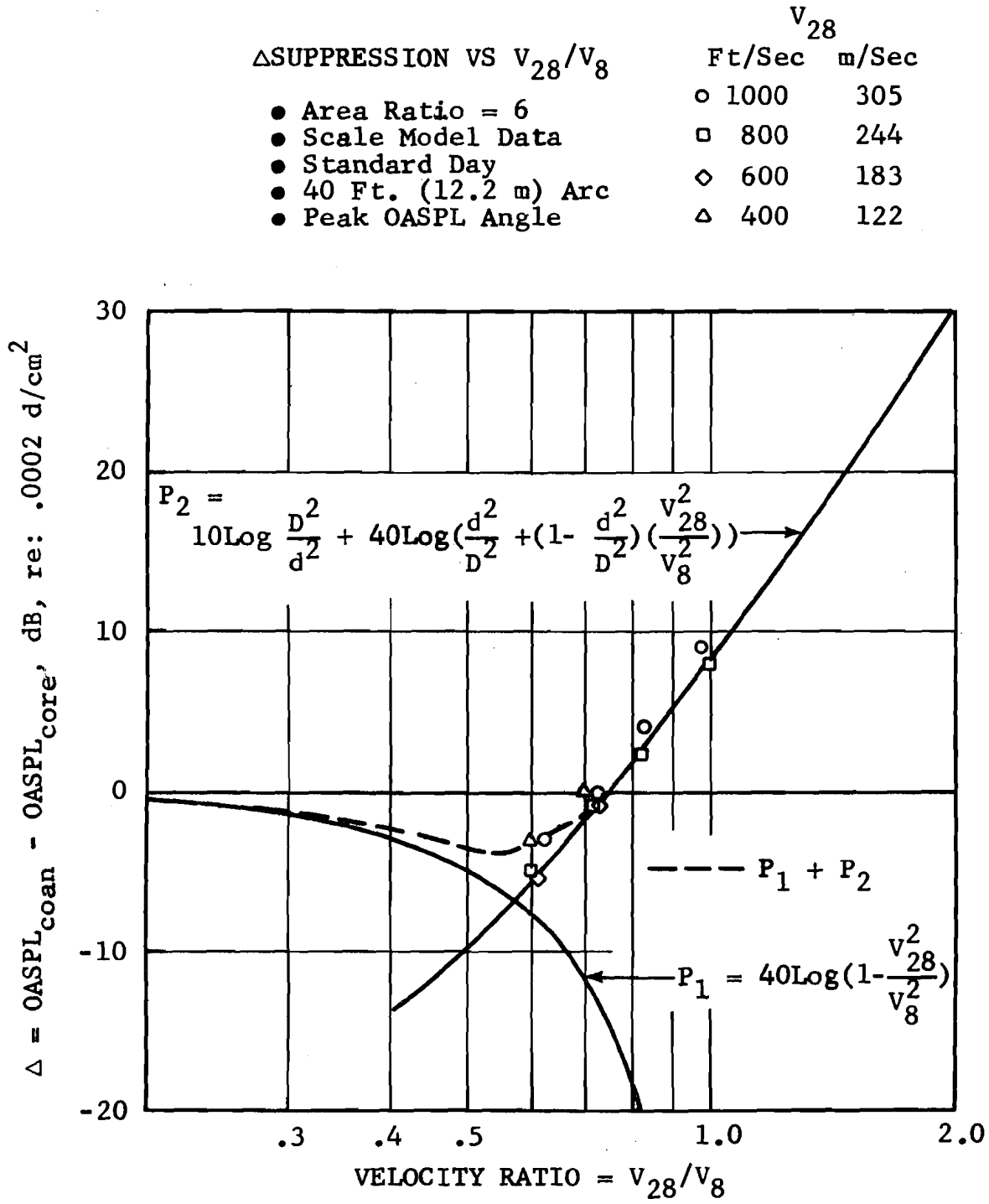

FIGURE 2.2.5.2-15 Δ SUPPRESSION VS V_{28}/V_8 FOR AREA RATIO = 6

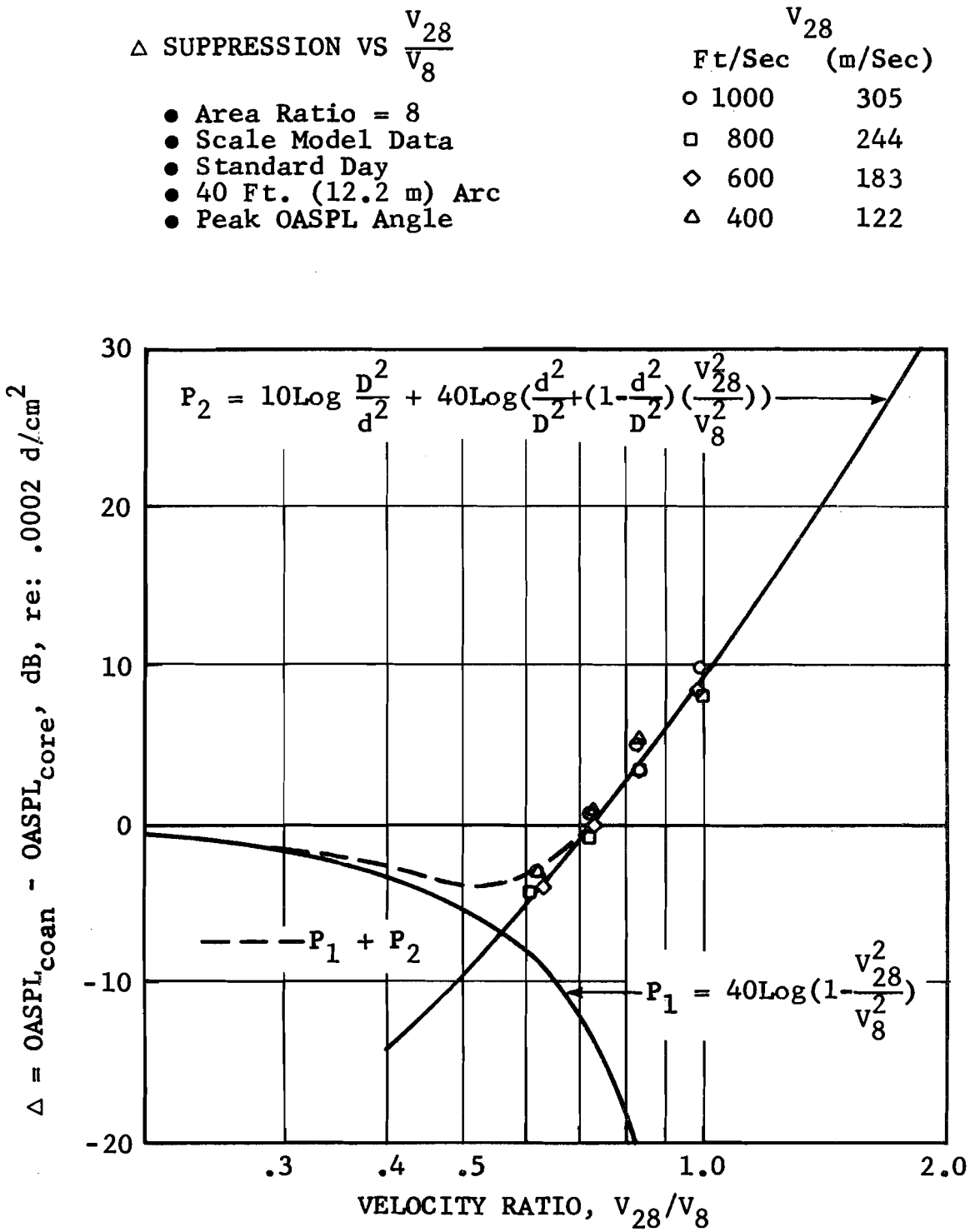

FIGURE 2.2.5.2-16 Δ SUPPRESSION VS V_{28}/V_8 FOR AREA RATIO = 8

1. The introduction of secondary air (fan flow) causes an initial reduction in the noise output (OASPL or OAPWL) of the dual flow system relative to the conical nozzle.

2. This observed noise reduction reaches a maximum when the ratio of fan velocity to core velocity is of the order of 0.5.

3. The maximum value of the observed noise reduction is increased when the area ratio (fan flow area to core flow area) is increased.

4. At a velocity ratio of approximately 0.75, the noise output of the dual flow system is equivalent to the single core jet. Further increases in velocity ratio produce a dual flow noise output which is consistent with the fully mixed jet region.

5. A substantial data bank of coannular flow has been made available to provide the basis for a prediction method.

2.3 UPSTREAM TURBULENCE TESTS

2.3.1 Objectives

The objectives of the test series were to conduct a series of experiments to determine the effect of changes in upstream turbulence intensity levels on low velocity jet noise and to perform a detailed survey of the turbulence characteristics of the exhaust plume using the laser velocimeter.

2.3.2 Test Procedure and Facility Description

2.3.2.1 Cold Flow Acoustic Duct Test

Before these objectives could be met, a series of tests were conducted in the cold flow acoustic duct to determine the turbulence generation characteristics of five designs, which incorporate either rods or plates. These configurations are defined in Figure 2.3.2-1. A schematic of the test setup in the cold flow duct is shown in Figure 2.3.2-2.

The most important parameters of the scale model farfield acoustic test were simulated in this cold flow duct test. These parameters are summarized as follows:

- The axial distance from the turbulence generation plane to nozzle exit plane.
- The incident Mach number into the turbulence generators.
- The Mach number in the acoustically treated section.
- The Mach number in the section where the cross-correlations measurements were made using the acoustic correlation probe.

The hot film anemometer was used to measure the turbulence levels generated by the various designs at the simulated nozzle exit plane. Hot film probe traverses were made across the duct to determine the mean velocity profile and the fluctuating u' profile. These data facilitated the calculation of the turbulence intensity profile across the duct for each design tested. For each configuration, the turbulence intensity profile is shown in Figure 2.3.2-3.

The most successful design was configuration 5 which incorporated axially staggered plates. This design generated turbulence intensity levels $(u'/\bar{U})$ of 22% and, unfortunately, a non-uniform mean velocity profile. The profile can be determined however, using the laser doppler velocimeter. In the process of generating high levels of turbulence intensity, the interaction of flow and the plate also generates another fluctuating pressure level which may be described as either flow noise or obstruction noise. It is essential in the farfield tests to measure the effect of changes in turbulence intensity levels on farfield noise and not the increase caused by flow noise. In order to determine the effect of flow noise, cross-correlation measurements were performed using

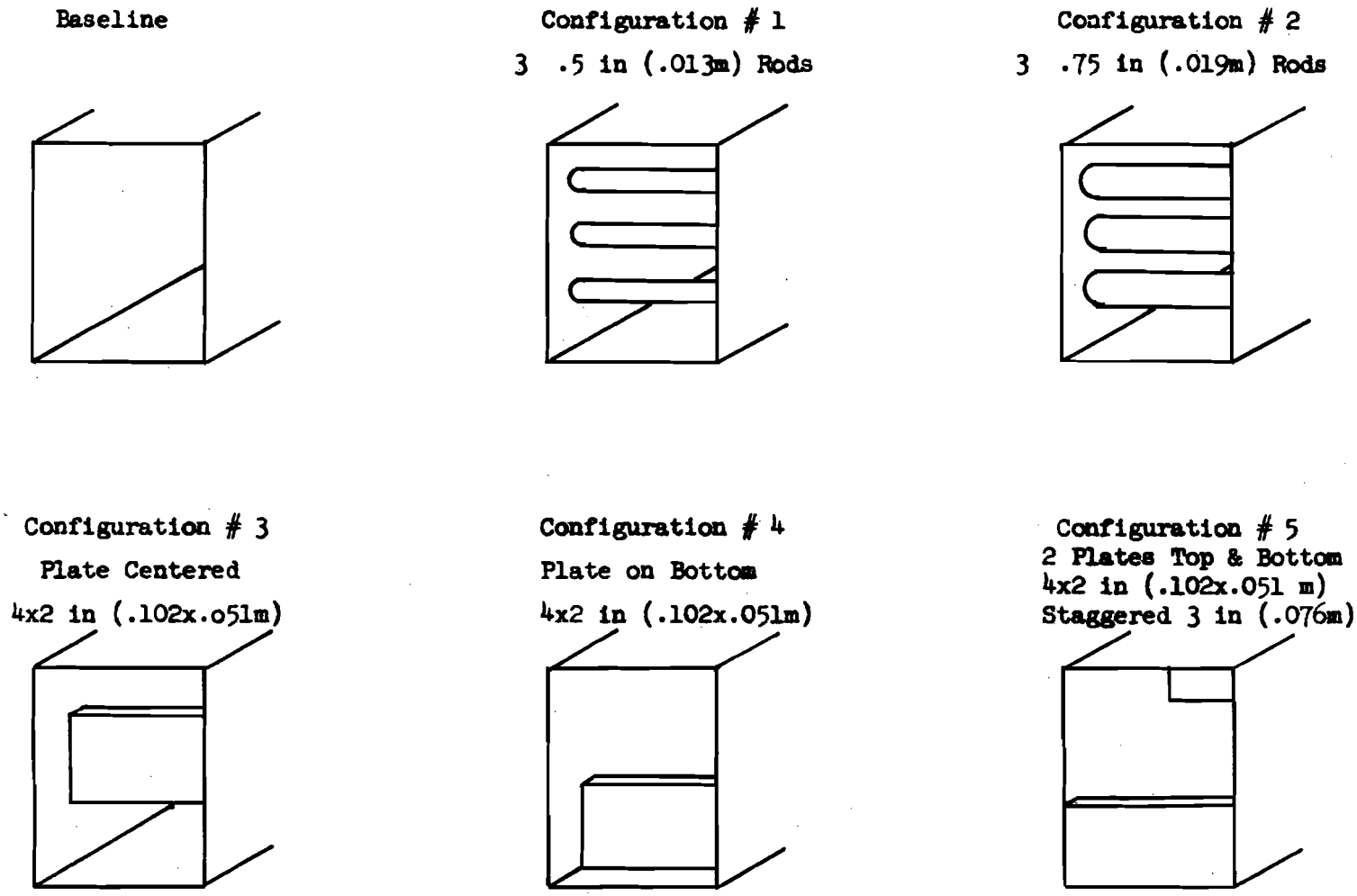

FIGURE 2.3.2 - 1 SCHEMATIC OF TURBULENCE GENERATORS USED IN COLD TURBULENCE TEST

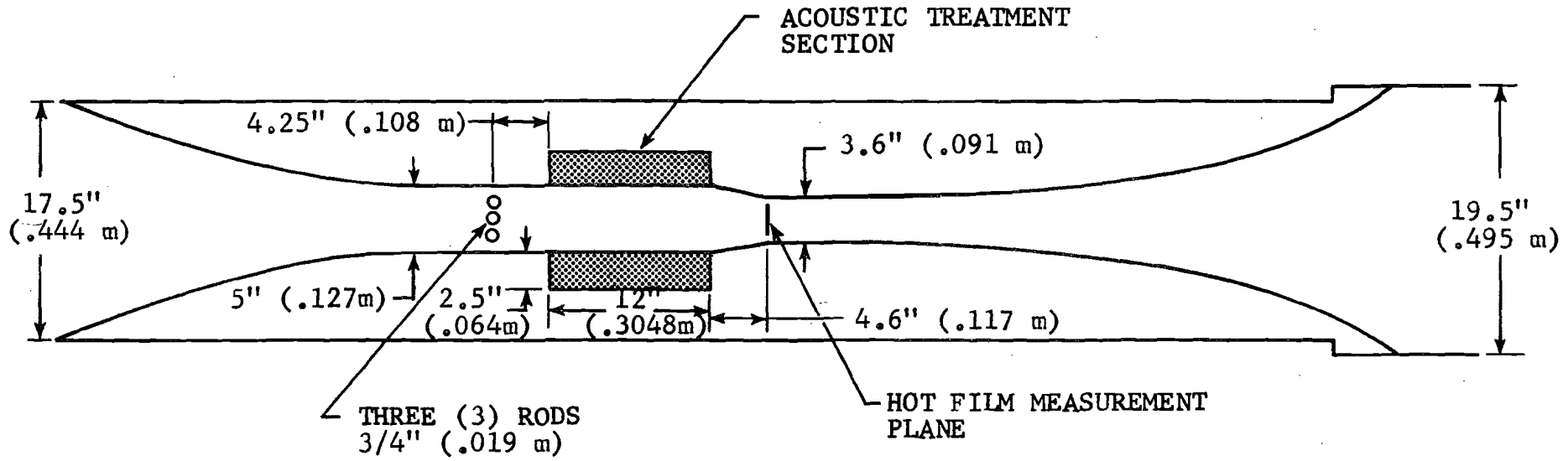

FIGURE 2.3.2-2 SCHEMATIC OF TEST SETUP IN COLD FLOW ACOUSTIC DUCT

CORE ENGINE NOISE CONTROL TEST

COLD FLOW ACOUSTIC DUCT TEST

MACH NUMBER ≈ .5

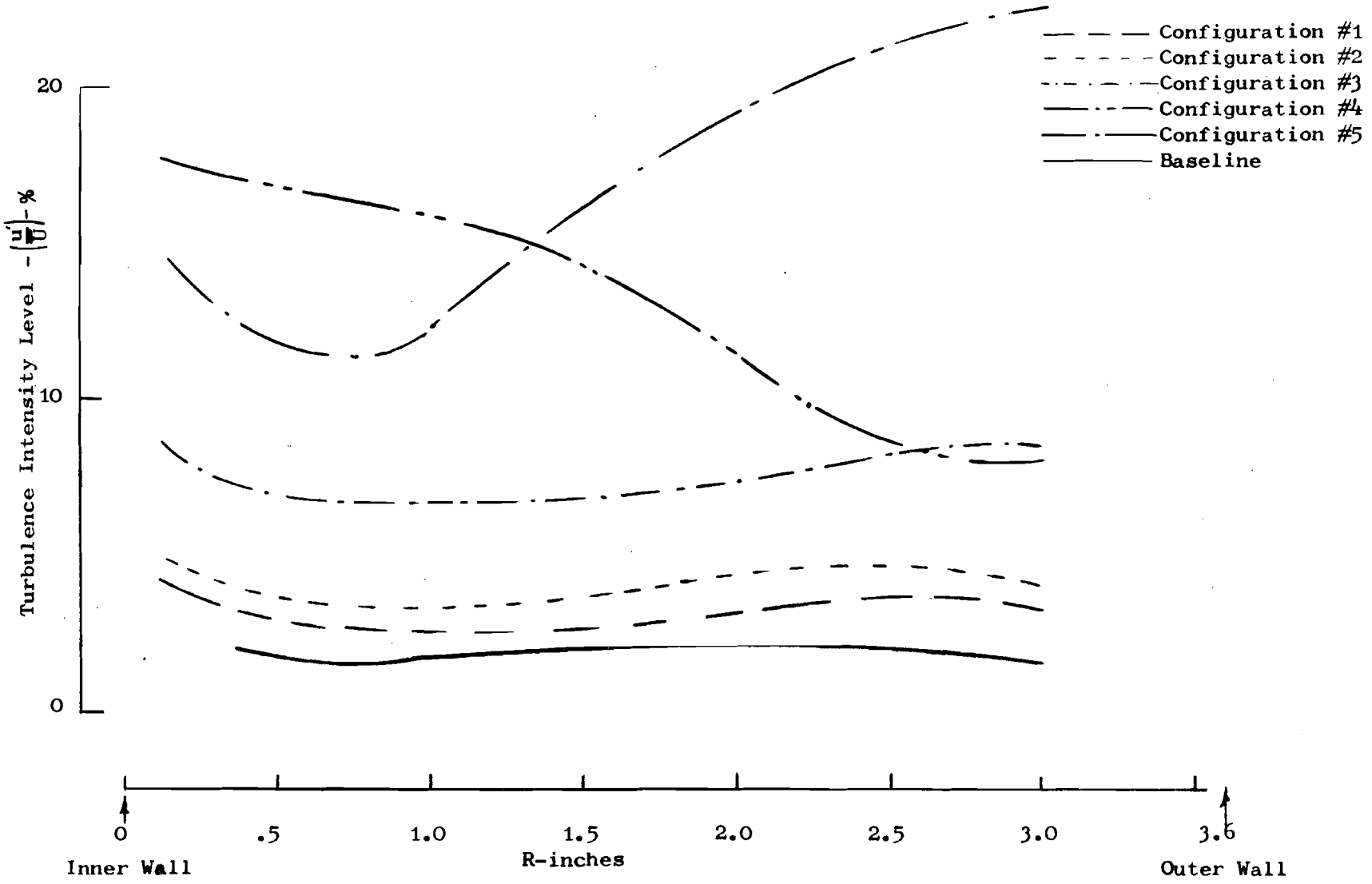

FIGURE 2.3.2-3 TURBULENCE INTENSITY LEVELS AT SIMULATED NOZZLE EXIT PLANE

an acoustic probe. The results of these measurements indicate a strong correlation with the amplitude of a pressure fluctuation traveling at the Mach number in the duct (i.e., turbulence level) and almost no correlation with a fluctuating pressure signal traveling at the duct Mach number plus the speed of sound in the duct (i.e., flow noise). These results indicate that the staggered plate design, configuration 5, is an acceptable means of increasing the turbulence intensity level at the nozzle exit plane without contaminating the farfield acoustic measurements with flow generated noises. As a result of this series of tests, the staggered plate design was used to generate the highest turbulence level for Jenots testing, the single plate (configuration 4) was used to generate the intermediate turbulence level, and the pipe with no obstruction was used as the baseline configuraton.

2.3.2.2 Jenots Test Series

After the turbulence generation devices were defined as the result of the cold flow acoustic duct test, a scale model test program was performed on the "Jet Exhaust Noise Outdoor Test Site," (Jenots). The facility has been described in Section 2.2.3. A schematic of the test hardware is presented in Figure 2.3.2-4. As labeled in Figure 2.3.2-4, the test configuration was divided into three sections. The sections are described as follows:

Section 1 - Turbulence Generation Section

This section has the capability to incorporate different designs which generate various levels of turbulence intensity. The designs used for this specific test series are presented in Figure 2.3.3-5. The configurations were: (1) staggered plates, (2) a single plate, (3) a semicircular screen, and (4) a smooth section with no obstructions. Selection of these turbulence generation designs was based on the results of the "Cold Flow Acoustic Duct Test." The staggered plates generated the highest turbulence level; the single plate, the intermediate level; and the smooth section provides baseline turbulence level. The purpose of the screen was to generate a velocity profile having the same shape as the designs incorporating the plates, but with low turbulence levels.

Section 2 - Acoustically Treated Section

The acoustically treated section was designed to suppress the flow noise generated by the exhaust stream-plate interaction. The cold flow acoustic duct test results showed that the plates introduced the desired high turbulence levels in the stream. A byproduct of the turbulence generation however, was flow noise. The objective of the test program was to determine the effect of turbulence intensity changes on low velocity jet noise and the acoustically treated section was to prevent the farfield acoustic measurements from being contaminated by an internally generated noise.

Section 3 - Core Nozzle

This section was designed to simulate the aerodynamic flow path of a typical engine exhaust nozzle. A mounting pad for an acoustic probe actuation system was also incorporated into the design. This actuation system enabled the probe to traverse radially across the duct.

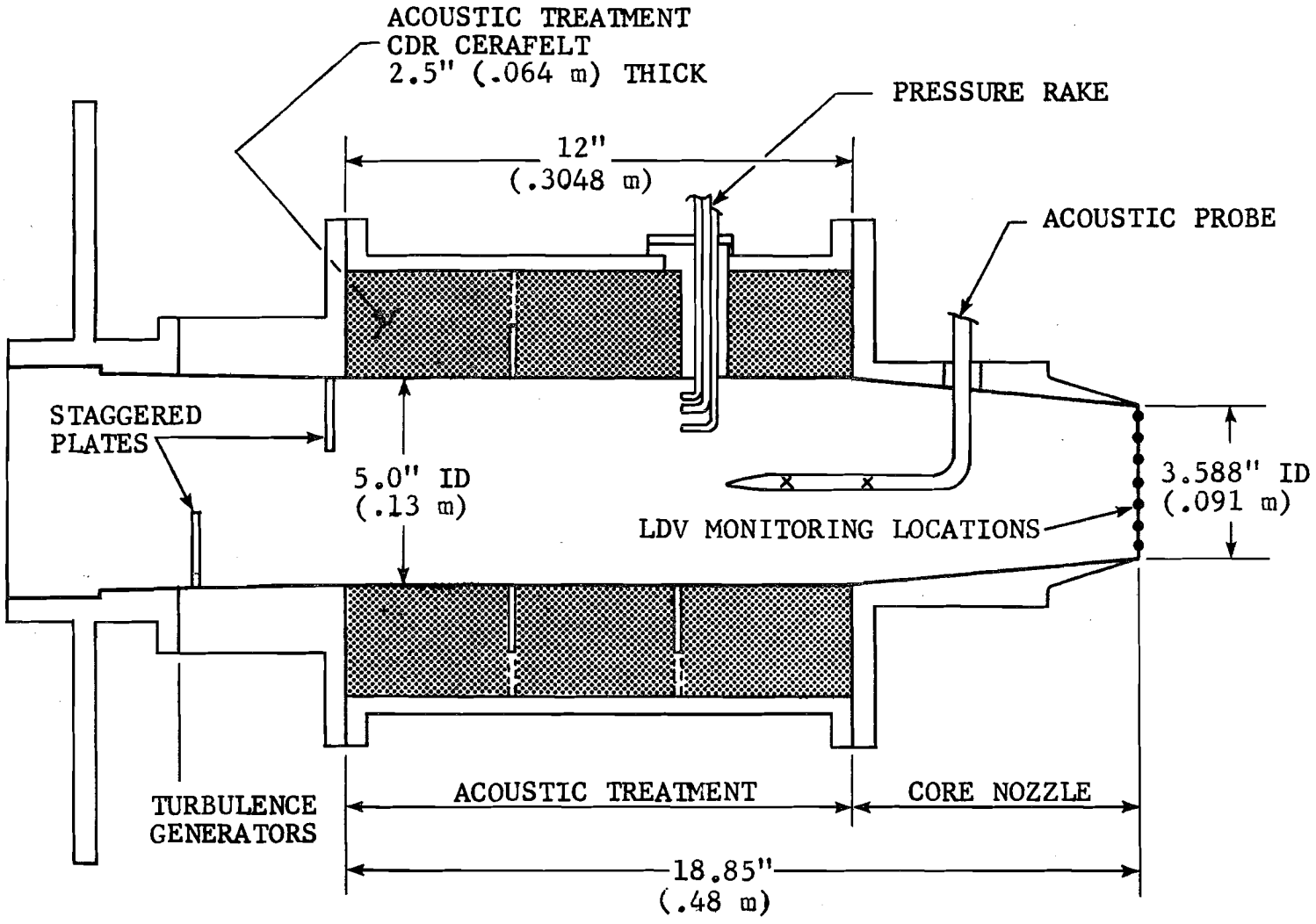

FIGURE 2.3.2-4 SCHEMATIC OF JENOTS TEST SETUP

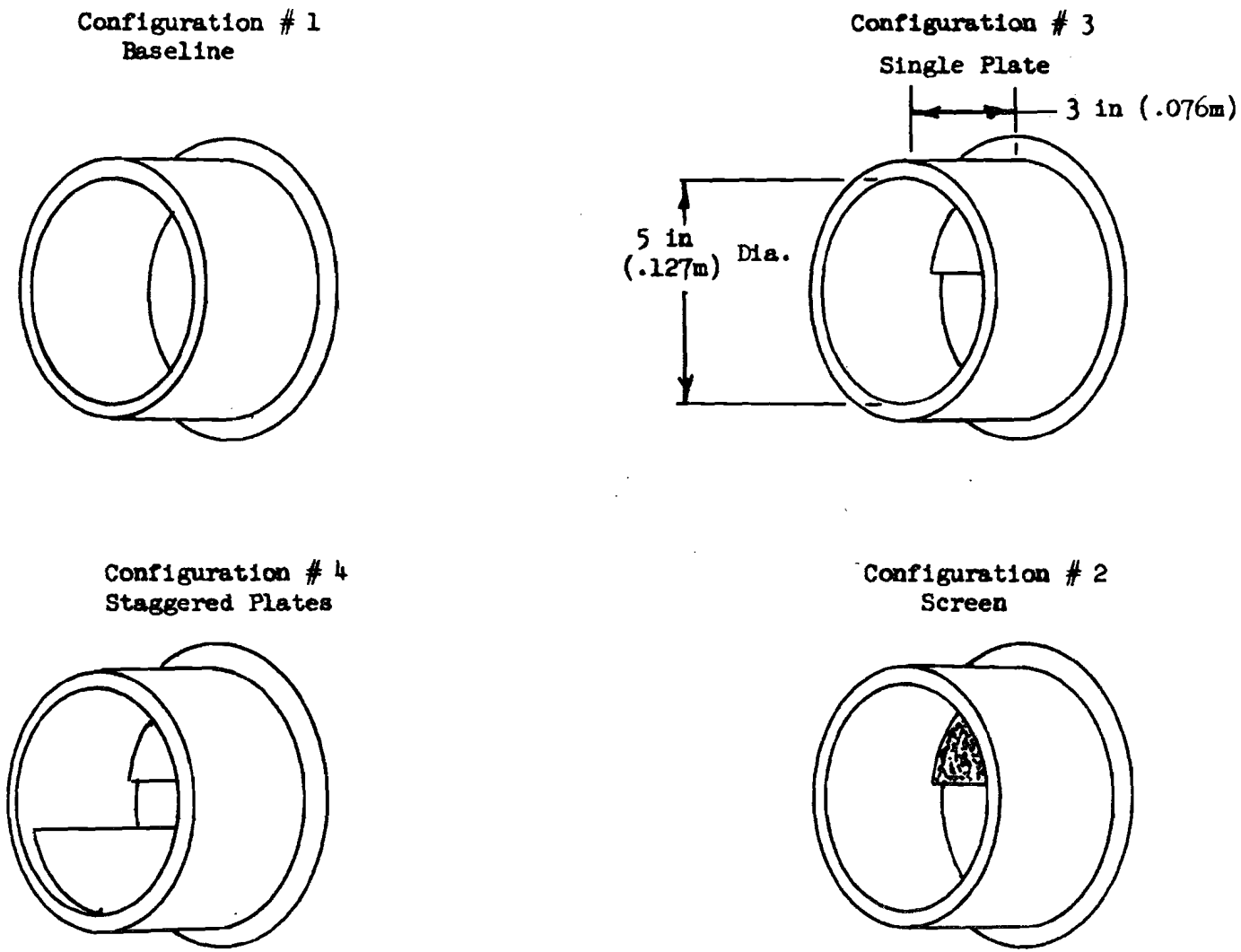

FIGURE 2.3.2 - 5 SCHEMATIC OF TURBULENCE GENERATORS USED IN HOT TURBULENCE TEST

The actual testing sequence was divided into three phases: laser velocimeter (LV), acoustic probe, and farfield noise measurements. The LV measurements were used to define the turbulence intensity levels for each of the test configurations. The acoustic probe data served a dual function: 1) to allow cross-correlation of the Kulite data, and 2) to allow the calculation of the duct acoustic power level for comparison with the measured acoustic power spectrum of the externally generated jet noise. The farfield measurements determined the change in jet noise due to turbulence intensity changes at the nozzle exit plane.

A schematic of LV monitoring points is given in Figure 2.3.3-6. The LV was used at each monitoring point to define the mean velocity, $\bar{U}$, and an axial fluctuating component, u'. From these two parameters, the turbulence intensity levels were calculated. To enhance the development of the analytical and empirical prediction procedures, a detailed exhaust plume LV survey was also made for baseline and staggered plate configurations at a jet velocity of 800 ft/sec (244 m/s). The planes where these traverses were made are defined in Figures 2.3.2-6 and 2.3.2-7. Typical velocity profiles at the nozzle exit plane to illustrate the data obtained for each of the configurations are presented in Figure 2.3.2-8.

The acoustic probe measurements were conducted after the LV measurement phase of the program was completed. The test matrix and a schematic defining the radial probe locations are presented in Figure 2.3.2-9. Data points 12P, 13P and 14P were completed, but during test point 15P, the pressure transducer mounted on the probe failed due to ice formation inside the nozzle. The preliminary results from the probe data that were obtained are presented on Figure 2.3.2-10. These results are from a cross-correlation analysis and show the maxmimum energy correlation as a function of time delay. Note the strong correlation with a time delay that corresponds to a signal traveling at the Mach Number of the exhaust duct (i.e., turbulence), and the weak correlation with the time delay of a signal traveling at the duct Mach Number plus the speed of sound (i.e., flow noise). This preliminary result indicates that the flow noise energy is much less than the turbulent energy. The test matrix for the farfield acoustic measurements is presented in Figure 2.3.2-11.

2.3.3 Discussion of Test Results

The test program consisted of aerodynamic flowfield surveys, acoustic probe results and farfield acoustic measurements. Figure 2.3.3-1 illustrates the turbulence levels produced at the nozzle exit plane by the various turbulence generation devices. To further illustrate the effect of changes in upstream turbulence levels on the turbulence levels in the exhaust plume, the contours of $u'/\bar{U}$ are presented in Figure 2.3.3-2. Analysis of the data supports the following trends.

- The mean velocity profiles for the baseline configuration were very uniform radially for all power settings.

- The staggered plate turbulence generator, configuration 4, caused an asymmetric mean velocity profile at the nozzle exit plane.

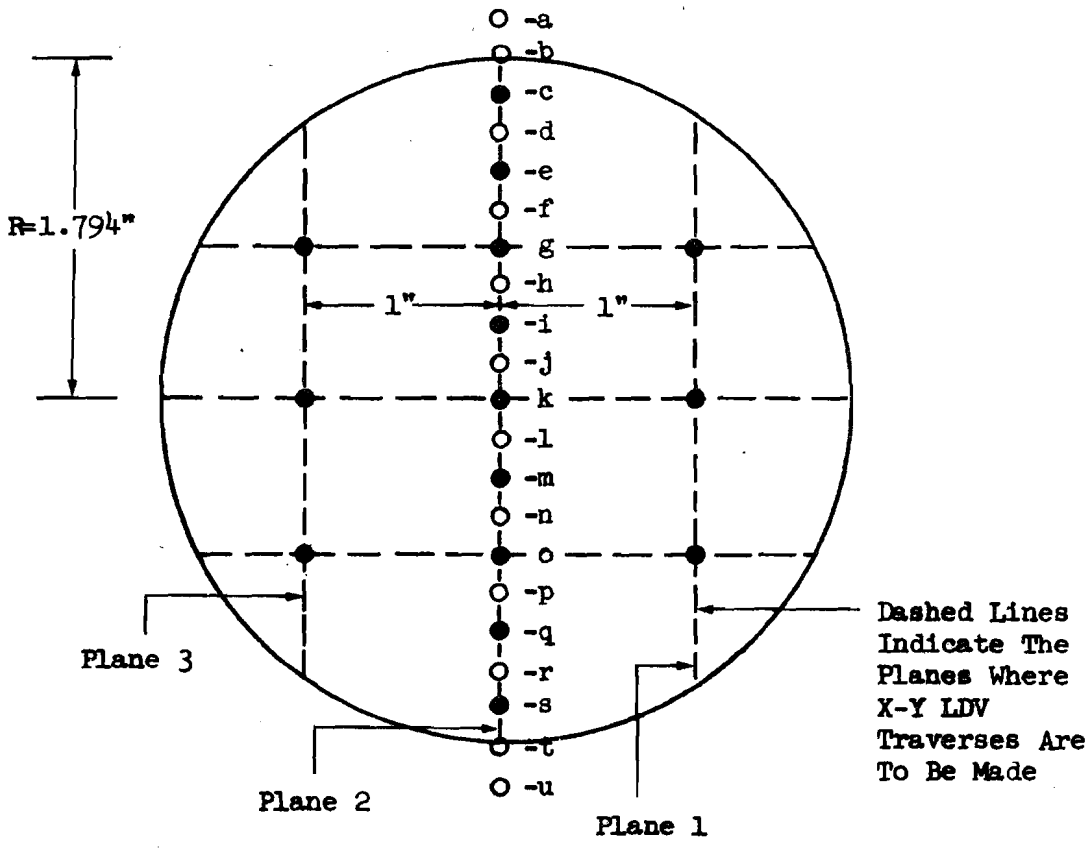

FIGURE 2.3.2-6 SCHEMATIC OF LASER VELOCIMETER MONITORING LOCATIONS

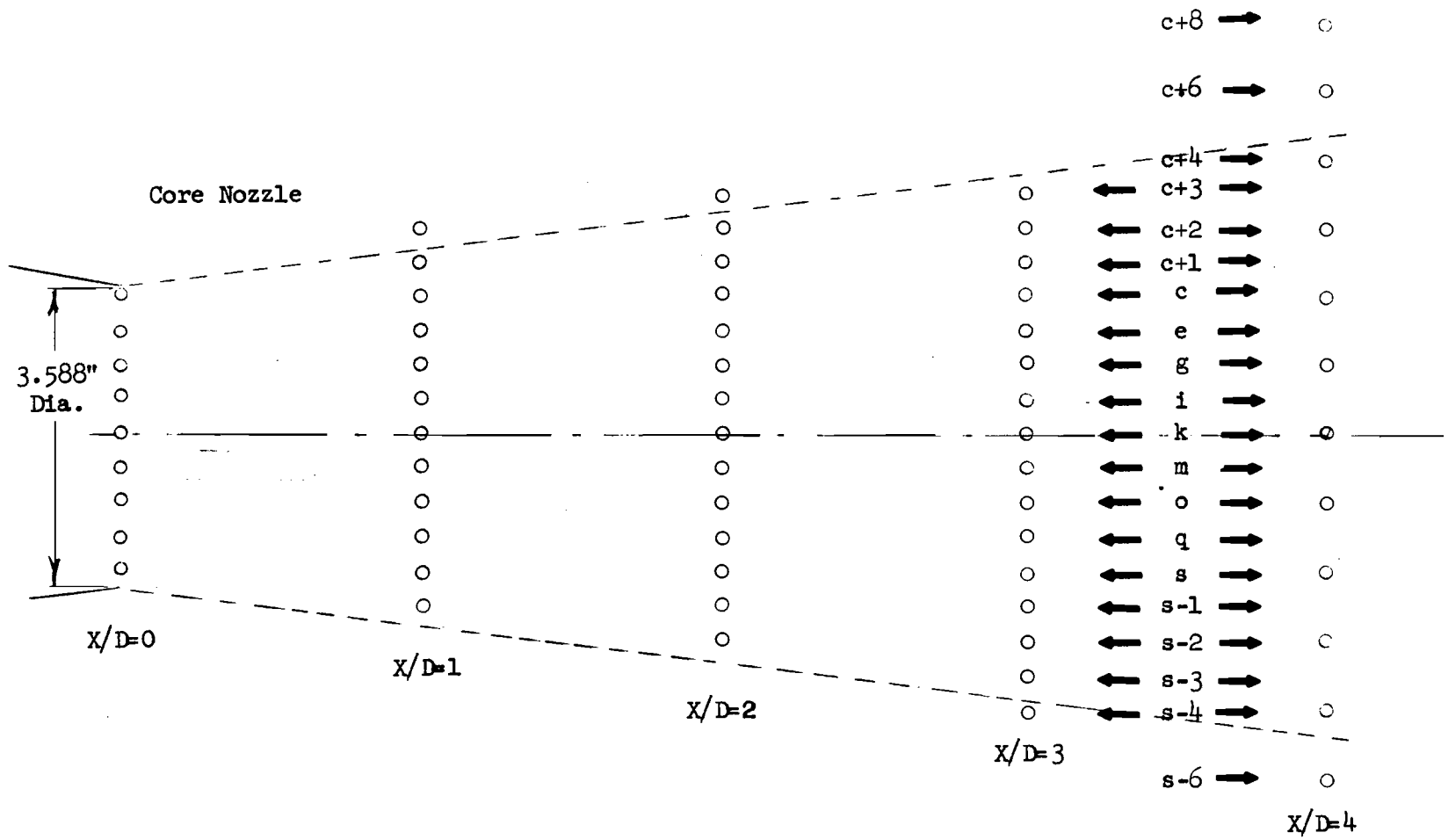

FIGURE 2.3.2-7 SCHEMATIC OF PLUME SURVEY POINTS

CORE ENGINE NOISE CONTROL - TEST 2

Vertical Traverse At Plane 2

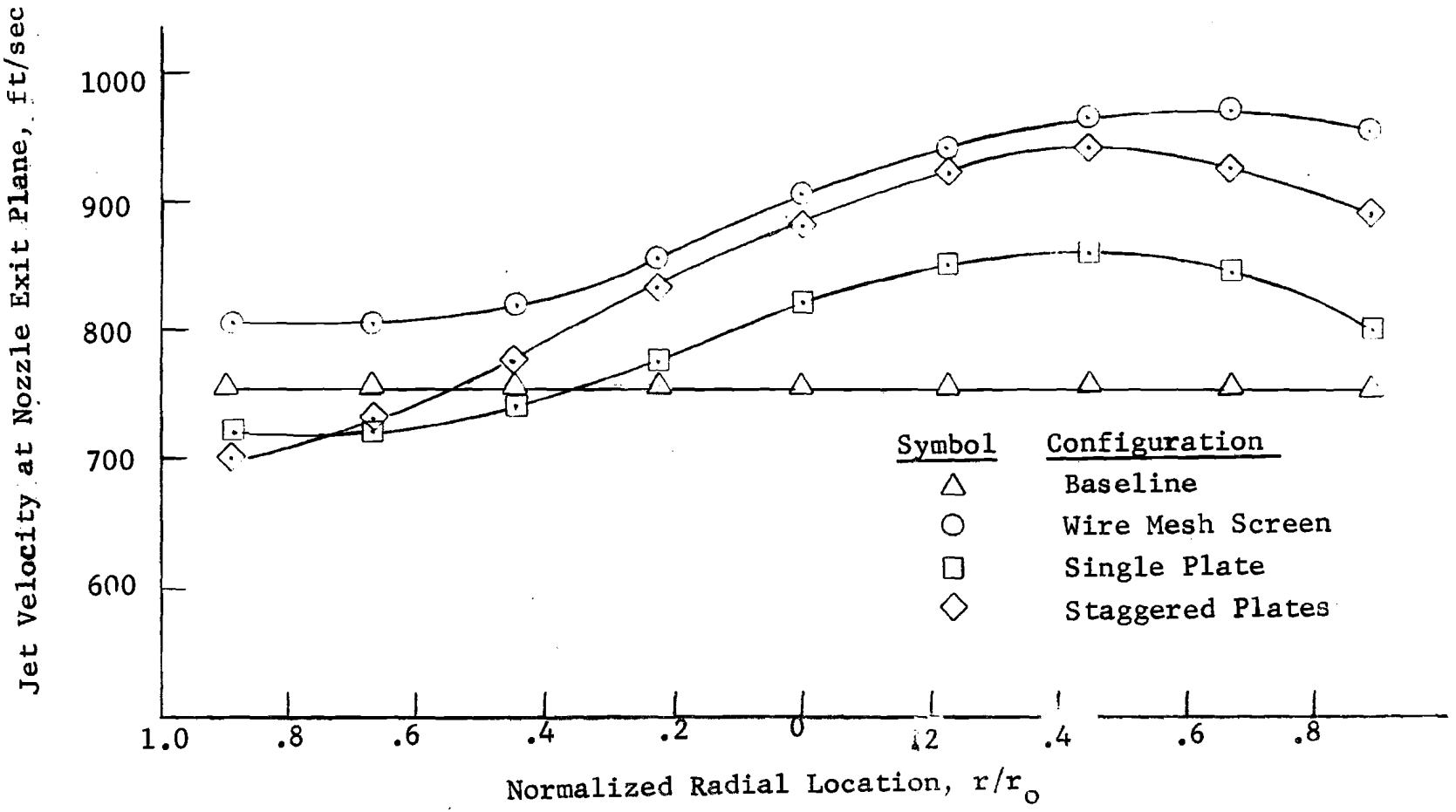

FIGURE 2.3.2-8 TYPICAL VELOCITY PROFILE SHAPES AT THE NOZZLE EXIT PLANE

CORE ENGINE NOISE CONTROL - TEST

Core Exhaust Velocity Ft/Sec	Configuration: Baseline	Baseline Non-Uniform Profile	Single Plate	Staggered Plate
500	1-P	4-P	7-P	12-P
600	2-P	5-P	8-P	13-P
700			9-P	14-P
800			10-P	15-P
900				
1000	3-P	6-P	11-P	16-P

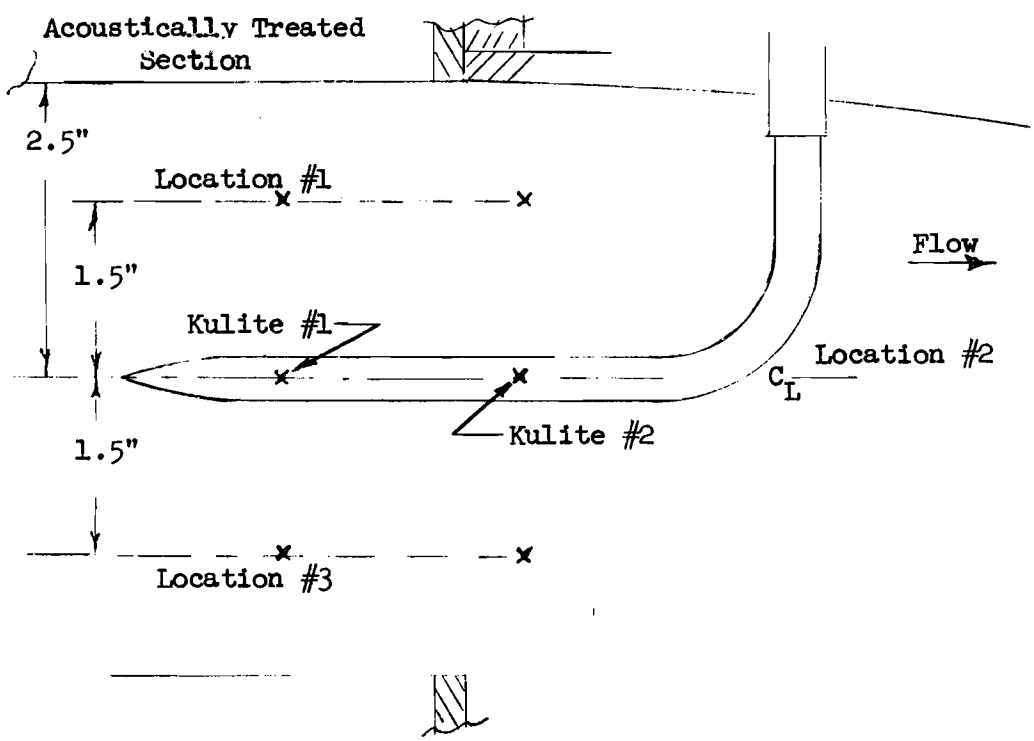

FIGURE 2.3.2-9 ACOUSTIC PROBE MONITORING LOCATIONS AND TEST MATRIX

CORE ENGINE NOISE CONRTOL - TEST II

* Data Point 14P, Position 2

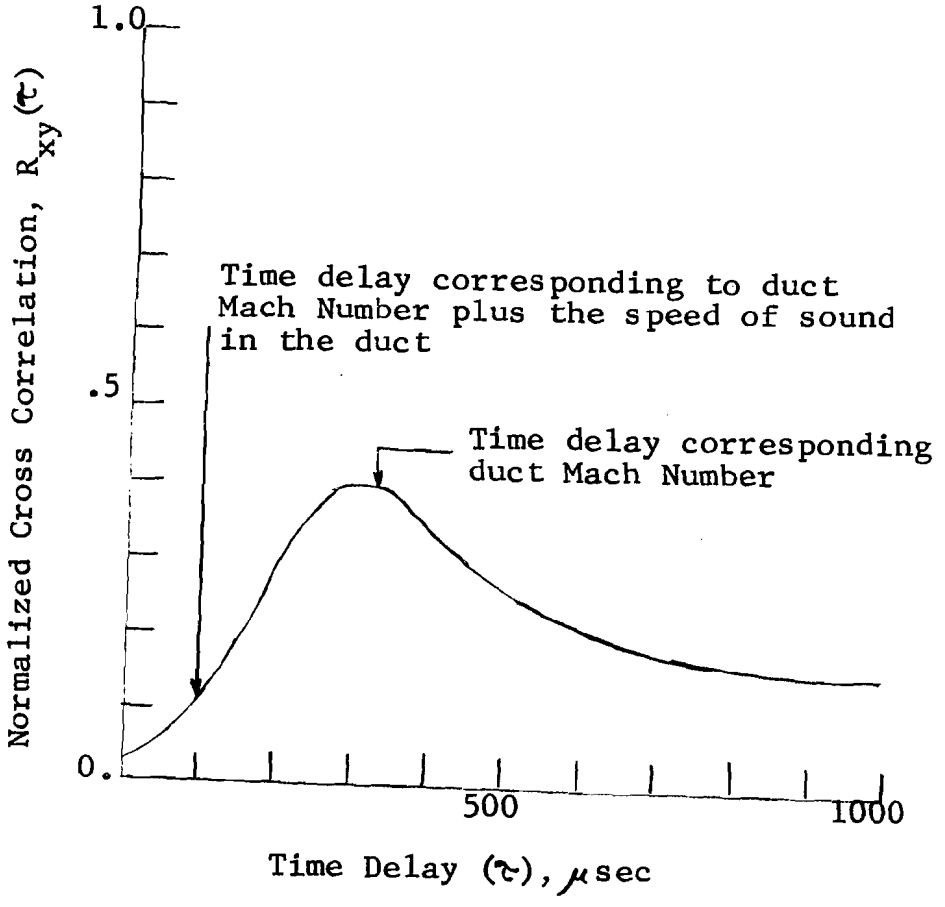

FIGURE 2.3.2-10 CROSS CORRELATION ANALYSIS OF ACOUSTIC PROBE DATA

Core Exhaust Velocity ft/sec	Configuration			
	Baseline	Baseline Non-Uniform Profile	Single Plate	Staggered Plate
	$T_{T8} \approx 750^{\circ}R$			
500	1-A	7-A	13-A	19-A
600	2-A	8-A	14-A	20-A
700	3-A	9-A	15-A	21-A
800	4-A	10-A	16-A	22-A
900	5-A	11-A	17-A	23-A
1000	6-A	12-A	18-A	24-A
	$T_{T8} \approx 1300\ ^{\circ}R$			
500	25-A	31-A	37-A	43-A
600	26-A	32-A	38-A	44-A
700	27-A	33-A	39-A	45-A
800	28-A	34-A	40-A	46-A
900	29-A	35-A	41-A	47-A
1000-	30-A	36-A	42-A	48-A

FIGURE 2.3.2-11 TEST MATRIX - FARFIELD ACOUSTIC MEASUREMENTS

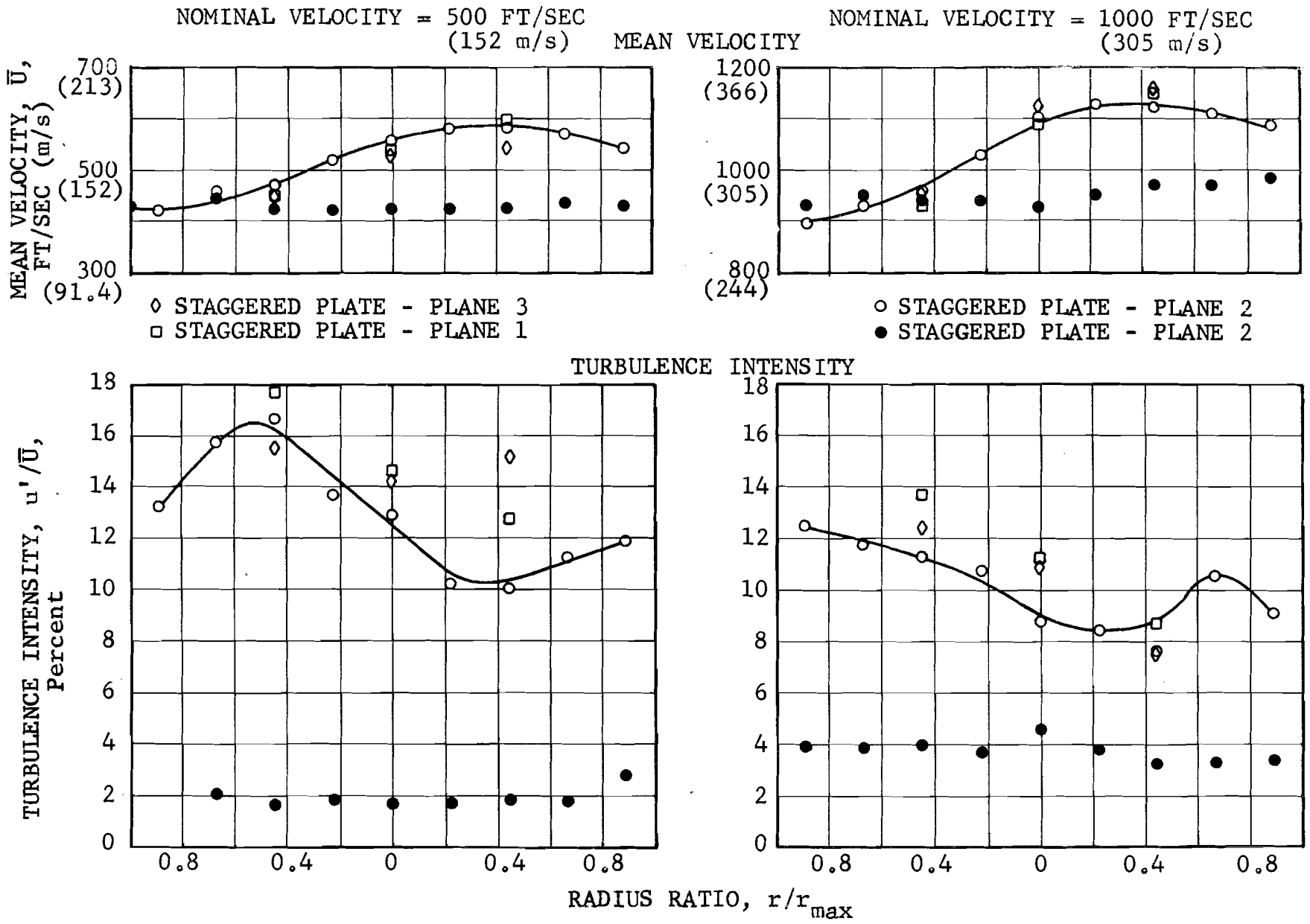

FIGURE 2.3.3-1 RADIAL PROFILES OF MEAN VELOCITY AND TURBULENCE INTENSITY AT NOZZLE EXIT PLANE, X/D = 0

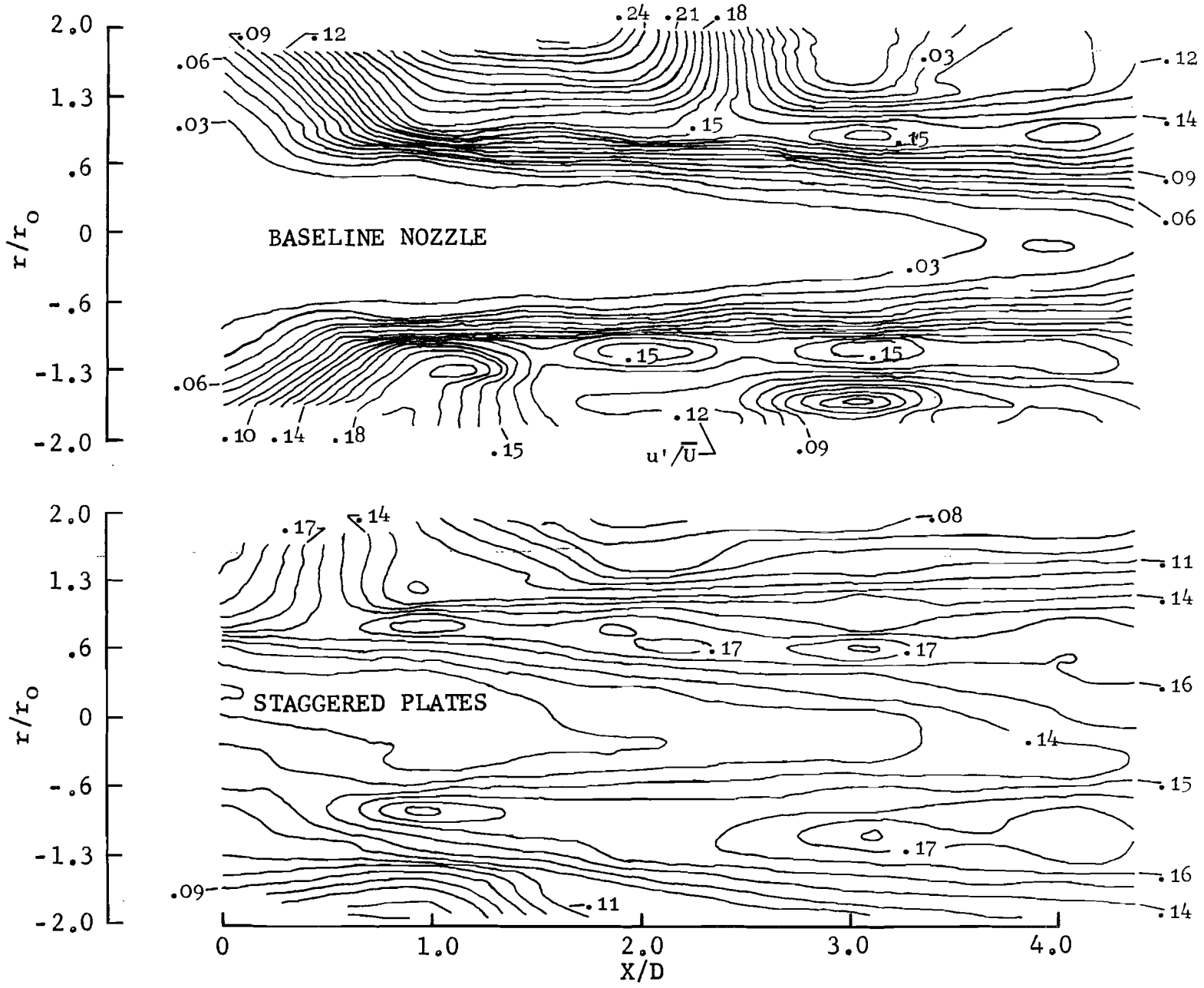

FIGURE 2.3.3-2 EXHAUST PLUME TURBULENCE INTENSITY LEVELS

- The turbulence intensity profiles for the baseline case were approximately between 2% and 4%.

- The turbulence intensity profiles for the staggered plate configuration were non-uniform with mean levels between 8% and 18%.

In addition to using the LV to define the turbulence levels at specific points in the nozzle exit plane, it was also used to perform a continuous traverse at the nozzle exhaust plane to define the mean velocity profiles for each of the configurations. Definition of these velocity profiles is essential in the analysis of the acoustic data because for three of the four configurations evaluated the velocity profiles were highly asymmetric. Based on a momentum weighted velocity calculation, the configurations all have the same mean velocity. Jet noise is dependent on exhaust velocity to the eighth power and hence the nozzles with the asymmetric velocity profiles would produce more jet noise than the baseline nozzle having the flat potential flow type velocity profile. Because of this effect, configuration 2 incorporated a semicircular screen designed to produce an asymmetric profile similar to the profile produced by the two high turbulence level configurations, but accompanied by a very low turbulence intensity level.

In presenting the farfield acoustic data average or momentum weighted values of jet velocity were used. The acoustic data for each of the configurations was measured at the same weight flows to insure the comparisons between the configurations would be made at the same mean velocity. In analyzing the acoustic data, the following important points should be noted.

- The comparisons of configurations 1 and 2 show the effect of having a non-uniform velocity profile only and not the effect of changes in turbulence intensity.

- Configuration 2 should be used as a baseline to determine the effect changes in turbulence levels had on farfield jet noise.

The peak OAPSL for each configuration is plotted as a function of jet velocity in Figure 2.3.3-3 to summarize the acoustic results. The maximum effect caused by change in turbulent intensity level is observed at the lowest jet velocity. Comparison of configurations 2 and 4 indicates that a change in overall turbulence intensity level of approximately 7% produced an 8 dB change in peak OASPL. In contrast, at the highest power setting only a 5dB increase is observed. This smaller difference at the higher power setting was due primarily to a decrease in turbulence level caused by an increase in Mach number.

For highly suppressed engines, the jet noise may be the major noise component at angles other than the jet peak. To show the effect that turbulence intensity has on these other angles, the directivity patterns for each of the four configurations evaluated are presented for the high and low power settings respectively, in Figures 2.3.3-4 and -5. These results indicate that at the higher power setting an increase in turbulence causes 8 dB increase in the forward quadrant as opposed to only a 5 - 6 dB increase in the aft quadrant. At the lower power setting, the trend is not clear because of the influence of ambient noise levels.

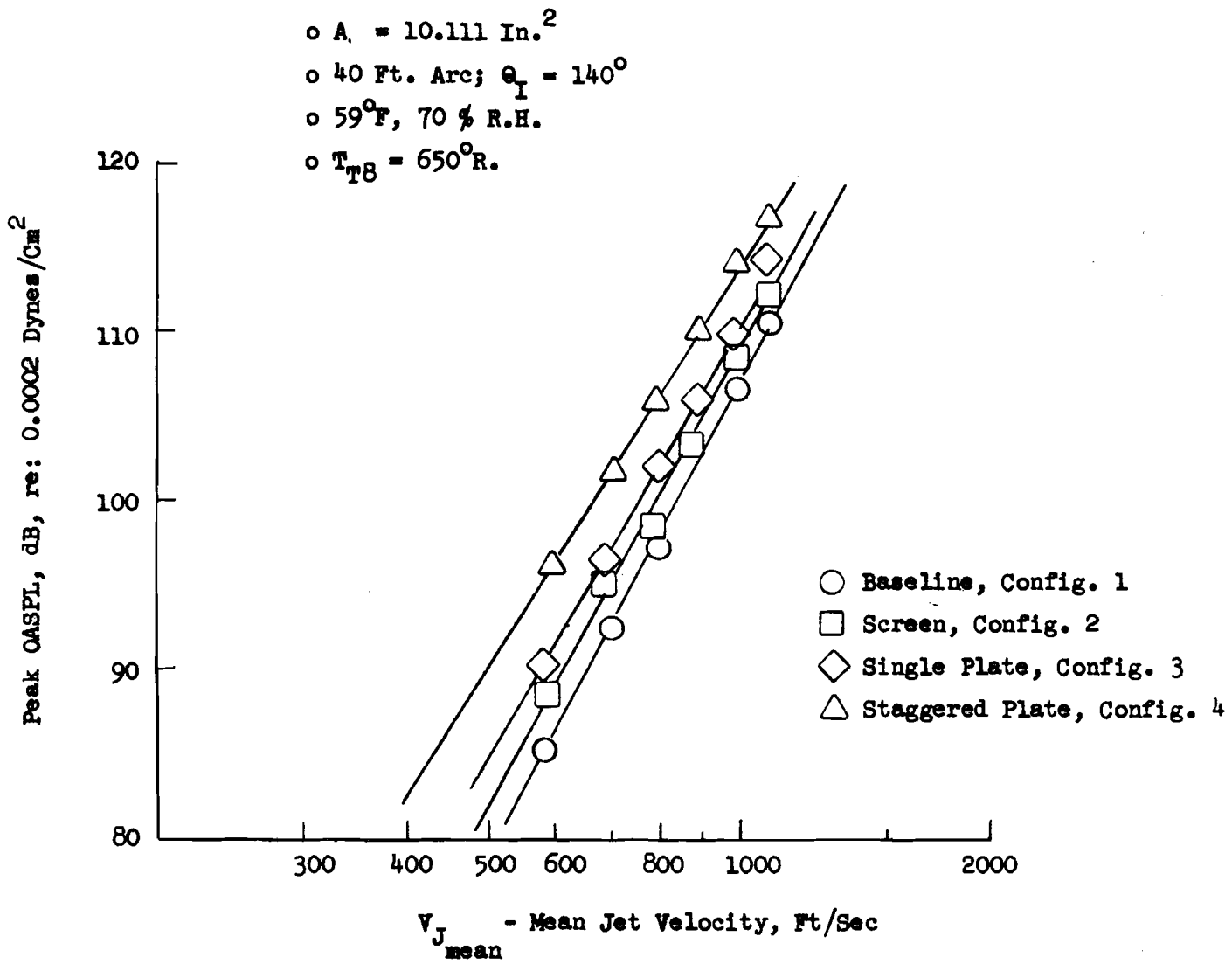

FIGURE 2.3.3-3 EFFECT OF TURBULENCE INTENSITY AS A FUNCTION OF JET VELOCITY

CORE ENGINE NOISE CONTROL - TEST II

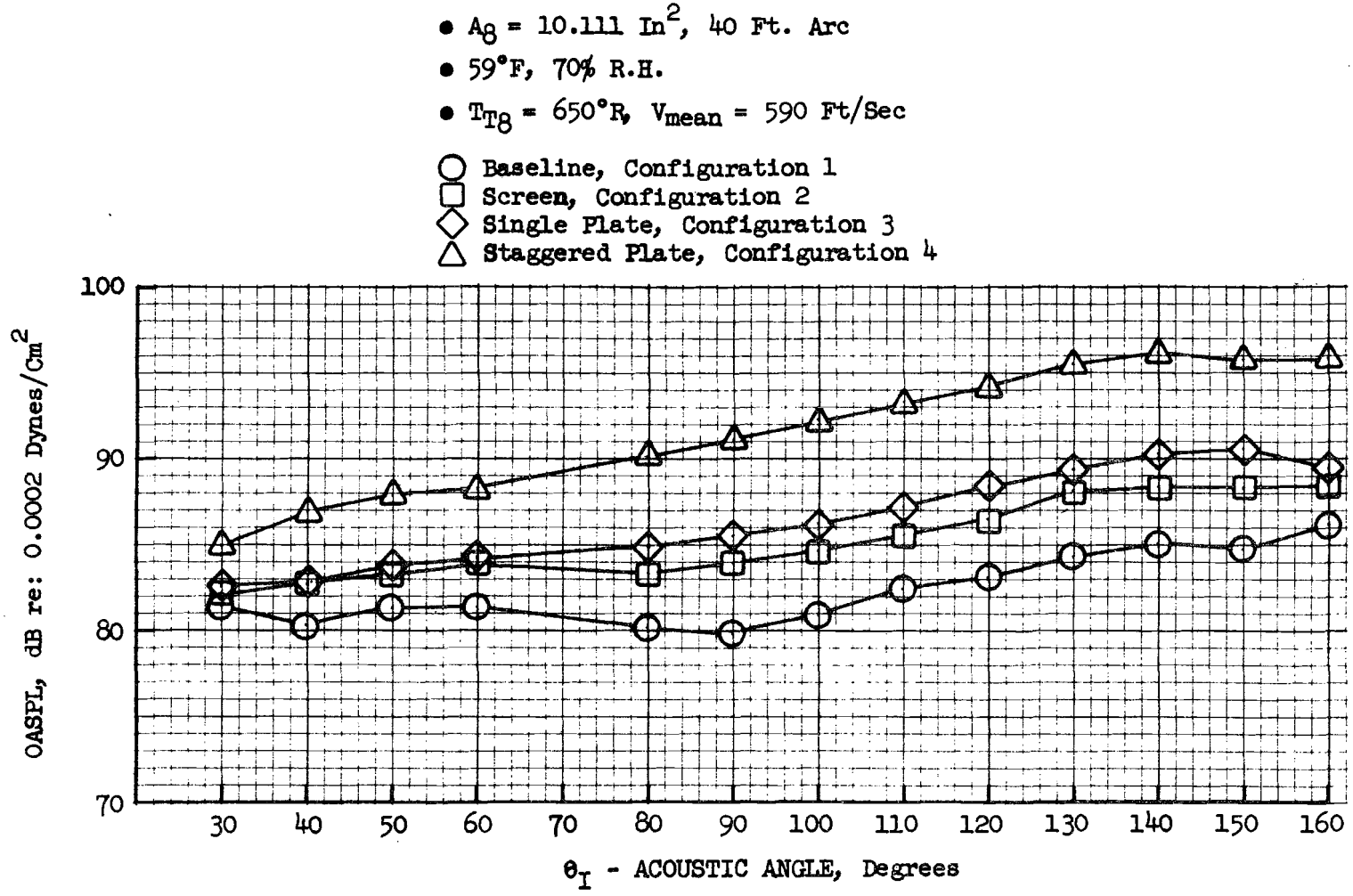

FIGURE 2.3.3-4 EFFECT OF TURBULENCE INTENSITY ON NOISE DIRECTIVITY PATTERNS, V_{MEAN} = 590 FT/SEC

CORE ENGINE NOISE CONTROL - TEST II

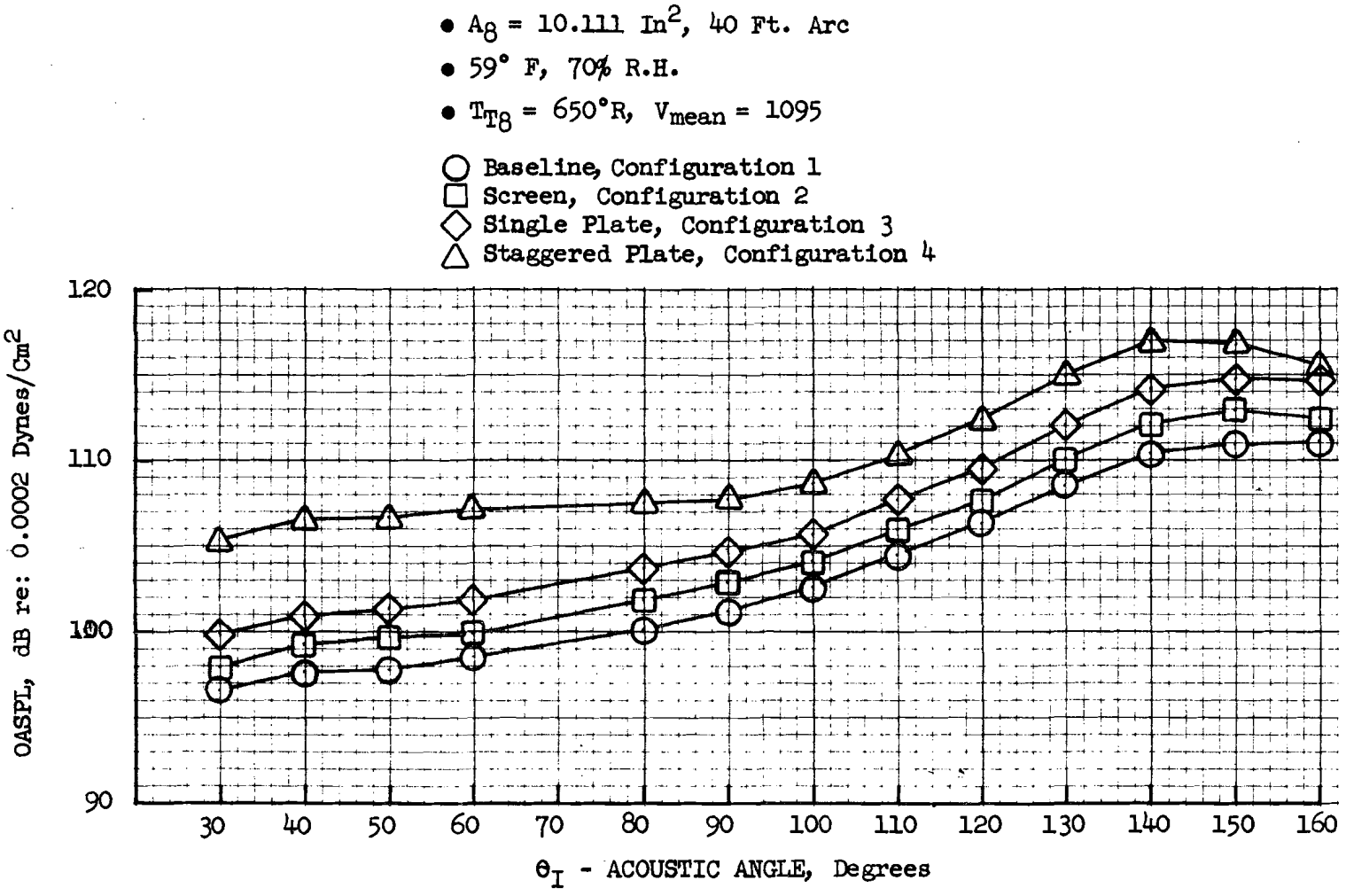

FIGURE 2.3.3-5 EFFECT OF TURBULENCE INTENSITY ON NOISE DIRECTIVITY PATTERNS, V_{MEAN} = 1095 FT/SEC

Up to this point, the acoustic results have been presented in terms of OASPL. In defining and understanding the mechanisms of noise generation, a spectral analysis was also considered. The effect of changing turbulence intensity level on peak angle spectrum shape is illustrated in Figures 2.3.3-6 and -7. Comparison of the high velocity spectra indicates that an increase in the turbulence intensity results in a uniform increase in SPL level across the entire spectrum. In contrast, at the low velocity point (590 ft/sec), the increase is 3-4 dB greater at high frequency than at low frequency. In analyzing this data, the data below 200 Hz was not considered, because on a scaled basis this data would not be used.

2.3.4 Conclusions

The analysis has shown that changes in the turbulence levels at the exhaust nozzle exit plane have a marked effect on the farfield noise signature of a conical nozzle. This effect is a function of jet velocity and acoustic angle. An increase in turbulence intensity level was found to result in an increase in the farfield level of a single flow system. This conclusion is also supported by the observation that a change in the turbulence intensity levels at the nozzle exit plane causes a change in the turbulence levels in the exhaust plume of the nozzle.

CORE ENGINE NOISE CONTROL - TEST II

- A_8 = 10.111 In^2
- 40 Ft. Arc
- 59°F, 70% R.H.
- T_{T8} = 650°R
- V_{mean} = 590 Ft/Sec, θ_I = 140°

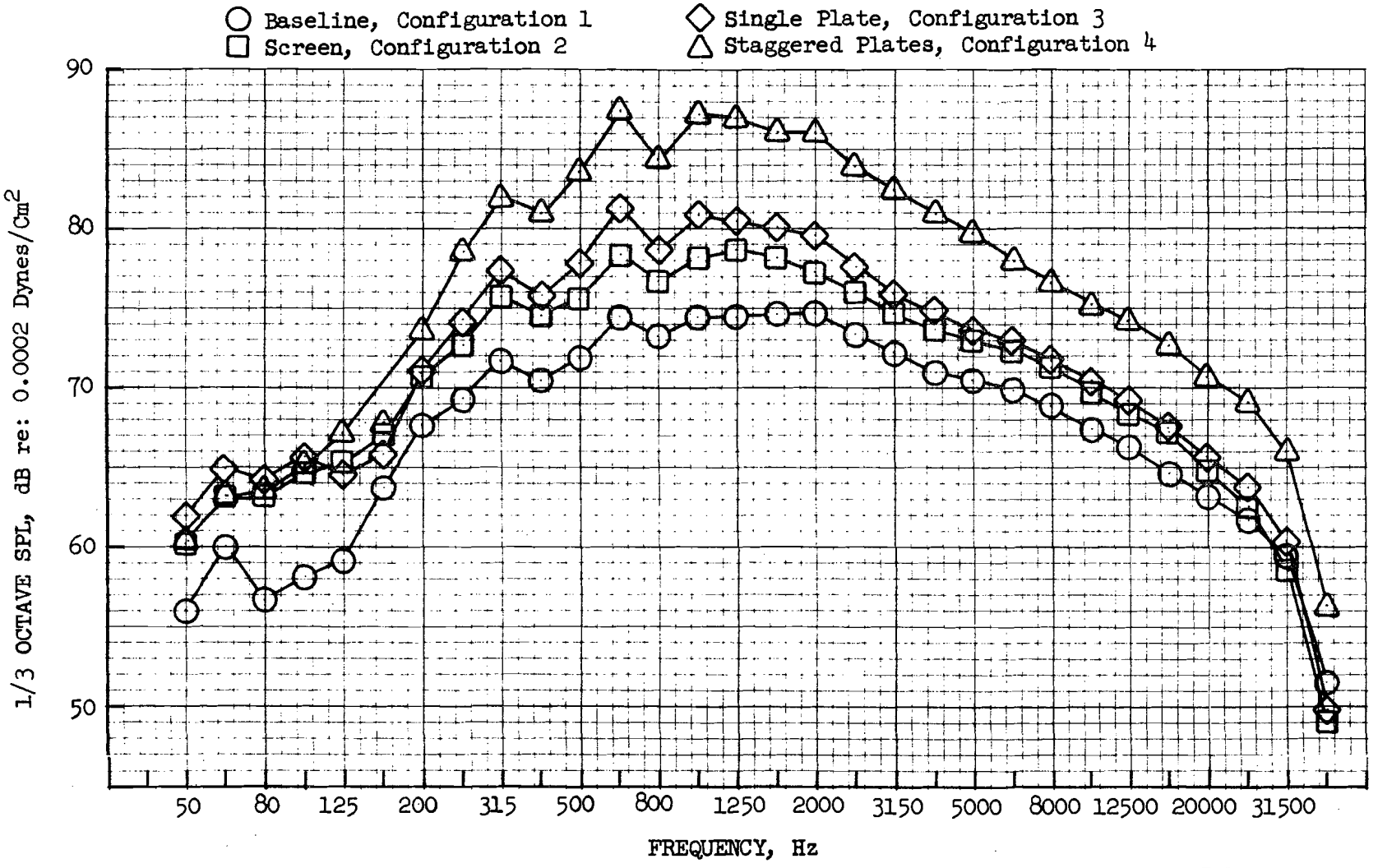

FIGURE 2.3.3-6 EFFECT OF TURBULENCE INTENSITY CHANGES ON PEAK ANGLE NOISE SPECTRA

CORE ENGINE NOISE CONTROL - TEST II

- A_8 = 10.111 In^2
- 40 Ft. Arc
- 59°F, 70% R.H.
- T_{T8} = 650°R

V_{mean} = 1095 Ft/Sec, θ_I = 140°

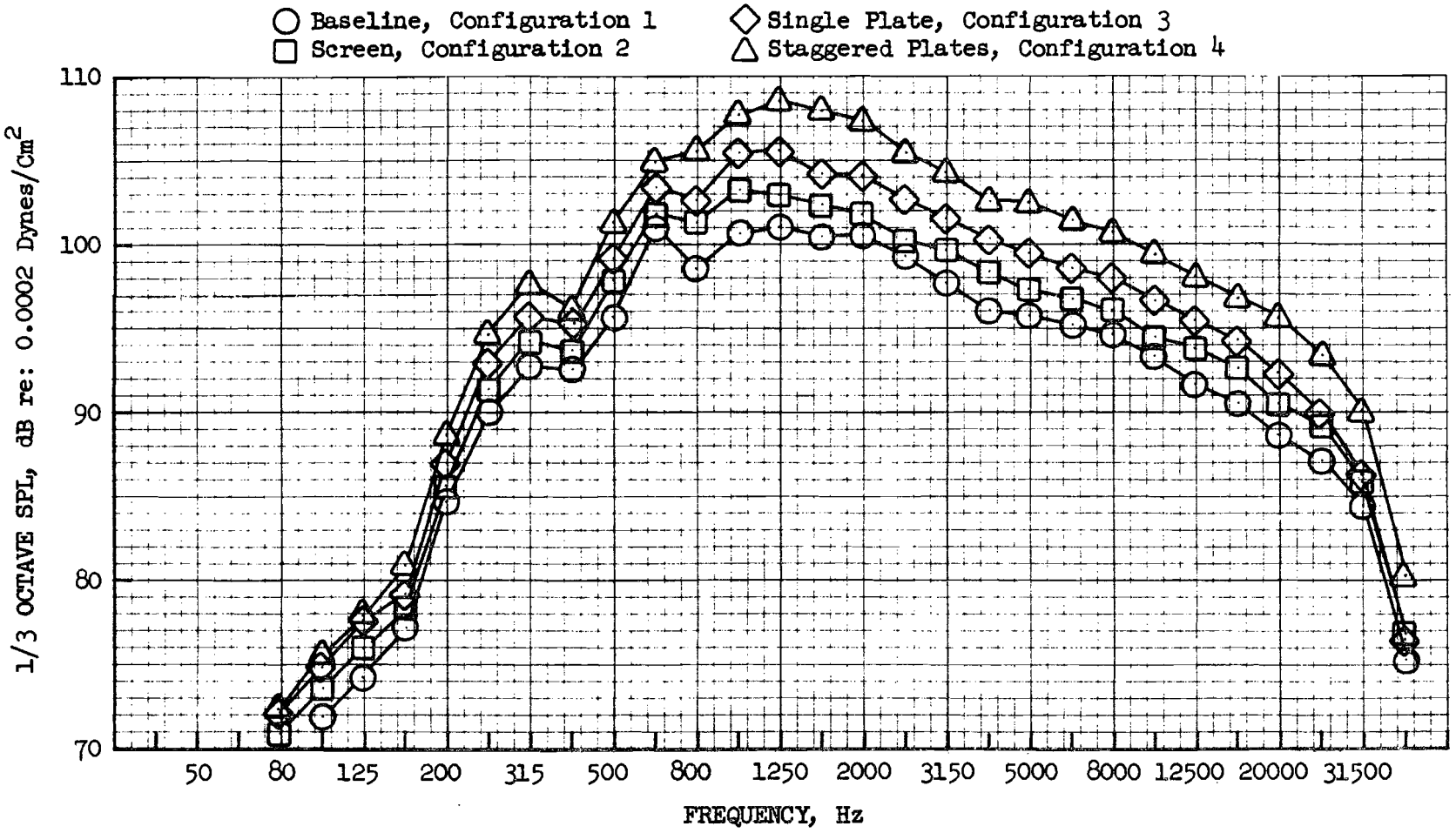

FIGURE 2.3.3-7 EFFECT OF TURBULENCE INTENSITY CHANGES ON PEAK ANGLE NOISE SPECTRA, V_J = 1095 FT/SEC

2.4 SUPPRESSOR TESTS

2.4.1 Objectives

- To examine existing single jet suppressor data and determine which configurations are compatible with the coannular flow environment.
- Test promising core suppressor configurations and determine their aero-acoustic characteristics.

2.4.2 Hardware Selection - Suppressor Configurations

In Section 2.2 the acoustic characteristics of coannular flow systems were determined. It was found that as the secondary flow velocity was increased in relation to a given primary jet velocity, an initial attenuation of the high frequency jet noise occurred. On further increasing the secondary jet velocity above a velocity ratio of about 0.75, the jet noise was in excess of that of the primary jet alone. The initial attenuation was found, on a spectral basis, to be due to large reductions of high frequency sound accompanied by small increases at the low frequency end of the spectrum (see Figure 2.4.2-1). It was hypothesized that the noise reduction associated with coaxial jets could be increased by designing core nozzle suppressors which promote more rapid mixing. The multi-lobe, the multi-tube, and the multi-spoke suppressor configurations are capable of providing mixing for single jets as summarized in Figure 2.4.2-2. The trends suggest that, for low velocity, the classical single flow suppressors provide little suppression. Test results from low area ratio (annulus area/core area) multi-element core jet suppressors (Figure 2.4.2-3) indicate a trend of increasing suppression with increasing number of elements. A low element number suppressor, however, has less mechanical complexity, less weight and will suffer fewer drag losses than a high element number design. Examination of the peak angle spectra in Figure 2.4.2-4 suggests that even though the single jet suppression is small, low element number core suppressors might be practical for coannular systems if the observed fan flow interaction effect continues to decrease high frequency noise.

Several types of suppressors were designed and built with the object of achieving the desired acoustic performance. An initial baseline configuration was also built and is shown in Figure 2.4.2-5. The configuration was chosen to simulate the geometry of a typical high bypass ratio turbofan engine with the fan nozzle exit plane located forward of the core nozzle exit plane to give a separate flow system. In this design the fan flow passes over the core waist cowl before interacting with the core flow. The initial suppressors evaluated were the multi-element type, 18 lobe daisy suppressors; one with an annulus area-to-core flow area of 2 and the other with an annulus area-to-core flow area of 4.8. This particular work was supported by Independent Research and Development but is reported here for completeness. Schematics of the two configurations are shown in Figures 2.4.2-6 and 2.4.2-7. Following initial testing, a design modification was instituted on the AR=2 multi-element configuration whereby the waist cowl contour was smoothed out by brazing metal caps in the lobe region (the flow of the fan air between the lobes remained unaltered). This configuration is shown in Figure 2.4.2-8. This modified suppressor was

SUPPRESSION EFFECTS
DUE TO FAN FLOW ON CORE NOZZLE OPERATION
• 200 FT. SIDELINE (61 m)

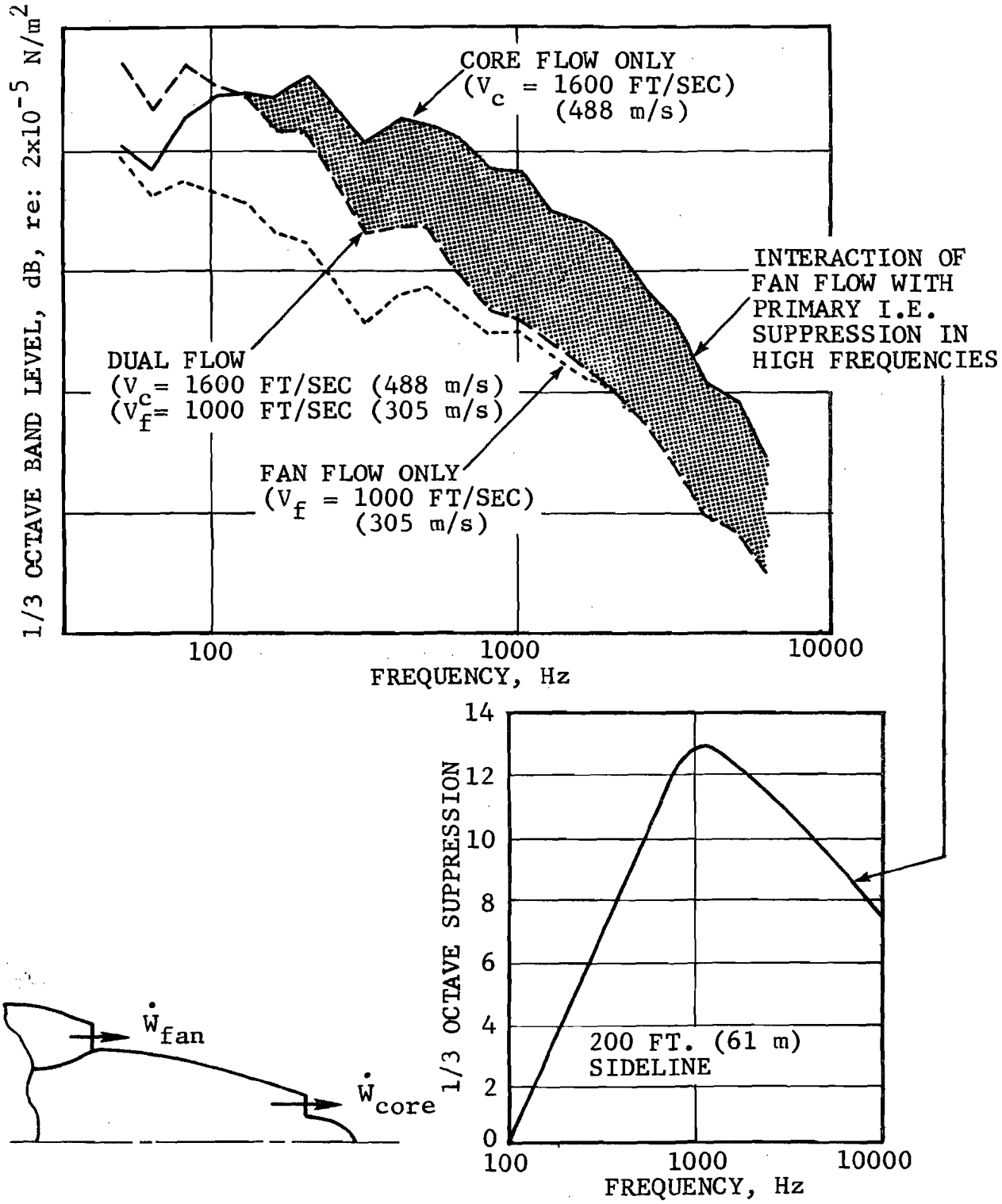

FIGURE 2.4.2-1 ACOUSTICAL CHARACTERISTICS OF UNSUPPRESSED COANNULAR NOZZLES

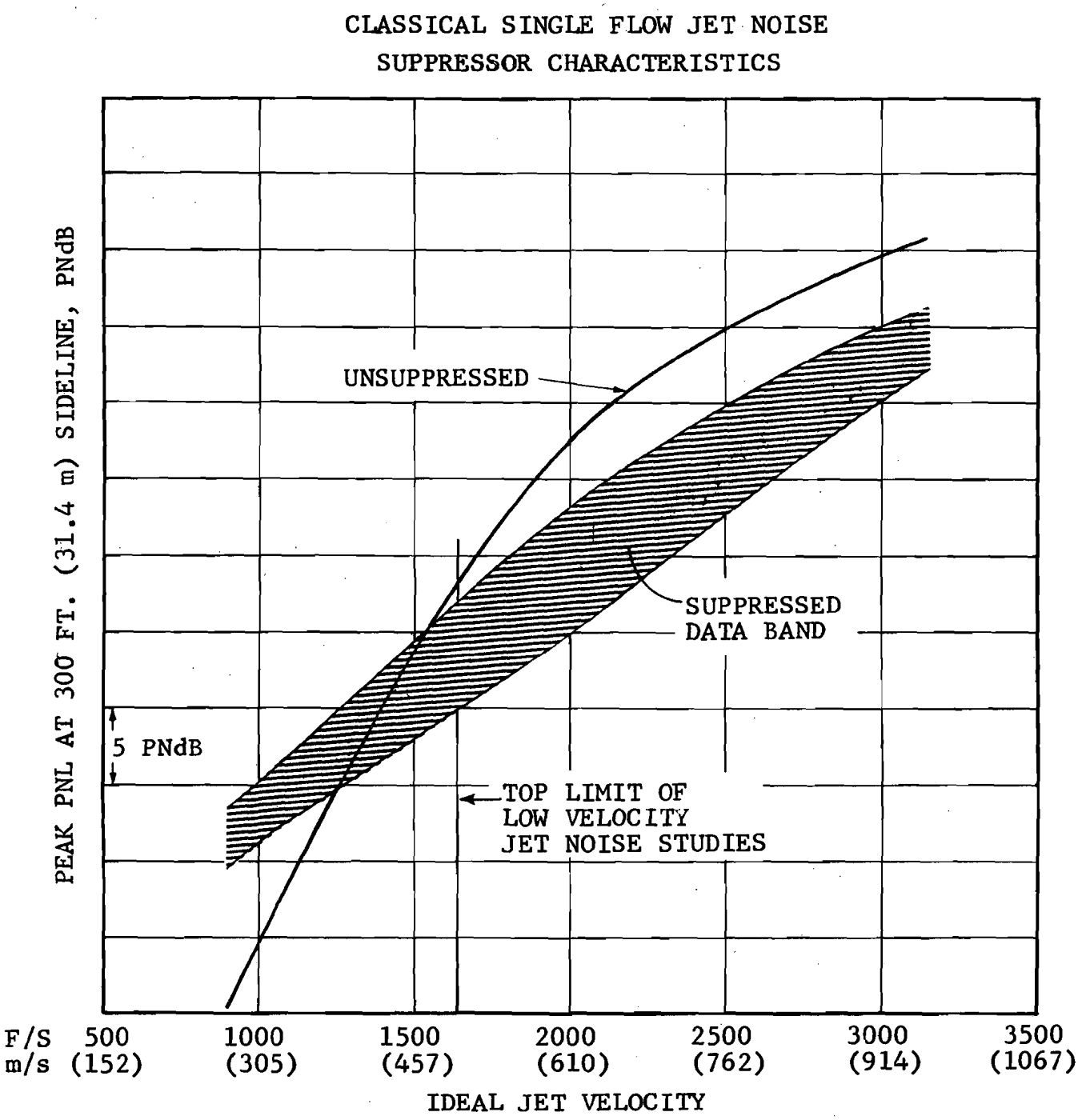

FIGURE 2.4.2-2 SUPPRESSION CHARACTERISTICS OF SINGLE FLOW MULTI-ELEMENT NOZZLES

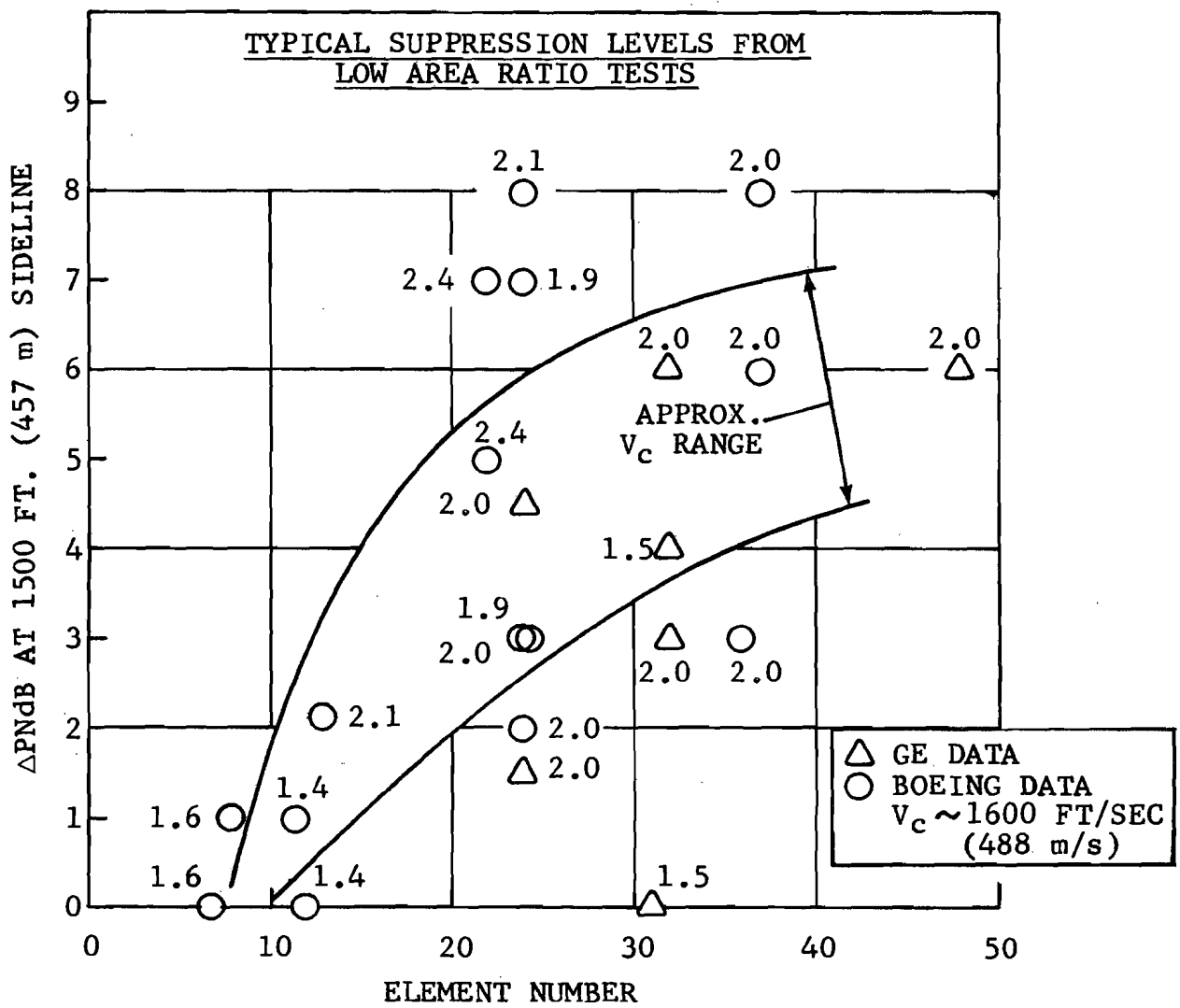

FIGURE 2.4.2-3 SUPPRESSION VS ELEMENT NUMBER FOR SINGLE FLOW SUPPRESSORS

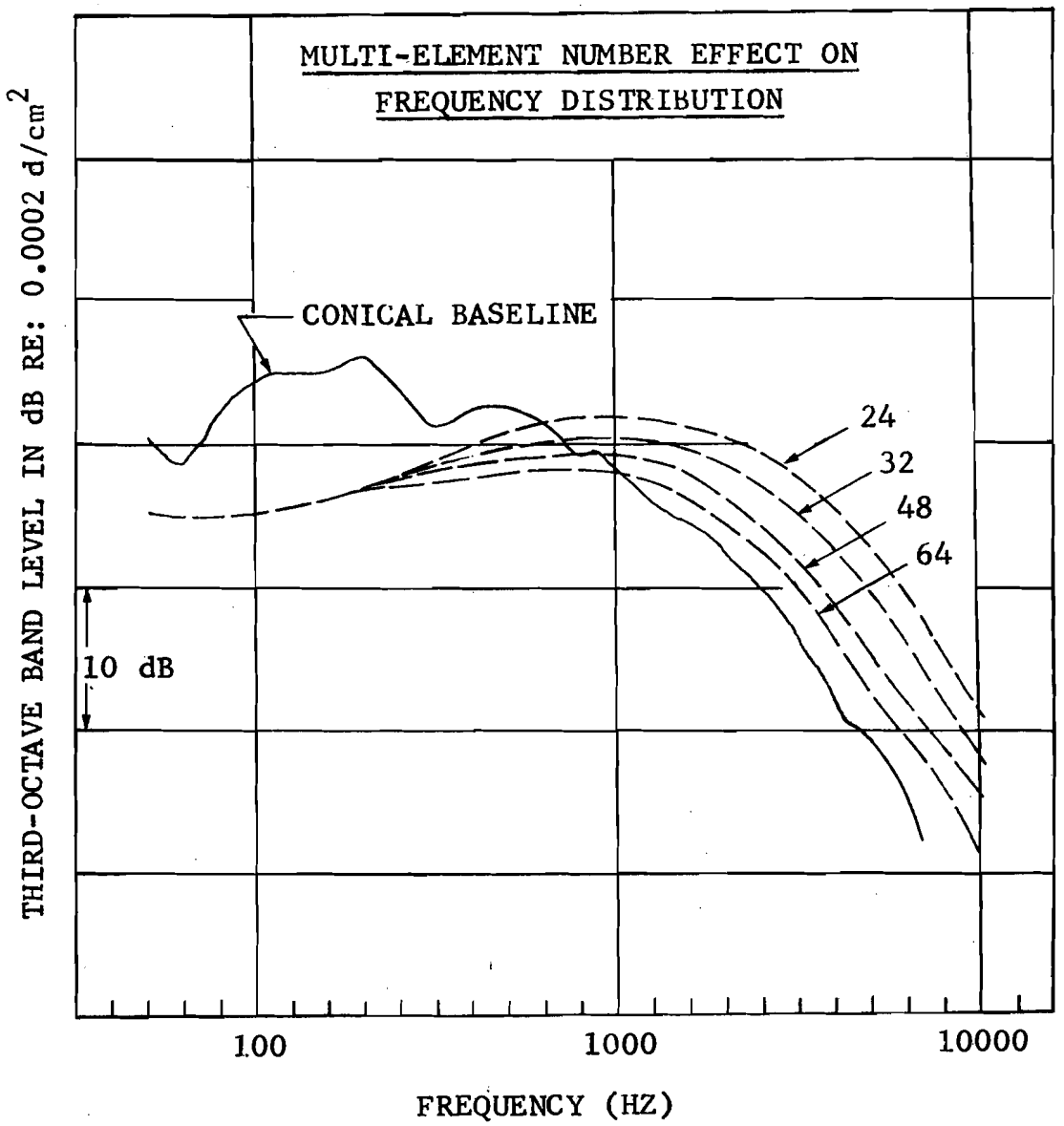

FIGURE 2.4.2-4 SPECTRAL CHARACTERISTICS OF MULTI-ELEMENT SINGLE FLOW SUPPRESSORS

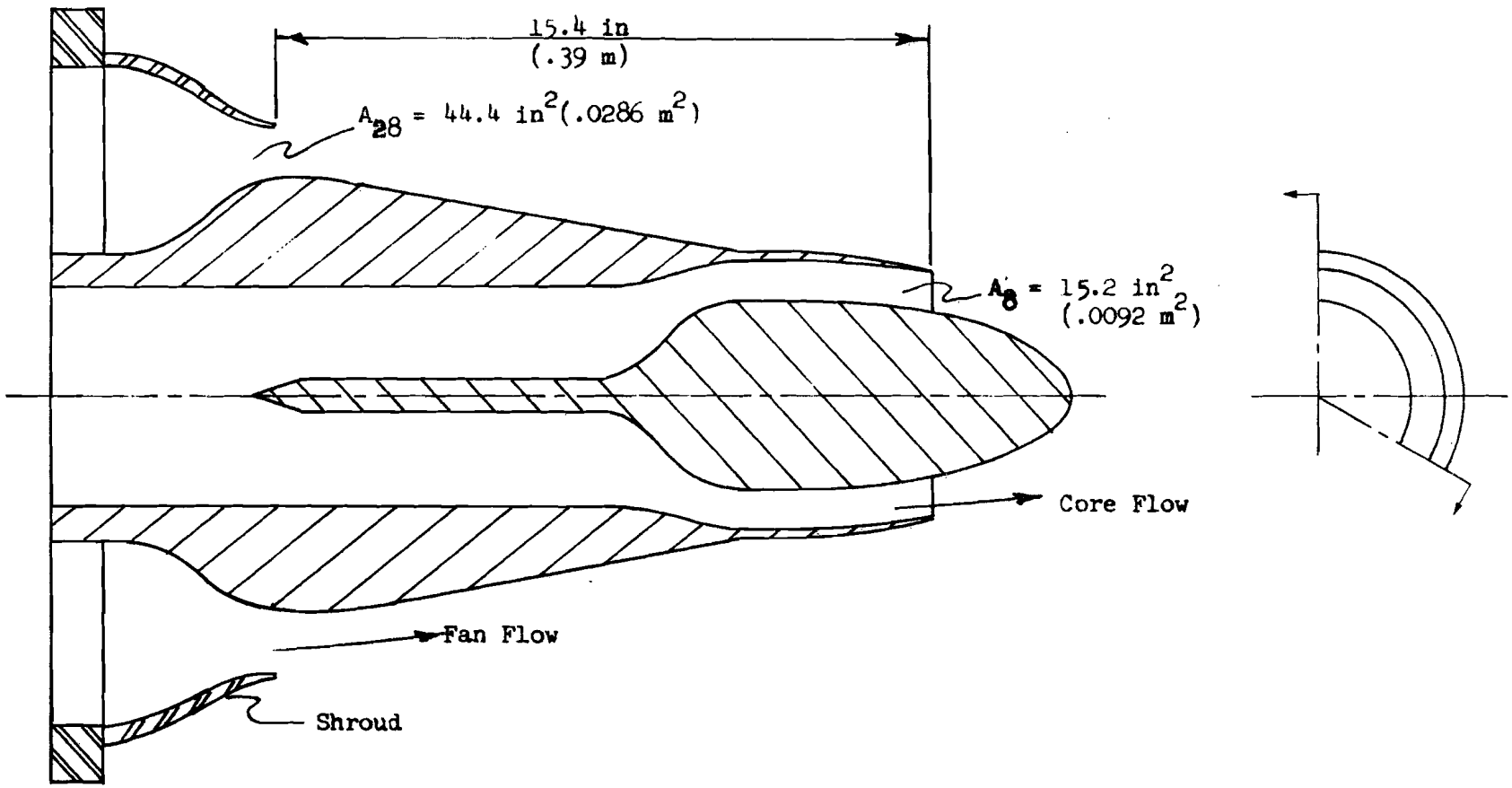

FIGURE 2.4.2 -5 CONFIGURATION 1 - BASELINE I USED IN SUPPRESSOR TEST

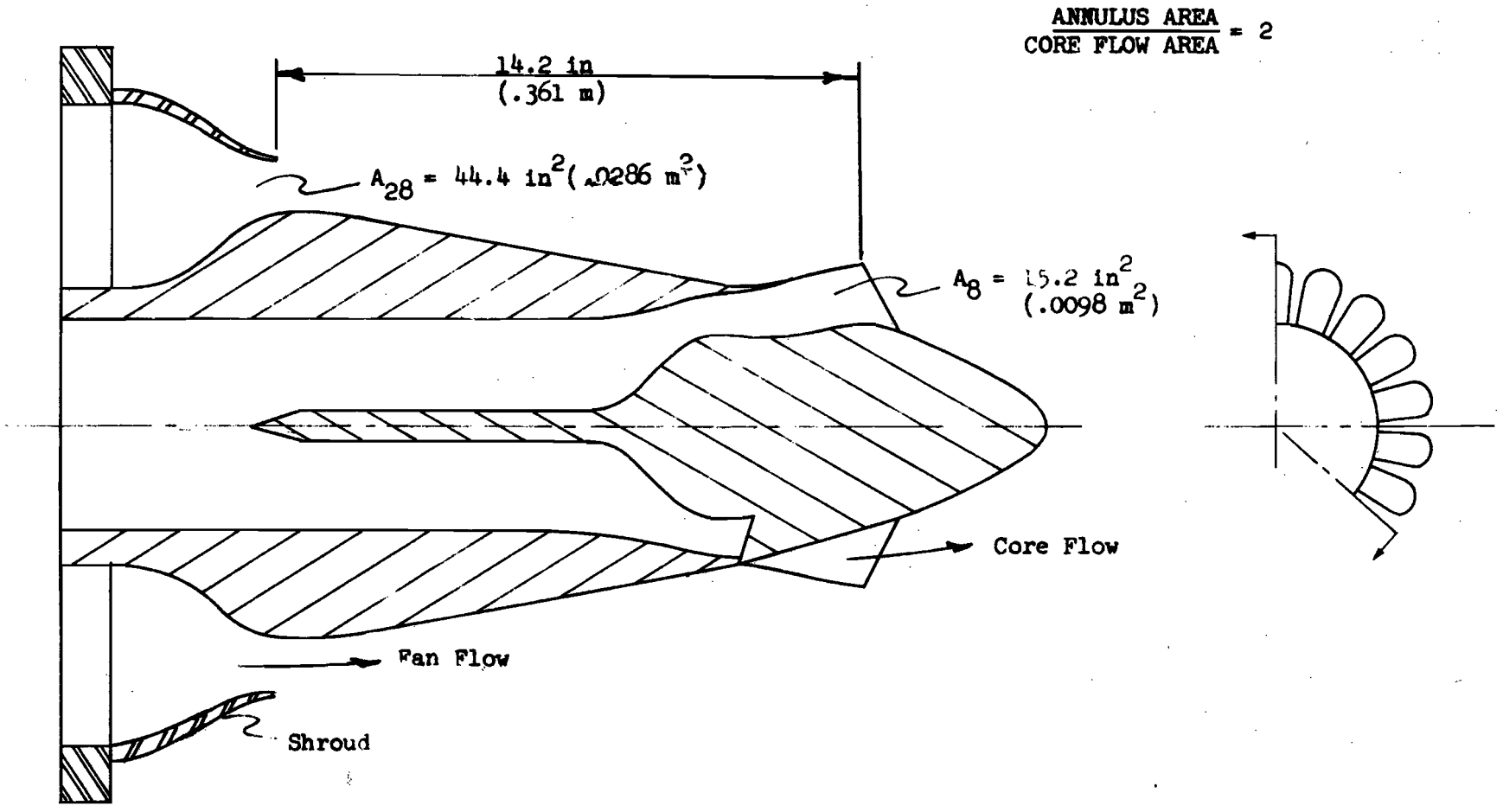

FIGURE 2.4.2 - 6 CONFIGURATION 2 - 18 LOBE CORE NOZZLE SUPPRESSOR AR = 2

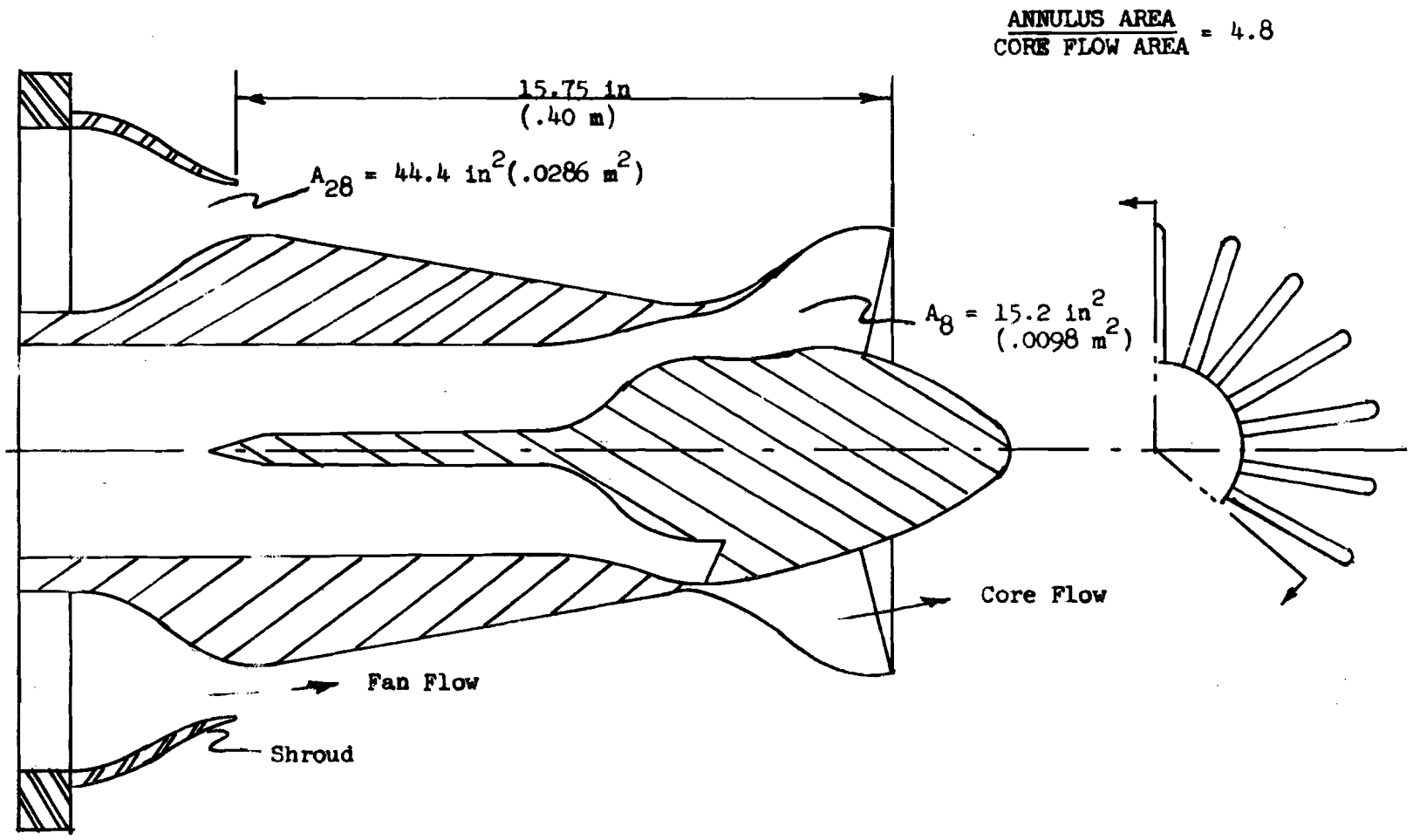

FIGURE 2.4.2 - 7 CONFIGURATION 3 - 18 LOBE CORE NOZZLE SUPPRESSOR AR = 4.8

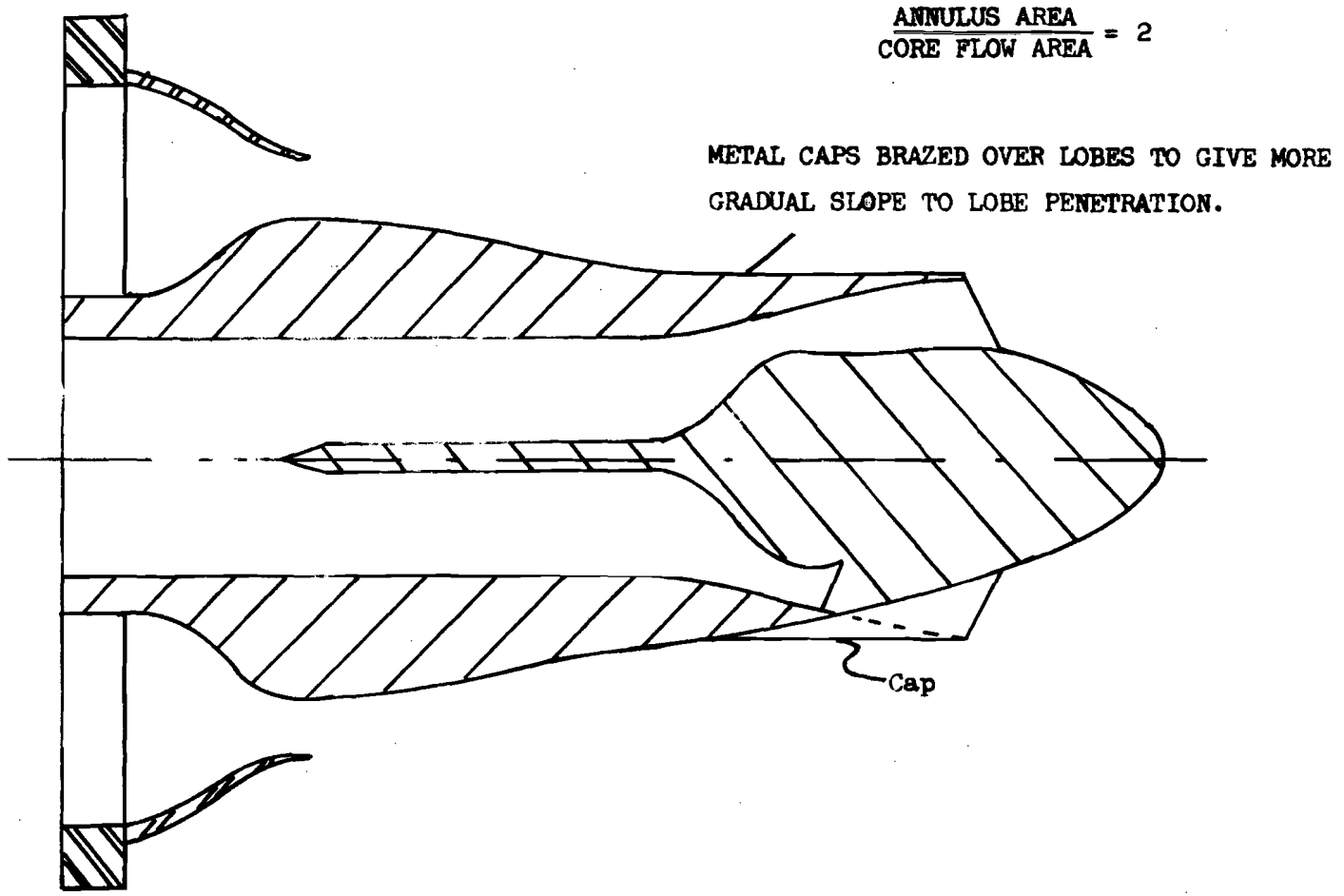

FIGURE 2.4.2 - 8 CONFIGURATION 4 - 18 "CAPPED" LOBE CORE NOZZLE SUPPRESSOR

also tested with a coplanar fan shroud (see Figure 2.4.2-9). Photographs of the above configurations are shown in Figures 2.4.2-10 to 2.4.2-12. The modification to the multi-lobe AR=2 suppressor consisted of an initial phase whereby the required contour was determined by applying clay to the lobes. This yielded the shape from which the metal caps were constructed as shown in Figure 2.4.2-13.

Additional test configurations were designed based upon the information obtained from these initial tests. A new reference nozzle, Baseline II, was constructed with a smoother, more accurate waist cowl geometry as is shown in Figure 2.4.2-14. The designs were comprised of easily assembled components. Figure 2.4.2-15 shows a photograph of the 24 hole core nozzle components. The assembly is shown in Figure 2.4.2-16. The final configuration, a 24 spoke nozzle is shown mounted on the coannular plenum in Figure 2.4.2-17. The dimensions of the configurations are given in Figures 2.4.2-18 to 2.4.2-20. Each model has an annulus area-to-core flow area of 2, and a secondary flow area-to-core flow area of 2.55.

2.4.3 Test program

Farfield acoustic measurements and aero-thermo data were recorded for the configurations previously described. The core flow noise and fan flow noise were measured independently, then together as a dual flow system. The independent variables were core and fan flow velocities. The core velocity ranged from 500 ft/sec (152 m/s) to 1600 ft/sec (488 m/s).

The test matrix for Suppressor Test 1 is outlined in Table 2.4.3-1. This test was comprised of Baseline I, the 18 uncapped lobes core suppressor AR=2, and 18 lobe core suppressor AR=4.8. The objective of the test matrix was to simulate the cycle parameters of a typical advanced technology turbofan engine from the approach power setting up to takeoff power conditions. The test matrix for Suppressor Test 2 is described in Table 2.4.3-2. This test consisted of the capped lobe suppressor in separate and coplanar configurations. Table 2.4.3-3 shows the test matrix for Suppressor Test 3. The configurations tested were Baseline II, the 24 hole core suppressor and the 24 spoke core suppressor. The aerodynamic data measured during the tests are tabulated in Appendix C. The data was scaled by a factor of 7.5 to represent engines in the 40000 lb (177.9×10^6N) thrust class. The acoustic data was scaled by the same factor and therefore represents full scale.

2.4.4 Test Results -Suppressor Test 1

The OASPL directional characteristics of the three configurations were compared at a farfield distance of 200 ft (61 m) sideline. Instrumentation difficulties prevented data processing of signals from microphones located forward of 100° (Figure 2.4.4-1) when the AR 4.8 core suppressor was being tested with core flow only; however, sufficient information was available to show that this suppressor provided some noise reduction at the extreme aft angles. In contrast, the AR 2 configuration increased the levels of the core jet. As the core jet velocity was increased from 660 ft/sec (201 m/s) to 1600 ft/sec (488 m/s) the effectiveness of both suppressors improved, as shown in

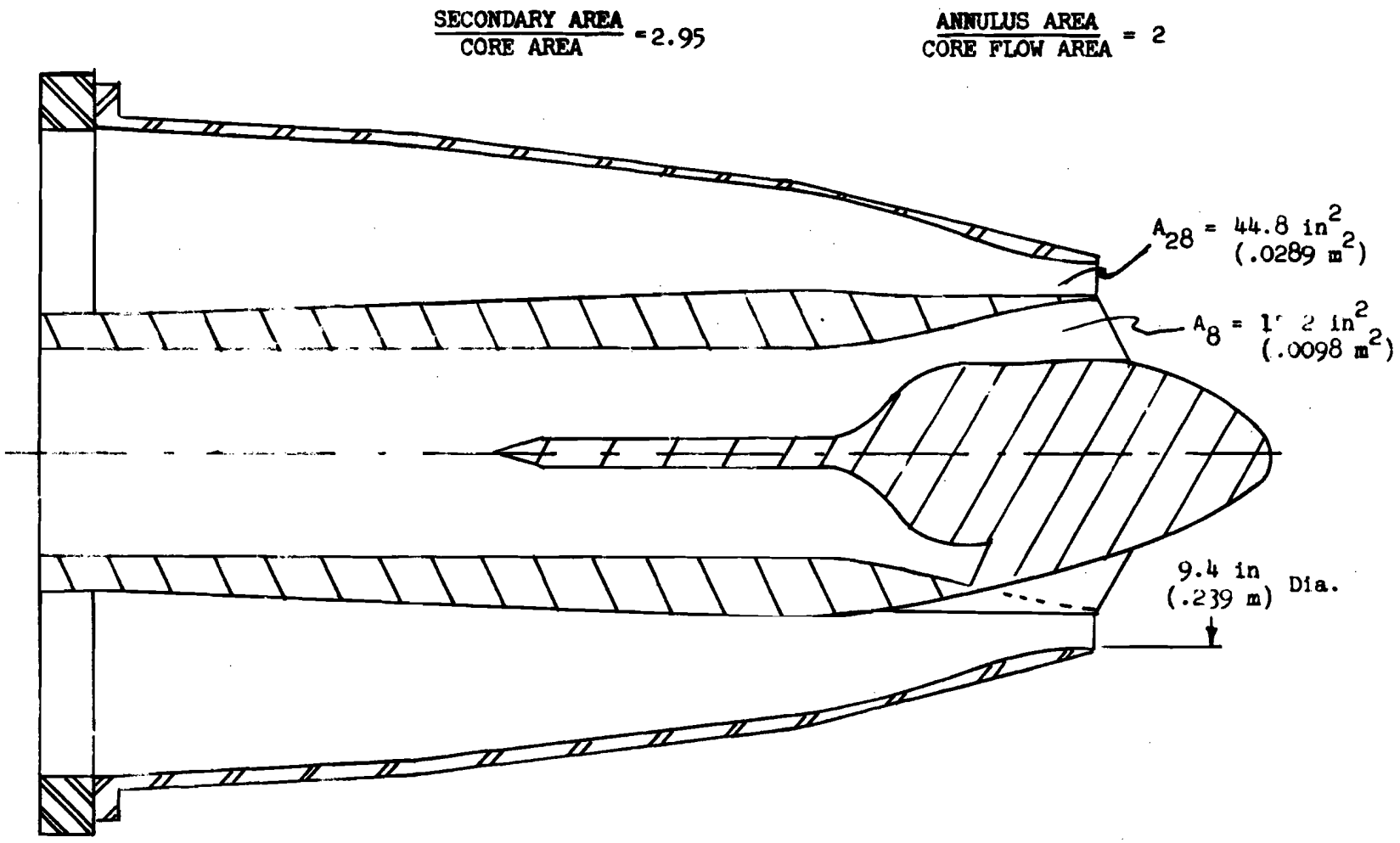

FIGURE 2.4.2 - 9 CONFIGURATION 5 - 18 "CAPPED" LOBE CORE NOZZLE SUPPRESSOR WITH COPLANAR SHROUD

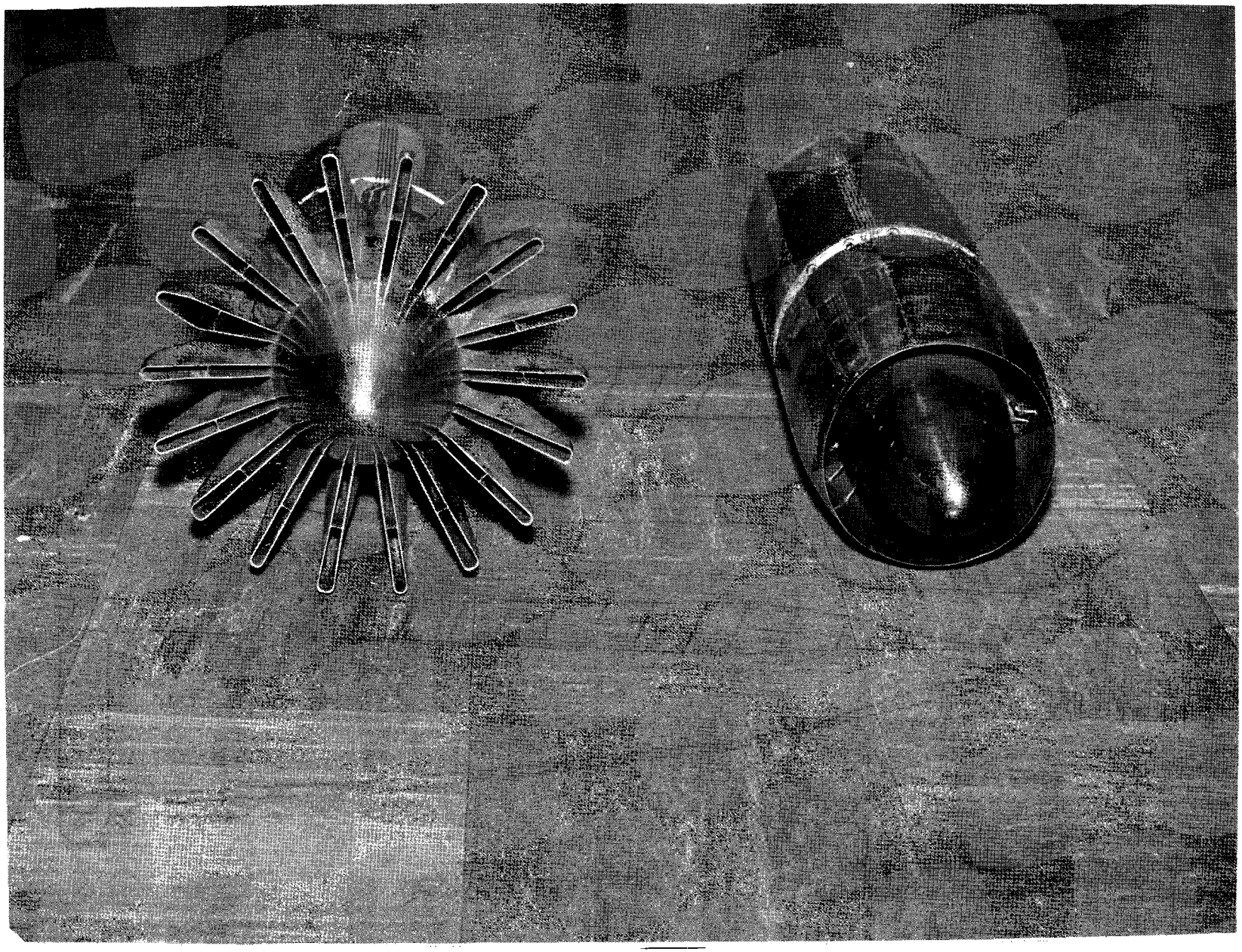

FIGURE 2.4.2-10 LOW VELOCITY JET NOISE EXPERIMENTAL INVESTIGATION. 18-LOBE DAISY-TYPE CORE SUPPRESSOR, ANNULUS-TO-ACTUAL FLOW AREA RATIO = 4.8, BASELINE CORE NOZZLE

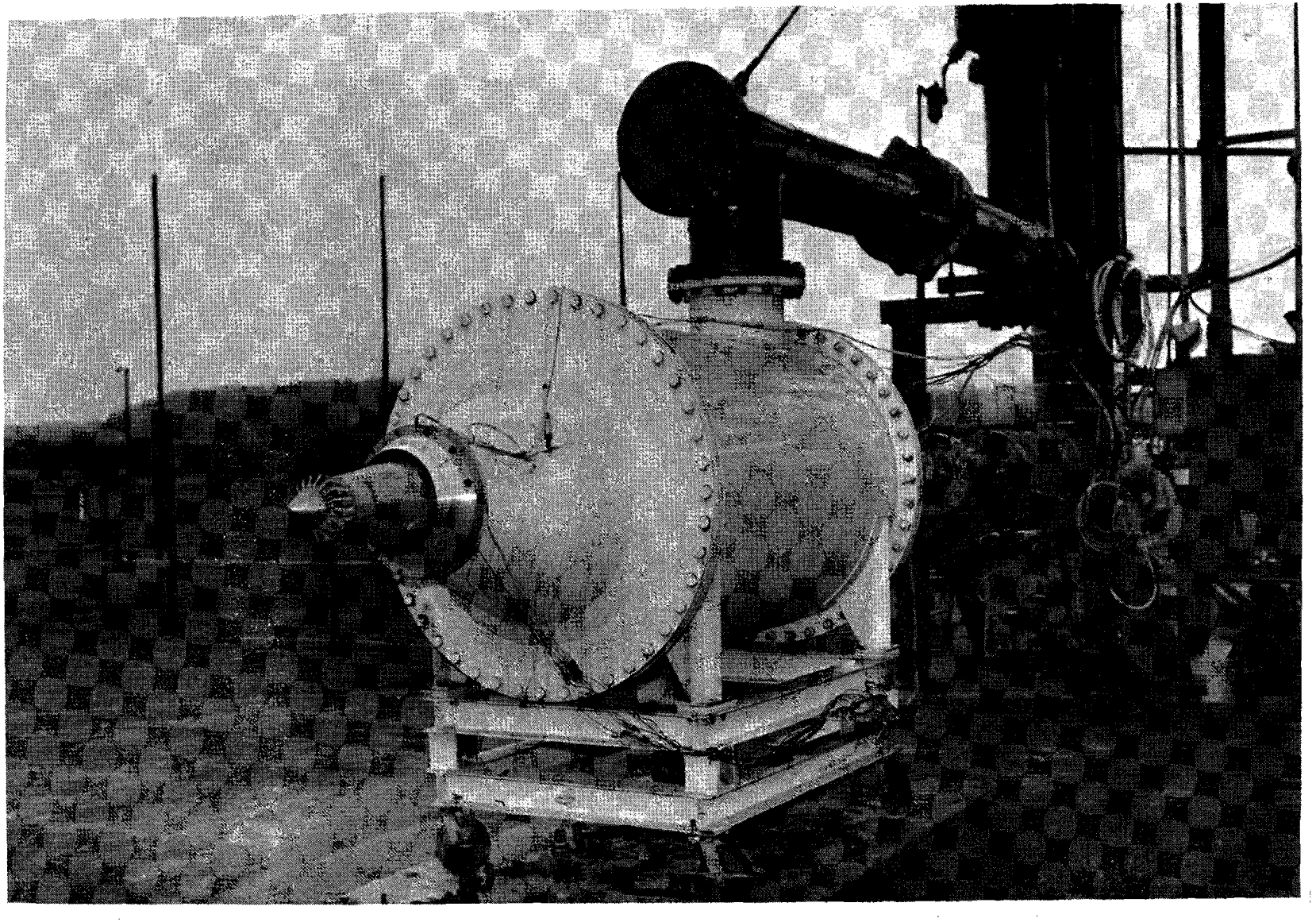

FIGURE 2.4.2-11 LOW VELOCITY JET NOISE EXPERIMENTAL INVESTIGATION. MULTI-ELEMENT NOZZLE TEST, 18-LOBE DAISY-TYPE CORE SUPPRESSOR ANNULUS AREA -TO-FLOW AREA RATIO = 2, CONNECTED TO TREATED PLENUM CHAMBER AT JENOTS

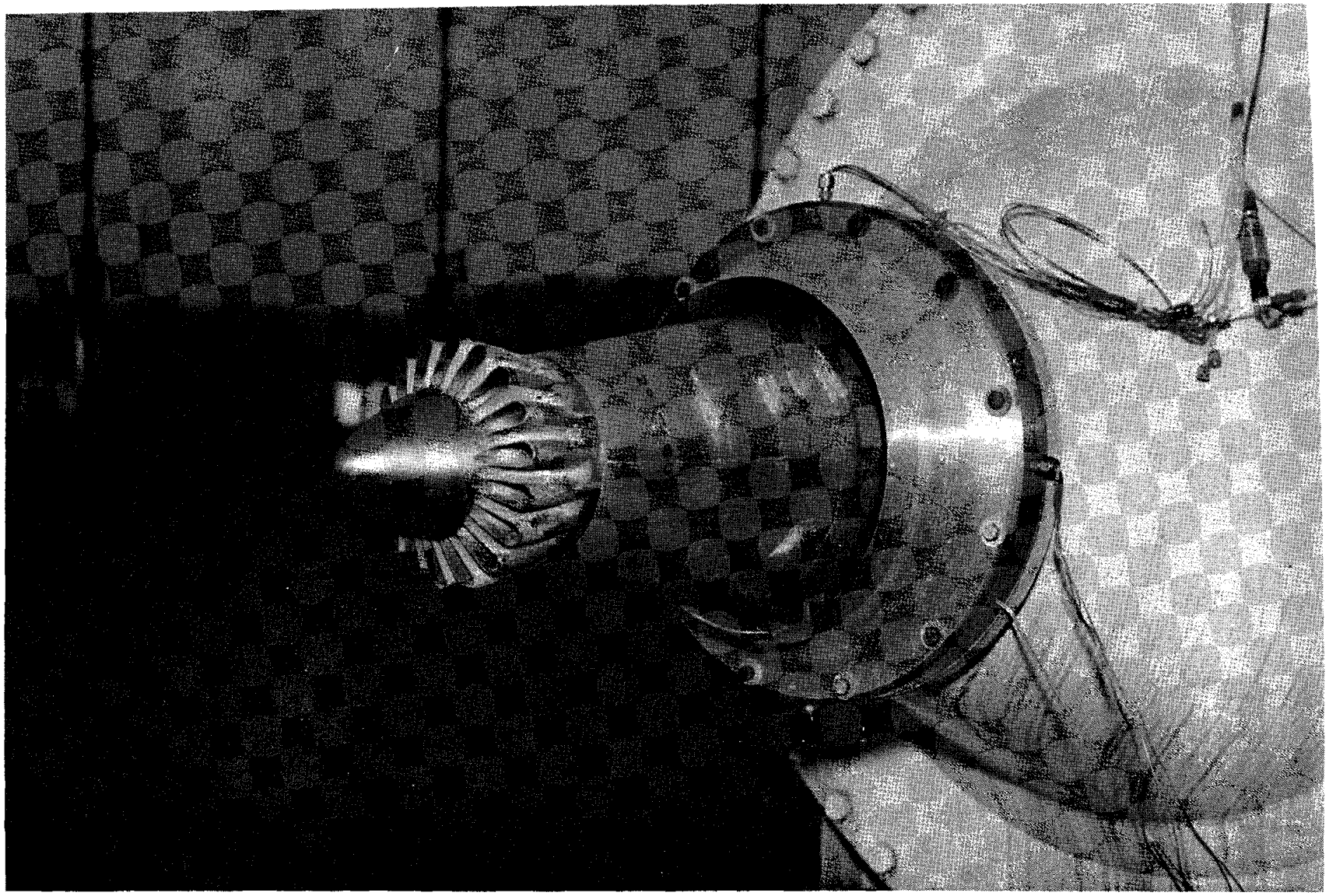

FIGURE 2.4.2-12 UNCAPPED 18-LOBE CORE SUPPRESSOR CONFIGURATION, AR = 2; LOBES PENETRATE ABRUPTLY INTO SECONDARY FLOW REGION

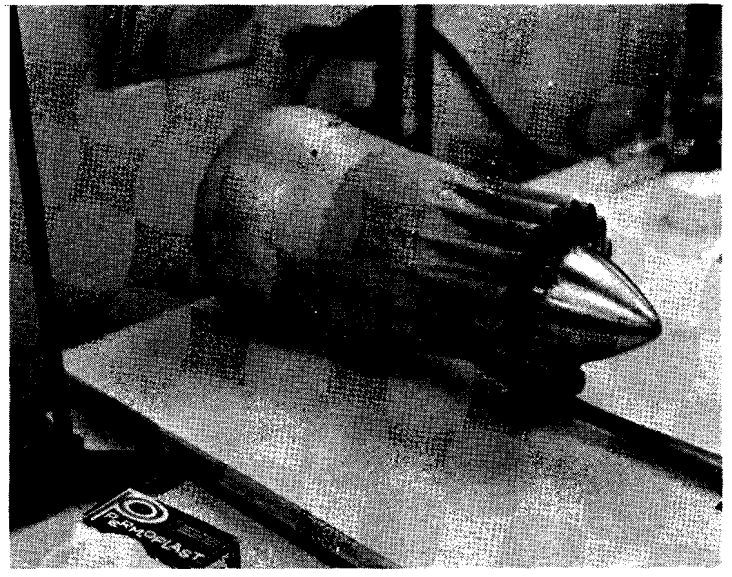

FIGURE 2.4.2-13 LOW VELOCITY SUPPRESSOR TEST, MODIFICATION 18-LOBE AR = 2 SUPPRESSOR

LOW VELOCITY JET NOISE SUPPRESSOR

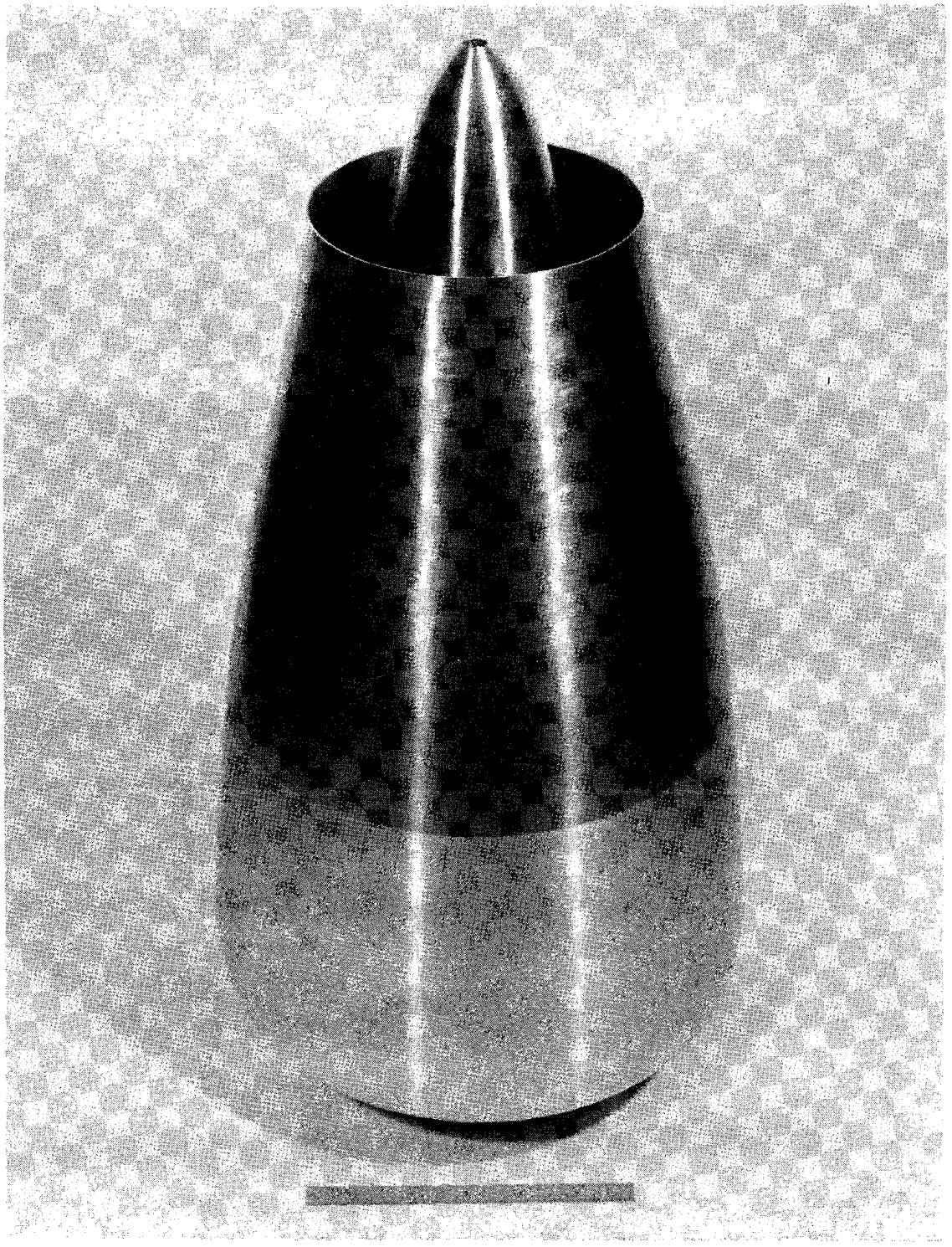

BASELINE CORE NOZZLE ASSEMBLY

FIGURE 2.4.2-14

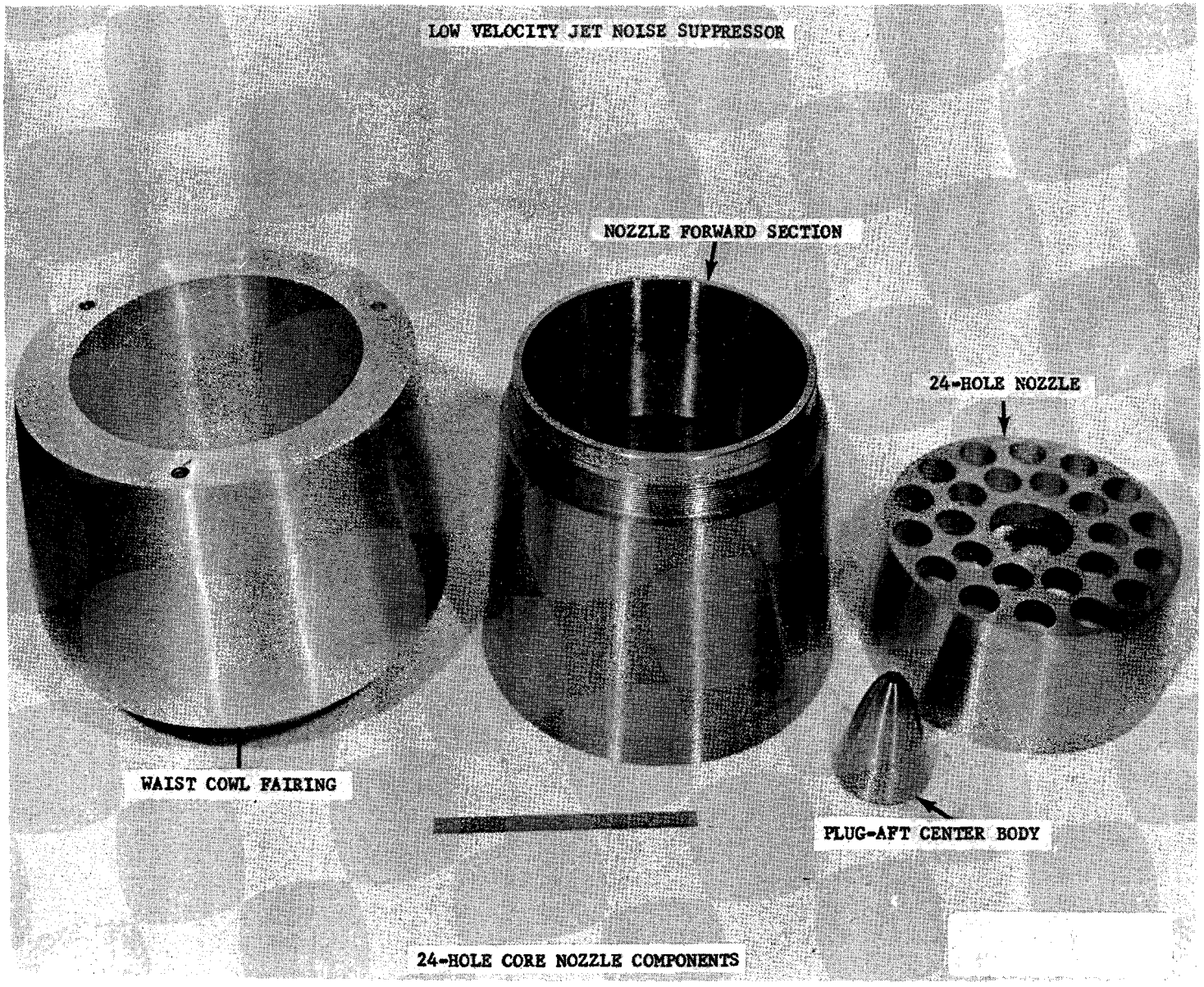

FIGURE 2.4.2-15

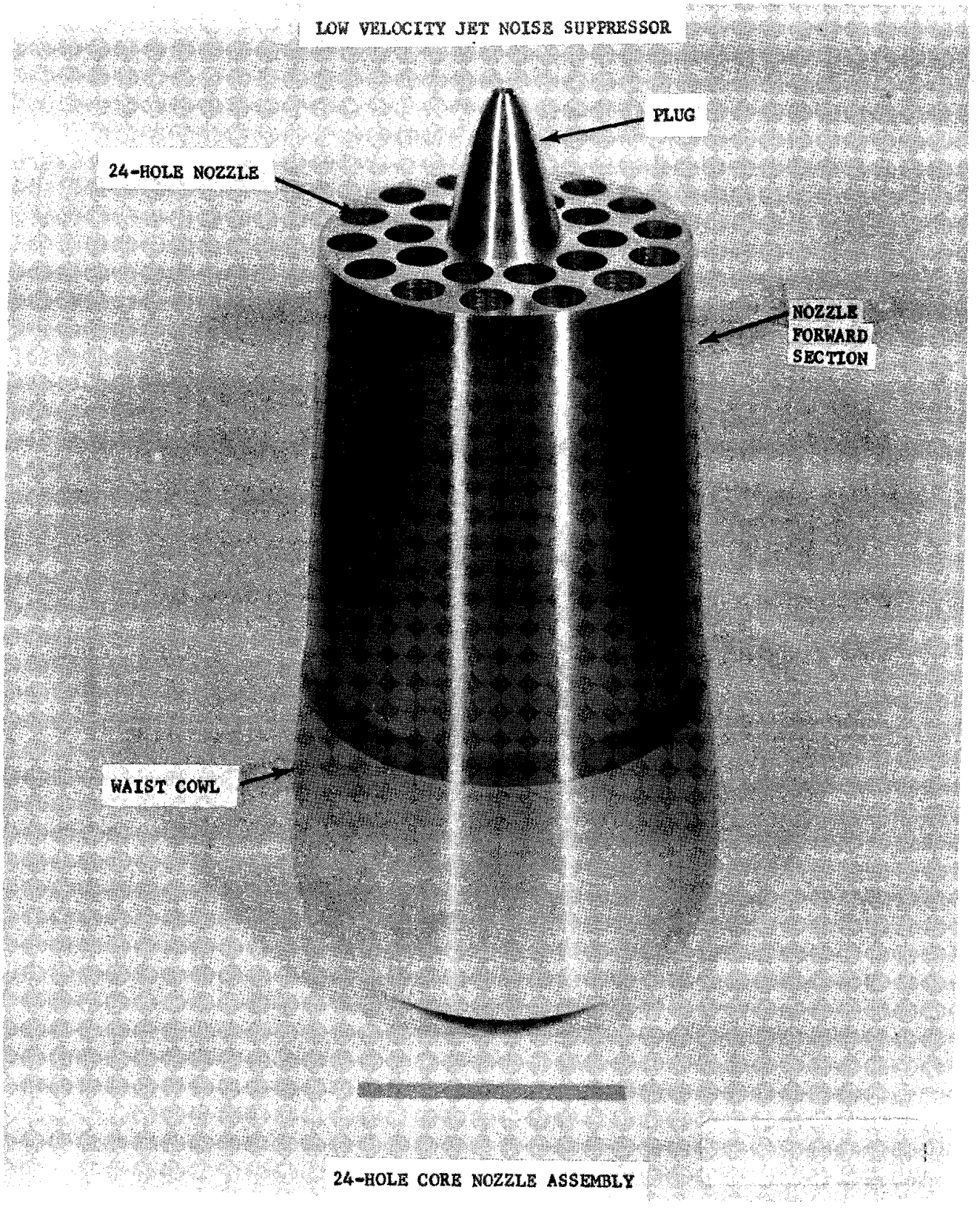

FIGURE 2.4.2-16

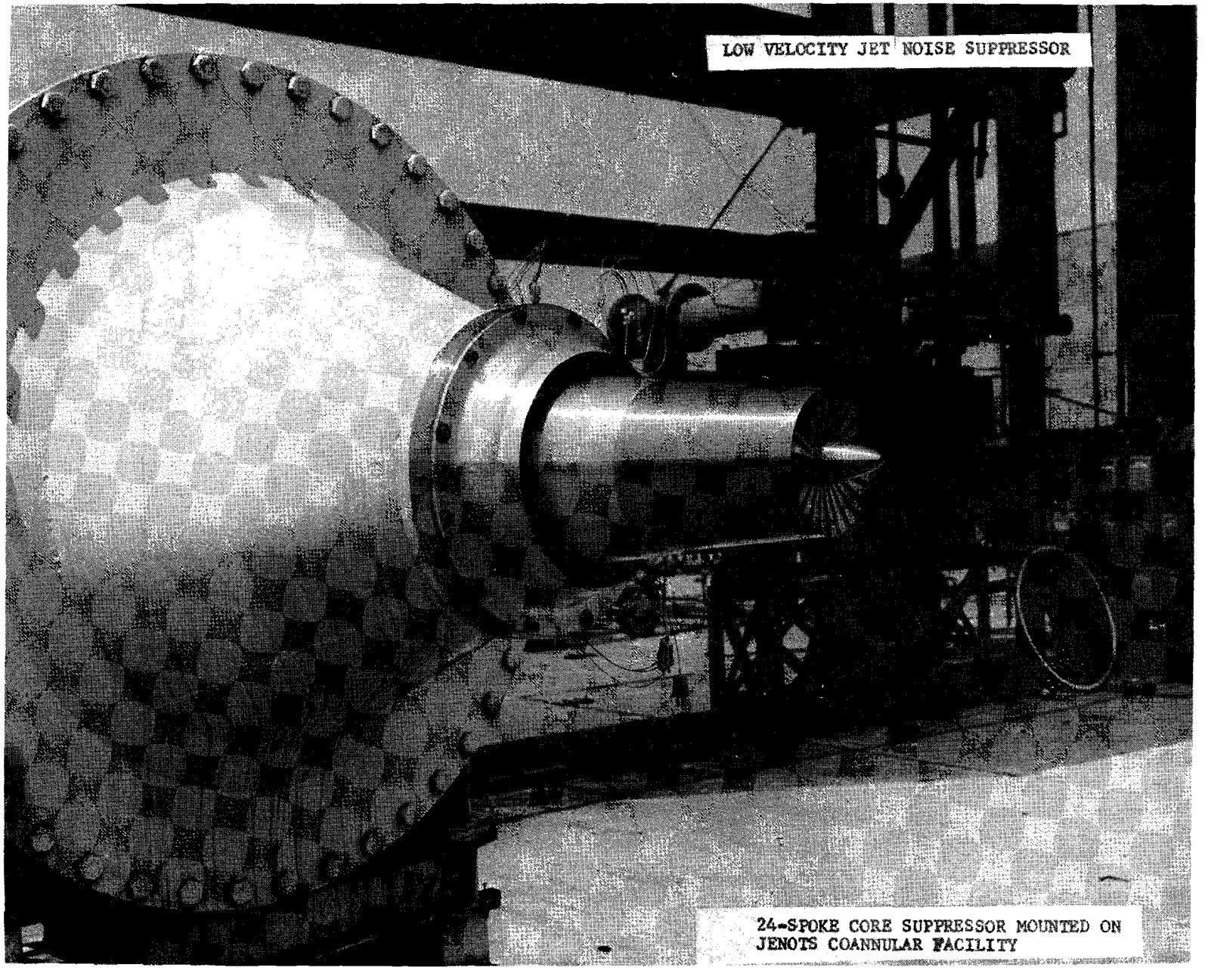

FIGURE 2.4.2-17

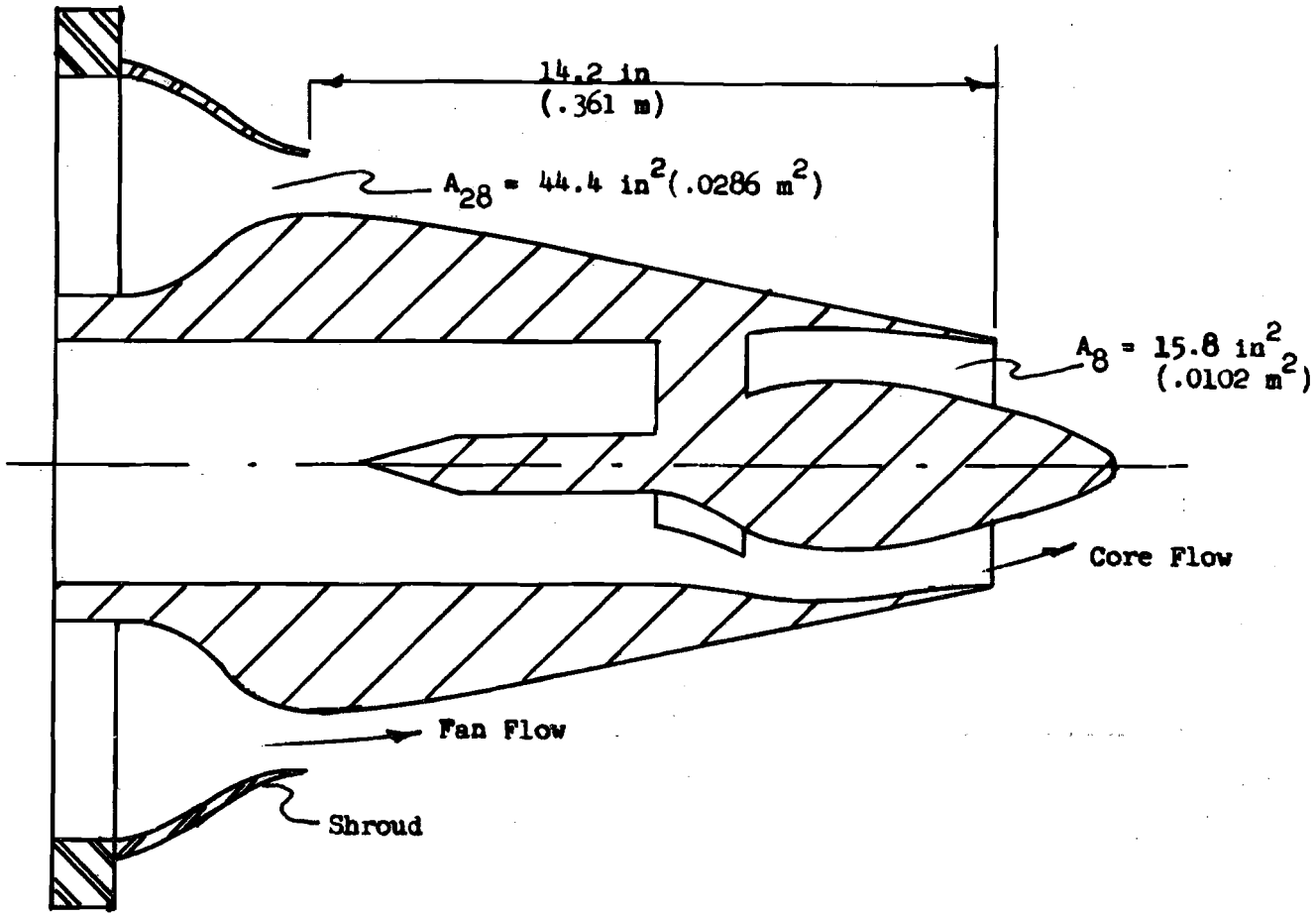

FIGURE 2.4.2 -18 CONFIGURATION 5 - BASELINE II USED IN SUPPRESSOR TEST

$$\frac{\text{ANNULUS AREA}}{\text{CORE FLOW AREA}} = 2$$

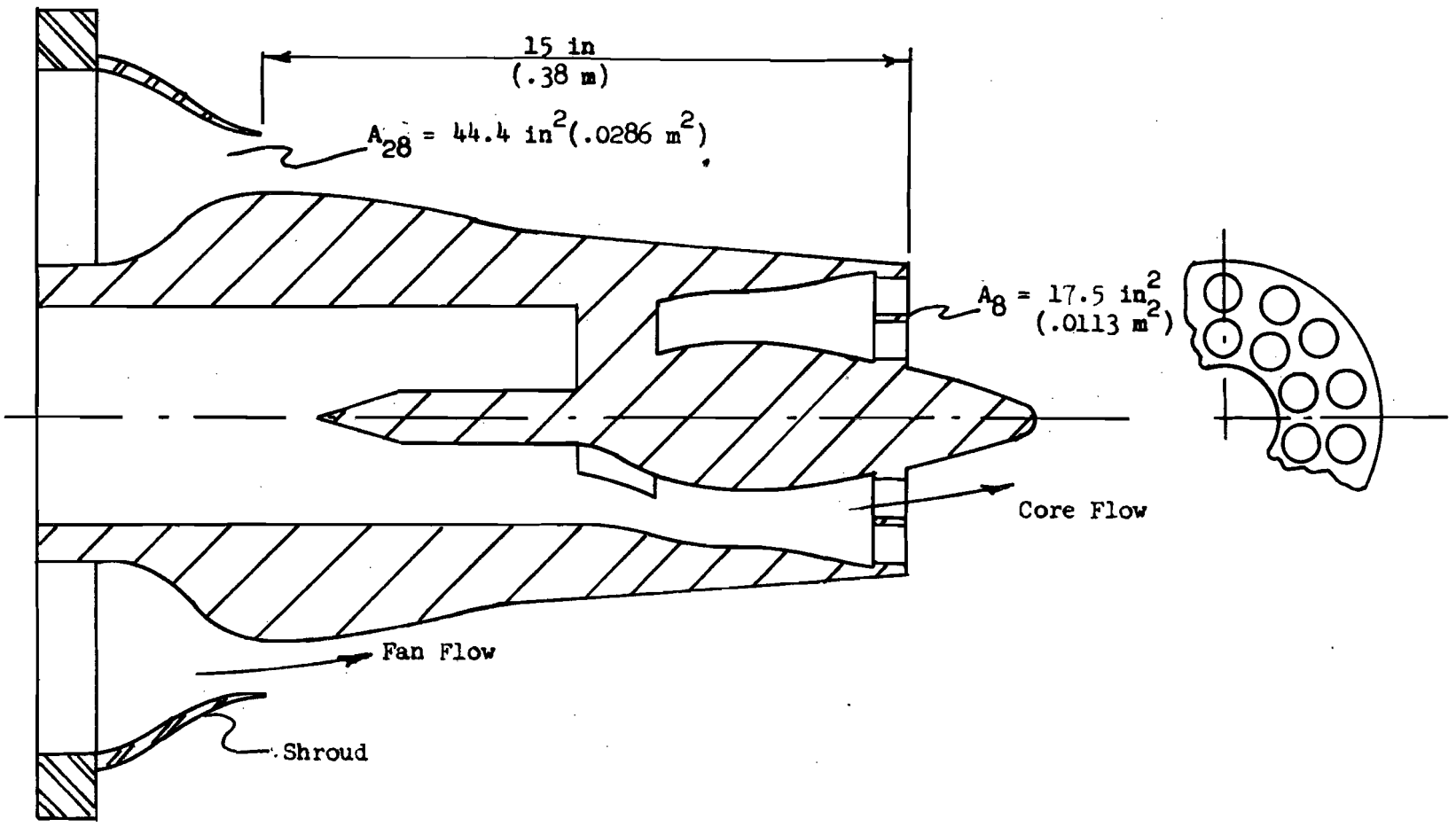

FIGURE 2.4.2 - 19 CONFIGURATION 7 - 24 HOLE CORE NOZZLE SUPPRESSOR

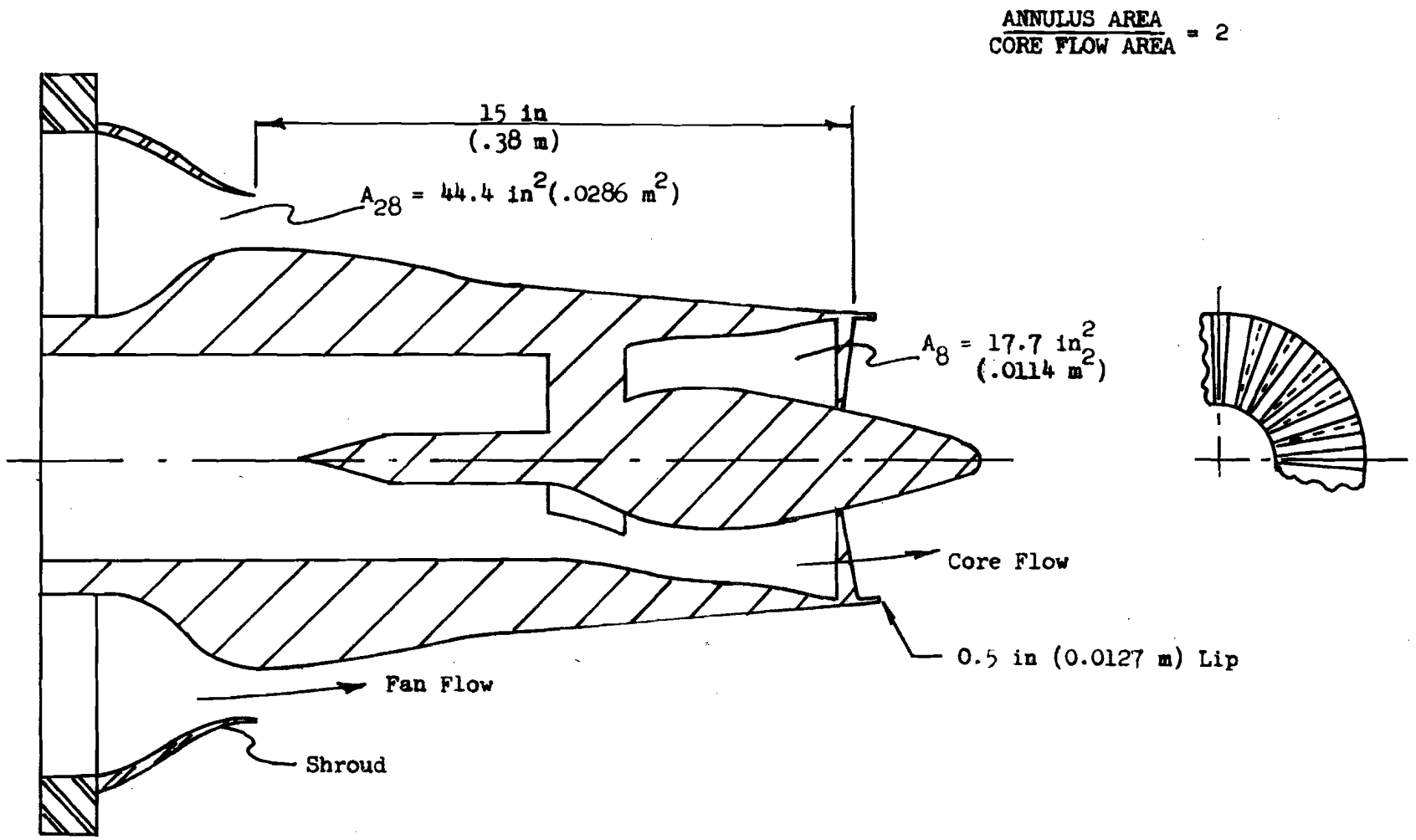

FIGURE 2.4.2 -20 CONFIGURATION 8 - 24 SPOKE CORE NOZZLE SUPPRESSOR

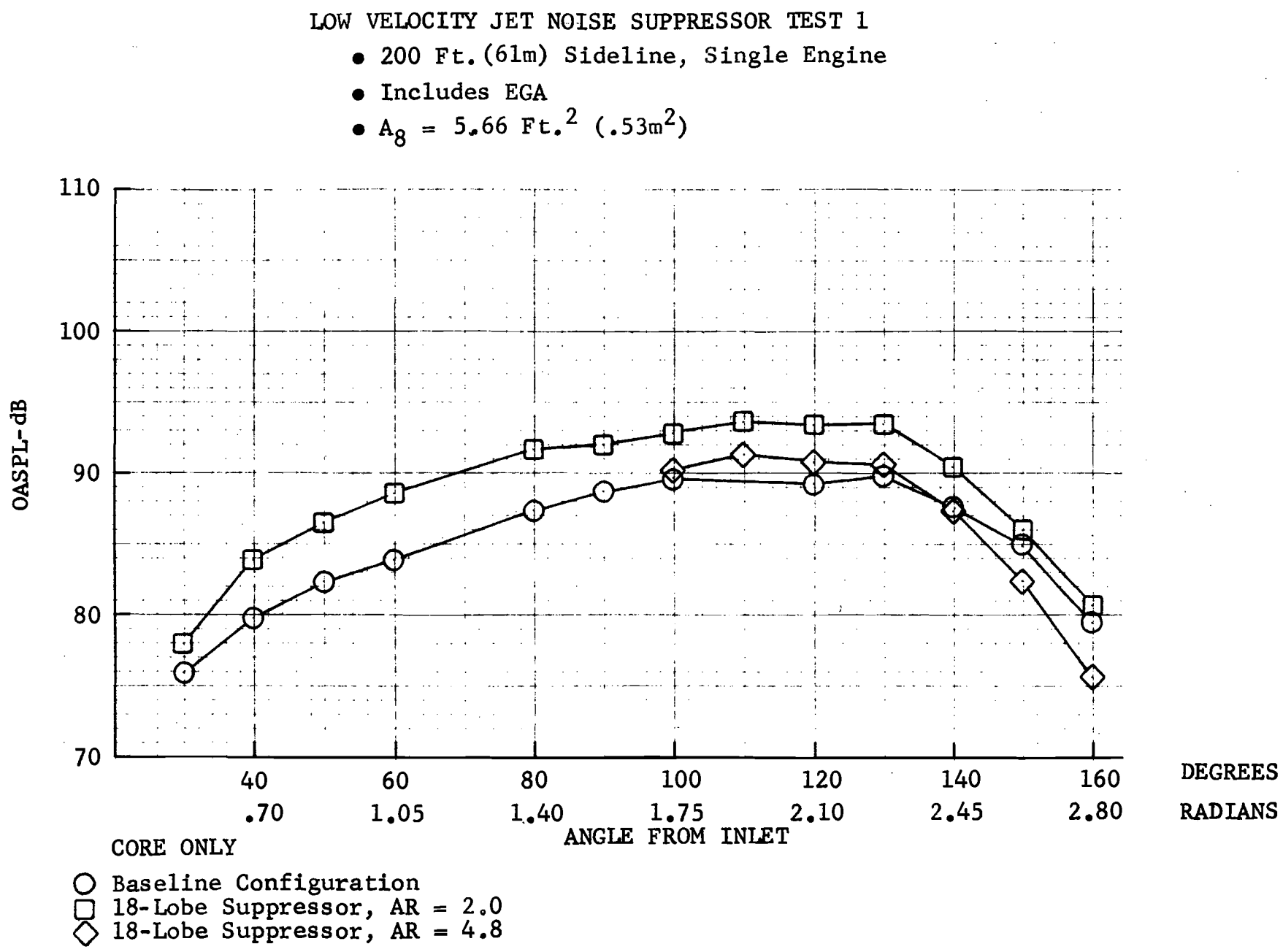

FIGURE 2.4.4-1 OASPL VS ACOUSTIC ANGLE, CORE ONLY, V_{CORE} = 660 FT/SEC (201 m/s)

Table 2.4.3-1. Test Matrix, Low Velocity Jet Noise Suppressor Test 1.

Core Only

Configuration 1 Baseline 1 (Test Points 1 through 6)
Configuration 2 18 Lobe Core Suppressor AR = 2 (Test Points 23 through 28)
Configuration 3 18 Lobe Core Suppressor AR = 4.8 (Test Pointes 45 through 50)

V_{core} ft/sec	T_{core} °R	V_{core} m/s	T_{core} °K
470	1086	143	603
670	1164	204	647
900	1254	274	697
1240	1381	378	767
1490	1473	454	818
1600	1516	488	542

Fan Only

Configuration 1 (Test Points 7 through 12)
Configuration 2 (Test Points 29 through 34)
Configuration 3 (Test Points 51 through 56)

V_{fan} ft/sec	T_{fan} °R	V_{fan} m/s	T_{fan} °K
468	Ambient	143	Ambient
609	Ambient	186	Ambient
755	Ambient	230	Ambient
926	Ambient	282	Ambient
1013	Ambient	309	Ambient
1039	Ambient	317	Ambient

Dual FLow

Configuration 1 (Test Points 13 through 22)
Configuration 2 (Test Points 35 through 44)
Configuration 3 (Test Points 57 through 66)

V_{core} ft/sec	V_{fan} ft/sec	T_{core} °R	T_{fan} °R	V_{core} m/s	V_{fan} m/s	T_{core} °K	T_{fan} °K
470	468	1086	Ambient	143	143	603	Ambient
670	609	1164	Ambient	204	186	647	Ambient
900	755	1254	Ambient	274	230	697	Ambient
1240	926	1381	Ambient	378	282	767	Ambient
1490	1013	1473	Ambient	454	309	818	Ambient
1600	1039	1516	Ambient	488	317	842	Ambient
1600	839	1516	Ambient	488	256	842	Ambient
1600	639	1516	Ambient	488	195	842	Ambient
670	450	1164	Ambient	204	137	647	Ambient
670	300	1164	Ambient	204	91	647	Ambient

Table 2.4.3-2. Test Matrix Low Velocity Jet Noise Suppressor Test II.

Core Only

Configuration 4, 18 Capped Lobe Suppressor AR = 2 Staggered Flow.
Configuration 5, 18 Capped Lobe Suppressor AR = 2 Coplanar Flow.

Test Points 1 thru 3

V_{core} ft/sec	T_{core} °R	V_{core} m/s	T_{core} °K
663	1165	202	647
1224	1379	373	766
1593	1515	486	842

Fan Only

Configuration 4
Configuration 5

Test Points 4 through 9

V_{fan} ft/sec	T_{fan} °R	V_{fan} m/s	T_{fan} °K
443	Ambient	135	Ambient
568	Ambient	173	Ambient
700	Ambient	213	Ambient
843	Ambient	257	Ambient
914	Ambient	279	Ambient
933	Ambient	284	Ambient

Dual Flow

Configuration 4
Configuration 5

Test Points 10 through 37

V_{core} ft/sec	V_{fan} ft/sec	T_{core} °R	T_{fan} °R	V_{core} m/s	V_{fan} m/s	T_{core} °K	T_{fan} °K
475	446	1070	Ambient	145	136	594	Ambient
656	563	1167	Ambient	200	172	648	Ambient
899	696	1255	Ambient	274	212	697	Ambient
1225	841	1362	Ambient	373	256	757	Ambient
1492	918	1477	Ambient	455	280	450	Ambient
1598	933	1516	Ambient	487	284	842	Ambient
1330	930	1520	Ambient	405	283	845	Ambient
1000	925	1523	Ambient	305	282	846	Ambient
671	424	1167	Ambient	205	129	648	Ambient
475	424	1163	Ambient	145	129	646	Ambient
660	424	1165	640	201	129	647	356
656	563	1165	640	200	172	647	356
1490	920	1520	640	454	280	845	356
1600	785	1520	675	488	239	845	375
1600	935	1520	675	488	285	845	375
1225	840	1360	675	373	256	756	375
1600	1040	1516	544	488	317	842	358
1556	1028	1498	641	474	313	832	356
1553	1027	1496	641	473	313	831	356
1490	1013	1473	638	454	309	818	354
1238	926	1381	624	377	282	767	347
901	755	1254	Ambient	275	230	697	Ambient
665	609	1164	Ambient	203	186	647	Ambient
462	468	1088	Ambient	141	143	605	Ambient
1477	1060	1516	647	450	323	842	359
1655	1083	1516	647	604	330	842	359
1477	1060	1516	Ambient	450	323	842	Ambient
1655	1083	1516	Ambient	504	330	842	Ambient

Fan Only

Configuration 4
Configuration 5

Test Points 38 through 47

V_{fan} ft/sec	T_{fan} °R	V_{fan} ft/sec	T_{fan} °K
424	640	129	356
563	675	172	375
620	675	189	375
785	675	239	375
900	640	274	356
800	640	244	356
1060	647	450	359
1083	647	330	359
1040	644	317	358
1028	641	313	356

Table 2.4.3-3. Test Matrix Low Velocity Jet Noise Suppressor Test III.

Core Only

Configuration 6 Baseline 2 Test Points 1 through 7
Configuration 7 24 Hole Core Suppressor. Test Points 26 through 32
Configuration 8 24 Spoke Core Nozzle Suppressor. Test Points 49 through 55

V_{core} ft/sec	T_{core} °R	V_{core} m/s	T_{core} °K
1656	1508	505	838
1600	1516	488	842
1553	1496	473	831
1490	1473	454	818
1238	1381	377	767
901	1254	275	697
665	1164	203	647

Fan Only

Configuration 6 Test Points 8 through 14
Configuration 7 Test Points 33 through 39
Configuration 8 Test Points 56 through 62

V_{fan} ft/sec	T_{fan} °R	V_{fan} m/s	T_{fan} °K
1064	643	324	357
1040	643	317	357
1027	641	313	356
1013	638	309	354
926	624	282	347
755	598	230	332
609	598	186	332

Dual Flow

Configuration 6 Test Points 15 through 25
Configuration 7 Test Points 40 through 48
Configuration 8 Test Points 63 through 71

V_{core}	V_{fan} ft/sec	T_{core}	T_{fan} °R	V_{core}	V_{fan} m/s	T_{core}	T_{fan} °K
1656	1064	1508	643	505	324	838	357
1600	1040	1516	643	488	317	842	357
1553	1027	1496	641	473	313	831	356
1490	1013	1473	638	454	309	818	354
1238	926	1381	624	377	282	767	347
901	755	1254	598	275	230	697	332
665	609	1164	598	203	186	647	332
1558	1078	1485	646	475	329	825	359
1464	1090	1465	649	446	332	814	361
1409	1098	1455	651	429	335	808	362
1347	1108	1442	653	411	338	801	363

Figure 2.4.4-2. Noise reduction, relative to the baseline, was obtained by both suppressors in the aft quadrant. The angle of maximum noise shifted from 130° in the unsuppressed mode to 120° in the suppressed mode. Single flow jet noise was more effectively reduced by the AR 4.8 suppressor.

The directional characteristics of fan flow only at approach power is shown in Figure 2.4.4-3. The flow noise was increased relative to the baseline for both configurations. The deeper penetration into the fan flow of the AR 4.8 suppressor caused an increase of 10 dB in the OASPL at each angle. At the take-off power setting shown in Figure 2.4.4-4, the AR 4.8 configuration causes large increases in noise level of the order of 15 dB. The AR 2 lobes do not penetrate the fan flow stream so deeply and the impingement noise associated with that configuration is only of the order of 3dB above the baseline.

The OASPL directional characteristics of dual flow at approach power is shown in Figure 2.4.4-5. The fan flow impingement noise was sufficient to cause noise level increases at all angles and was particularly severe for the AR 4.8 suppressor. At the take off power setting shown in Figure 2.4.4-6 the more favorable geometry of the AR 2 core suppressor provided modest amounts of noise reduction at the angles above 110° and no increase at other angles. The AR 4.8 configuration however, continued to amplify the noise levels at all angles. In order to understand this result, it is necessary to examine the SPL spectral distribution at the peak noise angle. In Figure 2.4.4-7, the peak angle spectra for core flow noise at approach power is shown for each configuration. Both configurations increase the sound levels at all frequencies above 100 Hz. Noise reduction is achieved below 100 Hz, but it does not effect OASPL significantly. As the core velocity is increased the frequency conversion becomes more pronounced as is observed for the takeoff power case shown in Figure 2.4.4-8. Both suppressor configurations successfully attenuate low frequency noise up to 630 Hz.

The peak angle spectrum plots of the fan only at the two extremes of velocity are shown in Figure 2.4.4-9 and 2.4.4-10. At approach power, the lobes of the AR 4.8 configuration increase the SPL in each frequency band by approximately 10 dB. In Figure 2.4.4-10, the higher fan flow velocity caused discrete tones to be generated from the AR 4.8 configuration; the general increase in SPL over the frequency range is again about 10 dB. It is not certain if the tones would be generated at these frequencies (if at all) on the full size engine since they were shifted in accordance with the scaling laws. An increase in the mid and high frequency bands is observed for the AR 2 configuration. The fan flow noise levels increased so much during their passage over the lobes that they control the spectral characteristics of the dual flow operation. In Figure 2.4.4-11, at approach power, both dual flow spectra of the suppressed configurations are higher than the reference baseline. At takeoff power, as is shown in Figure 2.4.4-12, a small noise reduction is achieved by the AR 2 configuration in the low frequency region. The AR 4.8 configuration increased the SPL at all frequencies with the exception of the 50 Hz and 63 Hz 1/3 octave bands.

The relationship between single flow OAPWL and core jet velocity is shown in Figure 2.4.4-13. The baseline nozzle has a $V^{6.5}$ relationship, the AR 2 suppressor nozzle has a $V^{5.5}$ relationship. Power level reductions are generally

LOW VELOCITY JET NOISE SUPPRESSOR TEST 1

- 200 Ft.(61m) Sideline, Single Engine
- Includes EGA
- A_8 = 5.66 Ft.^{2} (.53m^2)

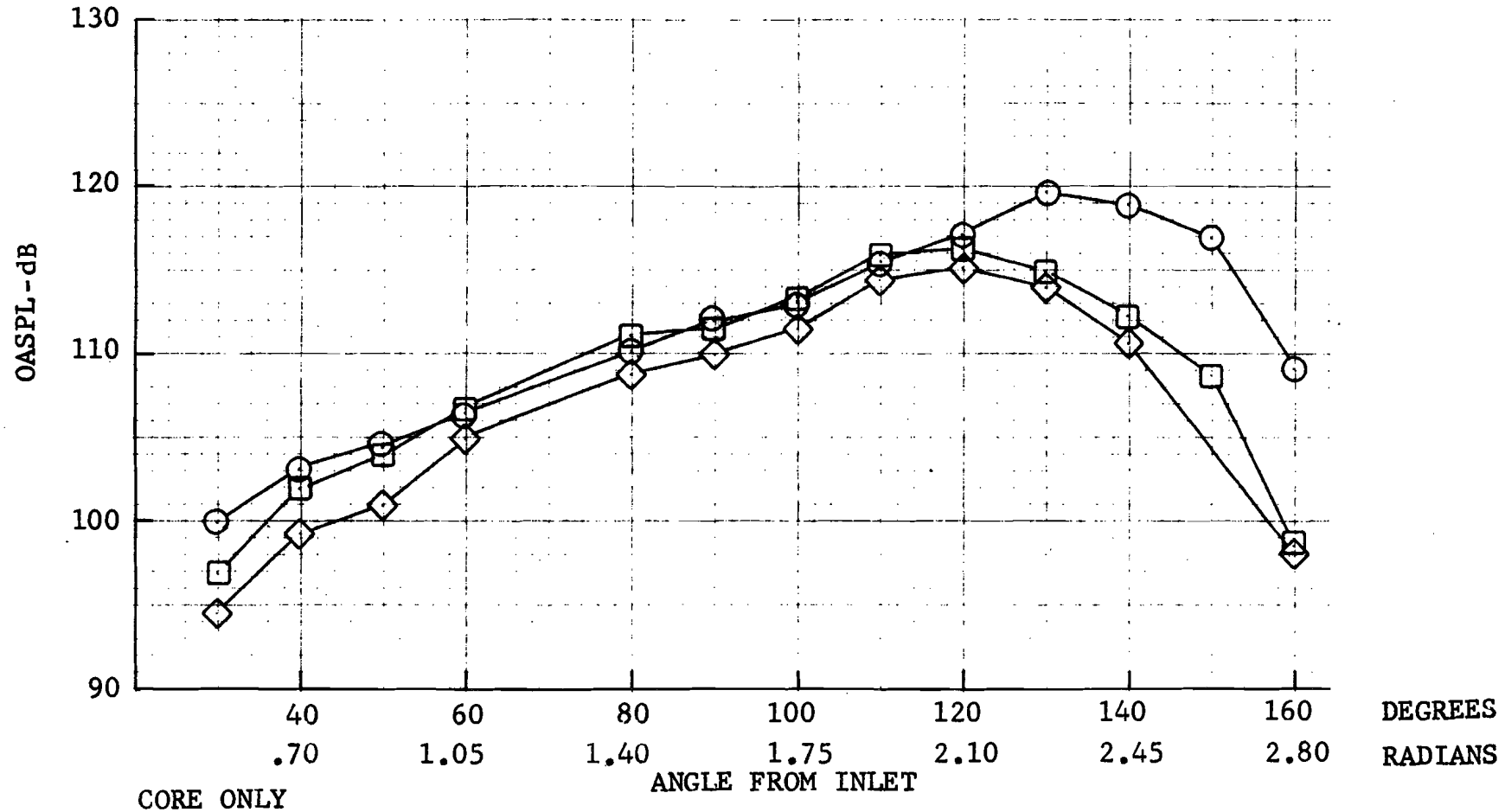

CORE ONLY
○ Baseline Configuration
□ 18-Lobe Suppressor, AR = 2.0
◇ 18-Lobe Suppressor, AR = 4.8

FIGURE 2.4.4-2 OASPL VS ACOUSTIC ANGLE, CORE ONLY, V_{CORE} = 1600 FT/SEC (488 m/s)

LOW VELOCITY JET NOISE SUPPRESSOR TEST 1

- 200 Ft. (61m) Sideline, Single Engine
- Includes EGA
- A_{28} = 17.28 Ft.^{2} (1.61m^2)

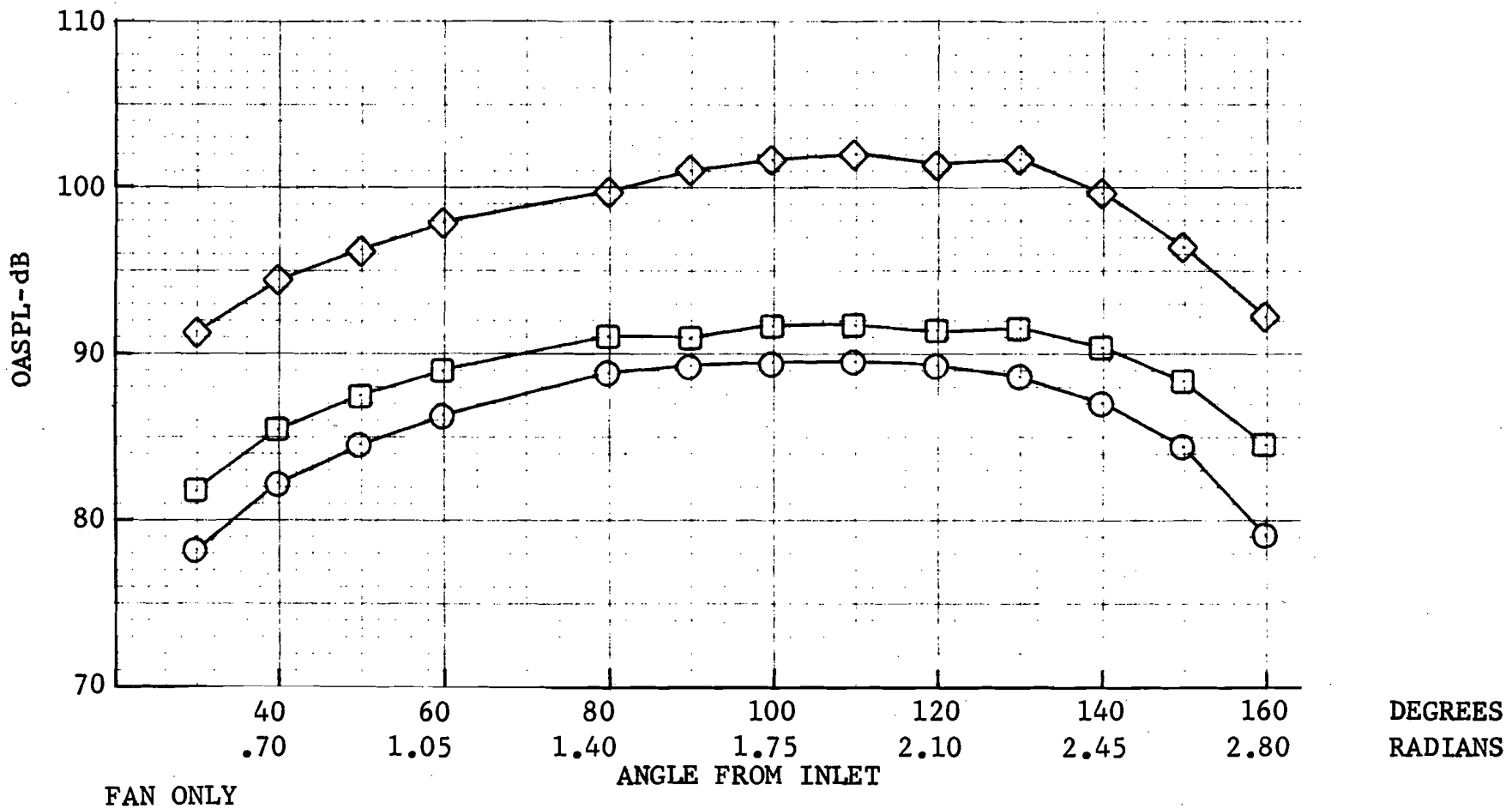

FAN ONLY

○ Baseline Configuration
□ 18-Lobe Suppressor, AR = 2.0
◇ 18-Lobe Suppressor, AR = 4.8

FIGURE 2.4.4-3 OASPL VS ACOUSTIC ANGLE, FAN ONLY, V_{FAN} = 580 FT/SEC (177 m/s)

LOW VELOCITY JET NOISE SUPPRESSOR TEST 1

- 200 Ft.(61m) Sideline, Single Engine
- Includes EGA
- A_{28} = 17.28 Ft.^{2} (1.61m^2).

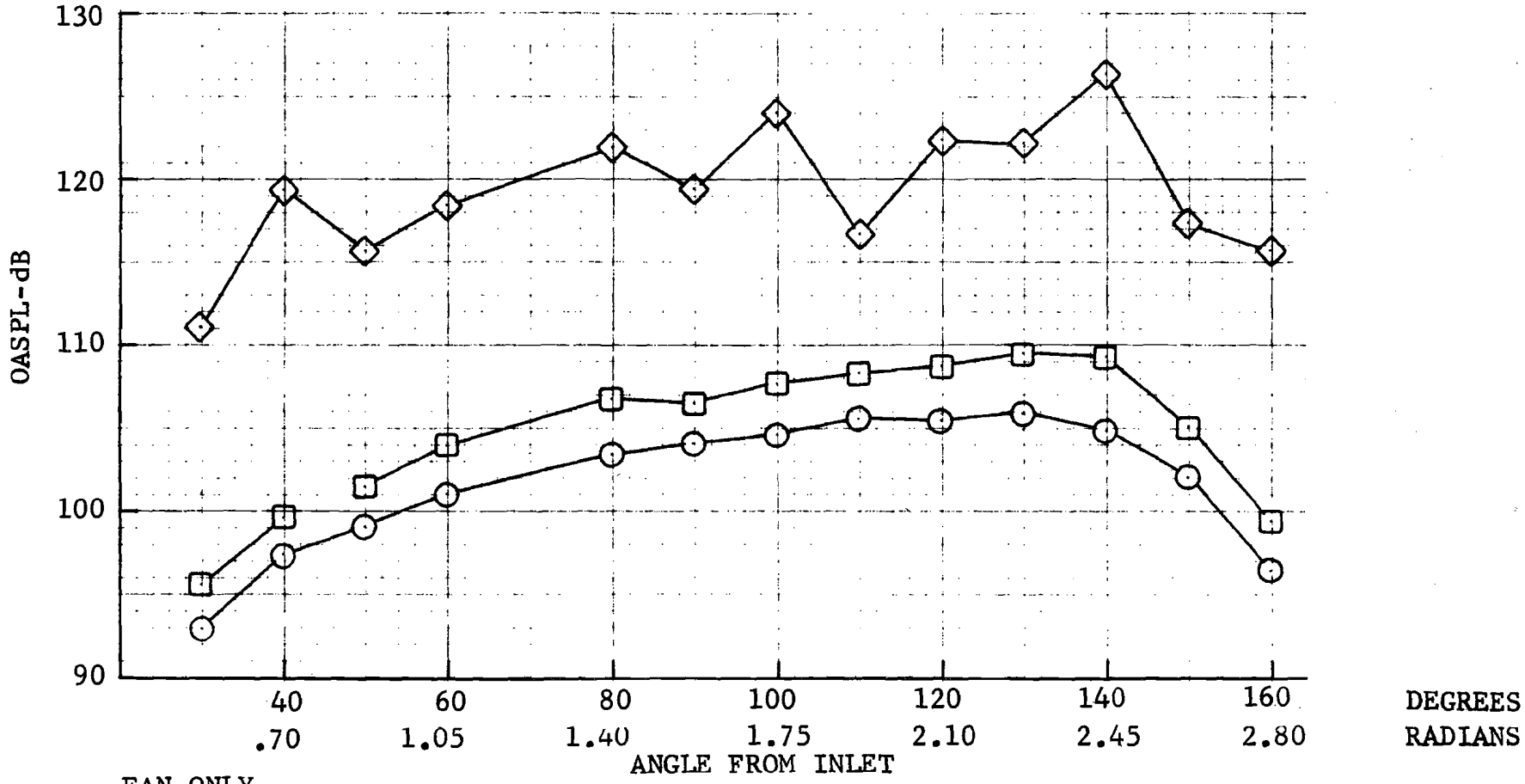

FAN ONLY

○ Baseline Configuration
□ 18-Lobe Suppressor, AR = 2.0
◇ 18-Lobe Suppressor, AR = 4.8

FIGURE 2.4.4-4 OASPL VS ACOUSTIC ANGLE, FAN ONLY, V_{FAN} = 950 FT/SEC (290 m/s)

LOW VELOCITY JET NOISE SUPPRESSOR TEST 1

- 200 Ft.(61m) Sideline, Single Engine
- Includes EGA
- A_8 = 5.66 Ft.^{2} (.53m^2); A_{28} = 17.28 Ft.^{2} (1.61m^2)

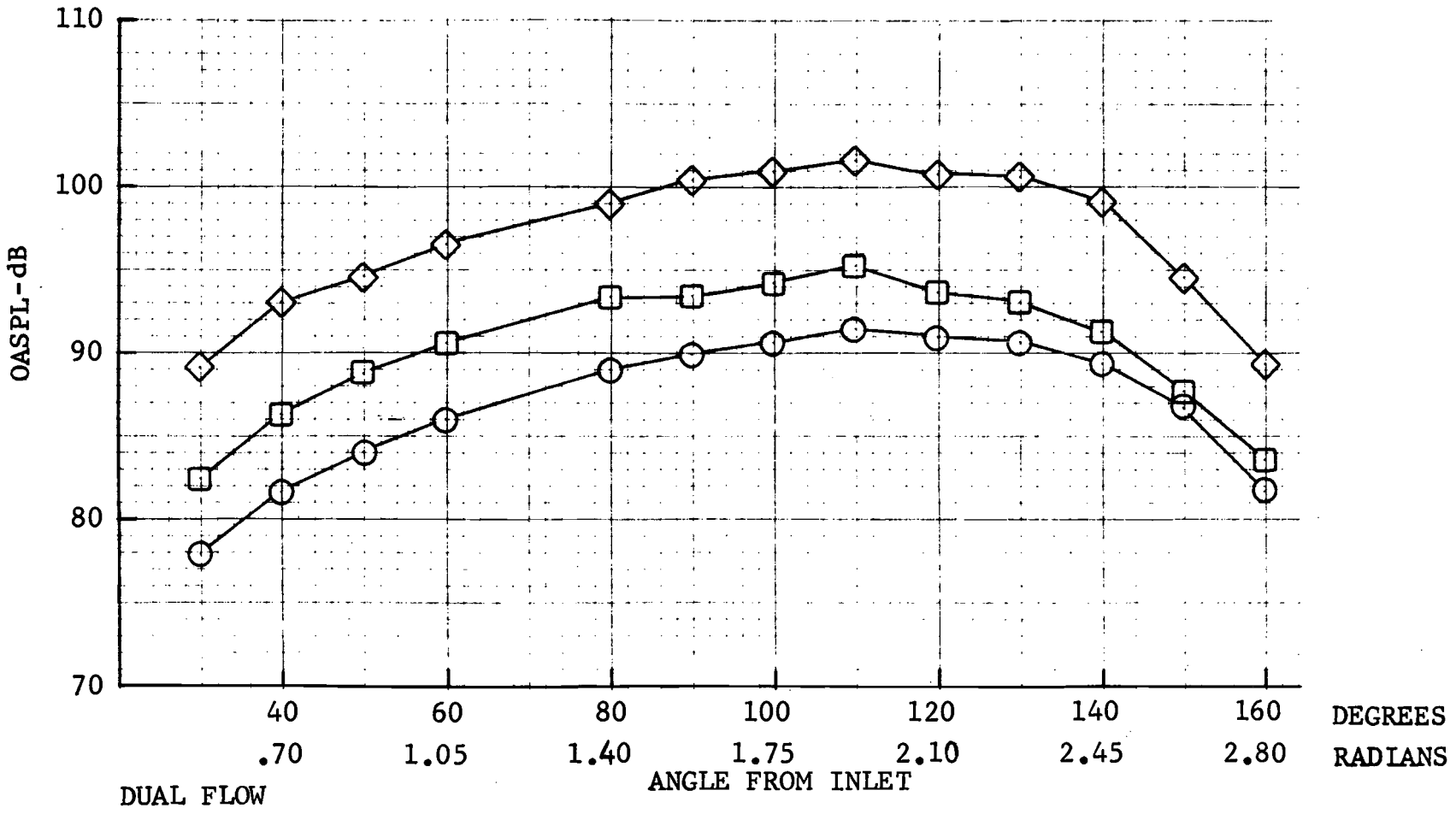

DUAL FLOW

○ Baseline Configuration
□ 18-Lobe Suppressor, AR = 2.0
◇ 18-Lobe Suppressor, AR = 4.8

FIGURE 2.4.4-5 OASPL VS ACOUSTIC ANGLE, DUAL FLOW, V_{CORE}=660 FT/SEC (201 m/s), V_{FAN}= 580 FT/SEC (177 m/s)

LOW VELOCITY JET NOISE SUPPRESSOR TEST 1

- 200 Ft. (61m) Sideline, Single Engine
- Includes EGA
- A_8 = 5.66 Ft.^{2} (.53m^2); A_{28} = 17.28 Ft.^{2} (1.61m^2)

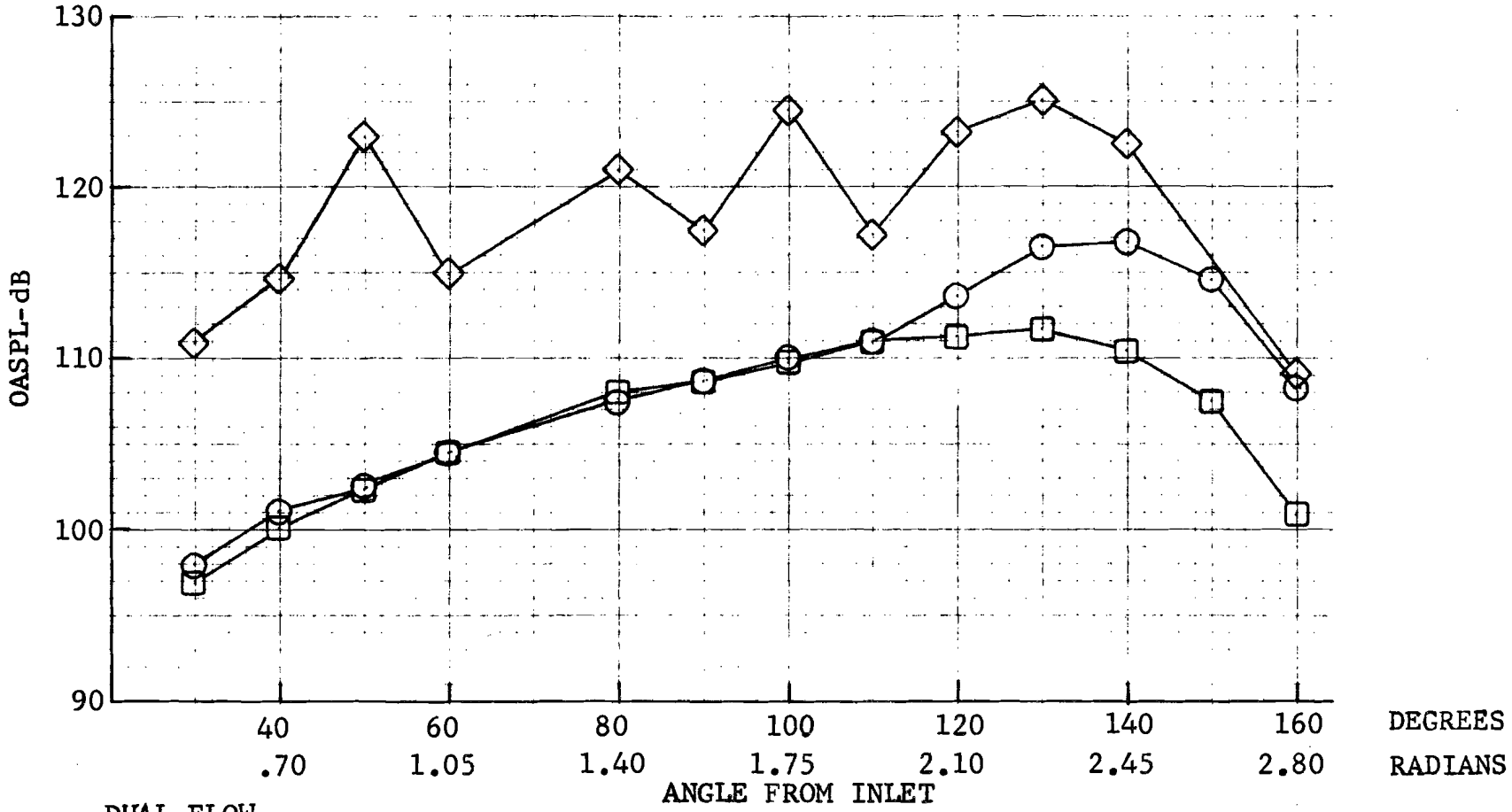

DUAL FLOW

○ Baseline Configuration
□ 18-Lobe Suppressor, AR = 2.0
◇ 18-Lobe Suppressor, AR = 4.8

FIGURE 2.4.4-6 OASPL VS ACOUSTIC ANGLE, DUAL FLOW, V_{CORE}=1600 FT/SEC (488 m/s), V_{FAN}= 950 FT/SEC (290 m/s)

LOW VELOCITY JET NOISE SUPPRESSOR TEST 1

* 200 ft. (61m) SIDELINE
* PEAK ANGLE SPECTRA
* INCLUDES EGA
* A_8 = 5.66 ft^2 (.53m^2)

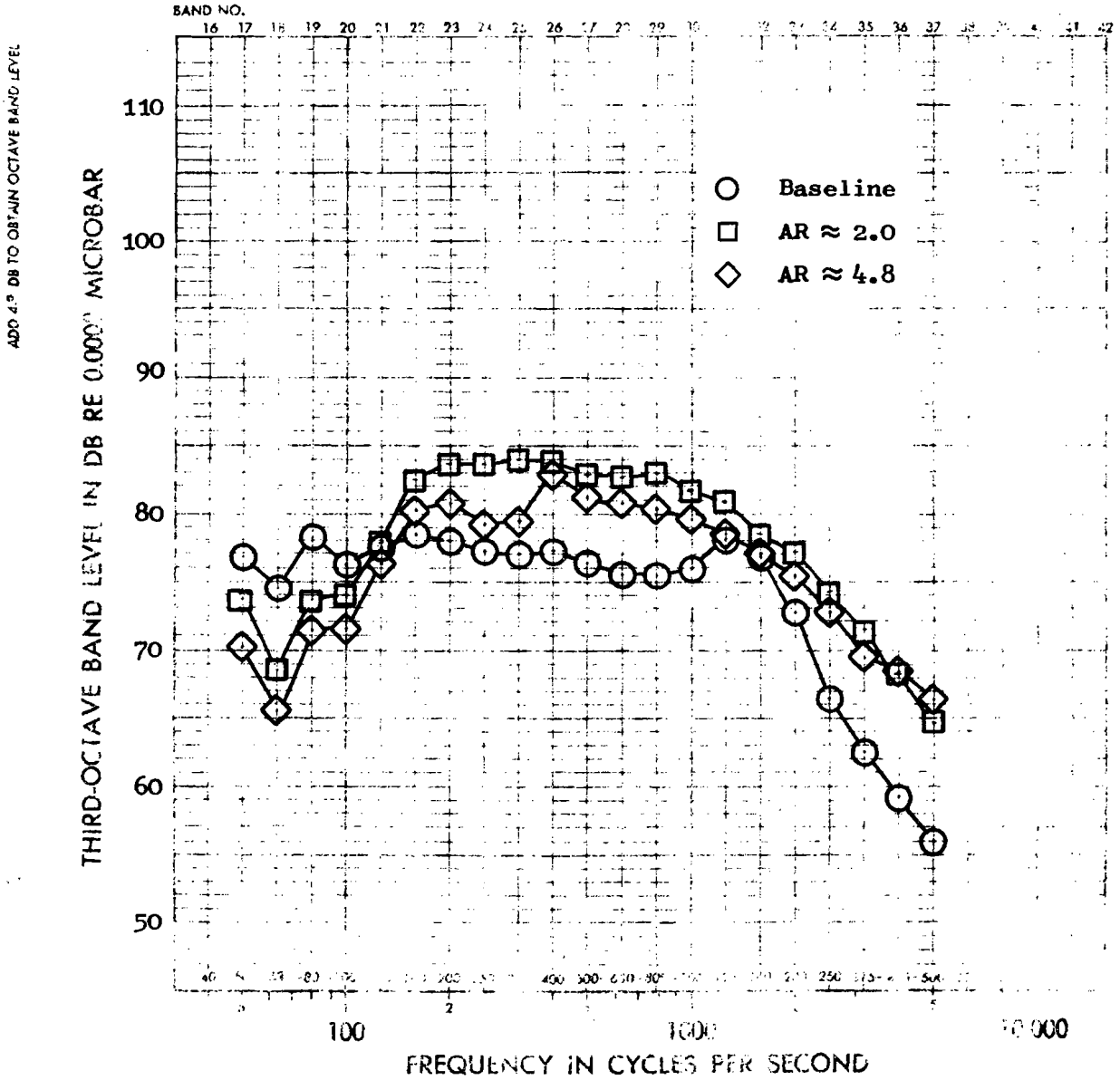

FIGURE 2.4.4-7 PEAK ANGLE SPECTRA, CORE ONLY, V_{CORE} = 660 FT/SEC (201 m/s)

LOW VELOCITY JET NOISE SUPPRESSOR TEST 1

* 200 ft. (61m) SIDELINE
* PEAK ANGLE SPECTRA
* INCLUDES EGA
* A_8 = 5.66 ft^2 (.53m^2)

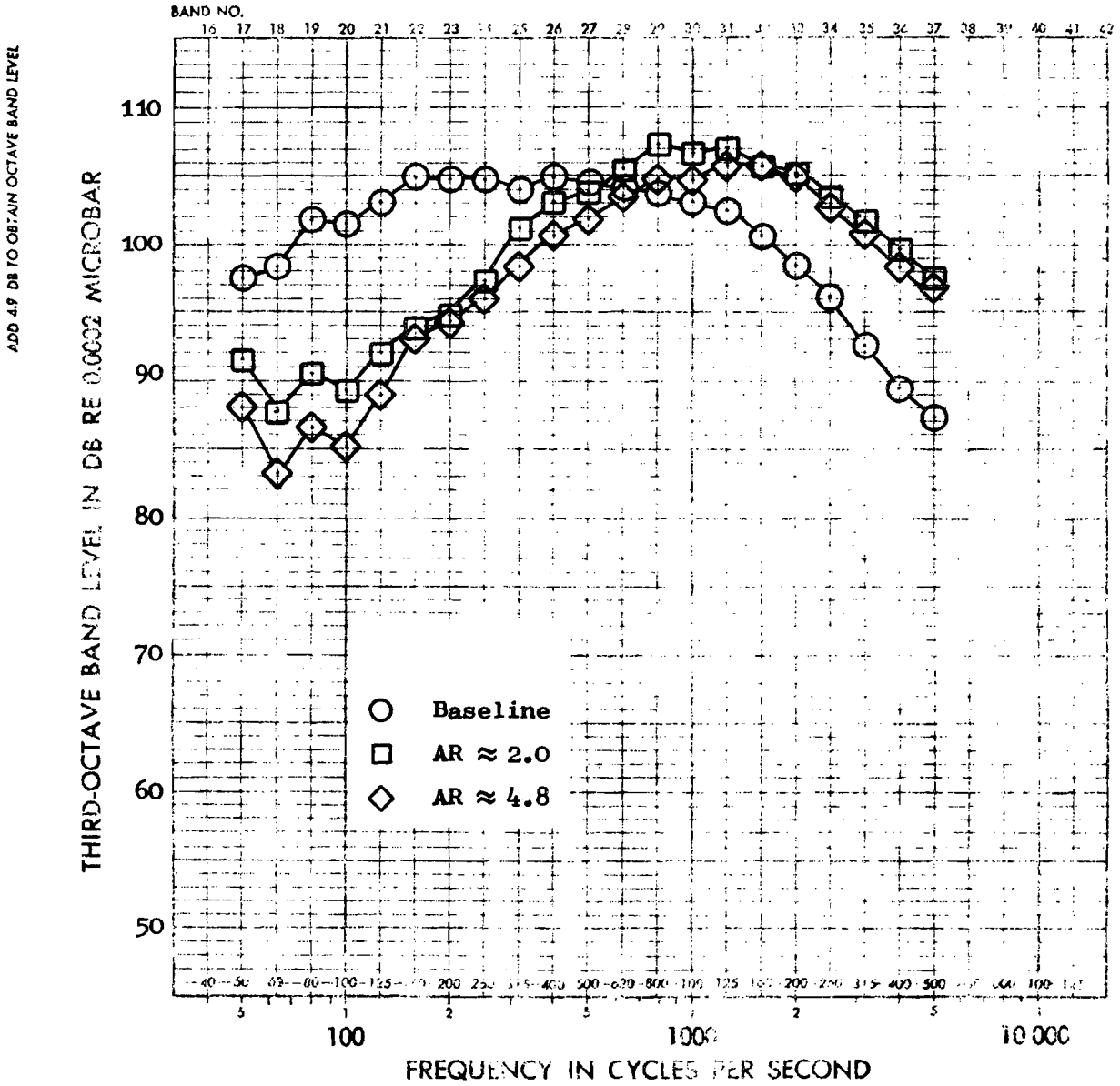

FIGURE 2.4.4-8 PEAK ANGLE SPECTRA, CORE ONLY, V_{CORE} 1600 FT/SEC (488m/s)

LOW VELOCITY JET NOISE SUPPRESSOR TEST 1

* 200 ft. (61m) SIDELINE
* PEAK ANGLE SPECTRA
* INCLUDES EGA
* A_{28} = 17.28 ft^2 (1.61m^2)

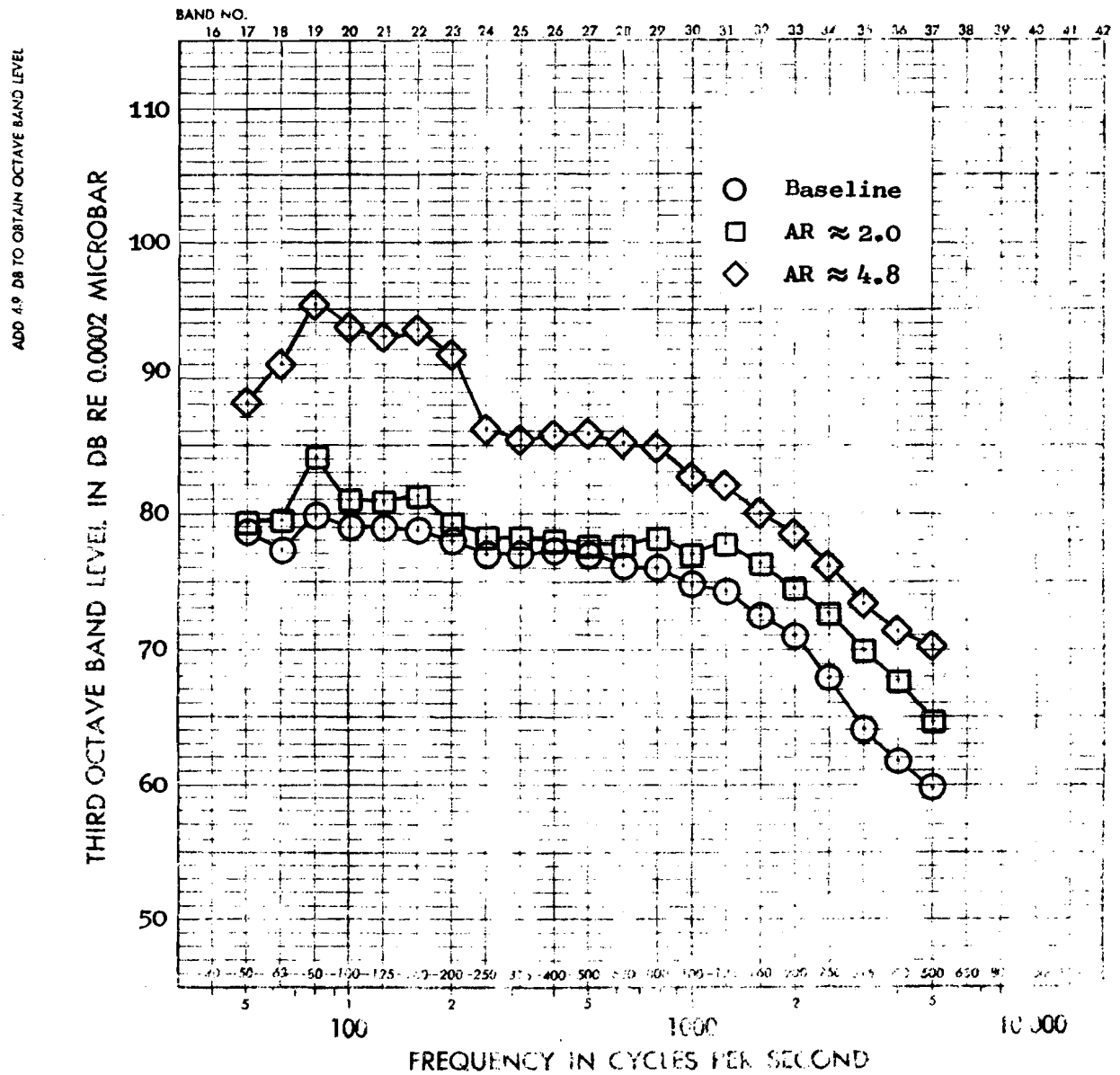

FIGURE 2.4.4-9 PEAK ANGLE SPECTRA, FAN ONLY, V_{FAN} 580 FT/SEC (177m/s)

LOW VELOCITY JET NOISE SUPPRESSOR TEST 1

* 200 ft. (61m) SIDELINE
* PEAK ANGLE SPECTRA
* INCLUDES EGA
* A_{28} = 17.28 ft^2 (1.61m^2)

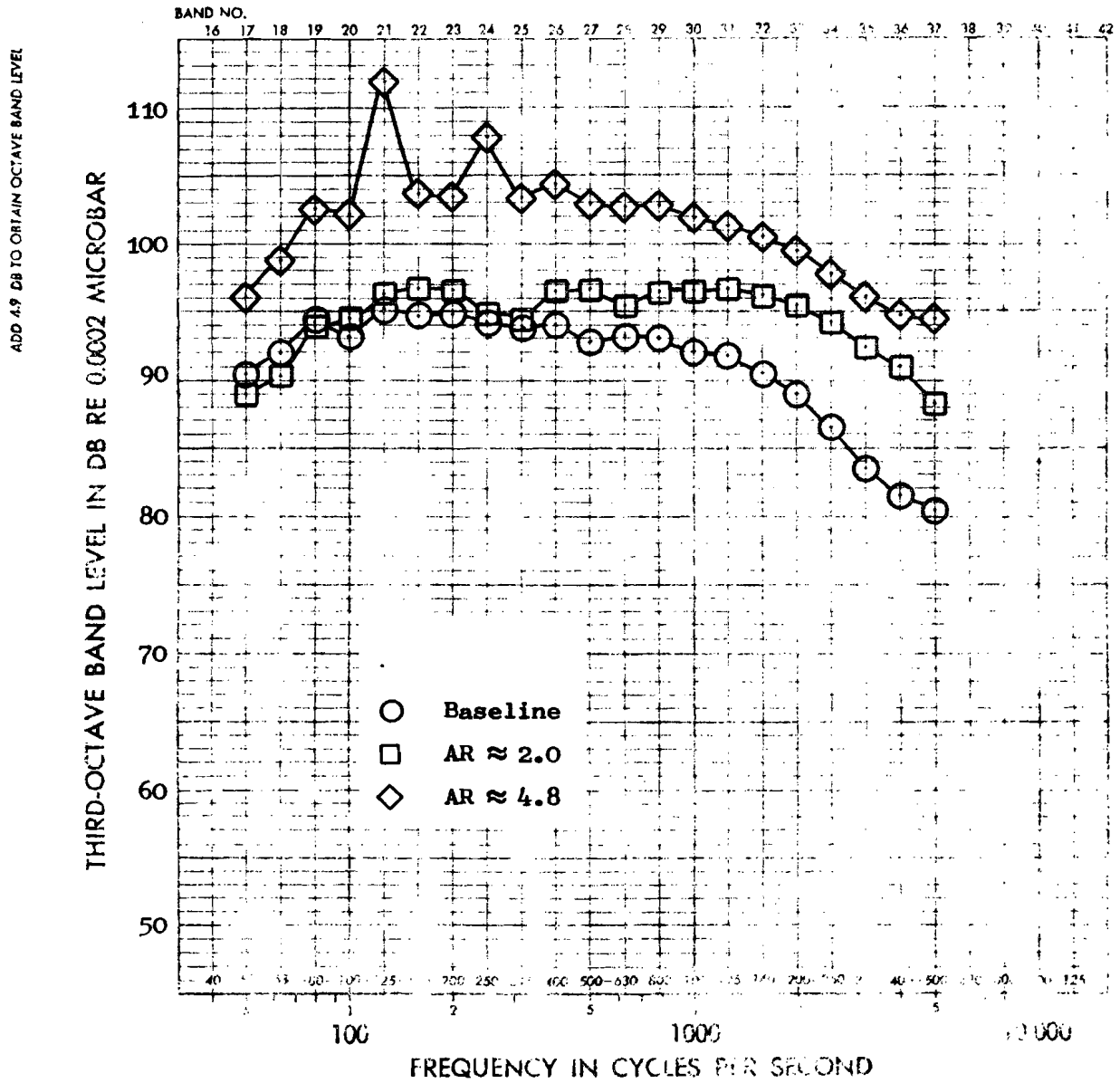

FIGURE 2.4.4-10 PEAK ANGLE SPECTRA, FAN ONLY, V_{FAN} 950 FT/SEC (290m/s)

LOW VELOCITY JET NOISE SUPPRESSOR TEST 1

* 200 ft. (61m) SIDELINE
* PEAK ANGLE SPECTRA
* INCLUDES EGA
* A_8 = 5.66 ft^2 (.53m^2); A_{28} = 17.28 ft^2 (1.61m^2)

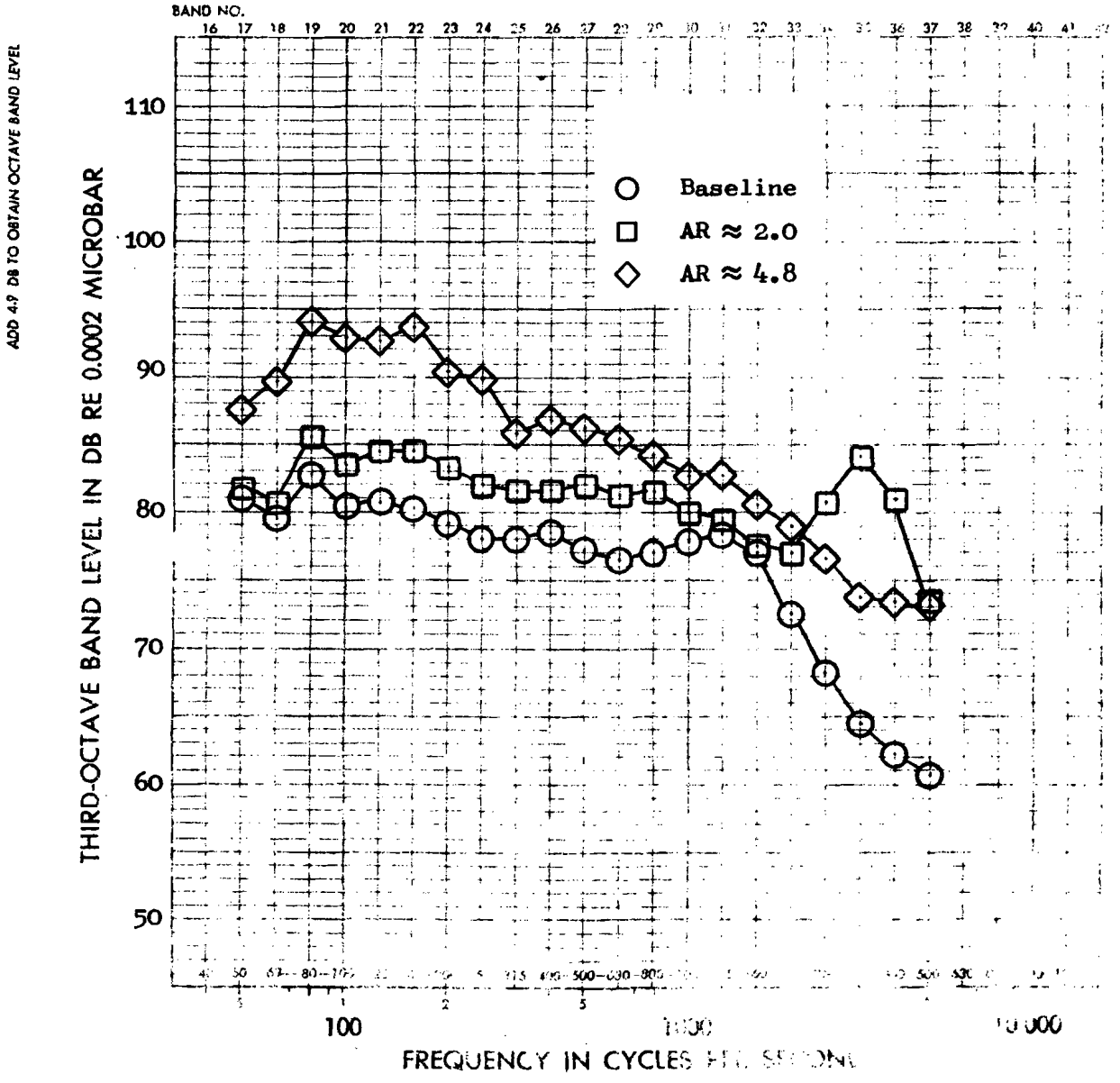

FIGURE 2.4.4-11 PEAK ANGLE SPECTRA, DUAL FLOW, V_{CORE} =660 FT/SEC (201 m/s), V_{FAN} = 580 FT/SEC (177 m/s)

LOW VELOCITY JET NOISE SUPPRESSOR TEST 1

* 200 ft. (61m) SIDELINE
* PEAK ANGLE SPECTRA
* INCLUDES EGA
* A_8 = 5.66 ft^2 (.53m^2); A_{28} = 17.28 ft^2 (1.61m^2)

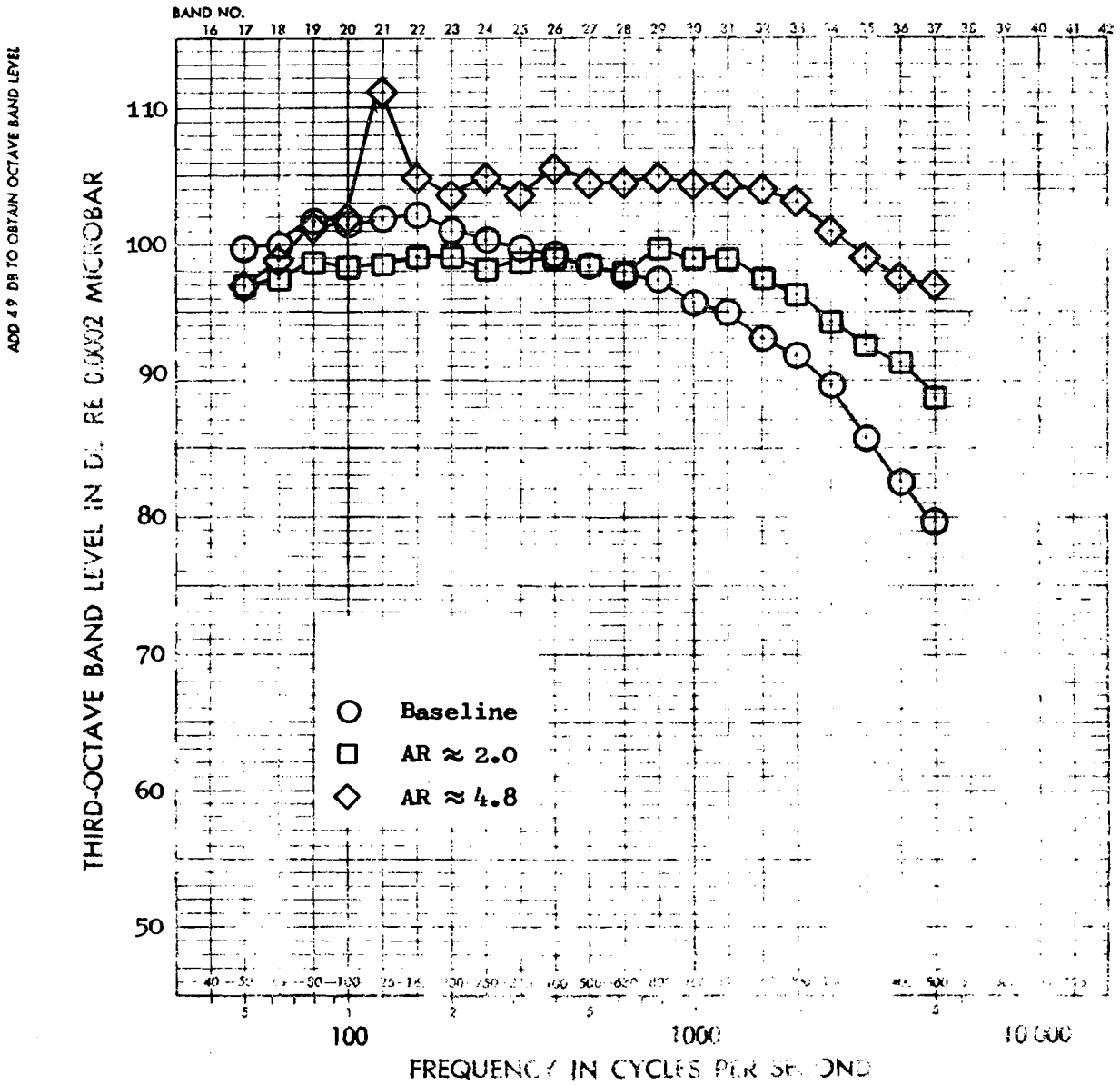

FIGURE 2.4.4-12 PEAK ANGLE SPECTRA, DUAL FLOW,
V_{CORE} = 1600 FT/SEC (488m/s)
V_{FAN} = 950 FT/SEC (290m/s)

LOW VELOCITY JET NOISE SUPPRESSOR TEST 1

- Single Flow;
- A_8 = 5.66 Ft^2 ($.53m^2$)

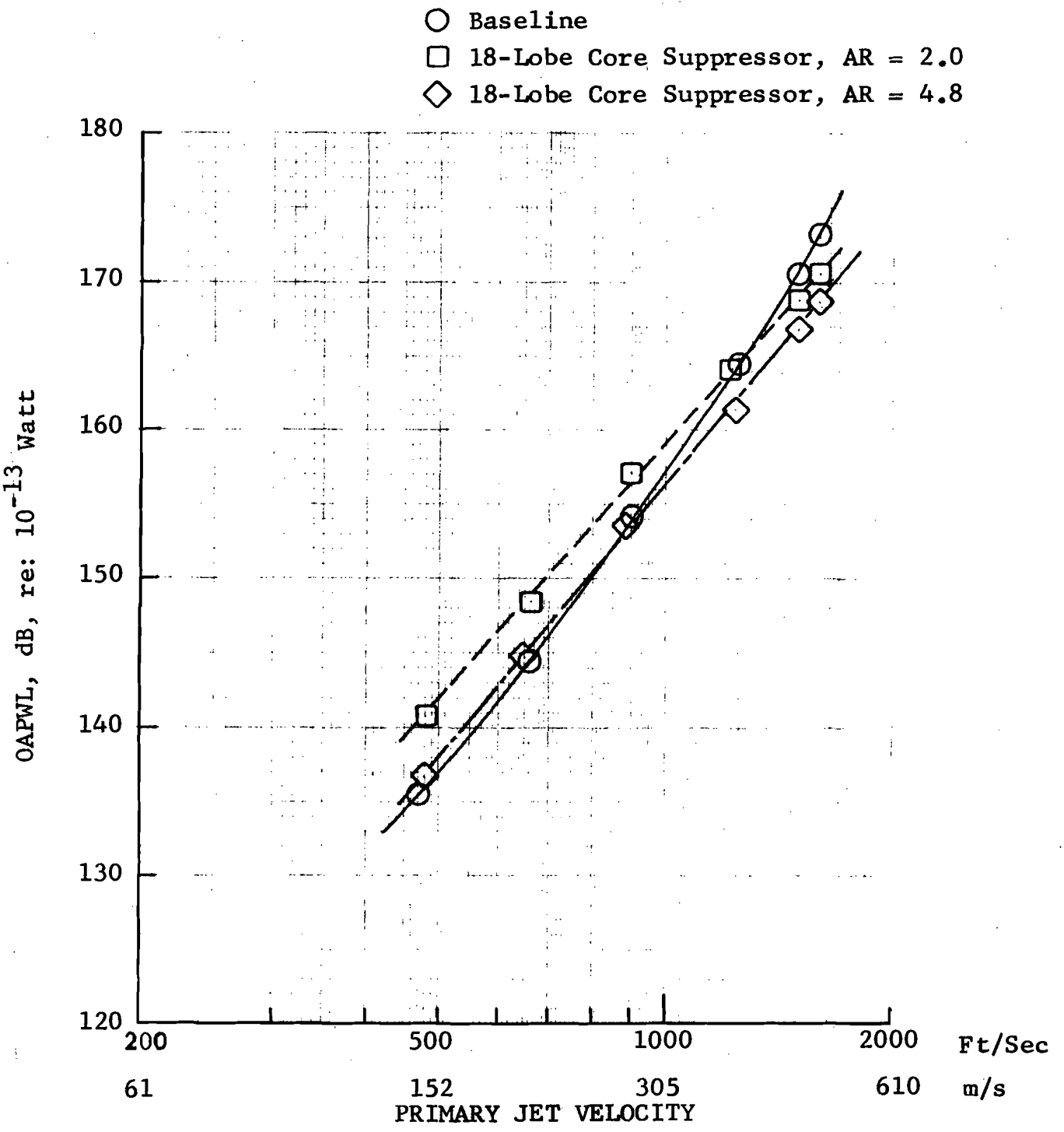

FIGURE 2.4.4-13 OAPWL VS V_{CORE}, SINGLE FLOW

small because these suppressor mechanisms are essentially that of the frequency conversion and little energy is extracted. This fact is shown in Figure 2.4.4-14 at a 1500 ft (474 m) sideline distance where OASPL reductions occur at core jet velocities below 1000 ft/sec (305 m/s). Since the suppressor mechanism forces energy into the higher frequencies the perceived noise level relationships at 1500 ft (474 m) shown in Figure 2.4.4-15 do not reflect the reduction obtained in OASPL.

The relationship between OAPWL and core jet velocity for the dual flow operation is shown in Figure 2.4.4-16. For the AR 4.8 configuration the increase in power level due to the fan impingement noise amounts to almost 10 dB throughout the velocity range. A similar result was obtained for peak OASPL and core velocity as seen in Figure 2.4.4-17. The peak perceived noise level characteristics follow similar trends as is shown in Figure 2.4.4-18. The relationships obtained for the AR 2 configuration were close enough to the baseline levels to suggest that if the increase in fan noise levels could be controlled by smoothing the flow contour over which the secondary air passes, a noise reduction might be obtained for dual flow operation.

2.4.5 Test Results, Suppressor Test 2

The 18 lobe daisy core nozzle suppressor was modified in an attempt to straighten the flow passing over the lobes by brazing metal caps in those locations. Apart from re-testing the "capped" lobe suppressor in its initial configuration, i.e., staggered exhaust planes, the capped suppressor was tested with a coplanar fan shroud to investigate possible improvements caused by this configuration. Since the modification did not alter the internal characteristics, the noise signature for single flow jet noise was unaffected. The results of the modification to the OASPL directional characteristics of fan flow noise at approach power is shown in Figure 2.4.5.1, where uncapped and capped lobe measurements are compared. The OASPL's from the tests on the capped lobe indicate a reduction at all angles relative to the initial design, particularly at forward angles. At this low velocity the modification did not reduce the levels down to the baseline. At the takeoff power setting, shown in Figure 2.4.5-2, the reduction in OASPL due to the capped lobe modification is sufficient to lower the levels to that of the baseline at all angles (with the exception of the aft angle locations of 120° to 150° where the levels are 2 dB above the baseline). The same results are obtained during dual flow operation (Figures 2.4.5-3 and 2.4.5-4). The modification is particularly successful at takeoff power where there is a 2 to 3 dB reduction in level at all angles relative to the "uncapped" design.

A further series of tests were conducted in order to examine another potential improvement possible with the capped lobe configuration; the fan shroud was replaced by another providing an extension in length sufficient to produce a coplanar system. Although not expected to effect core jet noise, it was hoped that the fan scrubbing noise might be shielded by the duct extension. In Figures 2.4.5-5 and 2.4.5-6 the OASPL directional characteristics of fan flow at approach and take power are compared for short and long (coplanar) duct configurations. The long duct provided a measurable shielding effect at all angles for both power settings particularly at approach power (see Figure

LOW VELOCITY JET NOISE SUPPRESSOR TEST 1

- 1500 Ft. (457m) Sideline
- A_8 = 5.66 Ft^2 (.53m^2); No EGA

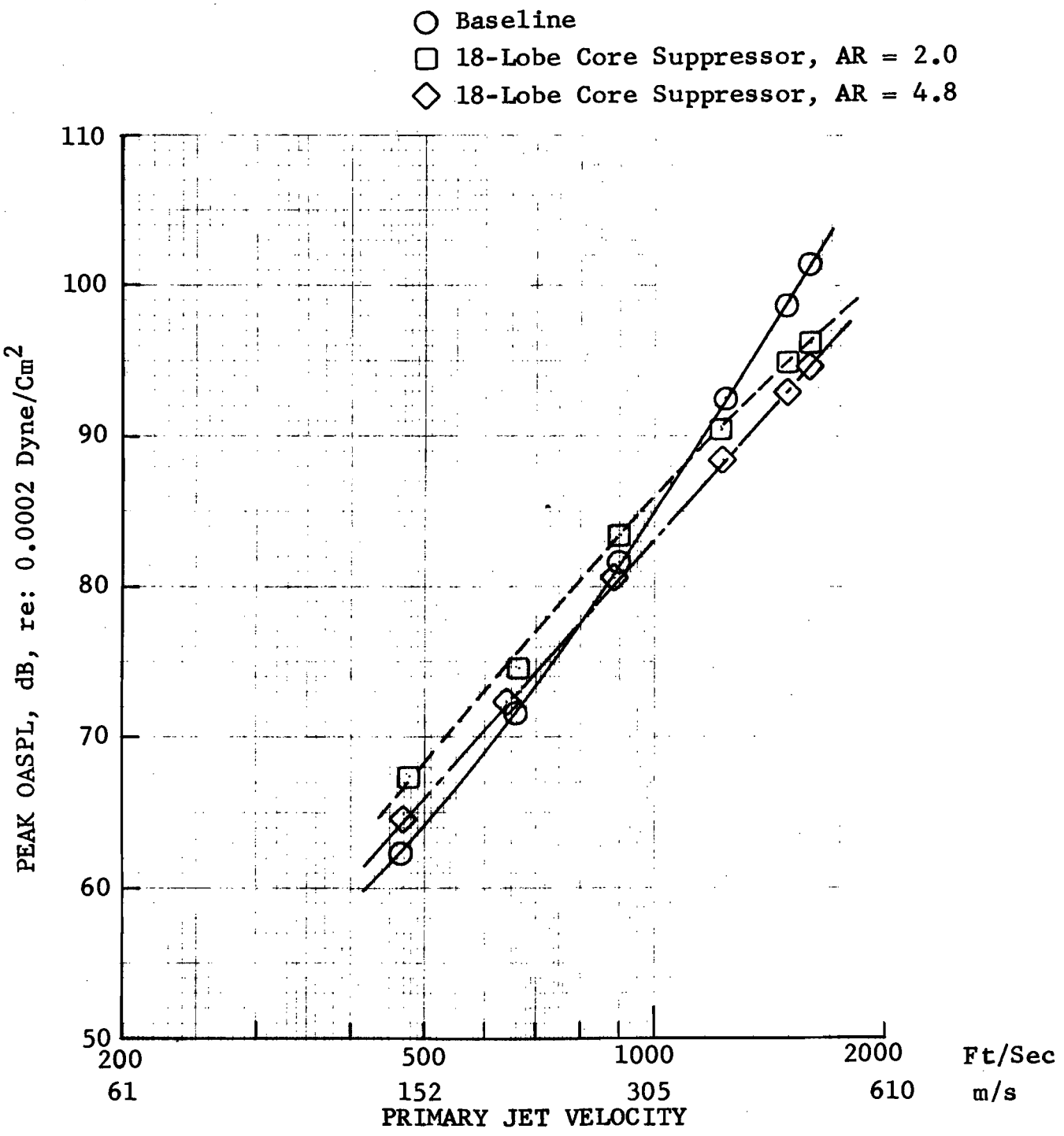

FIGURE 2.4.4-14 PEAK OASPL VS V_{CORE}, SINGLE FLOW

LOW VELOCITY JET NOISE SUPPRESSOR TEST 1

- 1500 Ft. (457m) Sideline
- A_8 = 5.66 Ft.^{2} (.53m^2); No EGA

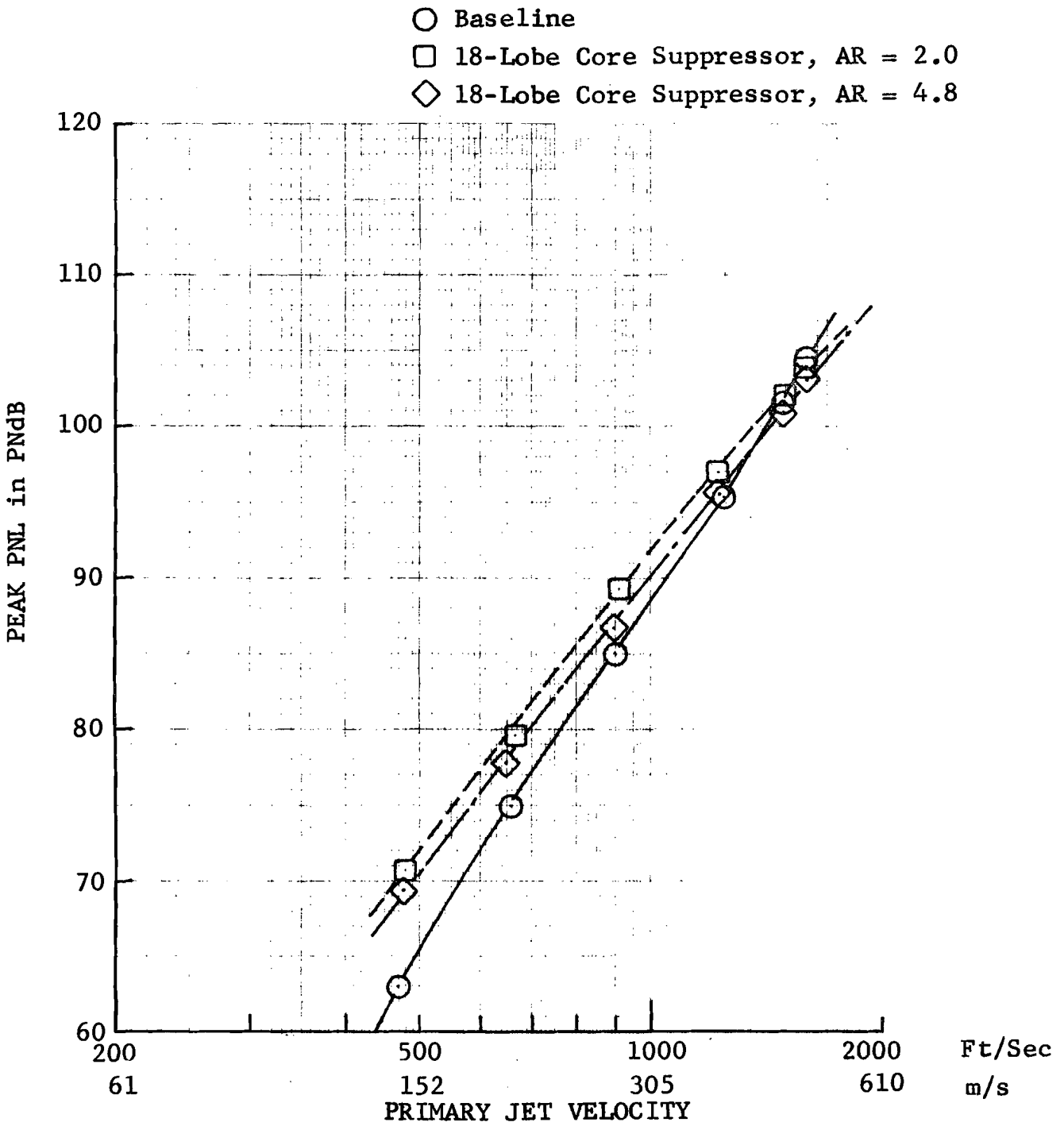

FIGURE 2.4.4-15 PEAK PNL VS V_{CORE}, SINGLE FLOW

LOW VELOCITY JET NOISE SUPPRESSOR TEST 1

- Dual Flow; No EGA
- A_8 = 5.66 Ft^2 (.53m^2), A_{28} = 17.28 Ft^2 (1.61m^2)

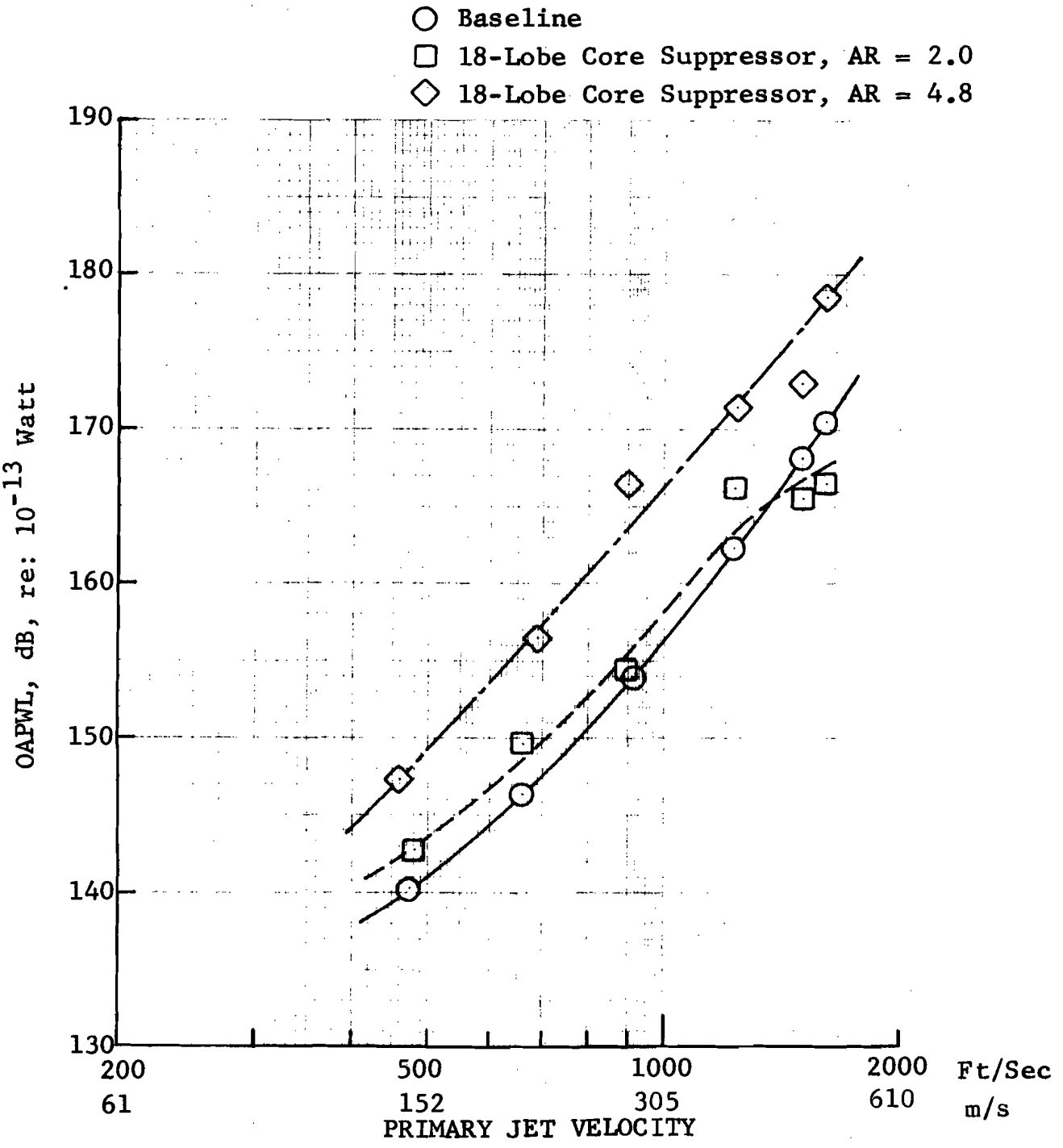

FIGURE 2.4.4-16 OAPWL VS V_{CORE}, DUAL FLOW

LOW VELOCITY JET NOISE SUPPRESSOR TEST 1

- 1500 Ft.(457m) Sideline, No EGA
- A_8 = 5.66 Ft^2(.53m^2); A_{28} = 17.28 Ft^2 (1.61m^2)

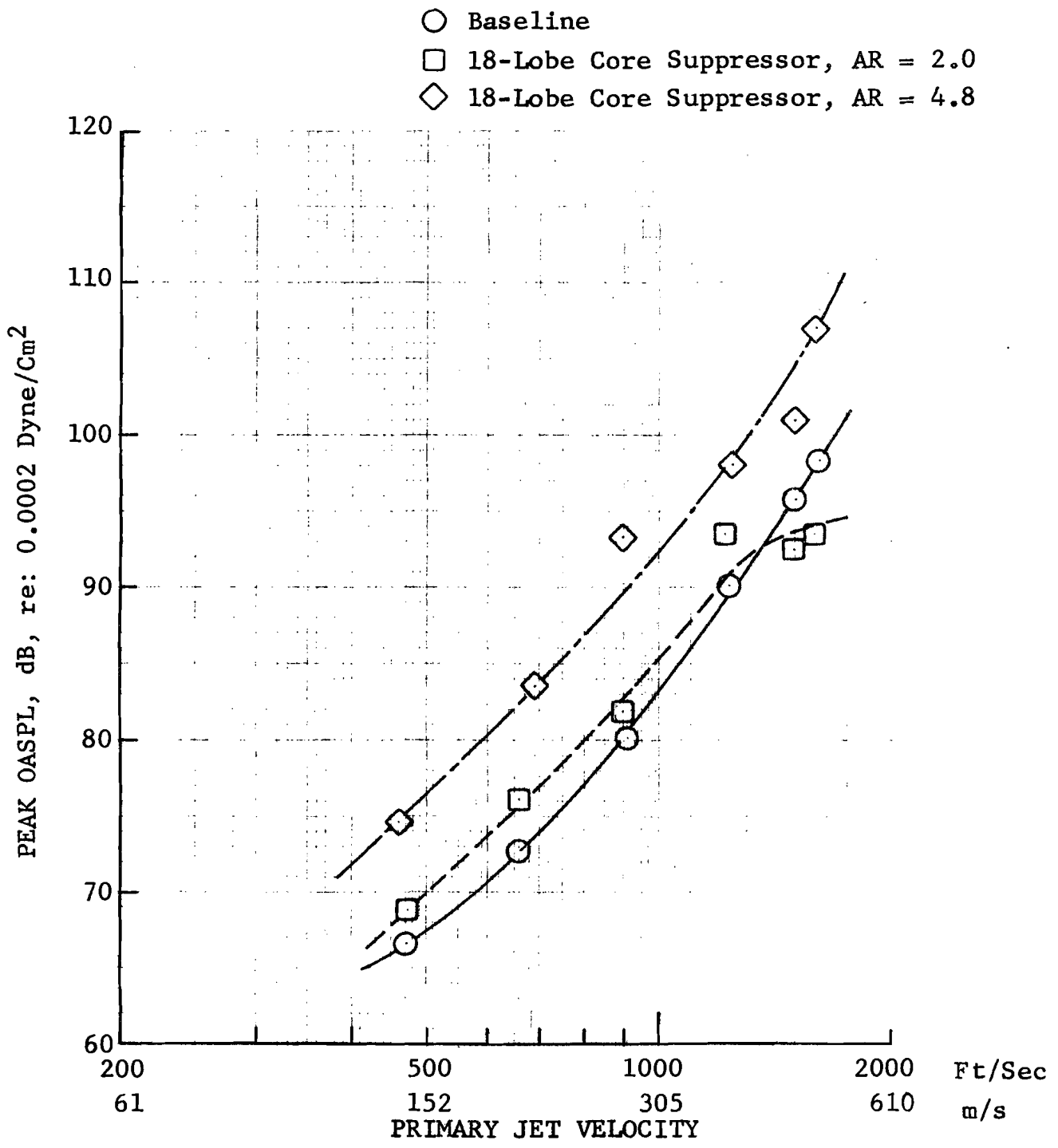

FIGURE 2.4.4-17 PEAK OASPL VS V_{CORE}, DUAL FLOW

LOW VELOCITY JET NOISE SUPPRESSOR TEST 1

- 1500 Ft. (457m) Sideline, No EGA
- A_8 = 5.66 Ft^2 (.53m^2); A_{28} = 17.28 Ft^2 (1.61m^2)

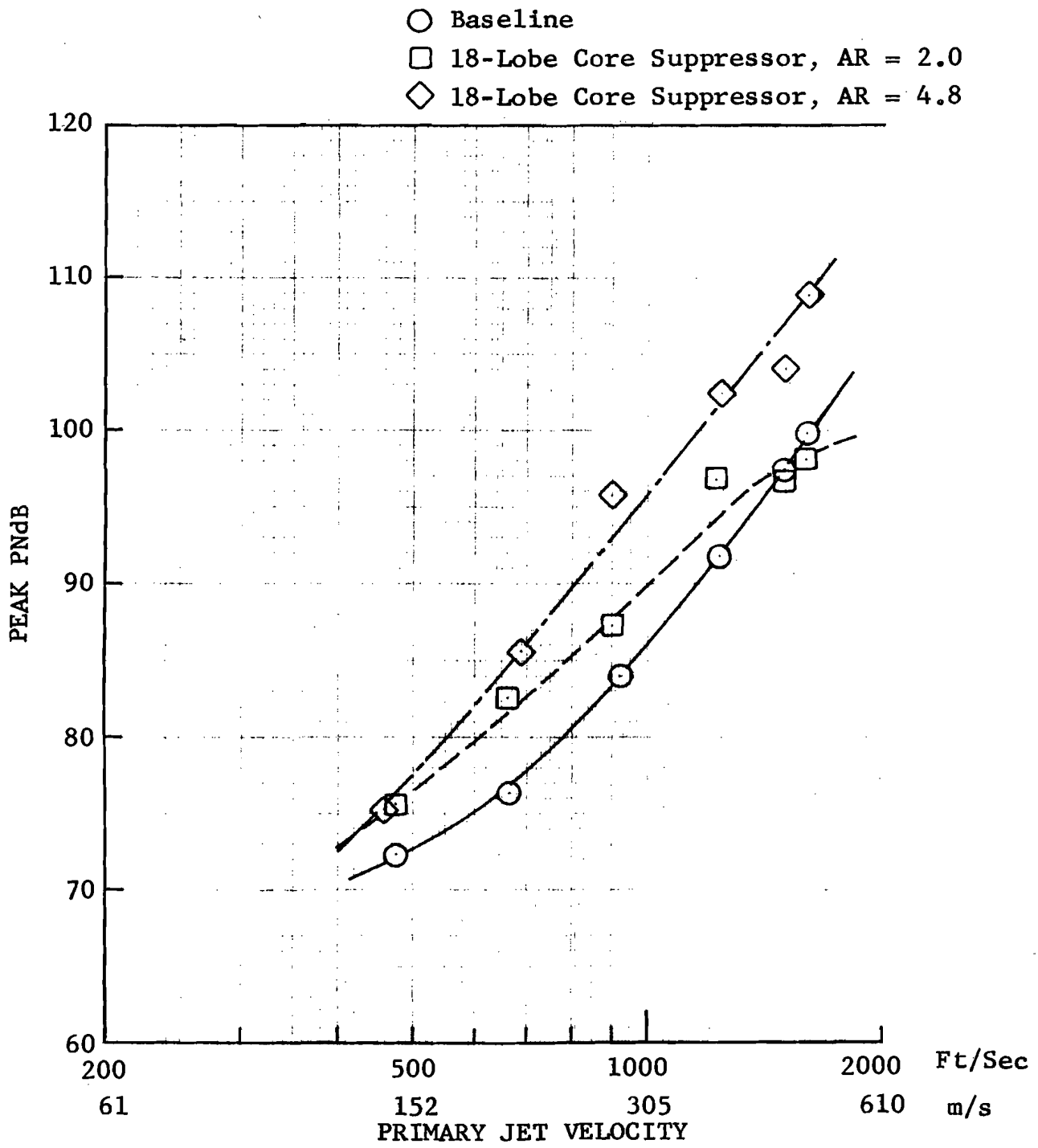

FIGURE 2.4.4-18 PEAK PNL VS V_{CORE}, DUAL FLOW

LOW VELOCITY JET NOISE SUPPRESSOR TEST 2
18-LOBE DAISY CORE NOZZLE, AR = 2.0, SHORT FAN DUCT

- 200 FT. (61 m) SIDELINE, SINGLE ENGINE
- INCLUDES EGA
- A_{FAN} = 17.28 FT^2 (1.61 m^2)

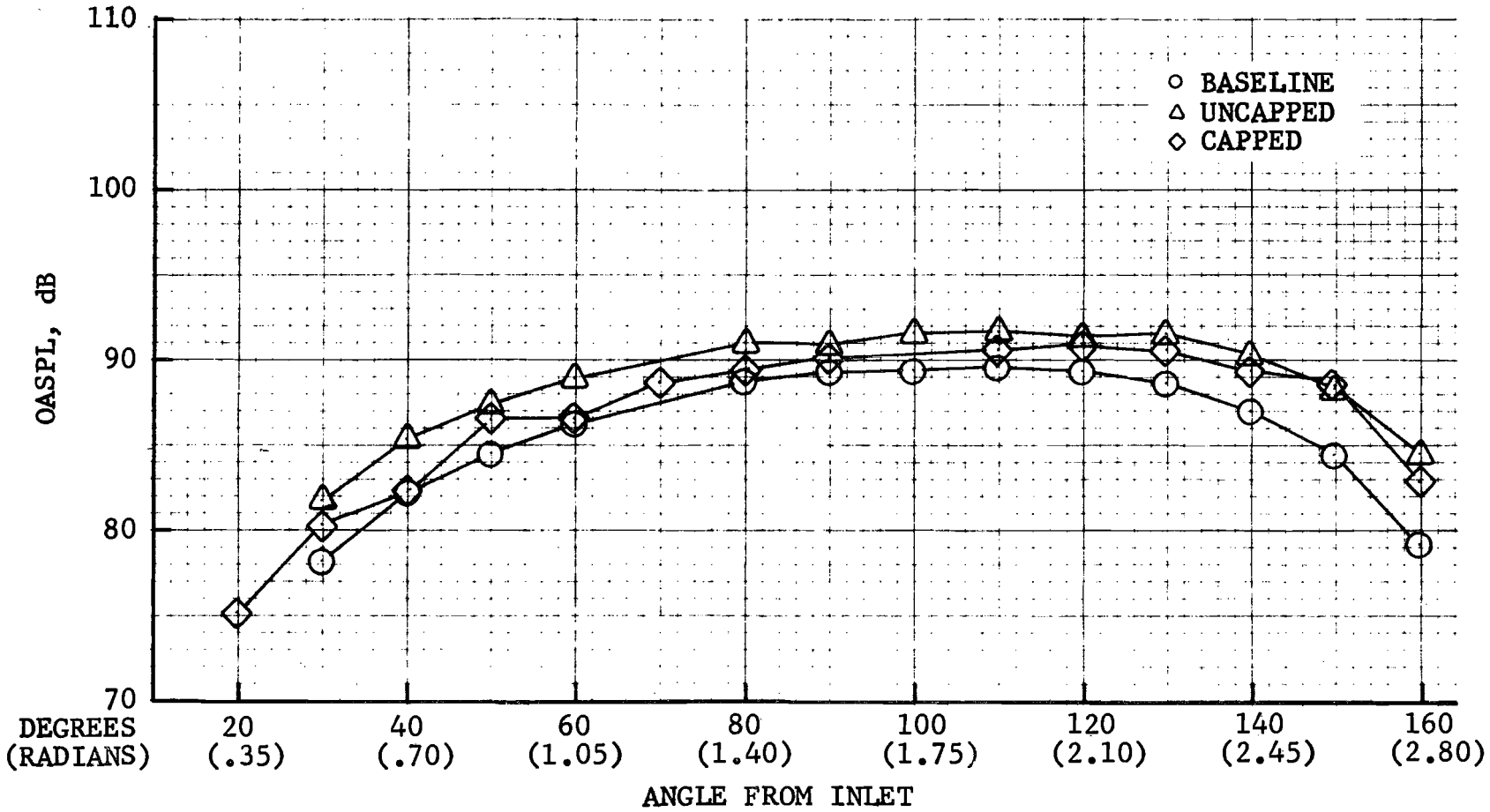

FIGURE 2.4.5-1 OASPL VS ACOUSTIC ANGLE, FAN ONLY, $V_{FAN} \approx 580$ FT/SEC (177 m/s)

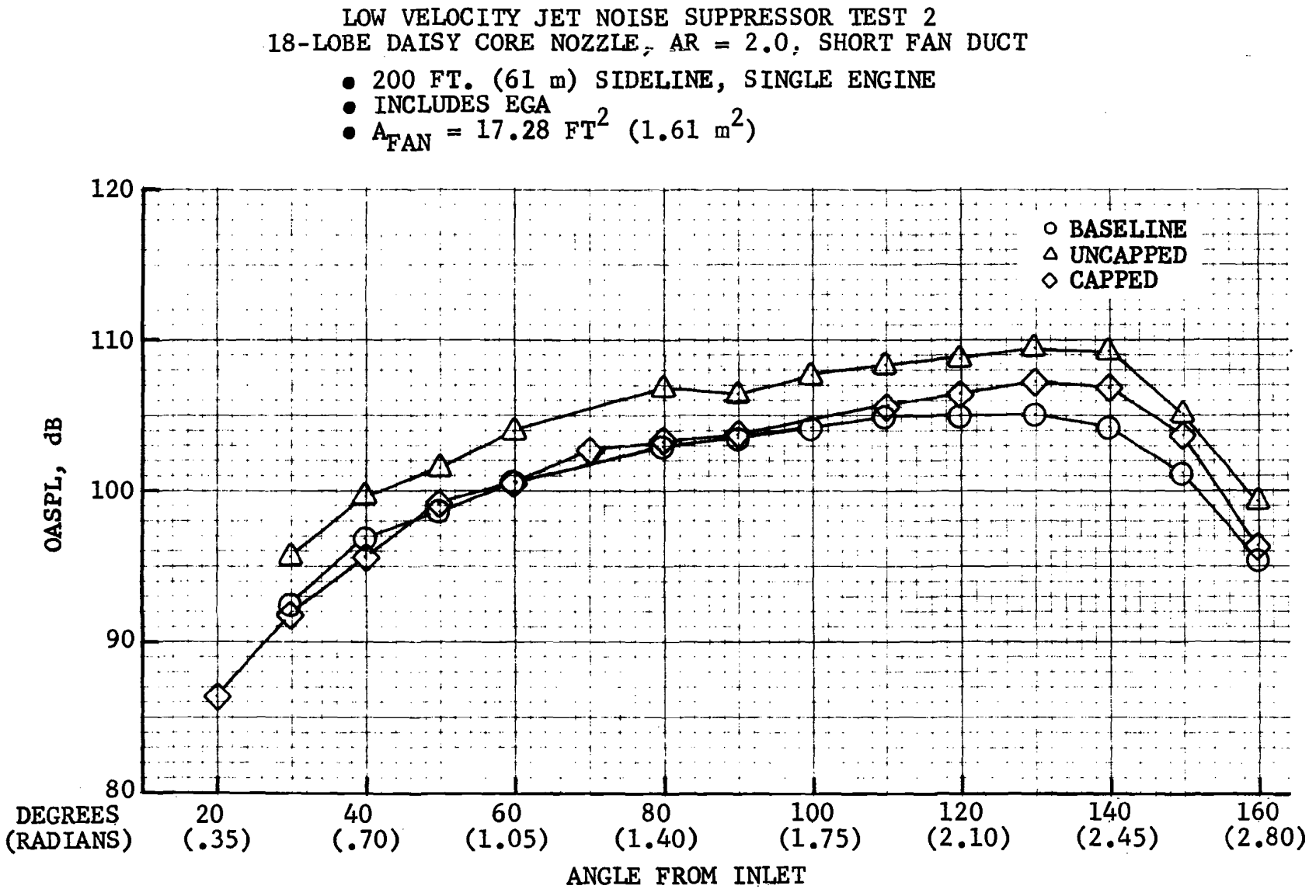

FIGURE 2.4.5-2 OASPL VS ACOUSTIC ANGLE, FAN ONLY, $V_{FAN} \approx 950$ FT/SEC (290 m/s)

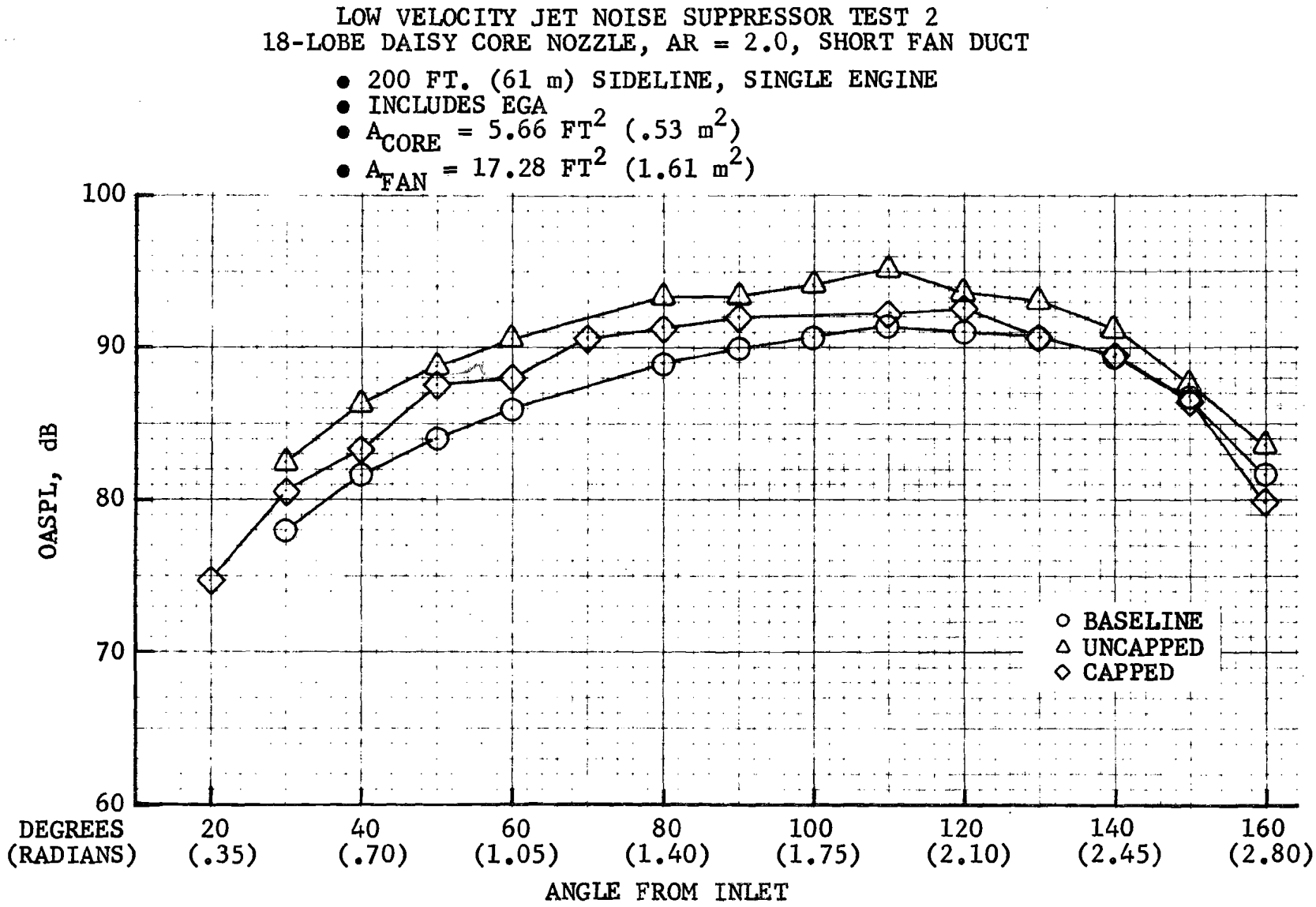

FIGURE 2.4.5-3 OASPL VS ACOUSTIC ANGLE, DUAL FLOW, $V_{CORE} \approx 660$ FT/SEC (201 m/s), $V_{FAN} \approx 580$ FT/SEC (177 m/s)

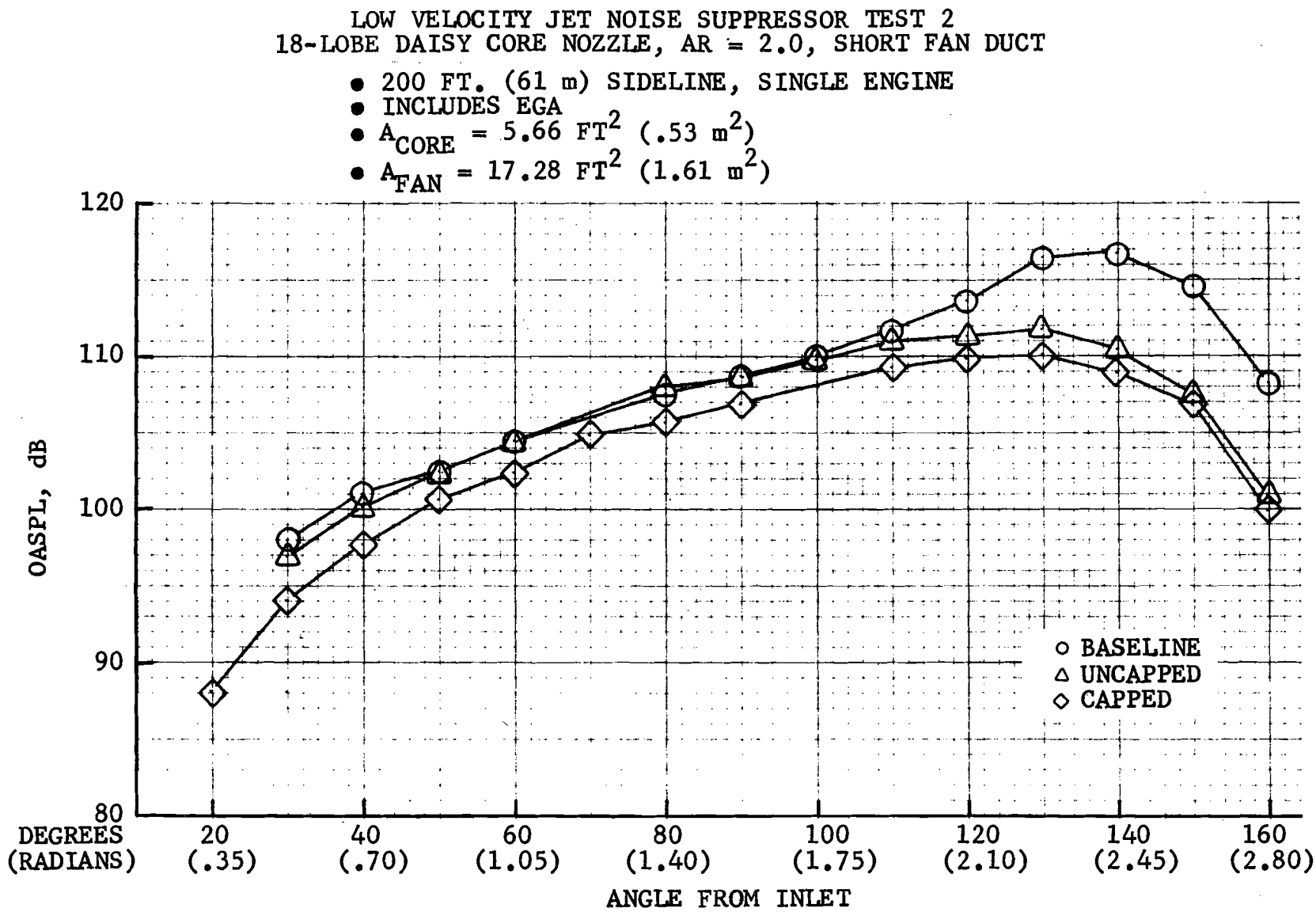

FIGURE 2.4.5-4 OASPL VS ACOUSTIC ANGLE, DUAL FLOW, $V_{CORE} \approx 1600$ FT/SEC (488 m/s), $V_{FAN} \approx 950$ FT/SEC (290 m/s)

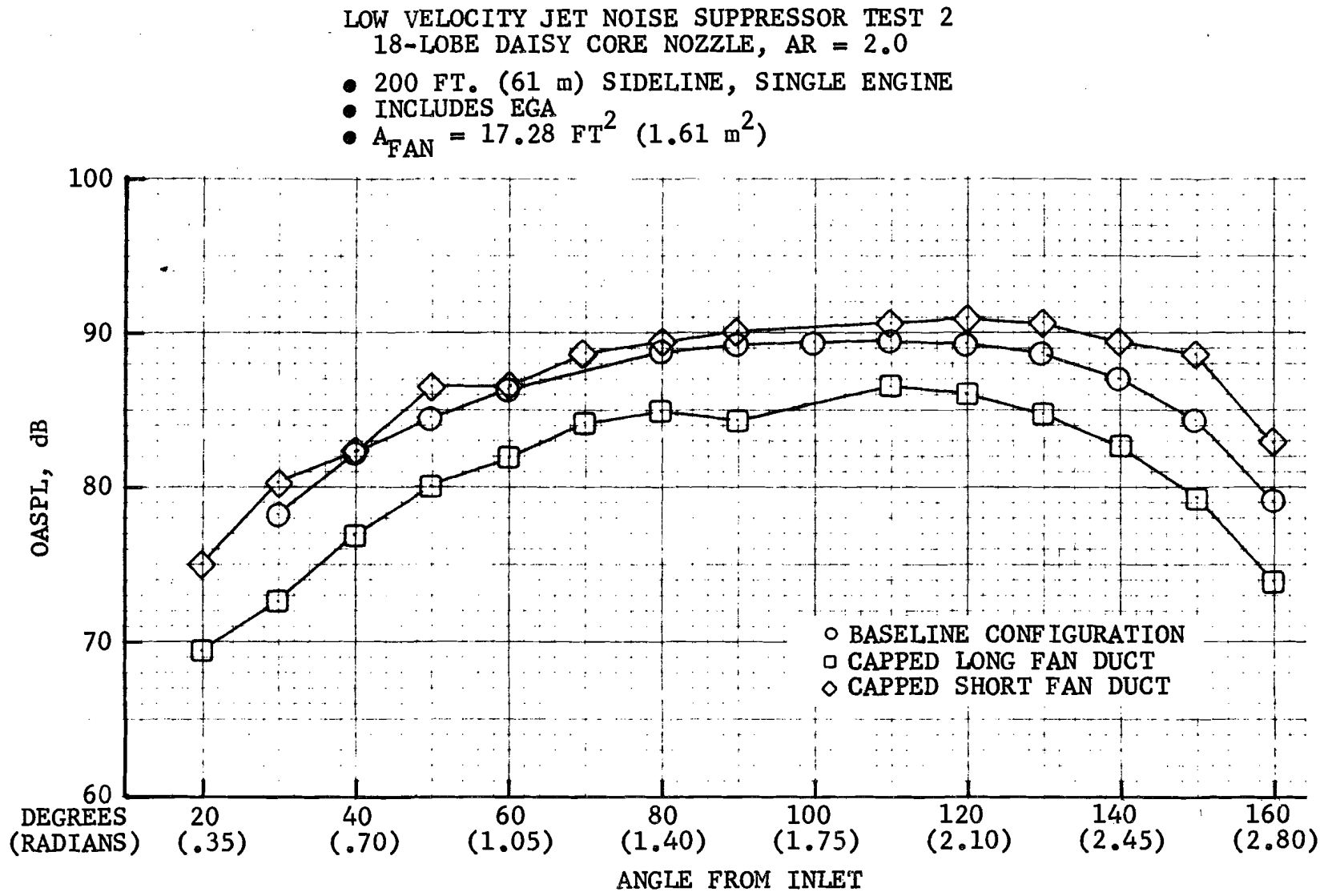

FIGURE 2.4.5-5 OASPL VS ACOUSTIC ANGLE, FAN ONLY, $V_{FAN} \approx 580$ FT/SEC (177 m/s)

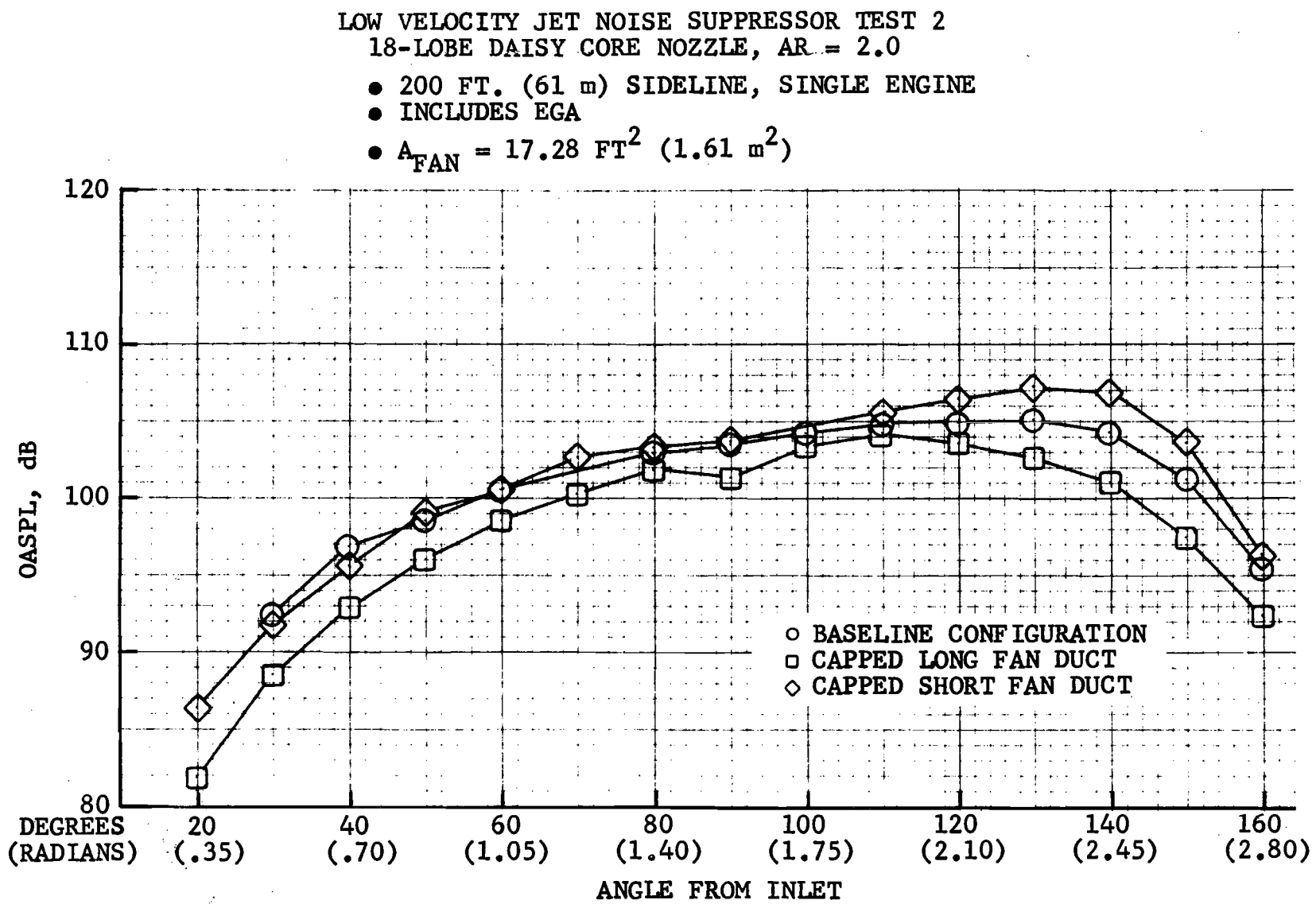

FIGURE 2.4.5-6 OASPL VS ACOUSTIC ANGLE, FAN ONLY, $V_{FAN} \approx 950$ FT/SEC (290 m/s)

2.4.5-5) where approximately 5 dB reduction in fan flow was measured at all forward angles and even greater reduction at aft angles. A comparison of both configurations with dual flow operation at approach and takeoff power are shown in Figures 2.4.5-7 and 2.4.5-8. The long duct did reduce the dual flow levels at the part power setting but no effect was observed at the full power setting where core jet noise is the primary noise source.

A comparison between the uncapped and capped lobe peak angle spectra are shown in Figures 2.4.5-9 to 2.4.5-12. The effect of the modification at the low fan velocity (Figure 2.4.5-9) was to lower the fan only SPL's by 2 to 3 dB in all frequency bands. At the complementary dual flow condition (Figure 2.4.5-11) the reduction in SPL's is greater than for the fan alone - 3 to 5 dB. The modification appears to have improved the interaction between fan and core flow, particularly at high frequencies. At the fan velocity simulating takeoff conditions (Figure 2.4.5-10) the fan only SPLs are reduced 4 to 5 dB in the high frequency range. With the dual flow system, Figure 2.4.5-12, levels are reduced in all frequency bands by 2 dB.

The peak angle spectra for the short and long duct configurations are shown in Figures 2.4.5-13 to 2.4.5-16. At low fan velocities (Figure 2.4.5-13) the long duct achieves shielding of low frequency fan flow generated noise; but there is no similar reduction in this portion of the spectra during dual flow operation (Figure 2.4.5-15). At the high fan velocity shown in Figure 2.4.5-14, low frequency fan flow noise is shielded by the long duct configuration; however, at the comparable dual flow condition the observed reduction does not materialize and a small increase in high frequency noise occurs (Figure 2.4.5-16). Thus the long duct configuration provides little or no improvement in dual flow jet noise levels over the velocity range of interest.

The relationship between dual flow OAPWL and core jet velocity for uncapped and capped configurations is shown in Figure 2.4.5-17. The modification provides OAPWL reductions down to 1000 ft/sec (305 m/s) and at the takeoff power results in 5 dB reduction relative to the baseline. The SPL data was extrapolated to 1500 ft (457 m.) sideline, without EGA, to simulate a microphone reading at a typical aircraft flyover situation. In Figure 2.4.5-18 the peak OASPL is shown related to core jet velocity. Relative to the baseline, the modified suppressor OASPL's are lower commencing at 900 ft/sec (275 m/s) and at the takeoff power setting achieve a total reduction of 7 dB. The relationship between perceived noise level and core jet velocity is shown in Figure 2.4.5-19. At the takeoff power condition the modified lobe core suppressor configuration provides 5 PNdB reduction in dual flow jet noise. The suppressor was effective down to a core jet velocity of 1100 ft/sec (335 m/s), whereas the original suppressor only achieved 2 PNdB suppression at the takeoff power and zero at a core jet velocity of 1500 ft/sec (457 m/s)

2.4.6 Test Results, Suppressor Test 3

The configurations evaluated in this test series include a new baseline configuration, a multi-hole configuration and a multi-spoke configuration. The core suppressors had annulus-to-core flow area ratios of 2; similar to the successful 18 capped lobe suppressor already evaluated. The directional

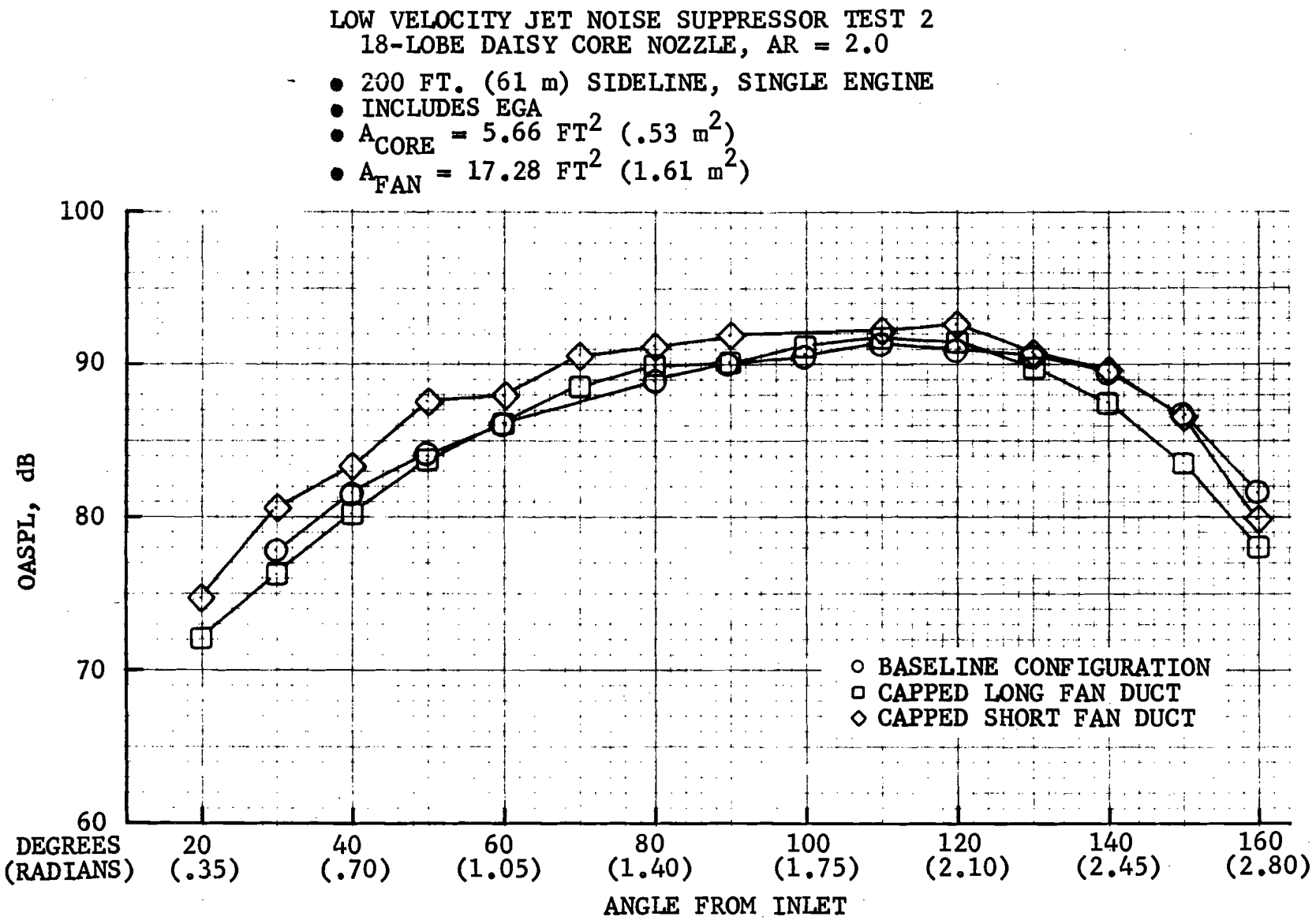

FIGURE 2.4.5-7 OASPL VS ACOUSTIC ANGLE, DUAL FLOW, $V_{CORE} \approx 660$ FT/SEC (201 m/s), $V_{FAN} \approx 580$ FT/SEC (177 m/s)

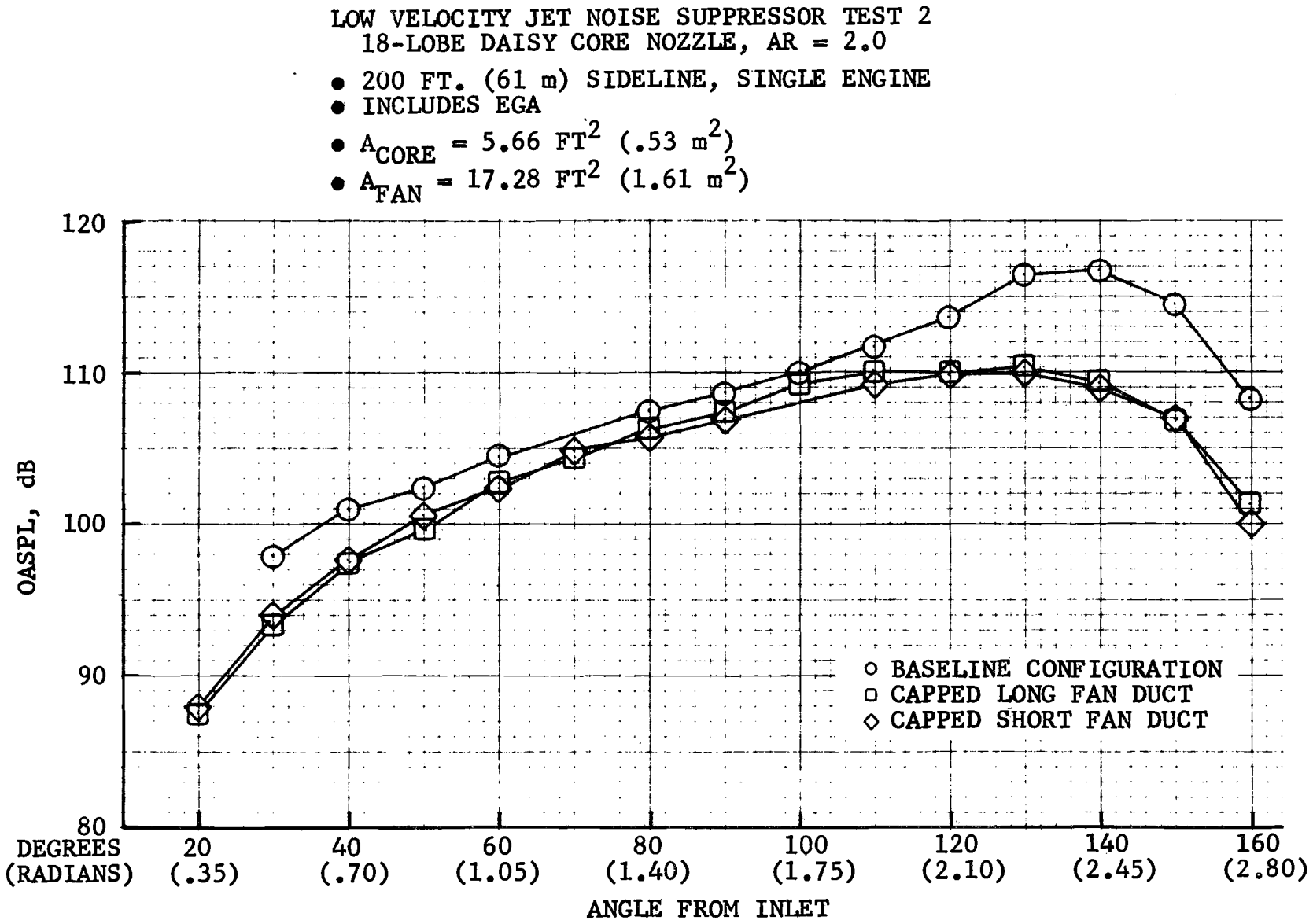

FIGURE 2.4.5-8 OASPL VS ACOUSTIC ANGLE, DUAL FLOW, $V_{CORE} \approx 1600$ FT/SEC (488 m/s), $V_{FAN} \approx 950$ FT/SEC (290 m/s)

LOW VELOCITY JET NOISE SUPPRESSOR TEST 2
18-LOBE DAISY CORE NOZZLE, AR = 2.0
SHORT FAN DUCT

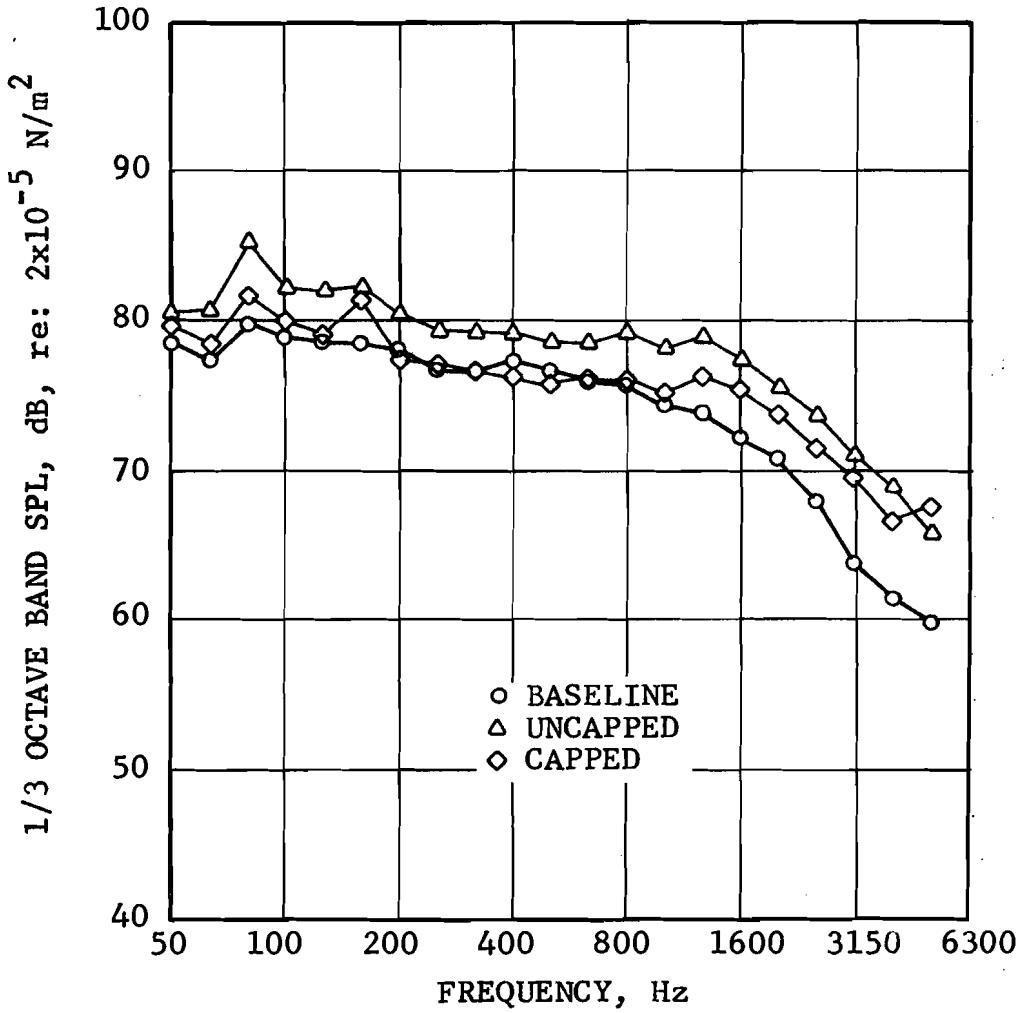

- 200 FT. (61 m) SIDELINE, SINGLE ENGINE
- INCLUDES EGA
- A_{FAN} = 17.28 FT^2 (1.61 m^2)

FIGURE 2.4.5-9 PEAK ANGLE SPECTRA, FAN ONLY, $V_{FAN} \approx 580$ FT/SEC (177 m/s)

LOW VELOCITY JET NOISE SUPPRESSOR TEST 2

18-LOBE DAISY CORE NOZZLE, AR = 2.0

SHORT FAN DUCT

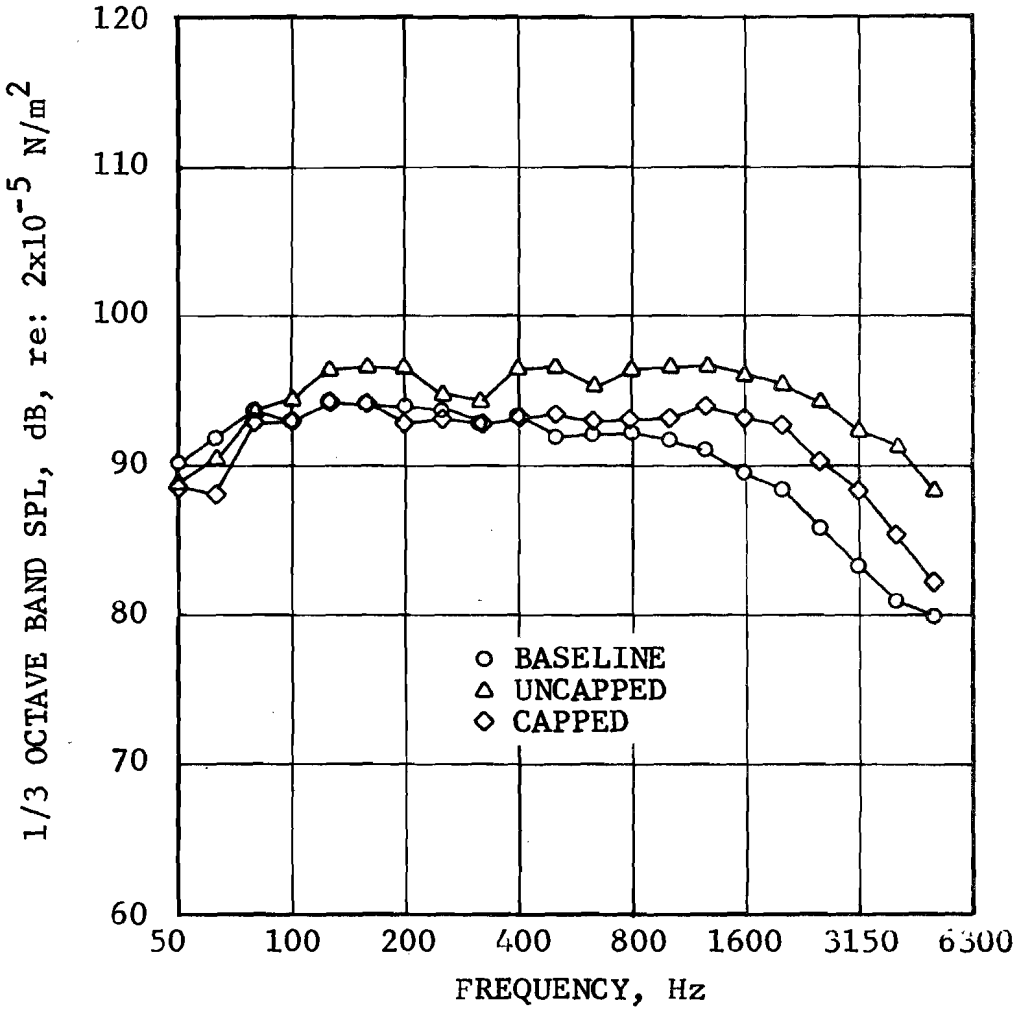

- o 200 FT. (61 m) SIDELINE, SINGLE ENGINE
- o INCLUDES EGA
- o A_{FAN} = 17.28 FT^2 (1.61 m^2)

FIGURE 2.4.5-10 PEAK ANGLE SPECTRA, FAN ONLY, $V_{FAN} \approx 950$ FT/SEC (250 m/s)

LOW VELOCITY JET NOISE SUPPRESSOR TEST 2
18-LOBE DAISY CORE NOZZLE, AR = 2.0
SHORT FAN DUCT

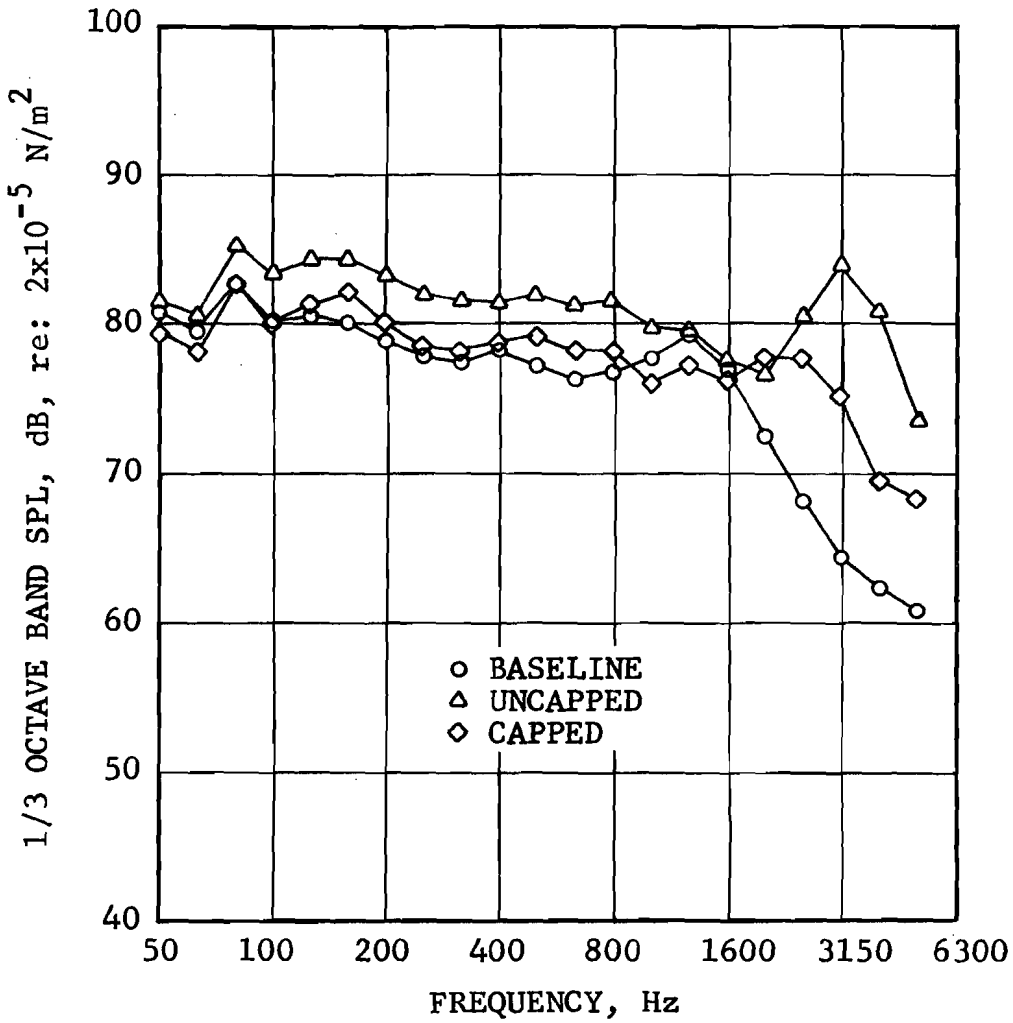

- 200 FT. (61 m) SIDELINE, SINGLE ENGINE
- INCLUDES EGA
- A_{CORE} = 5.66 FT^2 (.53 m^2)
- A_{FAN} = 17.28 FT^2 (1.61 m^2)

FIGURE 2.4.5-11 PEAK ANGLE SPECTRA, DUAL FLOW, $V_{CORE} \approx 660$ FT/SEC (201 m/s), $V_{FAN} \approx 580$ FT/SEC (177 m/s)

LOW VELOCITY JET NOISE SUPPRESSOR TEST 2

18-LOBE DAISY CORE NOZZLE, AR = 2.0

SHORT FAN DUCT

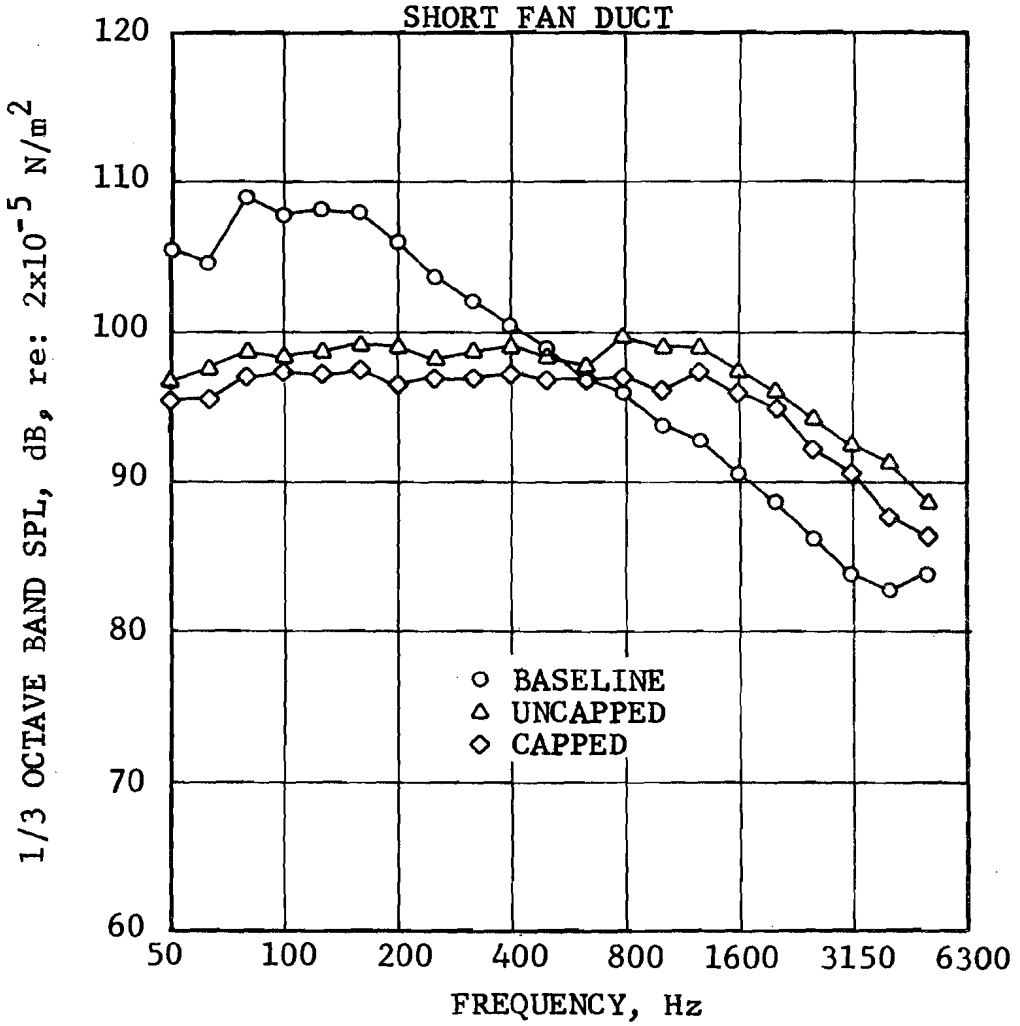

- 200 FT. (61 m) SIDELINE, SINGLE ENGINE
- INCLUDES EGA
- A_{CORE} = 5.66 FT^2 (.53 m^2)
- A_{FAN} = 17.28 FT^2 (1.61 m^2)

FIGURE 2.4.5-12 PEAK ANGLE SPECTRA, DUAL FLOW, $V_{CORE} \approx 1600$ FT/SEC (488 m/s), $V_{FAN} \approx 950$ FT/SEC (290 m/s)

LOW VELOCITY JET NOISE SUPPRESSOR TEST 2

18-LOBE DAISY CORE NOZZLE, AR = 2.0

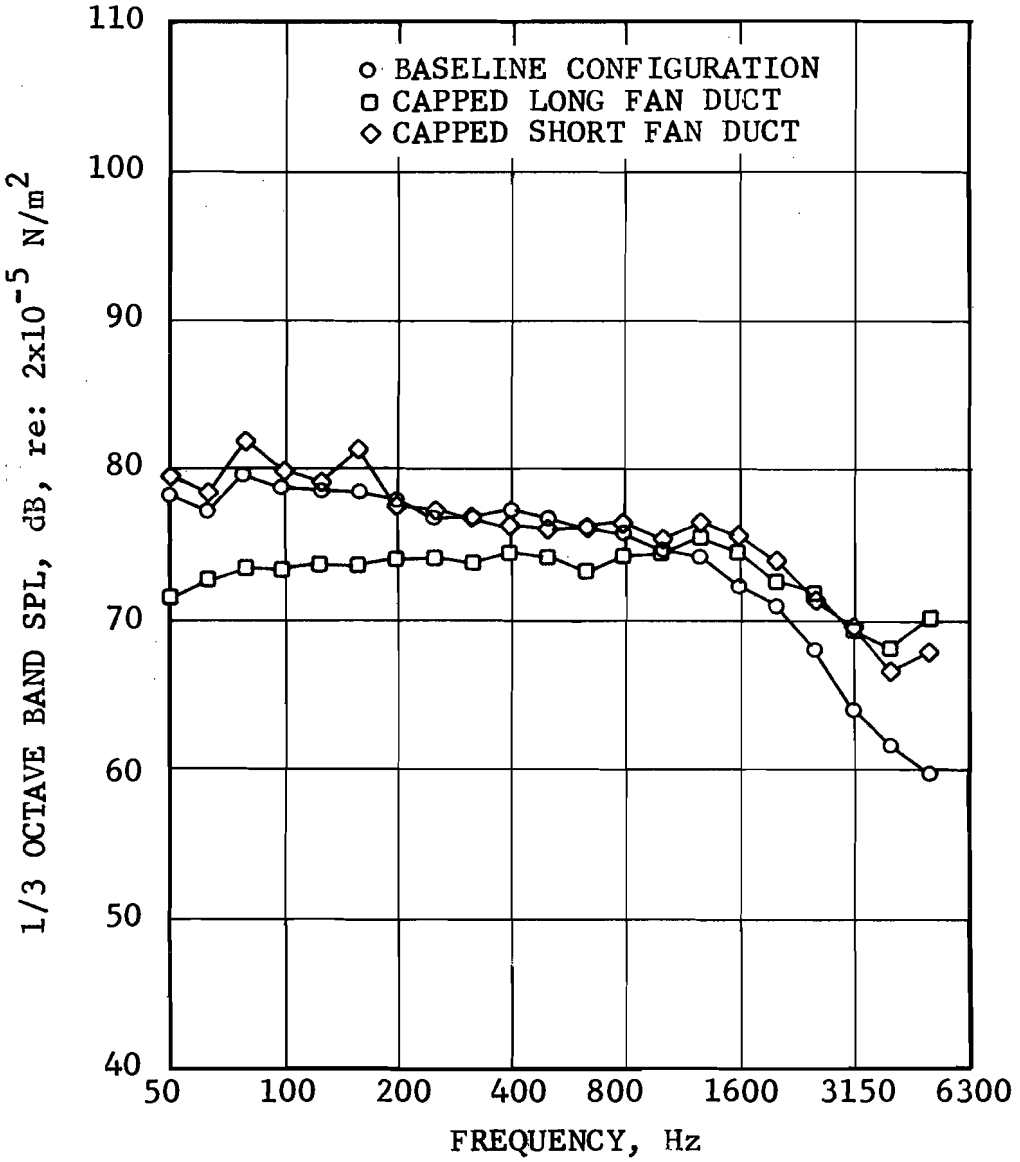

- 200 FT. (61 m) SIDELINE, SINGLE ENGINE
- INCLUDES EGA
- A_{28} = 17.28 FT^2 (1.61 m^2)

FIGURE 2.4.5-13 PEAK ANGLE SPECTRA, FAN ONLY, $V_{FAN} \approx 580$ FT/SEC (177 m/s)

LOW VELOCITY JET NOISE SUPPRESSOR TEST 2

18-LOBE DAISY CORE NOZZLE, AR = 2.0

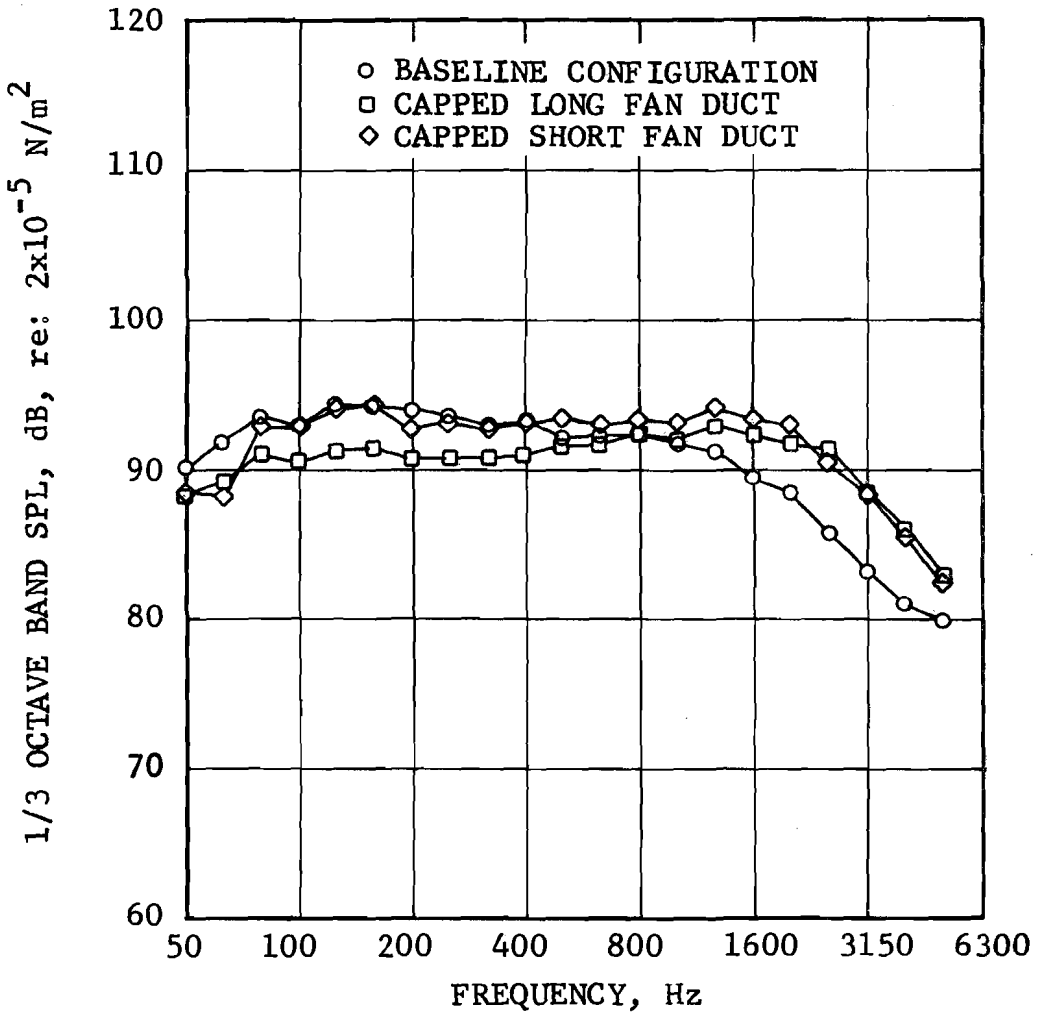

- 200 FT. (61 m) SIDELINE, SINGLE ENGINE
- INCLUDES EGA
- A_{28} = 17.28 FT^2 (1.61 m^2)

FIGURE 2.4.5-14 PEAK ANGLE SPECTRA, FAN ONLY, $V_{FAN} \approx 950$ FT/SEC (290 m/s)

LOW VELOCITY JET NOISE SUPPRESSOR TEST 2

18-LOBE DAISY CORE NOZZLE, AR = 2.0

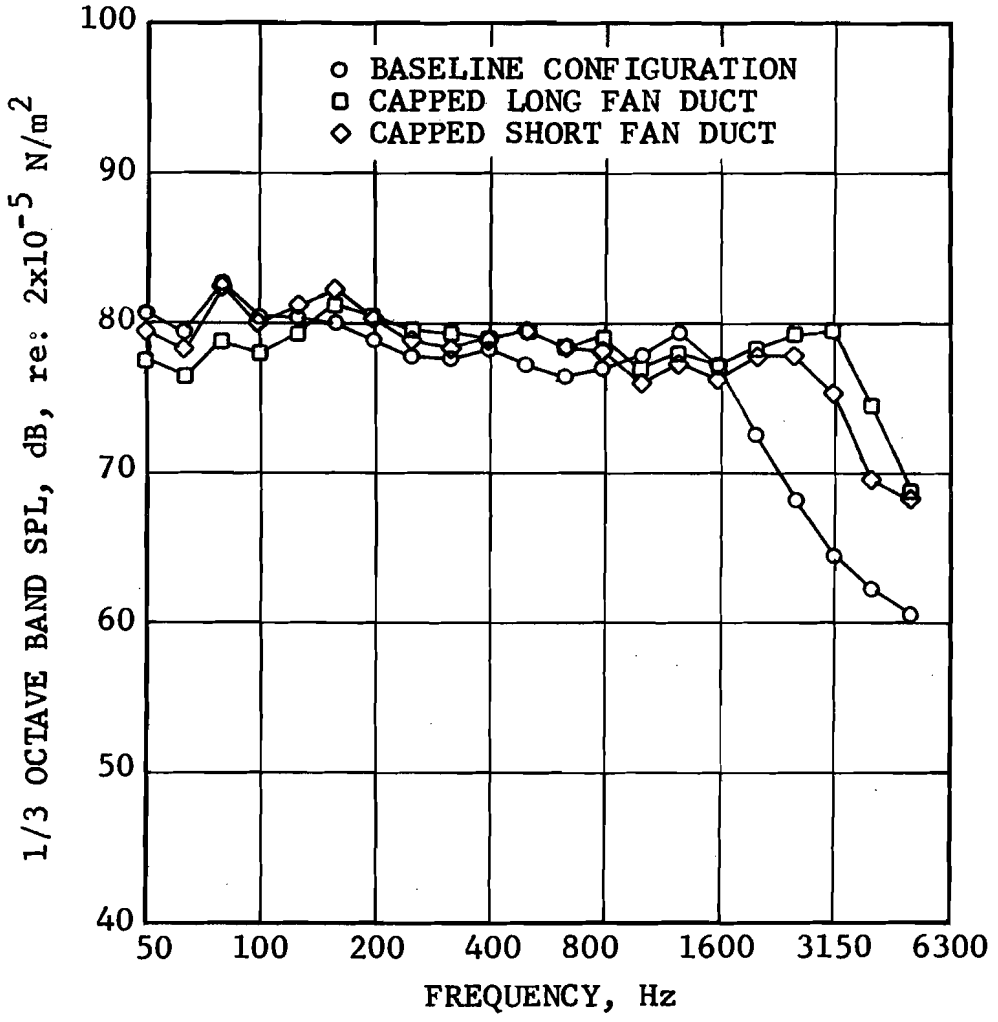

- o 200 FT. (61 m) SIDELINE, SINGLE ENGINE
- o INCLUDES EGA
- o A_8 = 5.66 FT^2 (.53 m^2)
- o A_{28} = 17.28 FT^2 (1.61 m^2)

FIGURE 2.4.5-15 PEAK ANGLE SPECTRA, DUAL FLOW, $V_{CORE} \approx 660$ FT/SEC (201 m/s), $V_{FAN} \approx 580$ FT/SEC (177 m/s)

LOW VELOCITY JET NOISE SUPPRESSOR TEST 2

18-LOBE DAISY CORE NOZZLE, AR = 2.0

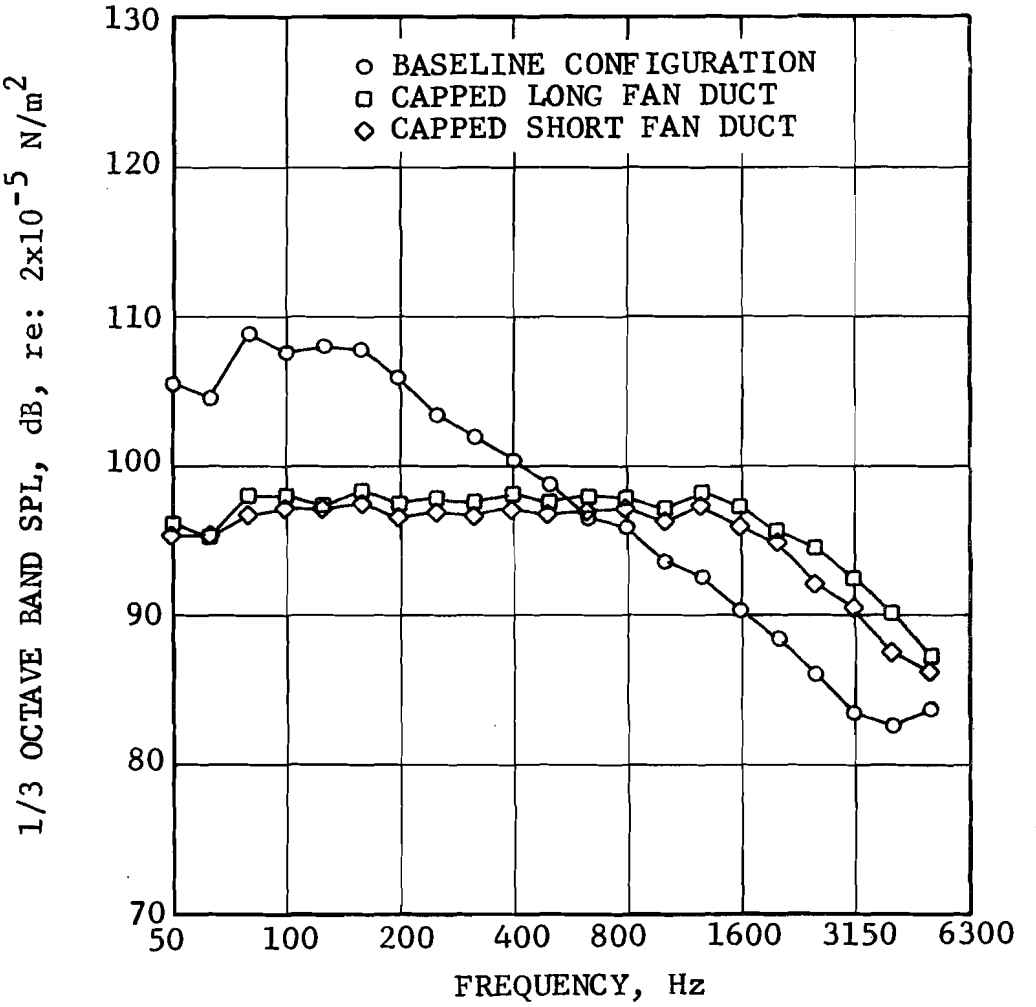

- o 200 FT. (61 m) SIDELINE, SINGLE ENGINE
- o INCLUDES EGA
- o A_8 = 5.66 FT^2(.53 m^2)
- o A_{28} = 17.28 FT^2(1.61 m^2)

FIGURE 2.4.5-16 PEAK ANGLE SPECTRA, DUAL FLOW, $V_{CORE} \approx 1600$ FT/SEC (488 m/s), $V_{FAN} \approx 950$ FT/SEC (290 m/s)

- SINGLE ENGINE, DUAL FLOW
- NO EGA
- A_{Core} = 5.6 FT^2 (1.7 m^2); A_{Fan} = 17.3 FT^2 (5.3 m^2)

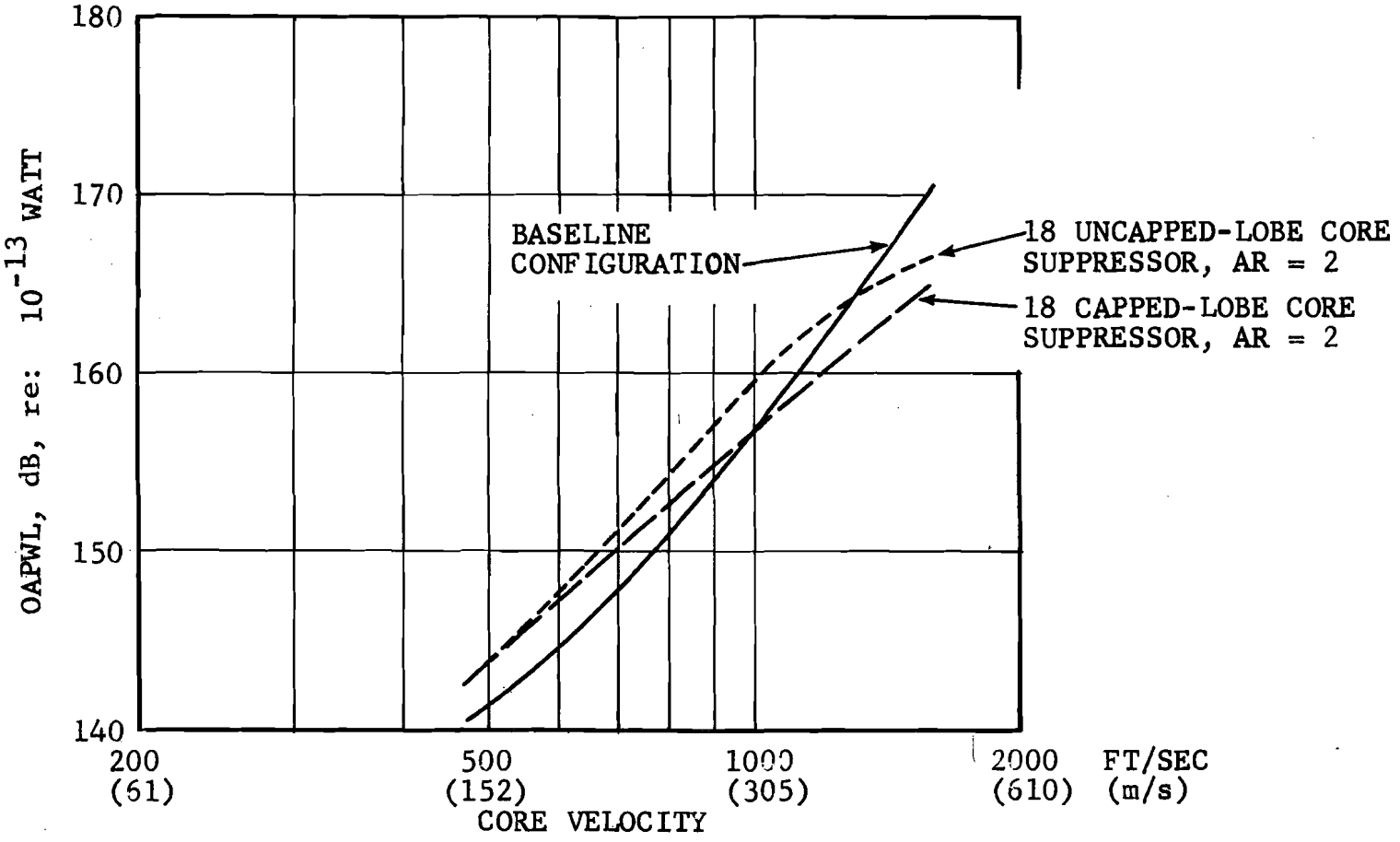

FIGURE 2.4.5-17 OAPWL VS CORE JET VELOCITY, DUAL FLOW, TEST 2

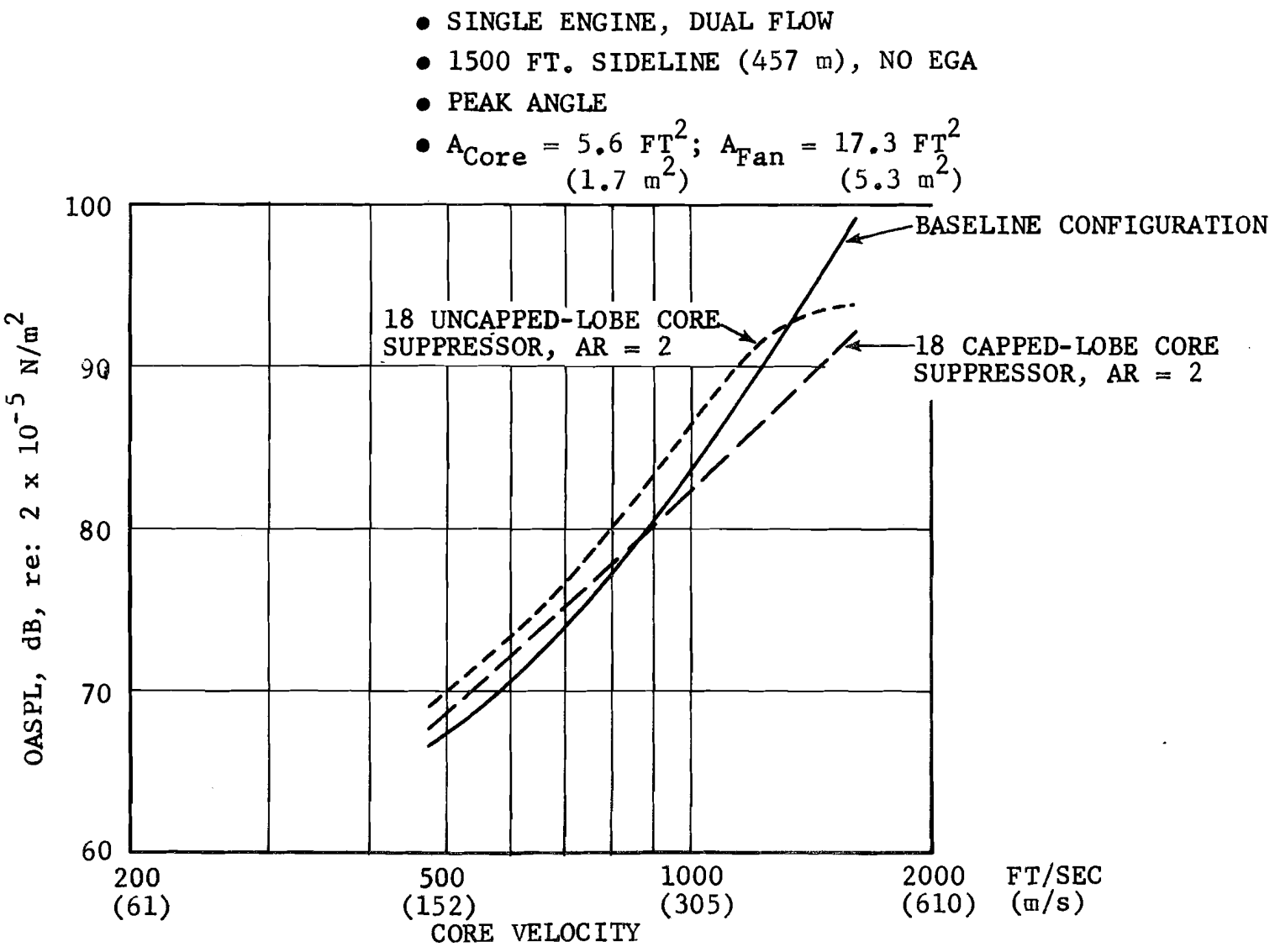

FIGURE 2.4.5-18 OASPL VS CORE JET VELOCITY, DUAL FLOW, TEST 2

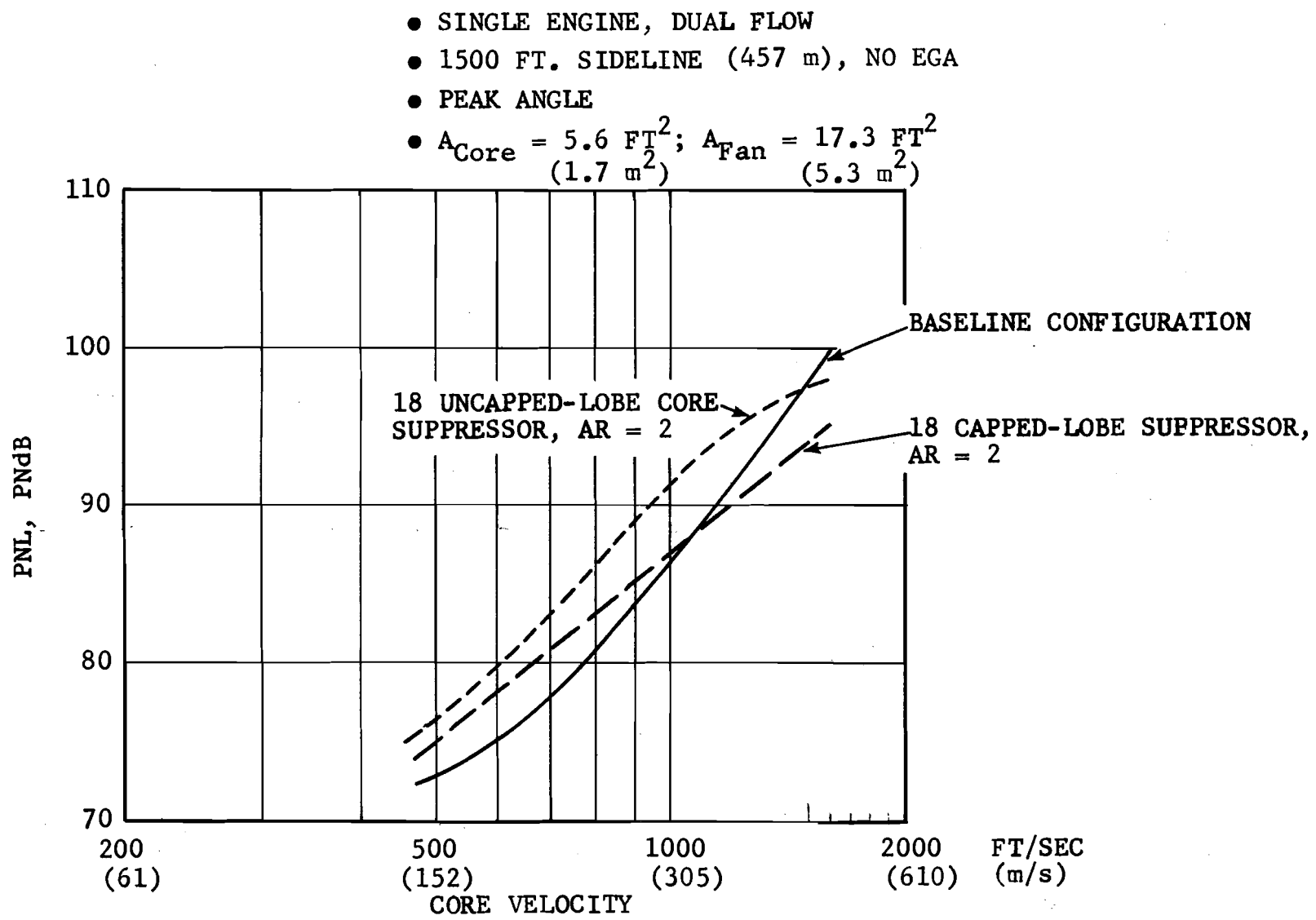

FIGURE 2.4.5-19 PNL VS CORE JET VELOCITY, DUAL FLOW, TEST 2

characteristics of these configurations for core jet only are shown in Figure 2.4.6-1 for the approach power case. Note that the SPL's have been extrapolated to a 1500 ft (457 m/s) sideline, without EGA. At this low velocity there is little noise suppression achieved by either suppressor. The multi-spoke suppressor actually produced an increase in noise at all but the extreme aft angles. At the core velocity corresponding to takeoff power (Figure 2.4.6-2) the multi-hole nozzle suppresses satisfactorily at all angles. The multi-spoke nozzle was more successful at aft angles above 120° (which was the peak angle for this configuration compared with 130° for the baseline and multi-hole core suppressor).

The fan only directional characteristics for approach power are shown in Figure 2.4.6-3. Fan flow noise increased when passing over the waist cowl of both suppressor configurations. This is unexplained since, apart from minor geometrical differences, the suppressor waist cowls are as clean as the baseline configuration. At the takeoff power velocity, shown in Figure 2.4.6-4, a discrete tone was observed when the 24 spoke configuration was being tested, it was sufficient in strength to cause increases in SPL's of at least 10 dB above the baseline levels. It is reasoned that a modification made to this configuration to strengthen the nozzle to withstand higher pressure ratios may be responsible for the tone generation. The design modification produced an 0.5 inch (.0127 m) lip which probably produced a ring tone dependent upon an acoustic feedback mechanism. The phenomena was investigated in a recent paper by W.A. Olsen, O. Guttierrez and R.G. Dorsch (Reference 2.4.6-1). The figures relating to this design modification include "as measured data," with no correction for the ring tone.

The directional characteristics of dual flow operation at approach power are shown in Figure 2.4.6-5. The levels of both suppressor configurations were greater than the baseline. At the takeoff power setting, shown in Figure 2.4.6-6, the multi-hole core suppressor provided suppression relative to the baseline at angles close to the jet axis; the multi-spoke levels. continued to be effected by the generation of tones. A better understanding of the directional plots is obtained by inspection of the peak angle spectra at the various conditions described.

The core only spectra at approach power is shown in Figure 2.4.6-7. The suppressor configurations are both successful in reducing low frequency noise but at the expense of increases in high frequency noise; this is typical of multi-element nozzles. The spectra at takeoff power is shown in Figure 2.4.6-8. The noise reduction of low and mid frequency noise is achieved by both suppressor configurations. The mid frequency suppression is superior to the multi-lobe core suppressor previously tested. The replacement of a circular jet by multi-elements tends to produce a greater proportion of high frequency noise Since the data has been extrapolated to a typical flyover altitude of 1500 ft (457 m), however, higher frequency sound is reduced due to greater atmospheric absorption. The multi-hole suppressor spectra was such that there is little difference with the baseline at high frequencies. The multi-spoke configuration was more efficient in transferring energy from low to high frequencies so consequently there is still high frequency noise present above the baseline spectra.

LOW VELOCITY JET NOISE SUPPRESSOR TEST 3

- 1500 FT.(457.2m) SIDELINE, NO EGA
- SINGLE ENGINE A_8 = 6.2 FT.^{2} (.58m^2)

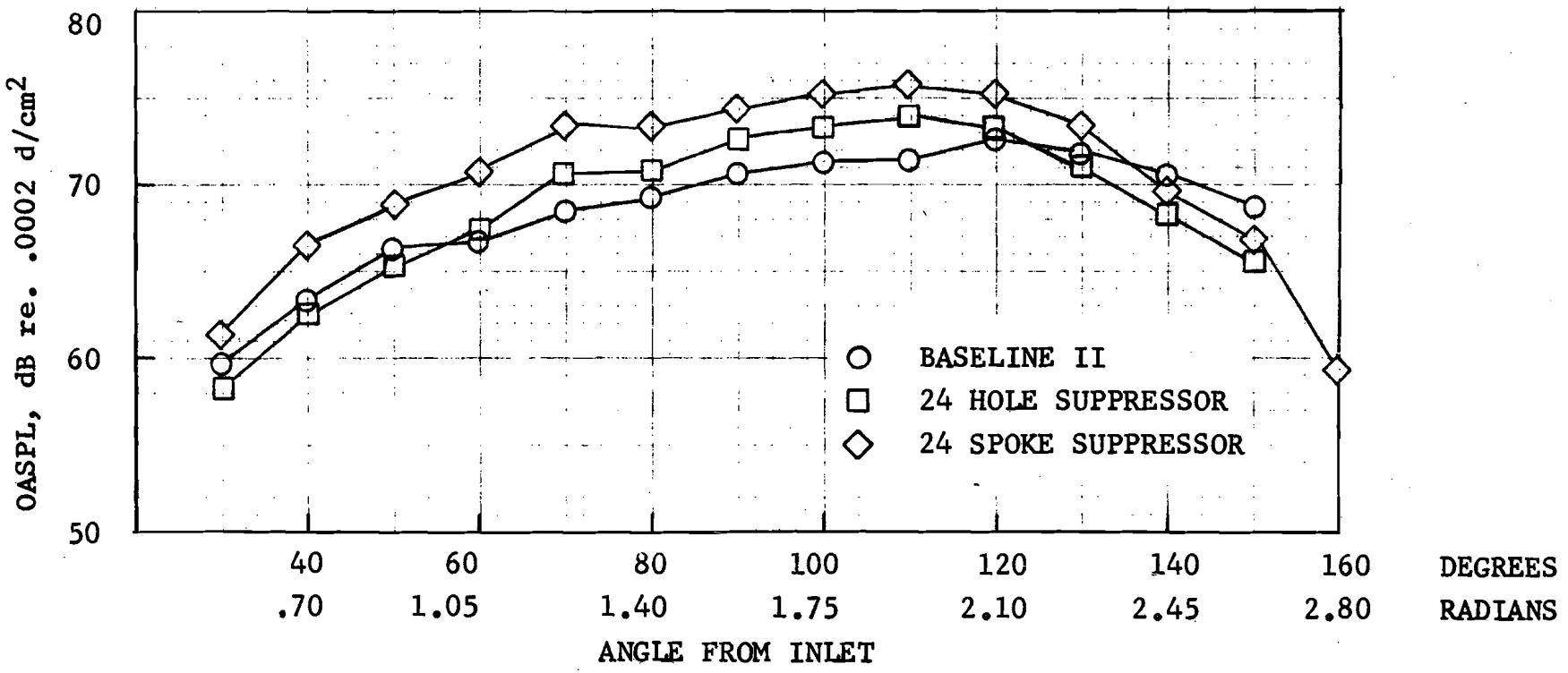

FIGURE 2.4.6-1 OASPL VS ACOUSTIC ANGLE, CORE ONLY, V_{CORE} 660 FT/SEC (201 m/s)

LOW VELOCITY JET NOISE SUPPRESSOR TEST 3

- 1500 FT.(457.2m) SIDELINE, NO EGA
- SINGLE ENGINE A_8 = 6.2 FT.^{2} (.58m^2)

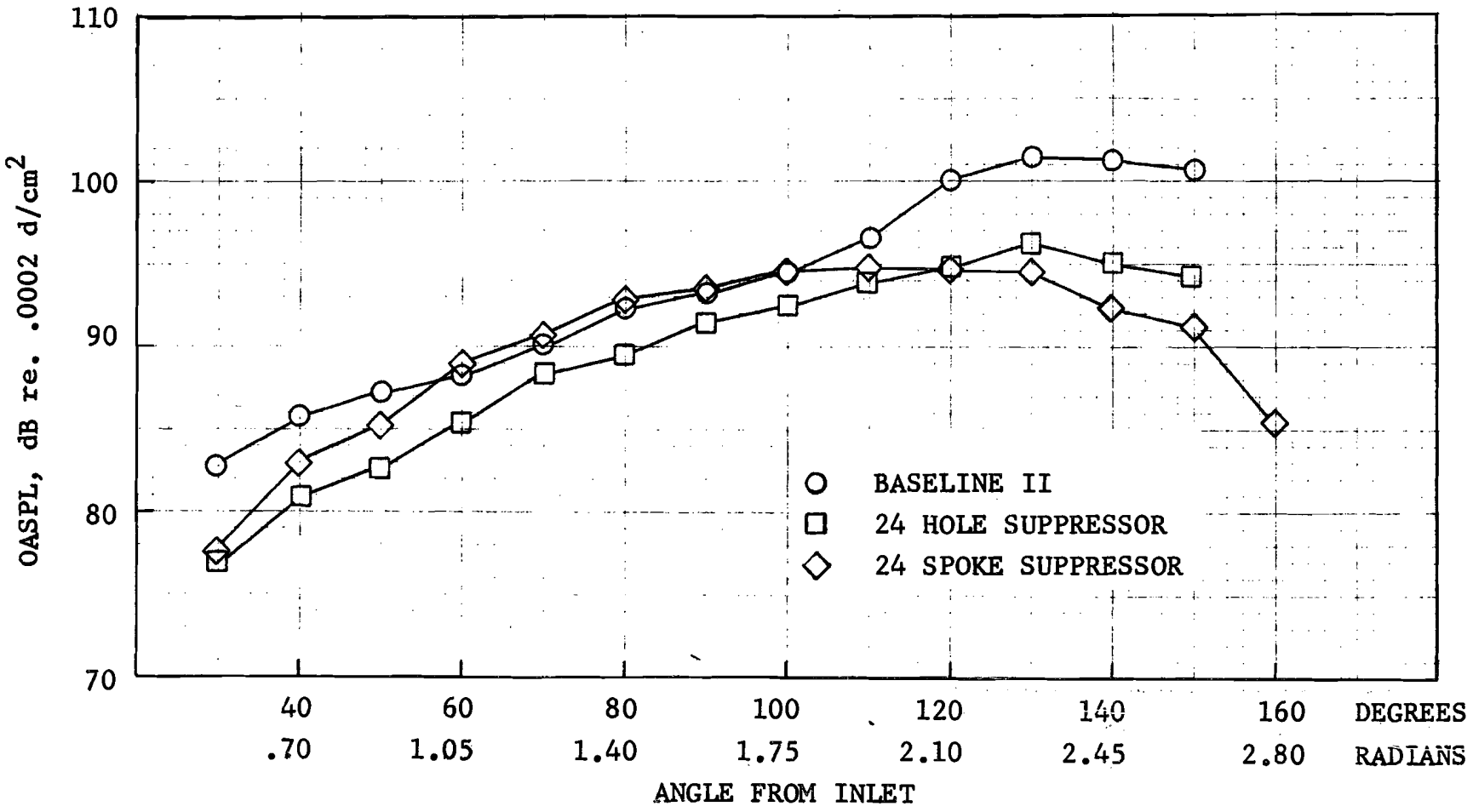

FIGURE 2.4.6-2 OASPL VS ACOUSTIC ANGLE, CORE ONLY, V_{CORE} 1600 FT/SEC (488 m/s)

LOW VELOCITY JET NOISE SUPPRESSOR TEST 3

- 1500 FT.(457.2m) SIDELINE, NO EGA
- SINGLE ENGINE A_{28} = 17.3 FT.^{2} (1.6m^2)

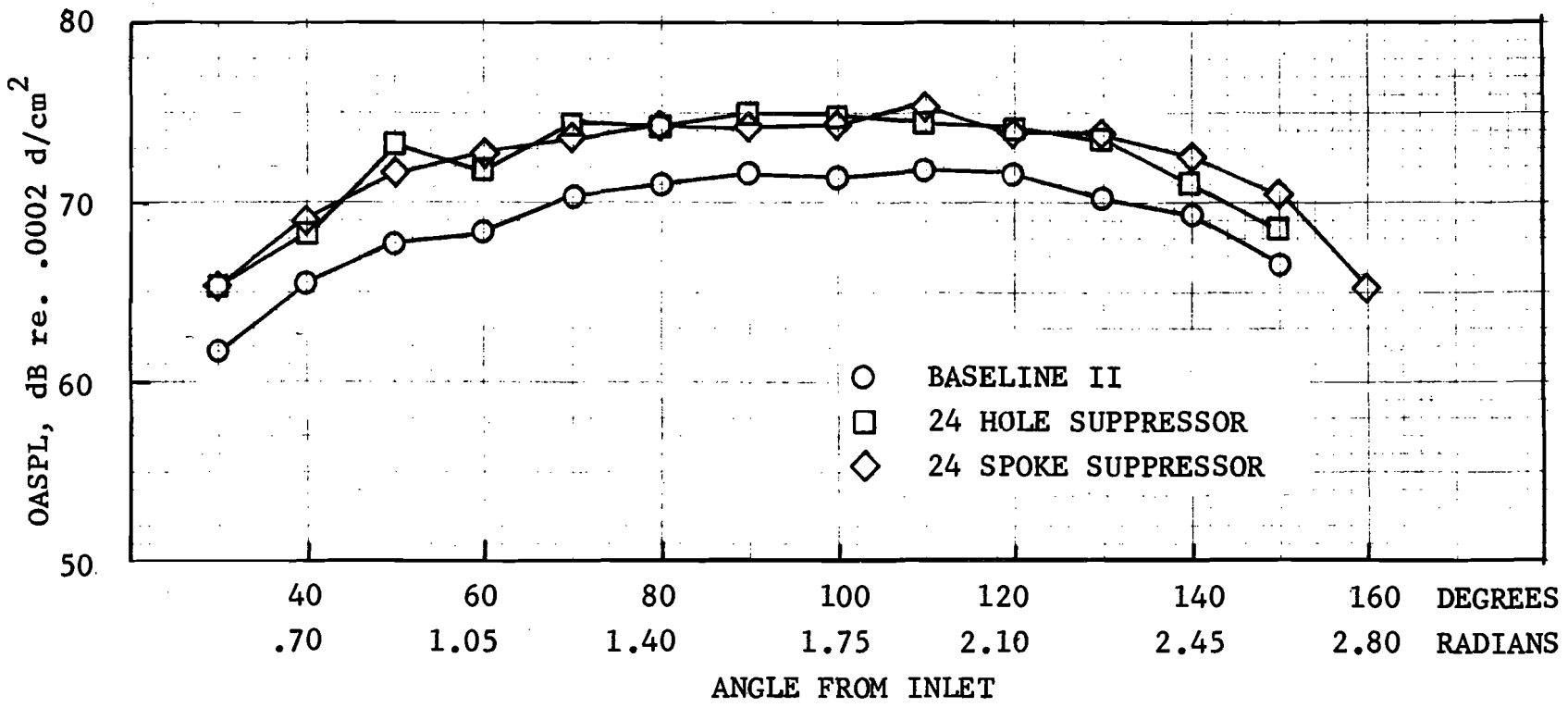

FIGURE 2.4.6-3 OASPL VS ACOUSTIC ANGLE, FAN ONLY, V_{FAN} 640 FT/SEC (195 m/s)

LOW VELOCITY JET NOISE SUPPRESSOR TEST 3

- 1500 FT.(457.2m) SIDELINE, NO EGA
- SINGLE ENGINE A_{28} = 17.3 FT.^{2} (1.6m^2)

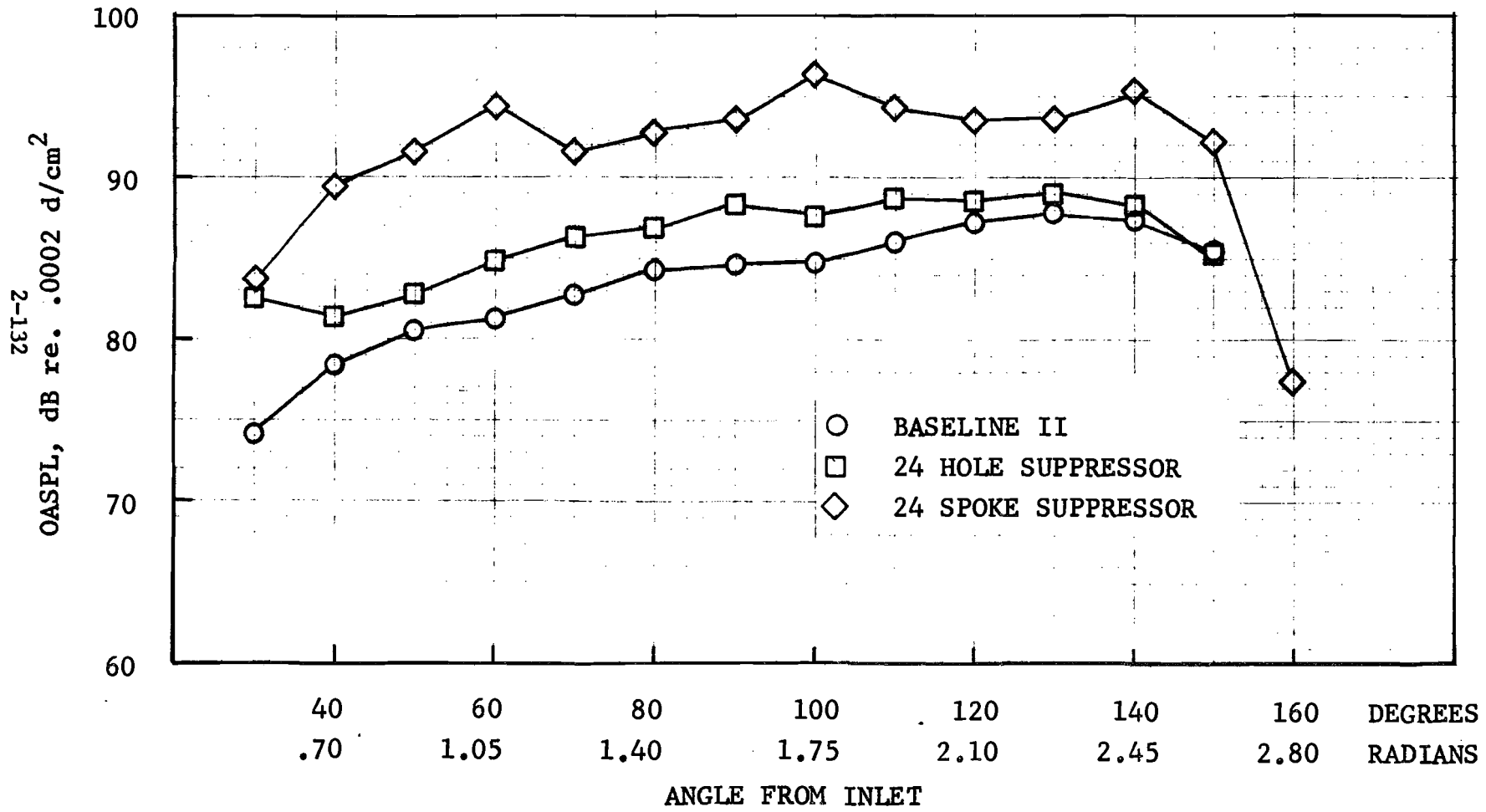

FIGURE 2.4.6-4 OASPL VS ACOUSTIC ANGLE, FAN ONLY, V_{FAN} 1000 FT/SEC (305 m/s)

LOW VELOCITY JET NOISE SUPPRESSOR TEST 3

- 1500 FT.(457.2m) SIDELINE, NO EGA
- SINGLE ENGINE A_8 = 6.2 $FT.^2$ (.58m^2) A_{28} = 17.3 $FT.^2$ (1.6m^2)

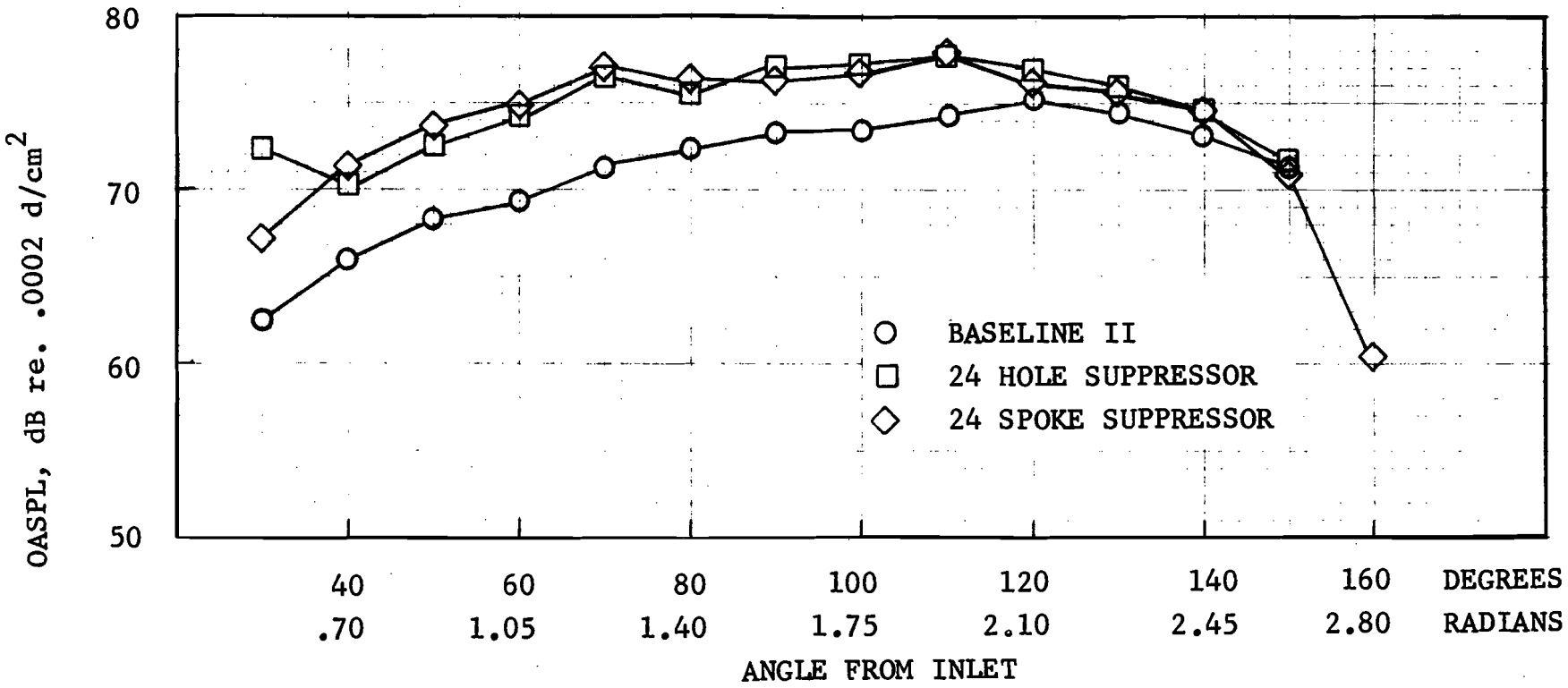

FIGURE 2.4.6-5 OASPL VS ACOUSTIC ANGLE, DUAL FLOW, V_{CORE} 660 FT/SEC (201 m/s), V_{FAN} 640 FT/SEC (195 m/s)

LOW VELOCITY JET NOISE SUPPRESSOR TEST 3

- 1500 FT.(457.2m) SIDELINE, NO EGA
- SINGLE ENGINE A_8 = 6.2 FT.^{2} (.58 ^{2}) A_{28} = 17.3 FT.^{2} (1.6m^2)

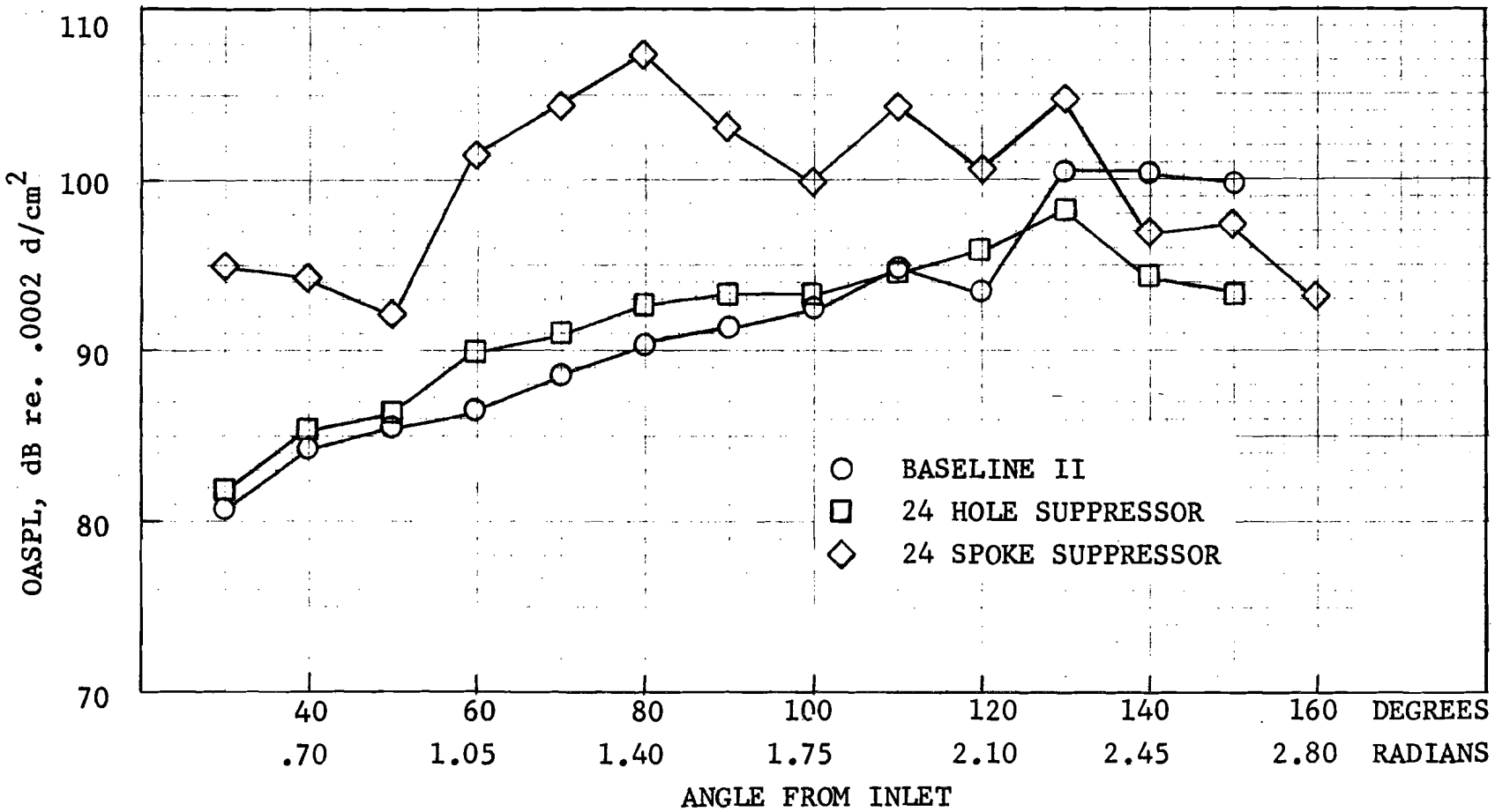

FIGURE 2.4.6-6 OASPL VS ACOUSTIC ANGLE, DUAL FLOW, V_{CORE} 1600 FT/SEC (488 m/s), V_{FAN} 1000 FT/SEC (305 m/s)

LOW VELOCITY JET NOISE SUPPRESSOR TEST 3

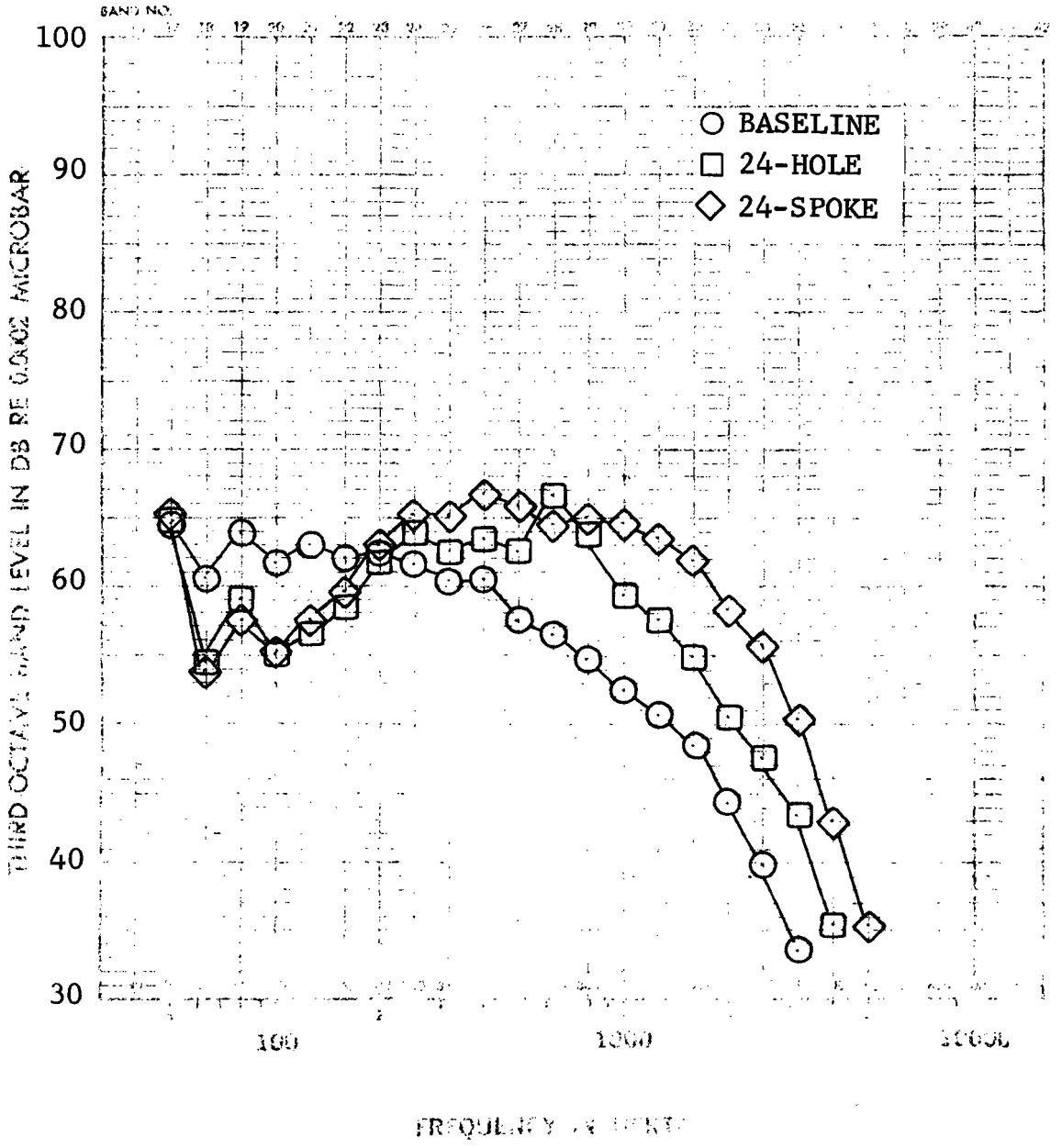

- 1500 FT (457m) SIDELINE, SINGLE ENGINE
- NO EGA
- A_8 = 6.2 FT^2 (.58m^2)

FIGURE 2.4.6-7 PEAK ANGLE SPECTRA, CORE ONLY
V_{CORE} = 660FT/SEC (201m/S)

LOW VELOCITY JET NOISE SUPPRESSOR TEST 3

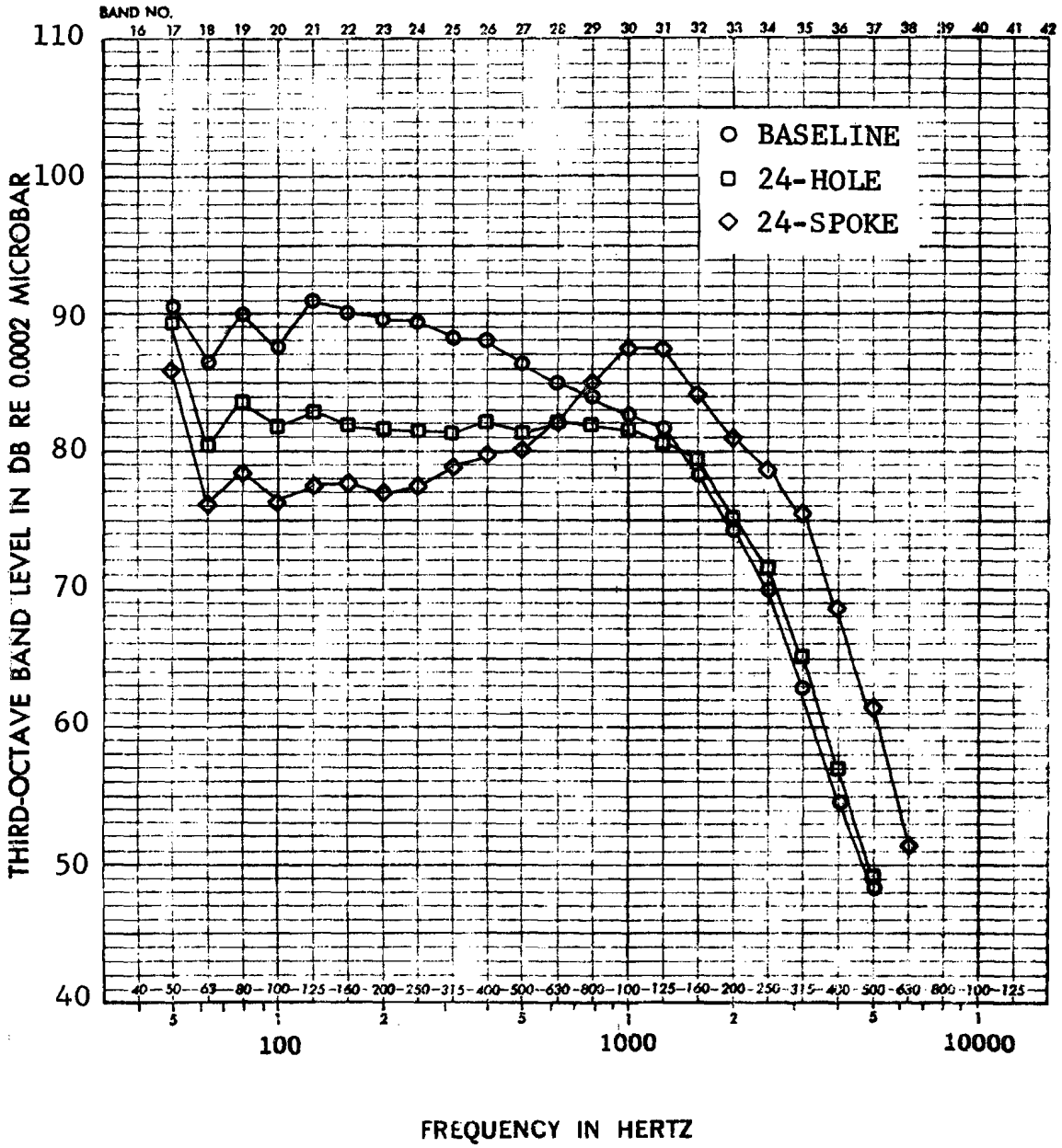

- 1500 FT (457m) SIDELINE
- NO EGA
- A_8 = 6.2 FT^2 (.58m^2)

FIGURE 2.4.6-8 PEAK ANGLE SPECTRA, CORE ONLY, V_{CORE} = 1600FT/SEC (488m/S)

The fan spectra at approach power is shown in Figure 2.4.6-9. The spectra levels exhibit minor increases in level, and the emergence of tones begins at 80Hz. The fan spectra at takeoff power is shown in Figure 2.4.6-10. The emergence of the tone phenomena associated with the multi-spoke configuration becomes quite pronounced at this fan velocity; however, noise levels associated with the fan flow over the multi-tube waist cowl showed minor increases relative to the baseline.

Observance of the spectra at this stage suggests the hypothesis that if the fan interaction effect is maintained, the dual flow results would show a reduction in high frequency noise thus providing an overall suppression of the coannular flow system. Analysis of the dual flow spectra at approach power however, (Figure 2.4.6-11) indicates increases in SPL's over the majority of the frequency range for both configurations. Inspection of the peak spectra at takeoff power (Figure 2.4.6-12) demonstrates similar results inconsistent with the hypothesis. The low frequency suppression attained during core flow only tests is reduced considerably (even if the measured pure tone is considered to be a phenomena associated with the specific model configuration only) and no reduction of high frequency noise is attained. This can be explained by considering the suppression mechanism of these suppressors, which essentially consists of replacing a single area jet by several smaller area elements. Unlike the multi-lobe arrangement, the turbulent mixing zone of the multi-tube and multi-spoke nozzles is not in direct contact with the secondary flow stream except in the vicinity of the jet periphery. The multi-lobe mechanism, on the other hand, simply increases the area over which the fan flow (if it is correctly introduced) can react favorably to reduce the turbulent shear. Thus, it may be concluded that core suppressors of the spoke and hole type will not reduce the dual flow noise for the velocity range being considered in this study.

Graphs summarizing the above tests are presented for the core flow only in Figures 2.4.6-13 to 2.4.6-15. The relationship between core only OAPWL and core jet velocity (Figure 2.4.6-13) shows that the multi-hole configuration produced OAPWL reductions down to 1000 ft/sec (305 m). The peak core only OASPL is related to core jet velocity in Figure 2.4.6-14. The multi-tube configuration is an effective suppressor over most of the velocity range. At the takeoff power setting the multi-spoke suppressor is more effective, providing 7 dB noise reduction. In Figure 2.4.6-15, the peak core only perceived noise level relationship demonstrates the subjective nature of the suppressor mechanisms. The conversion of low frequency energy into the high frequency regime is reflected in both suppressor curves, particularly in the case of the multi-spoke configuration.

For the purpose of constructing realistic summary plots of the configurations with dual flow operation, the tones measured during the test on the multi-spoke nozzle were considered not representative of a full scale design and thus were removed and the levels recalculated. On this basis the OAPWL is related to core jet velocity in Figure 2.4.6-16, the peak OASPL is related to core jet velocity in Figure 2.4.6-17, and the peak perceived noise level related to core jet velocity in Figure 2.4.6-18. Each of the curves is similar; the large increase in high frequency noise with a corresponding lack of fan interaction effect is the cause of the multi-spoke's poor performance.

LOW VELOCITY JET NOISE SUPPRESSOR TEST 3

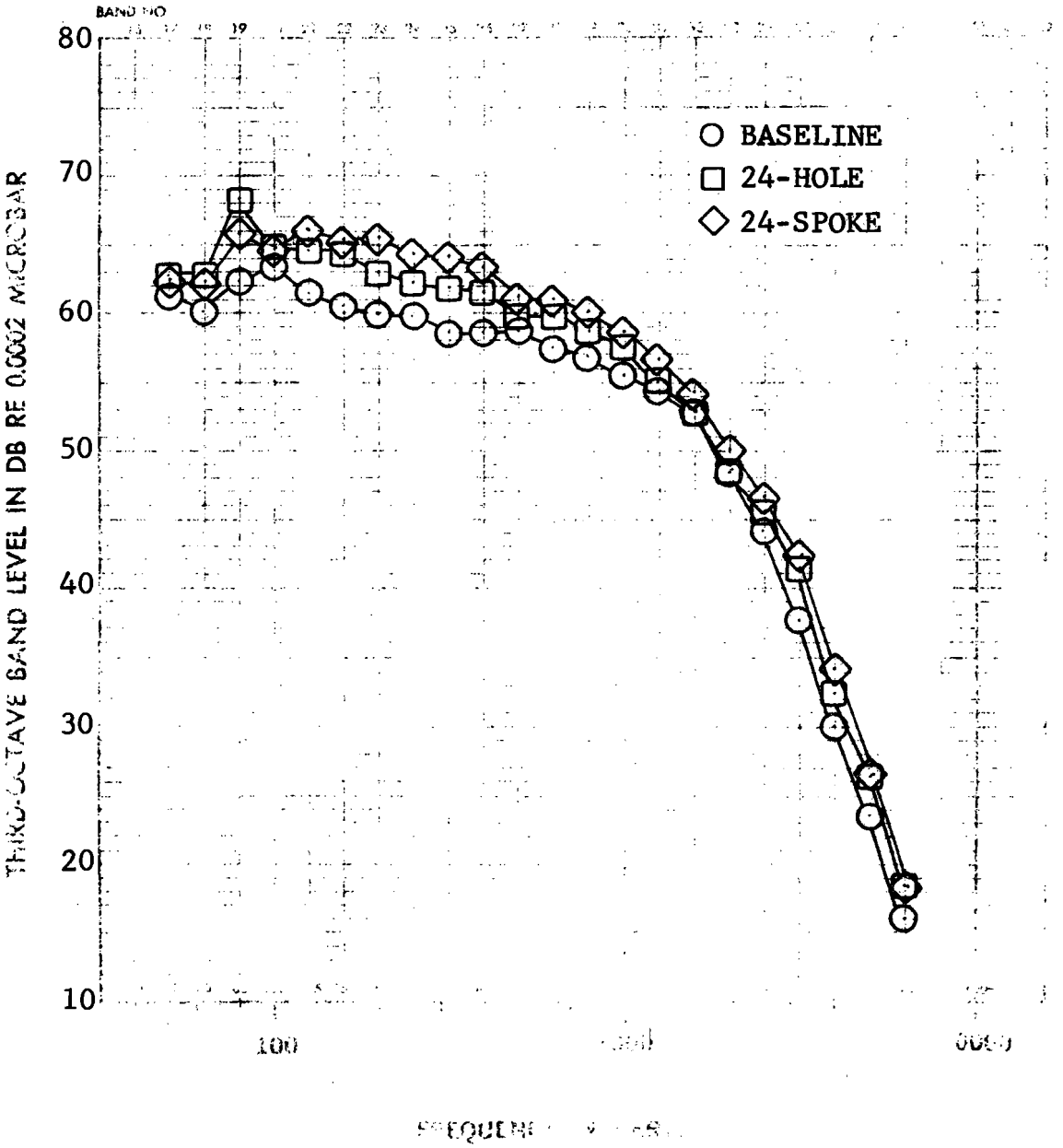

- 1500 FT (457m) SIDELINE, SINGLE ENGINE
- NO EGA
- A_{28}= 17.3 FT^2 (1.6m^2)

FIGURE 2.4.6-9 PEAK ANGLE SPECTRA, FAN ONLY, V_{FAN} = 640FT/SEC (195m/S)

LOW VELOCITY JET NOISE SUPPRESSOR TEST 3

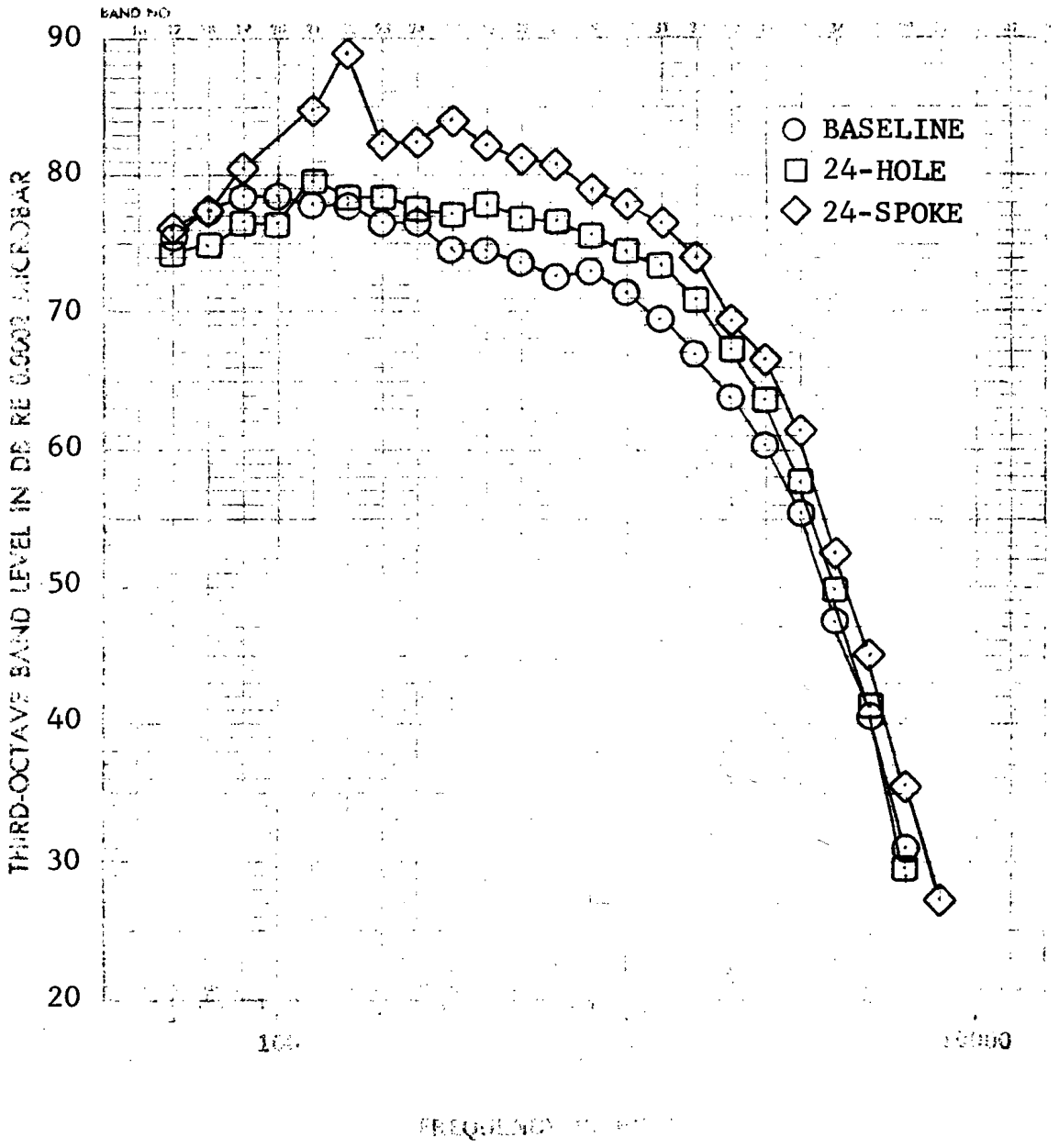

- 1500 FT (457m) SIDELINE, SINGLE ENGINE
- NO EGA
- A_{28} = 17.3 FT^2 (1.6m^2)

FIGURE 2.4.6-10 PEAK ANGLE SPECTRA, FAN ONLY, V_{FAN} 1000FT/SEC (305m/S)

LOW VELOCITY JET NOISE SUPPRESSOR TEST 3

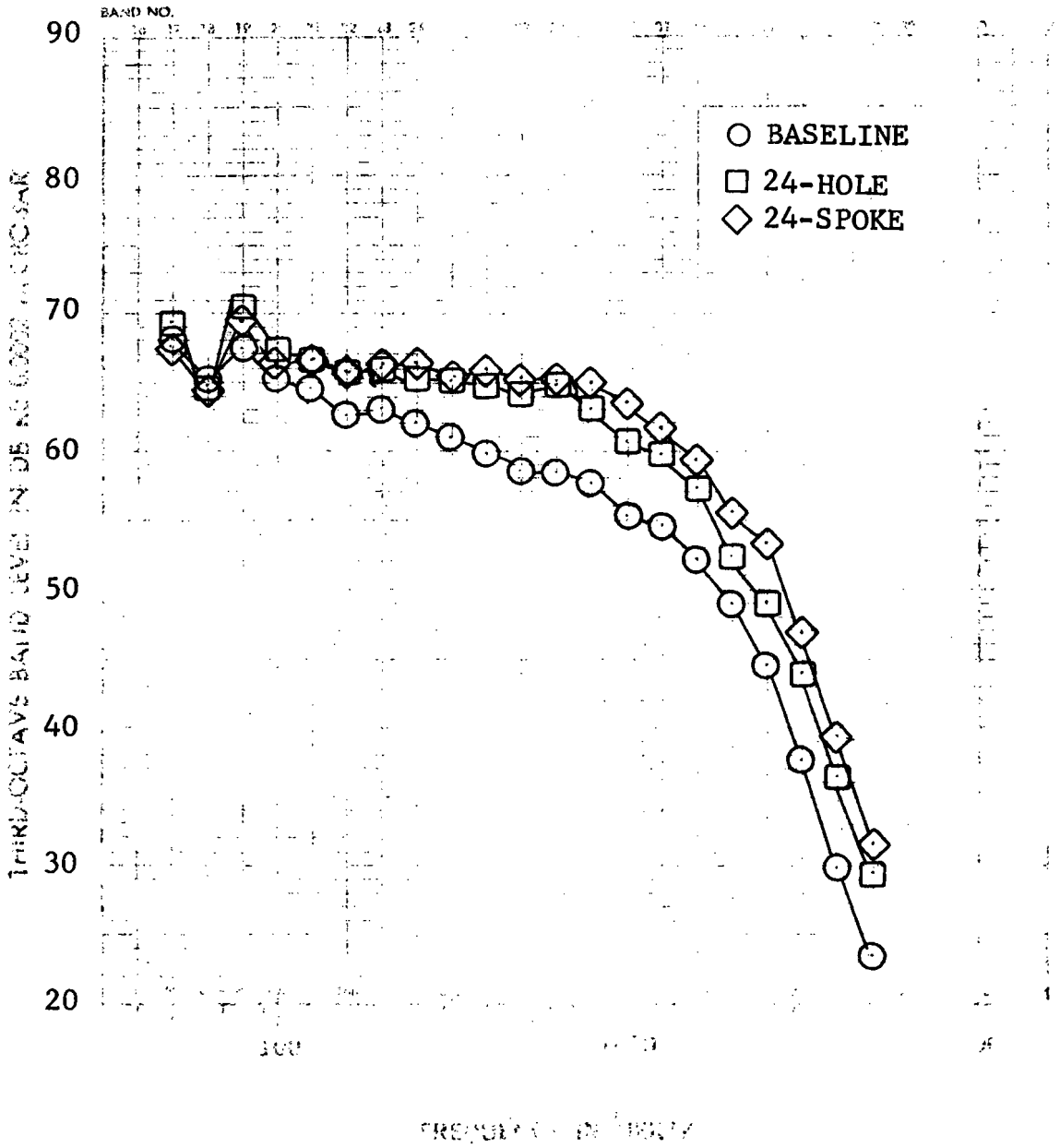

- 1500 FT (457m) SIDELINE, SINGLE ENGINE
- NO EGA
- A_8 = 6.2 FT^2 (.58m^2), A_{28} = 17.3 FT^2 (1.6m^2)

FIGURE 2.4.6-11 PEAK ANGLE SPECTRA, DUAL FLOW,
V_{CORE} 660FT/SEC (201m/S),
V_{FAN} 640FT/SEC (195m/S)

LOW VELOCITY JET NOISE SUPPRESSOR TEST 3

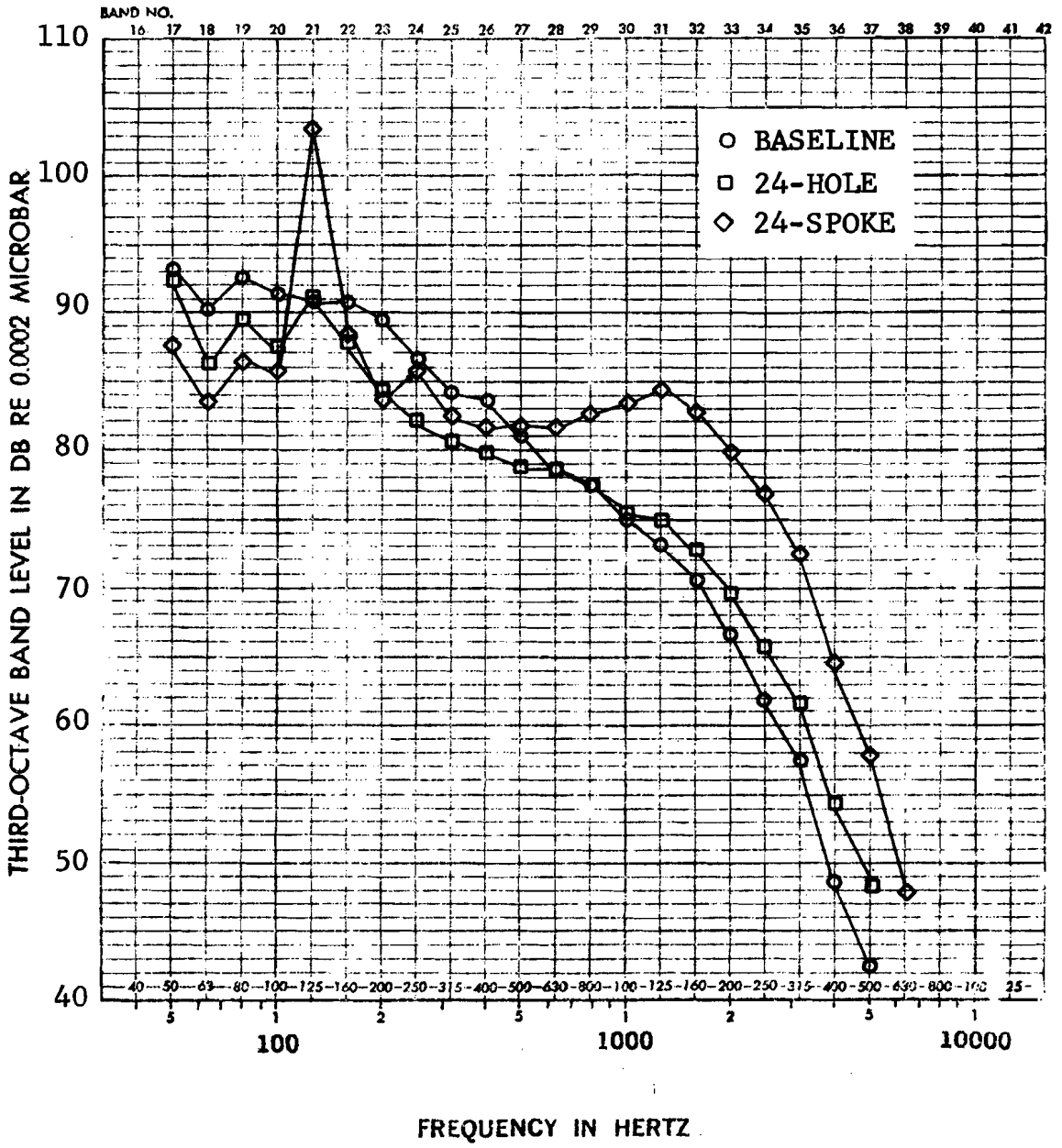

- 1500 FT (457m) SIDELINE
- NO EGA
- A_8 = 6.2 FT^2 (.58m^2), A_{28} = 17.3 FT^2 (1.6m^2)

FIGURE 2.4.6-12 PEAK ANGLE SPECTRA, DUAL FLOW,
V_{CORE} 1600FT/SEC (488m/S),
V_{FAN} 1000FT/SEC (305m/S)

- SINGLE ENGINE, CORE ONLY, NO EGA
- A_{Core} = 6.2 FT^2 (.58 m^2)

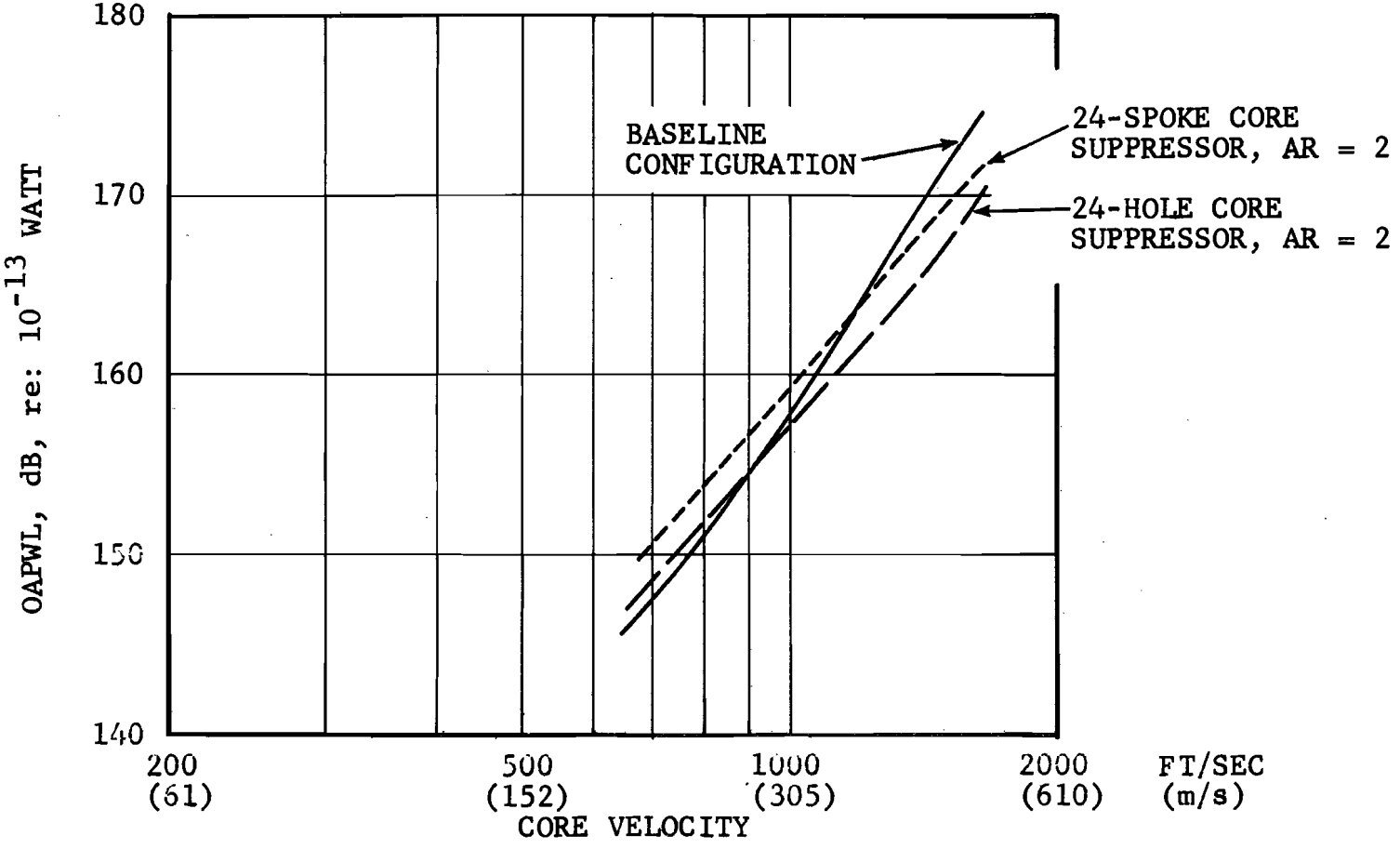

FIGURE 2.4.6-13 OAPWL VS CORE JET VELOCITY, CORE ONLY, TEST 3

- SINGLE ENGINE, CORE ONLY
- 1500 FT. (457 m) SIDELINE, NO EGA
- A_{Core} = 6.2 FT^2 (.58 m^2)

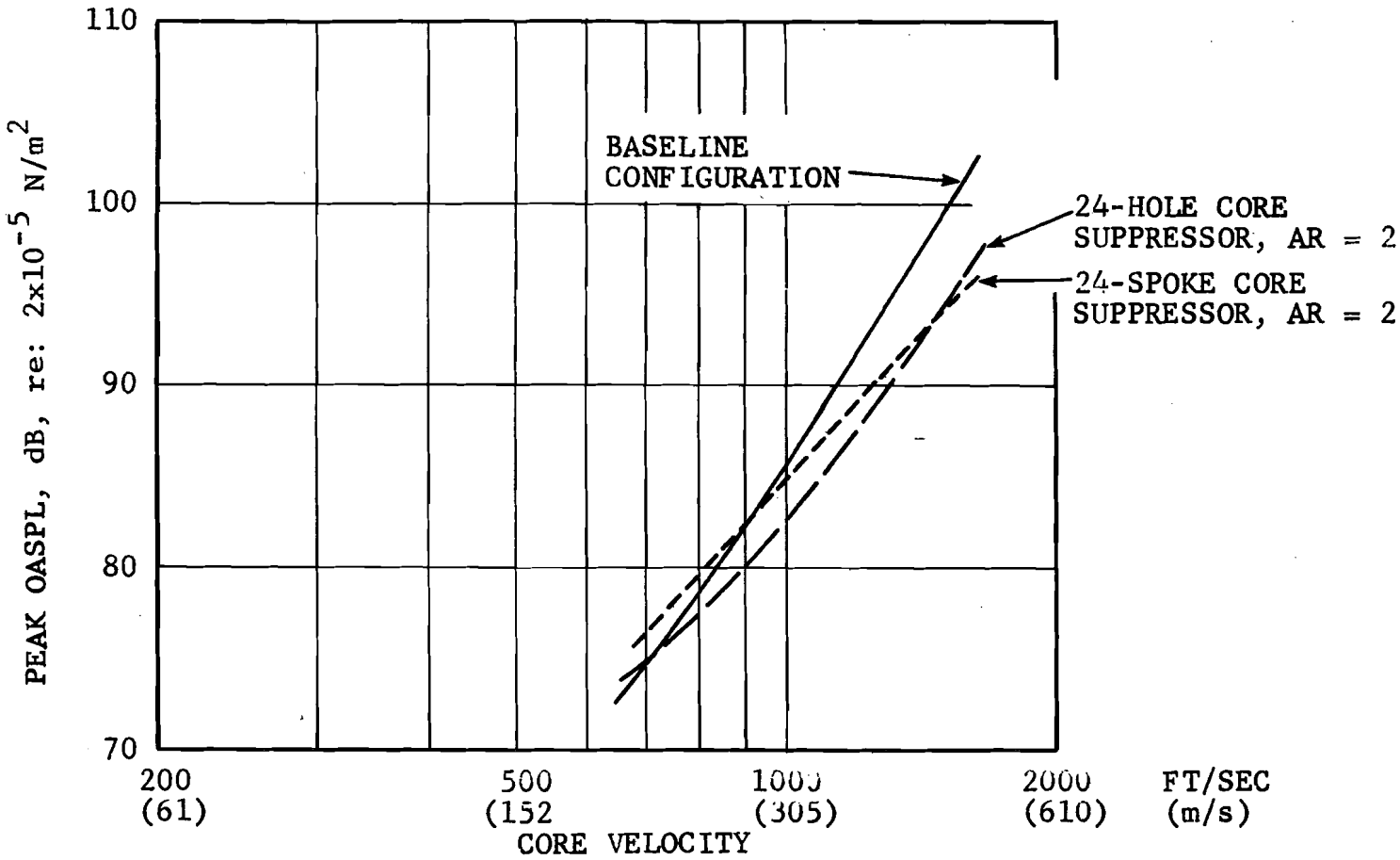

FIGURE 2.4.6-14 PEAK OASPL VS CORE JET VELOCITY, CORE ONLY, TEST 3

- SINGLE ENGINE, CORE ONLY
- 1500 FT. (457 m) SIDELINE, NO EGA
- A_{Core} = 6.2 FT^2 (.58 m^2)

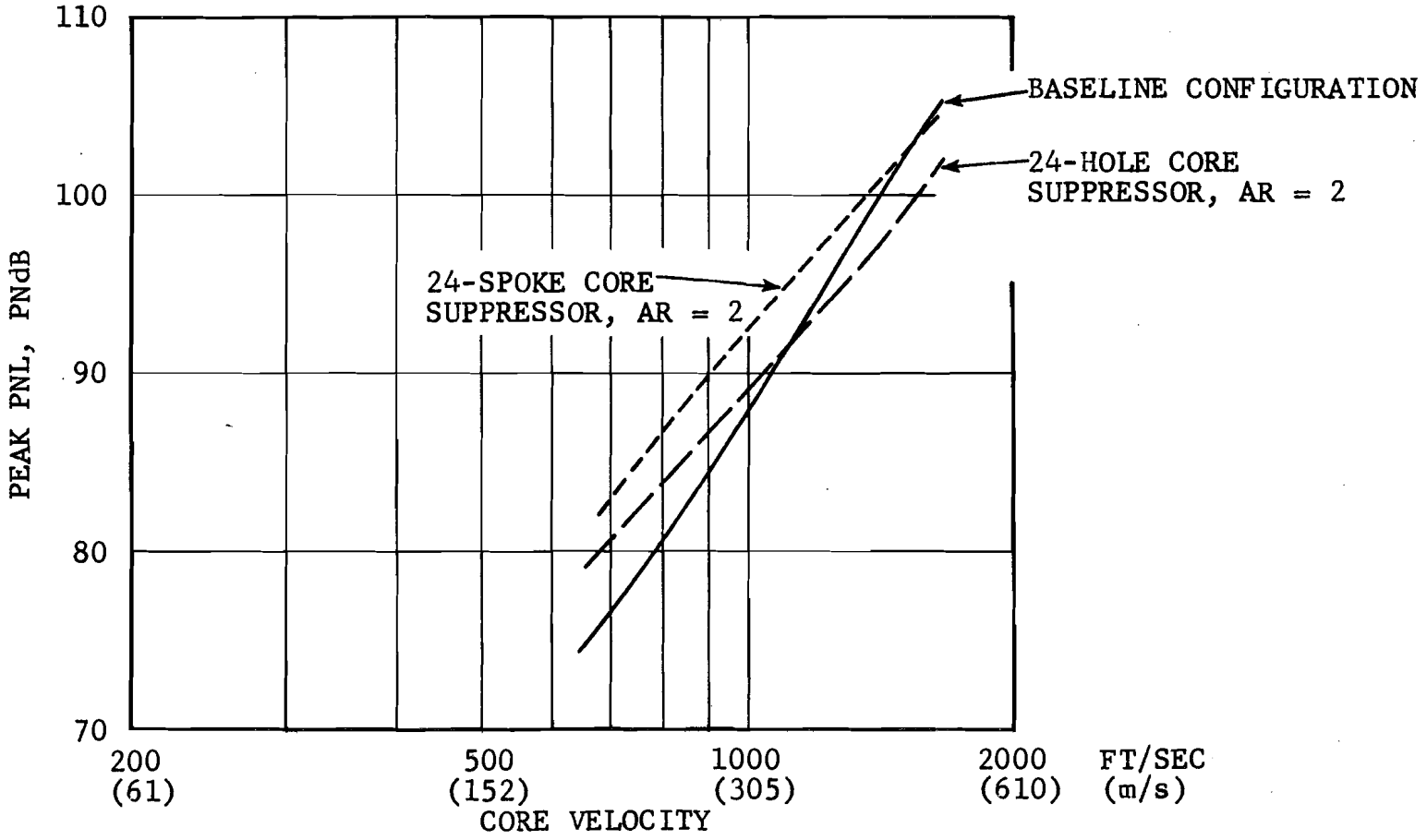

FIGURE 2.4.6-15 PEAK PNL VS CORE JET VELOCITY, CORE ONLY, TEST 3

- SINGLE ENGINE, DUAL FLOW, NO EGA
- A_{Core} = 6.2 FT^2 (.58 m^2); A_{Fan} = 17.3 FT^2 (1.6 m^2)

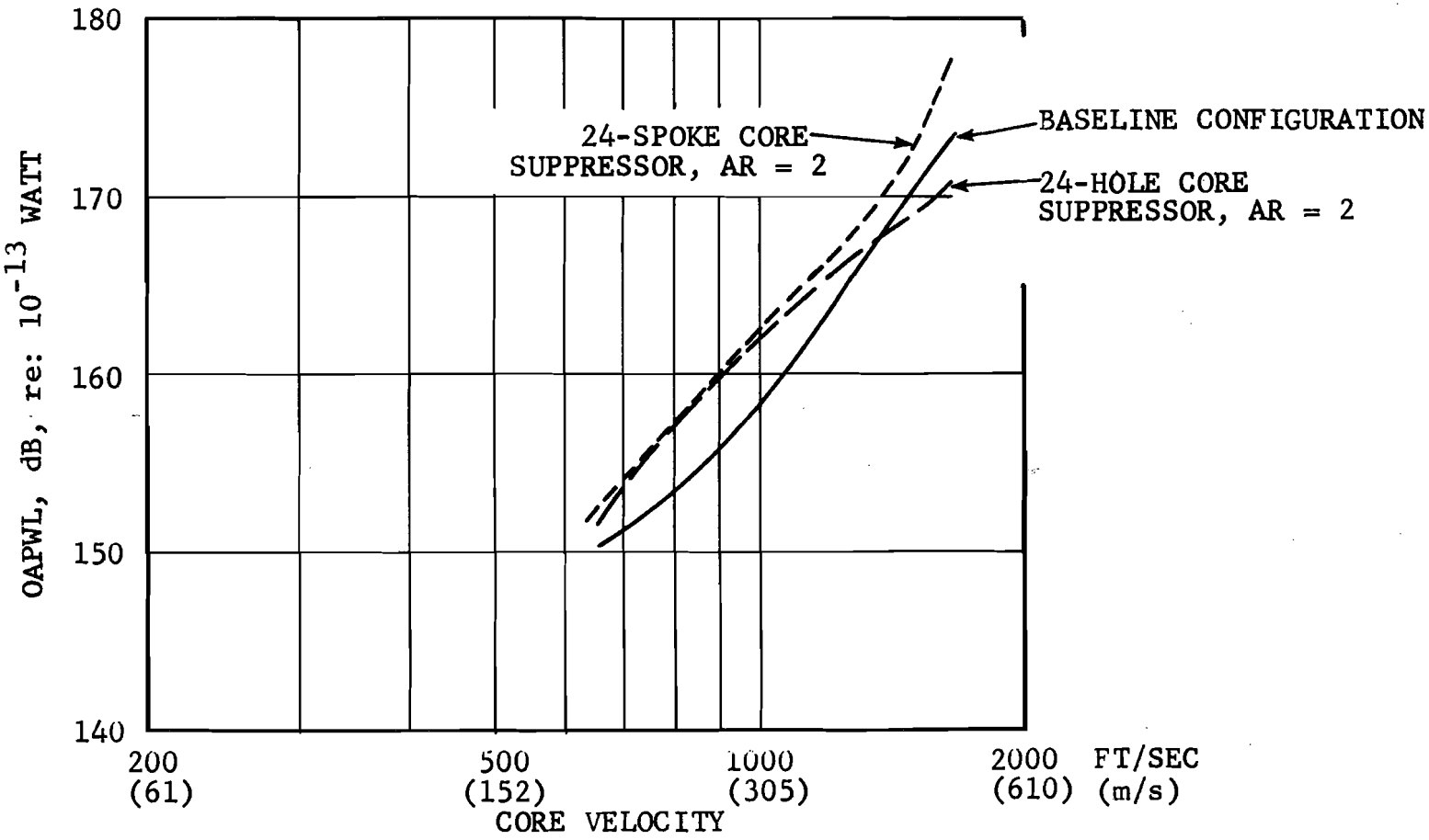

FIGURE 2.4.6-16 OAPWL VS CORE JET VELOCITY, DUAL FLOW, TEST 3

- SINGLE ENGINE, DUAL FLOW
- 1500 FT. (457 m) SIDELINE, NO EGA
- A_{Core} = 6.2 FT^2 (.58 m^2); A_{Fan} = 17.3 FT^2 (1.6 m^2)

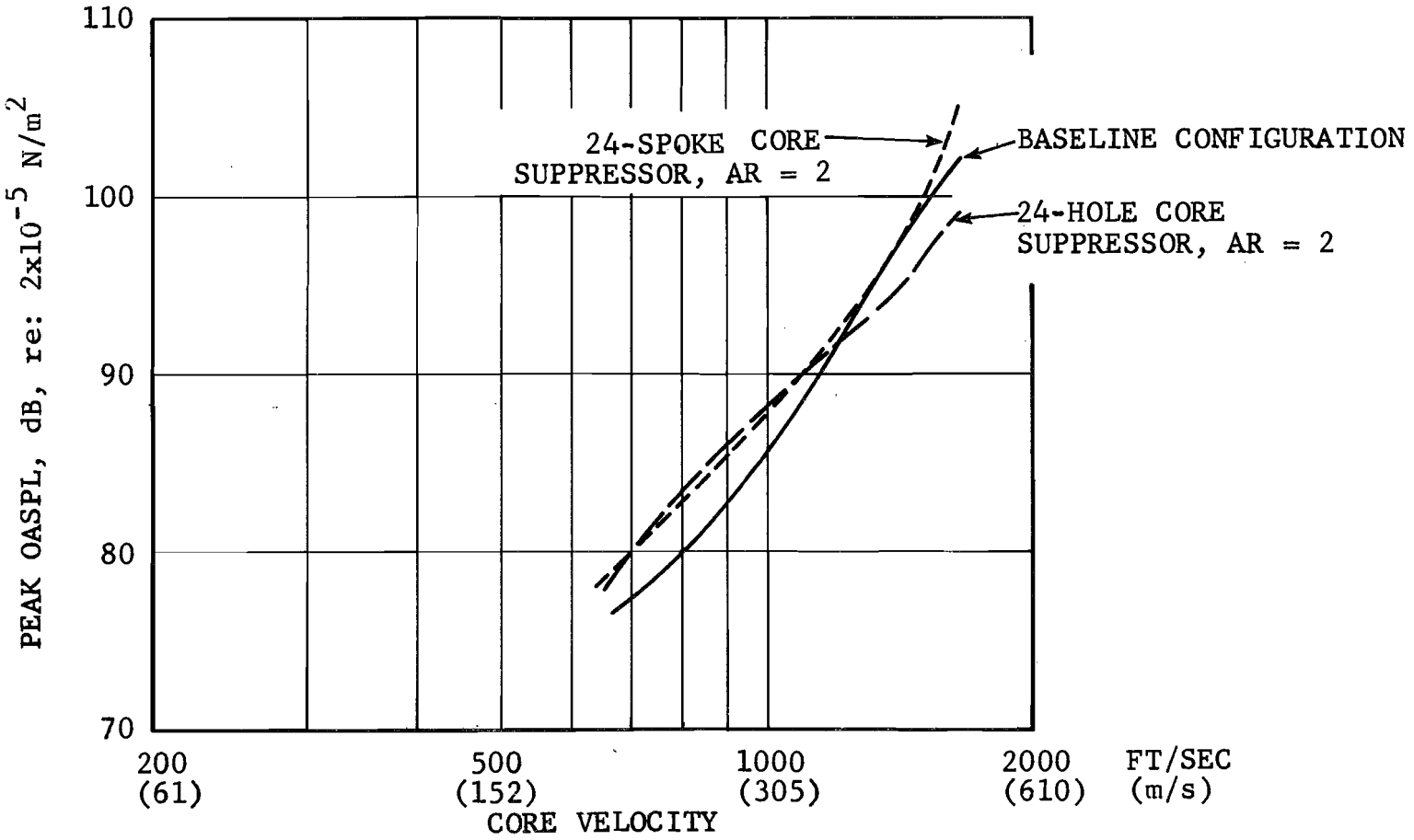

FIGURE 2.4.6-17 PEAK OASPL VS CORE JET VELOCITY, DUAL FLOW, TEST 3

- SINGLE ENGINE, DUAL FLOW
- 1500 FT. (457 m) SIDELINE, NO EGA
- A_{Core} = 6.2 FT^2 (.58 m^2); A_{Fan} = 17.3 FT^2 (1.6 m^2)

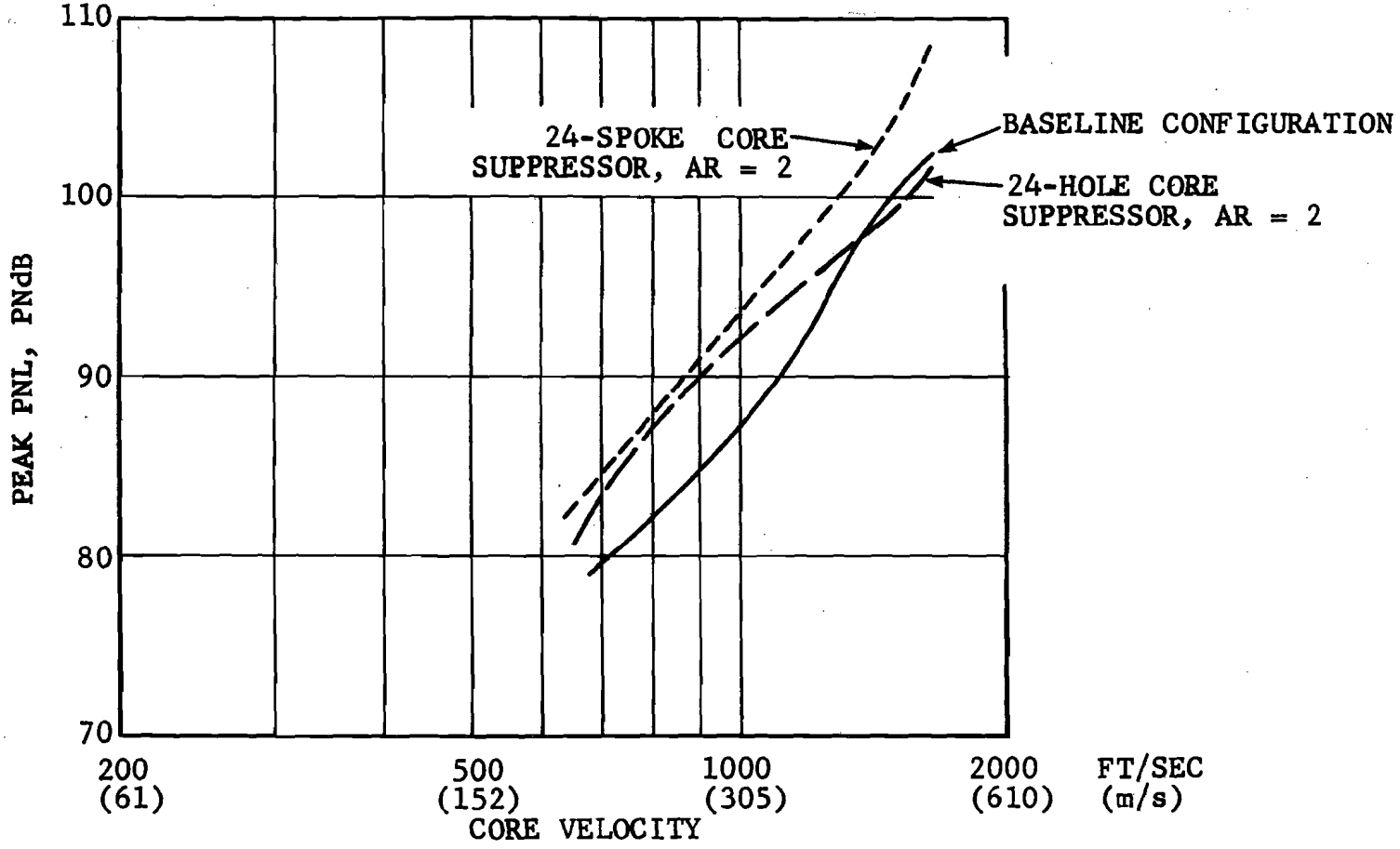

FIGURE 2.4.6-18 PEAK PNL VS CORE JET VELOCITY, DUAL FLOW, TEST 3

The small amount of suppression indicated for the multi-hole configuration was the result of its performance as a core jet suppressor only.

2.4.7 Summary and Discussion of Results

The selection of hardware for the suppressor tests was based on the assumption that certain suppressor configurations which cause premature mixing of the primary flow could be utilized to give additional suppression in conjunction with the secondary flow interaction effect. A study of existing data on multi-element core suppressors suggested that for the velocity range of interest, low area ratio/low element number designs might achieve the desired noise reduction goals. Suppressor Test 1 showed that the level of fan noise measured when passing over the baseline waist cowl could rise to unacceptable levels when a disturbance in the flow stream (such as the penetration of lobes) was allowed. This ruled out, for the present, multi-lobe suppressors with high ratios of annulus area to flow area. When the penetration of lobes is not too severe, as is the case with the annulus area-to-core flow area of 2, "capping" the lobes (brazing metal caps over lobes to maintain a smooth flow contour while still allowing the fan flow to mix with the core flow) resulted in a measurable reduction. This suppressor configuration was evaluated along with 24 spoke and 24 hole configurations all of which had area ratios (total annulus area/actual flow area) of 2.0.

The summary plots (Figures 2.4.4-13 to -18, 2.4.5-17 to -19, and 2.4.6-13 to -18) provide an ideal basis of comparison of the systems. Baseline I differs from Baseline II in that it had a smaller core area, a different plug geometry and a less tapered waist cowl. The noise reduction of the multi-spoke nozzle (and to a lesser degree, that of the multi-hole configuration) was affected by a discrete tone phenomenon which was not included in the noise level calculations since characteristic jet noise spectra is broadband in nature.

The multi-lobe configuration was the most successful relative to the baseline configuration in achieving the required acoustic objective. The multi-hole and the multi-spoke configurations were acoustically inferior when operating in the dual flow mode. This probably occurred because they did not sufficiently mix the two streams, as is necessary for the secondary flow interaction effect to occur. No effect was observed on dual flow noise levels as a result of extending the fan duct to a coplanar location.

2.4.8 Conclusion

A multi-lobe core suppressor configuration was found to be the most suitable method of capitalizing on the inherent suppression capability of a dual flow system. At typical takeoff power settings representing advanced turbofan engines, the reduction in perceived noise level was 5 PNdB at a 1500 ft (457 m) distance.

The foregoing numbers provided for the suppressor effects are conservative estimates in that they are obtained from a comparison with the Baseline I configuration. If Baseline II is used for the comparison as much as 2 PNdB extra suppression is indicated.

2.5 JET NOISE IN FLIGHT

2.5.1 Introduction

The study of noise generation and reduction has received a great deal of attention over the past twenty years. Most work has dealt with a stationary jet and the problems involved with moving jets have received somewhat less study. Enough data exists to show that the relative velocity effect is appreciable for unsuppressed single jets. The objective of this section is to illustrate how the noise generating mechanisms of ideal jets in flight can be modeled, based on existing knowledge, in an aero-acoustic manner such that gross overall parameters as well as spectral acoustic properties can be examined. The discussions will include single and dual flow nozzle exhaust systems.

2.5.2 Fundamental Analysis for the Flight Configuration

The acoustic analysis discussed here is a summary of the contributions of Lighthill, Ffowcs-Williams,and Ribner. The observer (e.g. a microphone) is at rest in a uniform acoustic medium also at rest. The source of noise is a turbulent flow which can be thought of as being generated by an engine of a moving aircraft.

The analysis of the acoustic field generated by turbulent flows has been formally developed by Lighthill (References 2.5.2-1, -2, -3) and Ribner (References 2.5.2-4 and -5). In their developments, the generalized equations of continuity and momentum conversation were formulated into a generalized wave equation as follows.

From conservation of mass we have:

$$\frac{\partial \rho}{\partial t} + \text{div}\ \rho\ u = 0 \qquad (2.5.2\text{-}1)$$

From conservation of momentum we have:

$$\frac{\partial \rho u}{\partial t} + \text{div}\ (\rho\ u\ u) = \text{div}\ \tau \qquad (2.5.2\text{-}2)$$

where

$$\bar{\bar{\tau}} = -\ p\ \bar{\bar{I}} + \bar{\bar{T}}'$$

p = thermodynamic pressure

$\bar{\bar{\tau}}' = \mu\ \text{def}\ u + \lambda\ \text{div}\ u\ \bar{\bar{I}}$ (viscous stress tensor)

$\text{def}\ u = \text{grad}\ u + (\text{grad}\ u)^T$

μ = first viscosity coefficient

λ = second viscosity coefficient ($\lambda \sim -2/3\ \mu$)

$\bar{\bar{I}}$ = unity tensor

Taking the time derivative of continuity, and the divergence on momentum and eliminating the flux of momentum flux term yields the following wave equation.

$$\frac{\partial^2 \rho}{\partial t^2} - a_o^2\ \nabla^2 \rho = \text{div div } (\rho\ u\ u - \bar{\bar{\tau}}') + \nabla^2\ (p - a_o^2\ \rho) \qquad (2.5.2\text{-}3)$$

or

$$\frac{\partial^2 \rho}{\partial t^2} - a_o^2\ \nabla^2 \rho = \text{div div } \bar{\bar{T}} \qquad (2.5.2\text{-}3a)$$

where $\bar{\bar{T}}$ = Lighthills stress tensor

$= p\bar{\bar{I}} - \bar{\bar{\tau}}' + \rho\ u\ u - a_o^2\ \rho\ \bar{\bar{I}}$

a_o = ambient speed of sound

In deriving this wave equation there are no restrictive assumptions that the fluid obeys an equation of state; in fact <u>all continuous flows</u> satisfy a wave equation such as equation (2.5.2-3) or (2.5.2-3a).

Far from the flow region itself, the right-hand side of equations (2.5.2-3) and (2.5.2-3a) must vanish identically. This leaves the well known homogeneous wave equation for acoustic wave propagation through a stationary-uniform medium. The right-hand side of either equation (2.5.2-3) or (2.5.2-3a) has the form of a quadruple source which is at rest. The stress sensor, $\bar{\bar{T}}$, is a stress produced by pressure, viscous shear stress, and momentum flux. One may now imagine the medium as being at rest at any point in space and interpret all the additional effects caused by the flow as a result of inhomogeneities, which are continuously distributed throughout a limited part of the medium.

The formal transformation of a differential equation of the Form (2.5.2-3a) into an integral equation is obtained by the well known Kirchhoff integral. Then the integral equation for the density perturbation field becomes:

$$\rho'(\tau,t) = (\rho - \rho_o) = \underbrace{\frac{1}{4\pi R}\iiint_{V_o} \text{div}_o\ \text{div}_o\ [\bar{\bar{T}}]\ dV_o}_{\text{Noise resulting from fluctuating shearing stresses}} \qquad (2.5.2\text{-}4)$$

$$+ \left[\begin{array}{c}\text{Noise resulting from the effect of} \\ \text{solid boundaries upon the flow}\end{array}\right]$$

Where the subscript, o, designates the turbulent source region and the bracket [] means evaluated at the retarded time $t - r/a_o$. (See the sketch below for the identification of the coordinate system). Physically, the retarded time effect means it takes a finite time for the sound emitted from the source region to travel the distance R, from the source to the observer.

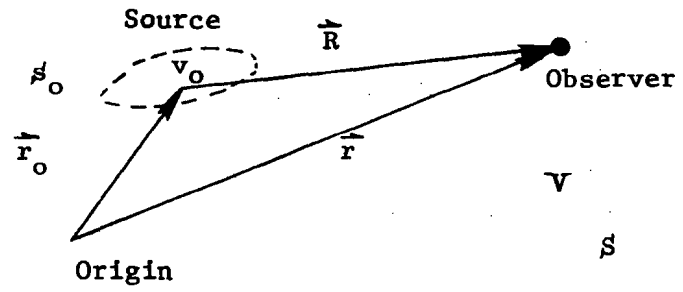

Generalized Coordinate System

Neglecting any solid boundaries as a noise source, it can be shown that equation (2.5.2-4) may be written as:

$$\rho'(r,t) = (\rho - \rho_o) = \text{div div} \iiint_{V_o} \frac{1}{R} [\bar{\bar{T}}] \, d V_o \qquad (2.5.2\text{-}5)$$

where ρ_o is the undisturbed density of the medium, r is the position of the observer, and r_o is the position in the turbulent region. The integral is evaluated over the entire region of turbulence. The solution given by equation (2.5.2-5) expresses the density disturbance at point r and time t which results from a region of turbulence which is at rest relative to the observer.

Now in the radiation field, differentiations in (2.5.2-5) can be carried out very simply. By defining:

$$r = x_1 \underline{i} + x_2 j + x_3 \underline{k}$$

$$r_o = y_1 \underline{i} + y_2 j + y_3 \underline{k}$$

and using an index notation equation (2.5.2-5) may be written as

$$\rho'(r,t) = \frac{(x_i - y_i)(x_i - y_i)}{a_o^2 R^3} \iiint_{V_o} \left[\frac{\partial^2 T_{ij}}{d+2}\right] d V_o \qquad (2.5.2\text{-}6)$$

where

$$\frac{\partial}{\partial x_i}\left(+ - \frac{R}{a_o}\right) = - \frac{x_i}{a_o R}$$

Now $\rho' = (\rho - \rho_o)$ and $(\rho - \rho_o)\, a_o^2 \sim p'(r, t)$, and for radiation in the far field we have:

$$p'(r,t) \sim \frac{x_i x_j}{4\pi a_o^2 R^3} \iiint_{V_o} \left[\frac{\partial T_{ij}}{\partial+2}\right] d V_o \qquad (2.5.2\text{-}7)$$

The acoustic intensity is then $I = (p')^2 / \rho_o a_o$ or

$$I(r,t) \doteq \frac{1}{16\pi^2 \rho_o = a_o^5} \frac{x_i x_j x_x x_i}{R^6} \int_{V_o'} \left\{ \int_{V_o} \left[\frac{\partial^2 T_{ij}}{\partial t^2}\right] dV_o \right\} \left[\frac{\partial^2 T_{kl}}{\partial t^2}\right] dV_o' \qquad (2.5.2\text{-}8)$$

2.5.3 Approximations for the Static Jet

Lighthill has shown (Reference 2.5.2-3) that for a stationary jet

$$I(r,\theta) \sim \frac{V_e\, \omega^4 \bar{T}^2}{\rho_o\, a_o^5} \frac{1}{4\pi R^2} \left[(1 - M_c(os\theta)^2 + \left(\frac{\omega \ell}{a_o}\right)^2\right]^{-5/2} \qquad (2.5.3\text{-}1)$$

Where R is the distance between the source of turbulence and the point of observation; V_e, the eddy volume; ω, the radiation frequency of fluctuation in a reference frame moving with eddy convection speed V_c; $\bar{T}^2$, the mean square value of the quadrupole strength; θ, the angle between the direction of sound emission and the jet axis; M_c, the ratio of eddy convection speed to sound speed of the ambient gas; and ℓ, the scale of turbulence.

The quantities in Equation (2.5.3-1) may be computed using the following assumptions. The eddy volume V_e was taken as ℓ^3; the quadrupole strength is assumed to be proportional to $\rho^2 U^4$; and the quantity $\omega\ell$ was approximated by 1.1 u' (the local turbulent velocity fluctuation). With these assumptions the mean square pressure fluctuation due to an individual circular ring volume element is:

$$p'^2 \sim \frac{1}{4\pi R^2} \frac{p^2 u'^4 \bar{U}^4}{p_o a_o^4} \left[(1 - M_c(os\theta)^2 + \left(\frac{1.1u'}{a_o}\right)^2 \right]^{-5/2} \qquad (2.5.3\text{-}2)$$

Equation (2.5.3-2) is seen to directly link the local aerodynamic properties with the acoustic farfield pressure field. By using the aerodynamic flow field analysis described above, the complete jet plume can be considered to consist of independent correlation volumes whose frequency content is specified by the P.O.A.L. Davies relation $\omega \ell^2 \sim 1.1\ u'$ (Reference 2.5.3-1).

The required local aerodynamic properties necessary for the evaluation of the noise generated by simple conical jets is well documented in References 2.5.2-2 through -5. The General Electric computational schedule necessary for calculating the detailed acoustic properties is represented in Figure 2.5.3-1. Individual volume elements are computationally constructed throughout the plume. Associated with each volume element are the local aerodynamic properties of ℓ, $\bar{U}$, $\bar{\rho}$, u'. Since these properties vary throughout the jet plume, so does the frequency and the acoustic source strength. The sound pressure levels can be computed, using Equation (2.5.3-2), stored, and summed for each one-third octave band at any emission angle. Through suitable integration, the overall power, power spectra, and overall sound pressure levels can also be computed.

The aeroacoustic relationship expressed by Equation (2.5.3-2) describes what is commonly referred to as "self-noise" generation; that is noise generated directly by a turbulence - turbulent interaction. Lilley (Ref. 2.5.3-6), Maestrello (Ref 2.5.3-7), Csanady (Ref. 2.5.3-8), Jones (Ref. 2.5.3-9), Krishnappa and Csanady (Ref. 2.5.3-10) have illustrated convective terms which deal with the turbulent and mean shear interaction field, which is referred to as shear noise. Reference (2.5.3-4) has illustrated that with a combination of self and shear noise radiation terms many of the observed acoustic characteristics of subsonic and supersonic stationary exhaust jets are illustrated.

2.5.4 Application of the Turbulent Mixing Model for Moving Jet Aircraft

If now the turbulence is being generated by the engine of an airplane which is in motion relative to the observer, the solution to equation (2.5.2-5) must be altered. This situation is considered by Ribner (Ref. 2.5.2-5) and Ffowcs-Williams (Ref. 2.5.4-1 and -2). The work here follows that of Ffowcs-Williams.

A new coordinate system is defined which moves with the aircraft at a velocity of $-a_o N$. In the new coordinate system, a point in the turbulence is moving along with the aircraft is identified by the position vector η. The relationship between the coordinate systems is $r_o = \eta - a_o Nt$ when both specify the same position in the turbulence. Signals received by the observer at time t were emitted at time $t - |R|/a_o$. At this time the relationship between coordinates is $r_o = \eta - a_o Nt + N|R|$ as shown in Figure 2.5.4-1. In the new coordinate system T_{ij} is a function of position η and retarded time $t - |R|/a_o$. The coordinate transformation has the property of changing the volume element in the turbulent region given by:

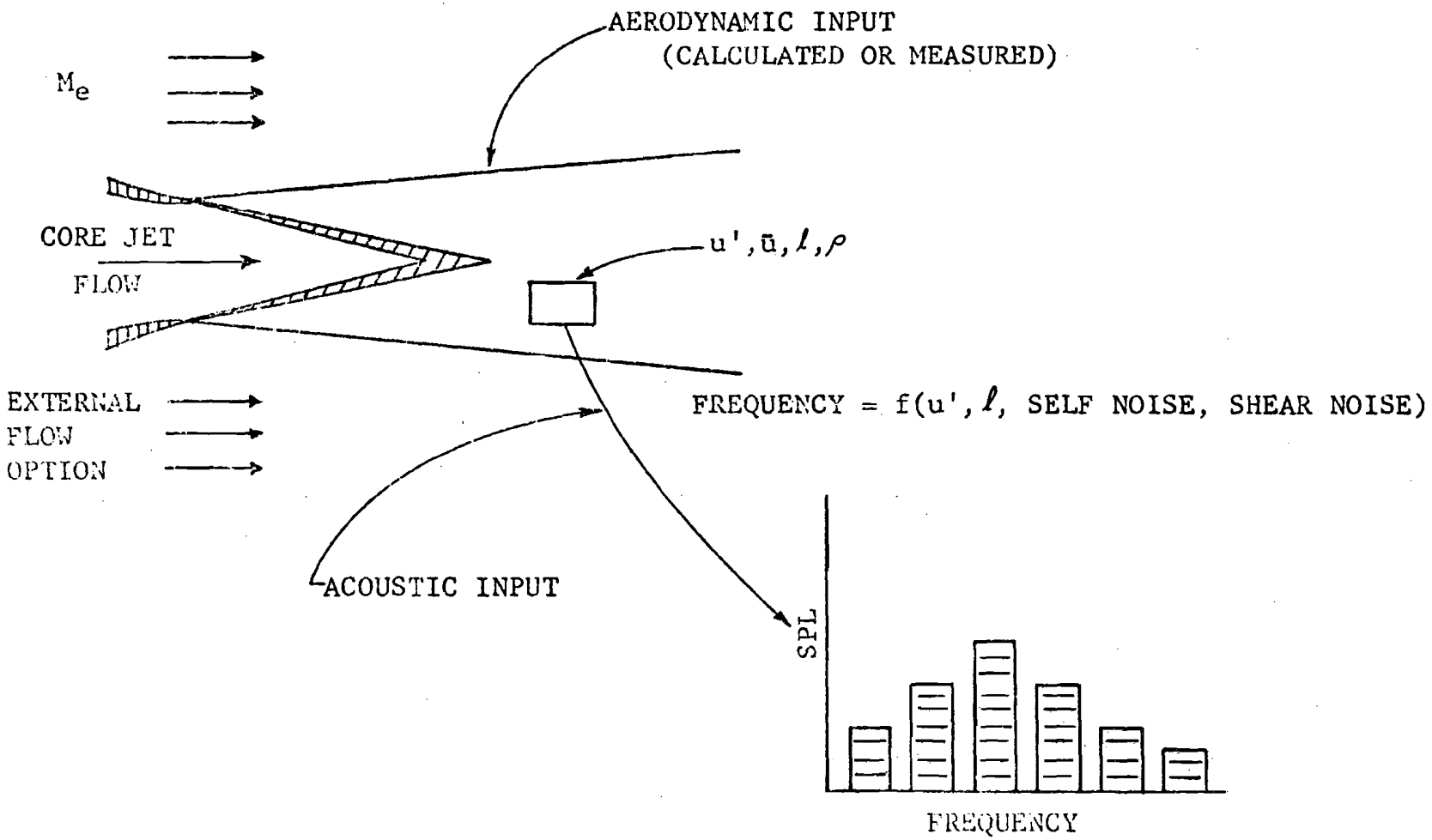

FIGURE 2.5.3-1 SCHEMATIC OF AERO ACOUSTIC RADIATION AND COMPUTATIONAL PROCESS

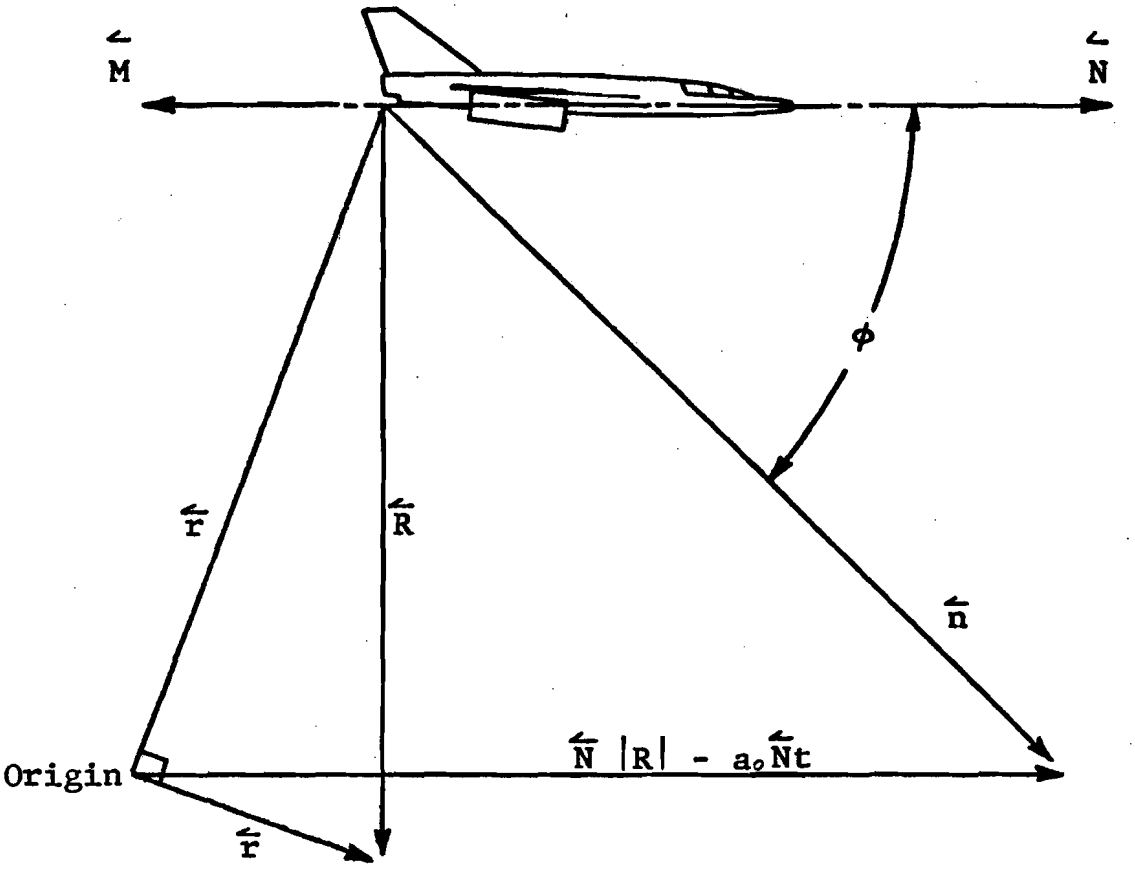

FIGURE 2.5.4-1 TURBULENCE DISTRIBUTION RELATIVE TO AIRCRAFT MOVING WITH VELOCITY $\vec{M}\cdot a_o$ IN OPPOSITE DIRECTION TO AIRCRAFT.

$$dV^{\eta} = dV^{y}\left[1 + \frac{N \cdot R}{|R|}\right]$$

The solution for the density disturbance which results from a turbulent region of fluid moving with the aircraft is:

$$(\rho(r,t) - \rho_o) = \frac{1}{4\pi a_o^2}\frac{\partial^2}{\partial x_i \partial x_j}\int \frac{T_{ij}\left(\eta, t - \frac{|R|}{a_o}\right)}{[|R| + N \cdot R]} dV^{\eta} \qquad (2.5.4\text{-}1)$$

or

$$(\rho(r,t) - \rho_o) \simeq \frac{1}{4\pi a_o^2}\int \frac{x_i x_j}{[|R| + N \cdot R]^3} \frac{\partial^2 T_{ij}(\eta,\tau)}{\partial t^2} dV^{\eta} \qquad (2.5.4\text{-}2)$$

where

$$\tau = t - \frac{|R|}{a_o}$$

The Doppler factor $[1 + N \cdot R/|R|]$ represents the influence of the movement of the sources. Ffowcs-Williams has shown that the acoustic intensity in the farfield can be written as:

$$I = \frac{1}{16\pi^2 a_o^5 \rho_o R^6} \frac{x_i x_j x_k x_\ell}{1 + \frac{N \cdot r}{|R|} \quad 1 - \frac{M \cdot r}{|R|}} \iint \frac{\partial^4 P_{ijk\ell}}{\partial \tau^4} dV^{\eta}\, dV^2 \qquad (2.5.4\text{-}3)$$

The acoustic intensity given by (2.5.4-3) is the field generated by the turbulent flow from the jet exhaust of an aircraft traveling at velocity $-a_o N$ through a uniform stationary medium. The acoustic intensity for the turbulent moving jet is approximated by:

$$I(r,t) \sim \frac{S}{\bar{\rho}_o R^2 a_o^5} \frac{(1 + N(os\phi)^{-1}}{\{(1 - \tilde{M}_c(os\theta)^2 + (\alpha M_c)^2\}^{-5/2}} \qquad (2.5.4\text{-}4)$$

where N is defined as the flight speed U_e, divided by the ambient speed of sound a_o; M_c is defined as: $0.63\ (U_j/a_o - N)$; U_j is the jet exit speed relative to the aircraft. The term α is the eddy decay parameter which is more complicated than the parameter used in the static jet noise case since the integral transverse and longitudinal turbulent length scales are affected by the relative motion of the fluids.

The source function in the acoustic intensity expression (2.5.3-2) can be handled by a method similar to the one used by Kobrynski (Reference 2.5.4-3). Recalling from the previous section on stationary jets, the source function per unit uncorrelated volume can be written as:

$$S \sim \bar{T}^2 \, \omega^4 \, V_e \qquad (2.5.4\text{-}5)$$

where $\bar{T}^2$ is the rms value of the fluctuations of the strength of the quadrupole, ω is the characteristic angular frequency of the fluctuations and V_e is the characteristic volume of the eddies. For a jet in flight the quantities in equation (2.5.4-5) may be written as:

$$\bar{T}^2 \sim \rho_j^2 \, (U_j - U_e)^4$$

$$\omega = \omega_e \, (1 + U_e/U_j)^2$$

$\omega_e = \omega_a \, (1 + N \cos \emptyset)$; characteristic angular frequency emitted by the stationary jet.

ω_a = The apparent observed frequency

$$V_e \sim L^3$$

Using this information detailed spectral computations can be formulated for the flight case in a fashion similar to the calculations performed for the stationary jets.

2.5.5 Influence of Flight on Single and Dual Flow Exhaust Nozzles Aerodynamics

Subsections 2.5.3 and 2.5.4 illustrated how the noise generating mechanisms of an exhaust jet can be related to the detailed turbulent flow properties of stationary and moving exhaust jets. In order to utilize the technique discussed, the aerodynamic flow properties must be available. For stationary single exhaust jets, General Electric's aerodynamic computation method is well documented (References 2.5.3-1 to -4). Discussed below are some parametric studies illustrating the influence of flight velocity on the turbulent and mean velocity distributions for a single and a dual flow nozzle. Since the basic turbulent mixing flight acoustic model relies directly on an aerodynamic source function, the aerodynamic properties are of interest to gain insight into the acoustic source characteristics.

Figures 2.5.5-1 and -2 illustrate predicted comparisons of radial mean and turbulence velocity profiles for a dual flow jet typical of the CF6, and a single jet at the same cycle condition as the dual flow core nozzle. Both predictions are shown for a relative flow (flight) environment. Figure 2.5.5-1 shows the mean velocity profiles for the single and dual flow jet at axial

D_{CORE} = 33.1" (0.851m) D_{FAN} = 54.3" (1.396 m)

$M_{j_{CORE}}$ = .9537 $M_{j_{FAN}}$ = .9429

$T_{j_{FAN}}$ = 1314°R (730°K) $T_{j_{FAN}}$ = 549°R (305°K)

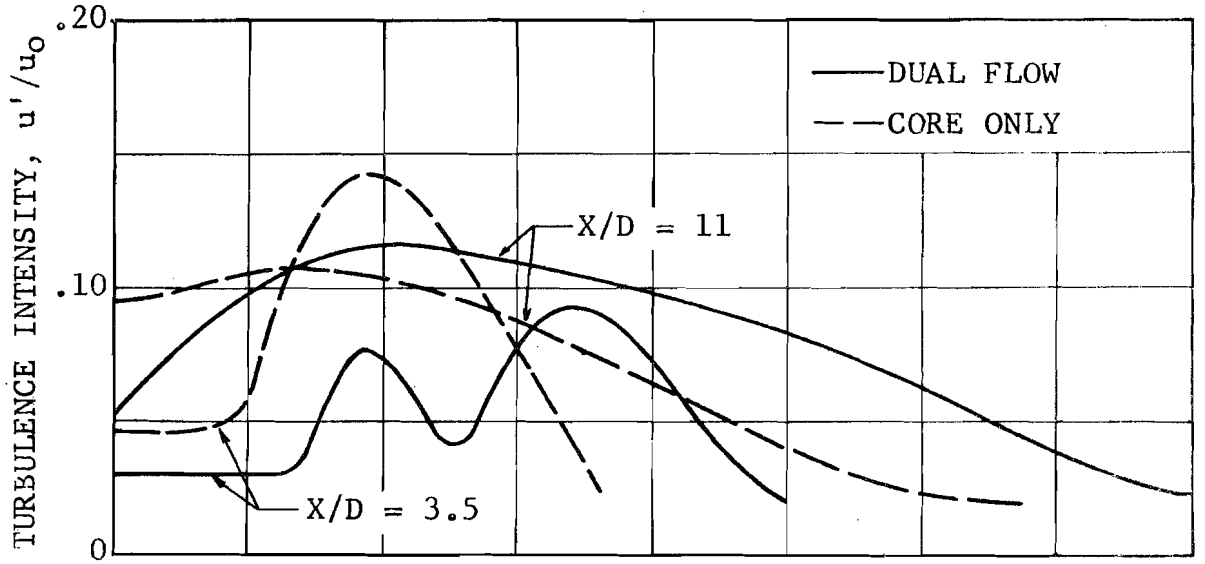

FIGURE 2.5.5-2 PREDICTED RADIAL TURBULENCE INTENSITY PROFILES AT AIRCRAFT MACH NUMBER = .1976

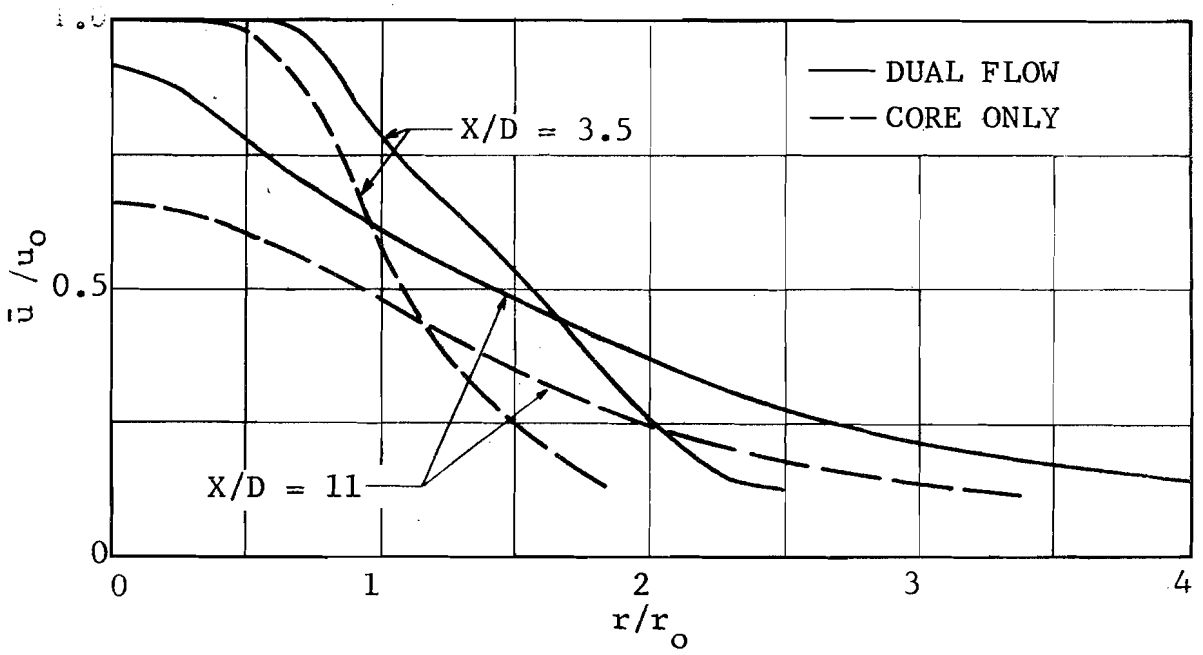

FIGURE 2.5.5-1 PREDICTED RADIAL MEAN VELOCITY PROFILES FOR DUAL FLOW AND SINGLE FLOW JETS AT AIRCRAFT MACH NUMBER = .1976

locations of 3.5 and 11 core jet diameters. The influence of the secondary fan flow on the mean velocity is readily apparent. For the dual flow nozzle conditions, the mean velocity profiles are seen to decay less rapidly than the mean velocity profile of the single jet in the same relative flow environment. The turbulence intensity profiles for the same two cases are shown in Figure 2.5.5-2. At the X/D = 3.5 location, the dual flow turbulence intensity profile is seen to have two "humps" of turbulence. One hump near the core jet lip, and a second hump near the fan jet nozzle lip. The level of turbulence for the dual flow jet is predicted to be some what less than the core jet alone case. However at X/D $\sim$ 11, the two "humps" of turbulence for the dual flow jet smooths out to a single hump which is broader and slightly higher in level than the single jet in flight.

Figures 2.5.5-3 and -4 illustrate the predicted axial mean velocity and turbulent velocity decay for the dual flow and single flow nozzles in flight. Figure 2.5.5-3 shows the influence of the additional fan flow on the mean velocity decay. The dual flow jet in flight has a less rapid mean velocity decay than the single jet case. This implies a somewhat longer, higher velocity, and smoother initial mixing region. Further downstream however, a more rapid mixing must take place since the mean velocity decay is seen to approach the single flow case.

The axial decay of turbulence intensity at the core jet nozzle lip for the dual flow and single flow jet in flight is shown in Figure 2.5.5-4. The different decay profiles are observed. The single jet has a peak very near the nozzle exit, while the dual flow jet turbulence intensity decay is seen to peak some 10 diameters downstream; thereafter higher levels of turbulence are predicted (contributing to the dual flow mean velocity decay approaching the single jet case shown in Figure 2.5.5-3).

2.5.6 Application of Turbulent Mixing Aero/Acoustic Models to Ideal Single and Dual Flow Moving Jets

2.5.6.1 Flight Predictions for a Single Jet

On a gross basis, it can be shown from dimensional arguments for turbulent mixing noise (Reference 2.5.3-2), that the sound power amplification for a moving jet is different than for a stationary jet and is given by

$$\frac{(U_j - U_e)^8}{(1 - U_e/U_j)^4} \qquad (2.5.6.1\text{-}1)$$

The jet mixing aerodynamics are of course modified with the movement of the jet. The amplification factor $(1-U_e/U_j)^{-4}$ is due to the elongation of the turbulent mixing region. As an illustration of how the actual data correlates with the above predicted velocity dependence, Figure 2.5.6.1-1 shows F-106/J85 flyover acoustic results. Shown on this figure are measured data, SAE prediction, and the noise levels predicted by the simple formulation above. The new velocity dependence is seen to be in better agreement with measurements than the SAE prediction.

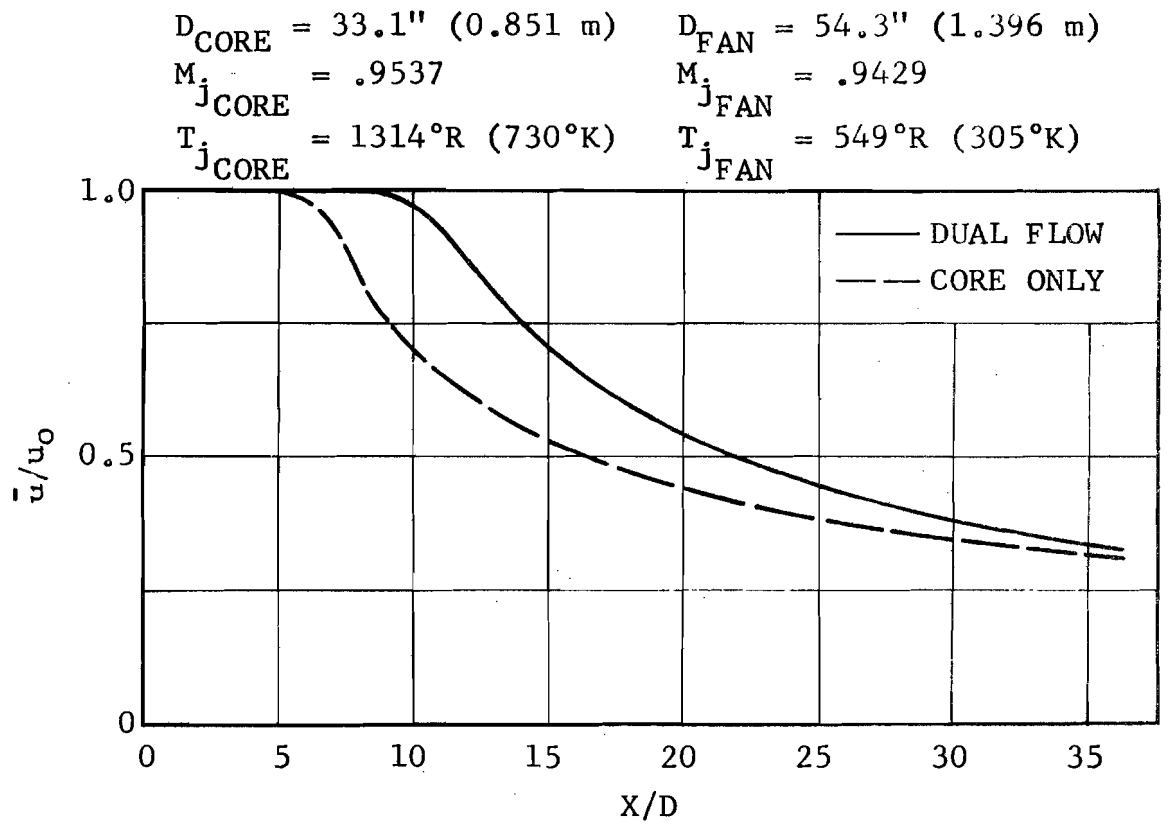

FIGURE 2.5.5-3 PREDICTED CENTERLINE AXIAL DECAY OF MEAN VELOCITY FOR DUAL FLOW AND SINGLE FLOW JETS AT AIRCRAFT MACH NUMBER = .1976

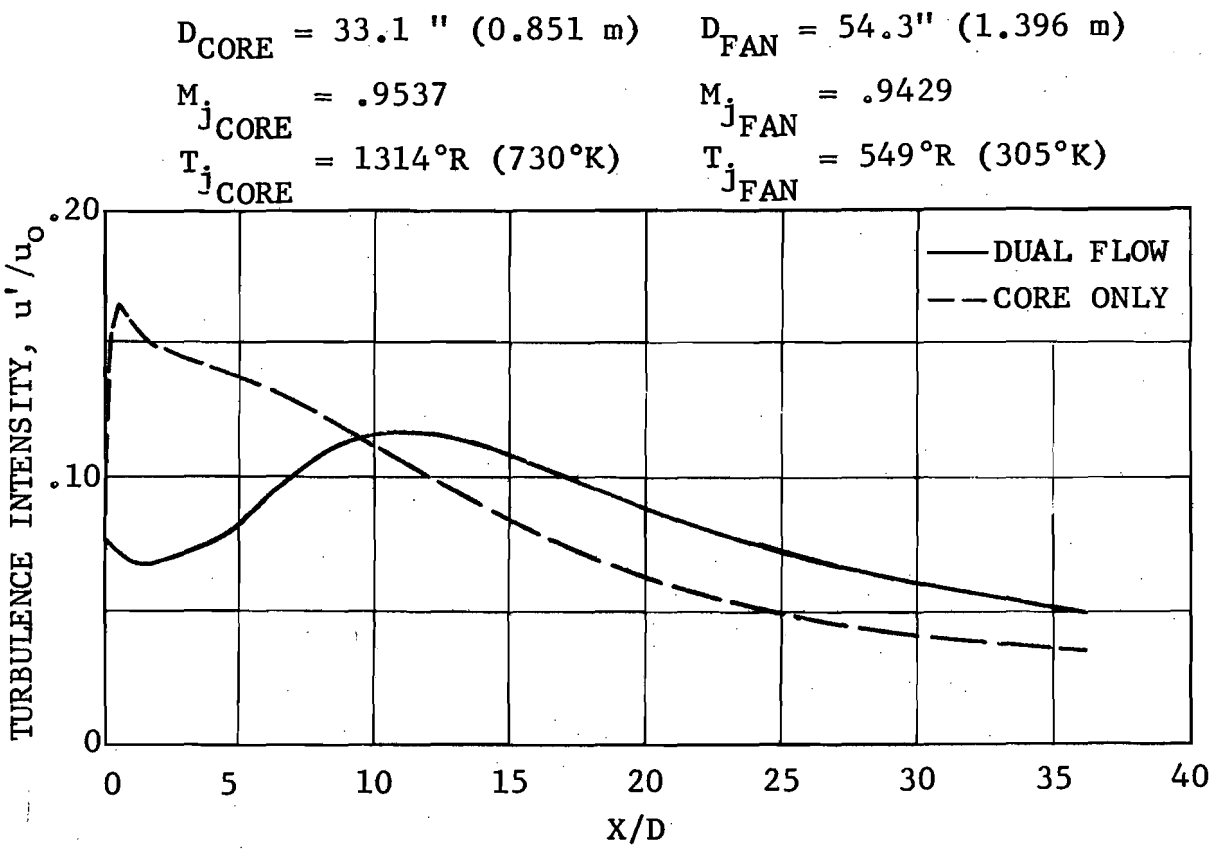

FIGURE 2.5.5-4 PREDICTED AXIAL DECAY OF TURBULENCE INTENSITY AT r/r_o = 1 FOR DUAL FLOW AND SINGLE FLOW JETS AT AIRCRAFT MACH NUMBER = .1976

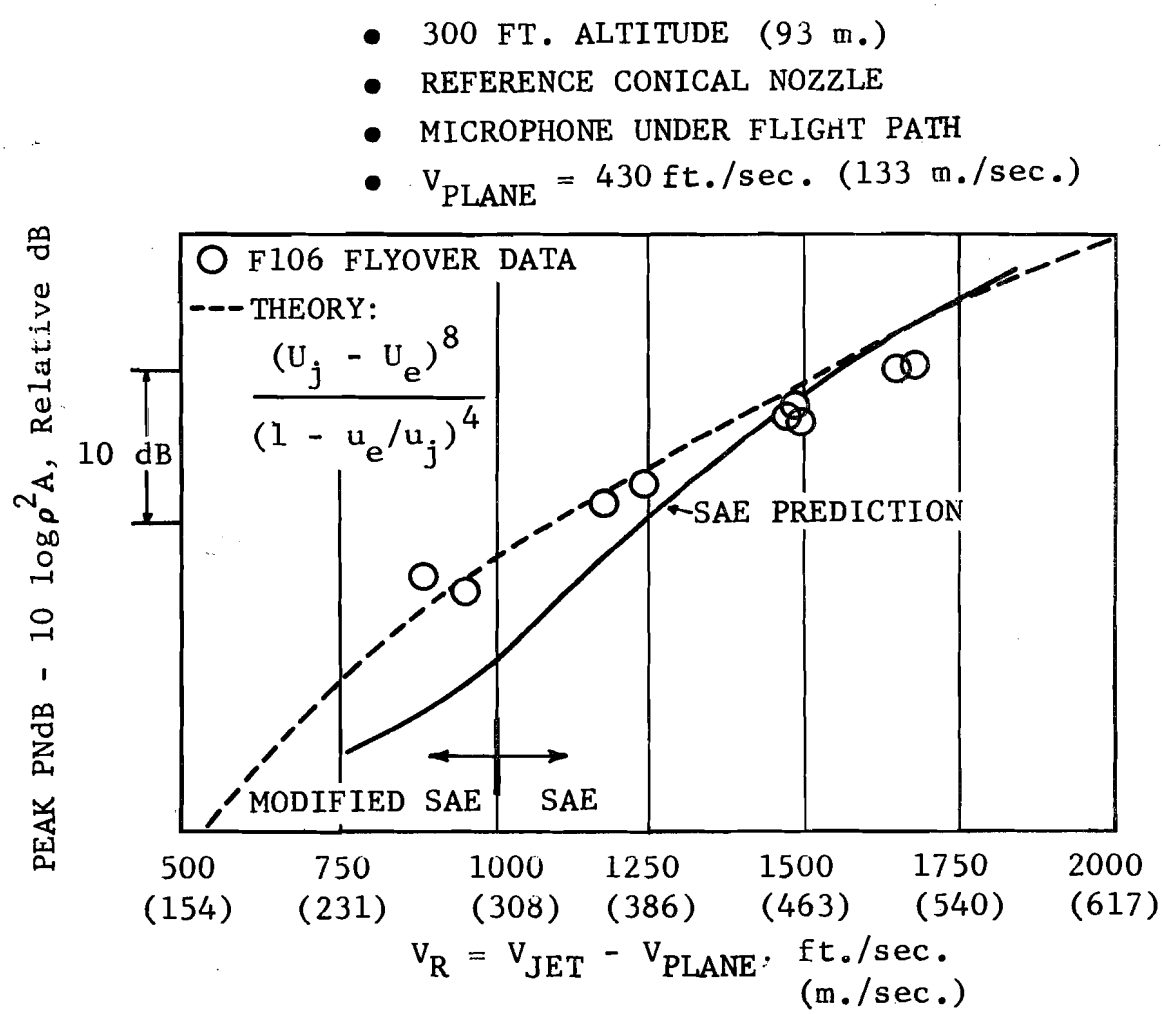

FIGURE 2.5.6.1-1 F106/J85 FLYOVER NOISE LEVELS

To illustrate some of the detailed predictions possible with this analysis, Figure 2.5.6.1-2 shows a theory/data comparison of the change of sound pressure level spectrum due to aircraft motion. Again F-106/J85 flight data is shown as a comparison. The reduction of noise in the low frequencies and amplification of noise in the high frequency jet exhaust noise due to aircraft motion is clearly shown by the theory and the data.

As an example of the directivity and spectral characteristics predicted by this method, Figures 2.5.6.1-3 and 2.5.6.1-4 show predicted trends of OASPL and 1/3 OBSPL for two types of turbulent mixing noise models (a self-noise model and a self-noise/shear-noise model). For static subsonic and supersonic jet noise predictions the self-noise/shear-noise model was found to be more representative of the ideal jet (see Reference 2.5.3-2 and 2.5.3-3).

2.5.6.2 Flight Predictions for a Dual Flow Nozzle

In Section 2.5.5 detailed aerodynamic predictions were presented showing the influence of flight on the plume characteristics of single and dual flow nozzles typical of the CF6 at takeoff conditions (see Figures 2.5.5-1 through -4). As a final illustration of the acoustic prediction, Figure 2.5.6.2-1 shows predicted jet noise OASPL versus jet angle for a dual flow nozzle in flight and stationary. The predictions show a reduction in jet noise due to flight at all jet angles. The jet cycle conditions choosen were typical of a CF6 at takeoff flight conditions.

2.5.7 Summary

In the above sections, the formulation of the generating mechanisms for simple exhaust nozzles based on existing turbulent mixing noise concepts were reviewed. It was shown how such turbulent mixing models can be formulated for computational studies, and how the acoustic model depends on the detailed mean velocity and turbulent velocity aerodynamic exhaust plume properties. Discussions and illustrations were given for single and dual flow nozzles.

Sections 2.5.1 through 2.5.4 reviewed the typical analysis used for turbulent mixing acoustic modeling for stationary and moving jets and how this type of analysis can be adapted for performing detailed calculations. Section 2.5.5 was a presentation of a study illustrating the influence of flight on the turbulent velocity and mean velocity exhaust jet distributions for single and dual flow jets. Inferences as to the noise generation distributions can be made from these results.

In Section 2.5.6 aero-acoustic predictions were presented for single and dual flow jets in motion. These rather simple acoustic models showed favorable agreement with observed velocity dependence of flight noise and the relative difference in sound-pressure-levels between a static jet and a jet in motion. The beneficial influence of flight on dual flow exhaust jet noise was also shown.

The aero acoustic model formulations presented herein can be used to predict the influence of flight on ideal jet exhaust noise. However, they can be

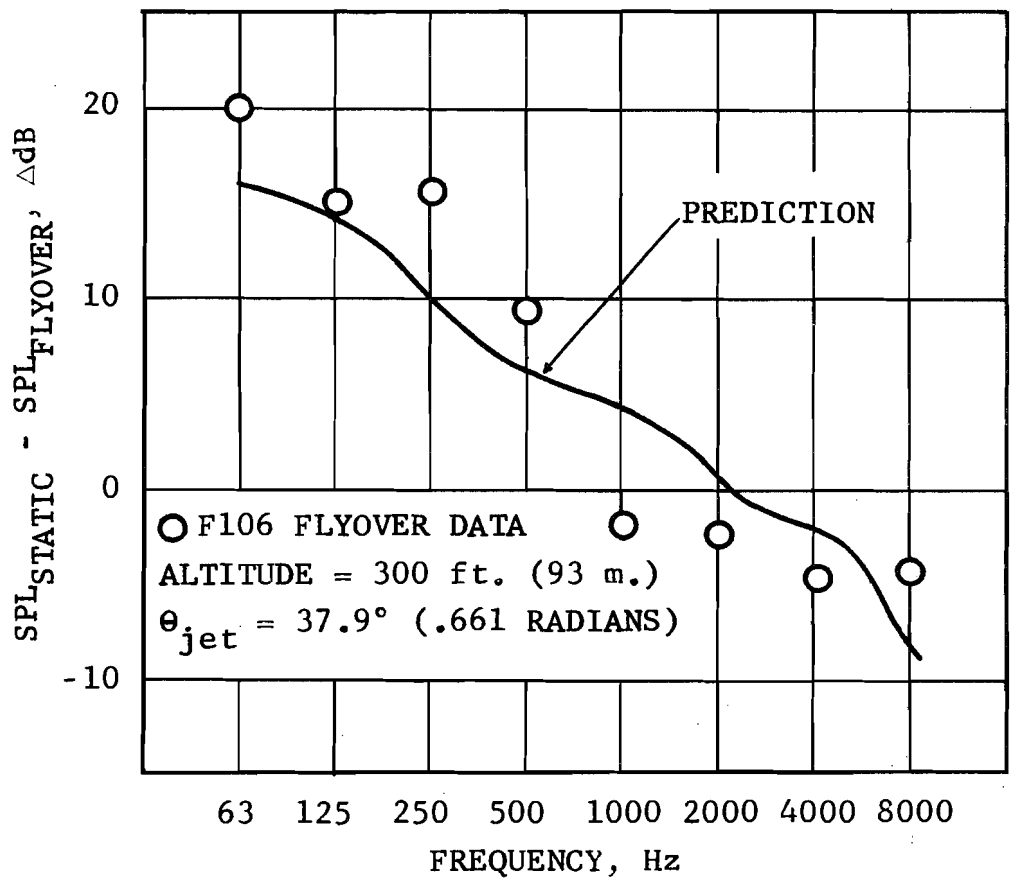

FIGURE 2.5.6.1-2 CHANGE OF SOUND PRESSURE SPECTRUM DUE TO FLIGHT (JET EXHAUST VELOCITY = 1328 ft./sec. (410 m./sec.), AIRCRAFT VELOCITY = 440 ft./sec. (136 m./sec.))

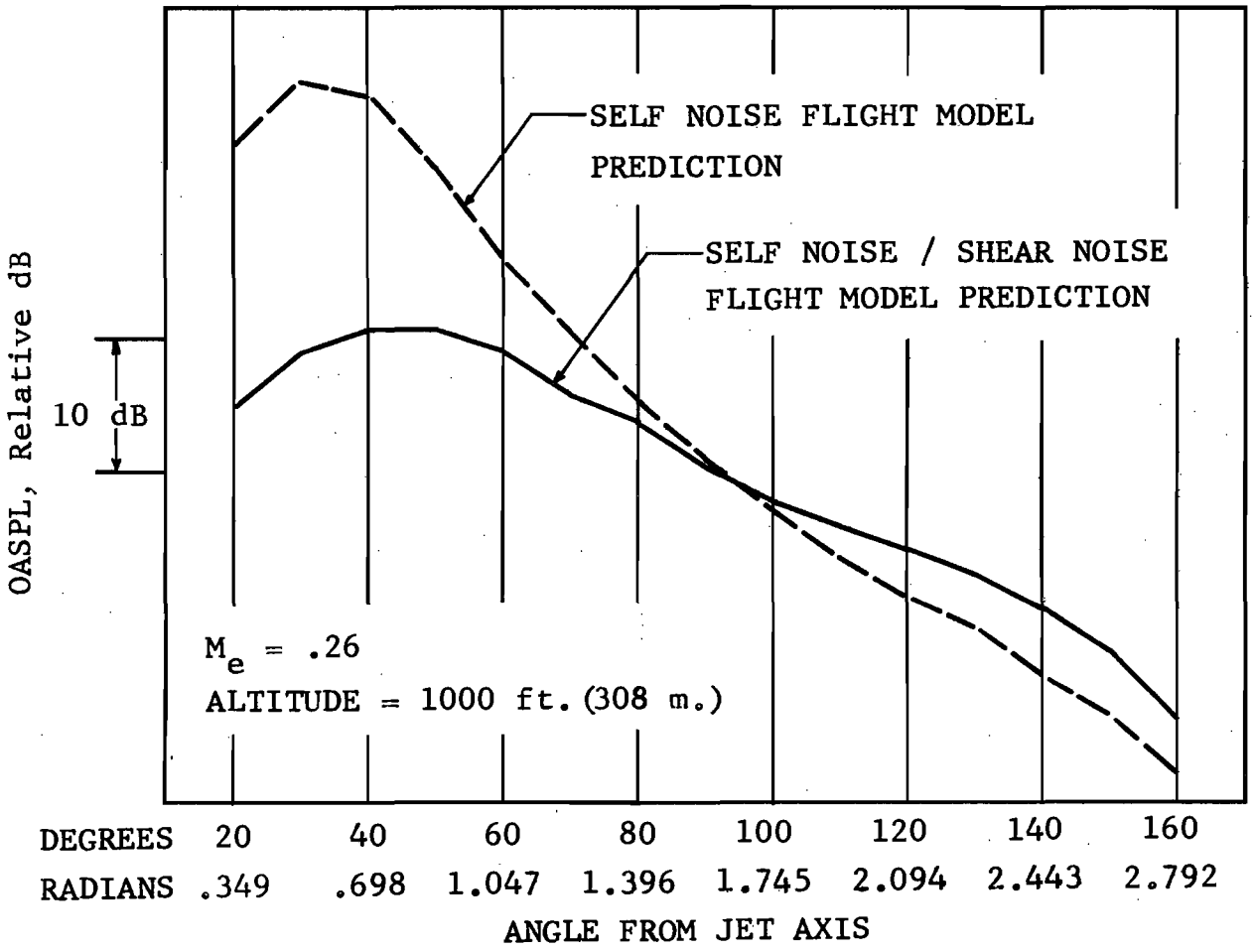

FIGURE 2.5.6.1-3 THEORY PREDICTION OF OASPL, 1000 ft. (308 m.) LEVEL FLYOVER NOISE, M_e = .26, V_j = 2165 ft./sec. (668 m./sec.), T_T = 1410°R (783°K)

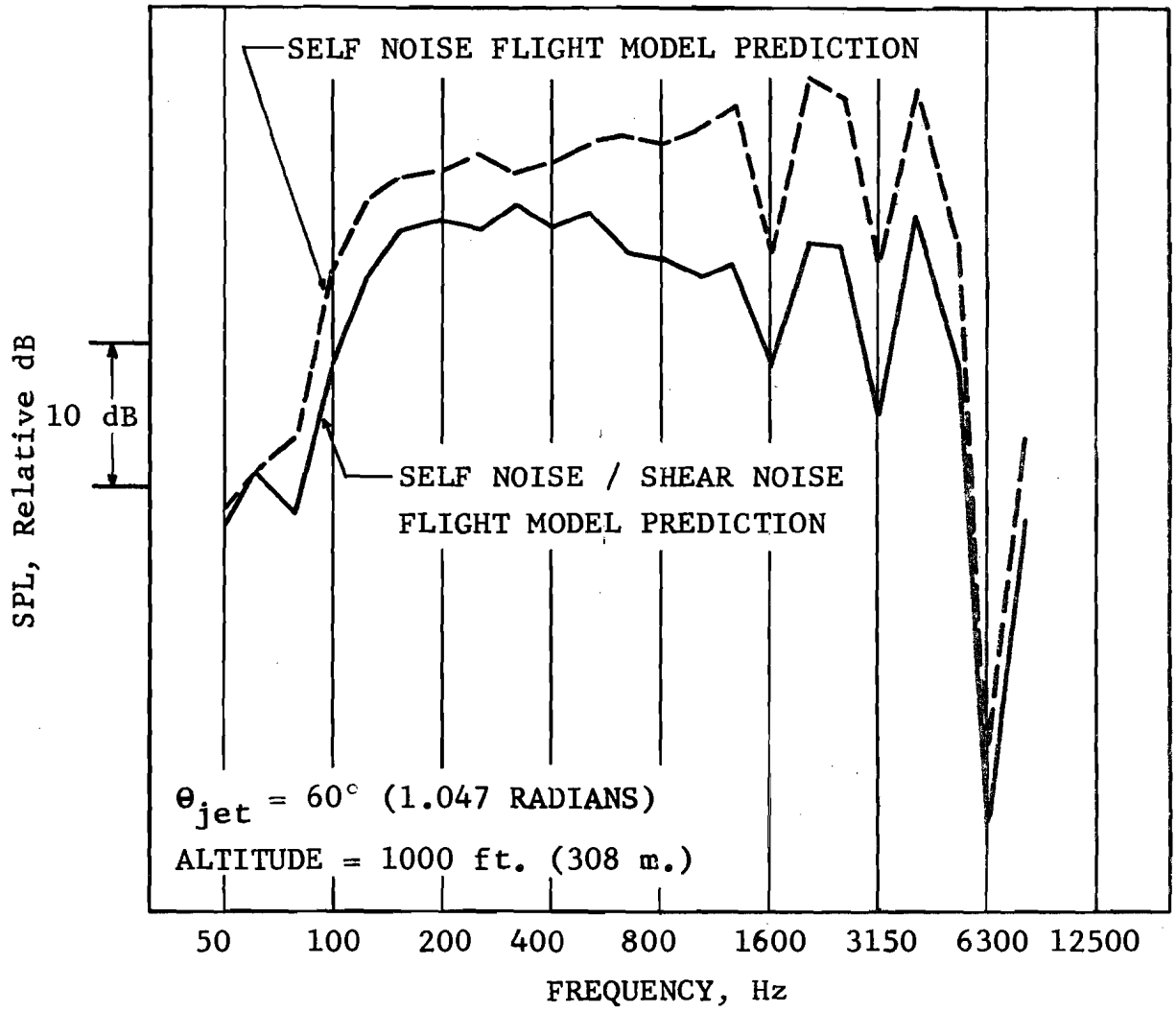

FIGURE 2.5.6.1-4 THEORY PREDICTION OF 1/3 OCTAVE BAND SPL SPECTRA, LEVEL FLYOVER NOISE, M_e = .26, V_j = 2165 ft./sec. (668 m./sec.), T_T = 1410°R (783°K)

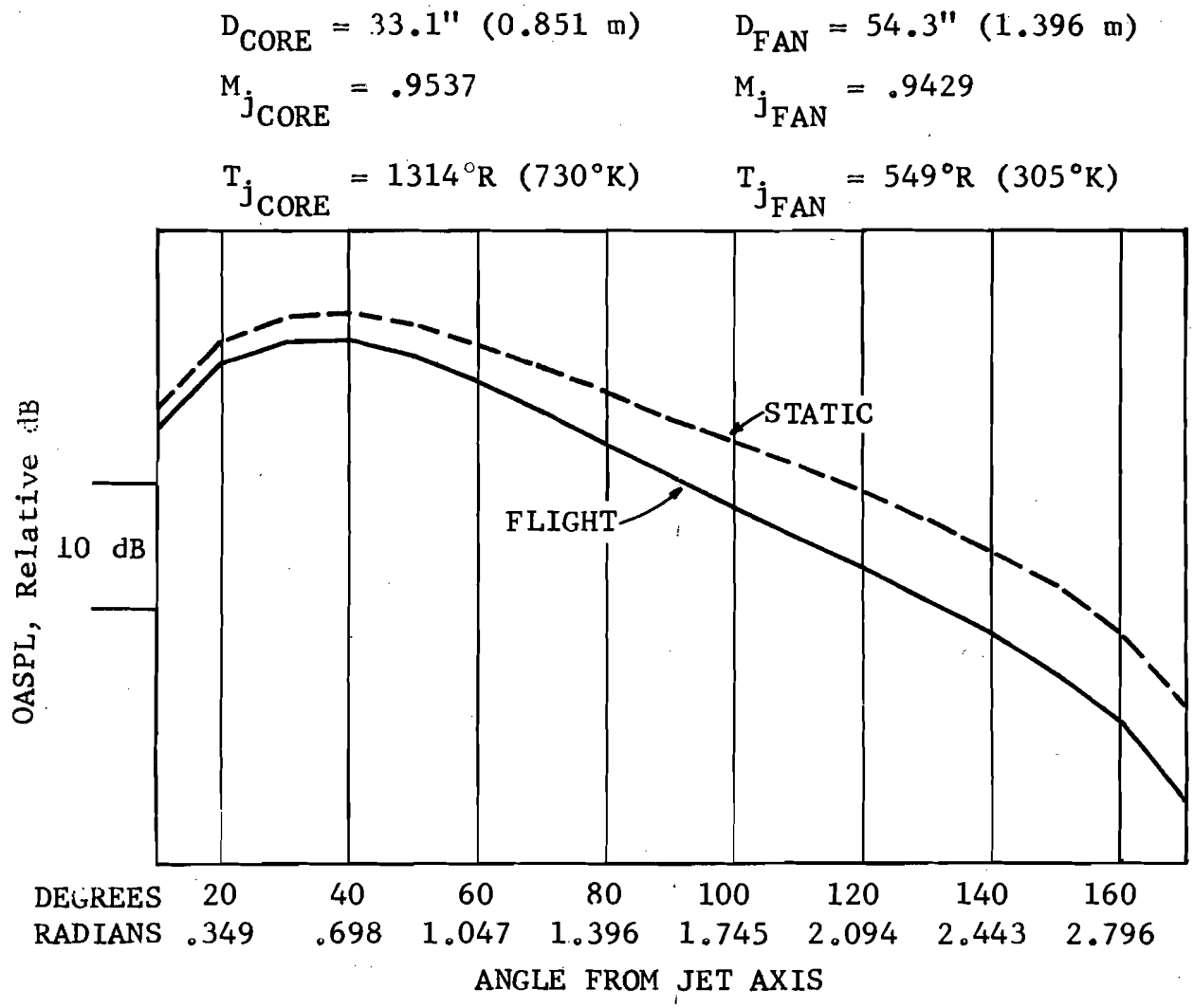

FIGURE 2.5.6.2-1 PREDICTED OASPL FOR A DUAL FLOW JET IN FLIGHT AND STATICALLY

improved. Areas of improvement include the proper acoustic modeling for jet density influences and a more exact model specification of the detailed spectral behavior of single and dual flow jets. The influence of the velocity and temperature gradients on the refraction of the sound also needs to be understood.

Due to the complexity of this analysis (see References 2.5.3-1 to -4), the lack of experimental data required for verification, and the needed improvements sighted above, this method is not being recommended as a general prediction procedure for relative velocity effects. This analysis will, however, prove very useful as a guide to further efforts on relative velocity effects.

References

2.1-1. Olsen, W., and Friedman, R.; "Jet Noise from Co-axial Nozzles Over a Wide Range of Geometric and Flow Parameters," NASA TM X-71503, February 1974.

2.1-2. Bielak, G.W.; "Coaxial Flow Jet Noise," DGE-1004-1, Boeing/Aeritalia Co., Seattle, Washington, 1972.

2.1-3. Eldred, K.; "Far Field Noise Generation by Coaxial Flow Jet Exhausts, Vol. I: Detailed Discussion," FAA-RD-71-101- Vol. 1, Wyle Laboratories, Inc., El Segundo, California, 1971.

2.1-4. Williams, T.J., Ali, M.R.M., and Anderson, J.S.; "Noise and Flow Characteristics of Coaxial Jets," Journal of Mechanical Engineering Science, Vol. II, No. 2, pp. 133-142, April 1969.

2.1-5. Hoch, R.G., DuPonchel, J.P., Cocking, B.J., Bryce, W.D.; "Studies of the Influence of Density on Jet Noise," presented at the First International Symposium on Air Breathing Engines, Marseille, France, 19-23 June 1972.

2.4.6-1 Olsen, W.A., Gutierrez, O., and Dorsch, R.G.; "The Effect of Nozzle Inlet Shape, Lip Thickness, and Exit Shape and Size on Subsonic Jet Noise," AIAA Paper No. 73-187, January 1973.

References

2.5.2-1 Lighthill, J.J.; "On Sound Generated Aerodynamically I - General Theory," Proc. Roy. Soc. A, 211 (1952).

2.5.2-2 Lighthill, J.J.; "On Sound Generated Aerodynamically II - Turbulence as a Source of Sound," Proc. Roy. Soc. A, 222 (1954).

2.5.2-3 Lighthill, J.J.; "The Bakerian Lecture. Sound Generated Aerodynamically." Proc. Roy. Soc. A., 267 (1962).

2.5.2-4 Ribner, H.S.; "Aerodynamic Sound from Fluid Dilatations, A Theory of the Sound from Jets and Other Flows," OTIA Report No. 86, July 1962.

2.5.2-5 Ribner, H.S.; Advances in Applied Mechanics, The Generation of Sound by Turbulent Jets, Vol. 8, Academic Press (1964).

2.5.3-1 Davies, P.O.A.L., Fisher, M.J. and Barratt, M.J.; "The Characteristics of the Turbulence in the Mixing Region of a Round Jet," J. Fluid Mech. 15, March 1963.

2.5.3-2 Heck, P.H. and Ferguson, D.R.; "Analytical Solution for Free Turbulent Mixing in Compressible Flows," AIAA No. 71-4 (1971).

2.5.3-3 Benzakein, M.J. and Knott, P.R.; "Supersonic Jet Exhaust Noise," AFAPL-TR-72-52 (August 1972).

2.5.3-4 Knott, P.R. and Benzakein, M.J.; "Analytical and Experimental Supersonic Jet Noise Research," AIAA 73-188 (1973).

2.5.3-5 Knott, P.R., et al.; "Supersonic Jet Exhaust Noise Investigation Interim Technical Report," AFAPL-TR-74 (February 1974).

2.5.3-6 G.M.; "On the Noise from Air Jets," ARC 20, 376 (1958).

2.5.3-7 Maestrello, L. and McDaid, E.; "Acoustic Characteristics of a High Subsonic Jet," AIAA 9, No. 6, 1058-1066 (1971).

2.5.3-8 Csanady, G.T.; "The Effect of Mean Velocity Variations on Jet Noise," J. Fluid Mech. 26, 183-197, (1966).

2.5.3-9 Jones, I.; "Aerodynamic Noise Dependent on Mean Shear," J. Fluid Mech., 33, 65-72 (1968).

2.5.3-10 Krishnappa, G. and Csanady, G.T.; "An Experimental Investigation of the Composition of Jet Noise," J. Fluid Mech. 36, 149-159 (1969).

2.5.4-1 Ffowcs-Williams, J.E.; "On Convected Turbulence and Its Relation to Near Field Pressure," Univ. Southampton Aero. Astr. Rept. No. 109 (1960).

References

2.5.4-2 Ffowcs-Williams, J.E.; "Jet Noise from Moving Aircraft," AGARD Conference Proc. No. 42 (1969).

2.5.4-3 Kobrynski, M.; "General Method for Calculating the Sound Pressure Field Emitted by Stationary or Moving Jets," Aerodynamic Noise Conference held at Toronto (1968).

SECTION 3.0

COMBUSTOR NOISE

3.1 BACKGROUND

In studying the noise generated by turbojet engines, it has been noted that as the jet velocity is decreased, the engine noise levels diverge from those predicted or measured for pure jet noise sources (Figure 3.1-1). At these lower velocities it is believed that broadband noise generated in the core of the engine is radiating from the exhaust nozzle. One of the possible sources for this frequency broadband noise is the combustor.

In order to determine the significant parameters which might affect the generation of combustor noise, a review of available published literature was made. One noise prediction equation, proposed by P.Y. Ho and R.N. Tedrick (Reference 3.1-1) was derived by using the Buckingham π - Theorem on a list of independent variables describing the combustor. The noise factor determined was:

$$F_1 = (T_4 - T_3)\sqrt{\frac{V_4 \; D_e \; P_4}{T_4}} \; (1 + f)$$

where the subscripts 3 and 4 denote conditions at combustor inlet and exit, respectively. P and T are the total pressure and temperature, V the velocity, f the fuel-air ratio and D_e the effective diameter.

Both engine and air rig component test data were used to obtain this above factor. There is, however, a conflict in the sound power levels. For air rig combustor component noise data:

$$\text{OAPWL} = 20 \log_{10} (F_1) + 81 \quad \text{dB, } r_e \; 10^{-13} \text{ Watt}$$

and for engine combustion noise data:

$$\text{OAPWL} = 40 \log_{10} (F_1) + 23 \quad \text{dB, } r_e \; 10^{-13} \text{ Watt}$$

This implies that the air rig combustor noise changes as F^2 and engine combustor noise changes as F^4.

Motsinger (Reference 3.1-2) uses an expression for the acoustic combustion efficiency which is expressed as:

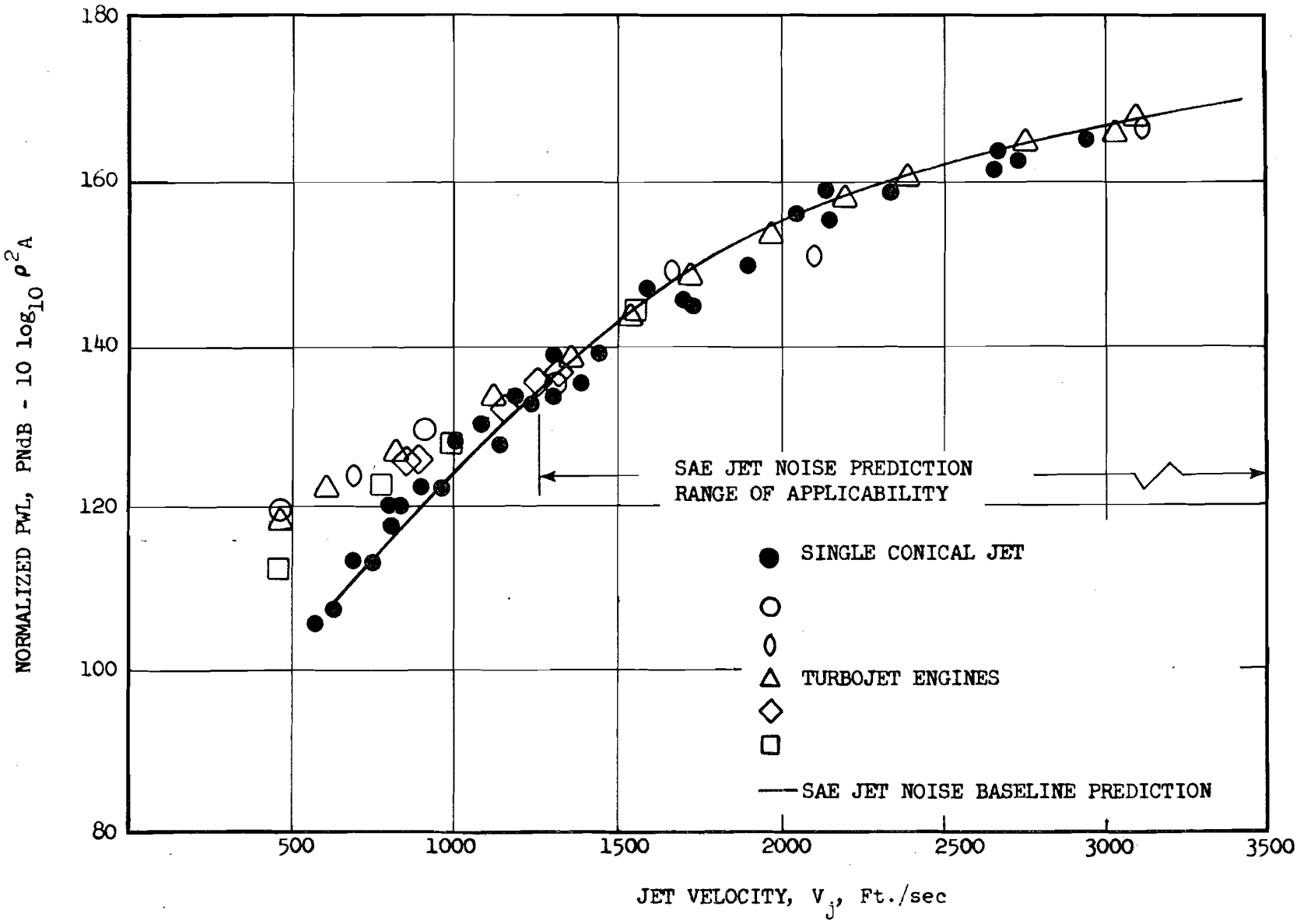

FIGURE 3.1-1 SINGLE CONICAL JET NOISE PREDICTION COMPARISON OF MEASURED TOTAL NOISE AND PREDICTED JET NOISE(SAE METHOD). PEAK NOISE BETWEEN 90° AND 160° FROM INLET, 300 Ft. SIDELINE DATA.

$$\eta = \frac{\text{Acoustic Power}}{\text{Heat Power}}$$

This expression can be put in terms of a noise factor similar to that of Ho and Tedrick's:

$$F_2 = \left[\sqrt{\dot{W}}\,\left(T_4 - T_3\right)\left(\frac{P_3}{P_o}\,\frac{T_o}{T_3}\right)\right]$$

The subscript 0 denotes ambient conditions and $\dot{W}$ is the air mass flow. Using this factor and the data from a T64 turboshaft engine, Motsinger recommends the following equation:

$$\text{OAPWL} = 20 \log_{10}\left(F_2\right) + 56.5 \quad \text{dB, re } 10^{-13} \text{ Watt}$$

which can be used to predict the overall sound power level for combustor noise from turboshaft engines.

Gerend, Kumasaka and Roundhill (Reference 3.1-3) propose using an engine core noise prediction that involves raising the turbine pressure ratio to the third power. Their prediction for OASPL at a 200 ft. sideline distance at the 110° angle (referenced to the engine inlet centerline), is:

$$\text{OASPL} = 10 \log_{10}\left[T_4^{\,2}\left(\frac{P_4}{P_5}\right)^3 \dot{W}\ \sqrt{\theta_4}/P_R\right] + \text{constant}$$

The subscript 5 denotes turbine exit conditions. Also, $\theta_4 = \frac{T_4}{518.7}$ and P_R is the compressor pressure ratio. The temperature and the mass flow are considered as important parameters.

Arnold (Reference 3.1-4) suggests a parameter proportional to the momentum changes that occur during combustion:

$$\text{POWER} = \frac{\dot{Q}V}{Aq_o\,[1-(\phi-1)]}\left(\frac{V_4}{V_3}\,\frac{T_4}{T_3} - 1\right)$$

where A is the exit area, q_o the specific stoichiometric heat of combustion, Q the heating value of the fuel, V the volume, and ϕ the equivalence ratio (fuel-air ratio/stoichiometric fuel-air ratio). The subscripted V's stand for velocity as above.

The velocities, temperatures, heat release and exit areas are considered the important parameters.

Strahle (Reference 3.1-5) states that the combustion power level will be proportional to the velocity and diameter cubed, the laminar flame speed squared, and a function of the reaction rate integrated over the reacting volume.

Current published work suggests based on the survey discussed above, that the air flow rate, temperature, pressure, and the temperature rise across the combustor are important noise parameters.

3.2 COMPONENT TESTS

In order to resolve some of the apparent differences in combustion noise prediction methods it was decided that the best results would be obtained by using full scale annular combustors for the component tests. By doing this it was anticipated that the combustor acoustic signatures would be more representative of aircraft engine combustor noise. A current technology CF6 and an advanced technology (A.T.) combustor were selected for the test.

3.2.1 Objectives

The goal of this investigation was to determine the most applicable equations for power level prediction, spectral shape characteristics, and directivity factors for combustion noise. Two combustors were tested over a wide range of temperature and flow rates in order to identify those parameters which would correlate combustor noise. The parameters considered most important were the air and fuel flow rates, the inlet temperature, pressure, and the inlet turbulence intensity. Acoustic data was obtained in both the nearfield and the farfield.

3.2.2 Hardware

Atomization Type Combustor

The CF6-6 engine combustor is of the conventional fuel nozzle atomization type. The axial swirler dome configuration was used for the test. Fuel is delivered by means of a dual orifice fuel nozzle that sprays the fuel into the combustor through two concentric sprays in these engines. The atomized fuel is mixed with air entering the axial swirler caps shown in Figure 3.2.2-1.

Carbureting Type Combustor

The A.T. combustor is a scroll or carbureting type premixing combustor. Fuel and air atomization and mixing are accomplished with the scroll device, as shown in Figure 3.2.2-2. The scroll device relies on the energy of the air stream to atomize and carburate the fuel, thus eliminating the need for a high pressure atomizing nozzle.

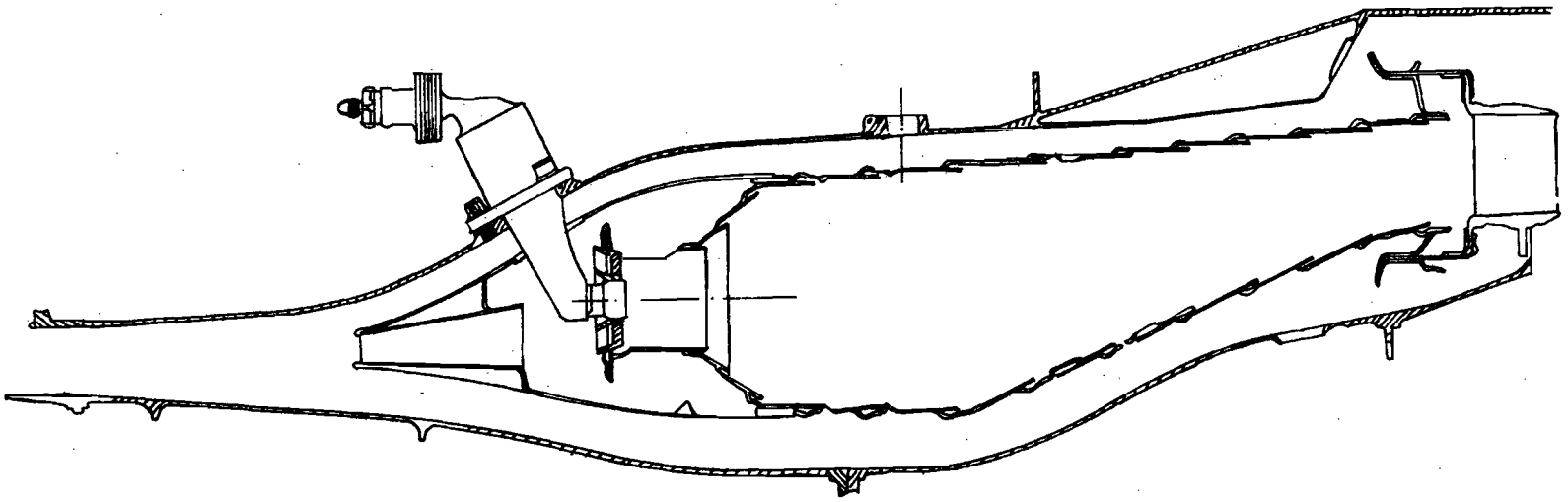

FIGURE 3.2.2-1 CF6 LOW SMOKE AXIAL SWIRLER COMBUSTOR FLOWPATH

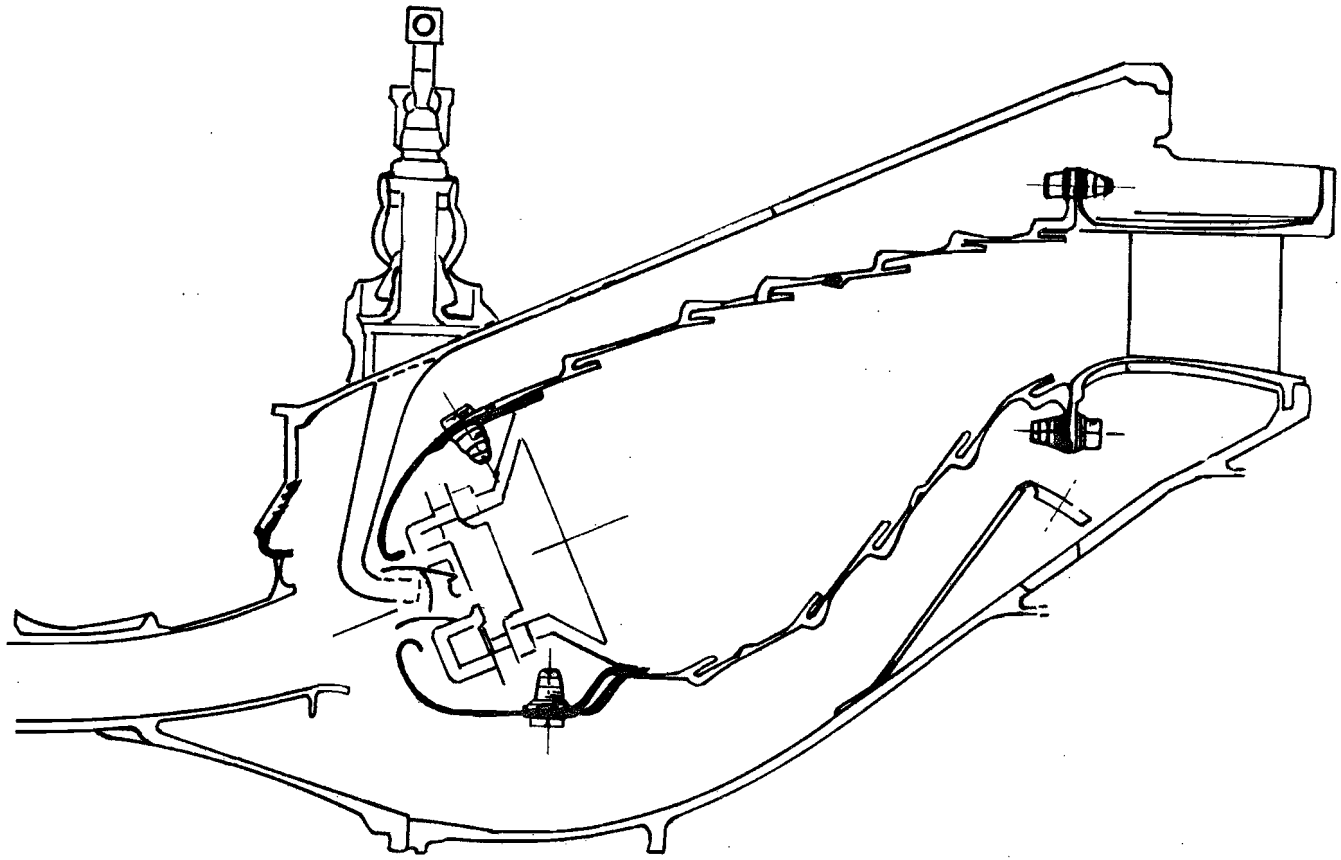

FIGURE 3.2.2-2 A.T. CARBURATING COMBUSTOR FLOW PATH.

Test Configuration

A cross section of the two combustors (Figures 33.2.2-3 and 3.2.2-4) show some of the differences in the liner shapes. The CF6 liner is relatively parallel to its centerline while the A.T. liner expands radially outward as the air travels through it. The A.T. liner is also shorter and smaller in diameter than the CF6. It was expected that the differences between these two combustors configurations would contribute to different levels of turbulent mixing.

Attached to each combustor rig is a horn and centercone. There are two reasons for this. It is possible that broadband jet noise could interfere with the similar broadband combustor noise signature. In order to minimize the jet noise contamination the exit velocities were diffused in the horn. The second reason for the horn was to provide an impedance coupling from the combustor liner to the farfield. The design of the horn was aimed at providing a high acoustic transmission coefficient down to frequencies below 100 Hz.

The combustor component tests were conducted on the JENOTS Facility. A detailed description of the JENOTS Facility was previously provided in Section 2.2.3. An instrumentation schematic of the combustor test at JENOTS can be seen in Figure 3.2.2-5. A heater was used upstream of the combustor to preheat the air. A bulk absorber muffler with a high porosity faceplate was installed ahead of the test combustor in order to reduce upstream noise. A single hot wire anemometer was used to monitor the turbulence intensity levels entering the combustor. A nearfield microphone probe was mounted at the liner exit plane for the CF6 test. Four rakes upstream and downstream of the combustor measured the total temperatures and pressures. The sound pressure levels were measured in the farfield by microphones on a 40 foot arc, at 10° intervals from 30° to 160° from the inlet. All acoustic data was recorded on magnetic tape. Photographs of the two combustors on the test stand can be seen in Figures 3.2.2-6 and 3.2.2-7.

3.2.3 Test Procedure

The test matrix was designed to isolate the effects of the temperature rise, airflow rate and inlet temperature. In order to do this over a wide range, it is necessary to understand certain limitations in combustion testing. Combustors are designed to operate within a range of ($\Delta P/P3$). An airflow rate of 7.5 lb/sec gives a ($\Delta P/P3$) that is close to the design value for both test combustors when operating at atmospheric pressure. Initial plans were to test the combustors at one half (3.75 lb/sec) and at two times (15 lb/sec) this flow rate. The A.T. combustor would not burn at the 15 lb/sec airflow rate however, and was therefore limited to a 10 lb/sec maximum flow in order to maintain proper burning.

At each of the selected airflow rates, fuel/air ratios were selected to give temperature rises of 1700, 1200, 700° F (945, 667, 389° C) and a no flame baseline. This matrix was initially set up to be tested two times, at 200° F

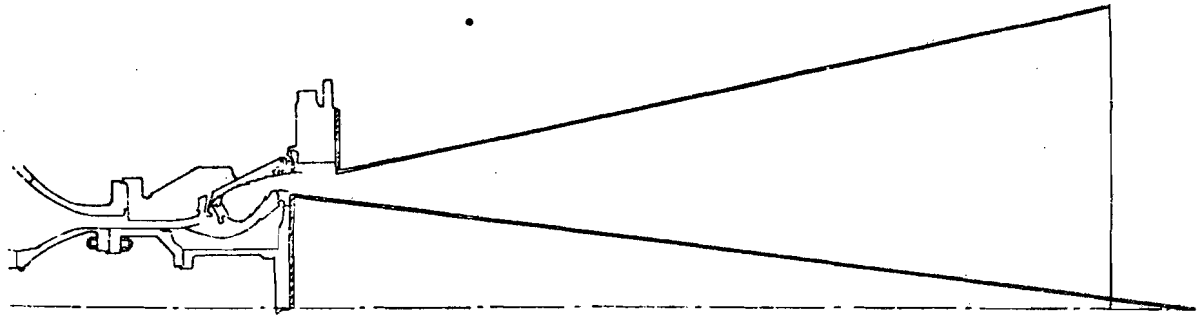

FIGURE 3.2.2-3 A.T. COMBUSTOR TEST CONFIGURATION

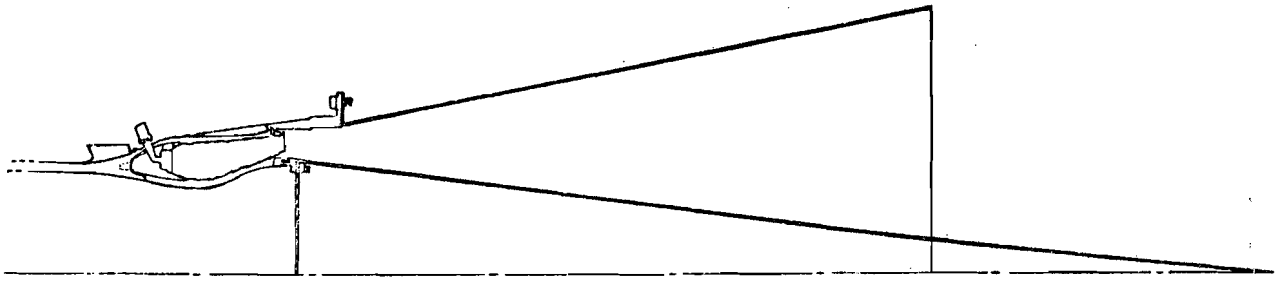

FIGURE 3.2.2-4 CF6 COMBUSTOR TEST CONFIGURATION

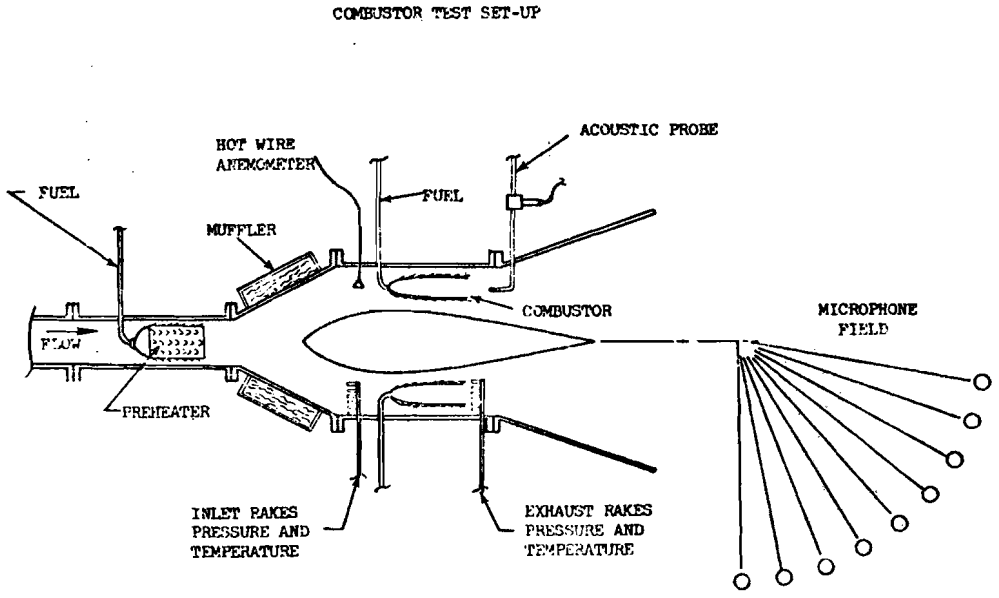

FIGURE 3.2.2-5 COMBUSTOR TEST SCHEMATIC

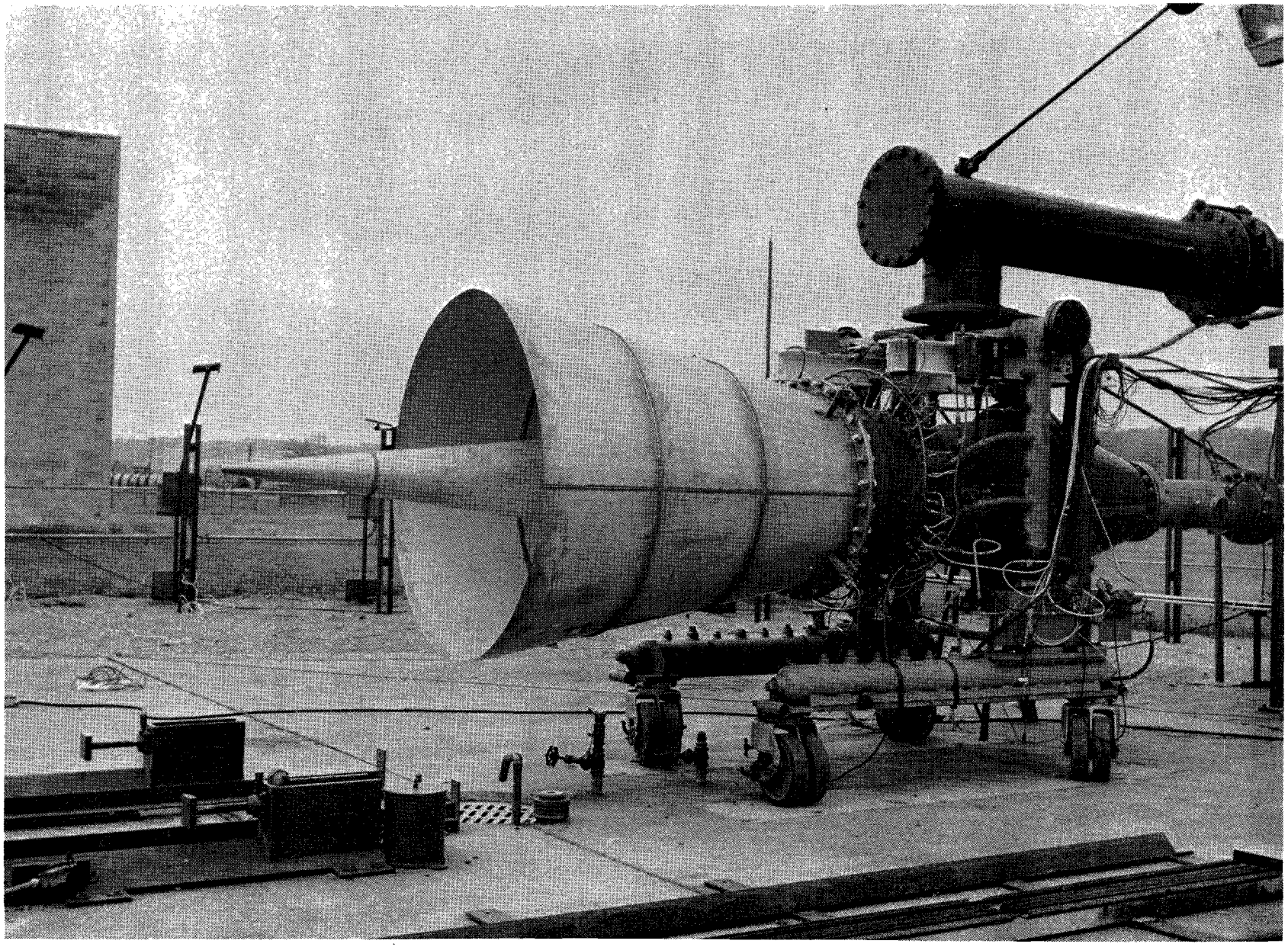

FIGURE 3.2.2-6 CF6 COMBUSTOR NOISE TEST

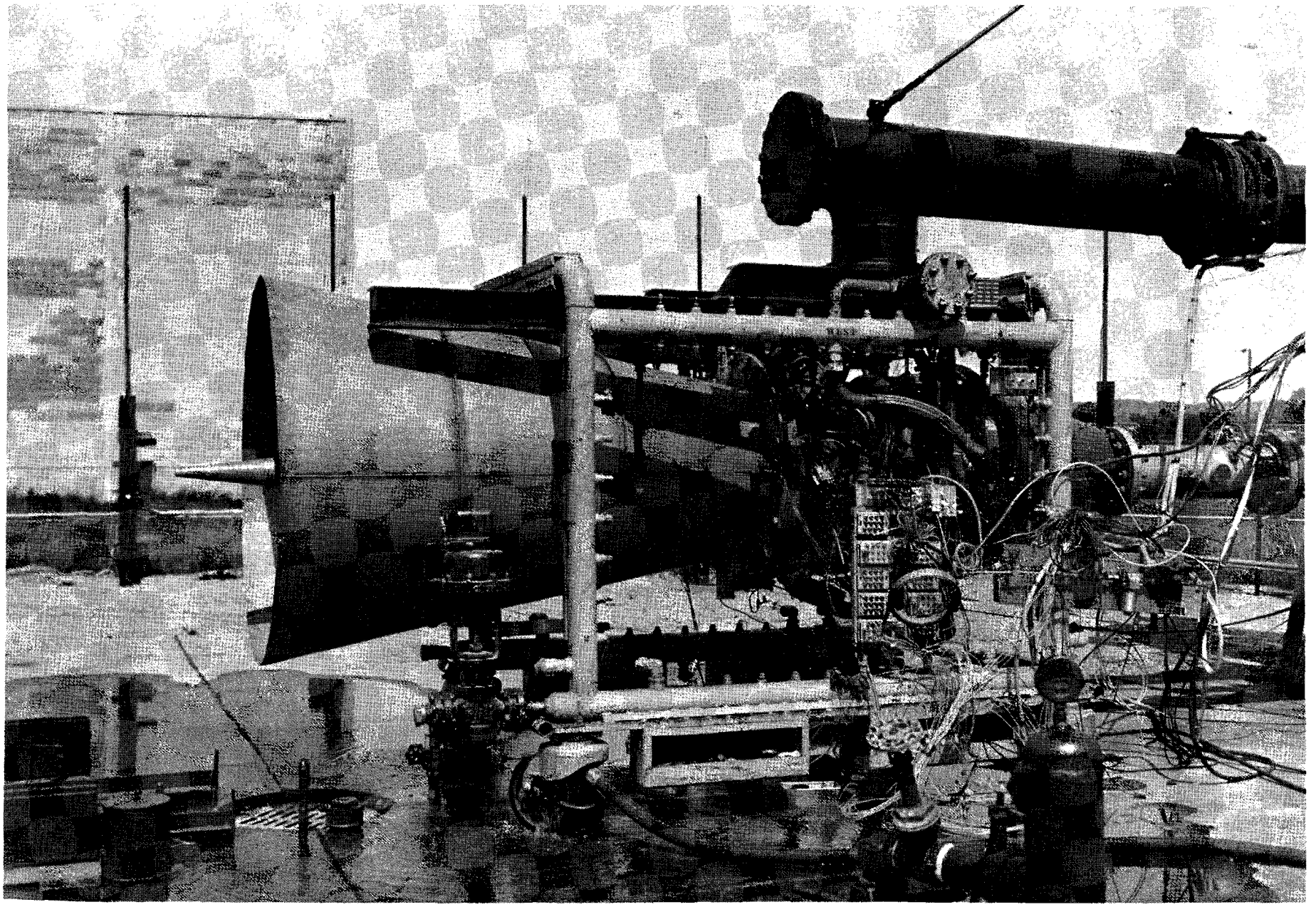

FIGURE 3.2.2-7 , A T COMBUSTOR NOISE TEST

(93.3° C) and 500° F (260° C) inlet temperatures. It was not possible to get all of the data at the 500° F (260° C) temperature. It was necessary to reduce the inlet temperature to 350° F (176.6° C) at the maximum airflow rates in order to get the combustors to burn properly. A table of test points, temperatures and pressures is presented in Appendix D.

3.2.4 Test Results

Acoustic Efficiency

The air and fuel flow rates plotted against the acoustic efficiency show trends that are similar to ones seen by Knott (Reference 3.2.4-1), (see Figures 3.2.4-1 and 3.2.4-2). Generally the acoustic efficiency increases with an increase in flow. The A.T. combustor, however, shows higher acoustic efficiency levels than the CF6 for the same air or fuel flow rate. In Figure 3.2.4-3, the CF6 efficiency does not markedly increase while the A.T. combustor does with an increase in the equivalence ratio (the fuel/air ratio divided by the stoichiometric fuel air ratio). This is believed to be due to the higher degree of turbulent mixing in the A.T. combustor. When the efficiency is compared to the exit velocity (Figure 3.2.4-4), the data seems to correlate better but it still includes the higher rate of increase in power level with fuel/air ratio for the A.T. combustor.

Acoustic Power Level

The overall power level (OAPWL) was calculated for each test point for a spectrum limited to the range from 100 to 2000 Hz. Above 2 KHz the noise levels were more than 20 dB below the peak one-third octave band level, which usually occurred between 200 and 400 Hz. The power level trends versus the mass flow and temperature rise can be seen in Figures 3.2.4-5 and 3.2.4-6. The power level increases with the temperature rise squared and with the air flow rate to the third power. Using these two terms by themselves will not, however, yield a good prediction parameter. A correlation (Figure 3.2.4-7) involving the mass flow cubed and the temperature rise squared has a standard deviation of 5.6 dB. Steps were taken to reduce this standard deviation. It was found that by changing the mass flow cubed to the mass flow times the exit velocity squared and dividing through by the exit area (Figure 3.2.4-8) would reduce the standard deviation to 3.2 dB. This correlation may be expressed as:

$$\text{OAPWL} \sim \left[\frac{\dot{W}\, V_4^2}{A_4} \; (T_4 - T_3)^2\right]$$

Since this results in a kinetic energy flux term per unit area times the temperature rise squared, the next step was to normalize the temperature rise by dividing through by the exit temperature (Figure 3.2.4-9):

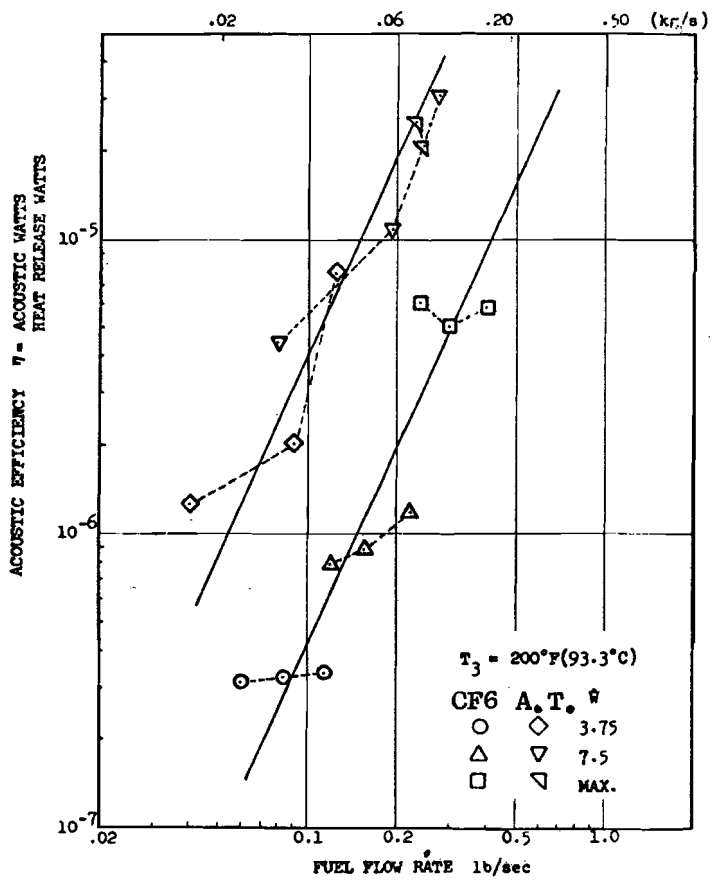

FIGURE 3.2.4-1 ACOUSTIC EFFICIENCY vs. FUEL FLOW RATE.

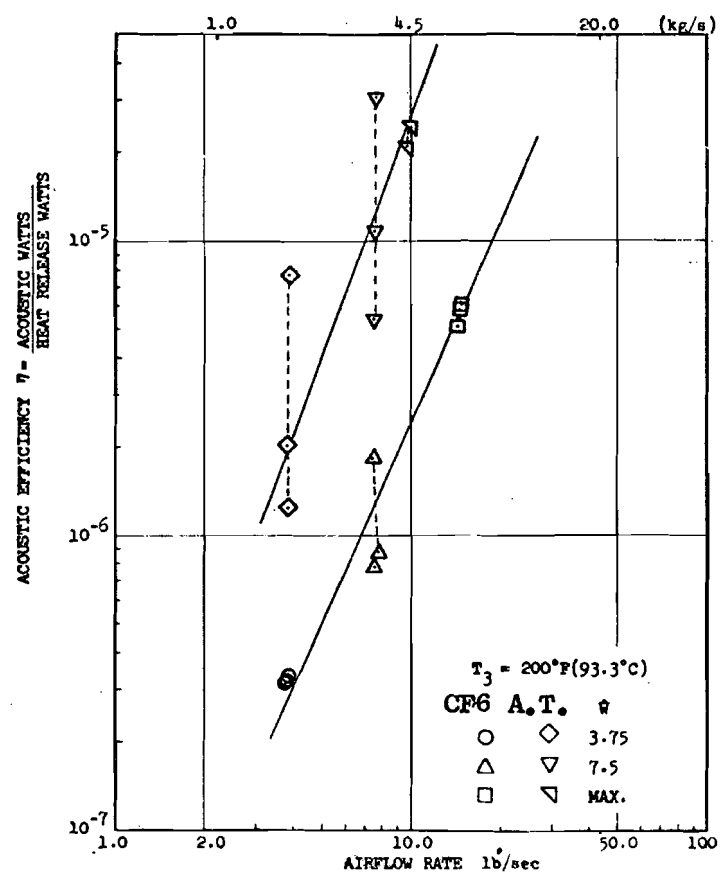

FIGURE 3.2.4-2 ACOUSTIC EFFICIENCY vs. AIR FLOW RATE.

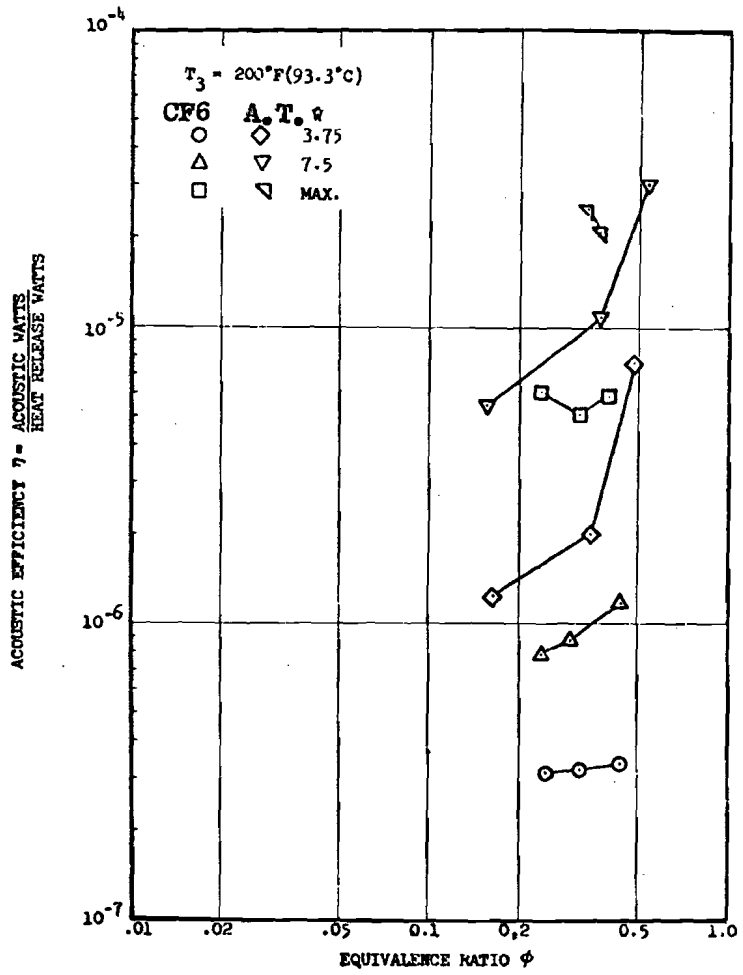

FIGURE 3.2.4-3 ACOUSTIC EFFICIENCY vs. EQUIVALENCE RATIO.

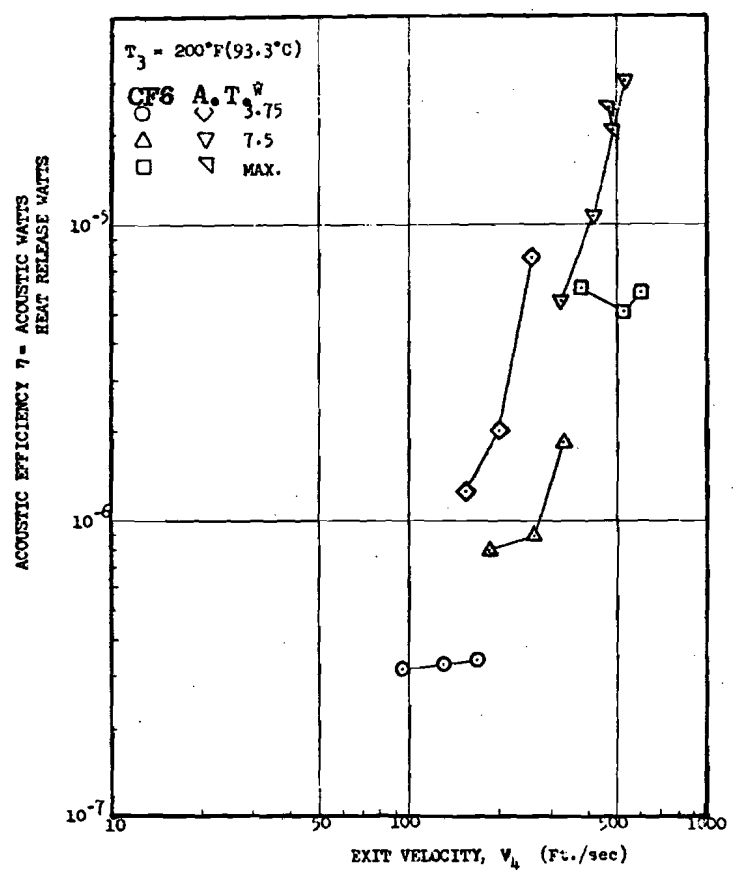

FIGURE 3.2.4-4 ACOUSTIC EFFICIENCY vs. EXIT VELOCITY.

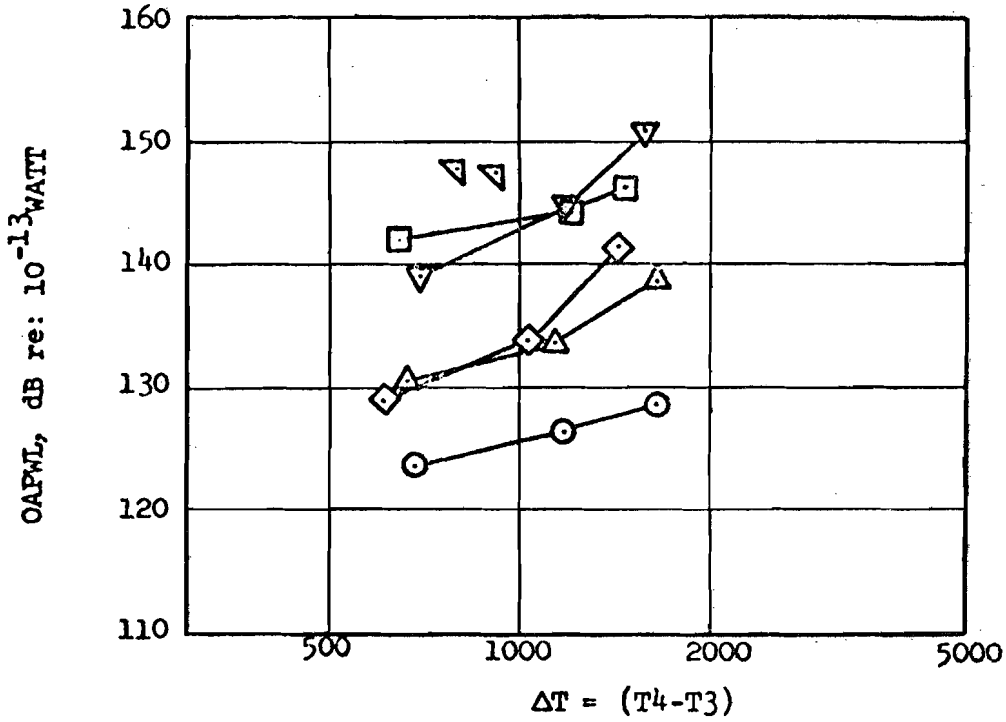

FIGURE 3.2.4-5 OAPWL vs. TEMPERATURE RISE.

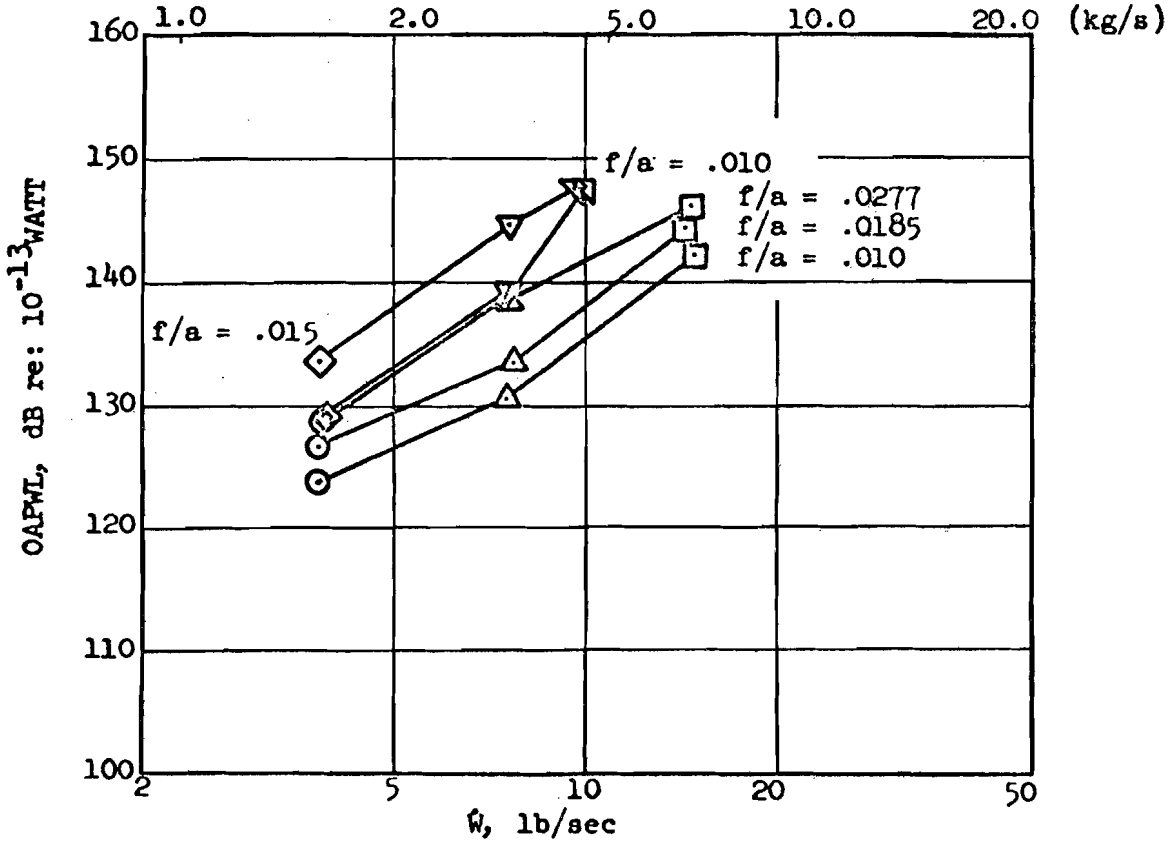

FIGURE 3.2.4-6 OAPWL vs. AIR FLOW RATE

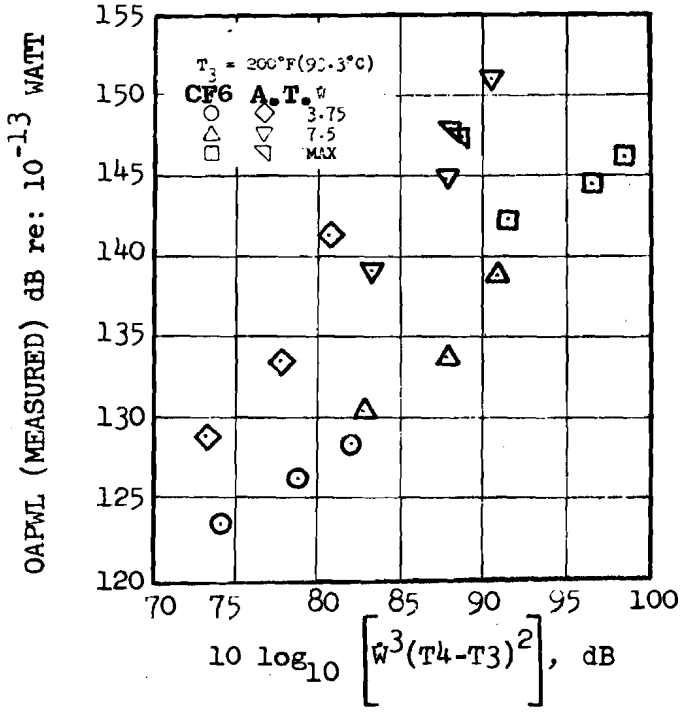

FIGURE 3.2.4-7 TEMPERATURE AND AIR FLOW CORRELATION

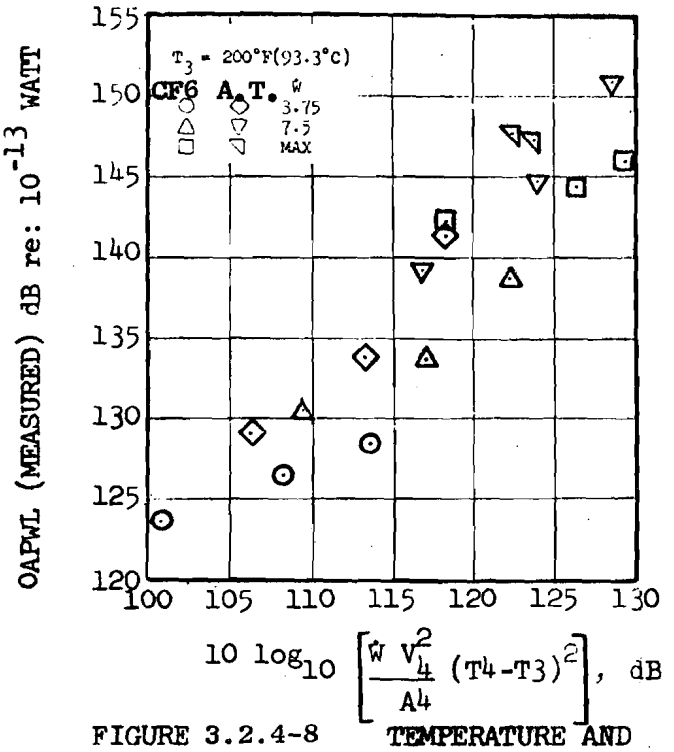

FIGURE 3.2.4-8 TEMPERATURE AND NORMALIZED KINETIC FLUX CORRELATION

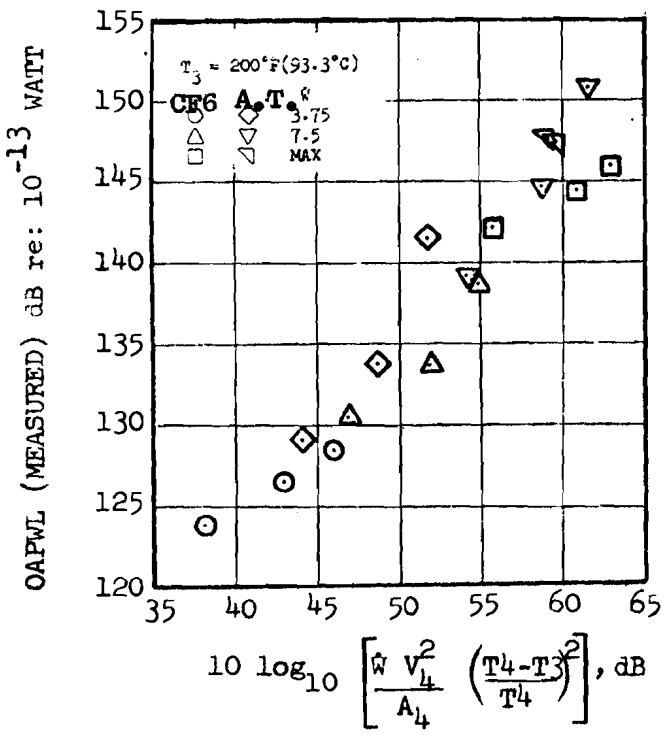

FIGURE 3.2.4-9 KINETIC ENERGY AND NORMALIZED TEMPERATURE CORRELATION

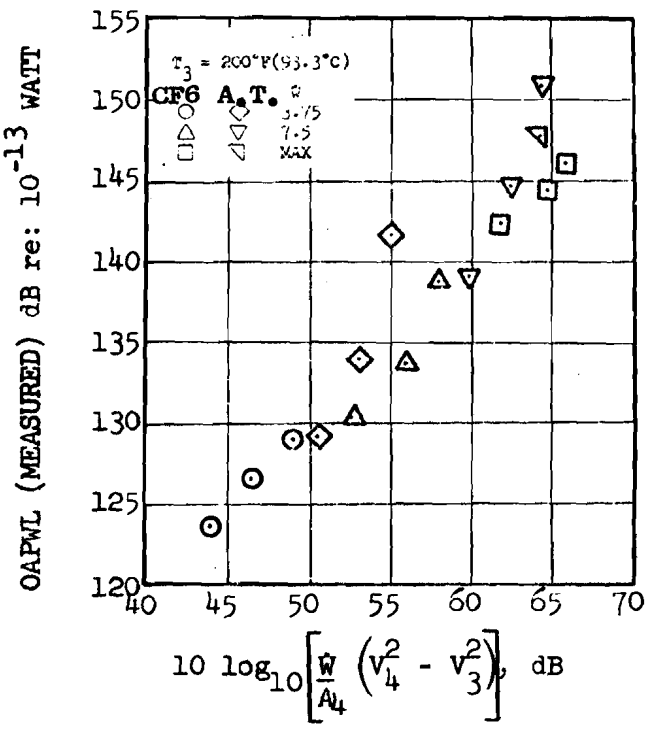

FIGURE 3.2.4-10 CHANGE IN KINETIC ENERGY FLUX CORRELATION

$$\text{OAPWL} \sim \left[\frac{\dot{W}\, V_4^2}{A_4} \left(\frac{T_4 - T_3}{T_4}\right)^2\right]$$

This reduced the standard deviation to 2.3 dB. Looking at this parameter, if $(T_4 - T_3)^2$ is assumed to be $T_4^2 - T_3^2$, neglecting the cross term, the OAPWL is proportional to the increase in kinetic energy flux through the combustor.

$$\text{OAPWL} \sim \left[\frac{\dot{W}}{A_4} (V_4^2 - V_3^2)\right]$$

This assumption changed the standard deviation to 2.4 dB. The parameter now has the units of Watts per unit area (Figure 3.2.4-10).

The kinetic energy flux at the exit station is more than ten times the kinetic energy flux at the inlet station just ahead of the fuel nozzles for any of the test point where the combustor was burning. Since the exit velocity is so much higher, the inlet velocity can be neglected and does not change the correlation. We are now left with a term which is directly related to the exit velocity to the third power since:

$$\frac{\dot{W}}{A_4} V_4^2 = \rho_4 V_4^3$$

Hence, OAPWL $\sim \rho_4 V_4^3$
The exit velocity to the third power correlates the data to the same 2.4 dB deviation (Figure 3.2.4-11) as above.

If all of the data are plotted in the form as jet noise (Figure 3.2.4-12), the same trend is realized. It can be seen from the slope of the data that the power level increases with the velocity to the third power. This is in agreement with Strahle's conclusions (Reference 3.1-5). The effect of the exit density can be seen in Figure 3.2.4-13. It is difficult to obtain any trend and it appears that it may safely be ignored in a correlation. The overall power level corrected for the exit velocity, (OAPWL - 10 Log_{10} V_4^3), is plotted against various temperature and pressure combinations in Figures 3.2.4-14 and 3.2.4-15. Again, no strong trend can be discerned. Similar difficulty is encountered in determining any trend with the combustor diameter or the liner exit area.

Directivity

Typical directivity patterns are shown in Figures 3.2.4-16 and 3.2.4-17. The CF6 combustor has its peak radiation between 110° and 130° from the inlet. The A.T. combustor has a broader directivity pattern that peaks in the range

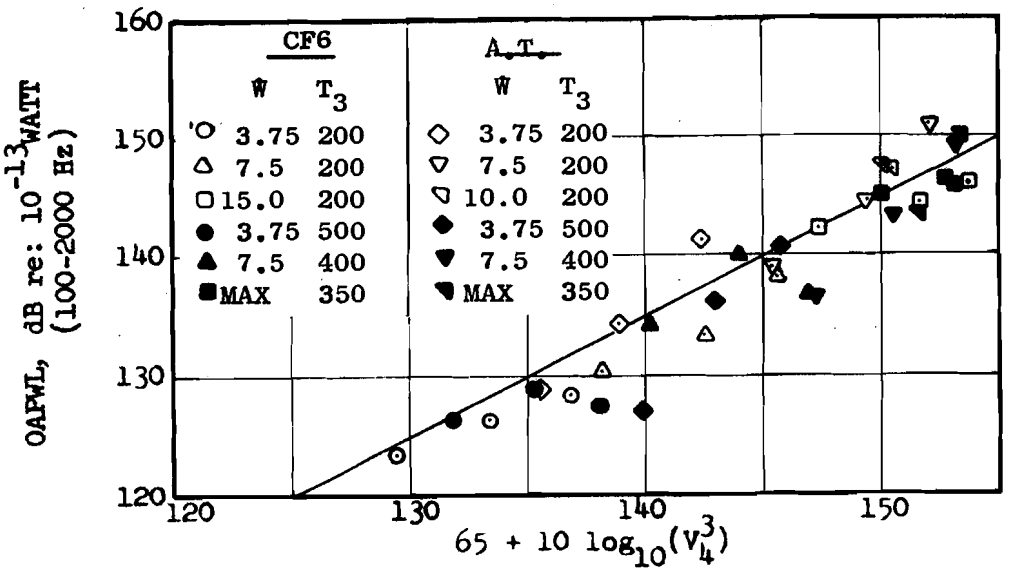

FIGURE 3.2.4-11 OVERALL POWER LEVEL vs. EXIT VELOCITY PREDICTION.

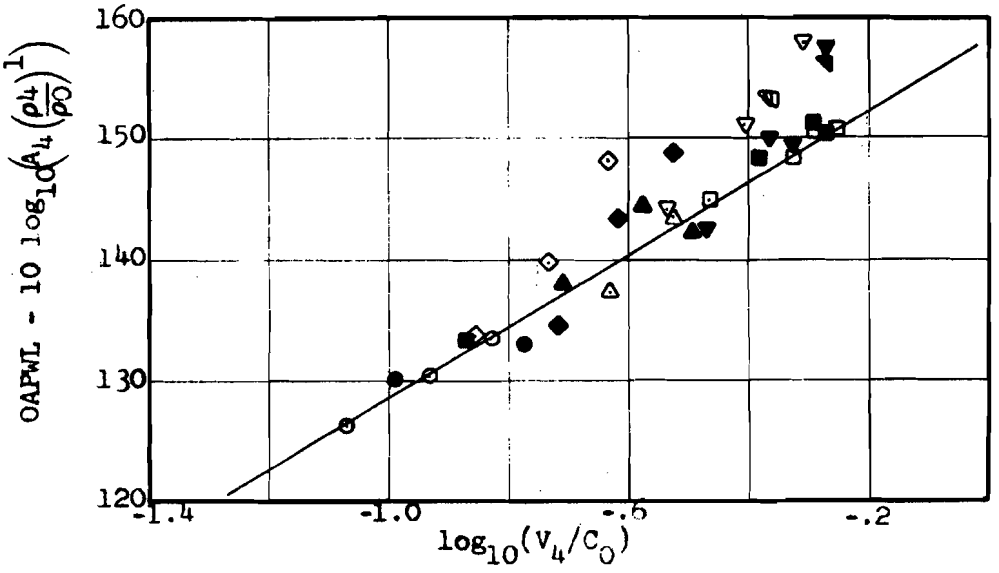

FIGURE 3.2.4-12 COMBUSTOR POWER LEVEL NORMALIZED FOR AREA AND DENSITY vs. NORMALIZED EXIT VELOCITY.

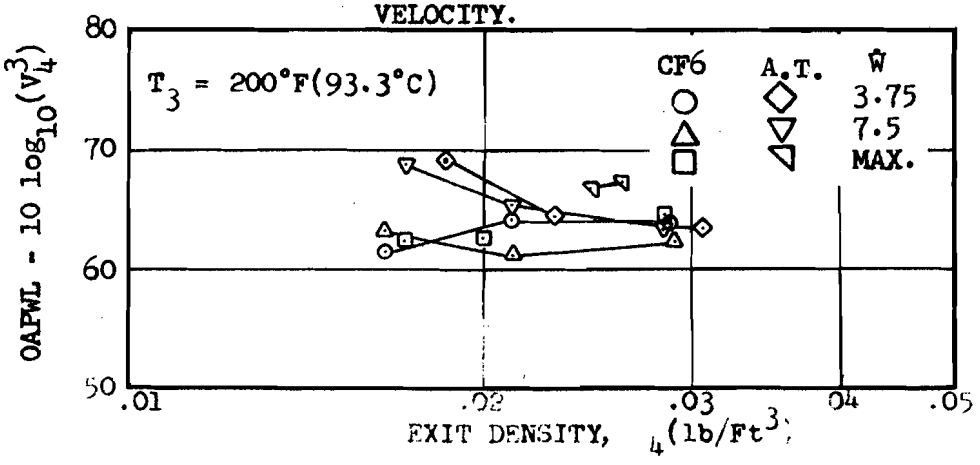

FIGURE 3.2.4-13 PARAMETER vs. EXIT DENSITY.

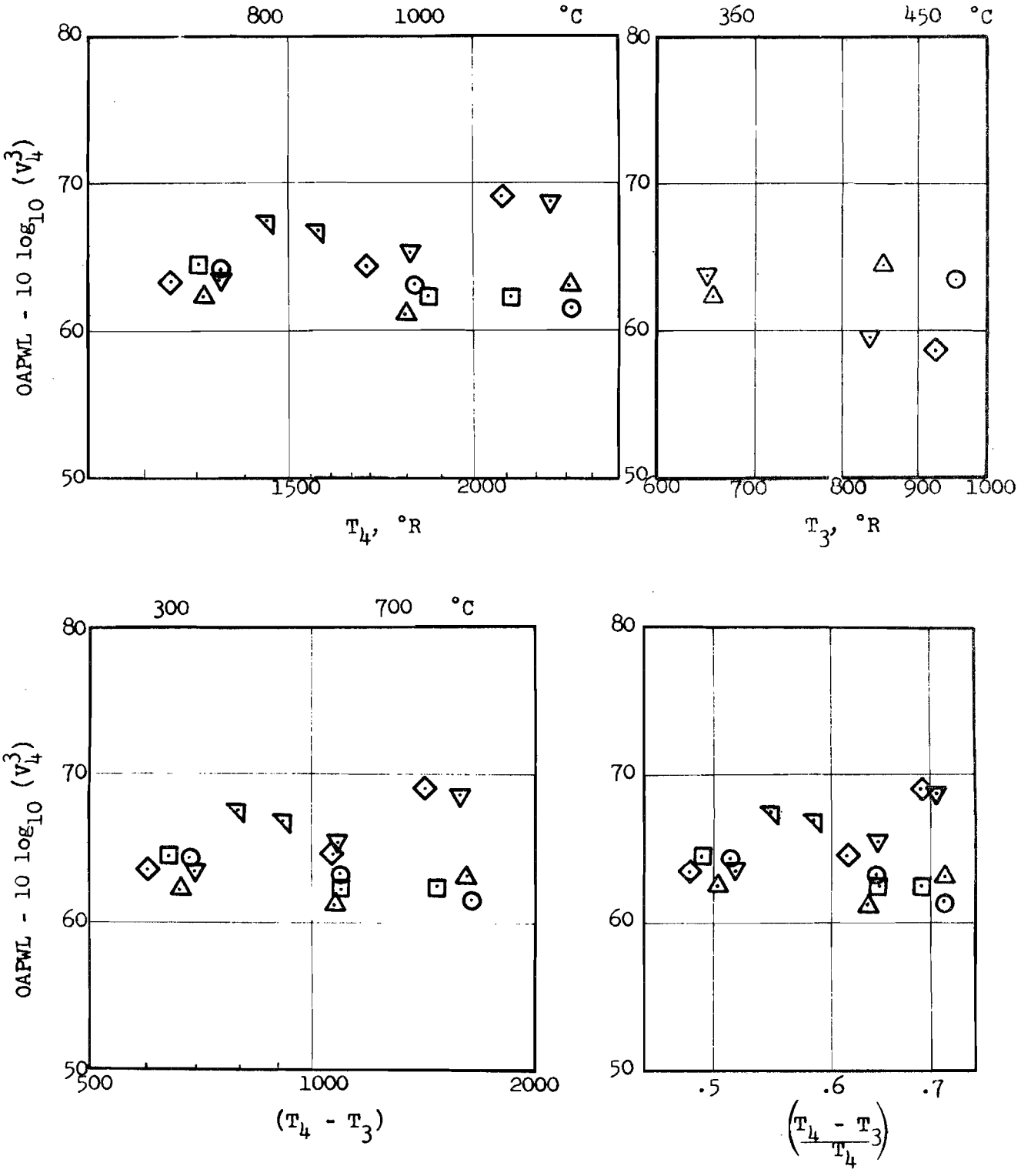

FIGURE 3.2.4-14 PARAMETER vs. TEMPERATURES

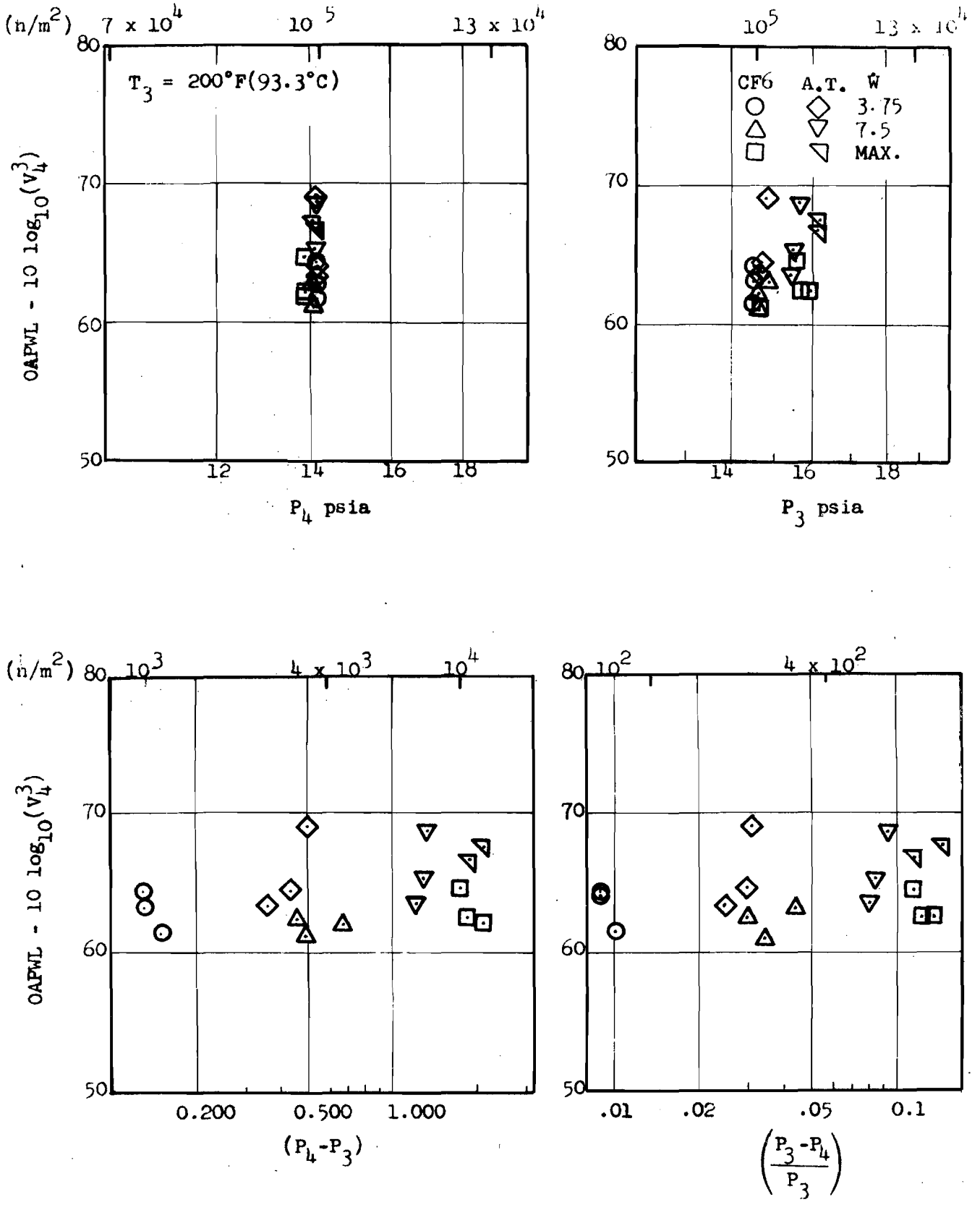

FIGURE 3.2.4-15 PARAMETER vs. PRESSURES

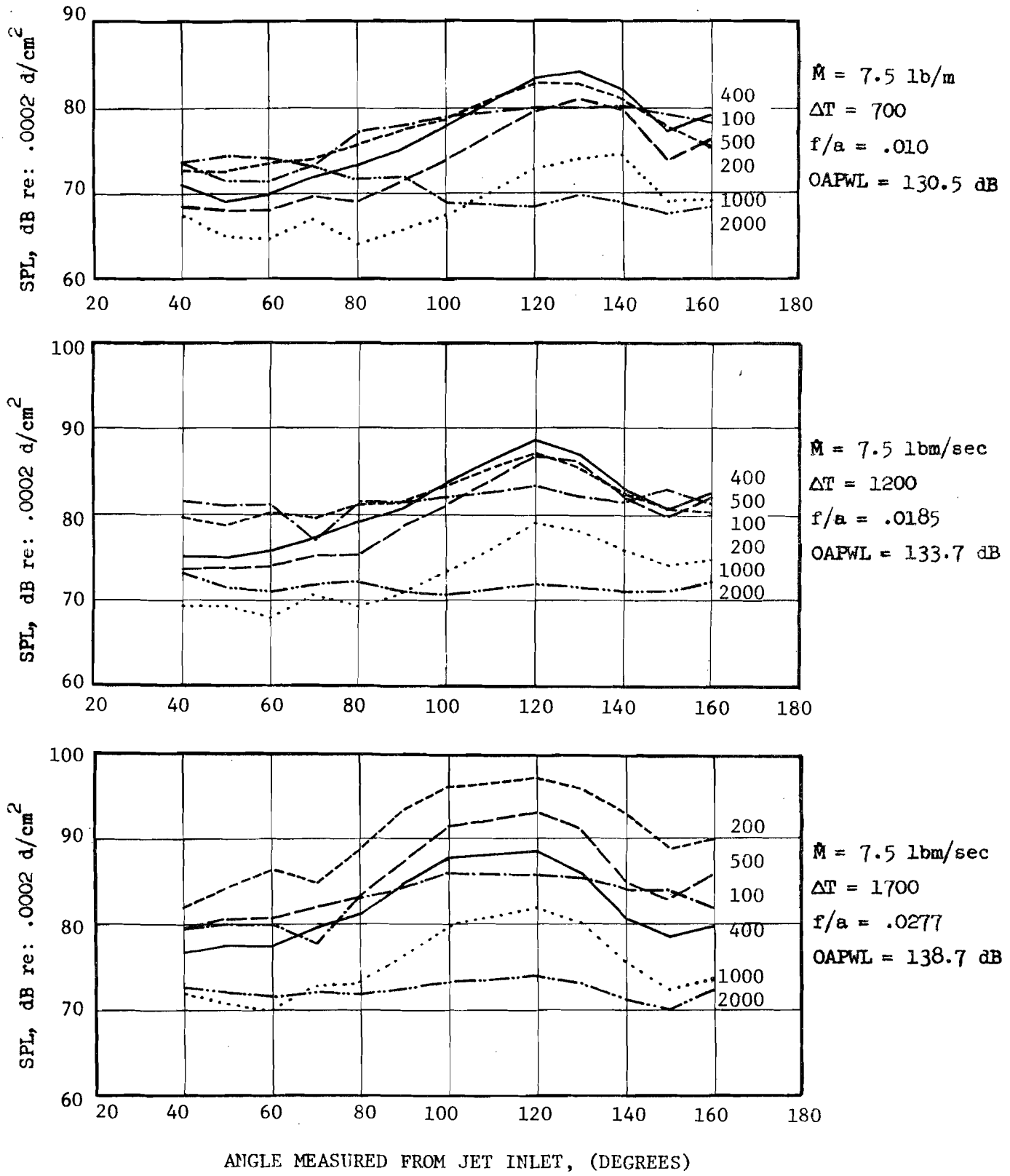

FIGURE 3.2.4-16 CF6 COMBUSTOR SOUND PRESSURE LEVEL DIRECTIVITY PATTERNS.

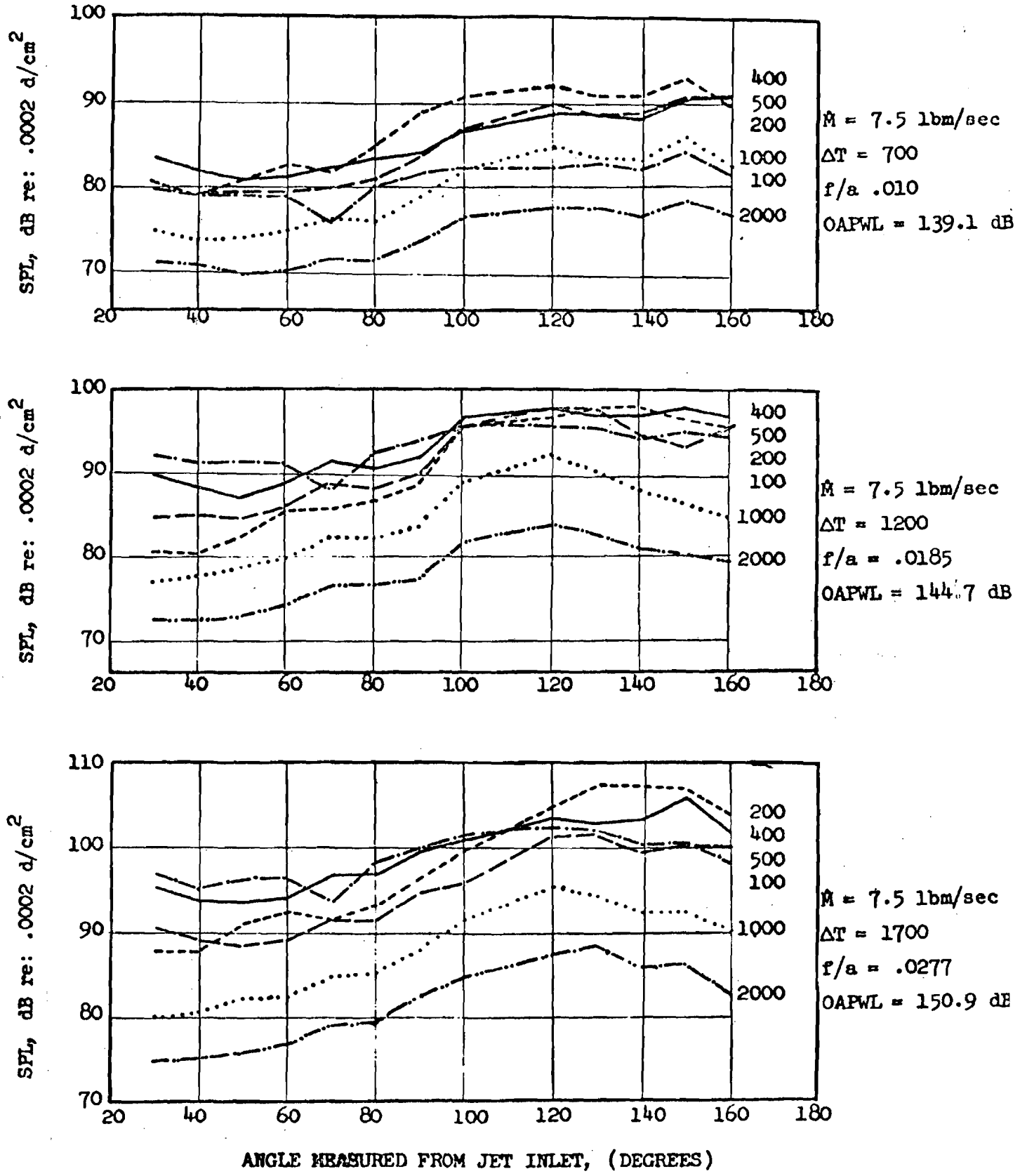

FIGURE 3.2.4-17 A.T. COMBUSTOR SOUND PRESSURE LEVEL DIRECTIVITY PATTERNS.

from 110° to 140°. The trends are applicable in the range of peak combustor noise frequencies. The difference in the directivity pattern is attributed to the difference in the radiation characteristics of the exit geometries. One of the differences between the two (Figures 3.2.2-3 and 3.2.2-4) was that the A.T. horn was a full foot longer than the CF6. Also, the centerbody of the CF6 extended about 40 inches (102 cm) past the exit plane of it's horn, while the A.T. centerbody projected only 14 inches (35.6 cm) beyond it's horn. Hence, the CF6 centerbody was about 10 inches (25.4 cm) in diameter versus 3 inches (7.6 cm) for the A.T. at the horn exit plane.

Spectrum

The one third octave spectra, normalized to the overall power level, are shown in Figures 3.2.4-18 and 3.2.4-19. There are ground reflections in this farfield data. The ground reflection first null occurs at 160 Hz and the first reinforcement is at 300 Hz. Since the ground reflection controls the farfield spectrum below 300 Hz, it is necessary use nearfield data to determine the true spectrum shape. Narrowband spectra for turbulence intensity, nearfield and farfield sound pressure levels are shown in Figure 3.2.4-20. The nearfield peak levels increase with the fuel/air ratio, while the spectral shape is roughly constant. The nearfield probe narrowbands also show that the peak frequency increases with the fuel/air ratio aand that this peak occurs between 100 and 200 Hz. However, the farfield microphone narrowbands show the spectra peaking between 200 and 300 Hz because of the ground reflection problem. Hence the slight increase in the peak frequency with fuel/air ratio cannot be discerned in the farfield data.

The turbulence entering the combustor appeared to determine the combustor noise spectrum, as is seen from Figure 3.2.4-20 which displays the close resemblance between corresponding turbulence and nearfield, probe-measured, noise spectra. During the tests, the inlet turbulence was found to vary only a few percentage points around an average intensity $u'/\overline{U}$ of 11%.

Conclusion

The tests on the two full scale, annular combustors with matched end impedance and at ambient pressure showed that:

- Combustor noise power level follows ∂ velocity to the third power scaling law.
- The directivity pattern will depend on the exit geometry.
- The spectrum shape will closely follow the turbulence spectrum entering the combustor.

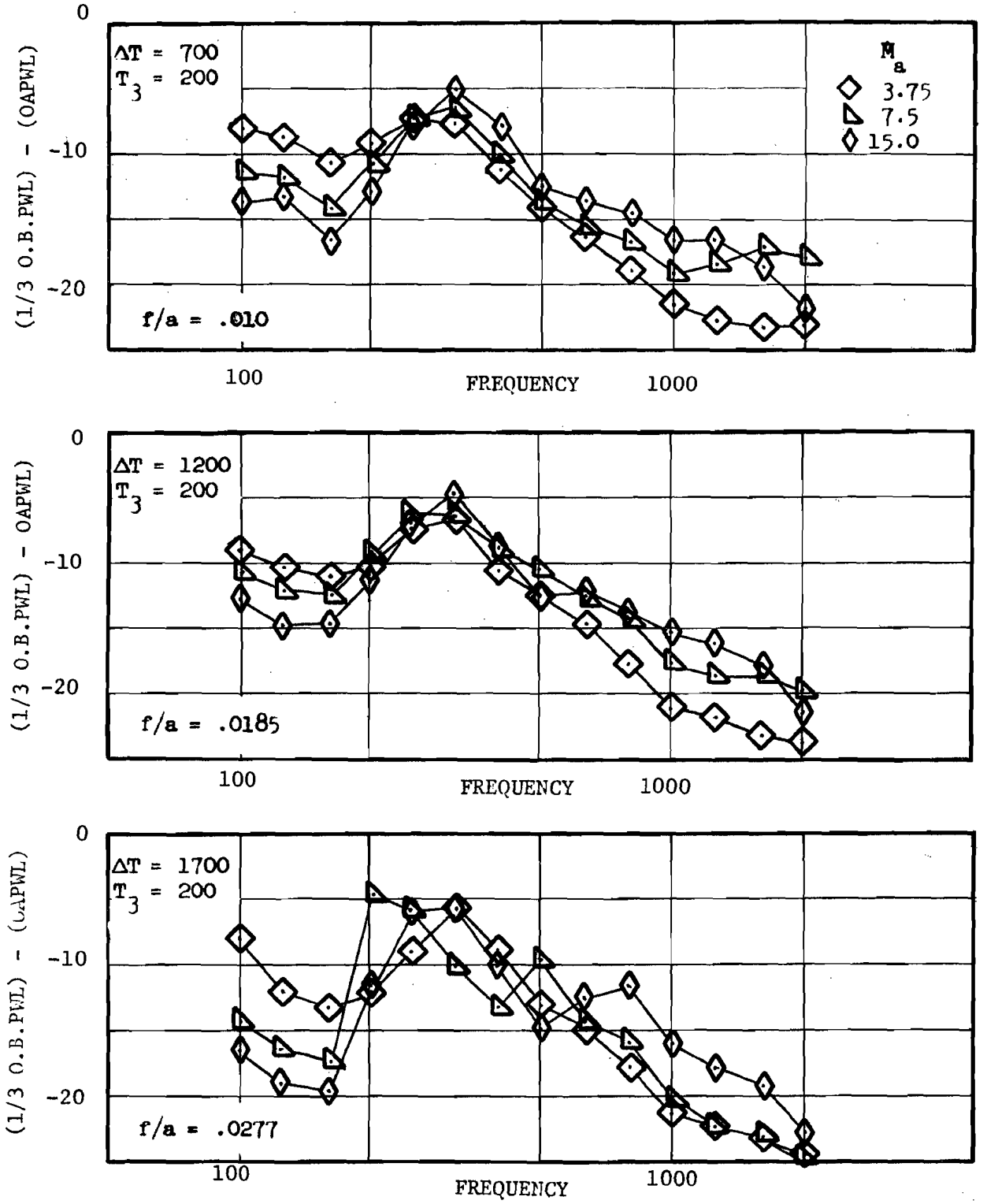

FIGURE 3.2.4-18 CF6 COMBUSTOR ONE-THIRD OCTAVE POWER LEVEL SPECTRUM SHAPE.

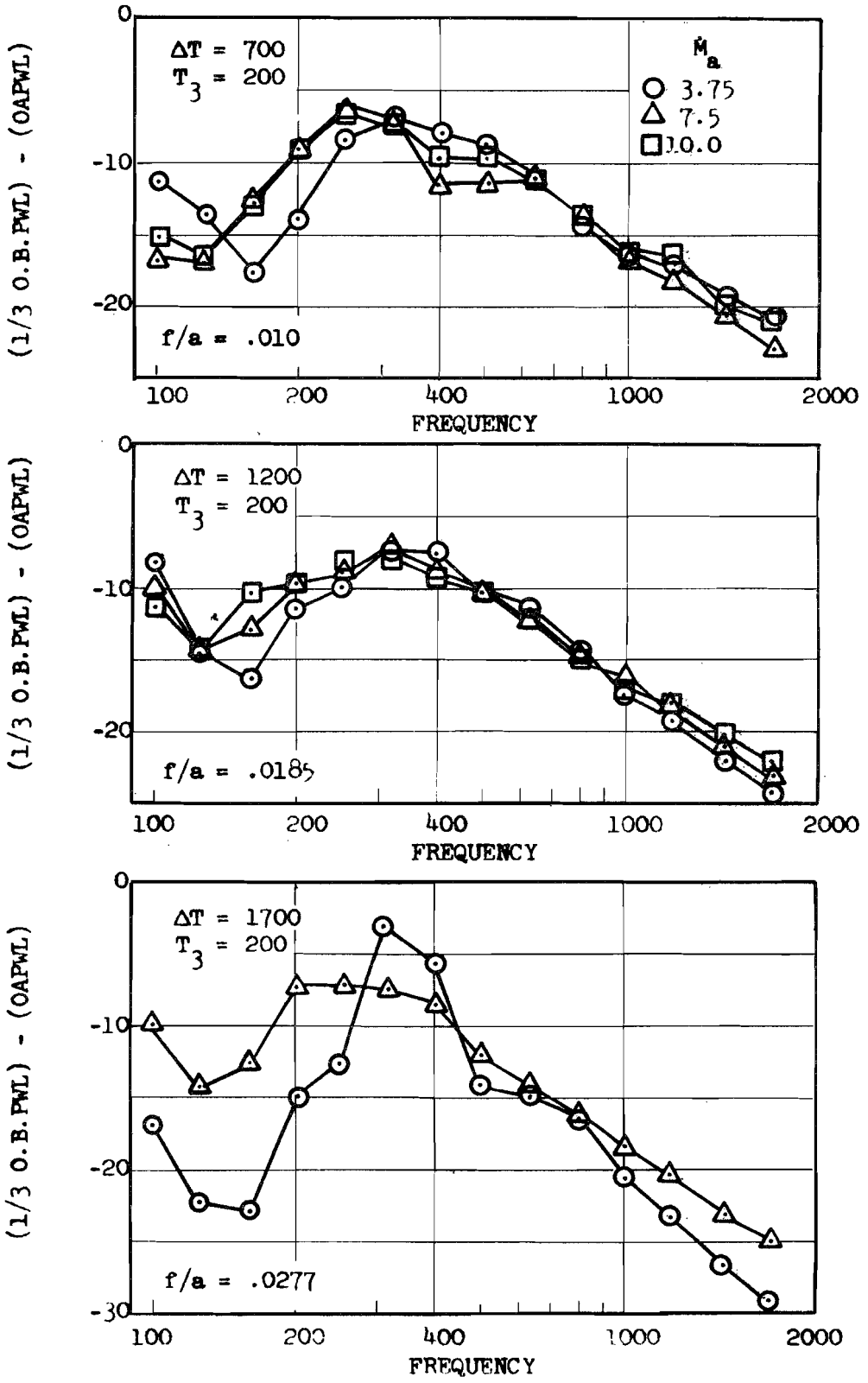

FIGURE 3.2.4-19 A.T. COMBUSTOR ONE-THIRD OCTAVE POWER LEVEL SPECTRUM SHAPE.

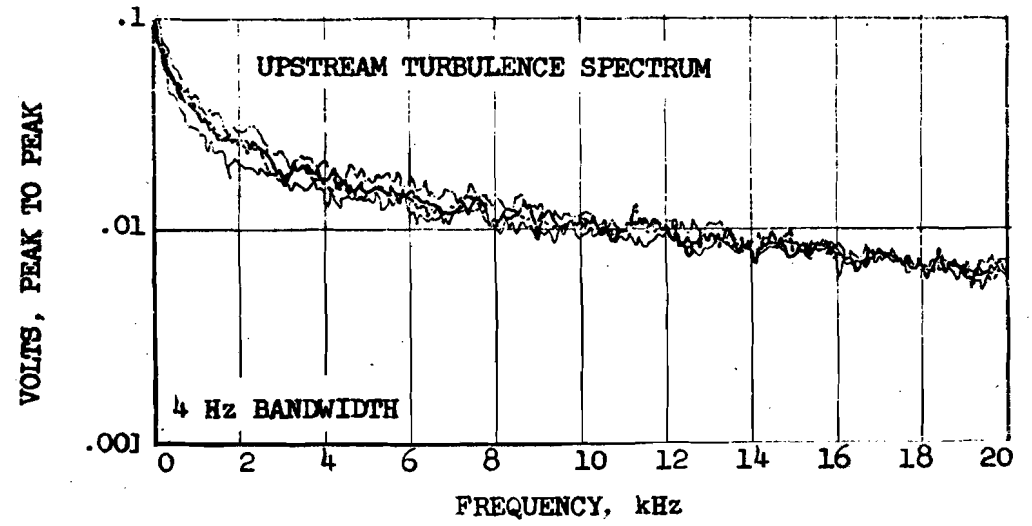

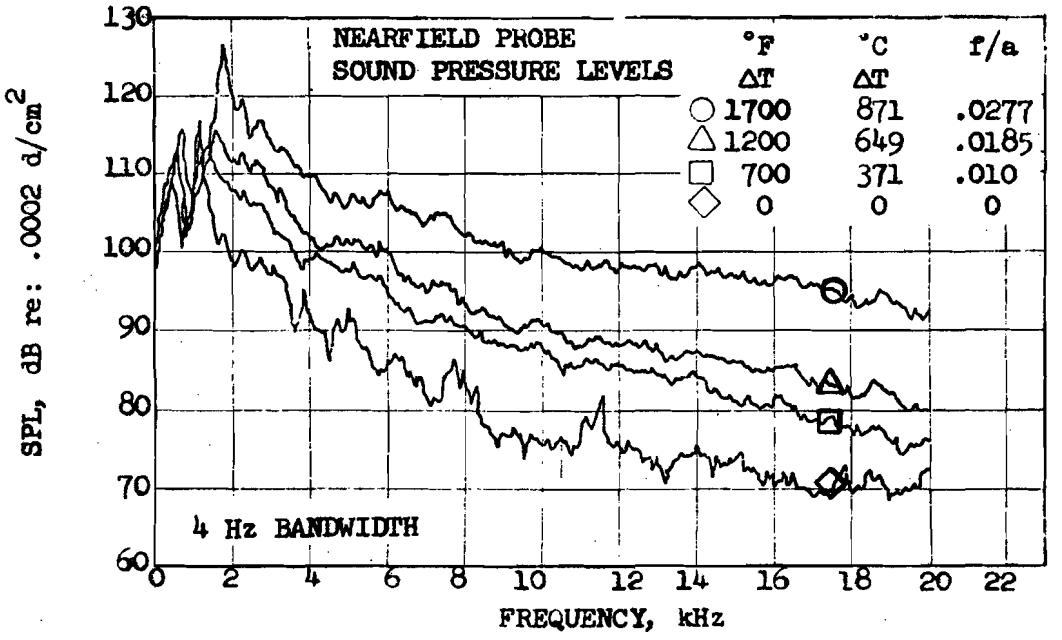

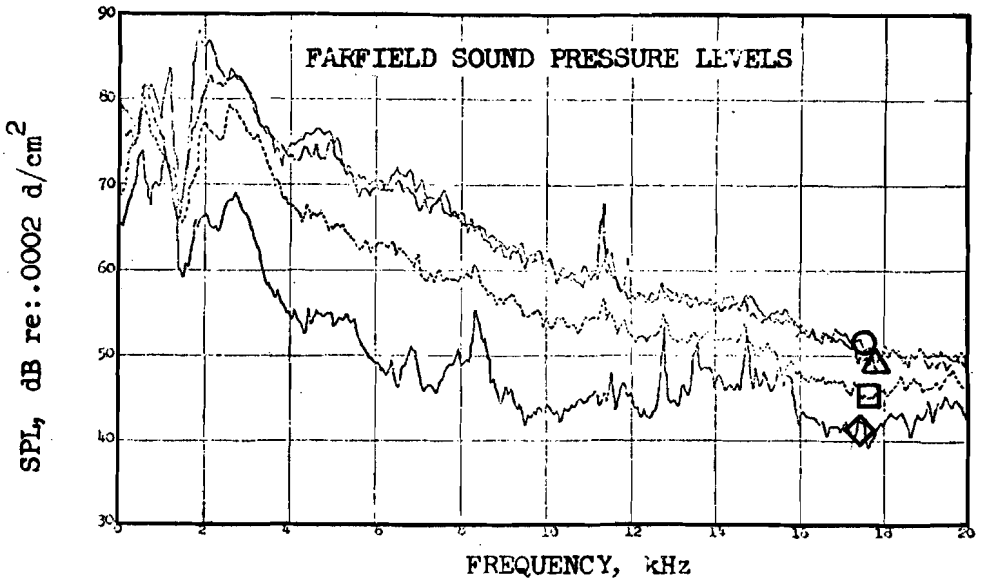

FIGURE 3.2.4-20 CF6 COMBUSTOR NARROWBAND SPECTRUMS

3.3 SUPPRESSOR TREATMENT SELECTION

Because of design constraints, it is apparent that the only viable technique of reducing combustor noise is through application of acoustic treatment. Several samples of different types of acoustic suppressors were examined and representative candidates were selected and tested. The tests were conducted under another FAA contract and details may be found in Reference 3.3-1. Although these selection tests were not conducted under the Core Engine Noise Control Program, a synopsis of the investigation is included here for completeness.

3.3.1 Objective

The purpose of these tests was to select the most desirable acoustic treatment from a mechanical and noise reduction point of view to function in a high temperature environment.

3.3.2 Hardware

A list of acoustic suppressor materials suitable for high temperature applications was drawn up. The list included various bulk absorbers constructed of fibers capable of withstanding high temperatures, ceramic material configurations, and resonators constructed of high temperature alloys. Two representative samples of each of the three types were selected. Details of the six selected samples can be seen in Figure 3.3.2-1. Cer-Vit is a ceramic material in the form of quarter wave tubes. The two samples differ in hole diameters and percent of open area exposed to the high temperature environment. The single degree of freedom (SDOF) resonators are fabricated from a high temperature alloy. The two samples differ in the percent of open area. The bulk absorber, Mono-Block, had two cavity depths and was retained during the test with a high porosity faceplate.

The samples were tested in the high temperature acoustic duct facility. A schematic of the duct can be seen in Figure 3.3.2-2. Two combustor cans placed upstream of the test section heated the duct up to 1800° F (982° C) and thermocouples were used to measure the temperature along the duct. A Hartman generator provided a pure tone source and ten acoustic probes, five upstream and five downstream, were used to measure the transmission loss of the samples.

3.3.3 Test Results

From the mechanical point of view, the ceramic material was too brittle. However, the ceramic had no difficulty with the temperature level or temperature changes during the test. The SDOF panels showed no deterioration other than the normal darkening in color and are mechanically desirable due to the fact that they can double as a load carrying surface in an engine. Upon examination after the test, the bulk absorber showed signs of deterioration. The binder used to hold the high temperature fibers in a fixed position had burned away leaving the fibers susceptible to being blown away by high velocity air flows.

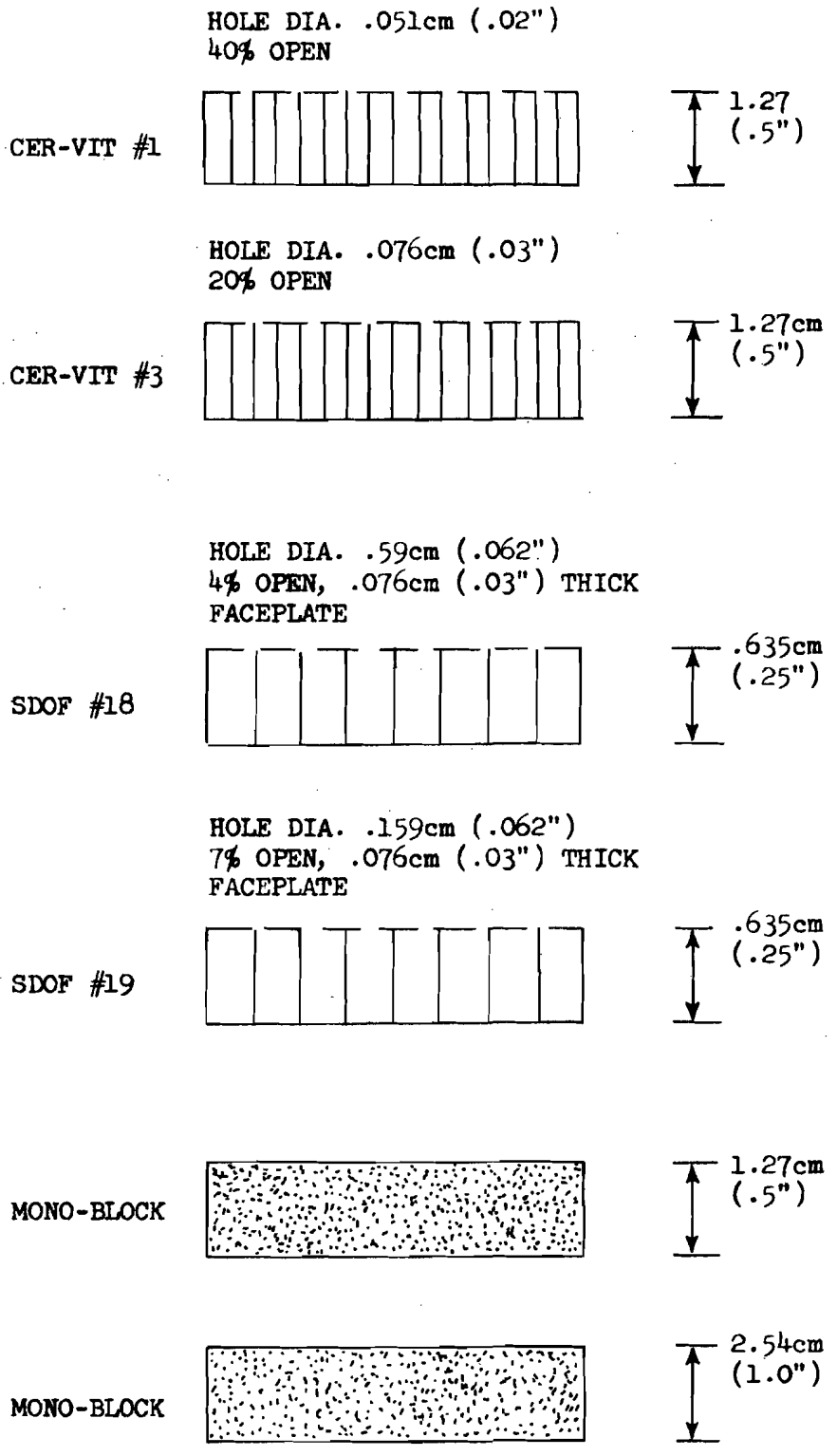

FIGURE 3.3.2-1 ACOUSTIC TREATMENT SAMPLES

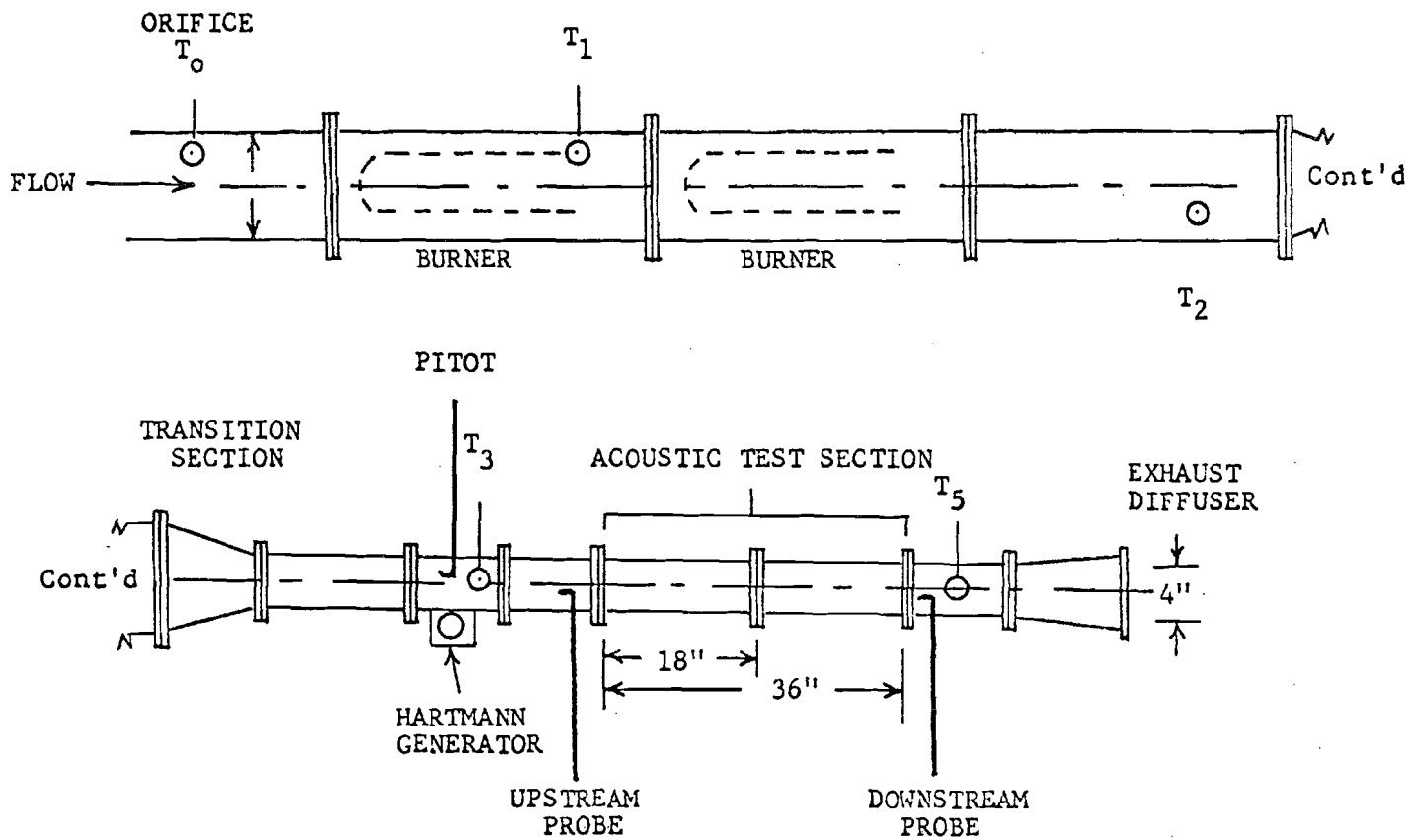

FIGURE 3.3.2-2 HIGH TEMPERATURE ACOUSTIC TREATMENT DUCT TEST FACILITY

3.3.4 Conclusions

The SDOF resonators displayed the best combination of suppression and structural integrity. The tests showed that the design method outlined in Reference 3.3.4-1 could successfully be used to design the high temperature treatment. It is a fairly straight forward procedure to extrapolate the suppressor design to peak at the low frequencies necessary for combustor noise application. It was found, however, that a resonator design peaking at 200 Hz, to match the combustor noise peak frequency, would be rather bulky for aircraft engine installations. It was felt, instead, that a suppressor could be designed peaking at 500 Hz and incorporating sufficient bandwidth to provide the required noise attenuation over the entire combustor noise spectrum. The size in this case, while still fairly large, would present far less problems in accommodating within the engine. Assuming an environment of 1500° F (816° C) and a Mach number of 0.3, the design requirement resulted in a suppressor cavity 12" (30.5 cm) deep. Details of the final design are shown in Figure 3.3.4-1. There are indications that the same suppression characteristics could be obtained through a judicious combination of various types of resonators which could result in a significantly reduced envelope.

3.4 SUPPRESSED COMBUSTOR TESTS

3.4.1 Objectives

The objective of the combustor suppressor test program was to demonstrate that the level of noise generated within the combustor could be reduced through application of acoustic treatment. The more advanced technology, full scale annular combustor was chosen as the baseline for this investigation. Nine test points, consisting of three air flow rates with three different fuel-air ratios each, were selected in order to demonstrate combustor noise suppression over a range of operating conditions. Further, to determine the suppressive effect of an abrupt impedance change on the propagation of combustor noise, a second configuration, which had the horn and centerbody removed, was included in the suppressor test plan.

3.4.2 Hardware

Farfield acoustic levels for the full scale suppressed A.T. annular combustor were measured at the JENOTS test facility. The test program and set-up for the two suppressed configurations which were examined were similar to the previous baseline testing at the same site. A photograph of the A.T. combustor mounted on the JENOTS test stand with the suppressor and horn installed is presented in Figure 3.4.2-1.

Acoustic data were recorded at the same microphone locations as for the baseline combustor testing. Thus the microphones were positioned at 10 degree intervals from 30° to 160° along the same 40 foot (12.2 m) arc. Additional details describing the JENOTS facility and sound field are contained in Section 2.2.2.

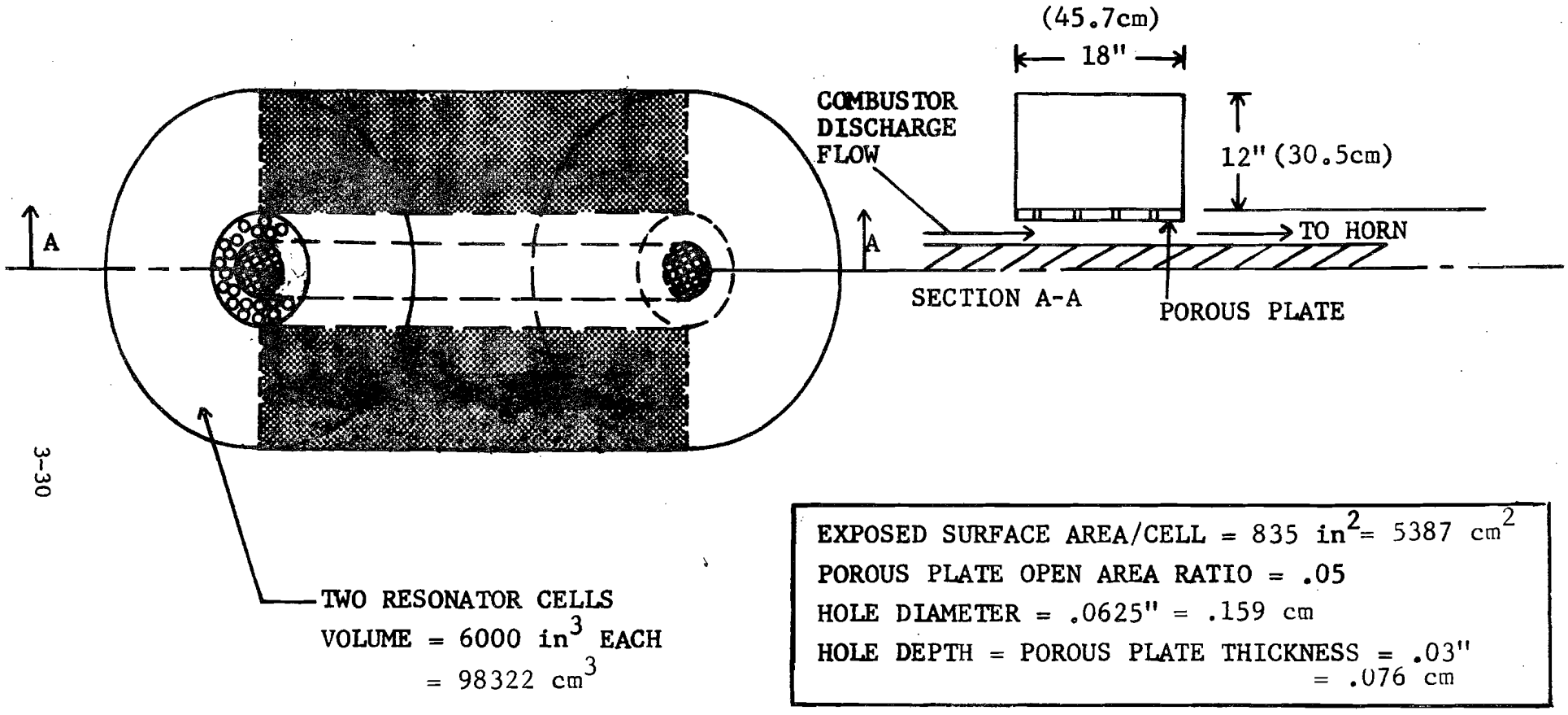

FIGURE 3.3.4-1 RESONATOR SUPPRESSOR DESIGN

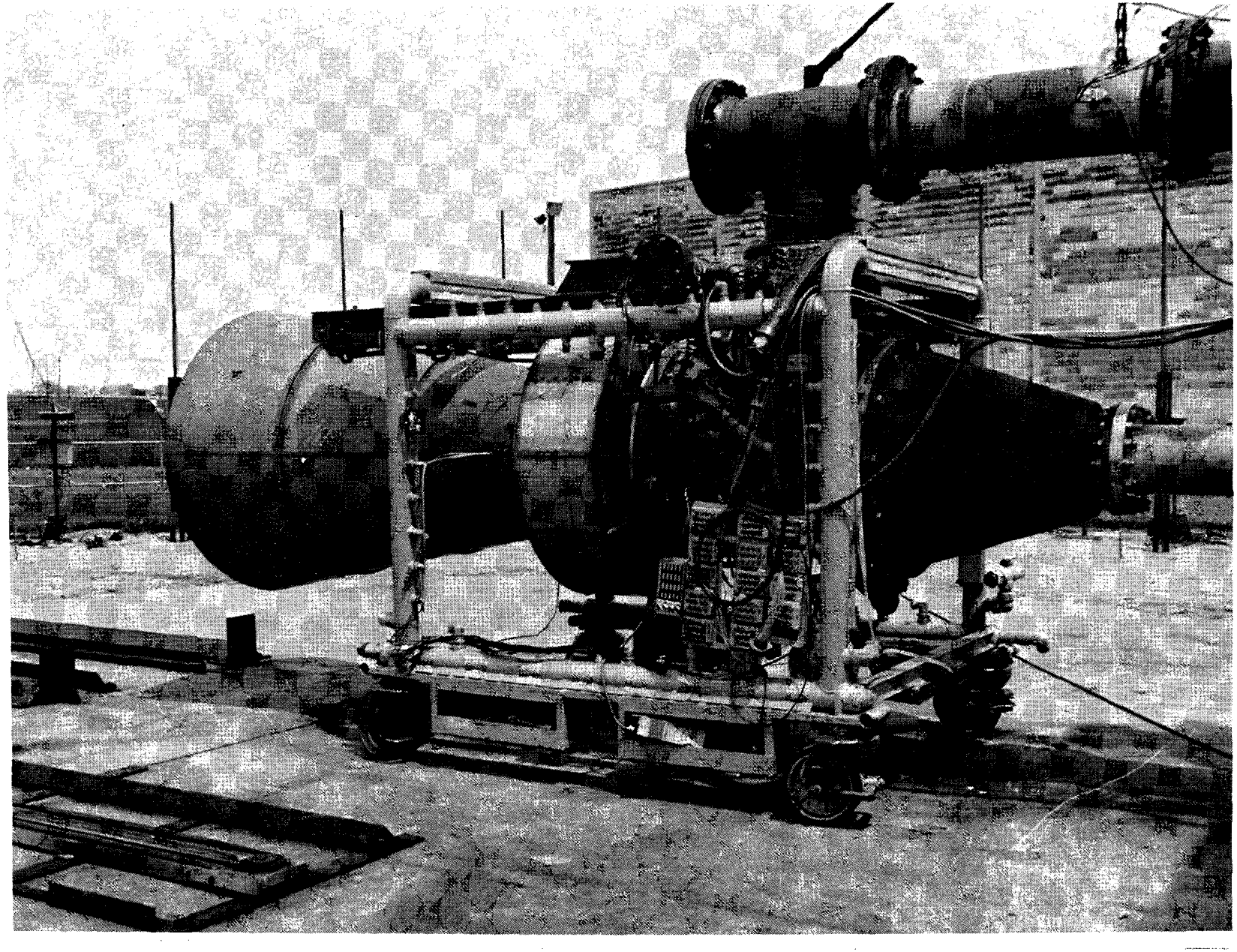

FIGURE 3.4.2-1 ACOUSTIC SUPPRESSOR TEST

A schematic of the combustor-suppressor test set-up is presented in Figure 3.4.2-2. The air flow was preheated to 200° F (93° C) upstream of the combustor to simulate air coming from a compressor. The muffler section, inlet rakes, and preheater were unchanged from the previous baseline A.T. combustor testing. The deep cavity suppressor, which was described in Section 3.3.4, was attached immediately downstream of the combustor for both suppressed configurations. The exhaust pressure and temperature rakes were thus located the length of the suppressor section farther downstream from the combustor than for the baseline test. The schematic, Figure 3.4.2-2, shows the horn and centerbody installed. For the second suppressed configuration, the horn and centerbody were both detached in order to examine the effects of an abrupt change in impedance.

The test matrix selected for the suppressor testing was nearly the same as the one for the baseline tests. Three air flow rates were again investigated - nominally these were 3.75 lbs/sec (1.7 kg/sec), 7.5 lbs/sec (3.4 kg/sec), and 10 lbs/sec (4.5 kg/sec). Three fuel-air ratios were tested for each weight flow giving a total of nine test points for each configuration. These were fuel-air ratios of zero, 0.011, and approximately 0.025. At the air flow rate of 10 lbs/sec, it was not possible to maintain combustion with the 0.011 fuel-air ratio. In place of this point, the higher fuel-air ratio of 0.025 was repeated.

A 200° F (93° C) inlet combustor temperature was used throughout the suppressor test program. The higher inlet temperature of 500° F (260° C), included in the baseline testing, was deleted from the suppressed combustor test plan due to the difficulty experienced holding that inlet temperature constant at the higher air flow rates. In addition, the highest fuel-air ratio examined during the baseline program was deleted in that the suppressor was not designed for the temperatures existing immediately downstream of the combustor at this power setting.

3.4.3 Test Results

The A.T. baseline combustor and the two suppressed combustor configurations are schematically shown in Figure 3.4.3-1. The deep cavity resonator was inserted between the combustor and the horn for the first suppressed configuration. This configuration was modified by removing the horn and centerbody for the second suppressed configuration. The farfield acoustic results measured for these configurations have been compared and analyzed to determine the amount of combustor noise reduction achieved with the matched end impedance and with the abrupt impedance change produced by removing the horn.

The results are presented through the frequency range of general interest for a combustor (100 Hz to 2000 Hz). These data have been corrected to Standard Day conditions of 59° F (15° C) temperature and 70% relative humidity. The sound pressure levels are presented for the 40 foot (12.2 m) arc distance at which they were measured.

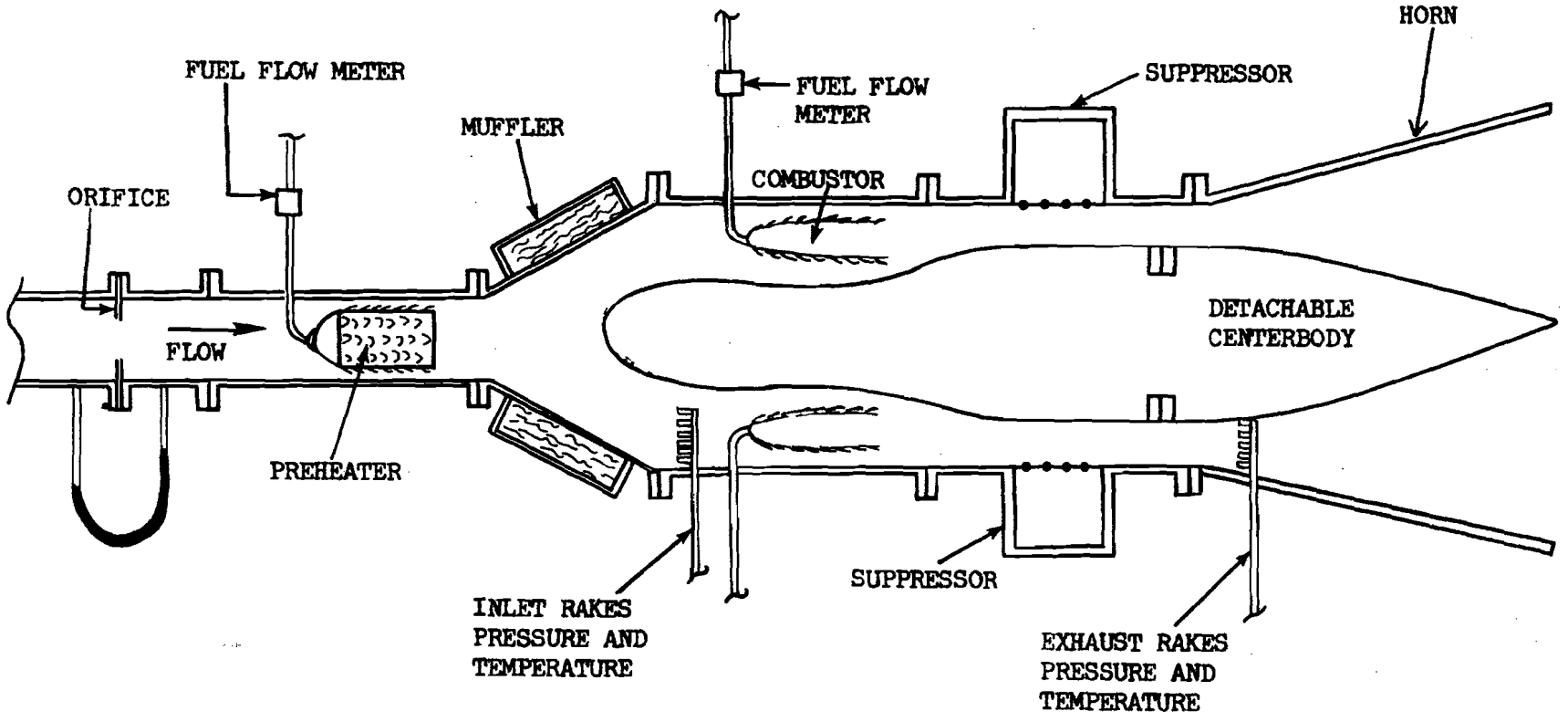

FIGURE 3.4.2-2 SCHEMATIC OF SUPPRESSED A.T. COMBUSTOR TEST SETUP.

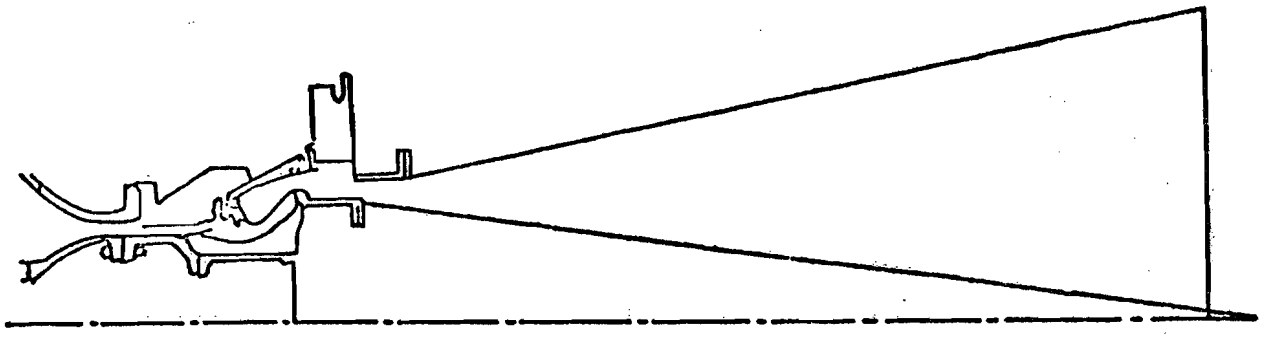

A.T. BASELINE COMBUSTOR

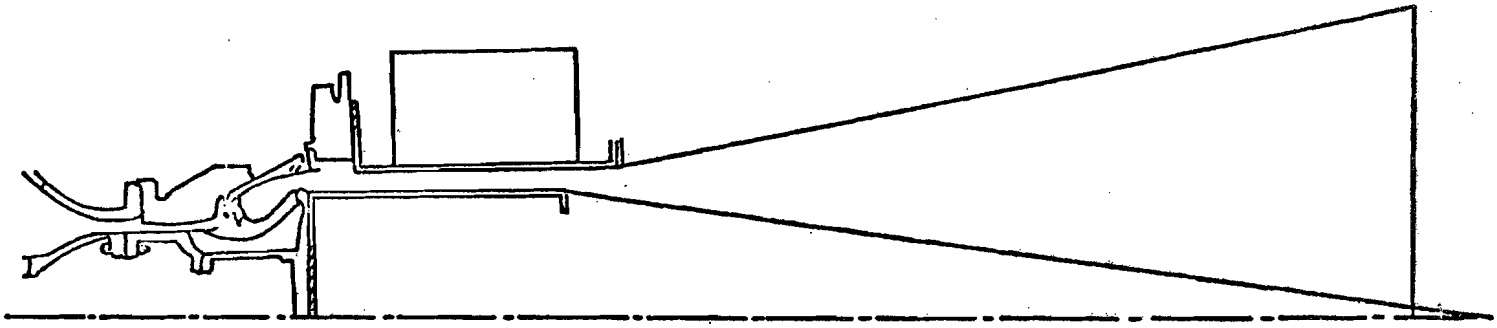

SUPPRESSED A.T. COMBUSTOR WITH HORN

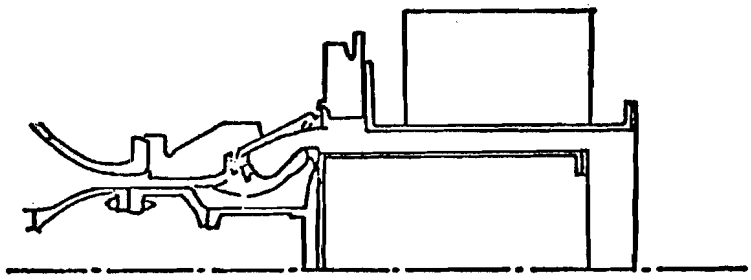

SUPPRESSED A.T. COMBUSTOR WITHOUT HORN

FIGURE 3.4.3-1 SCHEMATICS OF BASELINE AND TWO SUPPRESSED A.T. COMBUSTOR CONFIGURATIONS.

(1) Deep Cavity Resonator Suppression

Broad low frequency suppression was achieved by installing the deep cavity resonator downstream of the combustor. Comparisons of the PWL spectra for the baseline and the suppressed combustor with horn are presented in Figures 3.4.3-2 through 3.4.3-4. The test results are compared for three air flow rates - nominally 3.75 lbs/sec (1.7 kg/sec), 7.5 lbs/sec (3.4 kg/sec), and 10.0 lbs/sec (4.5 kg/sec) at three fuel-air ratios (f/a) each. (Note that the f/a of 0.011 has been replaced by a repeat of the higher fuel-air ratio for the 10 lbs/sec (4.5 kg/sec) flow rate). The delta PWL spectral reductions are shown in Figure 3.4.3-5 for the three air flow rates.

The suppression of the acoustic power levels for the case without combustion is shown for each air flow rate. The baseline PWL's were reduced 10 dB or more by the resonator from 100 Hz through 315 Hz. The maximum reduction occurred at 200 Hz and 250 Hz. As can be seen in Figure 3.4.3-5, the variation of delta PWL with frequency for a f/a of zero was very similar for the three air flow rates.

Several observations can be made concerning the baseline and suppressed combustor PWL comparisons, Figures 3.4.3-2 through 3.4.3-4. Ground reflection effects, which are related to the sound field setup and not the combustor, occurred from 125 Hz through 315 Hz. Below this frequency region, the power level at 100 Hz for the higher fuel-air ratio (likewise the higher exhaust velocities) seemed to have increased due to either higher turbulence levels or jet noise. The PWL's at the higher f/a appeared to have increased from the levels measured at the 0.011 f/a by the sixth to the eighth power of the corresponding exit velocity ratios. Jet noise is also believed to contribute some lesser amount to the PWL at 100 Hz for the 0.011 f/a. The test results further indicate an as yet unexplained increased PWL in the 800 Hz and/or 1000 Hz one third octave bands. This noise peak, which shows the same trend for each of the air flow rates, increased in frequency with increasing fuel-air ratio. Without combustion, the unexplained noise occurred within the 800 Hz band. It appeared to be split between both the 800 Hz and 1000 Hz bands at 0.011 f/a, and shifted to the 1000 Hz band at the higher fuel-air ratio. These peaks quite possibly could result from vortex shedding off of the exit measuring rakes and can be observed in the spectrum only when the combustor noise is suppressed sufficiently upstream of the rakes.

The baseline A.T. combustor noise PWL has previously been shown to peak between 250 Hz and 315 Hz for the fuel-air ratios examined. At these peak frequencies, the suppression achieved with the resonator varied from 8 to 17 dB PWL as shown in Figure 3.4.3-5. The suppressor also produced significant noise reduction over a wide range of frequencies. Between 160 Hz and 630 Hz inclusive, more than 9 dB PWL suppression was measured for the 3.75 lbs/sec (1.7 kg/sec) air flow rate for both of the fuel-air ratios examined. Likewise, more than 8 dB suppression was measured for 7.5 lbs/sec (3.4 kg/sec) and, with one exception, more than 7-1/2 dB suppression was measured for 10 lbs/sec (4.5 kg/sec) over the same frequency range.

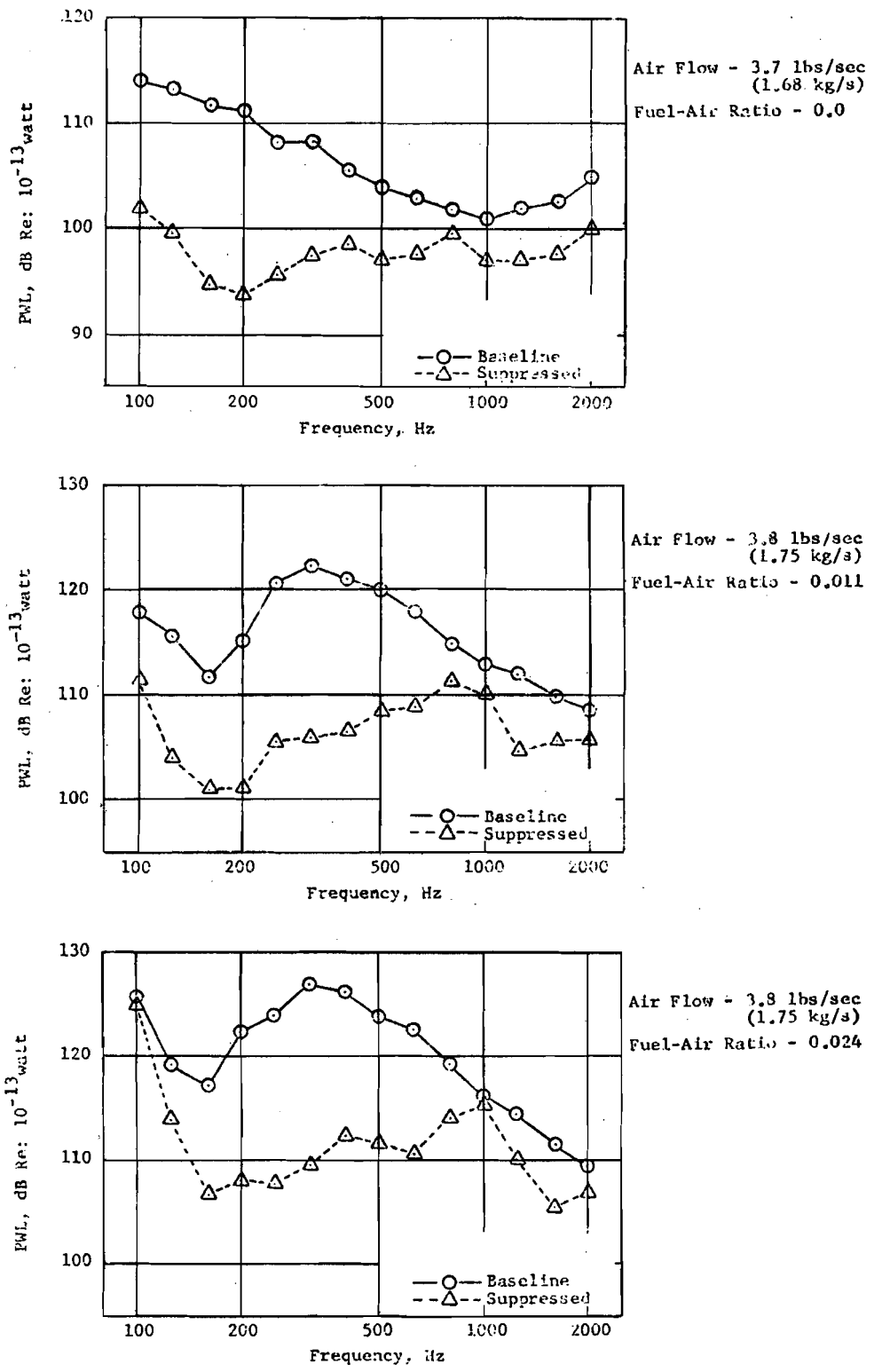

FIGURE 3.4.3-2 PWL REDUCTION FOR THE SUPPRESSED COMBUSTOR WITH HORN AT 3.75 lbs/sec(1.7 kg/sec) AIR FLOW RATE.

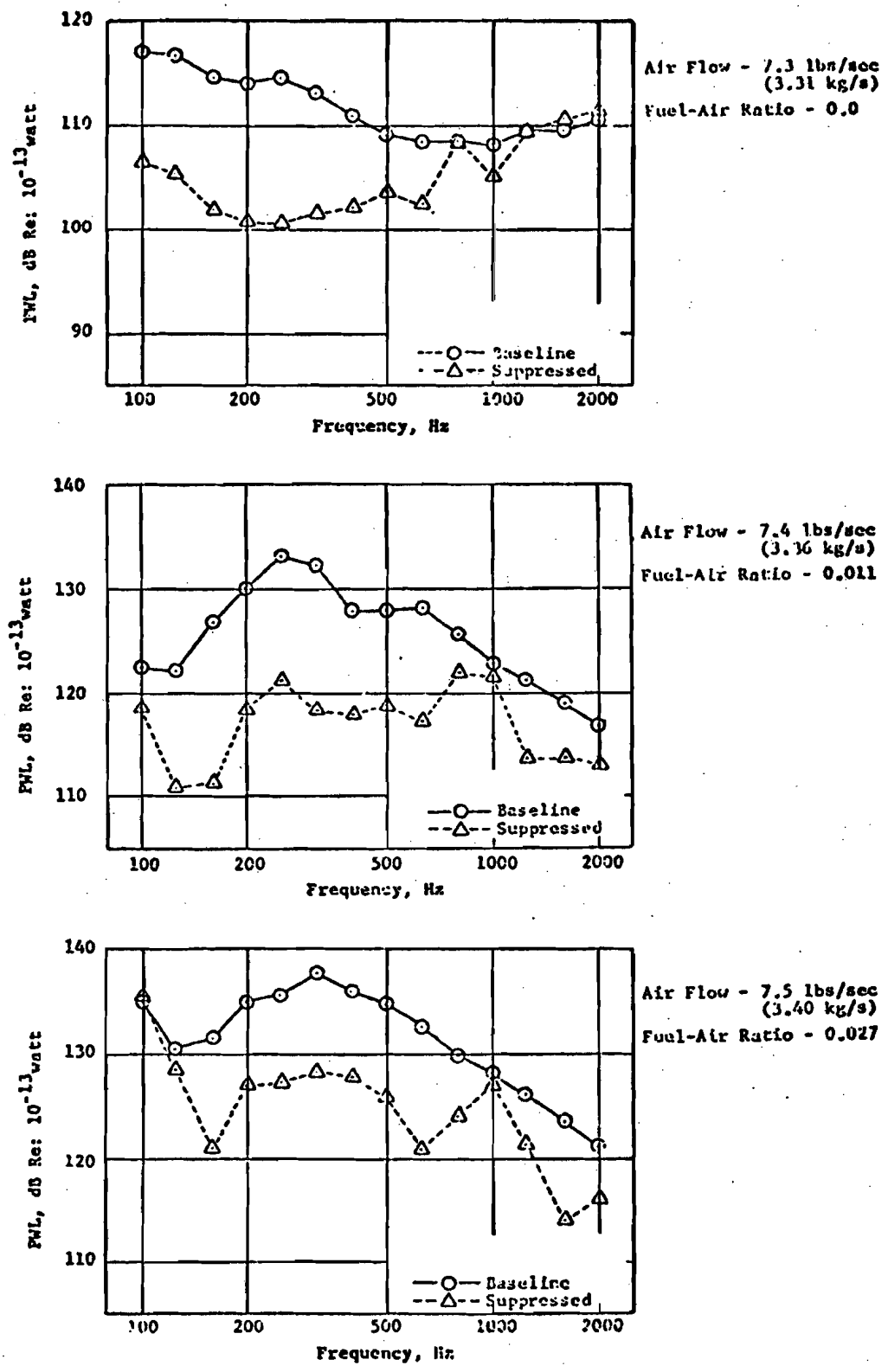

FIGURE 3.4.3-3 PWL REDUCTION FOR THE SUPPRESSED COMBUSTOR WITH HORN AT 7.5 lbs/sec(3.4 kg/sec) AIR FLOW RATE.

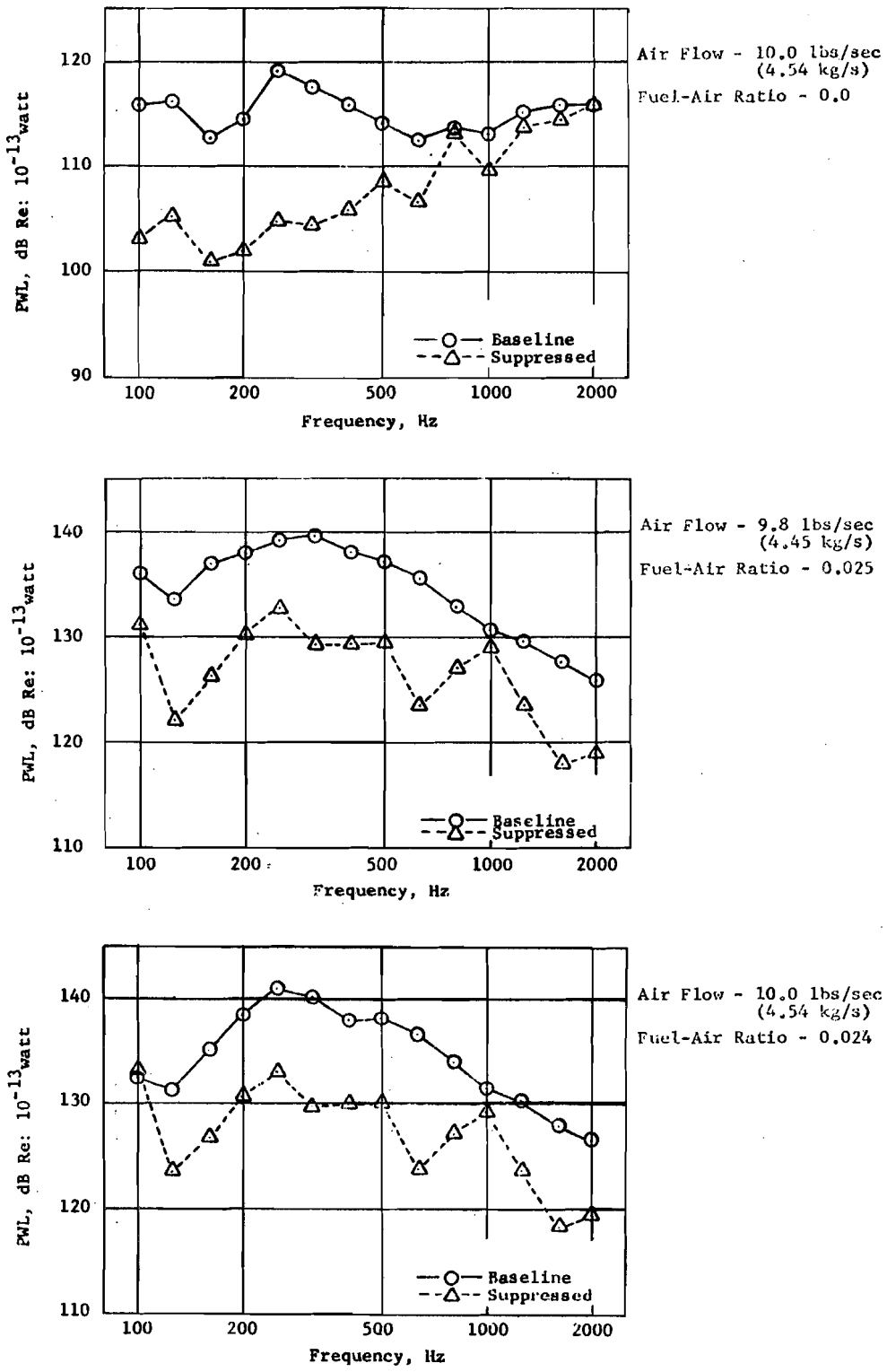

FIGURE 3.4.3-4 **PWL REDUCTION FOR THE SUPPRESSED COMBUSTOR WITH HORN AT 10.0 lbs/sec(4.5 kg/sec) AIR FLOW RATE.**

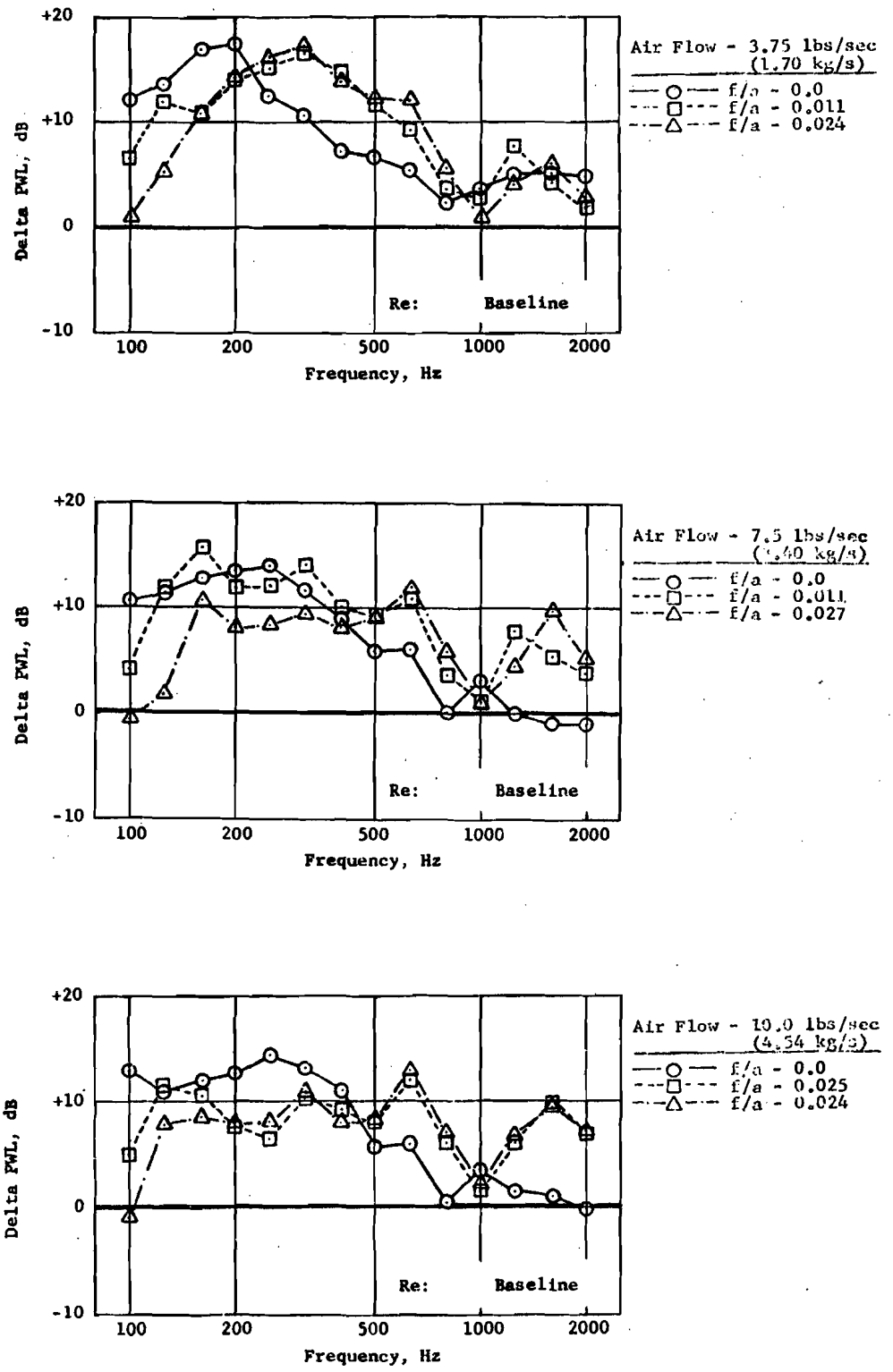

FIGURE 3.4.3-5 DELTA PWL FOR THE SUPPRESSED COMBUSTOR WITH HORN.

Inspection of the delta PWL's, relative to the baseline results, seems to indicate a general trend for the six combustor power settings examined. It appears that less noise reduction was attained from 160 Hz through 630 Hz as the velocity through the suppressor increased. (The exhaust velocities for the combustor with suppressor and horn are tabulated in Table 3.4.3-1. For the different power settings, the relative velocity levels within the suppressor section would exhibit a relationship similar to that at the exhaust plane).

Significantly less combustor noise suppression was measured at the intermediate air flow rate than at the lowest flow rate for both the 0.011 and 0.025 fuel-air ratios. The corresponding exit air velocities for the higher air flow rate were double those for the lower flow rate. (See Table 3.4.3-1). Likewise, a large difference in suppression existed between these two fuel-air ratios at the intermediate flow rate. Again, less suppression was achieved at the power setting with the higher exit air velocities. On the other hand, the suppression attained at combustor power settings with similar exit air velocities was very similar throughout the frequency range of 160 Hz to 630 Hz. Examples are the three power settings with the higher fuel-air ratio tested at the intermediate and highest air flow rates, and the two combustor fuel-air ratios tested at the lowest flow rate.

It can be postulated that scrubbing noise generated by flow over the resonator face plate increased with duct velocity at such a rate that a portion of the combustor noise reduction was negated. A non-uniform rippling of the face plate, observed at the conclusion of testing, undoubtedly increased the scrubbing effect. This rippling was believed to have occurred during the initial checkout point due to differential thermal expansion of the face plate.

The SPL directivities for all of the suppressed combustor test points are presented in Figures 3.4.3-6 through Figure 3.4.3-8 for selected one third octave bands along the 40 foot (12.2 m) arc. Generally the directivities were the same for each power setting. The levels start increasing markedly between 80° and 90°. They appeared to peak and level out at 150° and 160°.

Without combustion, the SPL diverged more (increasingly so with increased flow), and individually tended to be at a relatively constant level from 30° to 120°. The noise at 800 Hz was very prominent for these cases - more so with increasing flow.

With combustion, the SPL's for the majority of the bands increased from 80° until 130°. The levels were constant or increased slightly at 140° before they again increased to the peak values. The acoustic power levels that have been examined for the suppressed combustor were therefore based largely on the noise levels at these aft angles. The peak SPL's occurred further aft with the suppressor installed than for the baseline configuration. This is attributed to the horn exit extending past the arc centerline due to the additional length of the suppressor.

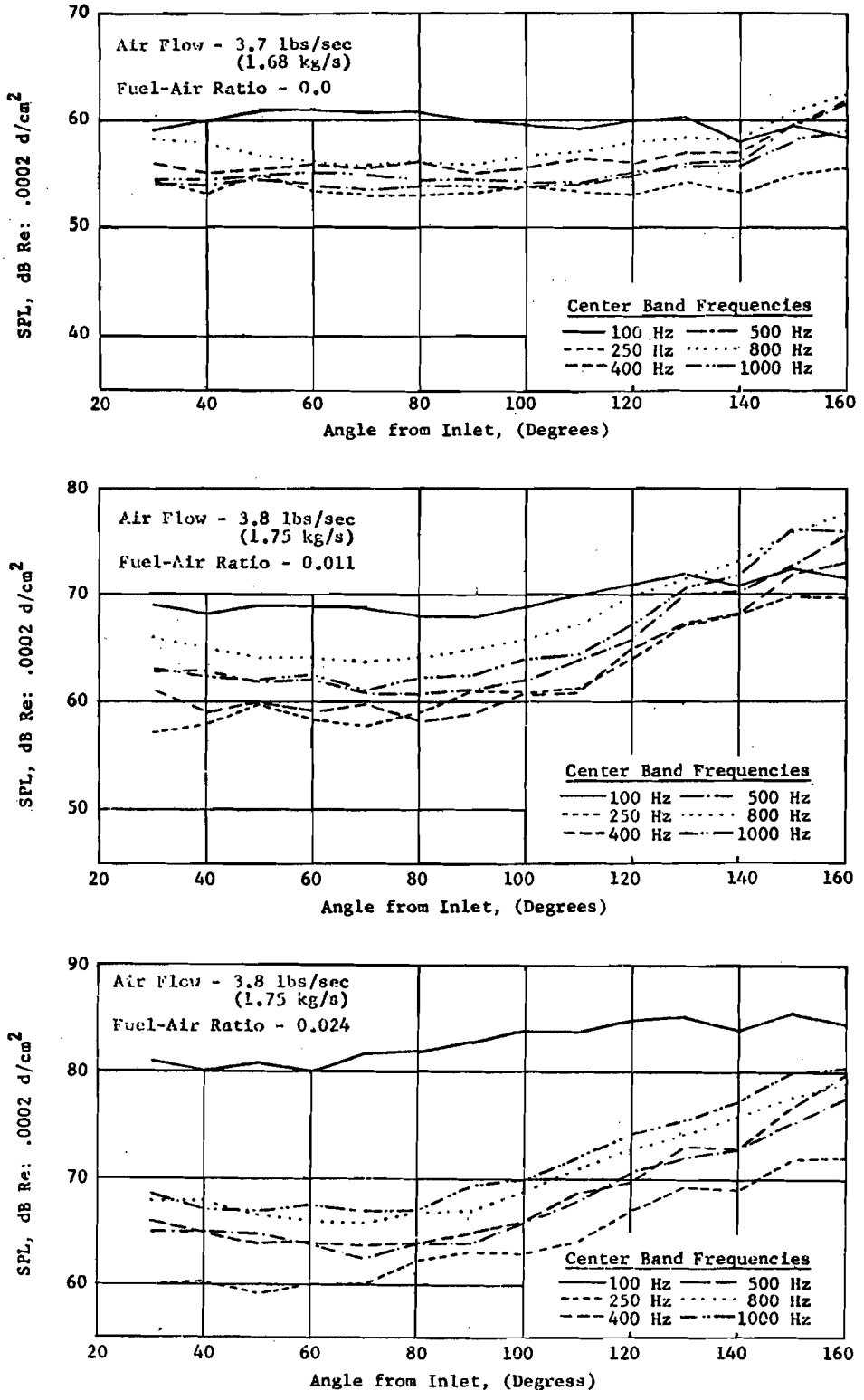

FIGURE 3.4.3-6 **SPL DIRECTIVITIES FOR THE SUPPRESSED COMBUSTOR WITH HORN AT 3.75 lbs/sec(1.7 kg/sec) AIR FLOW RATE.**

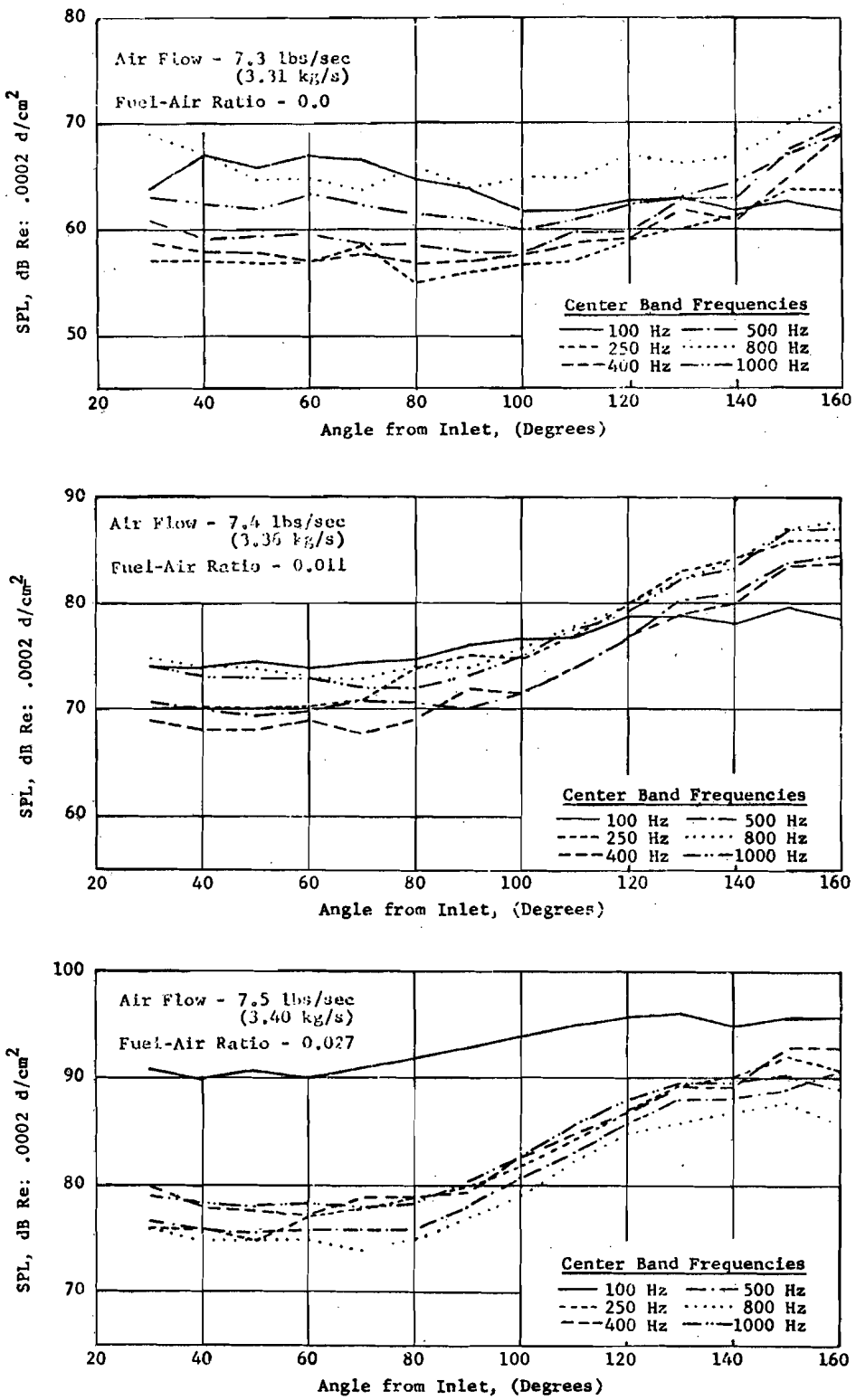

FIGURE 3.4.3-7 SPL DIRECTIVITIES FOR THE SUPPRESSED COMBUSTOR WITH HORN AT 7.5 lbs/sec(3.4 kg/sec) AIR FLOW RATE.

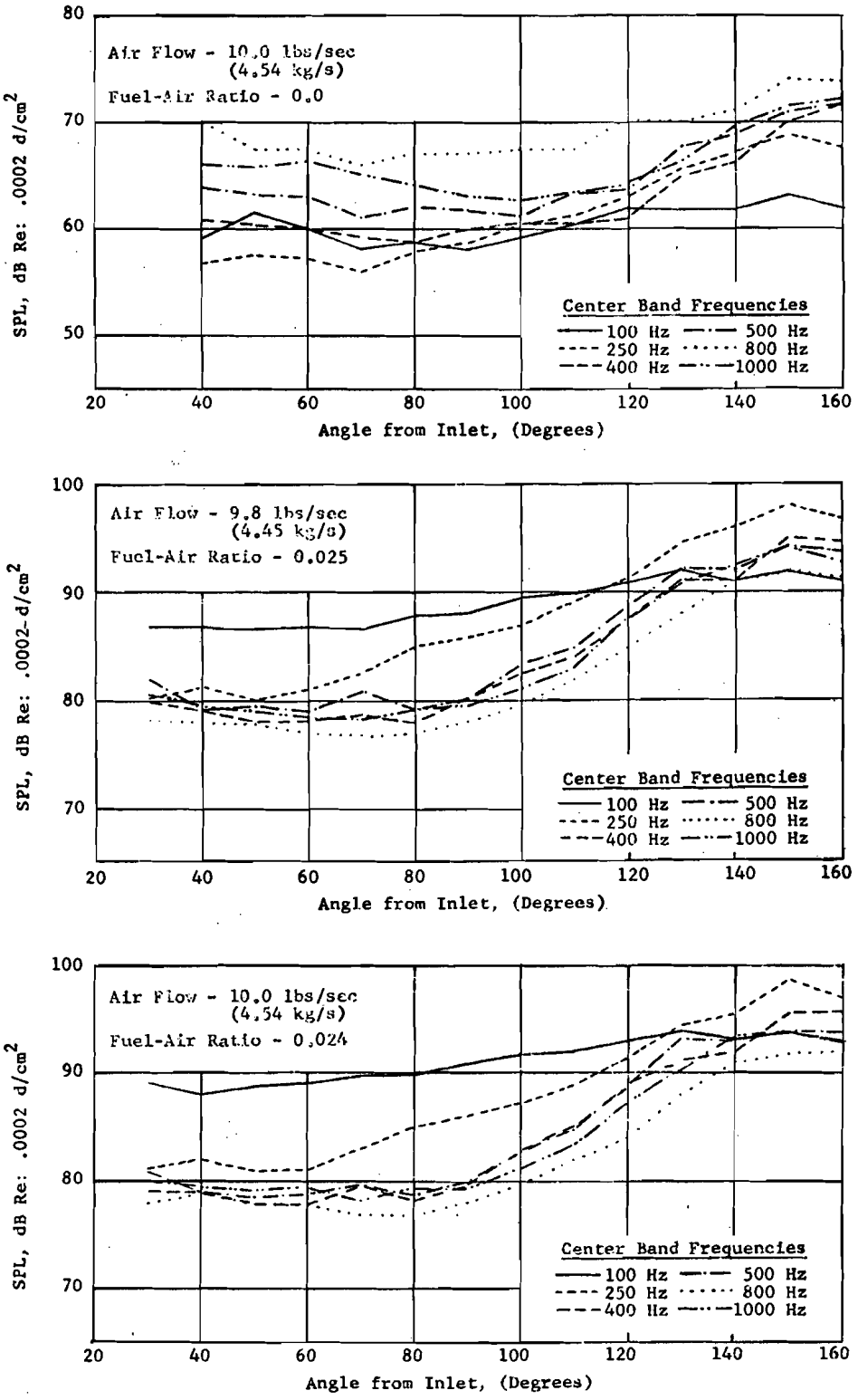

FIGURE 3.4.3-8 SPL DIRECTIVITIES FOR THE SUPPRESSED COMBUSTOR WITH HORN AT 10.0 lbs/sec(4.5 kg/sec) AIR FLOW RATE.

Table 3.4.3-1 A.T. Suppressed Combustor Test Points

Test Point	Air Mass Flow lbs/sec (kg/sec)	Fuel-Air Ratio	Exit Velocity ft/sec (m/sec)
1	3.7 (1.7)	0	77.2 (23.5)
2	3.8 (1.7)	0.011	152.0 (46.0)
3	3.8 (1.7)	0.024	244.4 (74.5)
4	7.3 (3.3)	0	156.0 (47.6)
5	7.4 (3.4)	0.011	315.0 (96.0)
6	7.5 (3.4)	0.027	501.5 (152.9)
7	10.0 (4.5)	0	211.0 (64.3)
8	9.8 (4.4)	0.025	465.9 (142.0)
9	10.0 (4.5)	0.024	493.9 (150.5)

(2) Effect of End Impedance

In order to determine the effect of end impedance on the results measured for the combustor with the deep cavity resonator, a second suppressor configuration was tested with significantly different end impedance. The suppressed configuration (which has been compared to the A.T. baseline) was designed to have a low impedance downstream of the resonator by gradually increasing the downstream area. A very abrupt change of impedance was produced for the second suppressed test by removing the horn and centerbody. This abrupt change of end impedance would increase the amount of sound energy reflected at the exhaust plane and thus generally result in lower or, possibly, unchanged far-field acoustic power levels.

Comparisons of the PWL spectra for the suppressed configurations with and without the horn are presented in Figures 3.4.3-9 through 3.4.3-11. These test results are compared at the same nominal air flow rates and fuel-air ratios as the previous comparisons.

At the lowest air flow rate (Figure 3.4.3-9) the 0.009 f/a yields the broadest reduction observed for these tests. One or more dB PWL reduction was observed between 100 Hz and 1000 Hz as well as at 1600 Hz. The maximum reduction of 4-1/2 dB occurred at 400 Hz and 500 Hz. No comparison could be made at the higher fuel-air ratio due to problems with the data acquisition at this point. Further, the noise levels measured without combustion were higher with the horn removed. This, however, was the only instance recorded where the suppressed configuration without the horn radiated higher acoustic power levels across the spectrum than with the horn. The reason for the increase is unexplained.

At the intermediate air flow rate, Figure 3.4.3-10, the acoustic power levels were generally the same for the cases without combustion as well as at the lower fuel-air ratio. Some differences occurred at several select frequencies for each case. On the other hand, without the horn, the suppressed power levels were measureably lower at the higher fuel-air ratio. Reductions of 4 dB and 5 dB PWL were observed in the 200 Hz and 500 Hz bands respectively. Lesser reductions of the acoustic power levels occurred within the 250 Hz and 800 Hz bands.

The PWL spectral results were similar for the higher air flow rate, without combustion (Figure 3.4.3-11). All of the acoustic power levels were within 2-1/2 dB. At the higher fuel-air ratio, marked reductions were measured for the configuration without the horn between the 160Hz and 500 Hz bands plus the 800 Hz band. The largest reduction of the propagating sound energy occurred in the 500 Hz band: 7 to 8 dB in the PWL. In the 160 Hz, 200 Hz, and 250 Hz bands the acoustic power levels were 3-1/2 to 4-1/2 dB lower without the horn. Similarly, the 400 Hz and 800 Hz bands were 2 to 3-1/2 dB lower without the horn. The level in the 120 Hz band was observed to increase 4-6 dB without the horn. Although the origin of this increase is unknown, it may be vortex lip noise created at the "sharp" exit from the suppressor.

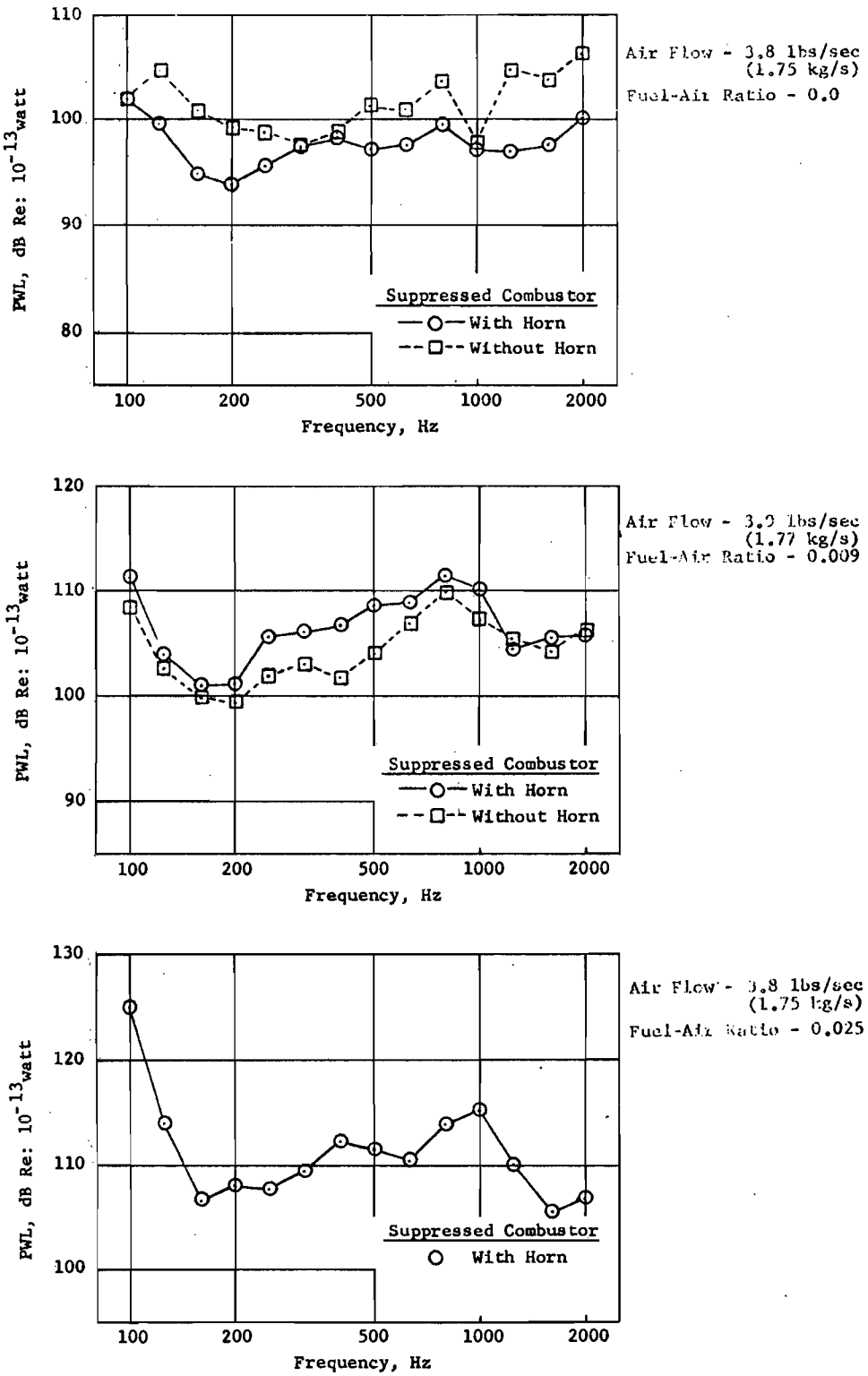

FIGURE 3.4.3-9 **PWL REDUCTION FOR THE SUPPRESSED COMBUSTOR WITHOUT HORN AT 3.75 lbs/sec(1.7 kg/sec) AIR FLOW RATE.**

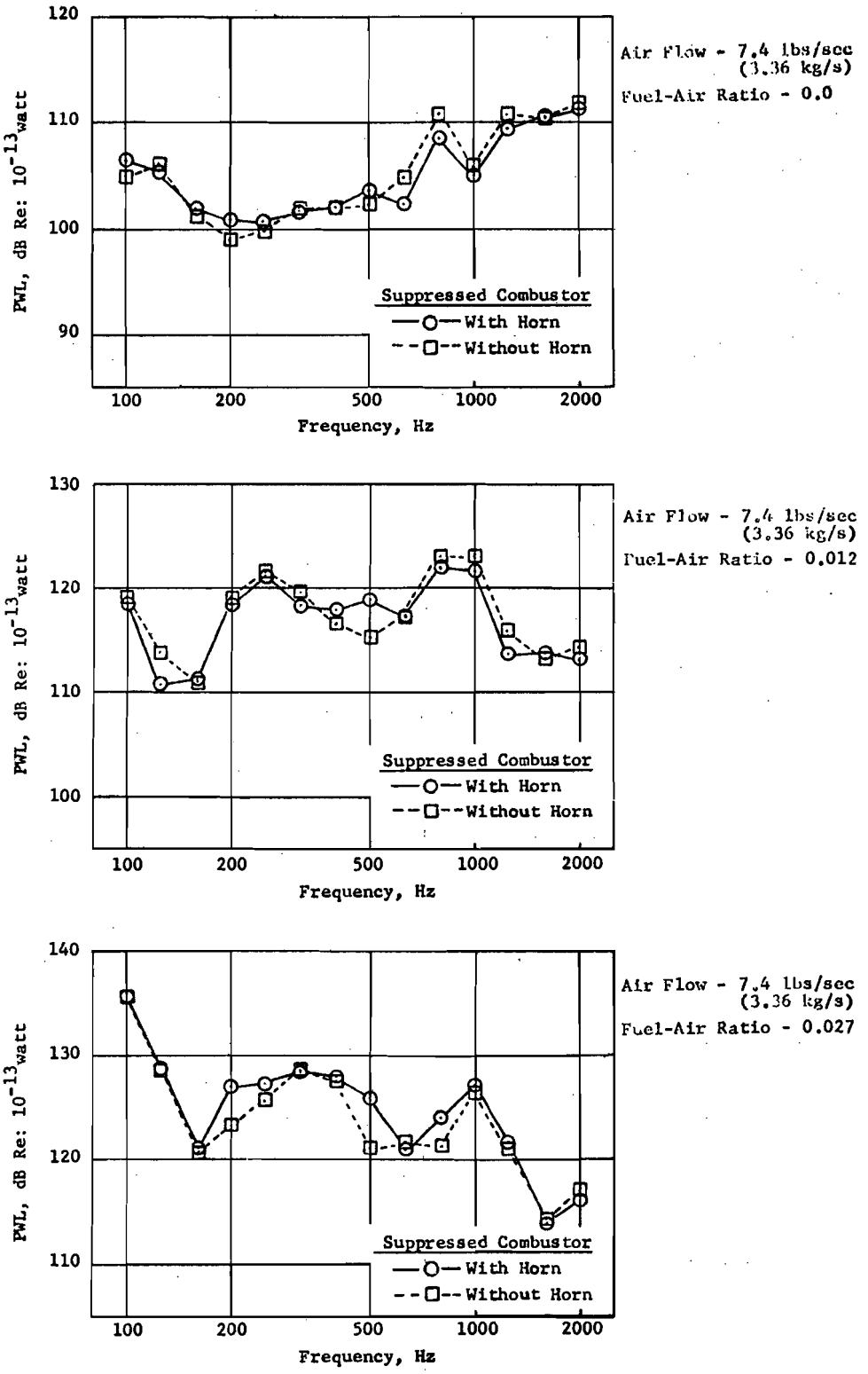

FIGURE 3.4.3-10 **PWL REDUCTION FOR THE SUPPRESSED COMBUSTOR WITHOUT HORN AT 7.5 lbs/sec(3.4 kg/sec) AIR FLOW RATE.**

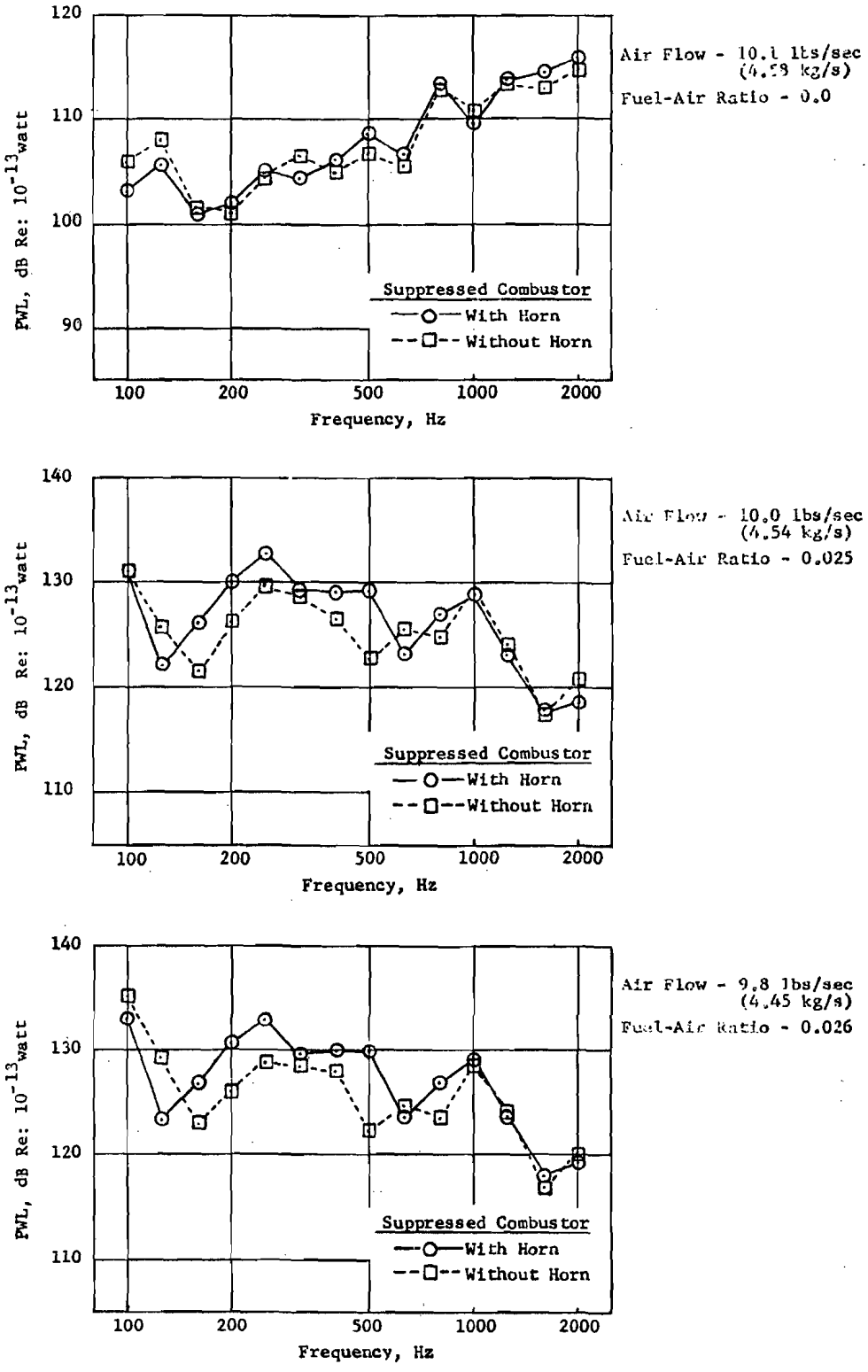

FIGURE 3.4.3-11 **PWL REDUCTION FOR THE SUPPRESSED COMBUSTOR WITHOUT HORN AT 10.0 lbs/sec(4.5 kg/sec) AIR FLOW RATE.**

The differences in the one third octave levels between these two configurations is not uniform over the spectrum as the end impedance is a function of the exit area change and the wavelength. Thus, some spectral variation is to be expected.

Typical SPL directivities are presented in Figure 3.4.3-12 for the suppressed configuration without the horn. These directivities have changed relative to those presented for the configuration with the horn. The maximum sound pressure levels have generally shifted from 150° and 160° to 120° through 140°. Note that the exhaust plane was farther away from the 150° and 160° microphones when the horn was removed, but only by the length of the horn.

3.4.4 Conclusions

The suppressed combustor results demonstrated that combustor noise can be substantially reduced over a broad range of low frequencies. Scrubbing noise over the resonator apparently increased with increasing velocity through the suppressor such that the overall combustor noise suppression was decreased with increasing exit velocity. Investigation of the two end impedances indicated measureable spectral differences occurred due to difference in reflectivity of sound energy at the exhaust plane (especially with the higher fuel-air ratios). Although neither end impedance examined simulates the impedance of an actual engine, the test results demonstrated that this characteristic is important for the design of combustors for low noise propagation.

3.5 SUMMARY

Two full scale annular combustors were used to determine a power level scaling and spectral shape for combustor noise. There was good agreement between this test series and the literature with regard to the power level being directly proportional to the exit velocity to the third power and the spectral shape being influenced by the turbulence spectrum. Based on this information, a suppressor was designed, built and tested to demonstrate the feasibility of suppressing the combustor noise close to the source. It was also shown that changing the end impedance (the tests with and without the horn) would result in changes in the spectrum shape and level of the low frequency signal in the farfield.

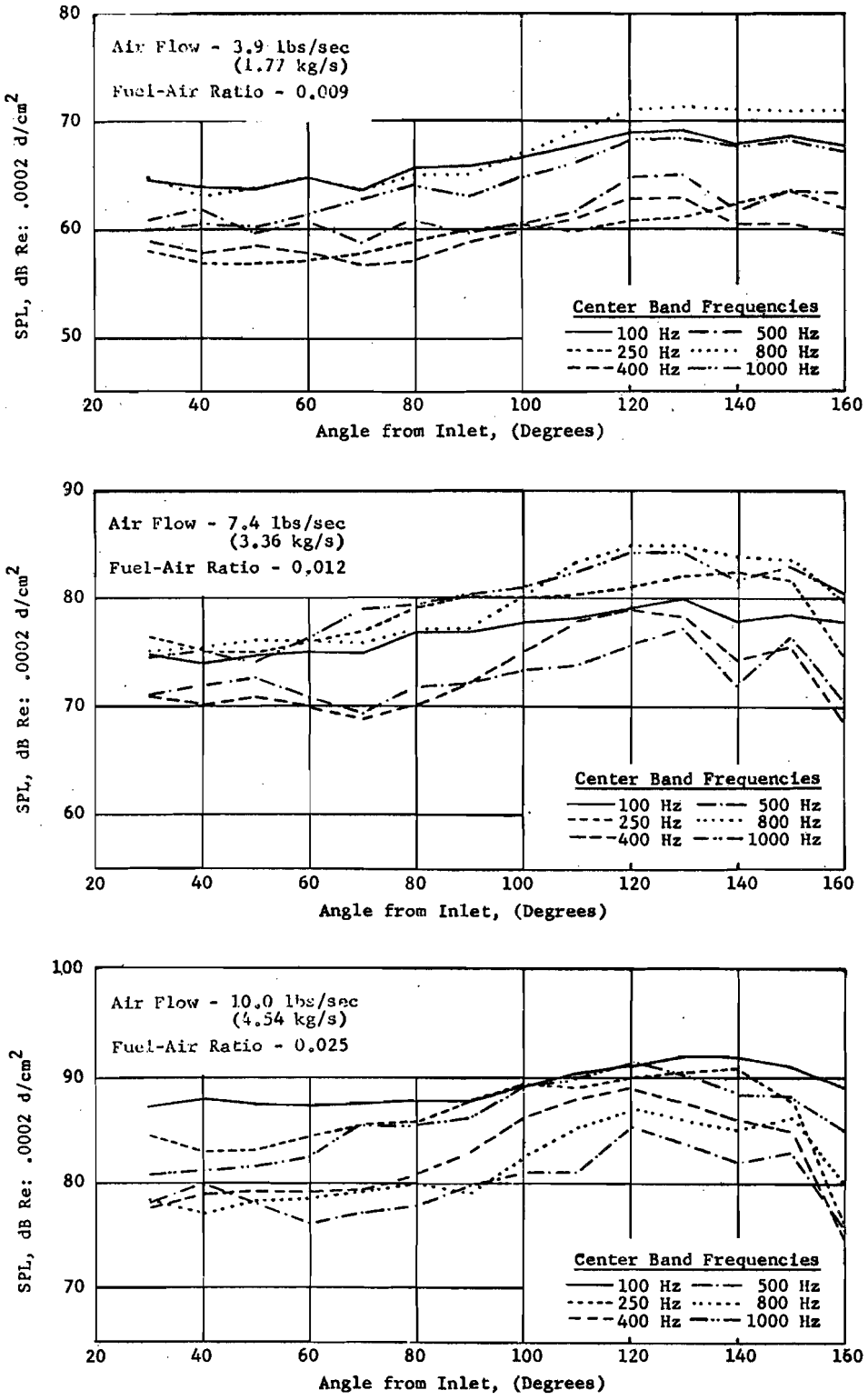

FIGURE 3.4.3-12 SPL DIRECTIVITIES FOR THE SUPPRESSED COMBUSTOR WITHOUT HORN.

References

3.1-1 Ho, P.Y. and Tedrick, R.N.; "Combustion Noise Prediction Techniques for Small Gas Turbine Engines," May 10, 1972, Garrett-AiResearch Report No. SD-8006.

3.1-2 Motsinger, R.; "Prediction of Engine Combustor Noise and Correlation with T64 Engine Low Frequency Noise," October 25, 1972, General Electric Report No. R72-AEG-313.

3.1-3 Gerend, R.P., Kumasaka, H.P. and Roundhill, J.P.; "Core Engine Noise," AIAA Paper No. 73-1027.

3.1-4 Arnold, J.S.; "Generation of Combustion Noise," The Journal of Acoustical Society of America, January 14, 1972.

3.1-5 Strahle, W.C.: "A Review of Combustion Generated Noise," AIAA Paper No. 73-1023.

3.2.4-1 Knott, P., "Noise Generated by Turbulent Non-Premixed Flames," AIAA Paper No. 71-732.

3.3-1 Fisk, W.S., Hehmann, H.W., Knott, P.R., Sandusky, G.T., "Supersonic Transport Noise Reduction Technology Summary" Report No. FAA-SS-72-43, December 1972.

3.3.4-1 Beranek, L.; NOISE AND VIBRATION CONTROL, McGraw-Hill, 1971.

SECTION 4.0

TURBINE NOISE

4.1 BACKGROUND

There was little need to investigate turbine generated noise until recently because the fan and the jet were the dominant noise sources in turbofan engines. Consequently, a general dearth of turbine acoustic data and information on the key parameters controlling turbine noise was initially encountered. The advent of the quiet fan installations (such as the CF6, JT9D and RB211) has increased the significance of noise from the turbine. Farfield measurements indicate that the unsuppressed turbine becomes a major contributor to the overall radiated noise as fan noise levels are reduced by either quieter fan design or through application of acoustic treatment. The need for basic turbine noise data, and an understanding of the noise generation and suppression mechanisms become necessary if the full benefits of the suppression of other noise sources are to be realized.

During the Phase II and III efforts of this program, basic, uncontaminated turbine noise data was accumulated through component tests on two turbine rigs: a single stage high pressure turbine and a 3 stage highly loaded fan turbine. The former test was used to investigate the effects of inlet turbulence and distortion on the noise generated. The latter test was used to establish parametric relationships between the noise generated and the turbomachinery aerodynamics. The effect of opened blade row spacing on the turbine noise generation was also examined with this rig. In addition, the acoustic data obtained was used to refine and extend an analytical model developed to predict turbine noise. Methods of turbine noise suppression studied included reduction at the source (through opened blade row spacing and leaned vanes) and use of acoustic treatment in the core nozzle. The first two are reported in the following sections. Details about the acoustic lining and the success achieved can be found in Reference 4.1-1 through 4.1-5. The references present data from the TF34 and the two NASA Quiet Engines "A" and "C". The design and testing of the acoustic lining is also provided in these references. Acoustic data is presented for configurations with and without acoustic treatment in the core nozzle, and with various degrees of fan suppression. The data include near- and far-field measurements as well as those taken with acoustic probes in the core nozzle. The data show the effect of core acoustic treatment on engine noise levels, and also provide information on turbine noise generation in an engine environment over a wide range of design parameters. This information was used along with CF6 data to formulate correlations for turbine noise generation (Volume III, Section 4).

4.2 SINGLE STAGE (HIGH PRESSURE) TURBINE TESTS

4.2.1 Background/Objectives

The objective of the single stage, high pressure turbine rig tests was to determine the effects of inlet distortion and turbulence on noise generation by a high pressure turbine. The turbine inlet is subject to flow distortions plus high, possibly varying, turbulence levels (arising, for example, from the combustor). If these nonuniformities were to be transmitted through the nozzles, they would interact with the rotor blades. This process has been analytically shown to significantly affect the noise generation (References 4.2.1-1 and -2), however, no published test data is available as to the actual effects.

Conducting a turbine acoustic test in an engine poses several problems, including high running costs and the possibility that noise from other sources, such as the combustor, might mask the turbine noise. Further, matching considerations between the turbine and the other engine components restrict the performance range to a single engine operating line, making it impossible to separate the effects of the various parameters, and also limiting the mechanical modifications which can be considered. A component turbine test, however, introduces the question of how representative the test is of the engine environment and how applicable the results are. A systematic investigation of the parameters is possible as a component test. An understanding of the basic processes occuring can therefore be achieved, and the results then extended (in terms of trends if not levels) to engine applications. This reasoning was substantiated by the results of the 3 stage turbine rig (Section 4.3) and the turbine noise correlations subsequently derived using engine data (Volume III).

4.2.2 Facility Description

The single stage turbine test was performed in General Electric Company's Evendale Air Turbine Test Facility, a dual purpose facility capable of evaluating either single stage high pressure turbine or multistage fan drive turbine performance. A typical test configuration is shown in Figure 4.2.2-1. The facility was used in investigations of both full scale and model turbines under stimulated operating pressures at low temperatures.

The flow enters the test region through a specially designed scroll which smooths out flow disturbances and provides a uniform stream to the turbine rig. The turbine discharges through a constant annular passage leading to the exhaust plenum. The turbine pressure ratio (Inlet/Exhaust) is set by controlling the inlet and exhaust pressures which can be maintained at any desired setting. The power generated is absorbed by means of a waterbrake which also serves to regulate the wheel speed (by changing the water flow rate and level in the brake). Hence the facility has the capability of independent variation of the pressure ratio and speed, two important parameters in turbomachinery noise generation. The actual test process consists of varying the wheel speed over

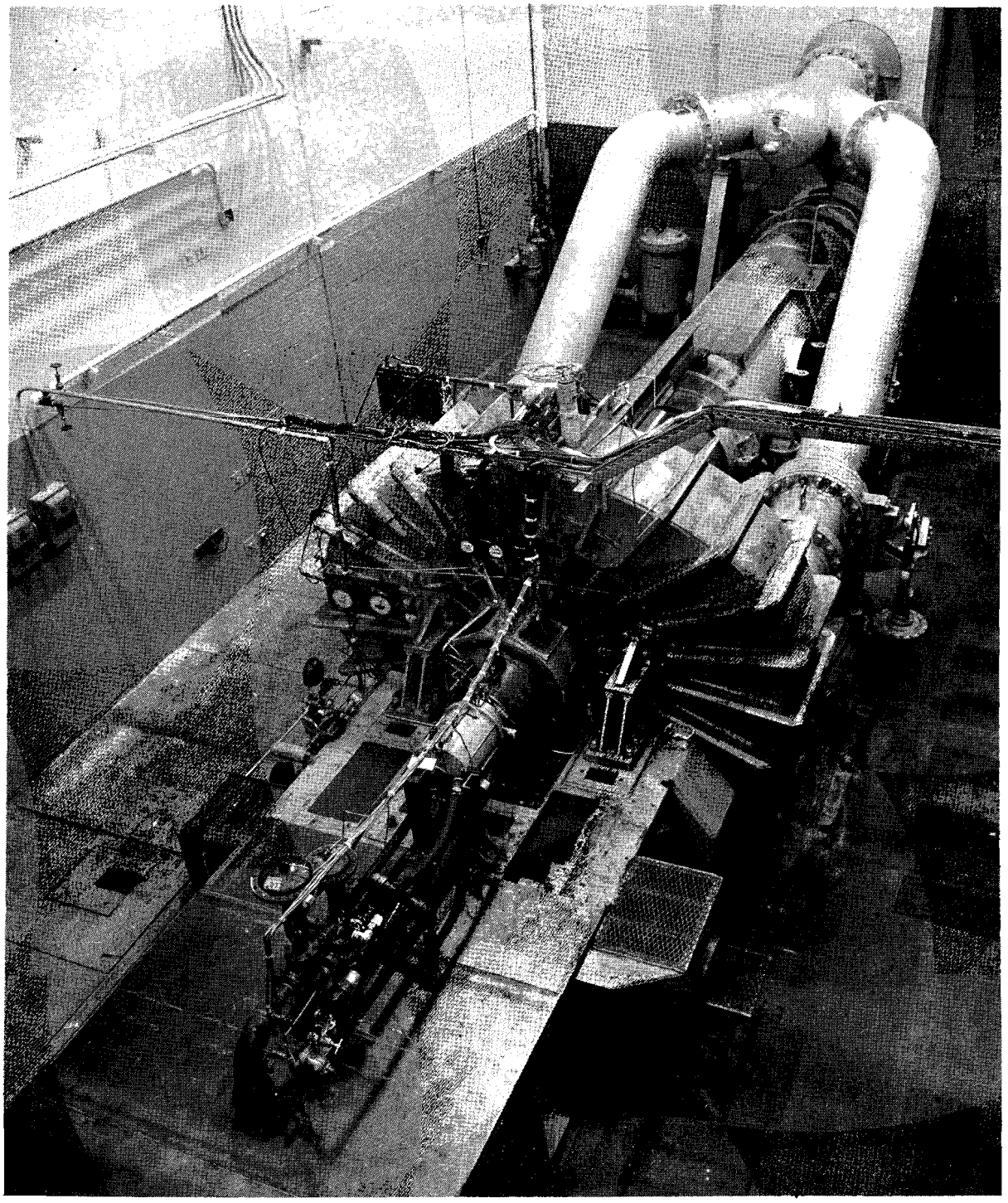

FIGURE 4.2.2-1 AIR TURBINE TEST FACILITY

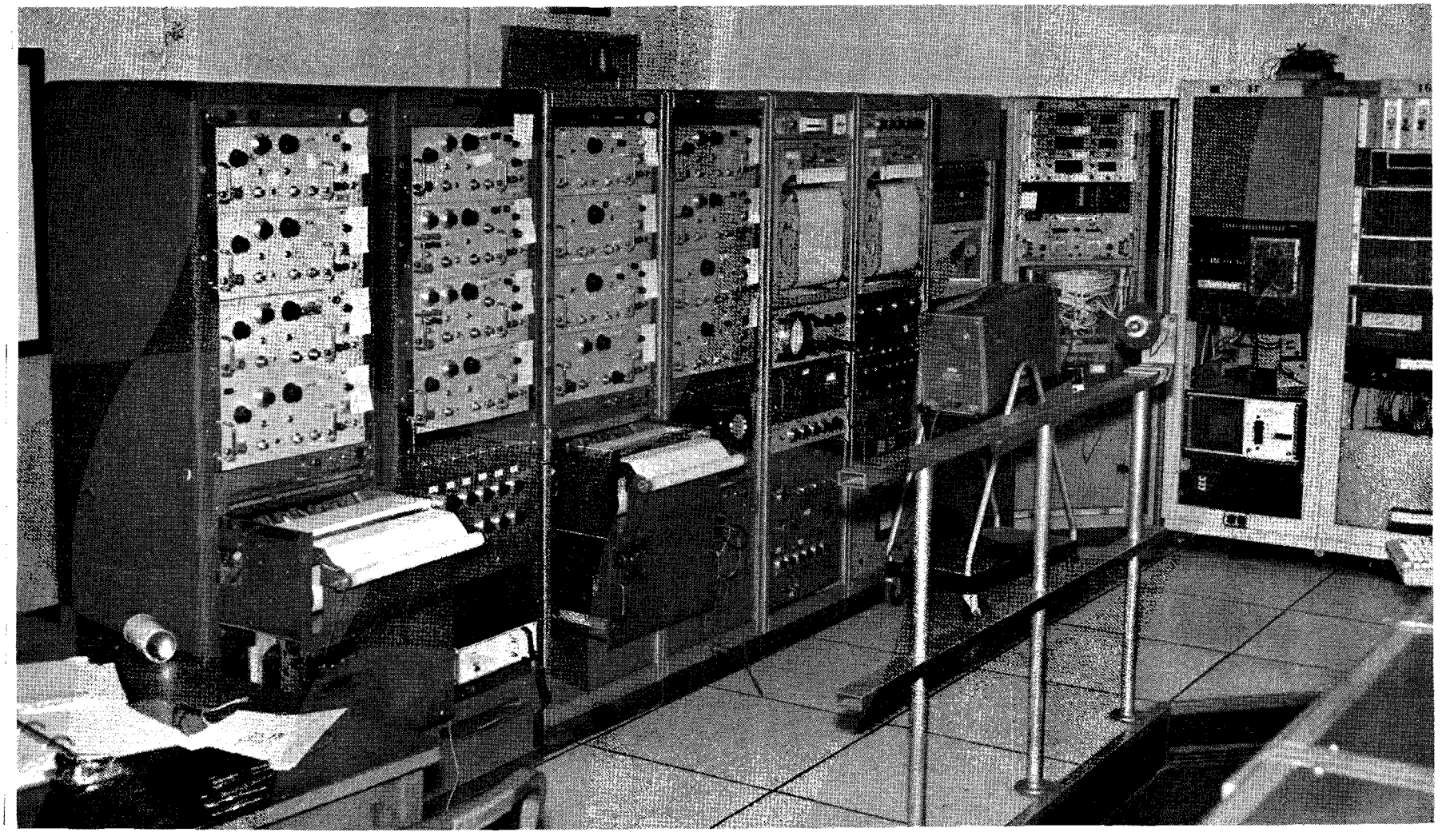

FIGURE 4.2.2-2 CONTROL ROOM FOR THE AIR TURBINE TEST FACILITY

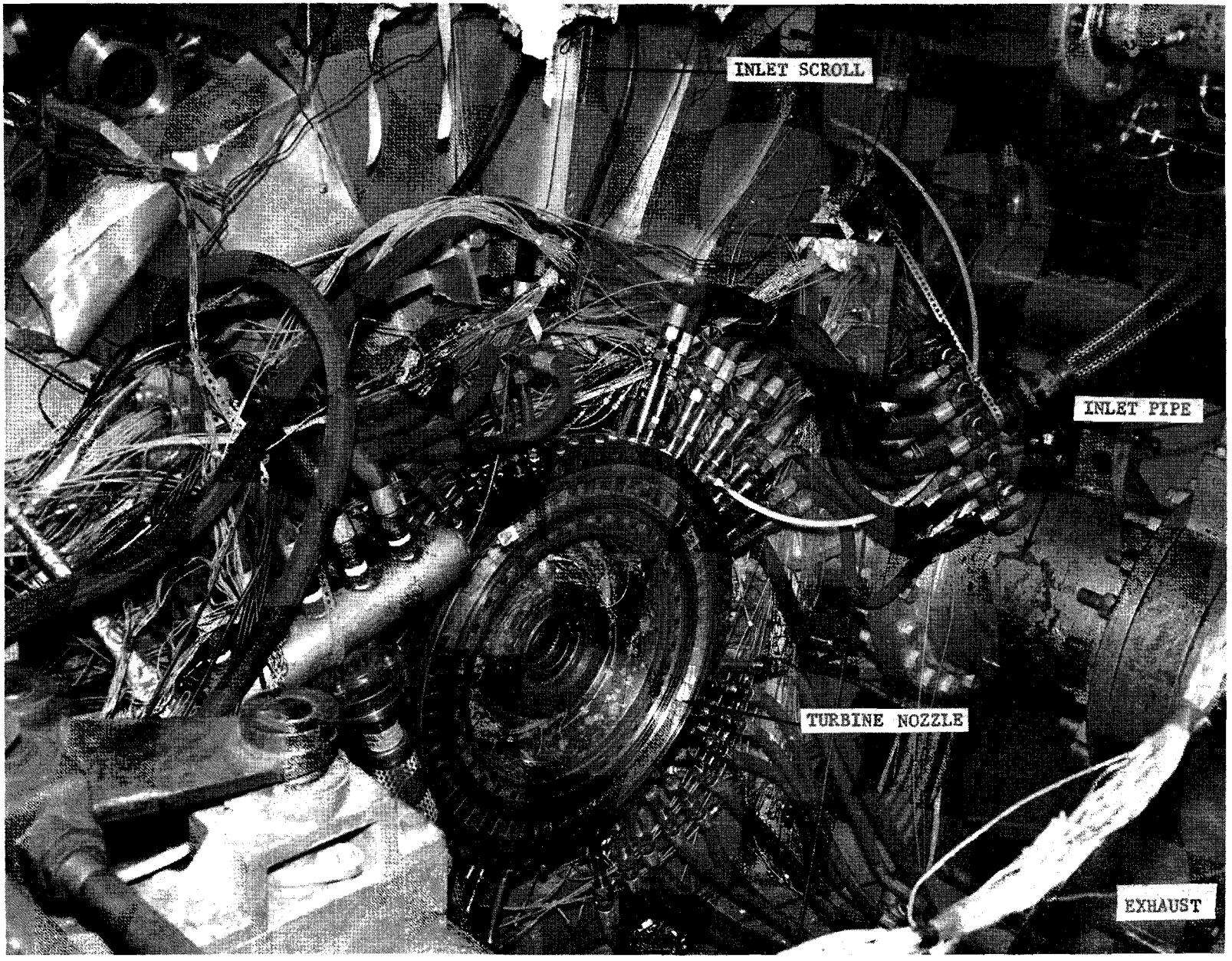

FIGURE 4.2.2-3 AIR TURBINE TEST FACILITY WITH SINGLE STAGE (H.P.) TURBINE RIG

the desired range for each pressure ratio setting.

The turbine facility controls (Figure 4.2.2-2) are set up in an adjoining room. Turbine parameters of inlet temperature, inlet pressure, discharge pressure, speed and rotor net thrust can all be maintained automatically at pre-set values.

The single stage high pressure turbine rig is shown in the early mounting stages in Figure 4.2.2-3. The basic design parameters for the turbine rig are provided in Table 4.2.2-1 and a schematic shown in Figure 4.2.2-4.

The turbulence and flow distortion were produced by inserting a knife-edged wedge in the inlet flowpath. Wire screens and meshes were considered but discarded when it became apparent they could not generate the high turbulence levels desired for the tests (see, for example, Section 2.3).The knife-edge ring designs were selected to produce data over a wide range of flow/velocity distortions and turbulence levels because there was little data available to indicate the type and level of distortion and turbulence which might be encountered in an engine. The configurations tested were: no blockage (baseline), 15% blockage, and 30% blockage, and are shown schematically in Figure 4.2.2-5.

The acoustic data was taken with five fixed wave-guide type probes immersed to "equal areas" in the turbine exhaust. The probes are displayed in Figure 4.2.2-6 and details of the construction can be found in Reference 4.2.2-1. The probes were calibrated in a standing (plane) wave tube (Figure 4.2.2-7) and a typical response curve is shown in Figure 4.2.2-8.

The immersions and circumferential locations of the acoustic probes are presented in Table 4.2.2-2. A block diagram of the acoustic instrumentation hook-up is shown in Figure 4.2.2-9. The microphone signals were recorded both direct and with the DC 0-1 kHz portion filtered out. The signals were filtered in order to insure that data would be available without high amplitude, low frequency (facility) noise influencing the signal-to-noise ratio in the frequency range of interest (7 kHz to 20 kHz).

Calibration of the microphone and data acquisition system was accomplished by the use of a Bruel and Kjaer (B&K) Pistonphone and recording the sound pressure level of the source (124 dB $\pm$ 0.2 dB). Because the pistonphone signal was affected by the filter, the filtered systems were calibrated by recording an equivalent voltage at a frequency above the filter cut off. The frequency response of the system was determined by applying a constant (known) voltage to the microphone cathode follower at a number of selected frequencies over the range 50 Hz to 22.5 kHz.

The system level (pistonphone) calibrations were included in the spectrum analysis and the frequency responses were included in the power level calculations.

The recorded signals were processed through a Federal Scientific "Ubiquitous" Spectrum Analyzer (UA6) to obtain narrow band spectra (Sound Pressure Level versus Frequency, 1 kHz - 20 kHz, with an effective 40 Hz bandwidth).

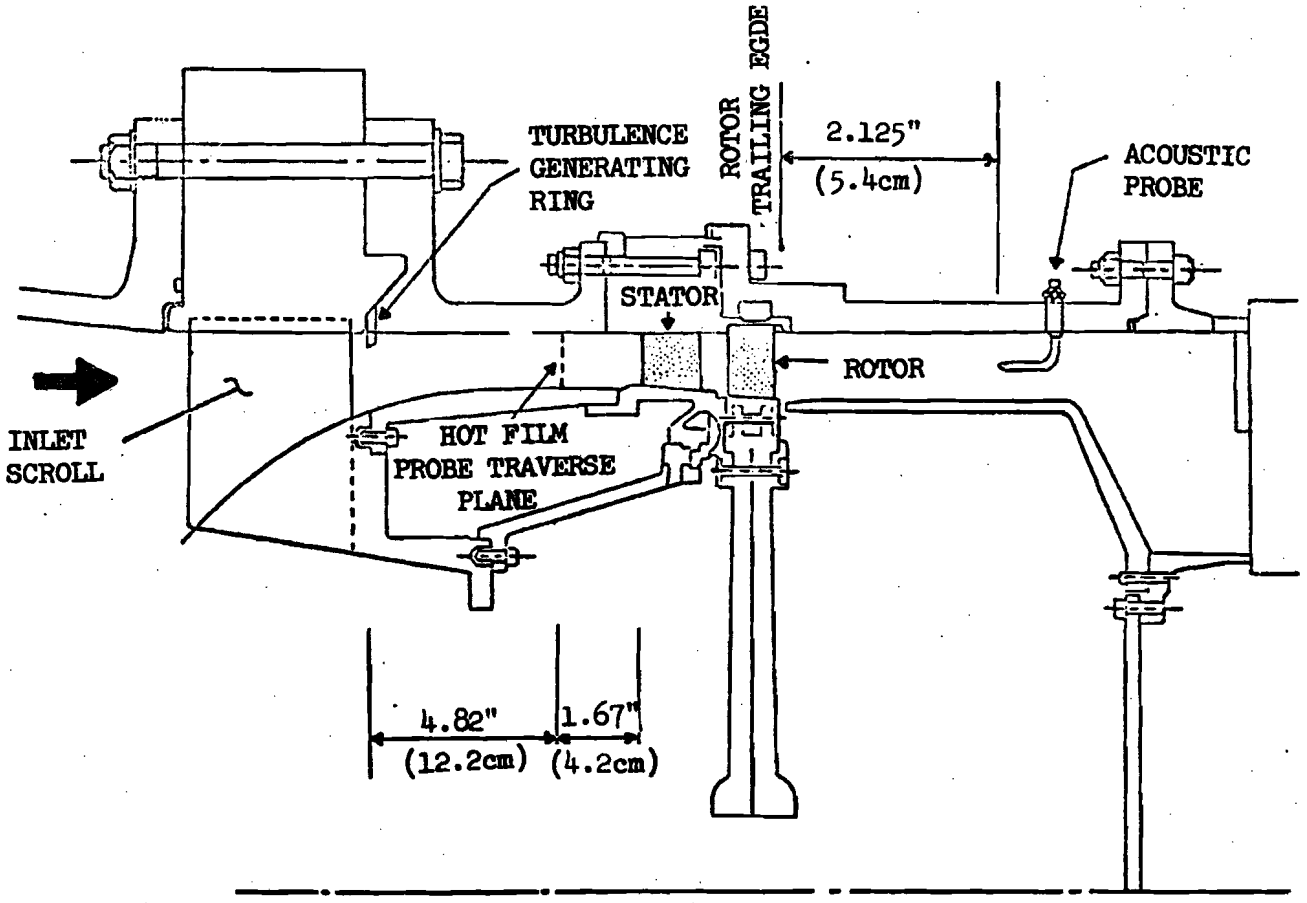

FIGURE 4.2.2-4 SCHEMATIC OF TEST CONFIGURATION FOR TURBULENCE AND DISTORTION TEST.(SINGLE STAGE TURBINE RIG)

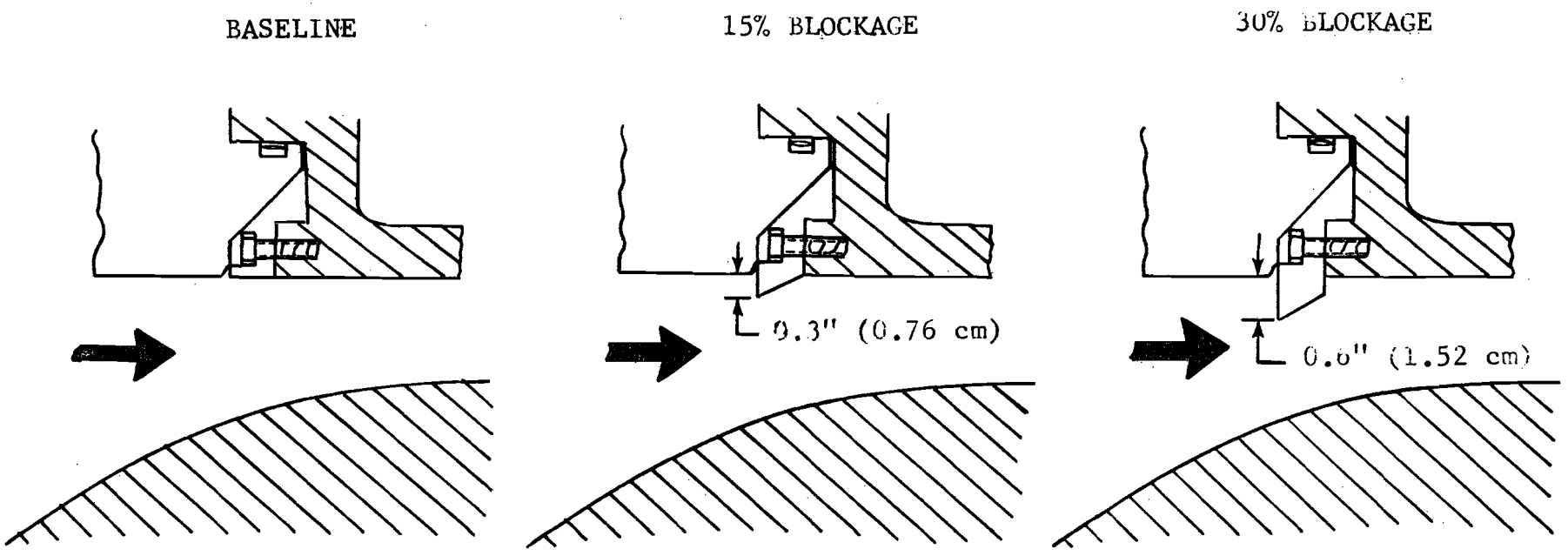

FIGURE 4.2.2-5 CONFIGURATIONS FOR TURBULENCE AND DISTORTION TESTS.

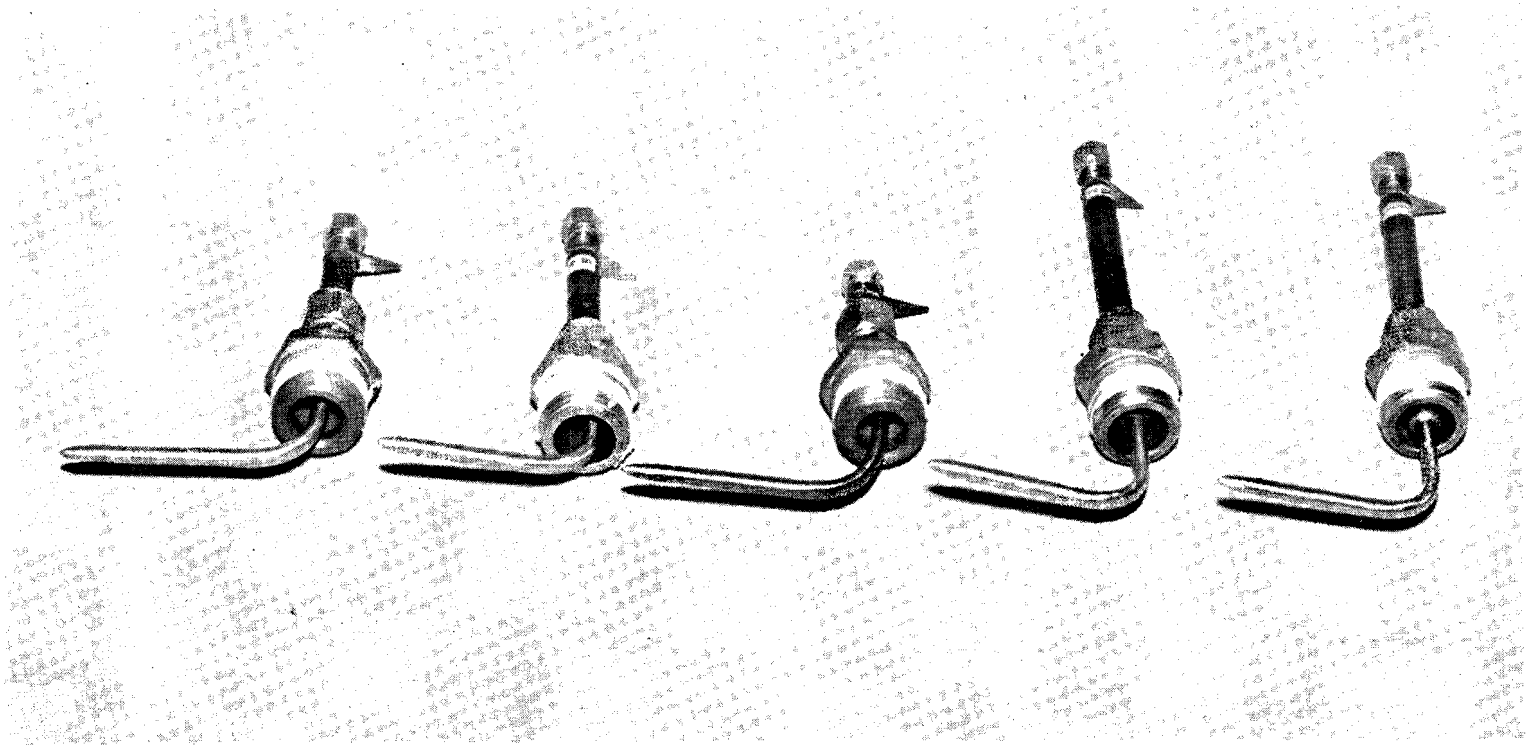

FIGURE 4.2.2-6 ACOUSTIC PROBES USED IN THE SINGLE STAGE (H.P.) TURBINE TESTS

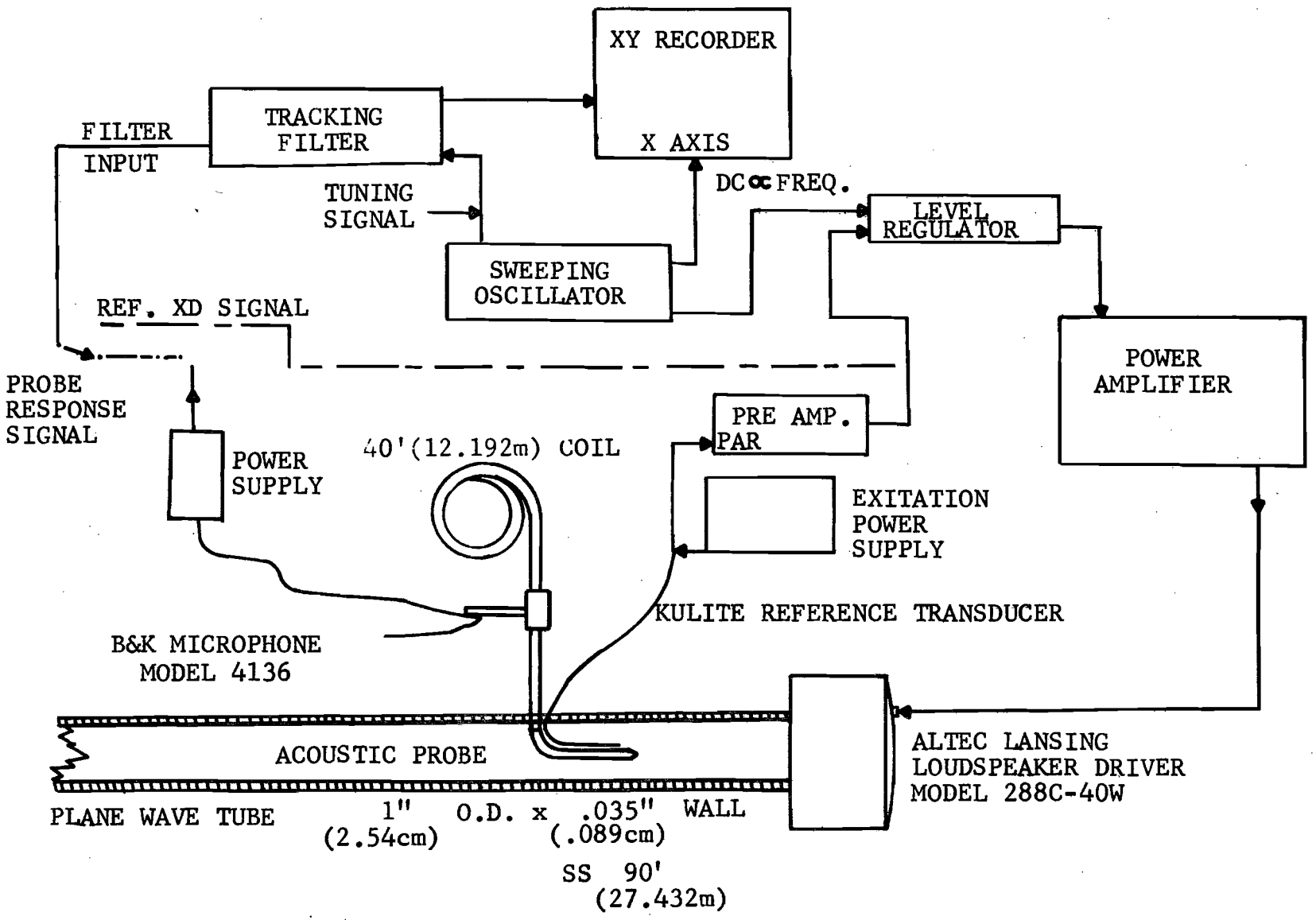

FIGURE 4.2.2-7 BLOCK DIAGRAM, ACOUSTIC PROBE CALIBRATION FACILITY

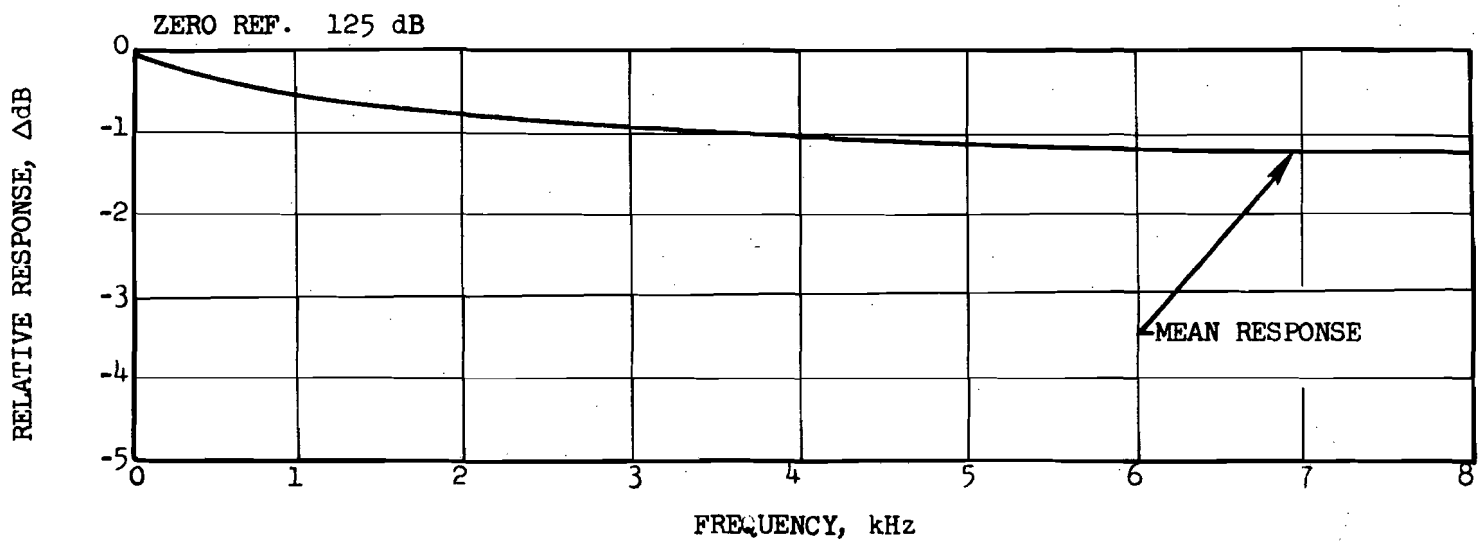

FIGURE 4.2.2-8 TYPICAL FREQUENCY RESPONSE, ACOUSTIC PROBE.

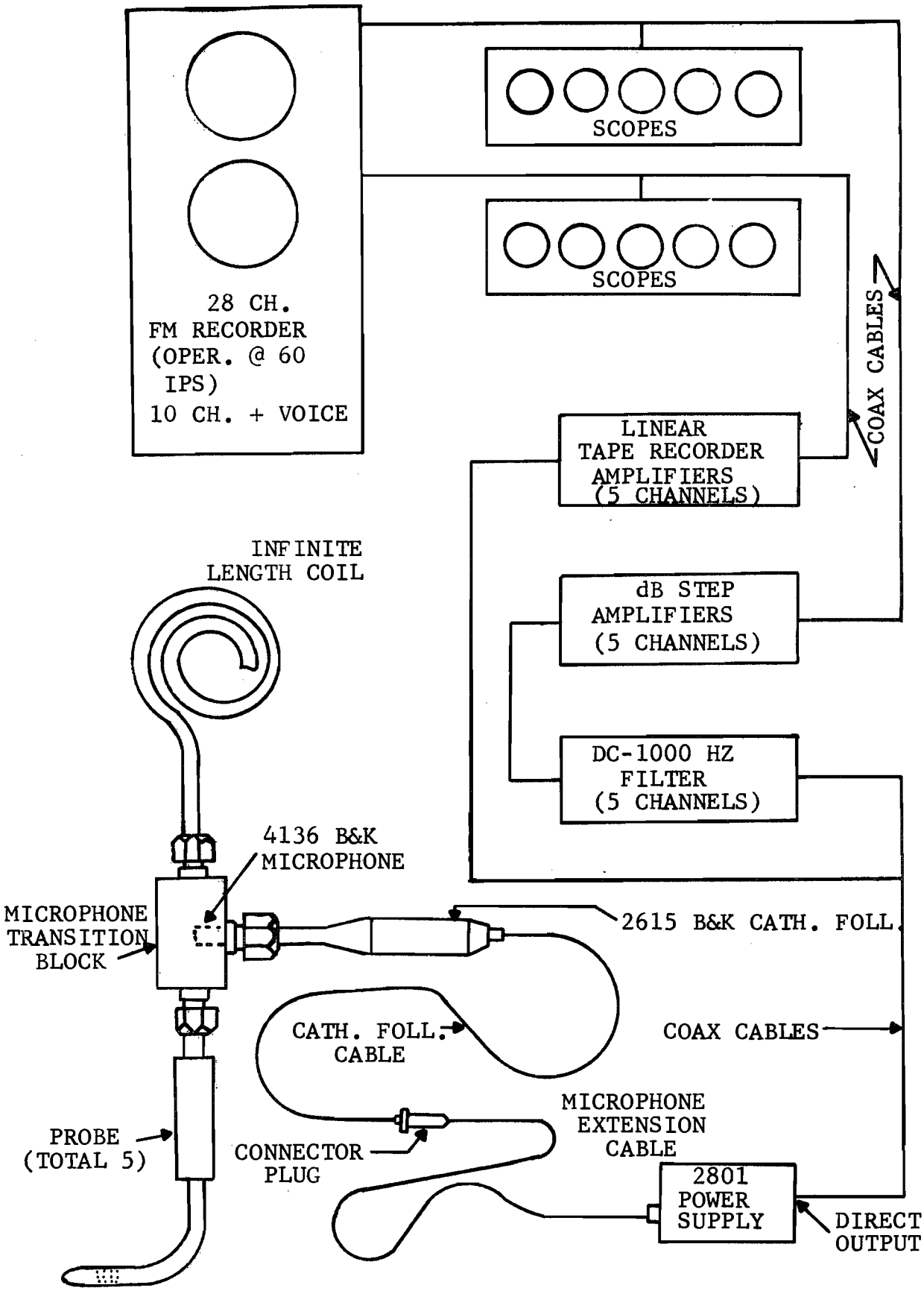

FIGURE 4.2.2-9 INSTRUMENTATION BLOCK DIAGRAM, HIGH PRESSURE TURBINE ACOUSTIC SPACING TEST

Table 4.2.2-1 Basic Design Parameters for the Single Stage High Pressure Turbine Rig

Work Coefficient $\frac{g\ J\ \Delta H}{2\ U_p^2}$	0.838
Nozzle Total-to-Static Pressure Ratio ($P_{T_{in}}/P_{out}$)	2.62
Design Speed	7380 rpm
Nozzle Exit Mach No.	1.23
Turbine Exit Axial Mach No.	0.494
Turbine Exit Absolute Mach No.	0.512
Turbine Exit Swirl Angle	15°
Number of Blades	80
Number of Vanes	56
Blade Passing Frequency	9840 Hz
Tip Speed	966 ft/sec (294 m/sec)
Blade Row Spacing	0.75 inch (1.905 cm)

Table 4.2.2-2. Acoustic Probe Immersions and Circumferential Position

Circumferential Location*	Immersion (From Tip) (inches)	(cm.)
3 o'clock	0.275**	0.698**
5 o'clock	0.525	1.333
7 o'clock	0.885	2.248
9 o'clock	1.225	3.111
11 o'clock	1.636	4.155

* Aft Looking Forward

** Minimum Immersion Possible for the Probe Geometry

A hot film anemometer traverse probe (X-Array) was located in the turbine inlet, providing turbulence intensity and velocity profile data at a series of immersions. A detailed discussion of the theory and application of hot film anemometry is presented in Reference 4.2.2-2. Outputs from the probe and its electronics consist of four voltage readings proportional to the axial velocity ($\bar{U}_{local}$), the circumferential velocity ($\bar{V}_{local}$), rms turbulent velocity-axial direction (u'), and rms turbulent velocity-circumferential direction (v'). Hot film data were taken at five immersion, presented in Table 4.2.2-3. The voltages were measured on line, using rms and DC voltmeters connected at the appropriate output terminals. The constant of proportionality between voltage and velocity is the same for all four outputs.

Because of the acoustic nature of the test, no total aerodynamic probe instrumentation was installed for this test, and the hot film probe was retracted from the flow stream when acoustic data were taken. The operating points were set based on static pressure measurements in the inlet and exhaust, plenum temperature and pressure measurements (inlet T_T and P_T), and flow rate measured using a venturi in the inlet ahead of the straightener scroll. Wheel speed was determined by a tachometer and torque output was obtained from strain gages on the shaft connecting the turbine and water brake. There is a total pressure loss for flow past a blockage (but no total temperature loss per Reference 4.2.2-3). The turbine used for these tests operates at constant corrected flow ($W \sqrt{T_T} / P_T$), since the nozzle passage is choked. By observing the apparent change in flow rate (based on plenum pressure), and interpreting the variation as an increased pressure requirement, the pressure loss across the turbulence generating rings was determined and used in setting the turbine pressure ratio.

Table 4.2.2-3 Hot Film Anemometer Probe Immersions

Immersion Number	Immersion from Tip (inches)	(cm)
1	0.202	.513
2	0.501	1.273
3	0.793	2.014
4	1.080	2.743
5	1.361	3.457

4.2.3 Test Results

The nominal test points were wheel speeds of 6220,6810 and 7380 rpm at a pressure ratio (total-to-static) of 5.1 with a repeat run at each setting.

Aerodynamic

As there was no total aerodynamic instrumentation, no attempt was made to determine the effect of inlet distortion and turbulence on turbine efficiency. Results from the hot film data are presented in Tables 4.2.3-1 through -3; the mean velocities (voltages) were determined using area weighted data from each immersion. The circumferential mean velocity in the inlet was negligible at all points.

Because the turbine operated at constant corrected weight flow (choked nozzle), the turbulence intensities and the velocity profiles do not vary over the operating range for a given configuration. The average turbulence and velocity profiles are presented in Table 4.2.3-4 and in Figure 4.2.3-1.

Acoustic

The procedure used to reduce the acoustic measurements was as follows:

- Narrow band spectral analysis from 0-20 kHz (40 Hz bandwidth) of the recorded data.
- Determination of the pure tone sound pressure levels (SPL's) at the fundamental blade passing frequency (BPF) and second harmonic (2 x BPF) for each operating point/immersion.
- Calculation of the sound power level (PWL) at each operating point for the fundamental and second harmonic. An area weighted average SPL was used for the duct PWL calculations.
- Calculation of the total power content of the pure tones (total PWL for fundamental and second harmonic).

Typical narrow band spectra are presented in Figures 4.2.3-2 through -6 for each of the five immersions. Due to instrumentation malfunction, only four immersions were recorded for the 30% blockage. The results of the narrow band spectrum analysis and the power level calculations are summarized in Figures 4.2.3-7 as PWL versus wheel speed for the three configurations.

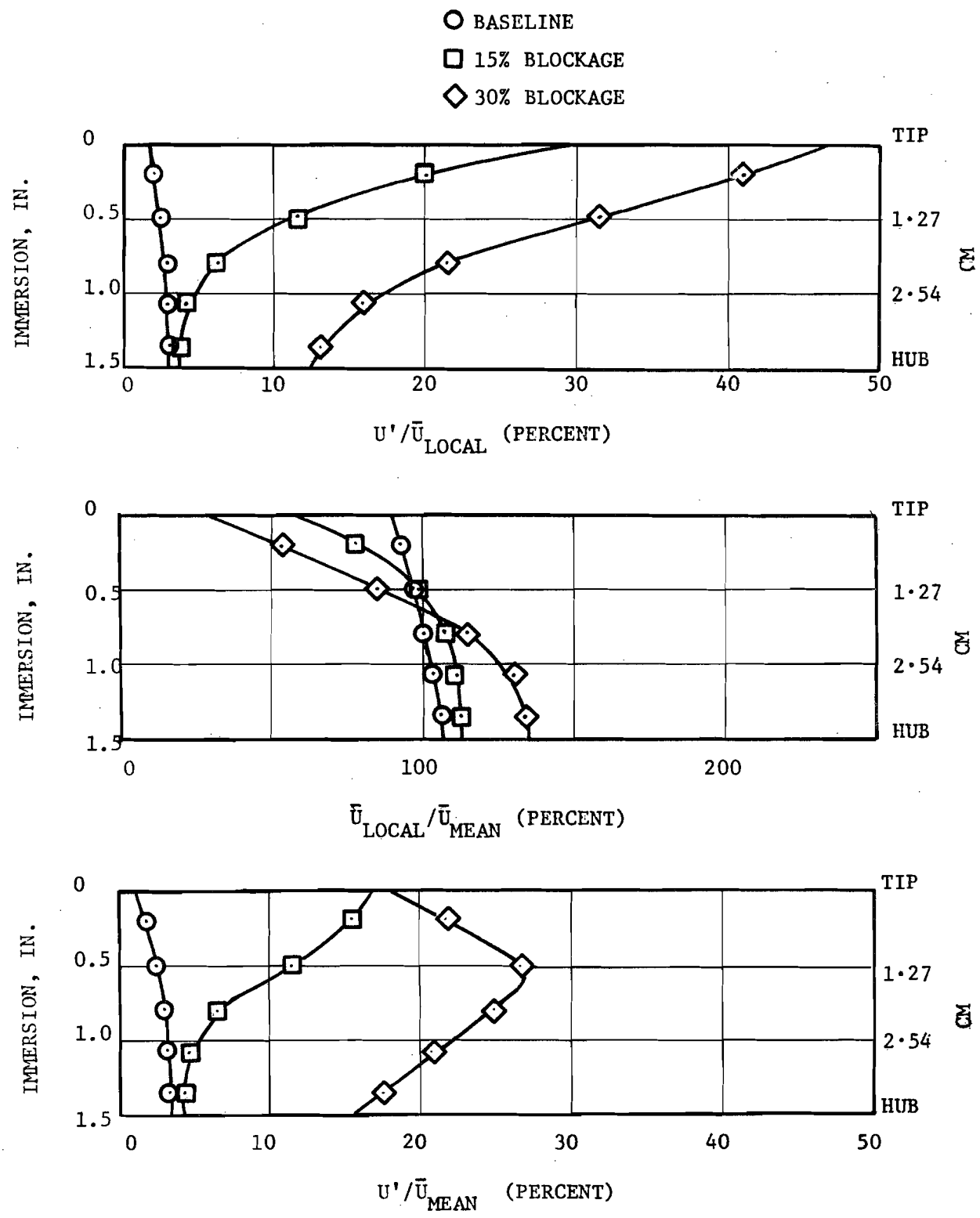

FIG. 4·2·3-1 AVERAGE TURBULENCE AND VELOCITY PROFILES

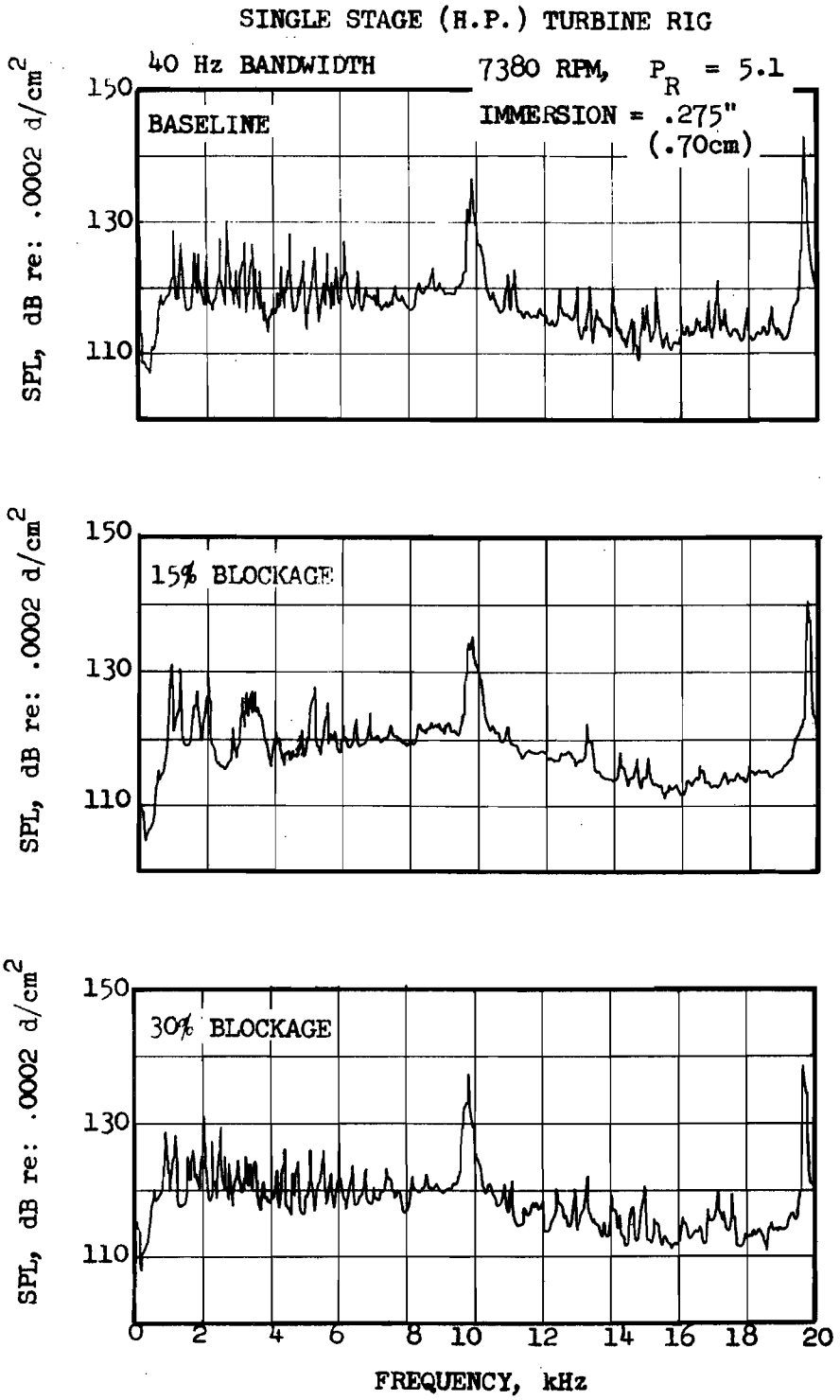

FIGURE 4.2.3-2 COMPARISON OF TYPICAL NARROWBAND SPECTRA FOR THE THREE CONFIGURATIONS (BASELINE, 15% BLOCKAGE, 30% BLOCKAGE).

SINGLE STAGE (H.P.) TURBINE RIG

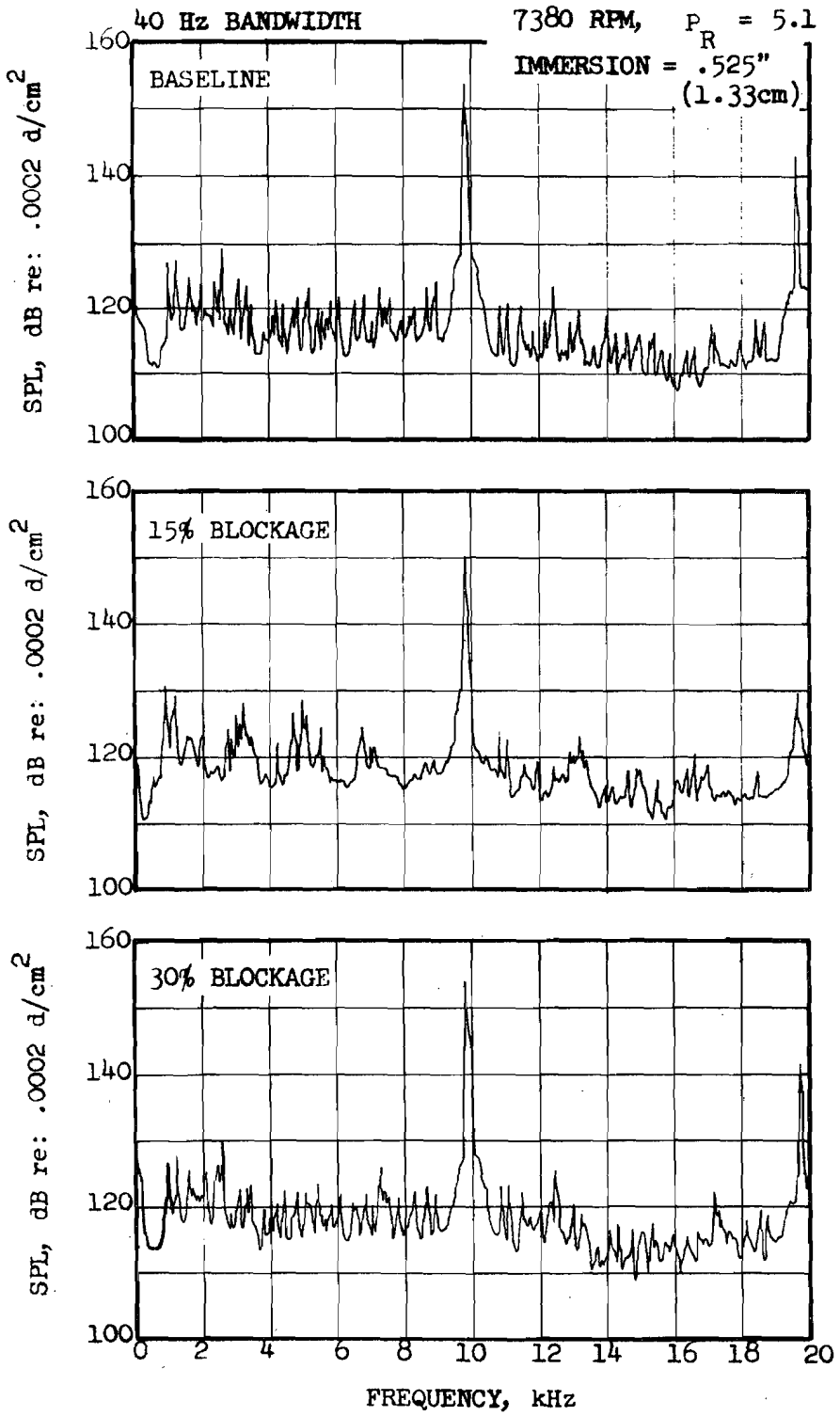

FIGURE 4.2.3-3 COMPARISON OF TYPICAL NARROWBAND SPECTRA FOR THE THREE CONFIGURATIONS (BASELINE, 15% BLOCKAGE, 30% BLOCKAGE).

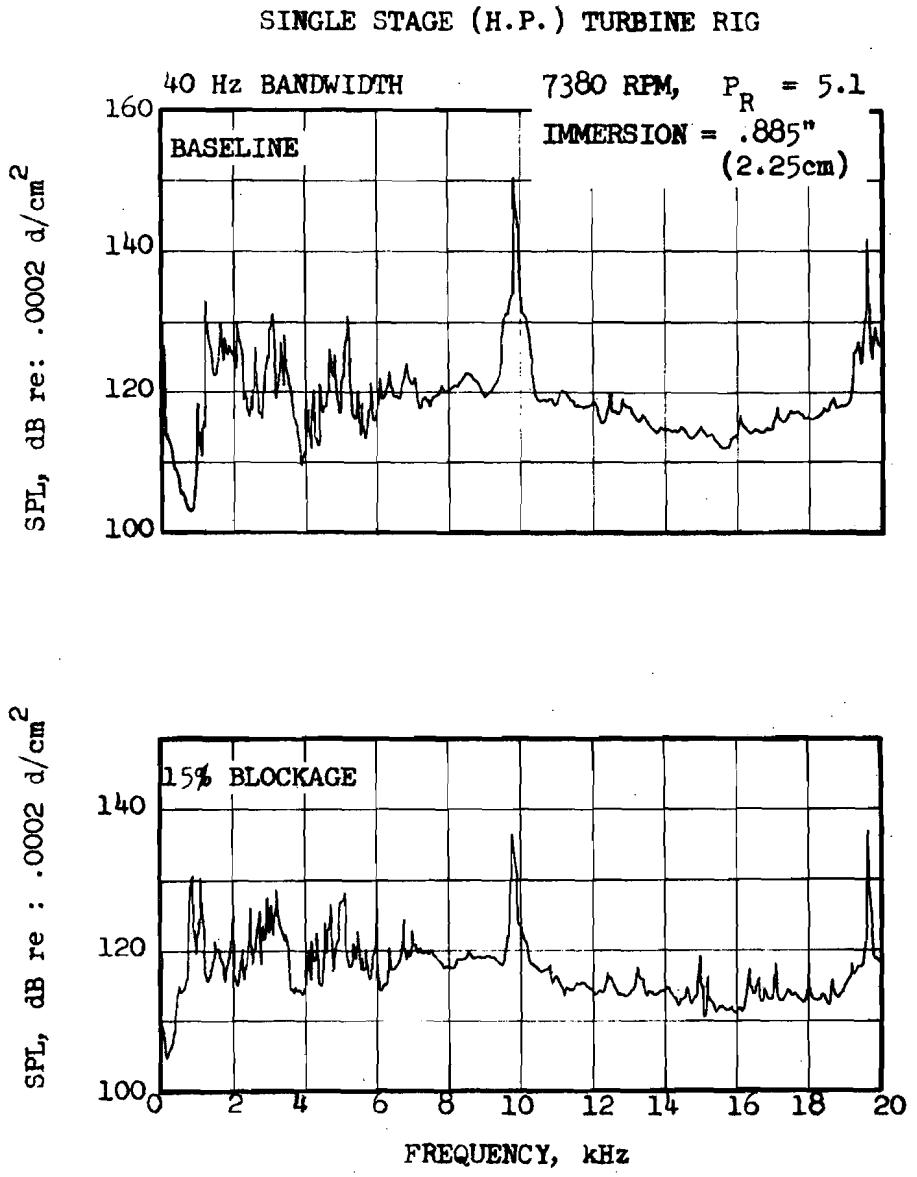

FIGURE 4.2.3-4 COMPARISON OF TYPICAL NARROWBAND SPECTRA FOR THE TWO CONFIGURATIONS (BASELINE, 15% BLOCKAGE).

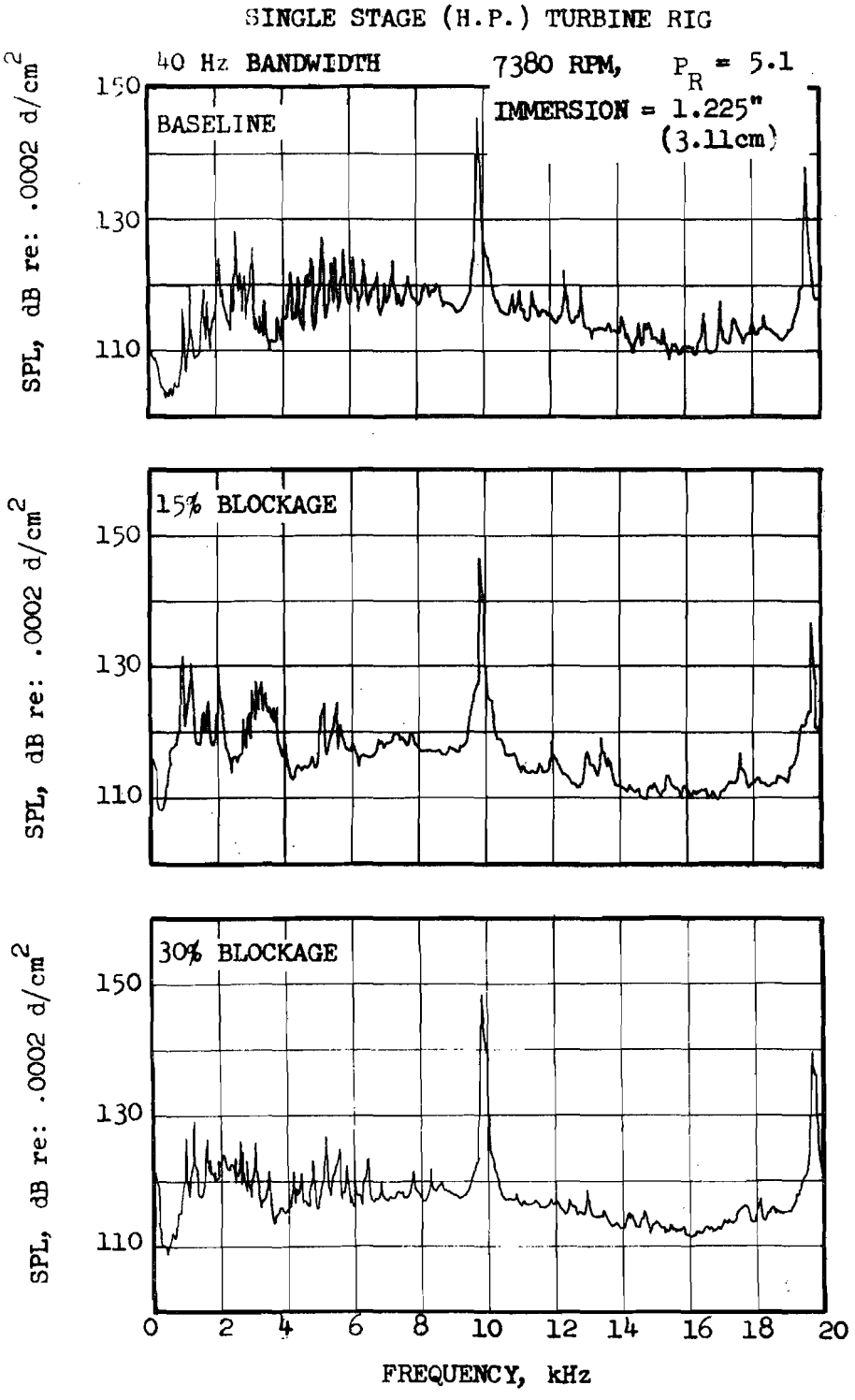

FIGURE 4.2.3-5 COMPARISON OF TYPICAL NARROWBAND SPECTRA FOR THE THREE CONFIGURATIONS (BASELINE, 15% BLOCKAGE, 30% BLOCKAGE).

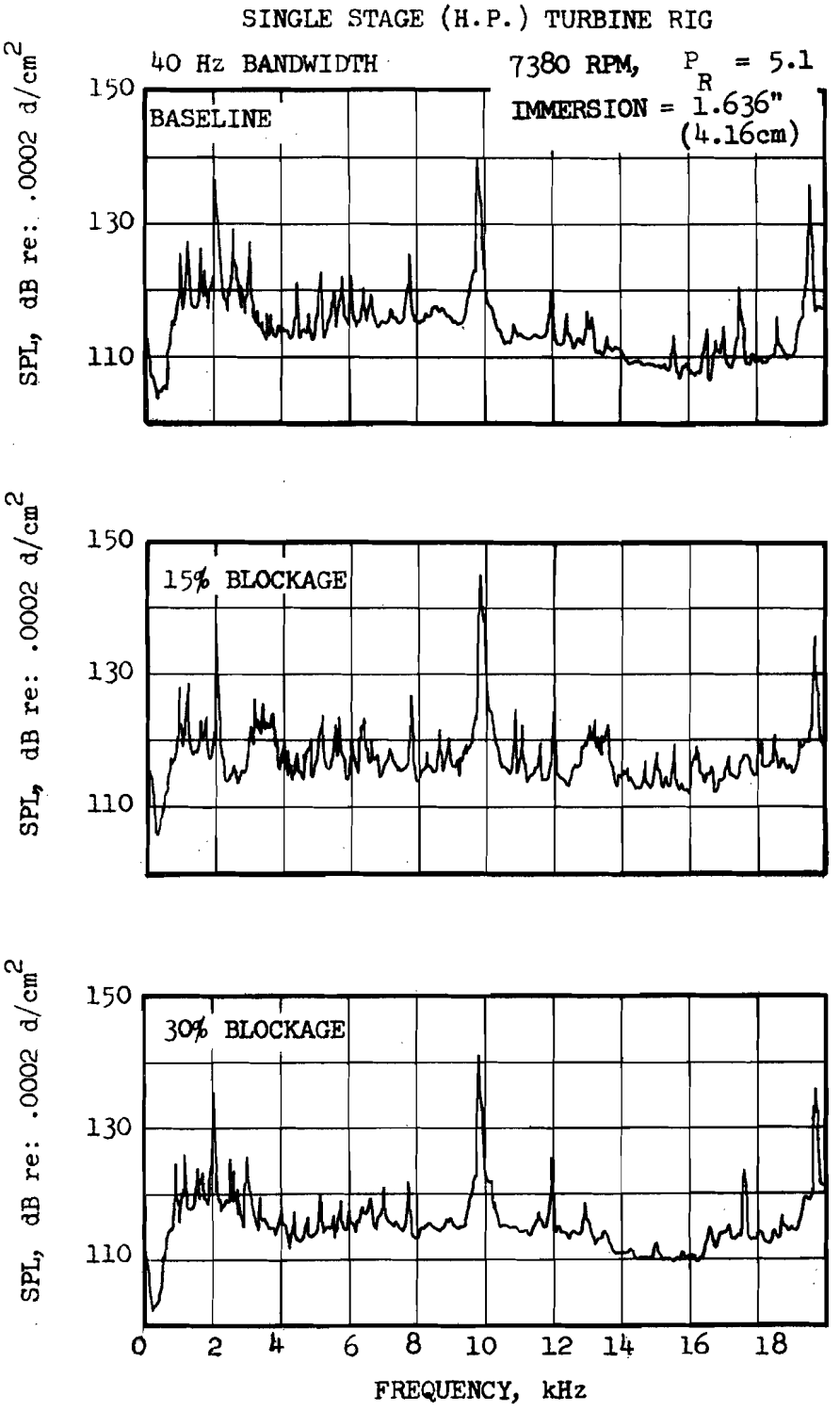

FIGURE 4.2.3-6 COMPARISON OF TYPICAL NARROWBAND SPECTRA FOR THE THREE CONFIGURATIONS (BASELINE, 15% BLOCKAGE, 30% BLOCKAGE).

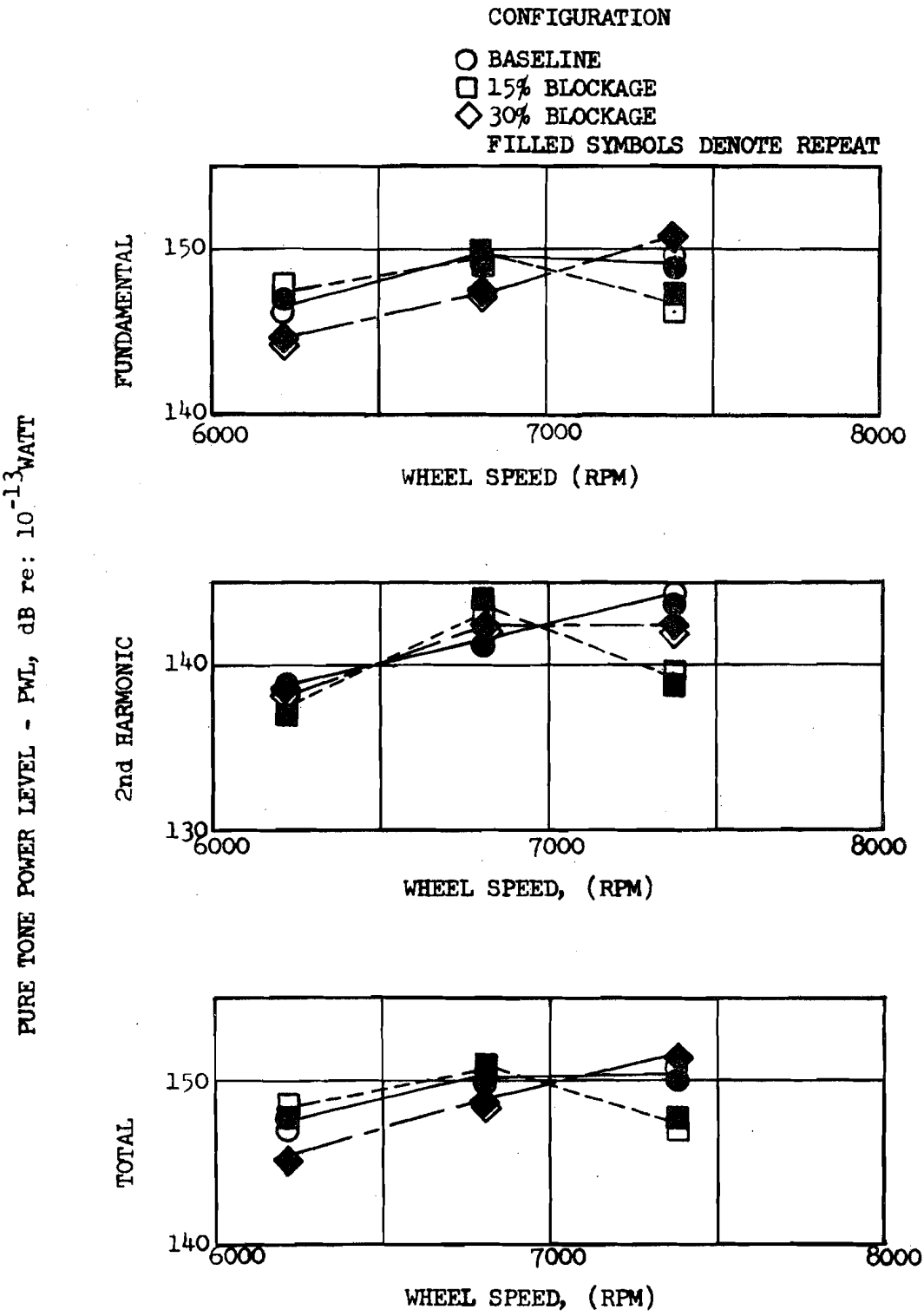

FIGURE 4.2.3-7 PWL VARIATION WITH WHEEL SPEED.

Table 4.2.3-1 Turbulence and Distortion Results - Baseline Configuration

Wheel Speed (RPM)	Immersion from Tip (inches)	Run $\frac{u'}{\bar{U}_{Local}}$ %	Run $\frac{v'}{\bar{U}_{local}}$ %	Run $\frac{\bar{U}_{local}}{\bar{U}_{mean}}$ %	Run $\frac{u'}{\bar{U}_{mean}}$ %	Repeat $\frac{u'}{\bar{U}_{local}}$ %	Repeat $\frac{v'}{\bar{U}_{local}}$ %	Repeat $\frac{U_{local}}{\bar{U}_{mean}}$ %	Repeat $\frac{u'}{\bar{U}_{mean}}$ %
6220	0.202	1.99	2.67	94.2	1.87	2.04	2.71	94.1	1.92
	0.501	2.54	2.82	97.4	2.47	2.57	2.80	97.4	2.50
	0.793	3.01	3.06	101.2	3.05	3.10	3.10	101.0	3.13
	1.080	3.05	3.45	103.5	3.16	3.13	3.41	103.7	3.25
	1.361	3.19	4.22	105.9	3.38	3.28	4.04	106.0	3.48
6810	0.202	2.07	2.77	93.9	1.94	-	-	-	-
	0.501	2.68	2.92	97.3	2.61	-	-	-	-
	0.793	3.03	3.03	101.4	3.07	-	-	-	-
	1.080	3.02	3.41	103.7	3.13	-	-	-	-
	1.361	3.01	4.04	106.0	3.19	-	-	-	-
7380	0.202	2.02	2.82	93.1	1.88	-	-	-	-
	0.501	2.63	2.92	96.6	2.54	-	-	-	-
	0.793	3.06	3.12	100.5	3.08	-	-	-	-
	1.080	3.07	3.40	103.9	3.19	-	-	-	-
	1.361	3.10	4.00	108.5	3.36	-	-	-	-

u' ∿ rms turbulent velocity-axial direction

v' ∿ rms turbulent velocity-circumferential direction

$\bar{U}_{local}$ ∿ local flow velocity - axial direction

$\bar{U}_{mean}$ ∿ weight flow averaged mean axial velocity

Table 4.2.3-2 Turbulence and Distortion Results - 15% Blockage

Wheel Speed (RPM)	Immersion From tip (inches)	Run $\frac{u'}{\bar{U}_{local}}$ %	Run $\frac{v'}{\bar{U}_{local}}$ %	Run $\frac{\bar{U}_{local}}{\bar{U}_{mean}}$ %	Run $\frac{u'}{\bar{U}_{mean}}$ %	Repeat $\frac{u'}{\bar{U}_{local}}$ %	Repeat $\frac{v'}{\bar{U}_{local}}$ %	Repeat $\frac{\bar{U}_{local}}{\bar{U}_{mean}}$ %	Repeat $\frac{u'}{\bar{U}_{mean}}$ %
6220	0.202	19.74	11.28	77.3	15.26	19.67	11.12	77.4	15.22
	0.501	11.54	5.94	98.8	11.40	11.64	5.86	98.8	11.50
	0.793	6.22	3.18	108.0	6.72	6.02	3.08	107.7	6.48
	1.080	4.18	2.80	110.7	4.63	4.08	2.84	110.8	4.52
	1.361	4.10	3.34	112.7	4.62	3.82	3.38	112.7	4.31
6810	0.202	19.96	11.26	77.2	15.41	19.80	10.96	77.5	15.34
	0.501	11.78	5.98	98.1	11.56	11.38	5.86	98.6	11.22
	0.793	6.20	3.10	108.0	6.70	6.06	3.07	107.5	6.51
	1.080	4.29	2.81	110.8	4.75	4.10	2.83	110.8	4.54
	1.361	3.84	3.40	113.5	4.36	3.77	3.29	113.0	4.26
7380	0.202	20.32	11.20	76.9	15.63	19.86	11.16	77.1	15.31
	0.501	11.54	5.94	98.4	11.36	11.54	5.86	99.0	11.42
	0.793	6.16	3.12	107.3	6.61	6.12	3.06	107.6	6.59
	1.080	4.16	2.77	111.0	4.62	4.12	2.74	110.6	4.56
	1.361	3.81	3.38	114.0	4.34	3.77	3.29	113.2	4.27

u' ∿ rms turbulent velocity - axial direction

v' ∿ rms turbulent velocity - axial - circumferential direction

$\bar{U}_{local}$ ∿ local flow velocity - axial direction

$\bar{U}_{mean}$ ∿ weight flow averaged mean axial velocity

Table 4.2.3-3 Turbulence and Distortion Results - 30% Blockage

Wheel Speed (RPM)	Immersion from tip (inches)	Run $\frac{u'}{\bar{U}_{local}}$ %	Run $\frac{v'}{\bar{U}_{local}}$ %	Run $\frac{\bar{U}_{local}}{\bar{U}_{mean}}$ %	Run $\frac{u'}{\bar{U}_{mean}}$ %	Repeat $\frac{u'}{\bar{U}_{local}}$ %	Repeat $\frac{v'}{\bar{U}_{local}}$ %	Repeat $\frac{\bar{U}_{local}}{\bar{U}_{mean}}$ %	Repeat $\frac{u'}{\bar{U}_{mean}}$ %
6220	0.202	41.46	21.60	52.6	21.81	40.70	21.45	53.0	21.57
	0.501	31.12	16.65	84.8	26.39	31.00	16.65	85.6	26.54
	0.793	21.47	10.80	115.0	24.69	21.51	10.82	114.8	24.69
	1.080	15.88	6.36	130.3	20.69	15.78	6.60	129.7	20.47
	1.361	13.13	6.06	134.3	17.63	12.16	6.01	133.6	16.25
6810	0.202	40.60	21.45	53.4	21.68	40.60	21.45	53.2	21.60
	0.501	31.60	17.16	84.7	26.76	31.60	16.99	84.3	26.64
	0.793	21.64	10.90	114.9	24.86	21.41	10.84	115.0	24.62
	1.080	15.92	6.62	130.3	20.74	15.76	6.30	130.2	20.52
	1.361	13.42	6.20	133.2	17.87	13.15	6.01	134.0	17.62
7380	0.202	40.58	21.26	53.5	21.71	41.10	21.28	53.0	21.78
	0.501	31.50	16.90	84.3	26.55	31.30	17.00	85.1	26.64
	0.793	21.06	10.59	116.0	25.06	21.54	10.84	115.0	24.77
	1.080	15.81	6.74	129.4	20.46	15.69	6.62	129.8	20.34
	1.361	13.30	6.08	133.4	17.74	13.06	6.13	133.9	17.49

$u' \sim$ rms turbulent velocity - axial direction

$v' \sim$ rms turbulent velocity - circumferential direction

$\bar{U}_{local} \sim$ local flow velocity - axial direction

$\bar{U}_{mean} \sim$ weight flow average mean axial velocity

Table 4.2.3-4 Average Turbulence and Velocity Profiles

Immersion From tip (in.)	Baseline $\frac{u'}{\bar{U}_{local}}$	Baseline $\frac{u'}{\bar{U}_{mean}}$	Baseline $\frac{\bar{U}_{local}}{\bar{U}_{mean}}$	15% Blockage $\frac{u'}{\bar{U}_{local}}$	15% Blockage $\frac{u'}{\bar{U}_{mean}}$	15% Blockage $\frac{\bar{U}_{local}}{\bar{U}_{mean}}$	30% Blockage $\frac{u'}{\bar{U}_{local}}$	30% Blockage $\frac{u'}{\bar{U}_{mean}}$	30% Blockage $\frac{\bar{U}_{local}}{\bar{U}_{mean}}$	Immersion From tip (cm.)
0.202	2.03	1.90	93.8	19.89	15.36	77.2	40.84	21.69	53.1	.513
0.501	2.60	2.53	97.2	11.57	11.41	98.6	31.35	26.59	84.8	1.273
0.783	3.05	3.08	101.0	6.13	6.60	107.7	21.44	24.78	115.1	2.014
1.080	3.08	3.18	103.7	4.16	4.60	110.8	15.81	20.54	130.0	2.743
1.361	3.14	3.35	106.6	3.85	4.36	113.2	13.04	17.43	133.7	3.457

4.2.4 Discussion of Results

Significant changes in the pure tone power levels, between configurations, are not evident (Figure 4.2.4-1). The differences that were measured are within the range of data scatter for the tests, considering that there was a vehicle/instrumentation teardown and reassembly between tests. Not only was the pure tone noise unaffected, but the broadband noise was also within normal data scatter, as may be seen from examination of the narrow band spectra (Figure 4.2.3-2 through -16).

The Mach number change through the turbine is illustrated in Figure 4.2.4-2. As indicated in the figure, the flow through the nozzle vanes is choked. Any radial weight flow (velocity) distortion entering the nozzles is attenuated by the choked section. Inlet velocity profiles are not transmitted and therefore do not interact with the rotor.

When the mean velocity of a turbulent flow is increased, the turbulence intensity ($u'/\bar{U}$) decreases because of the increase in the mean velocity, $\bar{U}$, and because of the readjustment of the turbulent components which takes place when the mean flow conditions change (Reference 4.2.4-1).

For this test, however, the inlet turbulence was varied, not the parameters which influence turbulence decay or growth, and therefore, the turbulence intensity variations in the turbine nozzle inlet may affect the turbulence levels at the rotor inlet plane. If turbulence - rotor interaction were the only noise source, the predicted change in this noise level (based on the turbulence ratios measured in the inlet) would be 13 dB between baseline and the 15% blockage configuration and 18 dB between baseline and the 30% blockage configuration (Reference 4.2.4-2).

This level of change is not evident in the test results so that either turbulence - rotor interaction is not a significant noise source as compared to others such as viscous wake interaction, or the effect of inlet turbulence variation on the total flow turbulence entering the rotor blades is negligible.

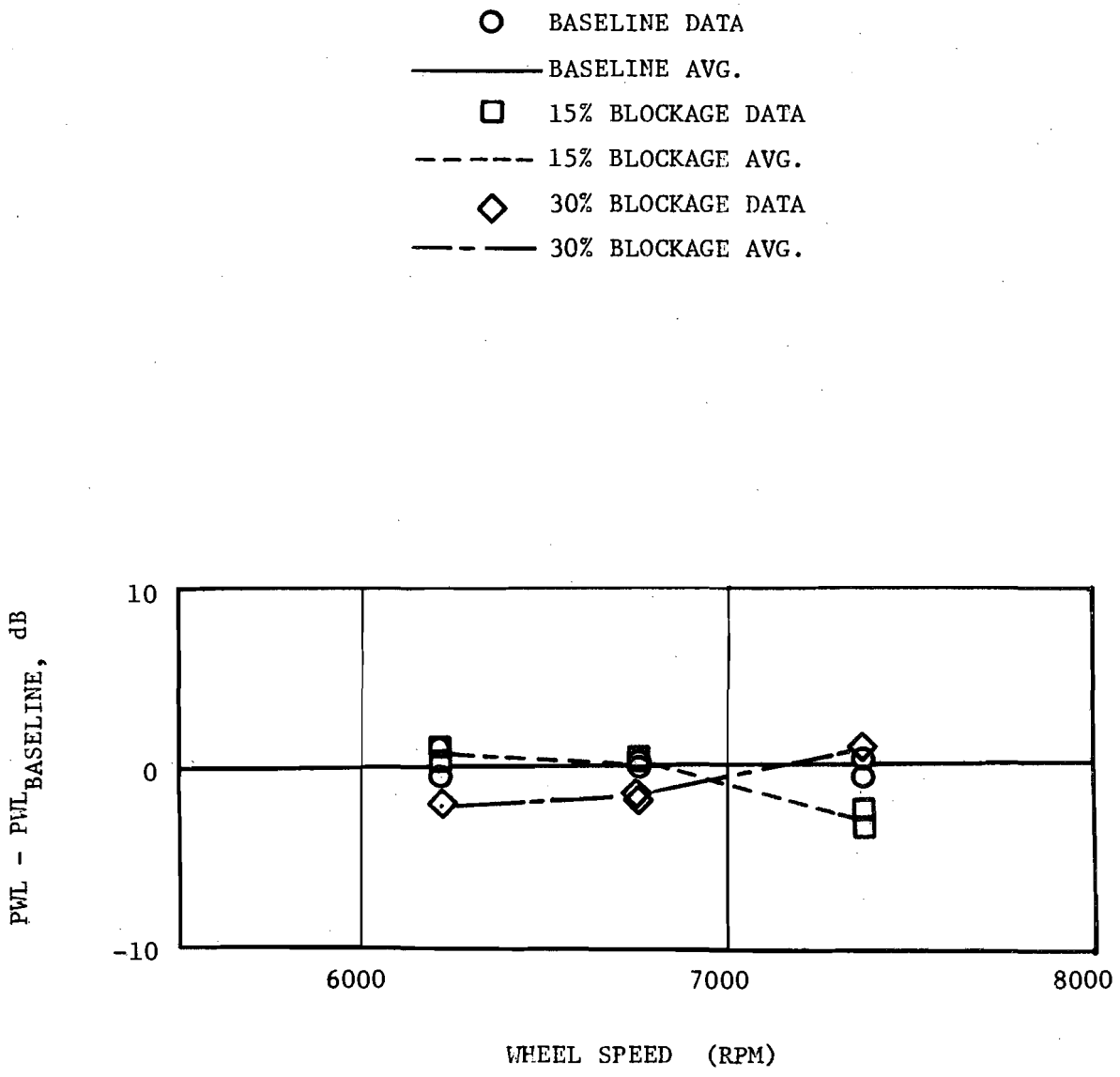

FIGURE 4.2.4-1 CHANGE IN PURE TONE PWL WITH INLET TURBULENCE AND DISTORTION

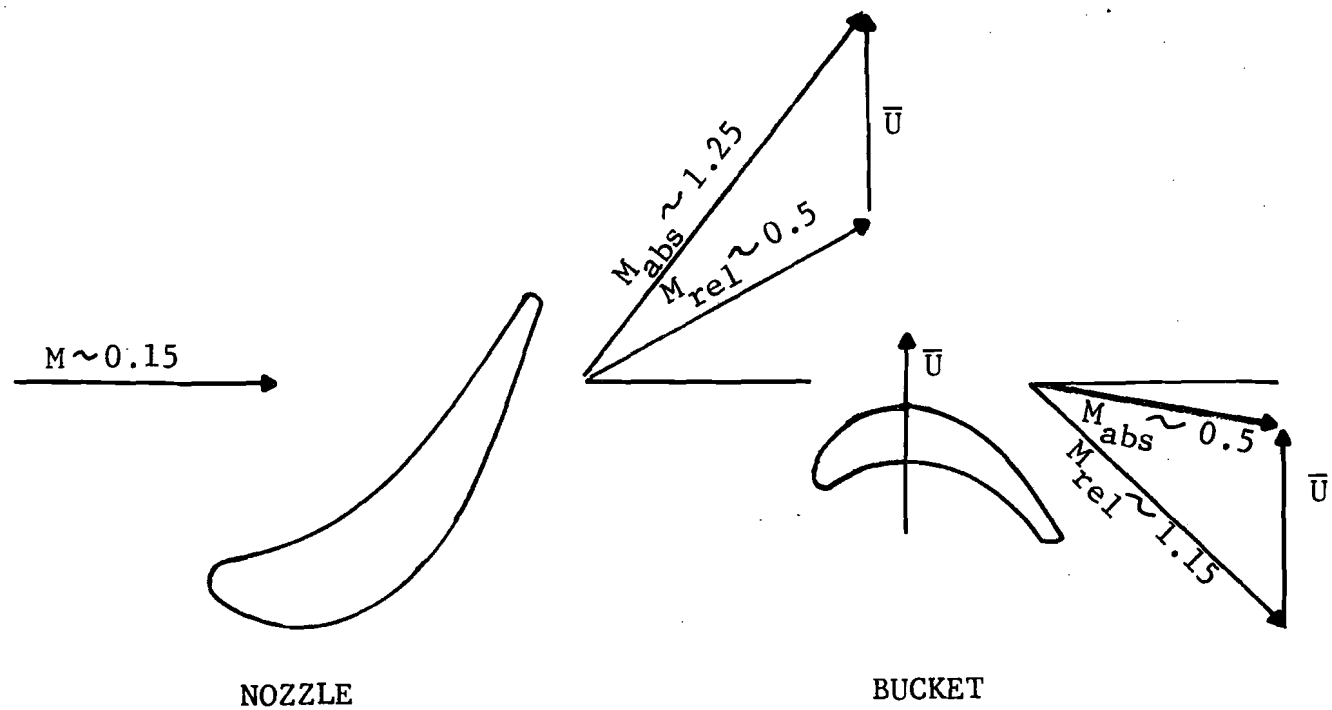

FIGURE 4.2.4-2 SCHEMATIC OF FLOW THROUGH TEST TURBINE

4.2.5 Conclusions

Inlet turbulence and distortion does not affect the noise generation of a high pressure turbine operating with a choked nozzle. Consequently, analytical predictions based on aerodynamic design data, and acoustic data from component testing are directly applicable to the turbine in an engine environment.

Adjustments to predictions or to component data may be necessary for turbines operating with nozzle pressure ratios less than choked that may permit inlet distortions to be transmitted through the turbine nozzles and affect the aerodynamics of the flow entering the rotor. Analytical predictions of the change in noise generation with distortion should be used in such cases until acoustic data becomes available defining these effects.

4.3 THREE STAGE (LOW PRESSURE) TURBINE TESTS

4.3.1 Objectives/Background

These tests were carried out in order to provide the following needed information:

- Basic relationships between low pressure (L.P.) turbine noise generation and the pertinent aerodynamic performance parameters.
- Data to check the analytical prediction method.
- Data on the effect of increased blade row axial spacing on noise levels.

As has been mentioned earlier, there is very little data available as to the effect of the various performance parameters like the pressure ratio and speed on the noise generated by turbines. The Air Turbine Facility described in Section 4.2 lends itself to such a parametric investigation because of the capability of varying pressure ratio and speed independently.

The tests provided clean, uncontaminated turbine noise data which was used to refine and extend the analytical prediction program for turbine discrete frequency (pure tone) noise. Extensive cascade and turbine aerodynamic performance data available from earlier test added to the usefulness of this particular machine. These data are required for the analytical prediction scheme and would also be essential in formulation of semi-empirical correlations for the noise generated.

The source reduction techniques devised from fan/compressor studies were expected to be applicable to turbine noise suppression. Because of the similarities between the noise generation mechanisms used to model turbine and fan/compressor noise.

As discussed in Reference 4.3.1-1, there are two major types of turbomachinery noise generation mechanisms: rotor alone noise and interaction noise. Rotor alone noise arises from the rotating pressure field attached to the rotor blades; interaction noise is generated by the mutual disturbance of the pressure fields of adjacent blade rows (potential interaction), and by the impingement of the viscous wakes produced by the upstream blade row on the downstream blades (viscous wake interaction) which causes a fluctuation in the blade loading (pressure field). When the rotor tip Mach numbers are less than one, the rotor alone noise generally does not propagate.

Increasing the axial spacing between adjacent blade rows has resulted in significant noise reductions in fan or compressor applications (References 4.3.1-2 and -3). The increased axial spacing essentially eliminates noise from the interaction of the pressure fields of the two adjacent blade rows and greatly reduces the viscous wake interaction noise.

Typical theoretical results (Reference 4.3.1-1) of the effect of axial spacing on the noise generation and the relative levels of the mechanisms discussed previously are presented in Figure 4.3.1-1.

The noise generated by turbomachinery is a function of the blading aerodynamics. The effect of spacing is therefore expected to vary from one turbine to the next and for single stage and multi-stage turbines, since considerable difference is encountered between the velocity triangles. The design differences between high pressure and low pressure (fan) turbines can also be significant determinants of the noise generation. An acoustic investigation of a high pressure turbine has already been conducted on a rig to study the effect of spacing (Reference 4.2.2-2). The same rig was used for the turbulence tests of section 4.2 and a schematic of a spaced configuration is provided in Figure 4.3.1-2. The results are summed up in Figure 4.3.1-3. The initial drop off in turbine tone power level (PWL) was about 20 log (spacing/chord) falling to about 10 log (spacing/chord) beyond spacing/chord $\simeq 0.5$. The suppression was accompanied by a significant drop in turbine efficiency.

The analysis described in Reference 4.2.2-1 incorporates the capability of predicting the noise reduction due to spacing and was used to define a maximum suppression configuration for the 3 stage low pressure turbine rig. The 3 stage turbine test provided not only data about the effects of spacing on noise generation by a multi-stage low pressure turbine but also the effect on the efficiency, that is, the trade-off involved.

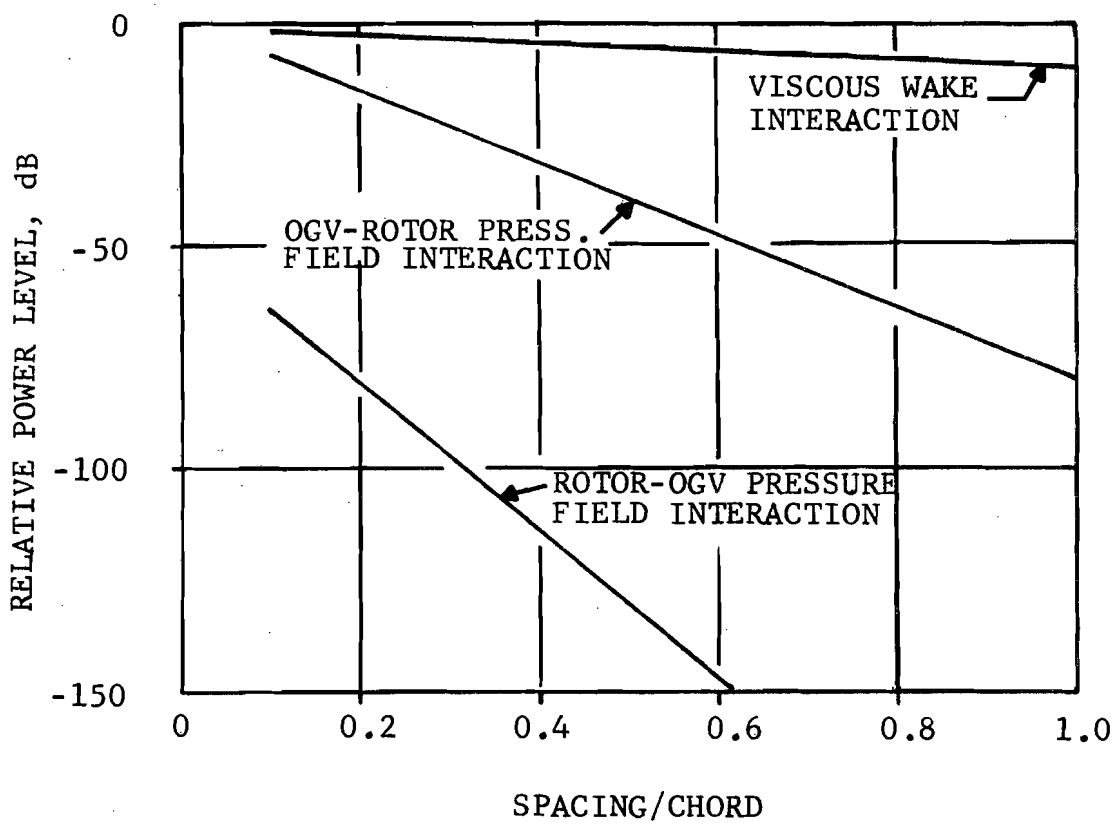

FIGURE 4.3.1-1 THEORETICAL EFFECT OF SPACING ON VISCOUS WAKE AND POTENTIAL INTERACTIONS (REFERENCE 4.3.1-2)

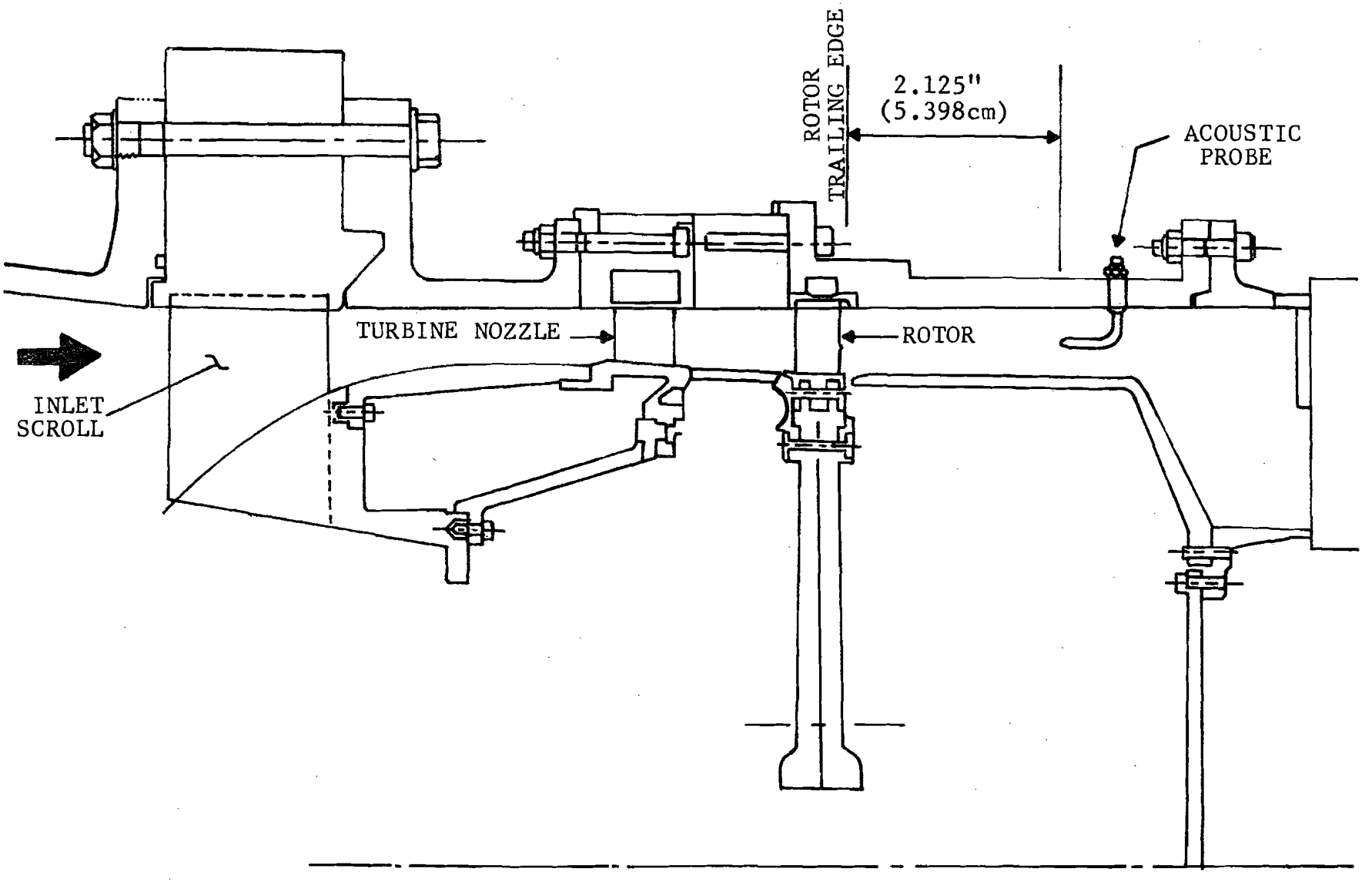

FIGURE 4.3.1-2 SCHEMATIC OF SINGLE STAGE TURBINE RIG WITH OPENED BLADE ROW SPACING (s/c = 1.3)

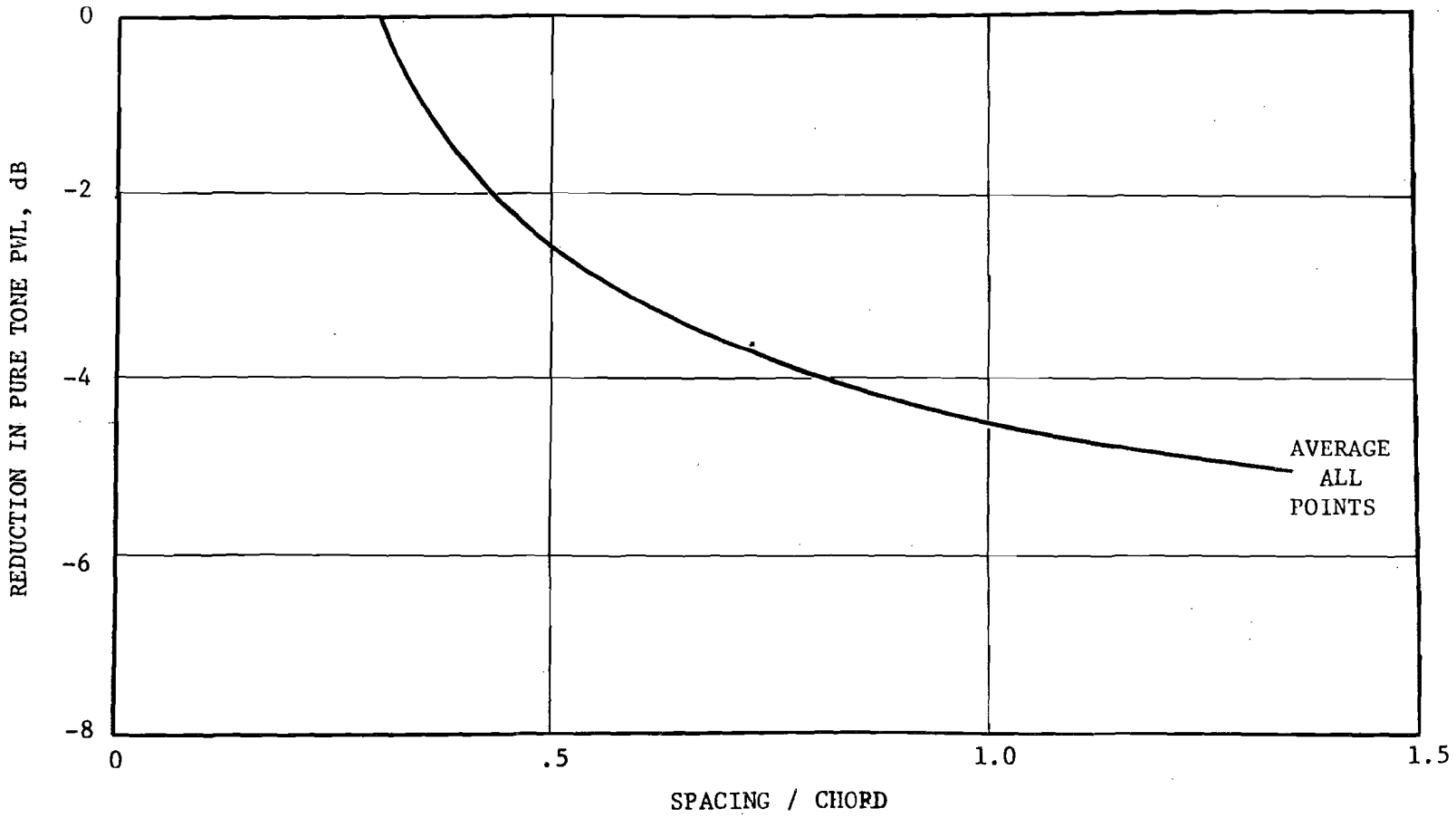

FIGURE 4.3.1-3 AVERAGE EFFECT OF SPACING ON TURBINE PURE TONE PWL FOR THE SINGLE STAGE TURBINE RIG

4.3.2 Facility Description

The 3 stage low pressure turbine rig was run at the Air Turbine Facility described in detail in Section 4.2.2.

The machine is the NASA 3 stage, highly loaded multi-stage fan turbine (HLMSFT) designed for projected future high bypass ratio aircraft engine application. Some basic design data are provided in Table 4.3.2-1. Greater details may be found in Reference 4.3.2-1. Two configurations were tested: a baseline and a spaced rig. The spacing, 1 inch (2.54 cm.) was introduced on either side of the second stage rotor and between the third stage rotor and nozzle, as is shown in Figure 4.3.2-1. The spacing to chord ratios for the two configurations are provided in Table 4.3.2-2.

Five fixed probes immersed to equal areas in the turbine exhaust were used to measure the acoustic levels. The immersions and locations are given in Table 4.3.2-3. The probes and the data acquisition system is as described in Section 4.2.2.

The aerodynamic performance data was obtained as described in Reference 4.2.2-1.

The test was run with the inlet temperature held constant at 700° R (389° K) and the inlet pressure at 30 psia (206850 N/m^2). At each pressure ratio, the turbine speed was varied over the operating range indicated by the aerodynamic performance mapping.

4.3.3 Test Results

The test matrix followed is given in Table 4.3.3-1. Data was recorded for 21 different settings for pressure ratios (total-to-static, P_{T_o}/P_{S_2}) ranging from 1.75 to 4.1 (design P_{T_o}/P_{S_2} = 3.83) and speeds from 60% to 120% of design value (N). For each configuration, repeat points were recorded for all pressure ratios except 2.6; giving a total of 38 data points in each instance.

Since the aerodynamic rakes from the exhaust were removed for the acoustic tests, the turbine efficiency was based on static pressure pickups in the casing wall. The efficiencies so obtained were compared to those determined with total pressure probes during the aerodynamic performance tests for the baseline configuration and found to be in good agreement. The efficiency figures presented herein for the effect of the increased spacing on the performance are therefore considered reliable. The variation of the turbine efficiency with the pressure ratio for speeds of 80, 100 and 120% design speed is given in Figure 4.3.3-1. The effect of the spacing on the efficiency is shown in Figure 4.3.3-2. The efficiency fell by about 0.3%, at design point but actually registered a gain at extreme off-design conditions (at low pressure ratios and speeds). The largest efficiency decrease (0.4%) resulted for P_{T_o}/P_{S_2} = 3.4 and 120% N. A gain of about 0.4% resulted at P_{T_o}/P_{S_2} = 1.75 and 60 and 70% N.

INTERACTION	BASELINE (S/C)t	SPACED (S/C)t
N2-R2	.19	.83
R2-N3	.32	1.143
N3-R3	.29	.89

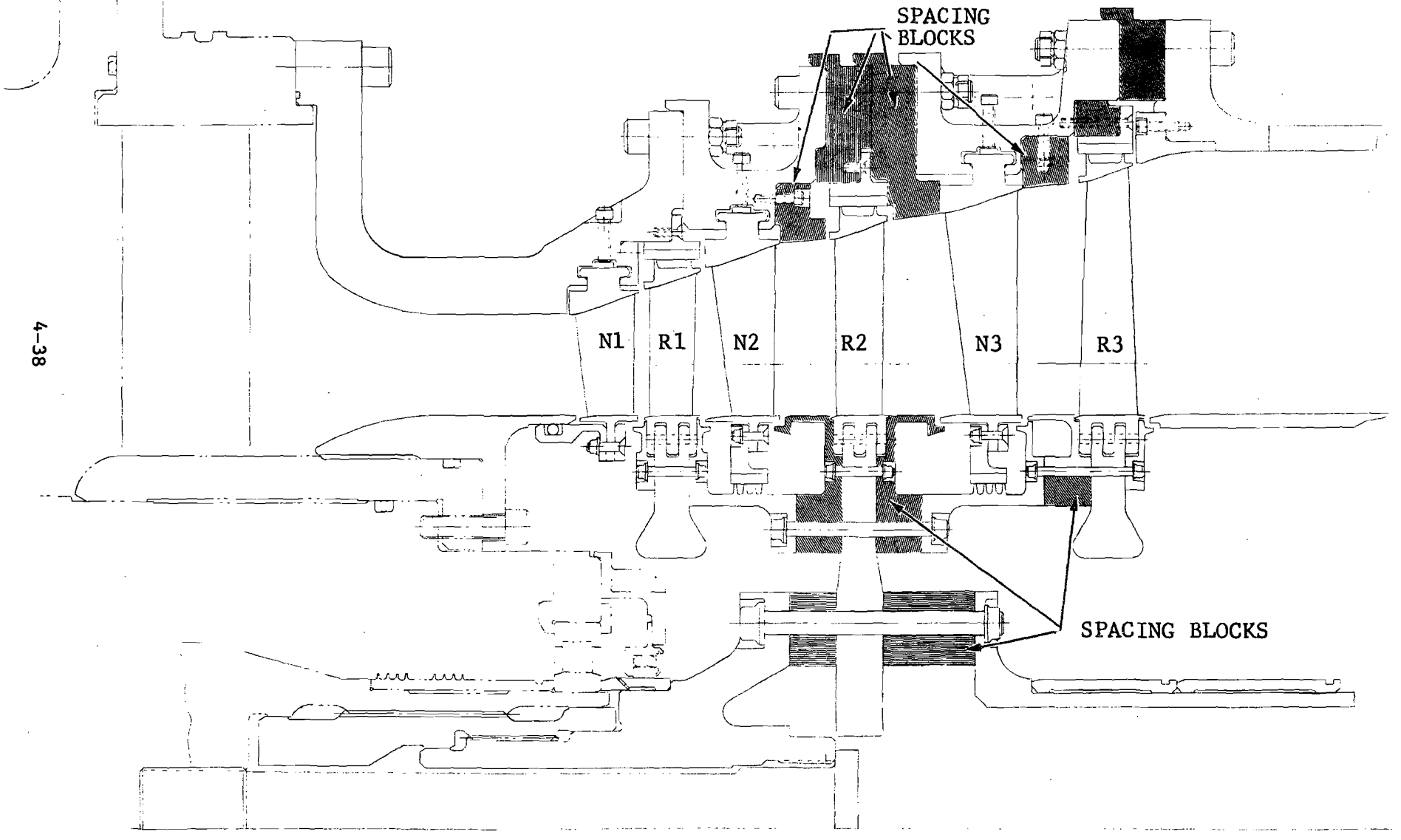

FIGURE 4.3.2-1 3-STAGE TURBINE SHOWING THE INCREASED SPACING

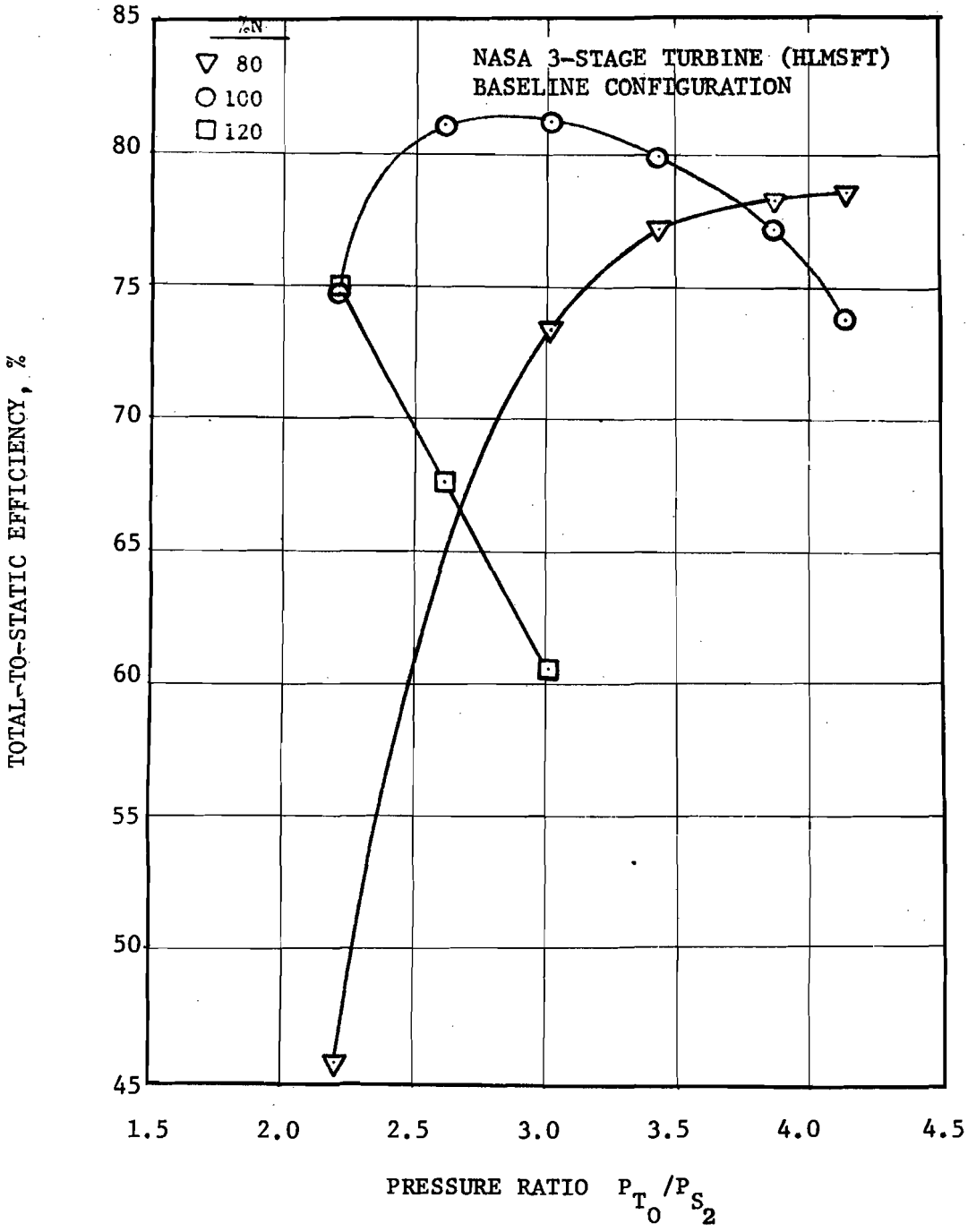

FIGURE 4.3.3-1 VARIATION OF THE TURBINE EFFICIENCY WITH PRESSURE RATIO, BASELINE CONFIGURATION

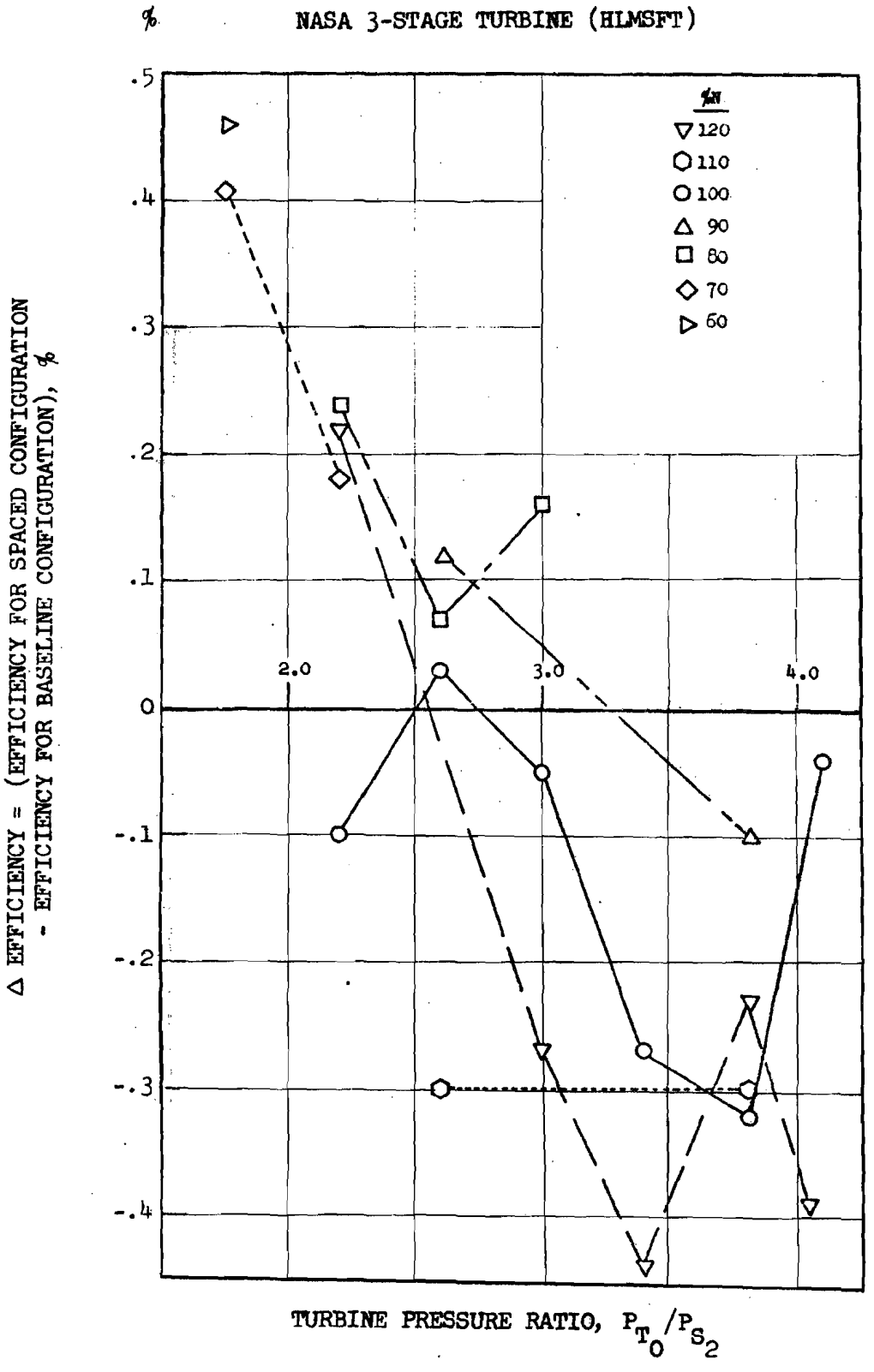

FIGURE 4.3.3-2 EFFECT OF SPACING ON THE TURBINE EFFICIENCY.

TABLE 4.3.2-1

NASA 3-STAGE TURBINE RIG

BASIC TURBINE DATA AT DESIGN

Average Pitch Loading, $\frac{gj\Delta h}{2\Sigma U_P^2}$	1.5
Equivalent Specific Work, E/θ_{cr}	33.0 Btu/lb (76753 J/kg)
Equivalent Rotative Speed, $N/\sqrt{\theta_r}$	3169.0 rpm
Equivalent Weight Flow, $W\sqrt{\theta_{cr}}\ \varepsilon/\delta$	28.0 lb/sec (12.7 kg/sec)
Inlet Swirl Angle	0 degrees
Exist Swirl Angle without Guide Vanes	$\leq$ 5 degrees
Maximum Tip Diameter	28.4 inches (72.1 cm)
Number of Stages	3
$W\sqrt{T_T}/P_T$ at inlet	43.16
$\Delta h/T_T$	0.0635
$N/\sqrt{T_T}$	138.98

Design Parameters	Stage 1	Stage 2	Stage 3
Pitch Loading, $\frac{gJ\Delta h}{2U_p^2}$	2.07	1.76	0.85
Exit Axial Mach No.	0.424	0.459	0.407
Exit Absolute Mach No.	0.593	0.602	0.408
Exit Swirl Angle (Degrees)	44	40	3
Number of Blades	106	102	112
Number of Vanes	64	108	100
Tip Speed (Ft/Sec)	384	418	456
Blade Row Spacing $(S/\ell)_p$	.237	.258	.298

s: Axial Spacing Between Blade Rows ℓ: Nozzle Chord Length

TABLE 4.3.2-2

NASA 3-STAGE TURBINE-SPACING/CHORD RATIOS

Interaction	Spacing/Upstream Chord (s/l)					
	Baseline			Spaced		
	Tip	Pitch	Hub	Tip	Pitch	Hub
N1R1	.192	.237	.281	.192	.237	.281
R1N2	.314	.598	.919	.314	.598	.919
N2R2	.186	.258	.373	.829	1.041	1.382
R2N3	.315	.590	.914	1.143	1.512	1.918
N2R3	.291	.298	.311	.886	1.026	1.252

TABLE 4.3.2-3

NASA 3-STAGE TURBINE - PROBE LOCATIONS AND IMMERSIONS

Channel		Probe	Circumferential Location* In Degrees Clockwise From TDC	Immersion From Outer Housing	
Unfiltered	Filtered			(in.)	(cm.)
1	6	A	350°	4.909	12.47
2	7	B	62°	3.625	9.21
3	8	C	134°	2.477	6.29
4	9	D	206°	1.430	3.63
5	10	E	278°	0.460	1.17

*AFT Looking Forward
Probe Stem is located 8.5 in. (21.6 cm.) aft of the turbine blading.

TABLE 4.3.3-1

3-STAGE TURBINE - TEST MATRIX

%N	N (rpm)	Total-To-Static Pressure Ratio P_{T_o}/P_{S_2}						
60	2206	1.75						
70	2574	1.75	2.2					
80	2942		2.2	2.6	3.0			
90	3309			2.6			3.83	
100	3677		2.2	2.6	3.0	3.4	3.83	4.1
110	4045			2.6			3.83	
120	4412		2.2		3.0	3.4	3.83	4.1

P_{T_o} = 30 psia (206850 N/m^2)

T_{T_o} = 700° R (389° K)

The procedure used to reduce the acoustic data was as follows:

- Narrowband spectral analysis from 0 to 20 kHz (40 Hz bandwidth) of selected points to determine the relative energy content in the fundamental and second harmonic of the tones.

- Since the second harmonic was found to be significantly (>6 dB) lower than the fundamental, the remaining data points were reduced using a 20 Hz bandwidth from 0 to 10 KHz. The 20 Hz bandwidth permitted discrimination between the first and second stage BPF's which were closely spaced in the spectrum.

- Calculation of the acoustic power level for the fundamental using an area-weighted SPL. The measurements were corrected for the flow as explained in Appendix E:

$$PWL = \sum_{n=1}^{5} \{SPL_n + C_n + \log_{10} \left(\frac{\Delta A}{144}\right)_n + 10 \log_{10} K$$

$$+20 \log_{10} (1 + \cdot 707M) + 10 \log_{10} \left(\frac{\sqrt{t_s}}{519} \cdot \frac{14-69}{P_s}\right)\} \qquad (4.3.3\text{-}1)$$

where PWL = acoustic power level, dB re 10^{-13} Watt.

SPL = sound pressure level, dB re .0002 dynes/cm^2

C = frequency response correction (including viscous losses), dB

P_s = static pressure at probe, psia

t_s = static temperature at probe, ° R

M = Mach number

ΔA = immersion area, sq. in.

K = constant .891

The flow corrections were essential in order that the absolute noise levels could be used for comparison with the analytical predictions, as well as to form correlations.

A typical narrowband spectrum for the baseline configuration is given in Figure 4.3.3-3 showing the fundamentals for all three stages. The typical effect of varying speed at constant pressure ratio is demonstrated in Figure 4.3-4. The variation of PWL with the pressure ratio at constant speed is shown in Figure 4.3.3-5.

The effect of the opened blade row spacing on the narrowband spectrum is shown in Figure 4.3.3-6. The trends with pressure ratio are compared for the two configurations in Figure 4.5.3-7. The noise reduction (Δ) achieved for each stage is summarized in Figure 4.3.3-8.

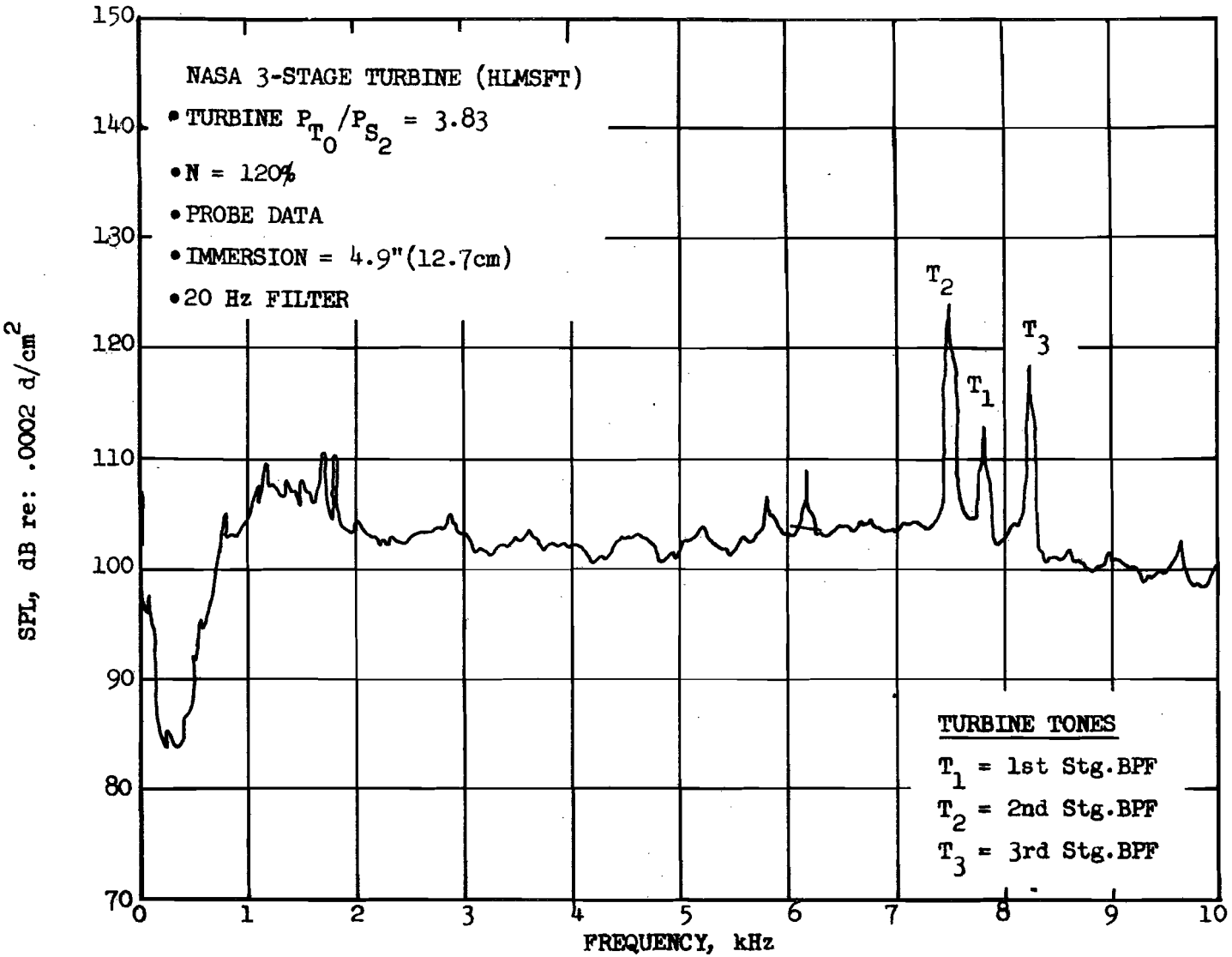

FIGURE 4.3.3-3 TYPICAL NOISE SPECTRUM FOR THE 3-STAGE TURBINE, BASELINE CONFIGURATION.

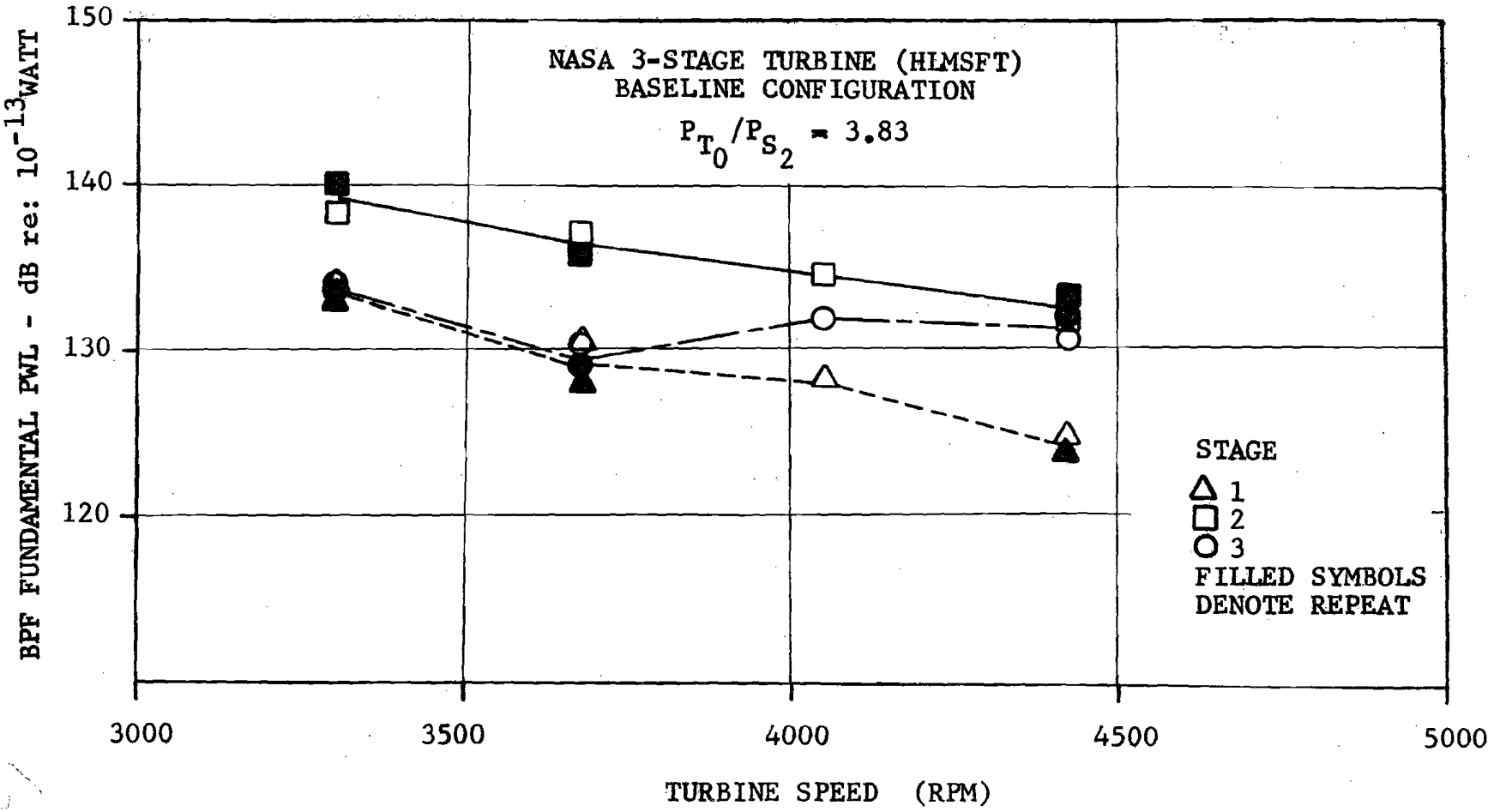

FIGURE 4.3.3-4 VARIATION OF TONE PWL WITH TURBINE SPEED

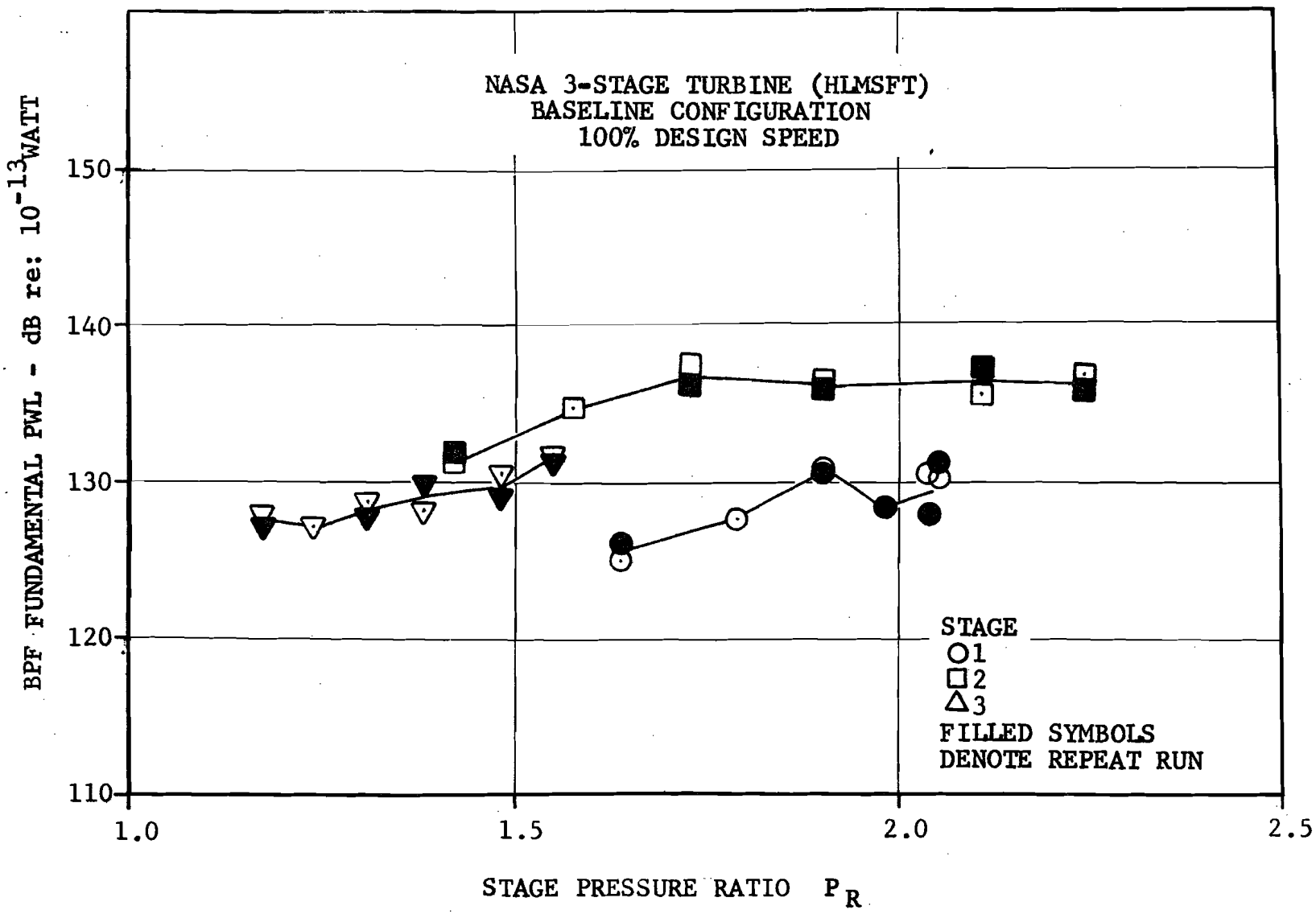

FIGURE 4.3.3-5 VARIATION OF TONE PWL WITH STAGE PRESSURE RATIO

4.3.4 Discussion of Results

Two trends are visible from Figures 4.3.3-1 -4 and -5 despite some data scatter: the tone PWL increases with the pressure ratio at constant speed and decreases with the wheel speed at constant pressure ratio. The latter trend may seem anomalous, in view of engine experience where noise increases with the engine speed. An engine runs on an operating line however, and the increasing speed is coupled to increasing power requirements and therefore to higher pressure ratios. The two effects cannot be separated in an engine. On the turbine rig, holding the pressure ratio constant corresponds to a constant work extraction, and increasing the wheel speed then results in reduced relative velocities and blade turning requirements and the lower noise generation follows. A similar effect was noted for fan discrete frequency noise (Reference 4.3.1-2).

The trends with pressure ratio and wheel speed suggest using the loading as a correlating parameter as is shown by Figure 4.3.4-1 for the third stage data. While an overall trend is evident however, the data scatter indicates that the loading cannot be the independent parameter. The loading is strongly dependent on the stage efficiency but may be less strongly dependent on the noise generated. It is also interesting that the entire set of data for the third stage may be collapsed by means of the pressure ratio, in the form of ideal work extraction, and the wheel speed (Figure 4.3.4-2). The correlating parameter is the ideal (isentropic) work extraction $[C_p(T_{in}-T_{out})]$ normalized by the initial enthalpy $[C_p\ T_{in}]$, where C_p is the coefficient of specific heat at constant pressure.

$$\frac{\Delta T}{T_{in}} = \frac{T_{in}\ T_{out}}{=[1-(\frac{1}{P_R})\ \frac{\alpha-1}{\alpha}]} \qquad (4.3.4\text{-}1)$$

where P_R = pressure ratio and γ = ratio of specific heats.

The subscript 0 is used for the inlet and 2 for the exit conditions hereon.

The relationship in Figure 4.3.4-2 may be expressed as:

$$PWL = 12\log_{10}(\frac{\Delta T}{T}) - 20\log_{10} U_T + \text{constant} \qquad (4.3.4\text{-}2)$$

where PWL = BPF fundamental acoustic power level, dB re 10^{-13} watt

and U_T = blade tip speed, ft/sec.

$(\frac{\Delta T}{T})$ is given by equation (4.3.4-1) where P_R is the stage total-to-static pressure ratio (P_{T_o}/P_{S_2}).

Only the third stage data were used in the correlation because of the uncertainties of the blade row attenuation on the other two stages.

Figure 4.3.3-6 shows narrowband spectra overlays for the two configurations: the blade row spacing yielded substantial reduction not only for the second and third stage tones but also for the "vortex" broadband type noise at the base of the tones. The added spacing did not, however, significantly alter the discrete frequency noise generation trends, as is demonstrated, for example by the PWL versus pressure ratio plots of Figure 4.3.3-7. The average noise reduction (Δ) achieved for the tones can be found on Figure 4.3.3-8 which provides Δ as a function of the pressure ratio for the 80, 100 and 120% speeds. Some scatter about the baseline noise levels is observed for the first stage, suggesting some effect of spacing in the downstream rows is propagating upstream. The mean Δ is a negligable 0.2 dB however, which is as expected since this stage did not involve any configuraion changes. The additional 2 inches (5.08 cm.) of spacing in the second stage resulted in a noise reduction of about 9 dB. The reduction was higher than had been predicted by the analysis (see Section 4.4).

The mean noise reduction resulting from the 1 inch (2.54 cm.) of added spacing in the third stage was about 3 dB.

The Δ's at the design point are given in Table 4.3.4-1 and are 8.7 dB for the second stage BPF fundamental and 3.1 dB for the third stage. These values correspond roughly (keeping in mind the discussion in the above paragraph) to a 10 log (s/l) relationship, where s is the spacing and l the chord of the upstream blading. The (s/l) values for the two configurations are provided in Figure 4.3.2-2. Hence a realistic value to be used for predicting tone PWL reduction with spacing is 3 dB per doubling. Smith and Bushell (Reference 4.3.4-1) had suggested using 6 dB per doubling till data became available as to the actual effect.

The spacing results in some loss in efficiency (at design point for example, the value decreased by 0.3%). The effect, however, is minimal, and at the lower pressure ratios (below 2.6) the efficiency actually increased (Figure 4.3.3-2), despite the step introduced in the outer flowpath by the spacers. Little can be done to eliminate the increased wall scrubbing losses due to the increased spacing. The losses would be lower, however, if the flowpath were smooth and if the turbine were designed for the unguided turning arising from the increased spacing in order to eliminate the mismatched incidence angles at the downstream blade row,

4.3.5 Conclusions

The three stage turbines tests demonstrated the following.

- For a multi-stage fan turbine, the pure tone PWL increases with pressure ratio for constant speed, and decreased with increasing speed for constant pressure ratio.

TABLE 4.3.4-1

THREE STAGE TURBINE NOISE GENERATION AT DESIGN POINT

(P_{T_o}/P_{S_2} = 3.83, N - 3677 RPM)

Stage	BPF Fundamental PWL Baseline Configuration (dB re 10^{-13} Watt)	Noise Reduction Due to Spacing (dB)	Additional Spacing (in.)	(cm.)
1	129.3	.3	0	0
2	136.5	8.7	2	5.08
3	129.6	3.1	1	2.54

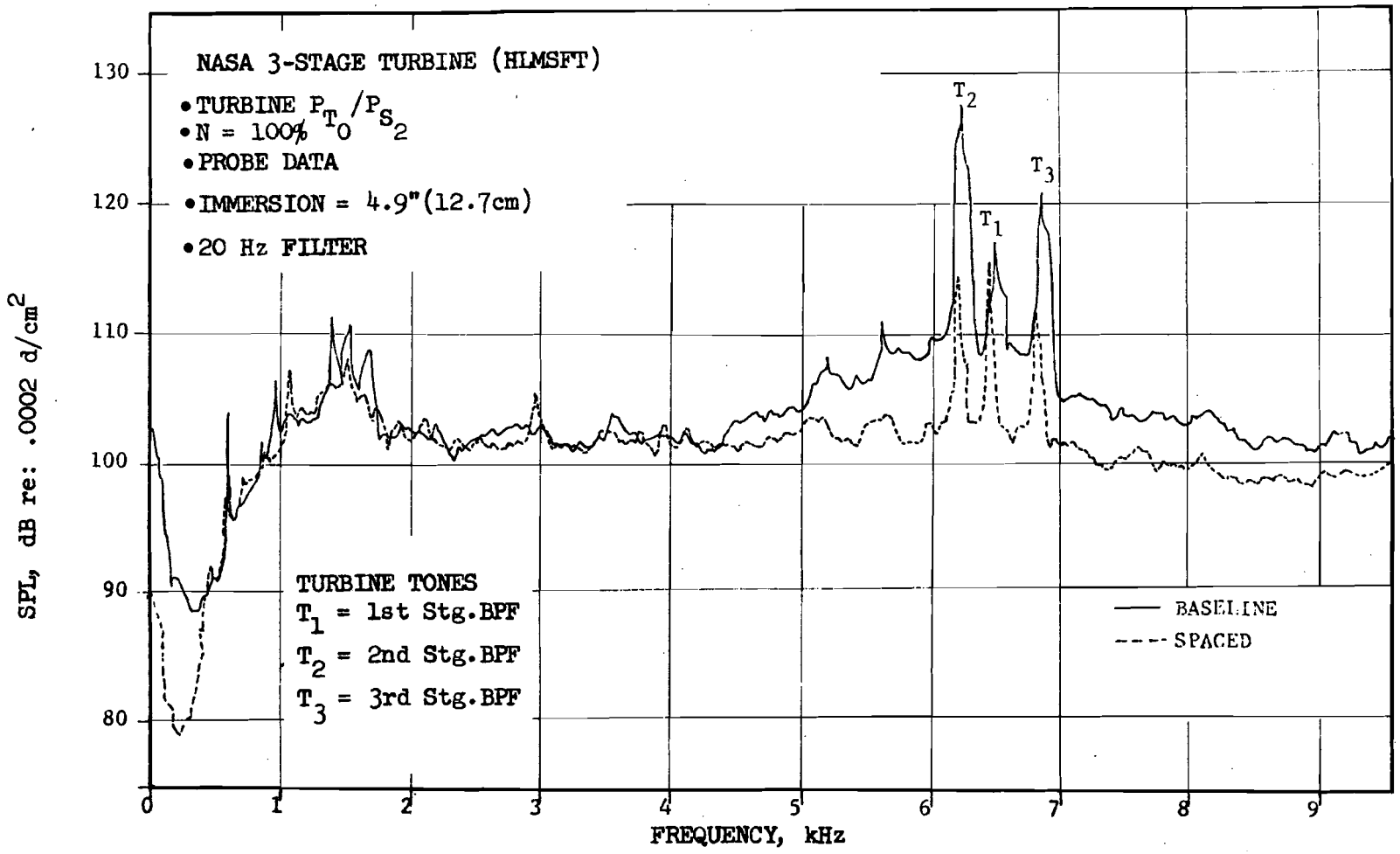

FIGURE 4.3.3-6 EFFECT OF SPACING ON TONE LEVELS.

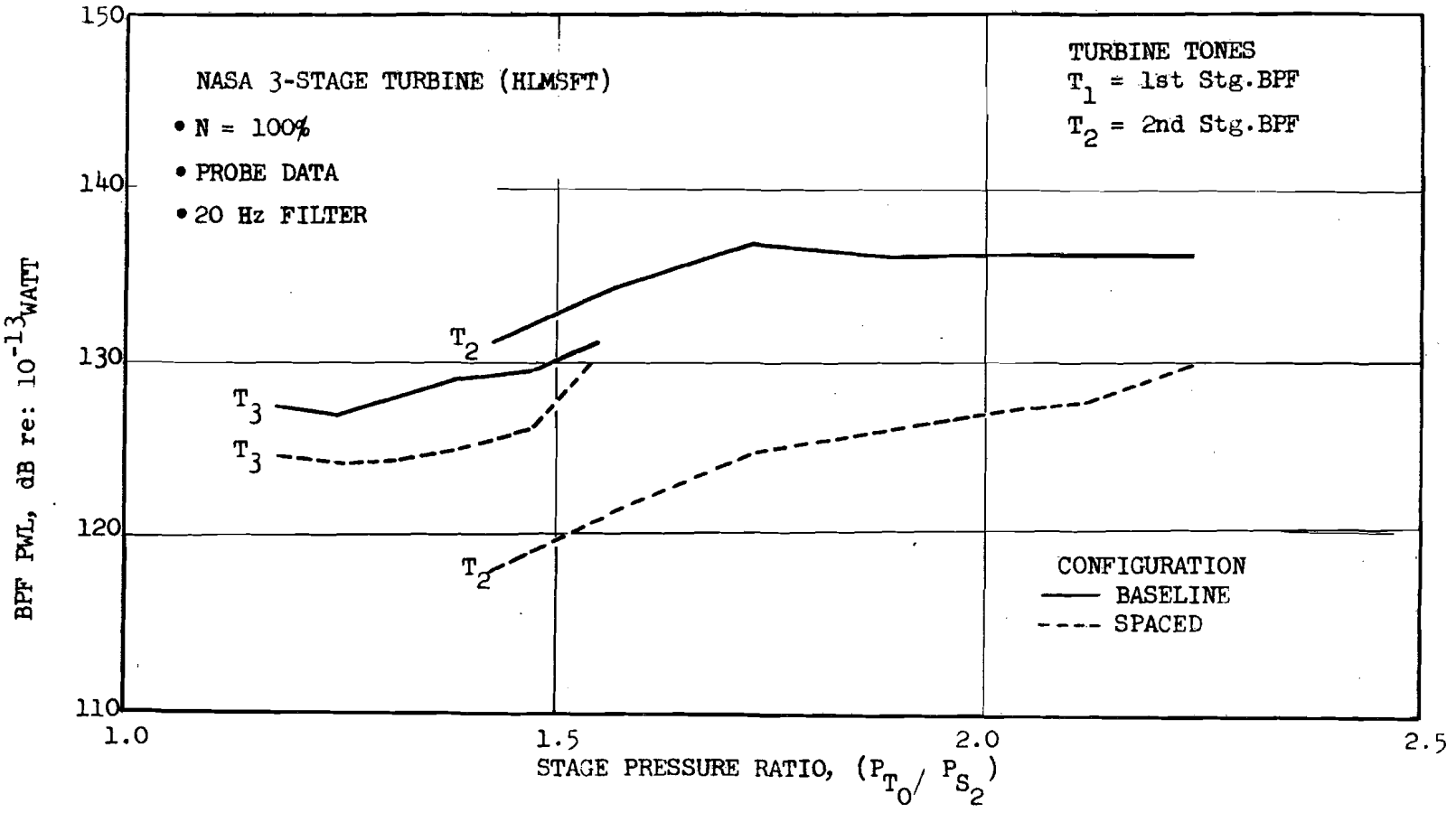

FIGURE 43.3-7 VARIATION OF TONE PWL WITH STAGE PRESSURE RATIO.

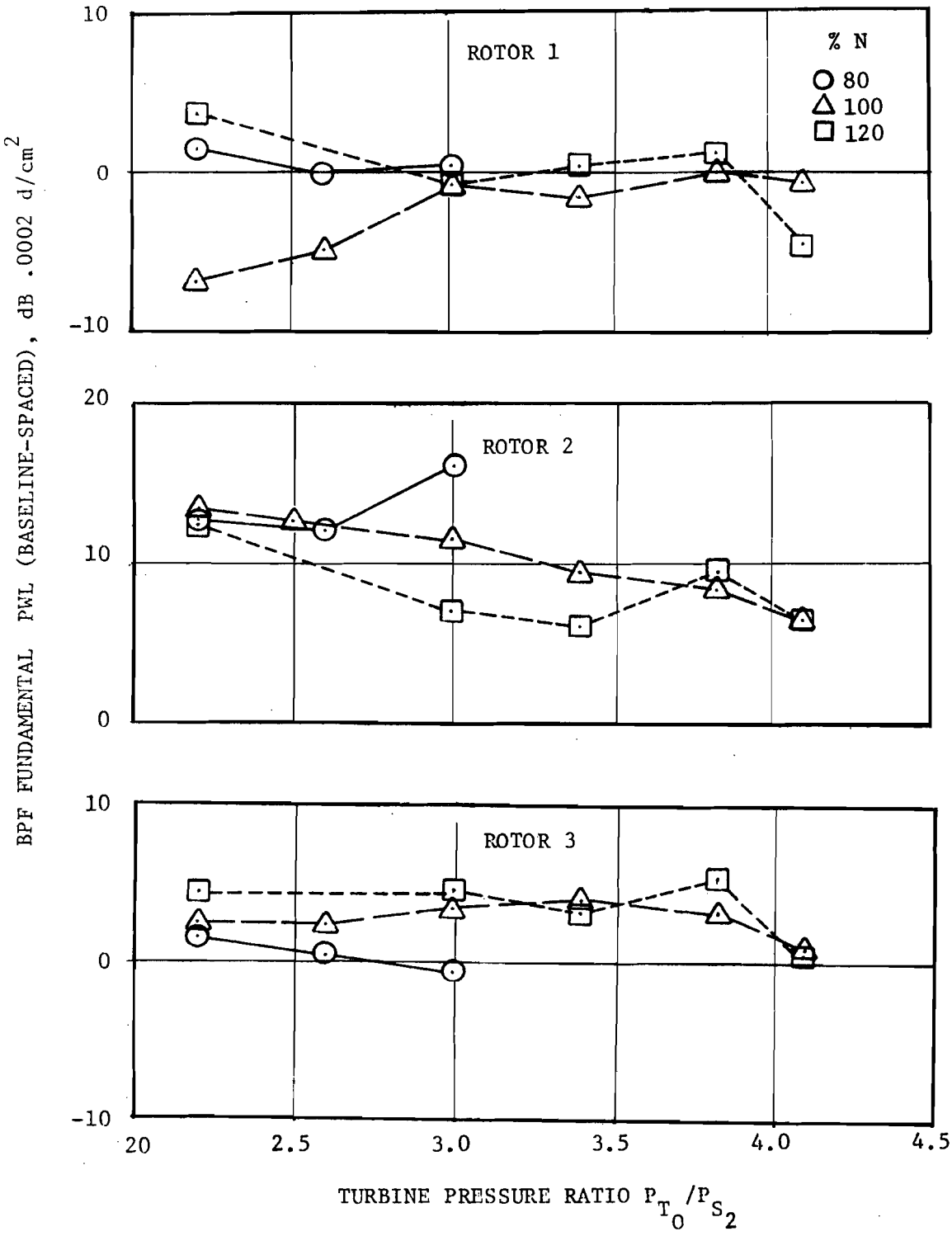

FIGURE 4.3.3-8 EFFECT OF SPACING ON TONE PWL, VARIATION WITH TURBINE PRESSURE RATIO

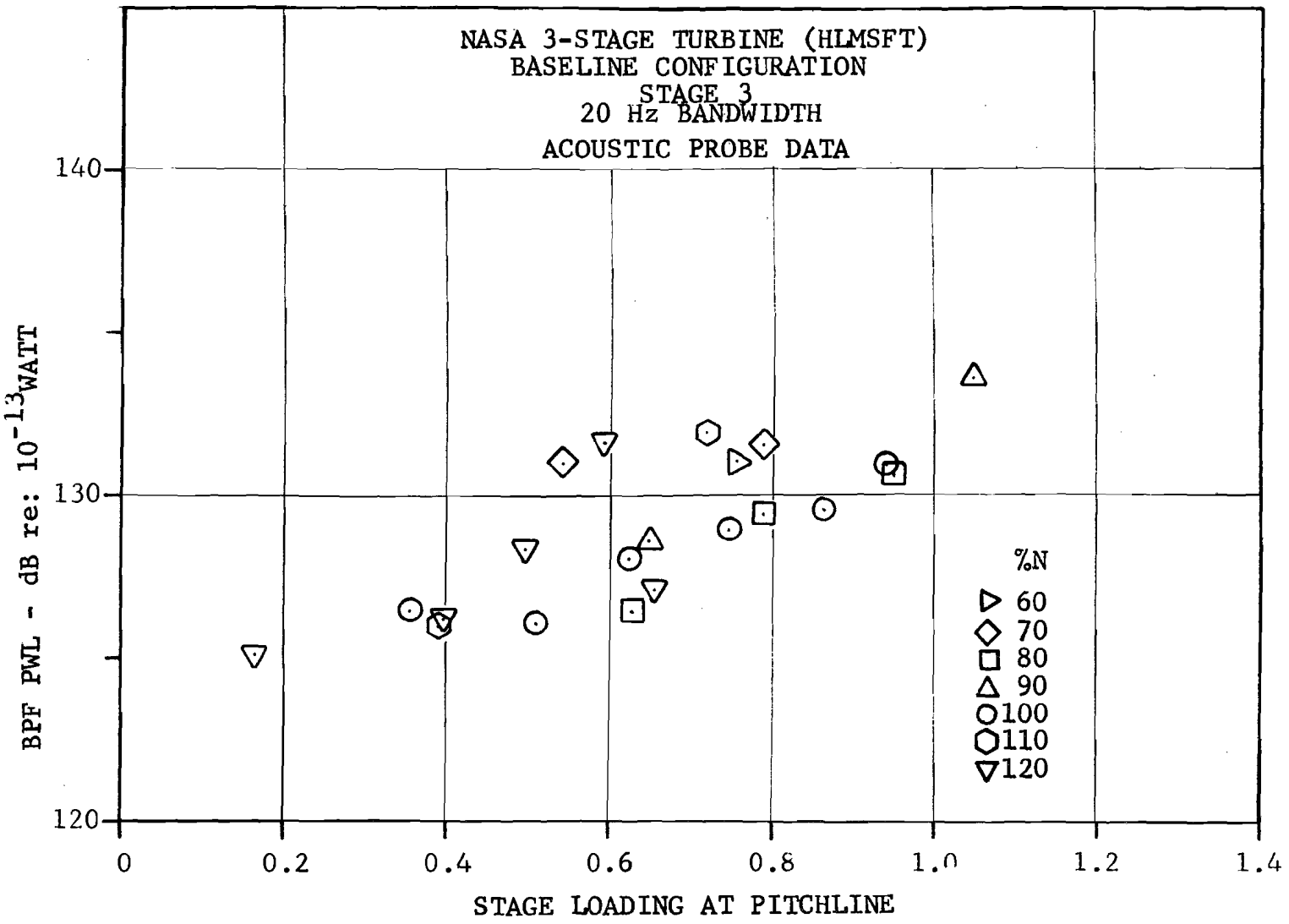

FIGURE 4.3.4-1 VARATION OF TONE PWL WITH STAGE LOADING

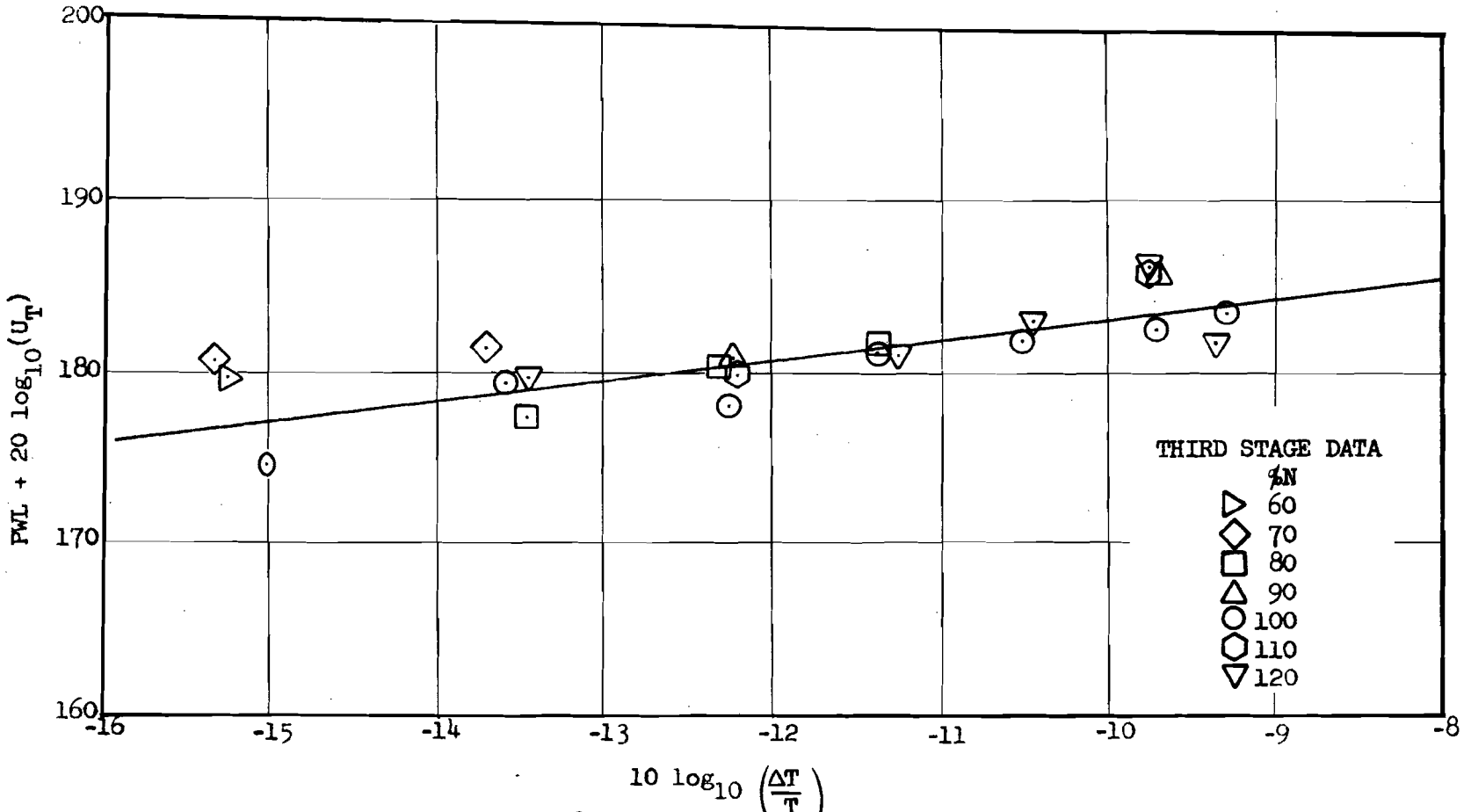

$$\frac{\Delta T}{T_a} = 1 - \left(\frac{1}{P_R}\right)^{\frac{\gamma-1}{\gamma}} \qquad P_R = P_{T_0}/P_{S_2}$$

FIGURE 4.3.4-2 VARIATION OF NORMALIZED PWL WITH IDEAL WORK EXTRACTION FOR THE LAST STAGE FUNDAMENTAL.

- For the final stage, the tone PWL correlates with the first power of the ideal work extraction and second power of the blade tip speed. The correlation provided a base for the semi-empirical turbine noise prediction method developed in Phase IV.

- The feasibility of using increased blade row spacing as a noise reduction technique in low pressure turbines. The reduction in tone PWL would be about 3 dB per doubling of the spacing.

- The associated penalty in performance loss is small (0.3% drop in efficiency at design point). Part of the loss was due to a step in the outer flowpath and part due to unguided turning in the increased spacing. Proper design of the turbine would mean even lower losses.

Valuable acoustic data was also accumulated in these tests for the purposes of evaluating the analytical prediction method for turbine discrete frequency noise (Section 4.4).

4.4 ANALYTICAL PREDICTION OF TURBINE DISCRETE FREQUENCY NOISE

4.4.1 Background

The objective was to develop an analytical turbine noise prediction method of sufficient scope to account for key aerodynamic performance and mechanical parameters.

Numerous studies have been conducted on the mechanisms of noise generation in fans/compressors and the task of predicting the discrete frequency (pure tone) noise has been successfully accomplished by analytic considerations of the various mechanisms (References 4.2.1-1, 4.3.1-1 and -2). The two major sources of discrete frequency noise are the rotor alone and the interaction between adjacent blade rows. The rotor alone noise arises from the rotating pressure field attached to the rotor blades and interaction noise from the mutual disturbance of the potential fields of adjacent blade rows and by the viscous wakes of the blading impinging on downstream blade rows.

These mechanisms are also applicable to turbines. Only the interaction mechanisms need be considered for fan turbines however because the rotor alone noise is generally "cut-off" (except when tip speed is supersonic). Consideration of the blade loadings and spacing indicates further that the major discrete frequency noise source for turbines should be the viscous wake induced noise. An analytical model was therefore developed for turbine wake interaction noise based on earlier General Electric experience with fan/compressor noise (References 4.2.1-1 and 45.3.1-2). The model couples the duct acoustic modes with the turbomachinery acoustics. The viscous wakes from any blade row impinging on a downstream row create unsteady circulation on the blading (Reference 4.4.1-1). The unsteady circulation, in turn, excites spinning modes in the duct which display both diametral (circumferential) and radial lobes (Reference 4.4.1-2). The acoustic pressure distribution is given by a Fourier series obtained by the summation of the pressure generation by all the spinning modes (Reference 4.3.1-2).

In order to calculate the unsteady circulation, it is necessary to provide a complete description of the viscous wake, including the velocity defect. The model used for fan/compressor work is derived from Reference 4.4.1-3 for uncambered blading. For purposes of a turbine noise analysis, the wake shape had to be redefined to reflect cambered blades with relatively large trailing edge thickness and the favorable pressure gradients characteristic of turbines. An initial attempt was made to accomodate turbine blading within the same model for fan/compressor blades, but with the constants redefined based on turbine cascade data. This effort (Reference 4.2.2-2) resulted in the following description of the wake thickness and velocity defect (see Figure 4.4.1-1).

$$Y = .669 C_D^{1/2}\, c \left[\frac{x}{c} - 1 + \frac{t^2 e/4}{.447 C, c^2}\right]^{1/2} \qquad (4.4.1\text{-}1)$$

and

$$\frac{u_c}{V} = -2.42 \frac{C_D^{1/2}}{\left(\frac{x}{c} - 0.4\right)} \qquad (4.4.1\text{-}2)$$

where:

Y = wake half width

x = axial distance downstream of the chord mid point

c = semi chord of the blade

t_e = trailing edge thickness of blade

C_D = profile drag coefficient

u_C = velocity defect in the wake

V = freestream velocity

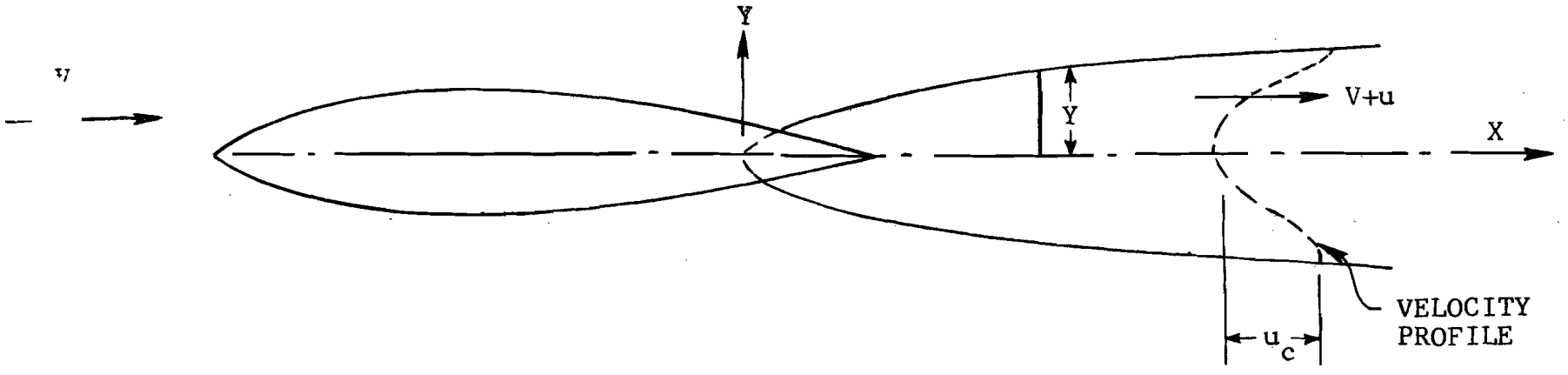

FIGURE 4.4.1-1 DEFINITION OF VISCOUS WAKE.

The computation of the unsteady circulation and acoustic pressures then proceeds as described in Reference 4.2.2-2.

The prediction program using equations (4.4.1-1) and (4.4.1-2) was found to correctly predict gross observed trends in turbine noise. However, a problem became evident when the absolute noise levels were predicted. The problem was related to the computation of a profile drag coefficient for turbine blading.

For a cascade, the profile drag coefficient may be related to the pressure loss coefficient, ζ_ρ, (see Figure 4.4.1-2) by

$$C_D = \zeta_\rho \left(\frac{t}{\ell}\right) \frac{\cos^3\alpha_m}{\cos^2\alpha_2} \qquad (4.4.1\text{-}3)$$

where t is the pitch and ℓ the chord of the cascade blades.

and

$$\zeta_\rho = \frac{\overline{P}_{01} - \overline{P}_{02}}{\overline{P}_{01} - \overline{p}_2} \qquad (4.4.1\text{-}4)$$

$\overline{P_{01}}$, $\overline{P_{02}}$ are the mass-averaged total pressures at inlet to and exit from the blade row and $\overline{p_2}$ the mass-averaged static pressure downstream of the blade row. It can be seen that the mean drag force and drag coefficient are associated with a mean direction and because of the large flow angles of turbine blading, this so called mean drag force can be, at times, quite different from the total profile drag of the blade. By changing the stagger, it is possible to generate greatly varying drag coefficients for the same blade. Obviously, then, the wake correlation had to be based on something other than the drag coefficient.

4.4.2 Development of a New Viscous Wake Model

The viscous wake thickness and velocity defect are functions of the profile drag on the blade and a correlation is merely a simplified representation of the actual relationship.

The profile drag for any general airfoil may be approximated by the total momentum loss in the wake (assuming no separation). Hence, for a flow in the axial direction, (see Figure 4.4.1-1)

$$D_p = \rho \int_{-\infty}^{\infty} u(V-u)\,dy \qquad u \ll \alpha \qquad (4.4.2\text{-}1)$$

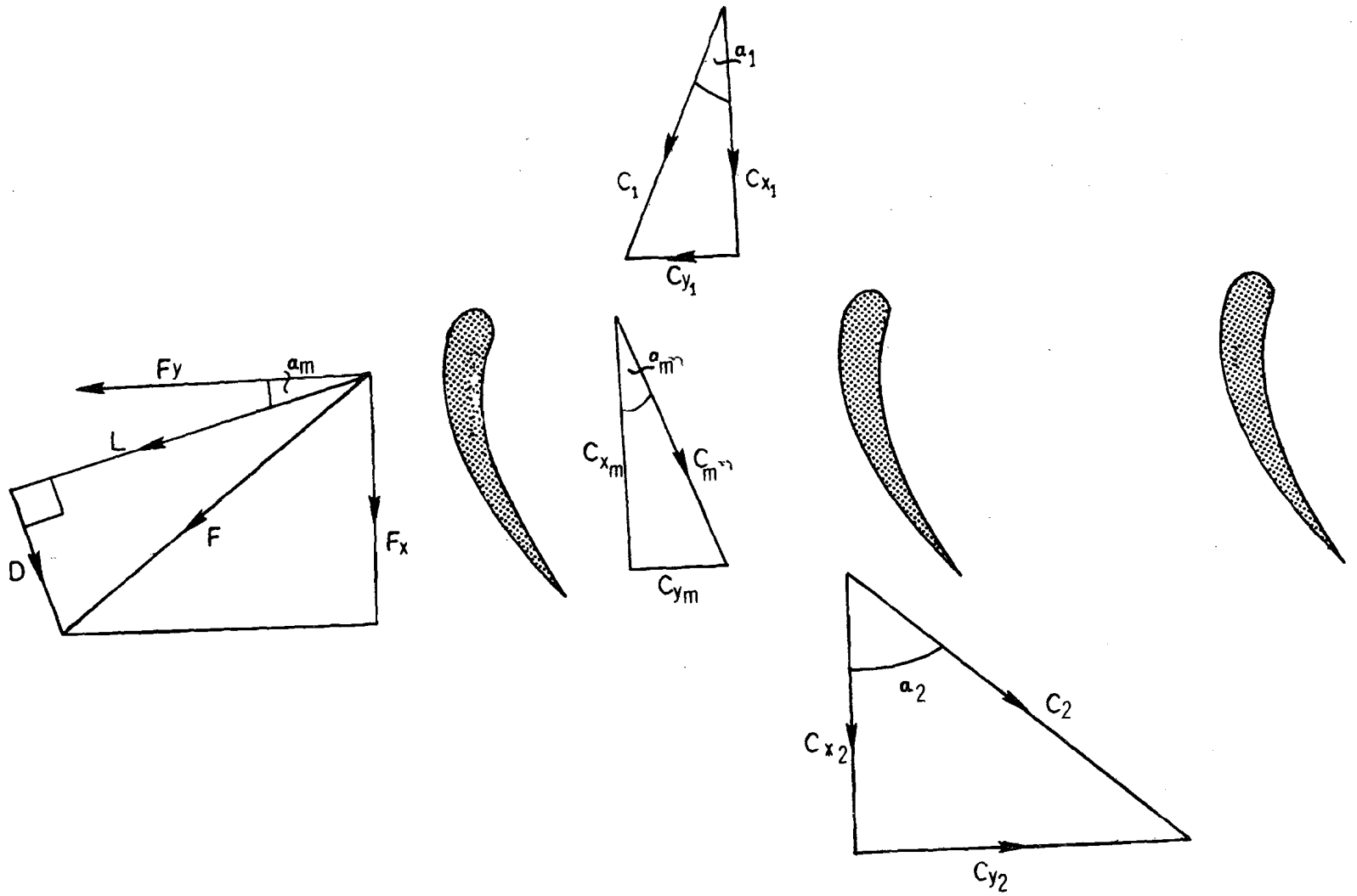

FIGURE 4.4.1-2 VELOCITY TRIANGLES FOR A CASCADE BLADE ROW

where D_p is the profile drag, ρ the fluid density, V the freestream velocity (axial direction), u the velocity defect at any point in the wake, y the coordinate normal to the wake axis and x the coordinate along the wake.

Immediately downstream of the trailing edge, the static pressure in the wake reaches the freestream value and equation (4.4.2-1) can be approximated by the following convenient non-dimensional form:

$$C_D = \frac{1}{\ell} \int_{-\gamma}^{\gamma} \left(1 - \frac{q}{q_\infty}\right) dy \qquad (4.4.2\text{-}2)$$

where $C_D = \dfrac{D_p}{\frac{1}{2}\rho V^2 \ell}$ (profile drag coefficient)

q/q_∞ = ratio of dynamic pressure in the wake to that in the freestream.

Excellent experimental verification of the relationship in equation (4.4.2-2) has been reported in Reference 4.4.1-3. The work, however, was performed on airfoils with comparatively little camber.

It can be shown analytically for turbulent flow (see, for example, Reference 4.4.2-1)that the relationships implied by (4.4.2-2) can be expressed as:

$$\gamma \propto C_D^{\frac{1}{2}} \chi^{\frac{1}{2}} \qquad (4.4.2\text{-}3)$$

and

$$\eta \propto \frac{C_D^{\frac{1}{2}}}{\chi^{\frac{1}{2}}} \qquad (4.4.2\text{-}4)$$

where $\eta = 1 - q_c/q_\infty$, the ratio of the dynamic pressure defect at the wake centerline to the free stream dynamic pressure (assumed in the analysis to be small near the trailing edge).

Experimentally, equation (4.4.2-3) was verified by Silverstein, et al., (Reference 4.4.1-3), but η was found to vary as

$$\eta \propto \frac{C_D^{1/2}}{\chi} \qquad (4.4.2\text{-}5)$$

It was suggested that the discrepancy occurs because the values of η were found to be large near the trailing edge and not small as assumed in the analysis. The above authors derived the following correlation.

$$\gamma = .68\, C_D^{1/2}\, \ell\, (\chi/\ell + .15)^{1/2} \qquad (4.4.2\text{-}6)$$

$$\eta = 2.42\ C_D^{1/2}/(x/\ell + .3) \qquad (4.4.2\text{-}7)$$

$$\eta^1/\eta = \cos^2 \frac{\pi}{2} (y/\gamma) \qquad (4.4.2\text{-}8)$$

where $\eta^1 = 1 - q/q_\infty$

The x-coordinate gives the distance downstream of the trailing edge. Equation (4.4.2-8) describes the velocity distribution in the wake.

It is recalled that the wake correlation was based on a profile drag and the drag coefficient was introduced as a convenient non-dimensional form. The pressure loss coefficient is clearly more representative of the profile drag for turbine blading than is the drag coefficient of equation (4.4.1-3).

The correlation represented by equations (4.4.2-6 to 4.4.2-8) was derived for relatively flat blades. Consider the case of one such blade aligned with the flow such that α_1 and α_2 are both very small and α_m is very small. Equation (4.4.1-5) then becomes:

$$C_D \simeq \zeta_p\ (t/\ell) \qquad (4.4.2\text{-}9)$$

2nd equation (4.4.2-6) and (4.4.2-7) become:

$$\gamma = k_1\ [\zeta_p\ (t/\ell]^{1/2}\ \ell\ (x/\ell + k_2)^{1/2} \qquad (4.4.2\text{-}10)$$

where the velocity distribution in the wake was assumed unchanged from equation (4.4.2-8).

The constants k_1, k_2, k_3 and k_4 were determined from cascade data for a number of blades (see Figures 5.4.2-1 through 5.4.2-4). The data labeled as FS3 came from a test with wake surveys at three axial locations downstream of the trailing edge. The rest of the blades come from the NASA 3 Stage Highly Loaded Multi-Stage Fan Drive Turbine cascade tests (Reference 4.4.2-2).* Some examples of the 3-stage turbine blades are shown in Figure 4.4.2-5.

Figure 4.4.2-1 shows that despite the data scatter, a dependence of wake half thickness on the square root of the pressure loss coefficient can be discerned. Figure 4.4.2-2 plots the half wake thickness as a function of $\ell[\zeta_p(s/\ell)(x/\ell + 0.2)]^{1/2}$ and was used to determine the constants k_1 and k_2. Figure 5.4.2-2 shows an attempt to obtain a correlation for the velocity defect as a function of pressure loss coefficient, solidity and axial distance downstream of the trailing edge. The FS3 tests were the only ones where a wake survey was conducted for more than one axial position downstream and hence provide the most reliable data on the wake decay with distance. These data are plotted in Figure 4.4.2-4 and were used to determine the velocity defect decay constants k_3 and k_4.

The result was the following wake correlation.

*A large amount of random variation was found during the wake surveys, resulting in some data scatter.

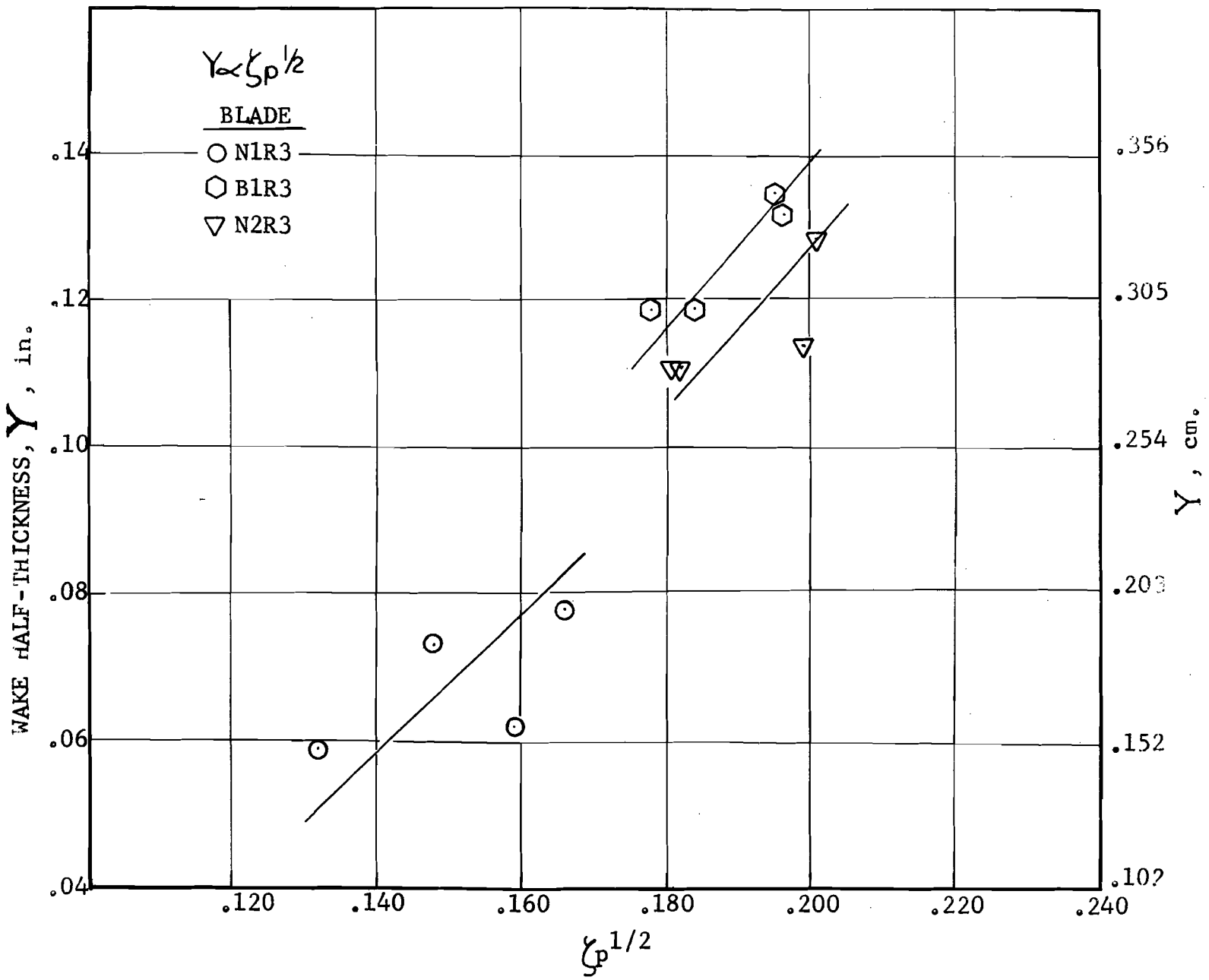

FIGURE 4.4.2-1 DEPENDANCE OF WAKE HALF THICKNESS ON PRESSURE LOSS COEFFICIENT.

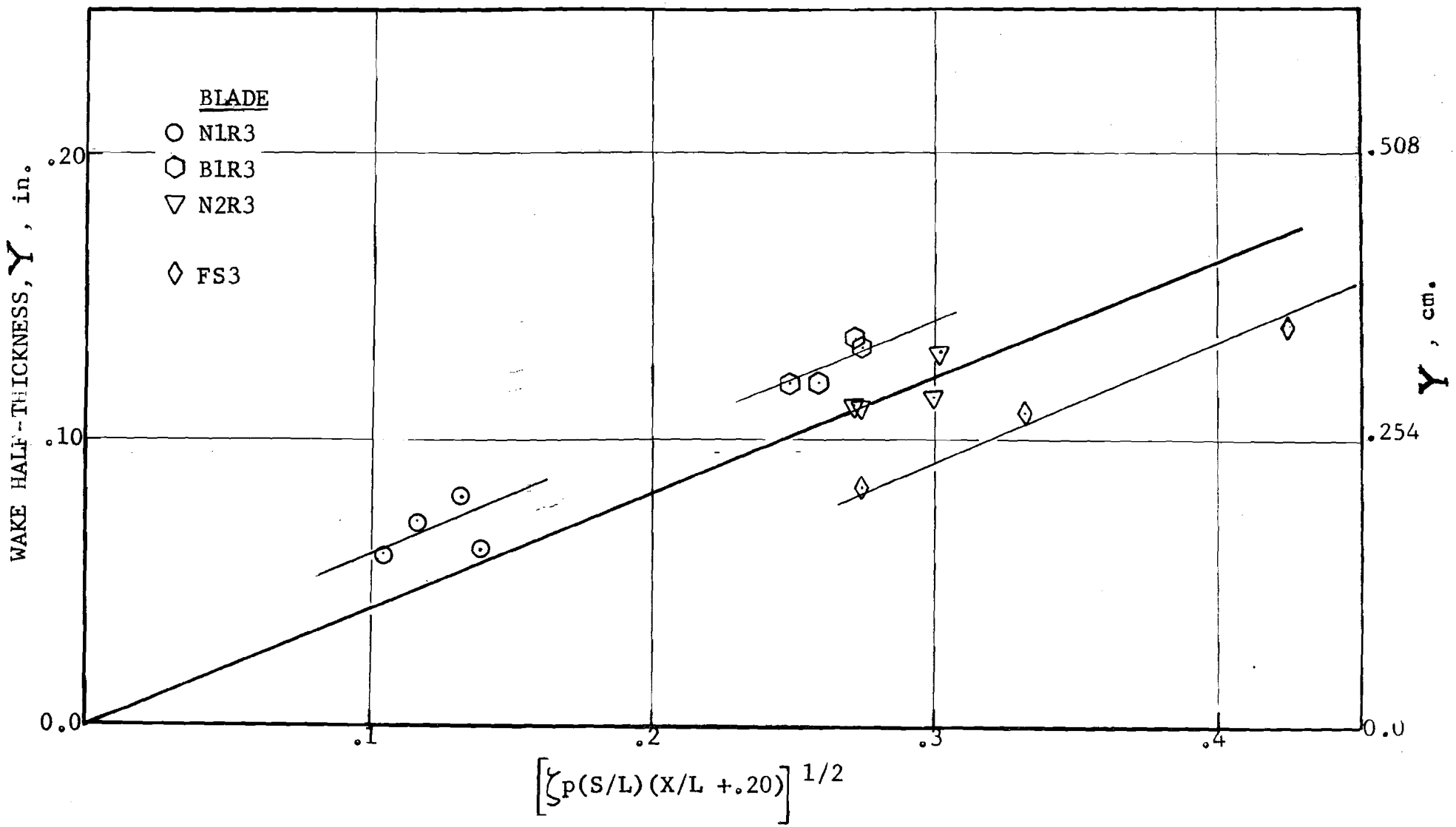

FIGURE 4.4.2-2 DETERMINATION OF HALF WAKE THICKNESS CONSTANTS.

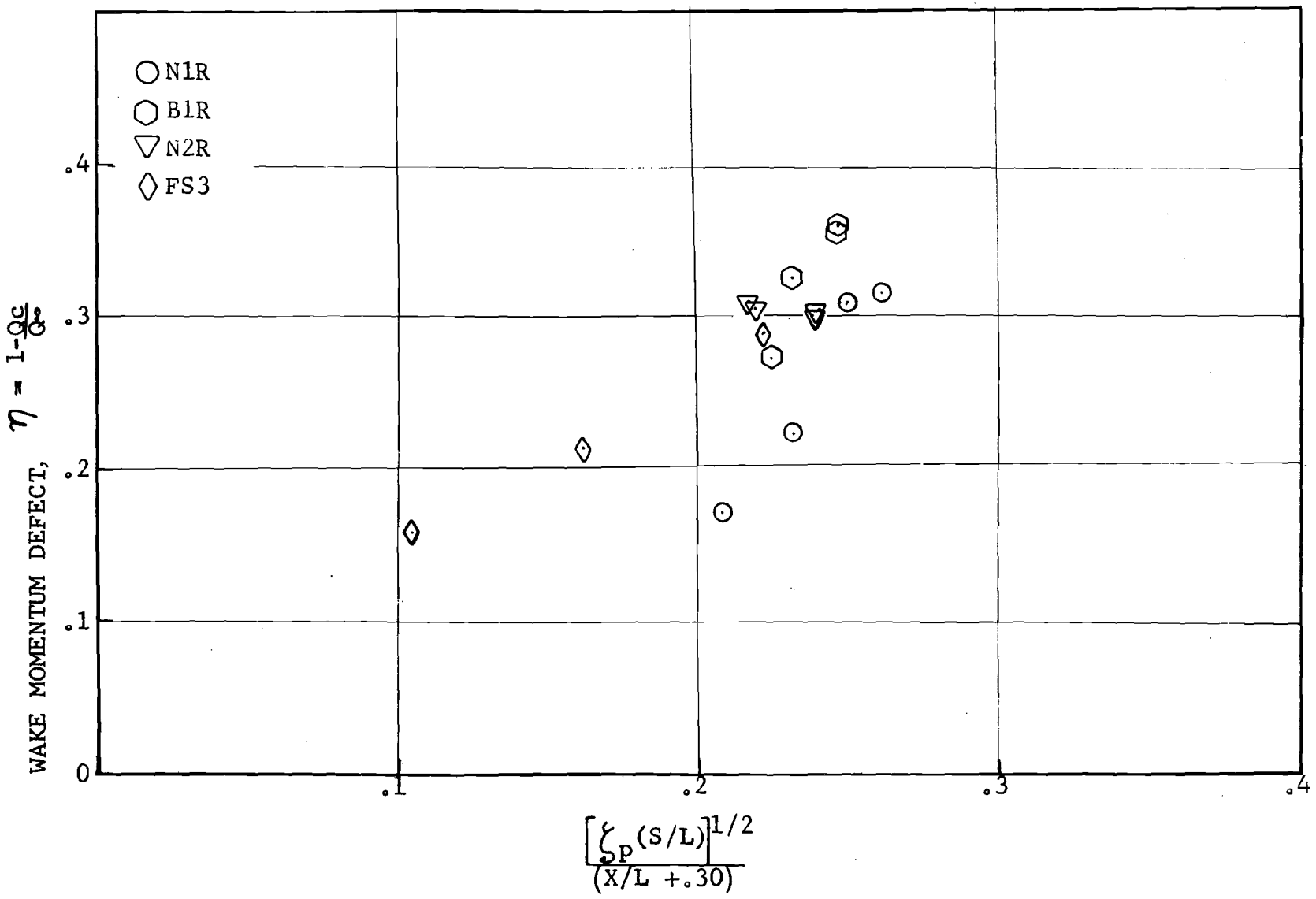

FIGURE 4.4.2-3 VARIATION OF VELOCITY DEFECT WITH PRESSURE LOSS COEFFICIENT, SOLIDITY AND AXIAL DISTANCE DOWNSTREAM.

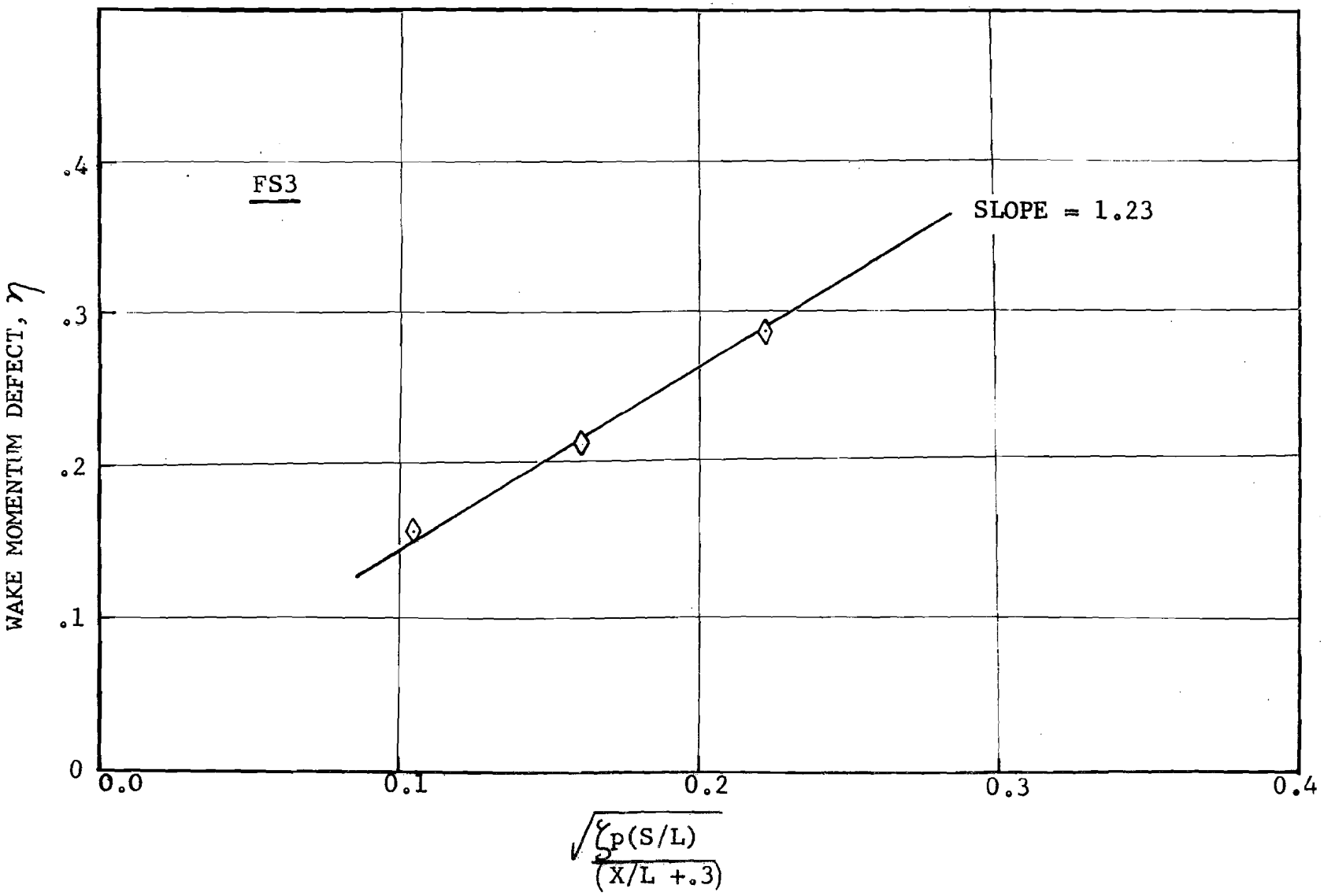

FIGURE 4.4.2-4 DETERMINATION OF VELOCITY DEFECT CONSTANTS.

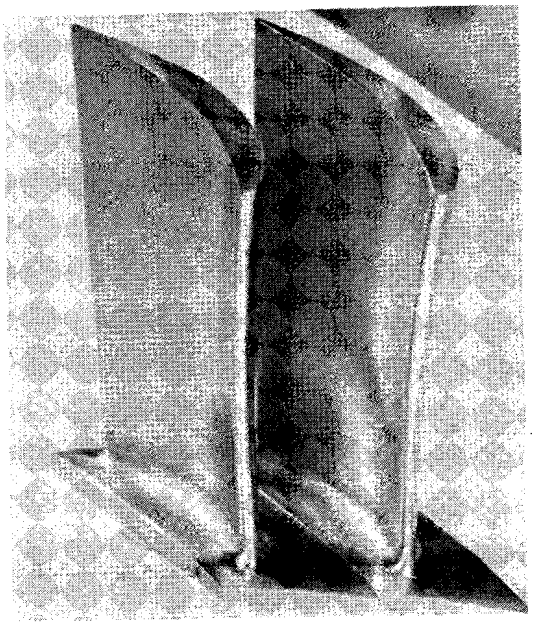

Stage One Plain Stator Airfoils.

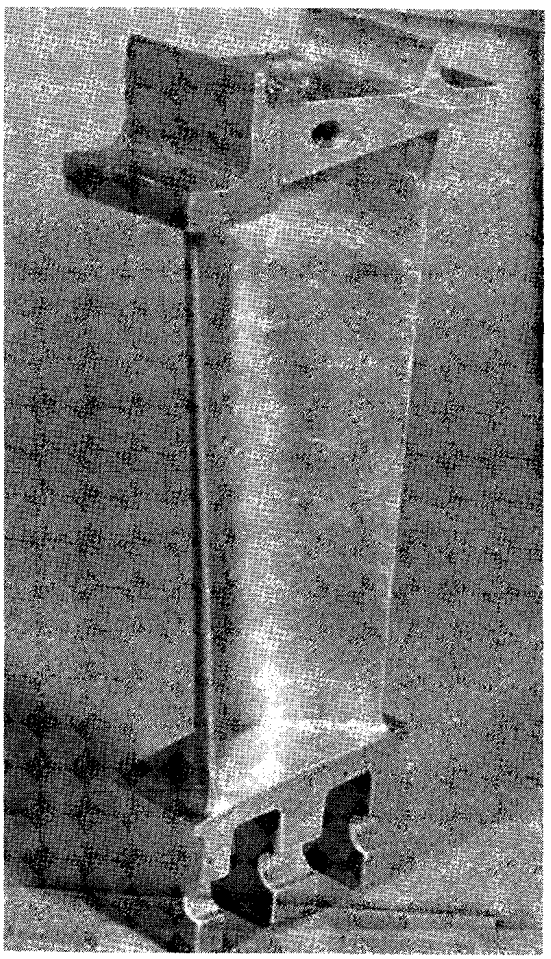

Stage One Rotor Plain Blade.

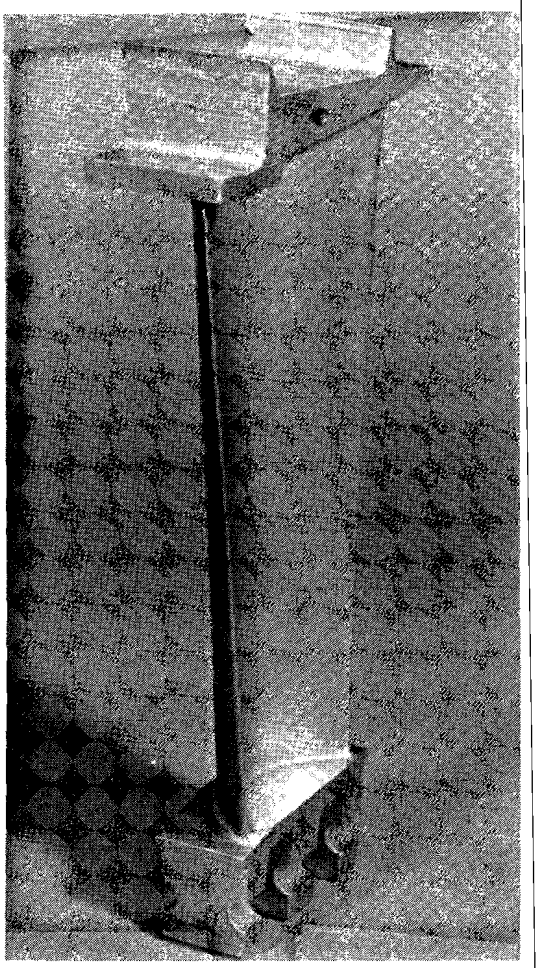

Stage Two Rotor Plain Blade.

FIGURE 4.4.2-5 BLADES FOR THE 3 STAGE TURBINE (HLMSFT)

$$Y = 0.4\ell[\zeta_p(t/\ell)(x/\ell+.2)]^{1/2} \quad (4.4.2\text{-}12)$$

$$\eta = \frac{1.23[\zeta_p(t/\ell)]^{1/2}}{(x/\ell+.3)} \quad (4.4.2\text{-}13)$$

$$\eta^1/\eta = \cos^2 \frac{\pi}{2}(y/Y) \quad (4.4.2\text{-}14)$$

Assuming that $|u_c| << V$ and dropping second order terms, equation (4.4.2-13) and (4.4.2-14) yield:

$$\frac{u_c}{V} \simeq - .615 \frac{[\zeta_p(t/\ell)]^{1/2}}{(x/\ell + .3)} \quad (4.4.2\text{-}15)$$

and

$$\frac{u}{u_c} = \cos^2 \frac{\pi}{2}(y/y) \quad (4.4.2\text{-}16)$$

Before this correlation can be used, it was necessary to find a means of computing the pressure loss coefficient, ζ_p. A study was conducted for the purposes of determining the best possible method.

The loss coefficient may be obtained through analytical determination of the boundary layer as is occasionally done at GE and is commonly found in Russian literature (see, for example, Reference 4.4.2-3). Unfortunately, a great many details such as the pressure profile over the blade are required (and are not always available), plus the data preparation can be quite cumbersome. Two empirical correlations exist, one by Soderberg and one by Ainley-Mathieson (Reference 4.4.2-4).

The Soderberg empirical correlation is based on the work of Zweifel and gives the enthalpy loss coefficient (ξ) as a function of the blade geometry, the thickness to chord ratio (t/ℓ), the aspect ratio (H/A_w), the Reynolds number (R_H) based on the hydraulic diameter (D_H), and the blade row solidity (ℓ/t). Here A_w is the axial chord and t, the circumferential spacing. For a turbine operating at a Reynolds number of 10^5, an aspect ratio of 3 and at zero incidence, the "nominal" loss coefficient ξ, is plotted as a function of the gas deflection ε for different t/ℓ. Correlations are then applied for conditions other than the above. The profile losses may be found by using an infinite blade length ($H/A_w \rightarrow \infty$).

The Soderberg correlation is simple in concept and use. It is considered oversimplified. The correlation implies that the effect of the profile shape is limited, for example, no correction is included for the trailing edge thickness. It also assumes that the stagger and the degree of reaction are unimportant as long as an optimum spacing to chord ratio is maintained. The resulting loss coefficients are consistently on the high side but the correlation useful in quick computational work.

The Ainley-Mathieson correlation is more comprehensive. The profile loss, expressed as a pressure loss coefficient ζ_p, is given as a function of the air angles (α_1, α_2), the pitch to chord ratio (t/ℓ), trailing-edge thickness to pitch ratio (t_e/t) and the Reynolds number. The correlation is provided for a Mach number of less than 0.6, but some experimental evidence is presented to show that for cascades of "straight-backed," blades there is little variation in ζ_p with Mach number in the range 0.6 - 1.0. Details of the correlation may be found in References 4.4.2-5 and 4.4.2-6.

The Ainley-Mathiesan correlation is provided for a Reynolds number of 2×10^5 based on the chord. Dunham and Came ((Reference 4.4.2-7) recommend that for Reynolds numbers other than 2×10^5 the following correction be used.

$$\frac{\zeta_p}{\zeta_p(R_e = 2 \times 10^5)} = \left(\frac{2 \times 10^5}{R_e}\right)^{1/5} \qquad (4.4.2\text{-}17)$$

The same authors also suggest the following penalty in performance in the case of choked flow when the blades have not specifically been designed for supersonic Mach numbers:

$$\frac{\zeta_p}{\zeta_p(M_2<1)} = [1 + 60\ (M_2 - 1)^2] \qquad M_2 > 1 \qquad (4.4.2\text{-}18)$$

Here M_2 is the relative Mach number at the exit of the blade row. Dunham and Came have verified that the Ainley-Mathieson scheme does a fairly good job in predicting off-design trends in performance.

At Mach numbers lower than 1, a compressibility correction may also be included by using:

$$\frac{\zeta_p}{\zeta_p(M_2 = 0)} = [1 - \frac{M_2^2}{4} + \frac{M_2^2}{40}] \qquad \underline{M_2 < 1} \qquad (4.4.2\text{-}19)$$

Since only the Ainley-Mathieson correlation provides for the variation of the loss coefficient with all the important turbine parameters, it was selected for use with the analytical prediction; this is especially important when noise predictions are required for off-design operating points.

4.4.3 Discussion of Results

The wake correlation for turbine blading described above compared to the viscous wake correlation used for fan/compressor noise predictions in Figure 4.4.3-1. Both correlations are based on the fact that the viscous wake thickness and the velocity defect are a function of the profile drag. The drag coefficient is a convenient means of non-dimensionalizing the profile drag for

FAN/COMPRESSOR BALDE WAKE CORRELATION
(Silverstein, Katzoff & Bullivant)

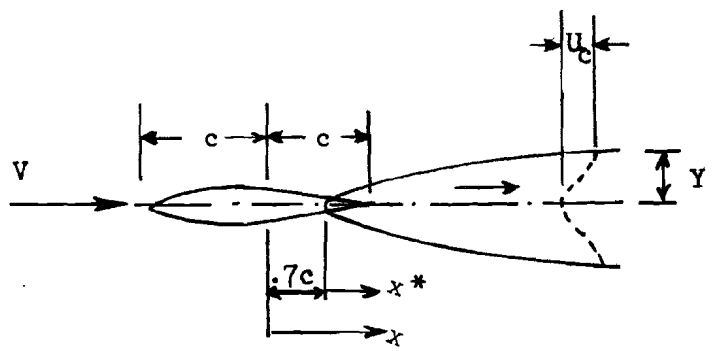

$$Y = .68\sqrt{2}\, C_D^{1/2}\ c\ (x/c - 0.7)^{1/2}$$

$$\frac{U_c}{V} = -\frac{2.42\ C_D^{1/2}}{(x/c - 0.4)}$$

$$C_D = \overline{\omega}_1\ (t/2c)\ \frac{\cos^3 \alpha m}{\cos^2 \alpha 2}$$

$$\overline{\omega}_1 = \frac{\overline{\Delta P}_0}{1/2\, \rho_1\, V^2}$$

TURBINE BLADE WAKE CORRELATION
(G.E.)

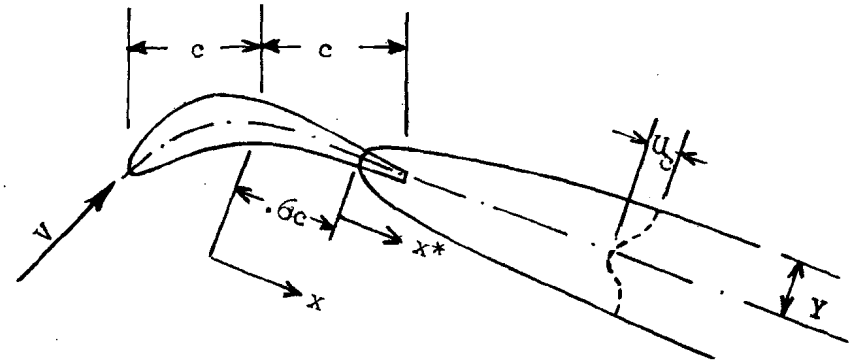

$$Y = .4\sqrt{2}\ [\zeta_p (t/2c)]^{1/2}\ c\ (x/c - 0.6)^{1/2}$$

$$\frac{u_c}{V} = -\frac{1.23\,[\zeta_p\ (t/2c)]^{1/2}}{(x/c - 0.4)}$$

$$\zeta_p = \frac{\overline{\Delta P_0}}{\overline{P}_{0_2} - \overline{P}_2}$$

FIGURE 4.4.3-1 COMPARISON OF VISCOUS WAKE CORRELATIONS.

uncambered airfoils, but so stated above, the pressure loss coefficient is believed to be the correct representation for highly cambered airfoils. The constants in the new correlation recognize turbine aerodynamics (they are based on turbine cascade data). Through use of the Ainley-Mathieson correlation for the pressure loss coefficient, it is possible to include the effects of the trailing edge and max thickness, the blade turning angle, changes in reaction, the angle of incidence and the operating Reynolds number and Mach number. The last few parameters permit prediction of the noise generation at off-design operating points.

Once the viscous wake has been defined, the unsteady circulation Γ may be computed as described in Reference 4.3.1-2:

$$|\Gamma| = C_2 V_2 \sum_{m=1}^{\infty} |G_m| \, |J9mw_2)| \, |S(mw_2)|$$

where $$J(mw_2) = |J_o^2(mw_2) + J_1^2(mw_2)|^{1/2} \qquad (4.4.3\text{-}1)$$

$$S(mw_2) = |\{imw_2[K_o(imw_2) + K_1\ (imw_2)]\}^{-1}|$$

J_0, J_1 are Bessel functions of Zeroeth and first order

and K_0, K_1 modified Bessel functions of the second kind.

Also, the reduced frequency ω_2 is given by:

$$\omega_2 = \frac{\pi C_2 \upsilon \sigma}{C_1 V_2}$$

where c = semi-chord

σ = solidity = $\frac{2c}{t}$

V = stream velocity

U = blade speed

The subscripts 1 and 2 on these parameters denote conditions for the upstream and downstream blade rows, respectively, as is illustrated in Figure 4.4.3-2 which gives a schematic of viscous wake interaction. G_m is the coefficient of unsteady upwash and is given by:

$$G_m = 1.391\ \pi\ \frac{V_1}{V_2}\ \frac{\zeta_{p1}\ \sin\beta}{(x^1/_c + .2)\ \cos\alpha_1}\ \left(\frac{x^1}{C_1}\right)^{1/2}$$

$$\exp\left[-\pi m^2\ \left(\frac{.283}{\cos\alpha_1}\right)^2\ \left(\zeta_{p1}\sigma_1 \frac{X1}{c_1}\right)\right] \qquad (4.4.3\text{-}2)$$

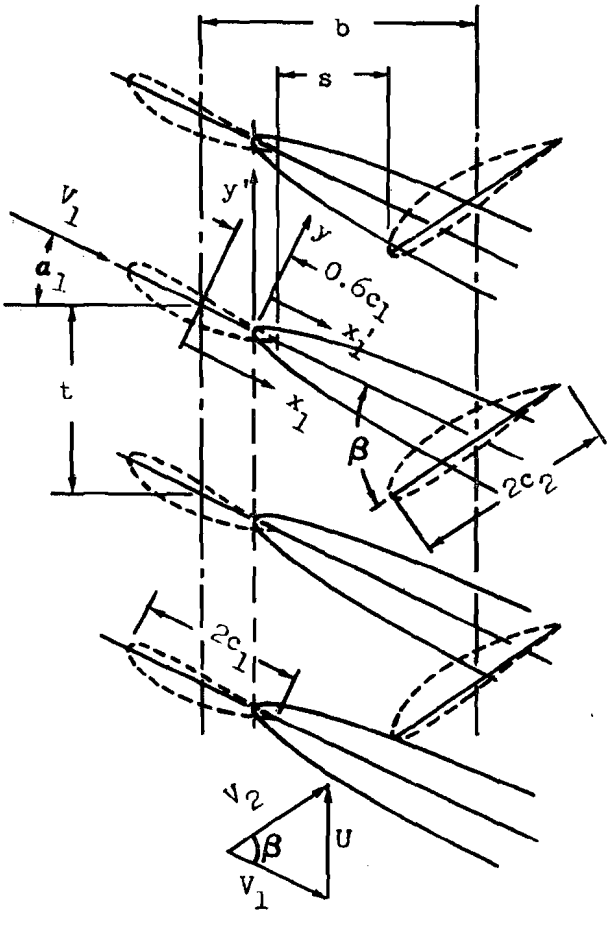

FIGURE 4.4.3-2 SCHEMATIC OF VISCOUS WAKE INTERACTION.

where

$$\frac{X1}{C_1} = \frac{C_2}{C_1}\left(\frac{b}{C_2\cos\alpha_1} + \frac{X2}{C_2}\frac{V_1}{V_2}\right) - .6 \qquad (4.4.3\text{-}3)$$

α_1 = stagger angle of blades (see Figure 4.4.3-2)

β = angle between stator and rotor blades

Normally, the center of pressure may be taken as the 1/4 chord point without incurring much error and hence $\frac{X2}{C_2} = \frac{1}{2}$ in equation (5.4.3-3).

As can be seen from equation (4.4.3-2), the analysis includes the effects of the blade geometry and the turbine aerodynamics. This analytical method then provides a powerful tool for the investigation of various mechanical and aerodynamic configuration changes on the discrete frequency noise generation. Since the pressure loss coefficient includes incidence, Mach number and Reynolds number effects, it is possible to predict the noise generated at off-design operating conditions. For example, the analytical prediction procedure was exercised for the NASA 3 stage turbine (HLMSFT) and the results are compared with the probe measured data in Figure 4.4.3-3. Excellent agreement was obtained over the entire operating range, including the fact that noise started to increase at the lowest pressure ratio (obviously a function of the high incidence).

The dependence of the noise generation on the pressure ratio, at constant wheel speed, has been clearly demonstrated. The noise reduction due to the opened spacing is correctly predicted.

A comparison for the low pressure turbines of Quiet Engines "A" and "C" is provided in Table 4.4.3-1. Again, good agreement is obtained. Finally, the analytic prediction scheme was also found to supply reasonable values for the noise generated by a turbine in a turbojet engine, as shown in Figure 4.4.3-4 for a speed range of 70 to 100% design.

As mentioned earlier, the prediction comparisons were limited to the last stage in each case because of the uncertainty of the effect of blade row attenuation.

4.4.4 Extension to Leaned Vanes

The earlier analysis of the pure tone noise resulting from the viscous wake interaction was for radial blading. Assuming that the wake coming off the upstream blade is also radial, the entire wake "slaps" into a downstream blade simultaneously from hub to tip. If the wake were leaned relative to the downstream blade row, a decrease in viscous wake interaction would result. The interaction would also be phased from hub to tip and some phase cancellation might result. Significant noise relief has, infact, been demonstrated for fans with leaned vanes (Reference 4.4.4-1). In addition to the noise suppression

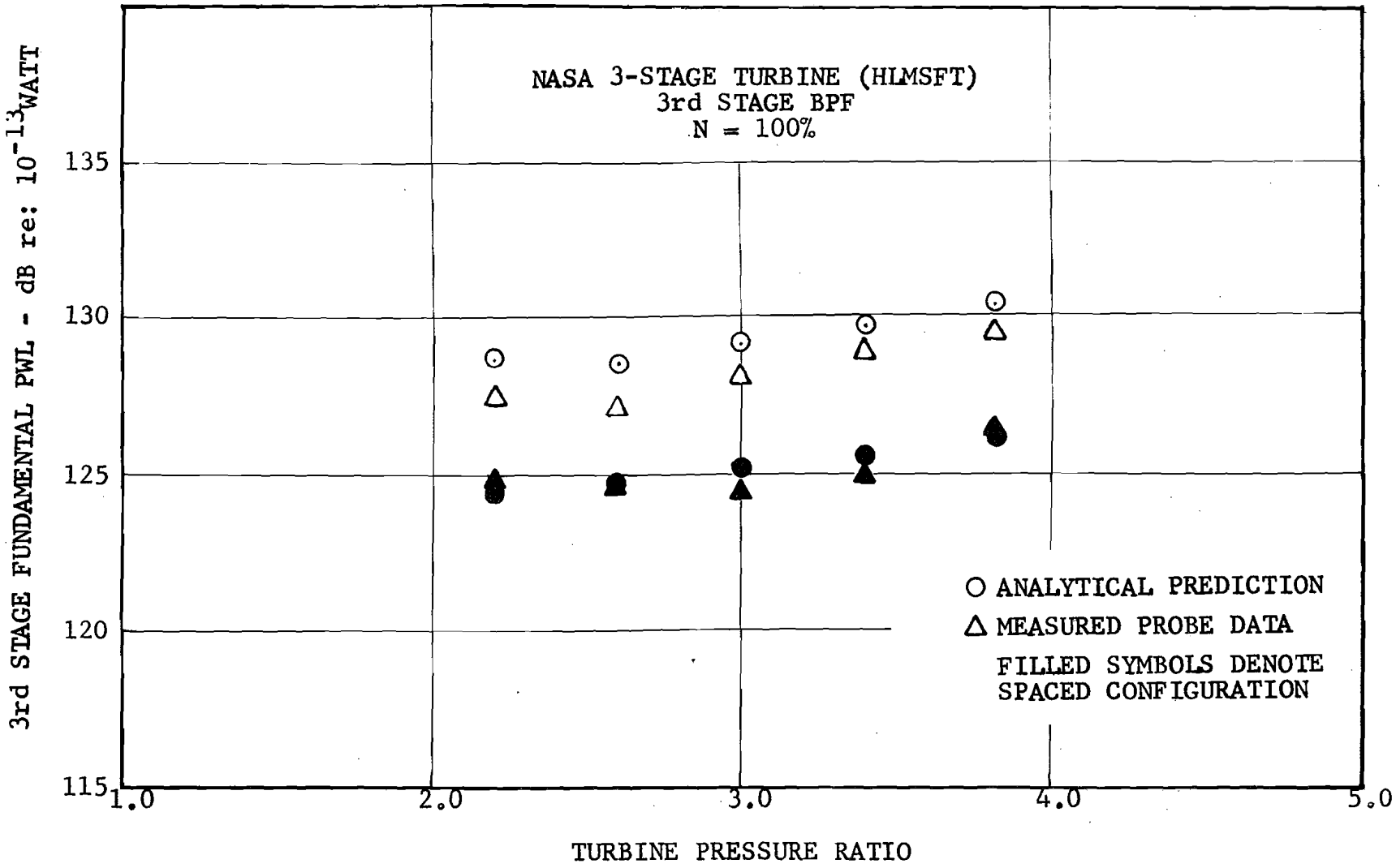

FIGURE 4.4.3-3 COMPARISON ANALYTICAL PREDICTION WITH MEASURED DATA FOR TURBINE TONES.

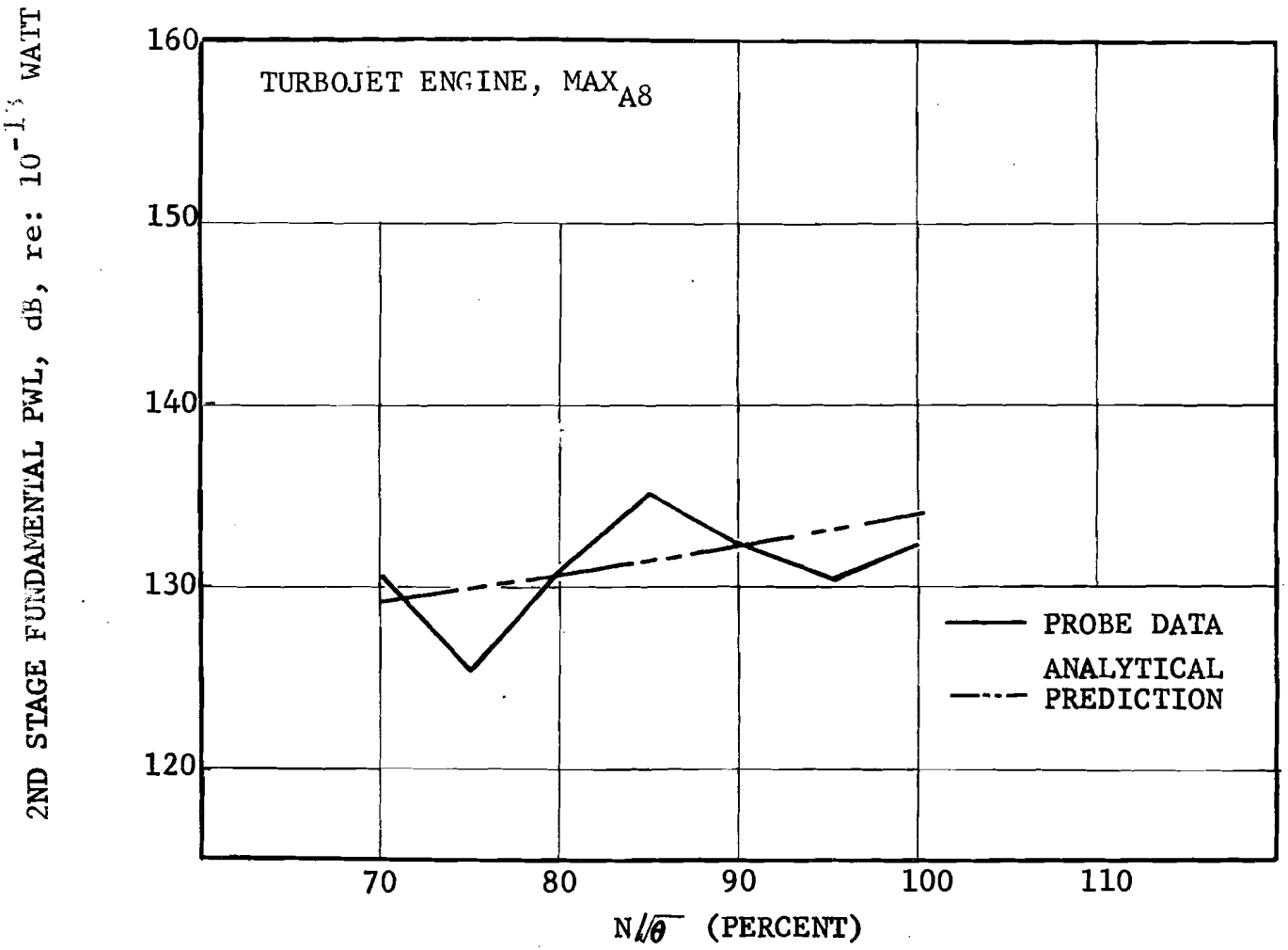

FIGURE 4.4.3-4 COMPARISON OF PREDICTED AND MEASURED TURBINE NOISE

Table 4.4.3-1. Comparison of Predicted and Measured Pure Tone PWL's.

(Last Stage BPF only)

Engine	Power Setting	Measured PWL,* dB	Predicted PWL, dB
"A"	Approach	125.0	126.3
"A"	T/O	131.0	131.4
"C"	Approach	135.5	133.3
"C"	T/O	142.0	141.0

*Includes probe corrections for flow. (∿3dB).

benefits, leaned vanes are also being considered as a means of improving turbine performance through reduction of secondary flow effects (Reference 4.4.4-2). A need therefore existed for a prediction method incorporating the effect of leaned vanes.

An effective lean is inherent in most machines because of the radial work variation and may be obtained by consideration of the velocity triangles at different radial locations. If the vanes are physically leaned in the tangential direction, a geometric lean is added to the effective aerodynamic lean, and the combined effect must be considered in determining the noise reduction.

The geometric lean, ψ, is in general a function of the radius and is easily computed for either curved or straight leaned vanes. Referring to Figure 4.4.4-1 and given the physical lean $\alpha(r)$, trignometric relationships yield:

$$\psi(r) = \alpha(r) - \delta(r)$$

$$\frac{r_{hub}}{\sin[\delta(r)]} = \frac{r}{\sin[\beta(r)]}$$

and

$$\beta(r) = 180° - \alpha(r)$$

$$\chi(r) = \alpha(r) = \sin^{-1}\left\{\frac{r_{hub}}{r}\sin\left[180° - \alpha(r)\right]\right\}$$

or

$$\chi(r) = \alpha(r) - \sin^{-1}\left\{\frac{r_{hub}}{r}\sin\left[\alpha(r)\right]\right\} \qquad (4.4.4\text{-}1)$$

Here a curved vane has been considered and $\alpha(r)$ is defined as the lean of a corresponding straight vane (as shown in Figure 4.4.4-1). δ is the angle between the tangent to the vane and the local radial line. For straight vanes, α is a constant and is independent of r.

While equation 4.4.4-1 appears relatively simple, application of such an expression as a boundary condition to the wave equation in an annular duct introduces several complications, specially in the determination of the radial mode eigenvalues.

The analytical prediction scheme was exercised for the NASA 3 stage turbine (HLMSFT) with lean in the third stage nozzle. The results are presented in Table 4.4.4-1 and should be considered as a first computational approximation. The projected results are somewhat disappointing in that suppression is not indicated for a range of lean encompassing 30° in either direction. This may result from either the multiplicity of overlapping blade interactions introduced by the lean or, possibly, from the approximations that have to be made in order to fit the complex boundary conditions to the problem. Hence the results must be viewed with some caution until the analysis can be evaluated further, or till some leaned vane turbine test data becomes available. Futher study is clearly indicated in view of the encouraging results obtained from fan tests with leaned vanes.

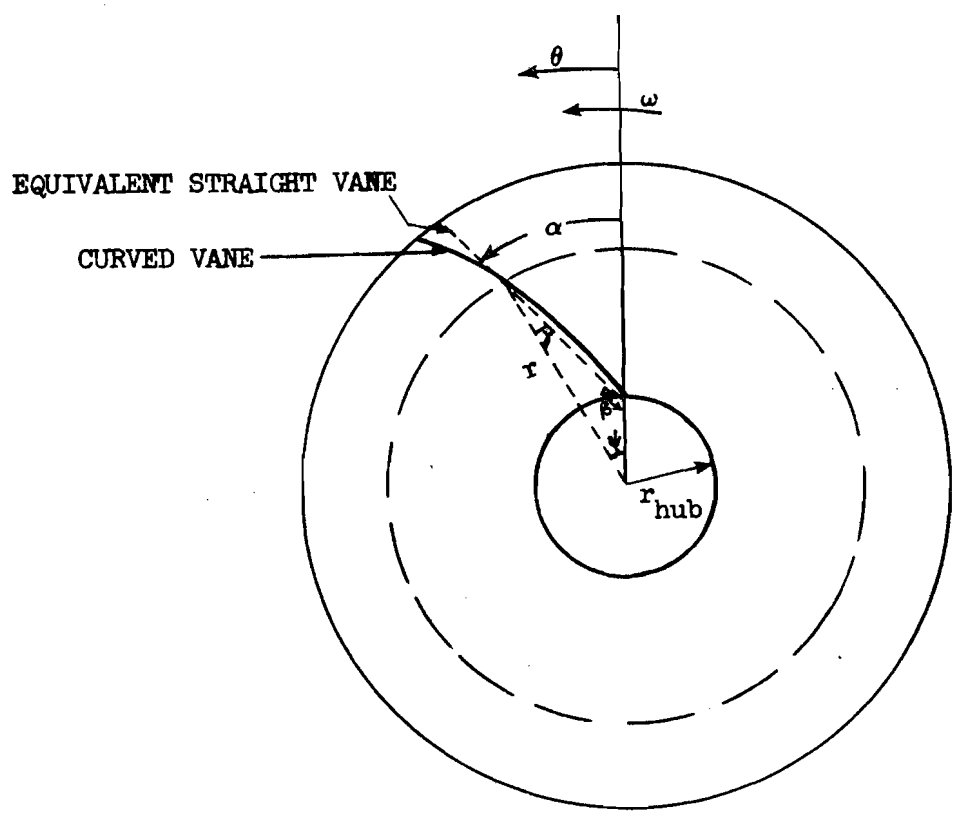

FIGURE 4.4.4-1 DETERMINATION OF THE GEOMETRIC LEAN.

Table 4.4.4-1 Leaned Vane Study NASA 3 Stage Turbine
Lean in direction of rotation is positive
SPEED N = 3677 rpm
Predictions are for the last stage

Lean (α)	PWL @ P_{T_o}/P_{S_2} 2.2	2.6	3.0	3.4	3.83	4.1
30°	129.9	128.3	128.1	128.7	129.4	130.2
20°	128.7	128.5	128.2	128.7	129.5	130.4
10°	126.6	126.2	125.8	126.2	127.0	128.1
0	126.7	126.2	125.8	126.2	127.0	128.1
-10°	126.7	126.1	125.8	126.2	126.9	128.1
-20°	128.5	127.1	126.8	127.4	128.1	129.0
-30°	129.8	129.4	129.1	129.7	130.5	131.3

4.4.5 Summary

Viscous wake interaction was identified as the most important discrete frequency noise generation mechanism and an analytical prediction method advanced for computing the noise generation. A semi-empirical correlation was derived for the viscous wake using cascade data. The correlation reflects the actual turbine aerodynamics and recognizes the highly cambered blading prevalent in turbines.

Comparison with measured data shows that the analysis is capable of accurately predicting noise levels not only for the design point, but also for off-design operating conditions. Further it correctly predicts the noise reduction due to opened spacing between blade rows. The analysis takes into account the effect of the blade geometry and aerodynamic parameters and provides a powerful tool for parametric investigation of various configuration changes.

REFERENCES

4.1-1 Kazin, S.B. and Paas, J.E., "NASA/GE Quiet Engine 'C' Acoustic Test Result," NASA CR-121176, April 1974.

4.1-2 Kazin, S.B. and Paas, J.E., "NASA/GE Quiet Engine 'A' Test Results," NASA CR-121175, October 1973.

4.1-3 Clemons, A., Hehmann, H. and Radecki, K., "Quiet Engine Program Turbine Noise Suppression, Volume I-General Treatment Evaluation and Measurement Techniques," NASA CR-134499, December 1973.

4.1-4 Clemons, A., Hehmann, H. and Radecki, K., "Quiet Engine Program Turbine Noise Suppression, Volume II-Treatment Selection, Installation, and Test Results," NASA CR-134499, December 1973.

4.1-5 Coward, W.E., Smith, E.G. and Sowers, H.D., "TF34 Quiet Nacelle Nearfield Acoustic Test Results," NASA CR-134604, March 1974.

REFERENCES

4.2.1-1 Benzakein, M.J. and Kazin, S.B., "Fan Compressor Noise Reduction," ASME 69-GT-9, Presented at the Gas Turbine Conference and Products Show, Cleveland, Ohio, March 1969.

4.2.1-2 Mani, R., "Noise Due to the Interaction of Inlet Turbulence with Isolated Stators and Rotors," J. Sound Vib, 17, part 2, p. 25, 1971.

4.2.2-1 Benzakein, M.J. and Smith, E.B., "Turbine Noise Generation and Suppression," ASME Paper No. 73-WA/GT-7.

4.2.2-2 "Hot Film and Hot Wire Anemometry, Theory and Application Bulletin TB5," Thermo-Systems Inc.

4.2.2-3 Cornell, W.G., "Losses in Flow Normal to Plane Screens," ASME Paper No. 57-F-19, June 1957.

4.2.4-1 Goldstein, S., Modern Developments in Fluid Dynamics, Volume 1, Dover Publications Inc. 1965.

4.2.4-2 Sharland, I.J., "Sources of Noise in Axial Flow Fans," J. Sound Vib. 1, part 3, 302-322, 1964.

REFERENCES

4.3.2-1 Evans, D.C. and Wolfmeyer, G.W., "Highly Loaded Multi-stage Fan Drive Turbine - Plain Blade Configuration Design", NASA CR-1964, Feb. 1972.

4.3.1-1 Benzakein, M.J., Kazin, S.B., "Theoretical Prediction of Aerodynamically Generated Noise in Fans and Compressors", Paper presented At the ASA Conference, Cleveland, Ohio, November 1968.

4.3.1-2 "Fan/Compressor Noise Research", Volume 1, Final Report under DOT/FAA Contract FA68WA-1960, Project Number 550-001-01H, General Electric Company (AEG), December 1970, FAS Report FAA-RD71-85, December 1971.

4.3.1-3 Kazin, S.B., Volk, L.J., "OF336 Lift Fan Modifications and Acoustic Test Program", NASA Report CR-1934, December 1971.

4.3.4-1 Smith, M.J.T. and Bushell, K.W., "Turbine Noise - Its Significance in the Civil Aircraft Noise Problem", ASME 69-WA/GT-12, 1969

REFERENCES

4.4.1-1 Tyler, J.M., and Sofrin, T.G.; "Axial Flow Compressor Noise Studies," SAE Transactions 70, pg. 309, 1962.

4.4.1-2 Kemp, N.H., and Sears, W.R.; "The Unsteady Forces Due to Viscous Wakes in Turbomachines," J. Aeronautical Sciences 22, pp. 478-483, 1965.

4.4.1-3 Silverstein, A., Katzoff, S., and Bullivant, W.K.; "Downwash and Wake Behind Plain and Flapped Airfoils," NACA Report 651, 1939.

4.4.2-1 Schlicting, H., Boundary Layer Theory, 6th Edition, transl. from German by J. Kestin, McGraw-Hill, New York, 1968.

4.4.2-2 Cherry, D.G., Staley, T.K., and Thomas, M.W.; "Highly Loaded Multi-Stage Fan Drive Turbine -- Cascade Test Program," NASA CR-2171, January 1973.

4.4.2-3 Markov, N.M., "Calculation of the Aerodynamic Characteristics of Turbine Blading," Transl. from Russian by Assoc. Tech Services (1958).

4.4.2-4 Horlock, J.H., Axial Flow Turbines, Butterworth and Co., (Publishers) Ltd. (1966).

4.4.2-5 Ainley, D.G., and Mathieson, G.C.R., "An Examination of the Flow and Pressure Losses in Blade Rows of Axial-Flow Turbines," N.G.T.E. Report R. 86 (1951), also ARC Tech. Report R & M No. 2891 (1955).

4.4.2-6 Ainley, D.G., and Mathieson, G.C.R., "A Method of Performance Estimation for Axial-Flow Turbines," N.G.T.E. Report R.111 (1952), also ARC Tech. Report R & M No. 2974 (1957).

4.4.2-7 Dunham, J., and Came, P.M., "Improvements to the Ainley-Mathieson Method of Turbine Performance Prediction," ASME Paper No. 70-GE-2, presented at the Gas Turbine Conference and Products Show, Brussels, Belgium, May 24-28, 1970 of the ASME.

REFERENCES

4.4.4-1 Wolfmeyer, G.W. and Thomas, M.W., "Highly Loaded Multi-Stage Fan Drive Turbine - Performance of Initial Seven Configurations," NASA CR-2362, February 1974.

SECTION 5.0

INTERACTION NOISE

5.1 BACKGROUND

Questions had been raised about the effects of fan and core exhaust stream interaction on the engine noise levels as a result of large humps of noise ("haystacks") observed in engine farfield narrowband spectra. The haystacking occurs in the frequency regime where fan and turbine blade-passing-frequency (BPF) tones normally appear, as is seen, for example, for Quiet Engine "A" in Figure 5.1.1. At the same time, the signal recorded by acoustic probes placed in the core nozzle indicate relatively pure tones emerging from the turbine, as given by discrete frequency spikes at each BPF location.

It was conceivable that the haystacking is a manifestation of a coupling interaction or feedback mechanism between the fan and core exhausts and this led to the speculation that the original engine noise levels are being amplified by this mechanism.

The objectives were to analytically and empirically:

- Isolate the source and the mechanisms involved.
- Determine whether any amplification takes place.
- Identify means of alleviating this condition.

5.2 IDENTIFICATION OF THE SOURCE AND RELEVANT MECHANISMS

Haystacks might conceivably result from any of the following:

(1) Turbine or fan tone modulation by the exhaust streams.

(2) Lip noise generation at the core nozzle tip.

(3) Flow separation at a step in the exhaust cowl.

(4) Flow over struts in the exhaust stream.

(5) Exhaust duct cavity resonance.

(6) Casing transmission.

(7) Modulation of combustor noise by turbine tones.

Most of these may be eliminated however, by consideration of available data and analytical reasoning. Acoustic data from the TF34 and Quiet Engines "A" and "C" pertinent to the haystack phenomenon are shown in Figures 5.2-1 through 5.2-6. The haystacks for the three engines appear to differ somewhat in character, in that discrete tone content is visible in some and not observed in others. There is also some doubt if they could all be attributed to a single common source. While it is possible to associate a turbine tone

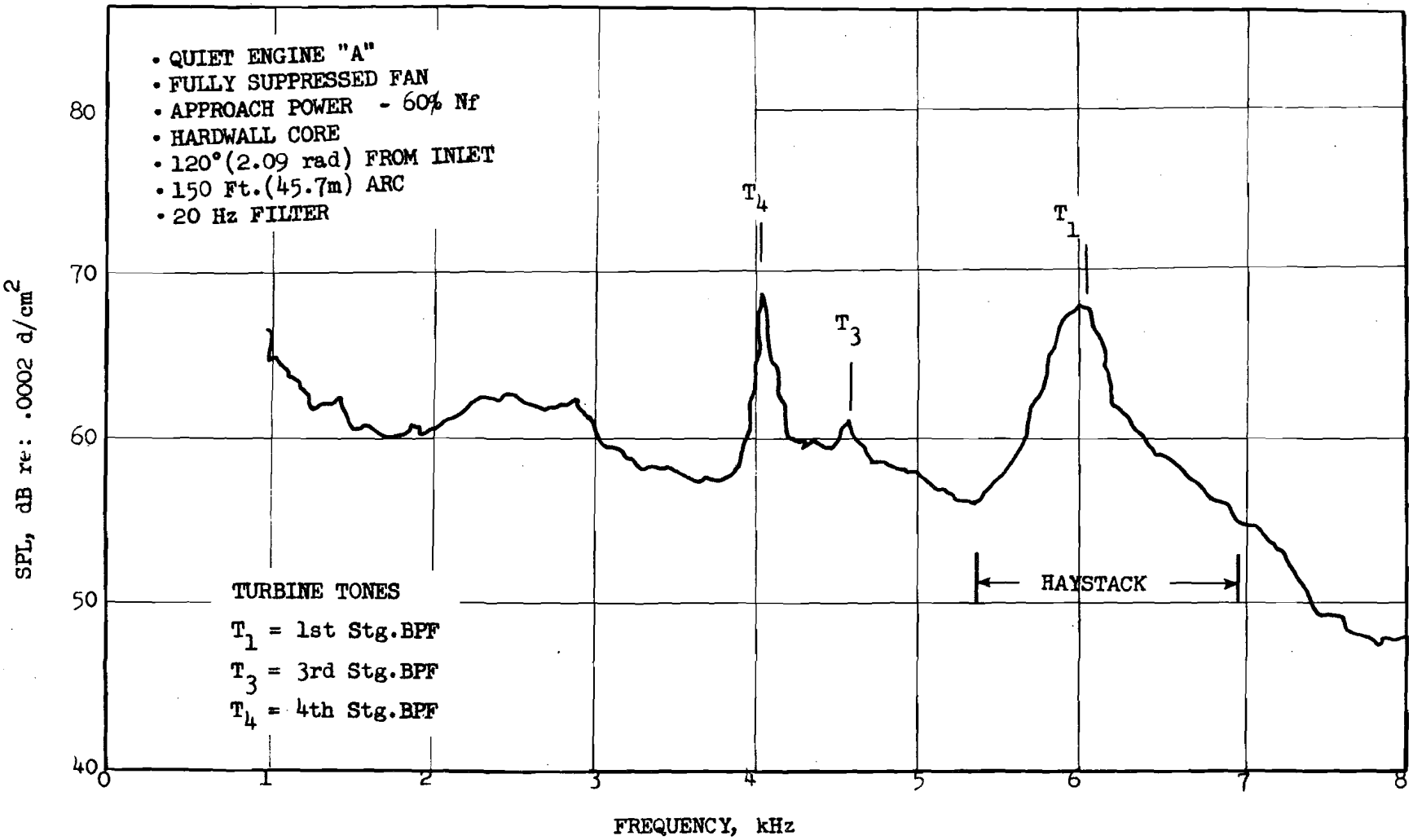

FIGURE 5.1-1 HIGH BYPASS ENGINE FARFIELD NARROWBAND SPECTRUM SHOWING "HAYSTACK".

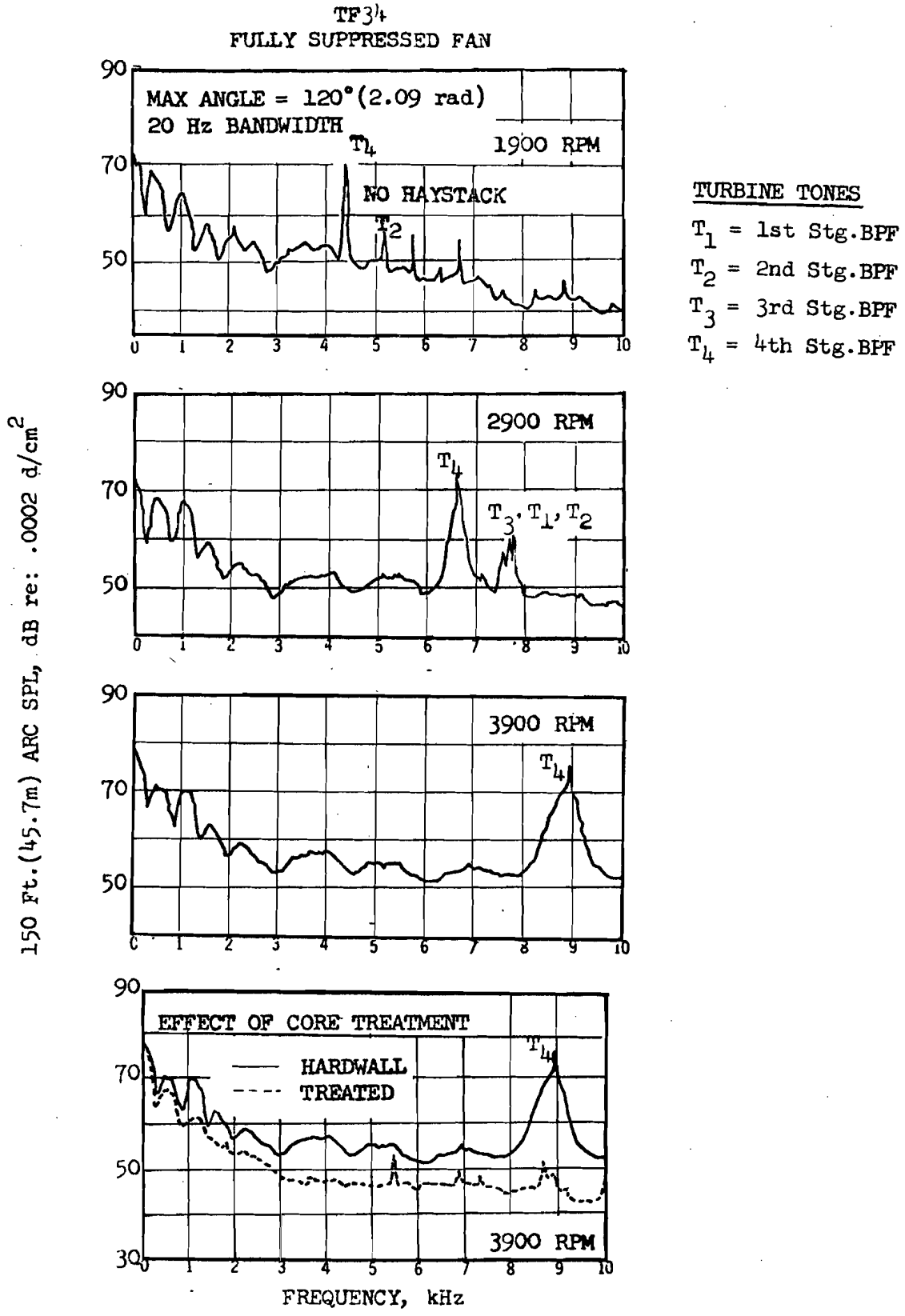

FIGURE 5.2-1 FARFIELD NARROWBAND SPECTRUM SHOWING HAYSTACKING GROWTH WITH SPEED AND THE EFFECT OF CORE ACOUSTIC TREATMENT.

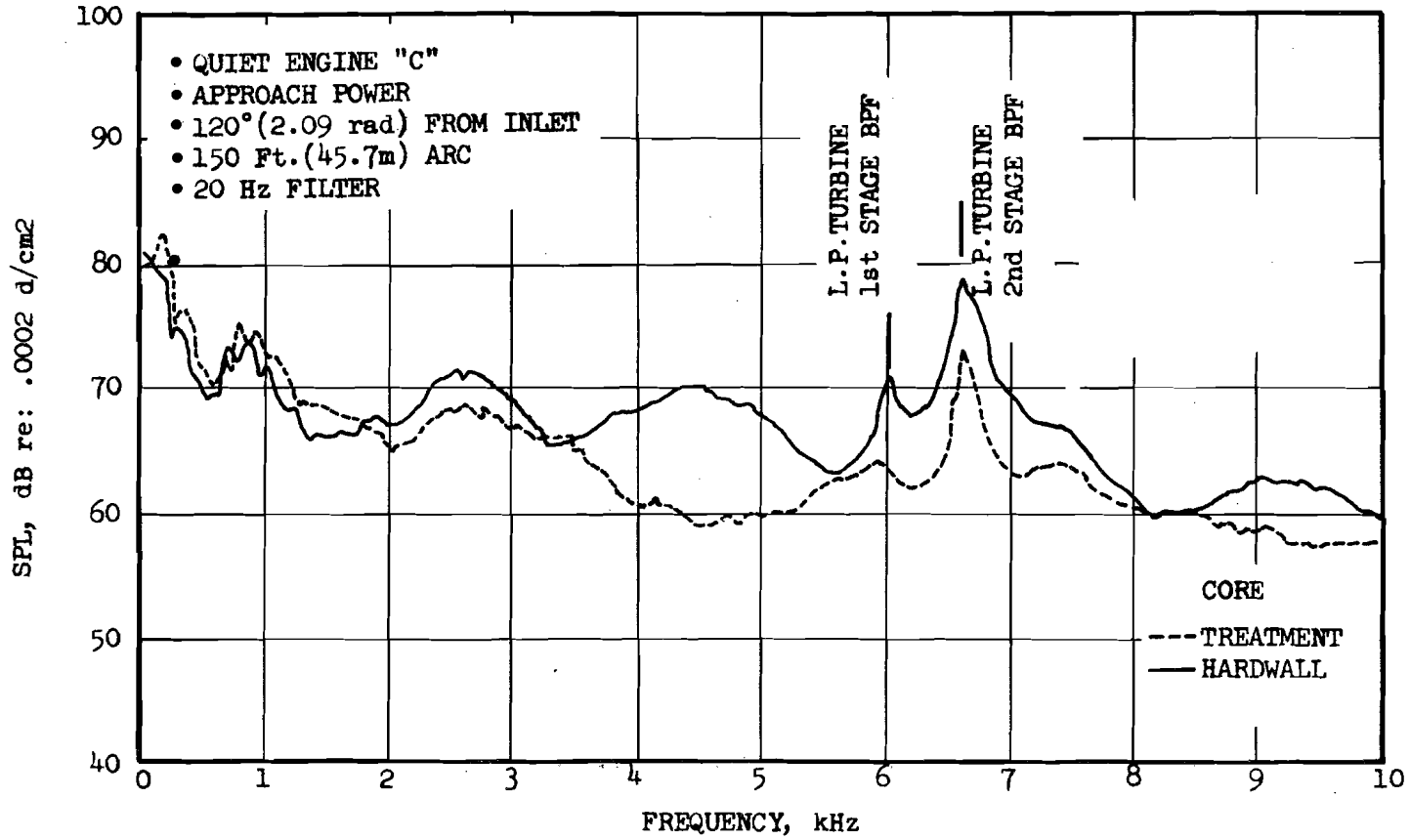

FIGURE 5.2-2 FARFIELD NARROWBAND SPECTRUM SHOWING HAYSTACKING AND THE EFFECT OF TREATMENT (CORRECTED TO HARDWALL CORE RPM).

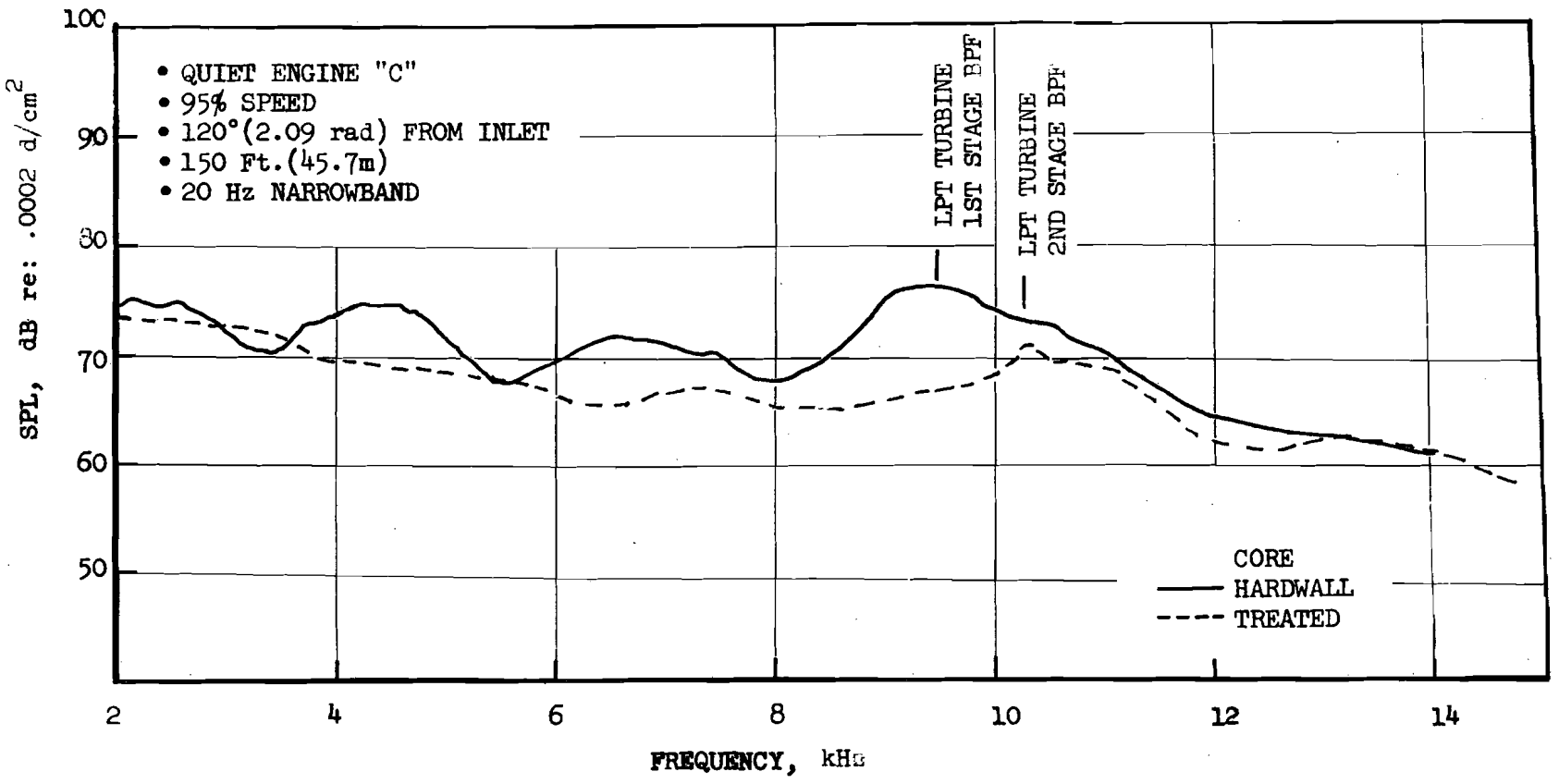

FIGURE 5.2-3 FARFIELD NARROWBAND SPECTRUM SHOWING THE "HAYSTACKING" AND THE EFFECT OF TREATMENT.

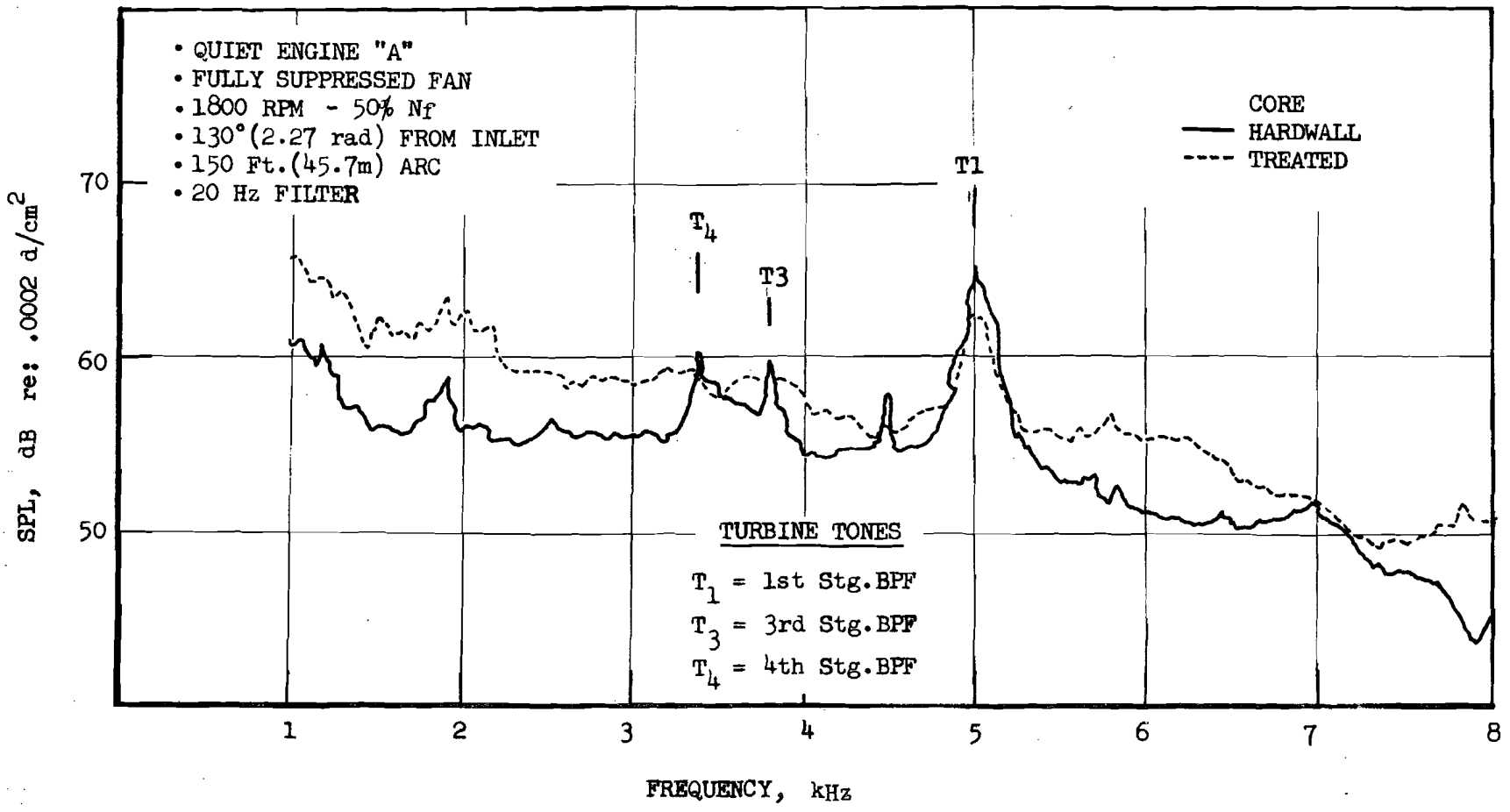

FIGURE 5.2-4 FARFIELD NARROWBAND SPECTRUM SHOWING "HAYSTACK" AT 130°
(CORRECTED TO UNTREATED RPM).

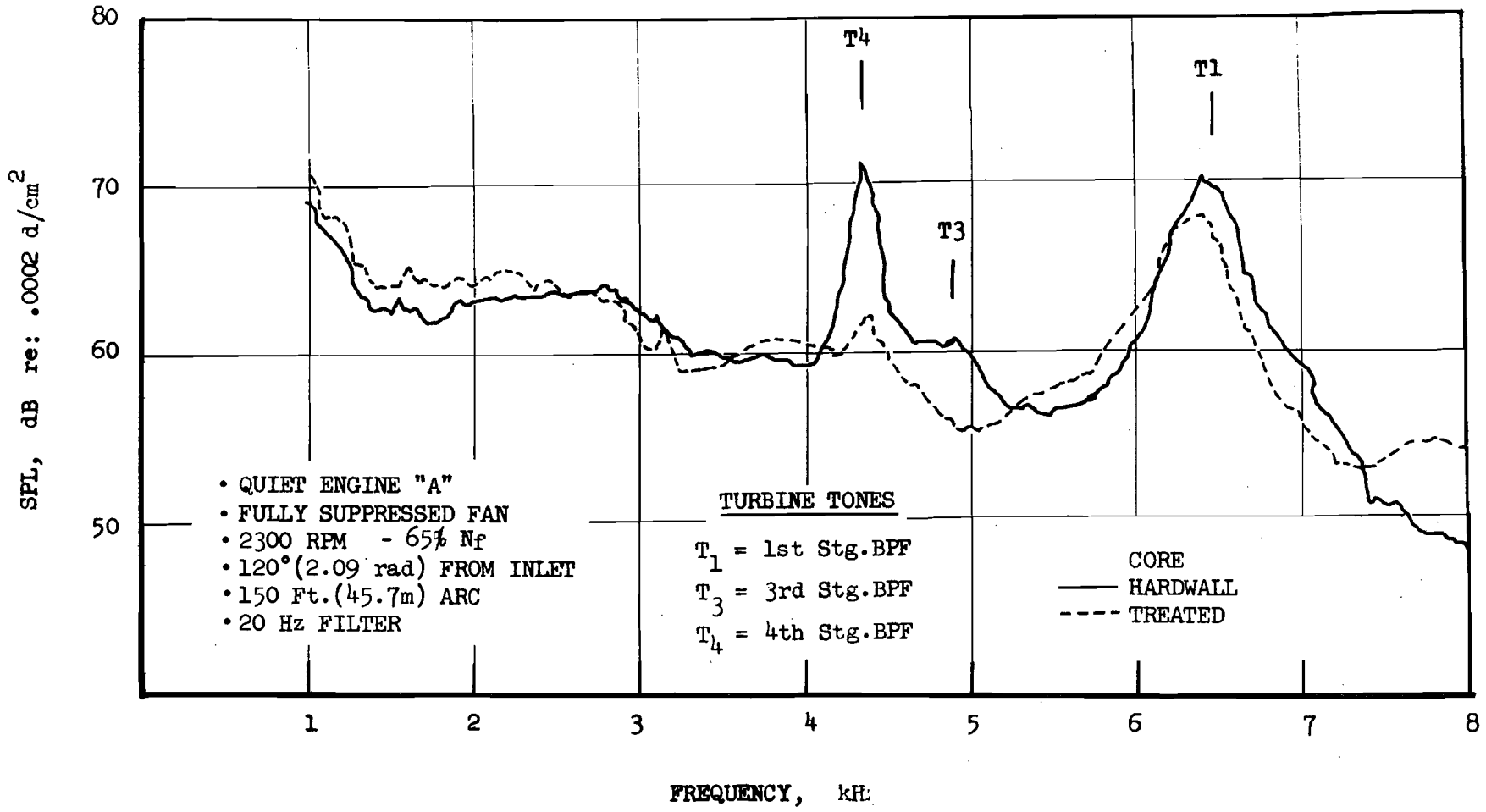

FIGURE 5.2-5 FARFIELD NARROWBAND SPECTRUM SHOWING "HAYSTACK" AT 120°
(CORRECTED TO UNTREATED RPM).

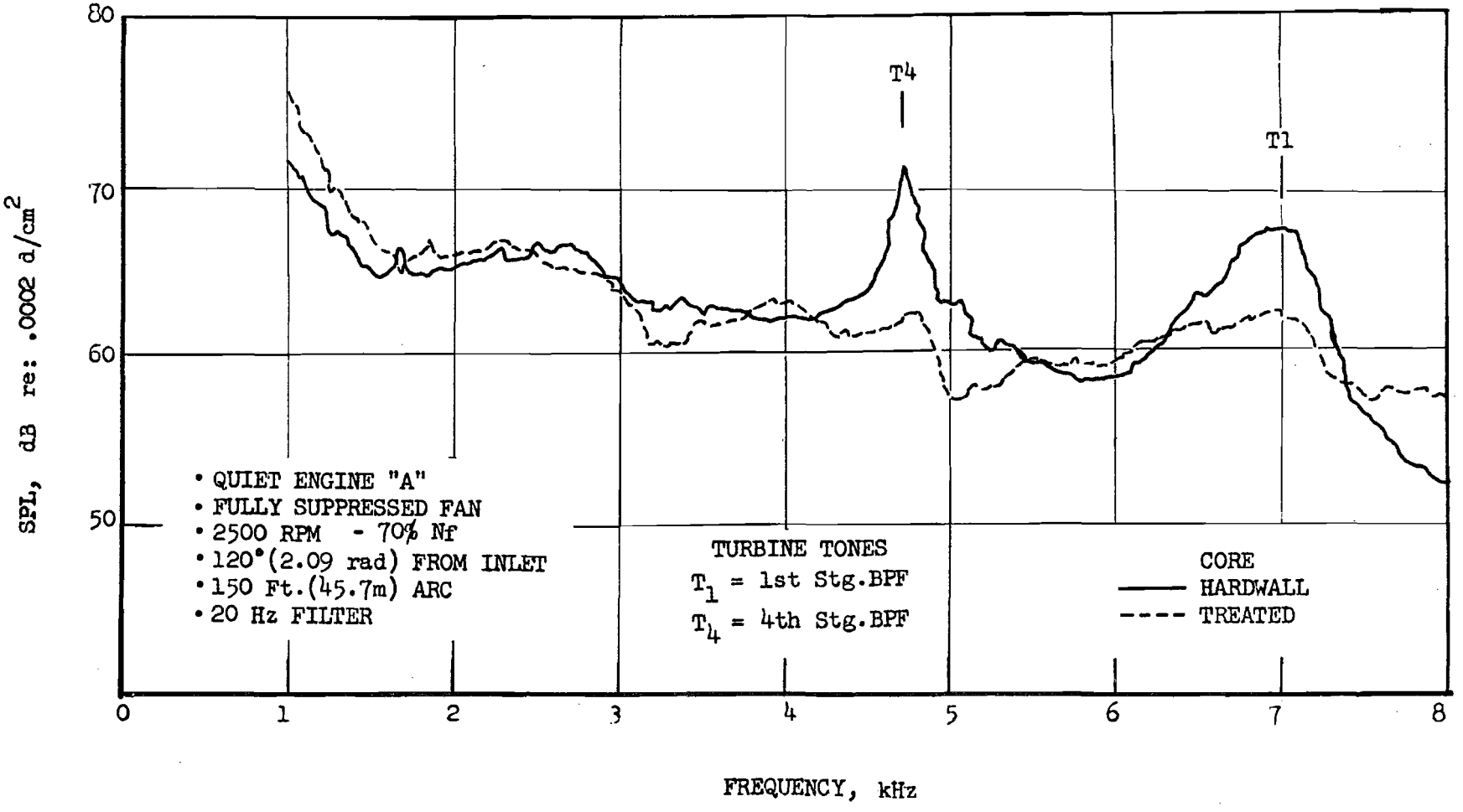

FIGURE 5.2-6 FARFIELD NARROWBAND SPECTRUM SHOWING "HAYSTACK" AT 120°
(CORRECTED TO UNTREATED RPM)

with each haystack, there exists the problem whether the haystacks merely obscure the tones in question or whether they are modulated forms of the tones.

The TF34 data of Figure 5.2-1 show a turbine tone experiencing a frequency broadening and developing a skirt as the speed is increased. The spectra in this Figure show the effect of inserting acoustic treatment into the core; both tone and the associated haystack are greatly attenuated.

Figures 5.2-2 and 5.2-3 show the Engine "C" haystack in two different stages, the former with still some visible tone content. Turbine treatment is again effective in removing the haystack.

Figures 5.2-4 through 5.2-6 demonstrate the haystacking phenomenon for Quiet Engine "A." The tone content of the 1st stage (T_1) haystack is barely visible at the lowest speed, but the last stage tone (T_4) very clearly shows the evolution into a haystack. The turbine treatment works well on the T_4 haystack but only marginally on the T_1 haystack. This however may be a consequence of a dip that exists in treatment effectiveness at 6 KHz.

The data of Figures 5.2-1 through 5.2-6 therefore indicate that the haystack source lies within the core, upstream of any core treatment and that the source is probably turbomachinery discrete frequency noise.

The differences in haystack appearance that were initially noted can be explained by assuming the same content, but a variable degree of modulation for each engine and engine speed. The degree of modulation experienced by a turbine tone depends, perhaps, on the turbulence level in the exhaust stream through which it must propagate and also on the level of the broadband noise floor. Both the turbulence level and the broadband floor rise for any engine, as the speed is increased, and therefore increasing tone modulation may be expected.

The observed effect of the core acoustic treatment would appear to eliminate the sources external to the core nozzle from further consideration. This would include flow separation on the exhaust casing and lip noise. Since the spectrum is normally fairly flat, the haystack could result from a "window" in the casing radiation transmission spectrum (see Section 7). The computed window was found to occur at much lower frequencies than the haystack for Quiet Engine "A" however. Wrapping the casing did not eliminate the haystack either. (see Figure 5.2-7).

The noise generated by flow over turbine rear frame struts in the core nozzle was eliminated as a haystack because the Strouhal peak frequencies (given by $ft/V \simeq .22$) were found to be incompatible with the haystack peak frequencies. Acoustic data taken with probes in the core nozzle also fail to show the presence of any such obstruction noise.

Hypothetically, cavity resonance could be important, since broadband noise can excite duct mode resonances causing tones to appear at the resonant frequencies. Turbine tones can also be enhanced when the duct resonances

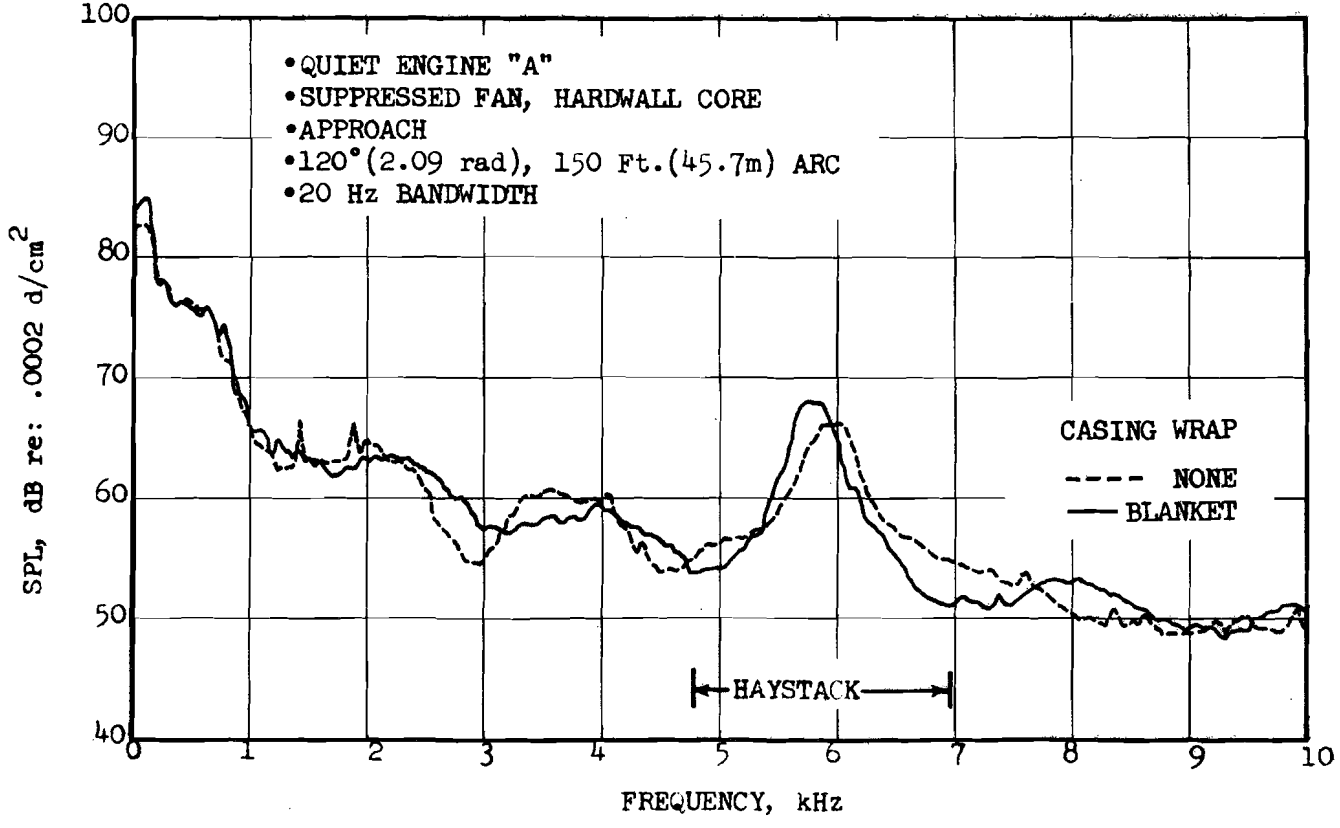

FIGURE 5.2-7 EFFECT OF WRAPPING THE ENGINE CASING.

coincide with the BPF's. In such an event, however, the tone level would vary sharply with engine speed as the driving frequency passed through a duct resonance. The haystack data shows a uniform trend however with rpm.

A basis for modulation of combustor noise by turbine tones to produce haystacks can be found in Reference 5.2-1. This requires two noise sources in series, as in the case of the combustor and turbine. However, for this mechanism, a coplanar fan and core exhaust would not be expected to change the haystacking, as was found for the Quiet Engine "C" coplanar configuration. (See Section 5.4).

The above considerations leave turbine tone modulation as the one viable mechanism that can produce haystacks.

5.3 ANALYSIS OF THE HAYSTACKING PHENOMENON

5.3.1 The Mechanisms Responsible for Tone Modulation

Modulation of turbine tones has been postulated to be responsible for the haystacks observed in the farfield acoustic data for many engines. The modulation must be a function of the interaction of, or with, the core and fan exhaust streams. Hence, referring to Figure 5.3.1-1, we seek a frequency dependent transfer function $T(\omega)$ such that an incident wave of intensity $I(\omega)$ is converted into a farfield signal characterized by the spectrum $O(\omega)$ where

$$O(\omega) = T(\omega)I(\omega)$$

This simple black box concept is complicated by the fact that a review of available literature indicates that two different mechanisms must be considered in determining $T(\omega)$: instability amplification by the shear layer(s) and scattering by the turbulence in the mixing region. For the range of frequencies and configurations of interest, however, it would appear only the latter is significant.

5.3.2 Tone Modulation by Shear Layer Instability

Excitation of the instability modes of free shear layers by periodic disturbances, injected parallel to the layers, is well known and discussion of the instability phenomenon may be found, for example, in Reference 5.3.2-1 through 5.3.2-7. This mechanism provides a possibility of amplification of tones traversing axially through a jet, as would be the case for turbomachinery discrete frequency noise propagating out of either exhaust nozzle. It is generally accepted that the disturbance frequency must coincide with the natural frequencies generated by the unstable jet before amplification can take place. There is some uncertainty as to whether a certain minimum amplitude is required.

INTERACTION MECHANISMS

TRANSFER FUNCTION $T(\omega)$ DETERMINED BY:

- Turbulence Scattering
- Instability Amplification

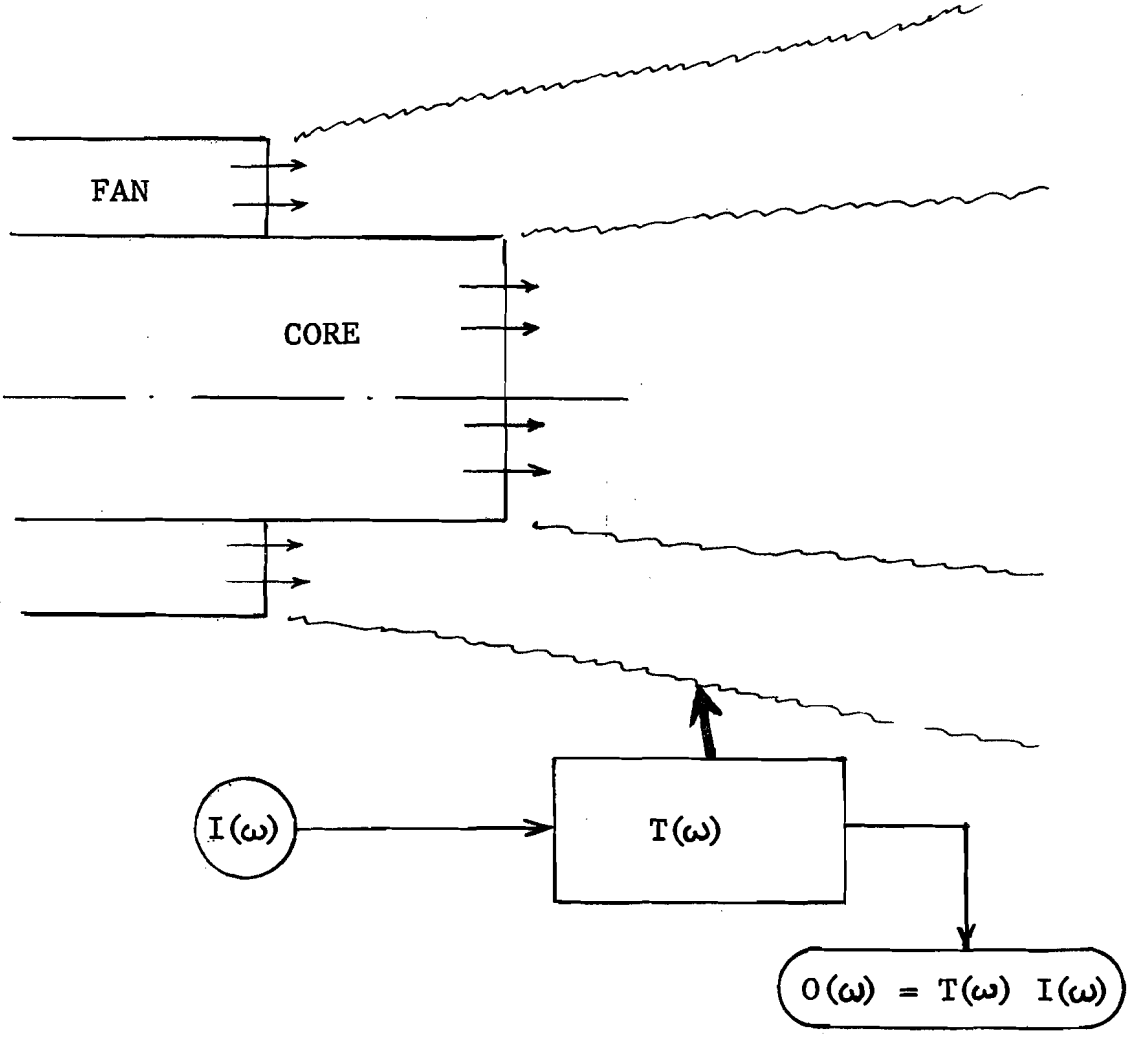

FIGURE 5.3.1-1

The authors of Reference 5.3.2-8 have presented some data displaying amplification. An acoustic signal simulating "core noise" was inserted into the central jet of a coannular flow and amplification was obtained for a tone-like peak at 450 Hz. Unfortunately, the evidence cannot be considered conclusive since the same 450 Hz peak was amplified for three different nozzle pressure ratios while a similar peak of higher magnitude at 300 Hz was left unaffected. Further, the source was placed far upstream of the nozzle exit plane and the observed phenomenon might well be a duct effect and therefore unique to the experiment.

Professor S.C. Crow (UCLA, unpublished reference) has indicated that because of the above-mentioned frequency matching criteria the instability phenomenon is inefficient over most velocities and frequencies and is significant only for Strouhal numbers in the range

$$\frac{fd}{V} \sim 0.2 \text{ to } 0.6$$

where f is the frequency of the periodic disturbance, d is the jet diameter and V the jet velocity. Hence, for a typical turbofan engine, no amplification would be encountered for turbine tones (which are well above 2 kHz) unless the core velocity becomes supersonic. The same reasoning could be applied to fan tones. This mechanism could be of significance however, either in the event that low frequency periodic noise was present in the core duct or in the case of turbojets at high power settings.

Other experiences by Professor Crow with core noise amplification can be found in Reference 5.3.2-9.

The above analysis indicates that there would not be any amplification of the tones. To verify these results, a comparison of noise levels of the modulated tones in the farfield was made with the turbine levels measured by acoustic probes in the core duct. The comparison was carried out for Quiet Engines "A" and "C" and the CF6. The farfield acoustic power levels (PWL) were based on 1/3 octave band data in order to include the tonal energy spread out into the sidebands and the duct PWL's on the 20 Hz bandwidth spectra. Typical results are provided in Table 5.3.2-1. The duct PWL's for Engines "A" and "C" include the probe frequency response corrections and those for the CF6 also include corrections for the flow and the acoustic impedance in the duct (Appendix F). The effect of including the two corrections for Engines "A" and "C" would be to raise the duct PWL's by about 3 to 4 dB.

Good agreement is found in Table 5.3.2-1 between the core and farfield PWL for the CF6 dominant turbine tones at this power setting. Both the 2nd and the 3rd stage BPF fall into the same 1/3 octave band. If the above flow corrections are used for Engines "A" and "C", a similar agreement is obtained for the two engines. It it therefore concluded that no tone amplification exists, and that the jet instability mechanism may be ignored for these engines.

TABLE 5.3.2-1

POWER LEVEL CORRELATION FOR TURBINE TONES

- HARDWALL CORE

Engine & Turb. Stage	Power Setting	Probe PWL (dB)	Farfield PWL For 1/3 O.B. with Tone(s) (dB)
"A" 1st Stg	Approach	128.9*	131.6
"A" 4th Stg	Approach	124.9*	128.7
"C" 1st & 2nd Stage	Approach	136*	140.6
"C" 1st & 2nd Stage	Takeoff	~145.0*	149.2
CF6 2nd & 3rd Stage	Low Power Approach	146.4	147.2
CF6 2nd & 3rd Stage	High Power Approach	151.2	150.6

* DO NOT INCLUDE MACH NUMBER OR (ρc) CORRECTION (Appendix F)

5.3.3 Tone Modulation by Turbulence Scattering

Turbulence scattering is analogous to the apparent twinkling of stars which occurs due to scattering of light rays by atmospheric turbulence. The scattering of sonar beams underwater which eventually results in loss of all beam width and coherence has been extensively investigated in underwater acoustics. Haystacks are hypothesized to be the result of modulation suffered by turbine tones while propagating through the intensely turbulent mixing regions associated with the exhaust jets (See Figure 5.3.3-1). The modulation can be attributed to the spatially incoherent distribution of turbulent velocity in the jet mixing region(s) through which the tones must propagate which results in redistribution of the acoustic energy contained in the tones. The random focusing and defocusing leads to fluctuation of the tone SPL in space and time.

The problem of scattering by jet turbulence has been analytically investigated in several forms in Reference 5.3.3-1 to 5.3.3-4. A simplified model displaying random turbulence cells in a stationary medium is analyzed herein. The turbulence cells in the mixing region (R) constitute zones in which the medium differs in acoustic properties from the rest of the medium. The difference is in the turbulent velocity $\vec{u}'$, perturbations in density δ_e, and variation in compressibility κ_e, where $\kappa_e = 1/\rho\ (\partial\rho/\partial p)$. If the perturbations in velocity and density due to an acoustic wave are given by $\vec{u}$ and δ, respectively, then for a stationary medium, the equations of motion become:

$$\frac{\partial}{\partial t}(\rho_o + \delta_e + \delta) = -\mathrm{div}[(\rho_o + \delta_e + \delta)(\vec{u}' + \vec{u})] \qquad (5.3.3\text{-}1)$$

and

$$(\rho_o + \delta_e + \delta)\frac{d(\vec{u}' + \vec{u})}{dt} = -\ \mathrm{grad}\ (\rho_o + \rho) \qquad (5.3.3\text{-}2)$$

Here ρ_o and p_o denote the averaged values of density and pressure and p the pressure perturbation. δ_e, κ_e and p are functions of the location, $\vec{r}$, and time, t.

Equations (5.3.3-1) and (5.3.3-2) can be manipulated into an "inhomogeneous" wave equation:

$$\nabla^2\rho - \frac{1}{c^2}\frac{\partial^2\rho}{\partial t^2} = \frac{1}{c^2}\frac{\partial^2\rho}{\partial t^2}\gamma_\kappa(\vec{r},t) + \mathrm{div}[\gamma_\rho(\vec{r},t)\,\mathrm{grad}\ \rho] - \nabla\cdot\left|\ \underset{\sim}{\overset{=}{\sim}}\ \right|\cdot\nabla \qquad (5.3.3\text{-}3)$$

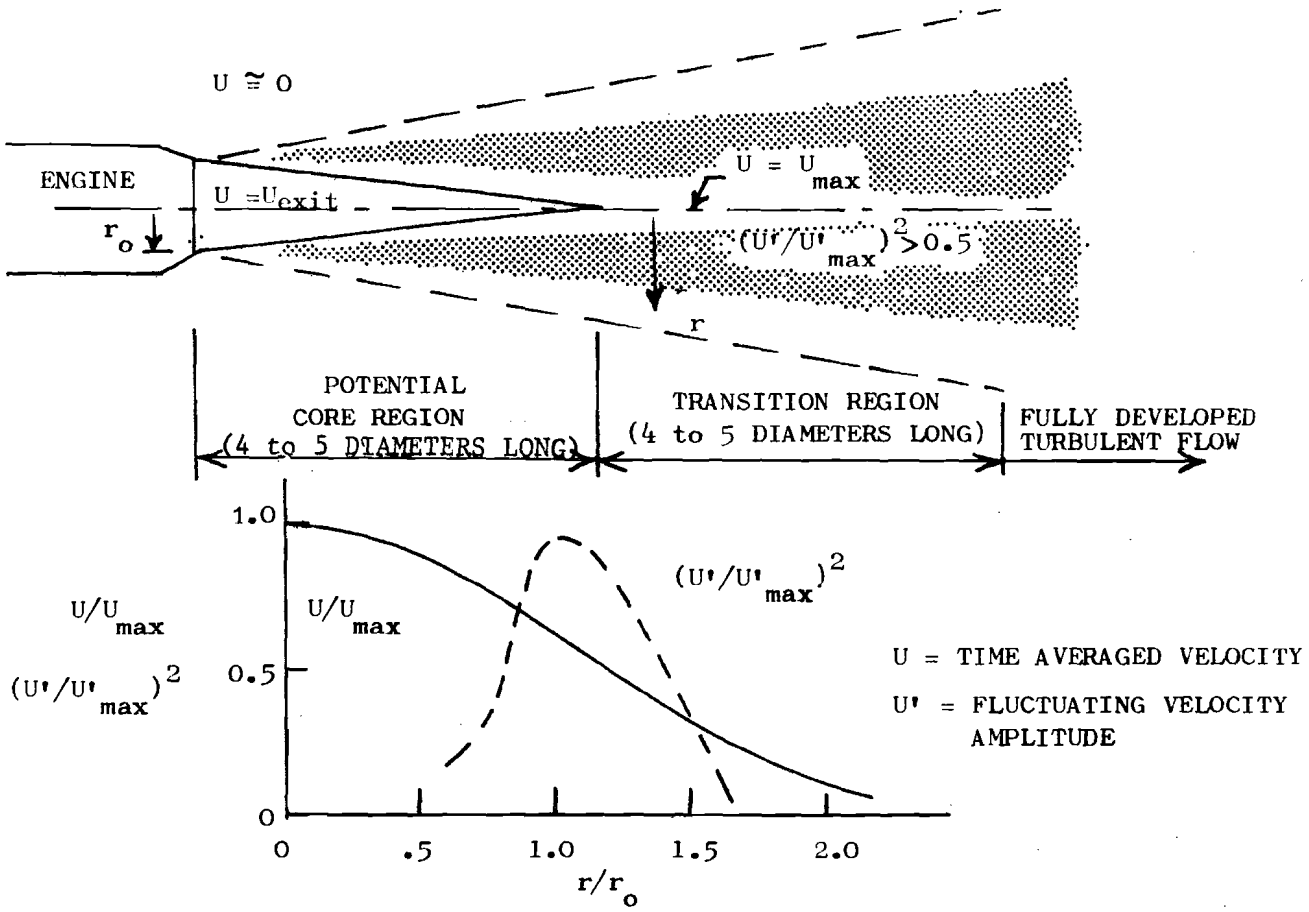

REF: ASD-TDR-62-578, "SUPPRESSION OF JET NOISE WITH EMPHASIS ON THE NEAR FIELD", K.M.ELDRED, et al, FEB. 1963, PAGE 4.

FIGURE 5.3.3-1 JET EXHAUST FLOW MIXING CHARACTERISTICS

where

$$\nabla \cdot \underset{\sim}{\overset{\overset{=}{\sim}}{|}} \cdot \nabla \simeq 2\left[\frac{\partial^2}{\partial x^2} R_{xx} + \frac{\partial^2}{\partial x \partial y}(R_{xy}+R_{yx}) + ---\right]$$

$$+\left[\frac{\partial^2}{\partial x^2}(u_x')^2 + 2\frac{\partial^2}{\partial x \partial y} u_x' u_y' + ----\right] \qquad (5.3.3\text{-}4)$$

$$R_{xx} = \rho u_x u_x'$$

$$R_{xy} = \frac{1}{2}\rho(u_x u_y' + u_y u_x')$$

and

$$\gamma_\kappa = \frac{\kappa_e - \kappa}{\kappa} \quad \text{inside R}$$

$$= 0 \quad \text{outside R}$$

$$\gamma_\rho = \frac{\rho_e - \rho}{\rho_e} \quad \text{inside R}$$

$$= 0 \quad \text{outside R}$$

$$c^2 = \frac{1}{\rho\kappa} \quad \text{assuming isentropic processes.}$$

The second order terms in the acoustic velocity have been neglected. Since we are interested only in the scattering of sound by the inhomogenities in the region R and not in the sound generated within r, the $u_i' u_j'$ terms in $\overset{\overset{=}{\sim}}{|}$ are from equation (5.3.3-2), as the latter represent sound sources and are independent of the acoustic wave incident upon R. The equation then becomes:

$$\nabla^2\rho - \frac{1}{c^2}\frac{\partial^2\rho}{\partial t^2} = \frac{1}{c^2}\frac{\partial^2\rho}{\partial t^2}\gamma_\kappa(\vec{r},t)$$

$$+ \operatorname{div}[\gamma_\rho(\vec{r},t)\operatorname{grad}\rho] - 2\,\nabla \cdot \overline{\overline{R}} \cdot \nabla \qquad (5.3.3\text{-}5)$$

where the tensor $\overline{\overline{R}}$ has the components R_{xy}, etc. It should be noted that the equation is homogeneous in p and "inhomogeneous" only in the sense that it has <u>source</u> terms (representing scattering) on the right hand side.

The solution to equation (5.3.3-5) can be approached in two different ways. The time dependence may be removed first by means of separating the forcing terms into their simple harmonic components through Fourier transforms.

The Fourier transform technique leads to the following integral equation:

$$p_\omega(\vec{r}) = p_i(\vec{r}) + \iiint_R f_\omega(\vec{r}_o) g_\omega(\vec{r}/\vec{r}_o)\, du_o \qquad (5.3.3\text{-}6)$$

where

$$g_\omega(\vec{r}/\vec{r}_o) = \frac{1}{4\pi|\vec{r}-\vec{r}_o|} \exp(ik|\vec{r}-\vec{r}_o|) \qquad (5.3.3\text{-}7)$$

$$k = \frac{2\pi}{\lambda} = \frac{\omega}{c}$$

Also, $f_\omega(\bar{r}_o)$ is the Fourier transform of the forcing terms, i.e. the right hand side of equation (5.3.3-5). The region R is represented by $\vec{r}_o$ and the measurement point by $\vec{r}$. The integration is over the region R and $g_\omega(\vec{r}/\vec{r}_o)$ is the spatial Green's function for the unbounded medium. The scattered wave is given by $P_\omega(\vec{r})$ and the incident wave represented by $p_i(\vec{r})$.

The integral equation is now inhomogeneous because of the term $p_i(\vec{r})$ and can be solved exactly only in rare instances. Generally, successive approximations are used instead:

$$P_\omega(\vec{r}) = p_i(\vec{r}) + p_1(\vec{r}) + p_2(\vec{r}) + \text{----} \qquad (5.3.3\text{-}8)$$

The first term $p_1(\vec{r})$ is found by using p_i for p_ω in the volume integral, $p_1(\vec{r}) = \iiint_R f_\omega(\vec{r}_o) g_\omega(\vec{r}/\vec{r}_o)\, d\, v_o$, the second term $p_2(\vec{r})$ by putting p_1 for p_ω in the integral and so on. In case $p_1 << p_i$ within R, then is sufficient to use

$$p_\omega(\vec{r}) \doteq p_i(\vec{r}) + p_1(\vec{r}) \qquad (5.3.3\text{-}9)$$

This last is known as the Born approximation.

The second approach to solving equation (5.3.3-5) is by means of the time dependent Green's function $(\vec{r}, t/\vec{r}_o, t_o)$ along with the source function $f(\vec{r},t)$ which is the right hand side of equation (5.3.3-5). If the γ's and R are small, the Born approximation is valid with p approximated by p_i in $f(\vec{r},t)$

$$f(\vec{r},t) \simeq -\frac{1}{c^2}\gamma_\kappa(\vec{r},t)\frac{\partial^2 p_i}{\partial t^2} - \text{div}[\gamma_\rho(\vec{r},t)\,\text{grad}\; p_i(\vec{r},t)] + 2\nabla\cdot\bar{\bar{R}}\cdot\nabla \qquad (5.3.3\text{-}10)$$

and

$$g(\vec{r},t/\vec{r}_o,t_o) = \frac{1}{4\pi|\vec{r}-\vec{r}_o|}\,\delta\left[t_o - t + \frac{|\vec{r}-\vec{r}_o|}{c}\right] \qquad (5.3.3\text{-}11)$$

Here δ [τ] represents the delta function. The solution is given by:

$$p_s(\vec{r},t) = \iiint_R d\, v_o \int_{-\infty}^{\infty} f(\vec{r}_o,t_o)\, g(\vec{r},t/\vec{r}_o,t_o)\, dt_o \qquad (5.3.3\text{-}12)$$

The pressure p_s $(\vec{r},t)$ represents only the scattered part of the wave. Taking the Fourier transform yields the spectrum. This process translates the random motion within R, as give by the variation of the γ's, into a frequency spread. This spread is determined by the reciprocal of the time correlation interval, τ_c, which represents the interval beyond which the autocorrelation function falls off rapidly to zero.

For example, assuming an incident plane wave $p = A_o \exp(i\vec{k}_i\vec{r} - ik_i ct)$, the solution to equation (5.3.3-12) may be expressed, after some manipulation, in terms of integrals over the turbulent region (R) and the retarded time $(t - \lambda/c + \vec{r}_o \cdot \hat{a}_r/c)$ over a suitable time interval (T). Taking the Fourier transform and assuming an auto-correlation function which correlation length ℓ_c and correlation time $1/\omega_c$, the spectral density of the <u>scattered</u> wave is given by:

$$I_\omega(\vec{r}) \simeq \frac{|A_o^2|}{\rho c r^2} \frac{VT\ell_c^3}{16\pi^2\omega_c} [k_i^4\langle\gamma_\kappa^2\rangle + k_i^2\langle\gamma_\rho^2\rangle(\frac{\omega}{c})^2\cos^2\Theta$$

$$+ 4(\frac{\omega}{c})^4\langle M_t^2\rangle\cos^2\Theta]\exp[-\frac{1}{2}\mu_s^2\ell_c^2 - \frac{1}{2}(\frac{\Delta_s}{\omega_c})^2] \qquad (5.3.3\text{-}13)$$

where

k_i = incident wave number = $\frac{\omega}{c}$

< > denotes a time and space averaged mean

V = volume of turbulence region

$M_t = \frac{u_r'}{c}$ where u_r' = turbulent velocity in the direction of the observer $(\vec{r})$.

$\hat{a}$ = unit vector = $\vec{k}/|\vec{k}|$ and the subscript denotes the direction

$\cos\Theta = \frac{\vec{k}_i \cdot \vec{k}_s}{k^2}$; the cosine of the angle between the observer and the incident plane wave

$\vec{M}_s = \frac{\omega}{c}\hat{a}_r - \vec{k}_i$

and

$\Delta_s = \omega - k_i c = \omega - \omega_o$

Equation (5.3.3-13) shows that the observed interaction effects could be a result of fluctuation in both density and compressibility in the mixing region (these two effects are of the same order) and a non-zero distribution of turbulence velocity component.

$I_\omega(r)$ gives the energy in the scattered wave for a given frequency and spatial location. Integrating over the frequency and space provides the total energy loss due to scattering. For example, integrating equation (5.3.3-13) over frequency and non-dimensionalizing yields:

$$\frac{I_s(\vec{r})}{|A_o^2|/\rho c r^2} \simeq \frac{V}{\sqrt{32\pi}\,\ell_c} \frac{\alpha^4}{\sqrt{1+\alpha^2}} \left\{ \eta^4 \langle\gamma_\kappa^2\rangle + \eta^2 \langle\gamma_\rho^2\rangle \frac{1+\eta^2(1+\alpha^2\cos^2\Theta)^2}{1+\alpha^2} \right.$$

$$\left. + 12\langle M_t^2\rangle \frac{1+2\eta^2(1+\alpha^2\cos^2\Theta)^2 + \frac{1}{3}\eta^4(1+\alpha^2\cos^2\Theta)^4}{(1+\alpha^2)^2} \right\}$$

$$\exp\left[-\frac{\eta^2\alpha^2}{2(1+\alpha^2)}\left(4\sin^2\frac{\Theta}{2} + \alpha^2\sin^2\Theta\right)\right] \qquad (5.3.3\text{-}14)$$

where $I_s(\vec{r})$ = overall scattered intensity at any location.

$$\eta = \omega_i/\omega_c$$

$$\alpha = k_c \ell_c$$

Equation (5.3.3-13) can be simplified for low turbulent Mach numbers, since normally γ_κ and γ_ρ vary as M_t^2 and therefore only the last term need be considered:

$$\frac{\bar{I}_\omega(\vec{r})}{|A_o^2|/\rho c r^2} \simeq \frac{V\ell_c^3}{4\pi^2\omega_c}\left(\frac{\omega}{c}\right)^4 \langle M_t^2\rangle \; H \qquad (5.3.3\text{-}15)$$

where $\bar{I}_\omega(\vec{r})$ is the time averaged value of $I_\omega(\vec{r})$

and $$H = \cos^2\Theta \exp\left[-\frac{1}{2}\mu_s^2\ell_c^2 - \frac{1}{2}\left(\frac{\Delta_s}{\omega_c}\right)^2\right] \qquad (5.3.3\text{-}16)$$

Taking ($10 \log_{10}$) of both sides, the left hand side would represent the difference (Δ) in decibels between the incident and scattered waves.

Also, imposing the Lighthill model for a subsonic jet (see Figure 5.3.3-2) and assuming that V=the mixing region volume, Equation (5.3.3-15) yields:

$$\Delta = 30\log_{10}D + 30\log_{10}x + 40\log_{10}\left(\frac{\omega}{c}\right) + 20\log_{10}M$$

$$+ 30\log_{10}\ell_c - 10\log_{10}\omega_c + 10\log_{10}{}^{H} + \text{constant (K)} \quad (5.3.3\text{-}17)$$

where

$$\Delta = 10\log_{10}\left[\bar{I}_\omega(\vec{r})/r^2\right] - 10\log_{10}|A_o^2|/\rho c$$

D = core nozzle diameter

x = axial distance downstream from the nozzle exit

Δ represents the energy lost by the scattering for a given frequency and angular location. Integrating over the frequency and angle gives the total energy dispersed by the scattering and therefore is a measure of the amplitude loss at the incident tone frequency.

An exact solution of equation (5.3.3-12) would require detailed knowledge of the turbulence region. The assumption of a coherence function permits the solution of equation (5.3.3-13). A simplified model, will be used below to show that turbulence modulation can yield a frequency spread.

Consider a region of discrete turbulence cells such that the incident tone propagates through unaltered in the absence of a turbulence cell in its path, and is completely cut off from the farfield when a cell interrupts the path. This constitutes a simple full OFF/full ON mechanism. Hence, in the farfield, the signal will be given by:

$$\begin{aligned} p(t) &= 0 && t<t_o \\ &= A_o\cos\omega_o t && t_o\leq t\leq t_o+\Delta t \\ &= 0 && t>t_o+\Delta t \end{aligned} \quad (5.3.3\text{-}18)$$

(Assuming that the entire content before time t_o and after t_1 is scattered or absorbed by turbulence cells).

The spectral content of such an interrupted signal is found by taking the Fourier transform,

$$\begin{aligned} p(\omega) &= \frac{1}{2\pi}\int_{\infty}^{\infty} p(t)e^{i\omega t}\,dt \\ &= \frac{A_o}{4\pi}\left[\frac{\sin(^{\omega}o-\omega)t}{(\omega_o-\omega)} + \frac{\sin(^{\omega}o+\omega)t}{(\omega_o+\omega)}\right]_{t_o}^{t_o+\Delta t} \end{aligned} \quad (5.3.3\text{-}19)$$

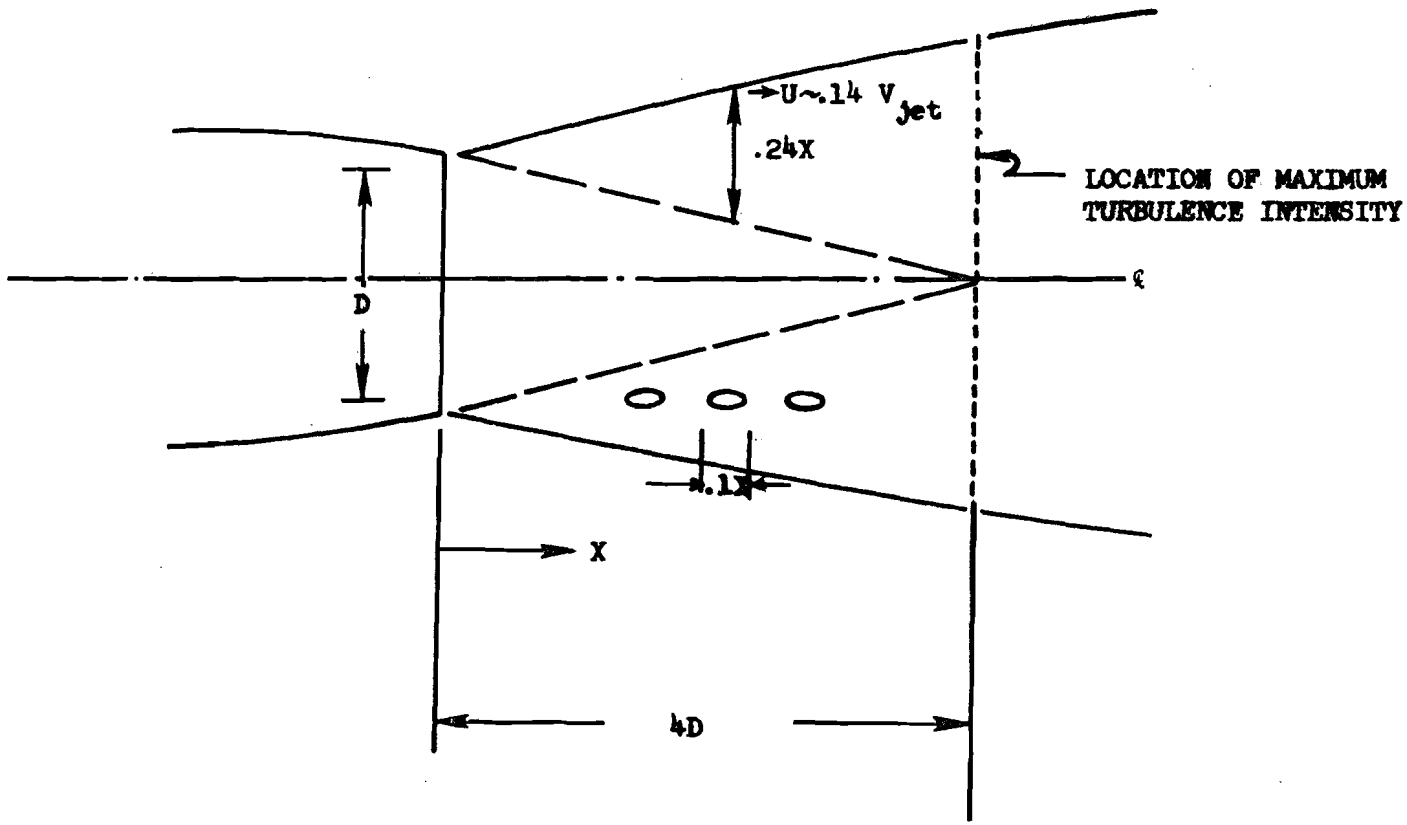

FIGURE 5.3.3-2 LIGHTHILL MODEL FOR A SUBSONIC JET.

Since ω is large ($=2\pi BPF$), $p(\omega)$ is small for all ω except near $(\omega_o-\omega)=0$. Hence, defining t_o as the time origin, equation (5.3.3-19) gives:

$$p(\omega) \simeq \frac{A_o}{4\pi} \frac{\sin(\omega_o-\omega)\Delta t}{(\omega_o-\omega)} \qquad (5.3.3\text{-}20)$$

This signal is shown in Figure 5.3.3-3 and displays a spectral broadening which is inversely proportional to the pulse time Δt. The peak value is achieved at $\omega=\omega_o$ and is given by

$$p(\omega_o) \simeq \frac{A_o}{4\pi} (\Delta t) \qquad \text{finite } \Delta t$$

In addition, the frequency where $p(\omega)=1/2\ p(\omega_o)$ is approximately given by:

$$|(\omega_o-\omega)| \simeq \frac{1}{2(\Delta t)}$$

Hence if $\Delta\omega$ is defined as the circular frequency range over which the signal stays within half the maximum value (6 dB point), the following approximate relationship holds:

$$(\Delta\omega)(\Delta t) \simeq 1 \qquad (5.3.3\text{-}21)$$

For an uninterrupted signal, $\Delta t \to \infty$ and a pure tone is recorded. On the other hand, short bursts of turbulence will broaden the received signal. Switching times can typically be of the order of a millisecond, giving frequency spreads of about 200 Hz (consistent with observations). As the jet speed is increased, the convection velocity of the turbulence cells increases and therefore the switching time decreases, resulting in increased frequency spread as was found for the engines surveyed in Section 5.2.

While a full OFF/full ON switching mechanism is not encountered in engine configurations, there is considerable variation in amplitude and phase, of the signal propagating through the jet mixing regions, imposed by the incoherent inhomogeneities inherent in this regime. Equation (5.3.3-13) shows that this is manifested as a drop in the peak amplitude and a frequency spread. The nature of the frequency spread can be inferred from the form of the time auto-correlation of the amplitude and phase fluctuations.

5.3.4 Discussion of the Results of the Analysis

The analytical model indicates that the acoustic signal recorded by the farfield microphones consists of an "incident" and a scattered wave. The "incident" wave contains the coherent part of the signal transmitted through

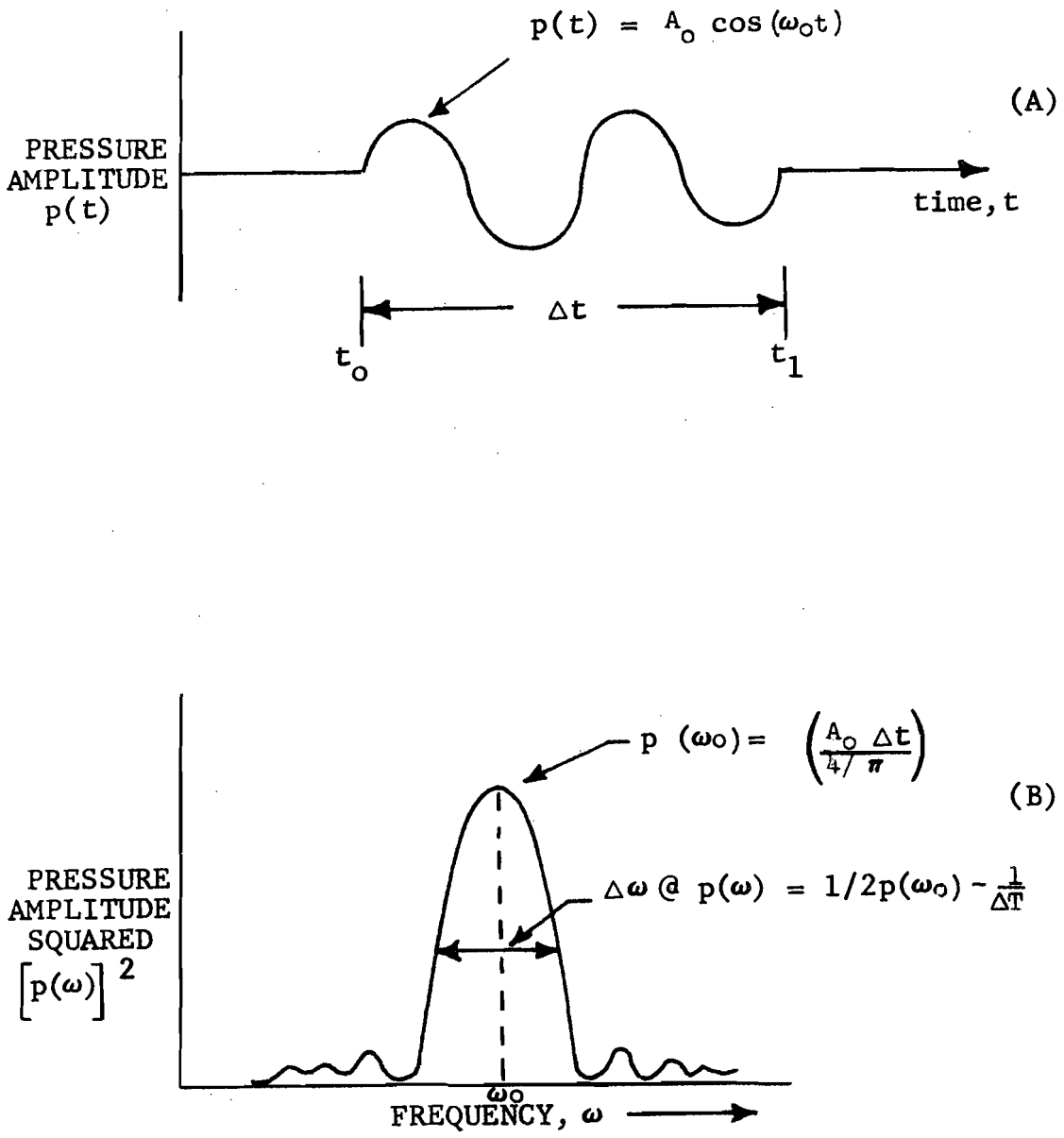

FIGURE 5.3.3-3 BROADENING OF PURE TONE DUE TO MODULATION

the turbulence region. The coherent part provides a discrete frequency spike in the narrowband spectrum and the scattered wave a broadband hump which would intuitively be expected to peak near the incident tone frequency. The shape of the resulting haystack is determined by the relative energy distribution between the two component waves. At the lower engine power settings it is reasonable that, the turbulence level in the exhaust jets is comparatively low and the scattered wave content correspondingly small. The haystack would then exhibit a visible tone content and be defined by a discrete frequency spike centered at the tone frequency, just as occurs for the TF34 and Quiet Engine "C" and "A" in Figures 5.2-1, 5.2-2 and 5.2-4, respectively. The higher power settings however, would result a large amount of scattered energy through increased turbulence levels and the scattered wave would overshadow the "incident" coherent part of the signal giving the tone-less haystacks of Figures 5.2-3, 5.2-5, and 5.2-6 for the two Quiet Engines.

The turbulence scatterers act as the "source" of the scattered wave and hence a Doppler effect may be imposed on this wave as the scatterers are in motion. The haystack will therefore exhibit a frequency shift with angle when the scattered wave obscures the "incident" coherent signal, as occurs for Engine "A" in Figure 5.3.4-1.

Equations (5.3.3-13) and (5.3.3-14) can be used to determine parametric trends for the scattering effects, but the low Mach number approximation expressed in equations (5.3.3-15) and (5.3.3-17) is somewhat easier to interpret.

In general, it can be seen that the interaction effect will vary as:

- The intensity $[|A_0^2|/\rho c]$ of the incident tone
- The size ℓ_c of the eddies in the mixing zone
- The Mach number M_t of the turbulent velocity fluctuations
- The volume of the turbulence region, that is, the axial location downstream of the nozzle exhaust plane where the tones propagate out to the surrounding air.

In addition, when the compressibility and density perturbations imposed by the turbulence cells cannot be ignored, the following become significant parameters:

- The frequency, $\frac{\omega_o}{2\pi}$, of the incident tone
- The difference between the eddy and freestream density and compressibility. Loosely interpreted, this would be a function of the difference between the fan and core stream temperatures.

The above effects are in agreement with the experimental trends observed for the three high bypass engines in Section 5.2.

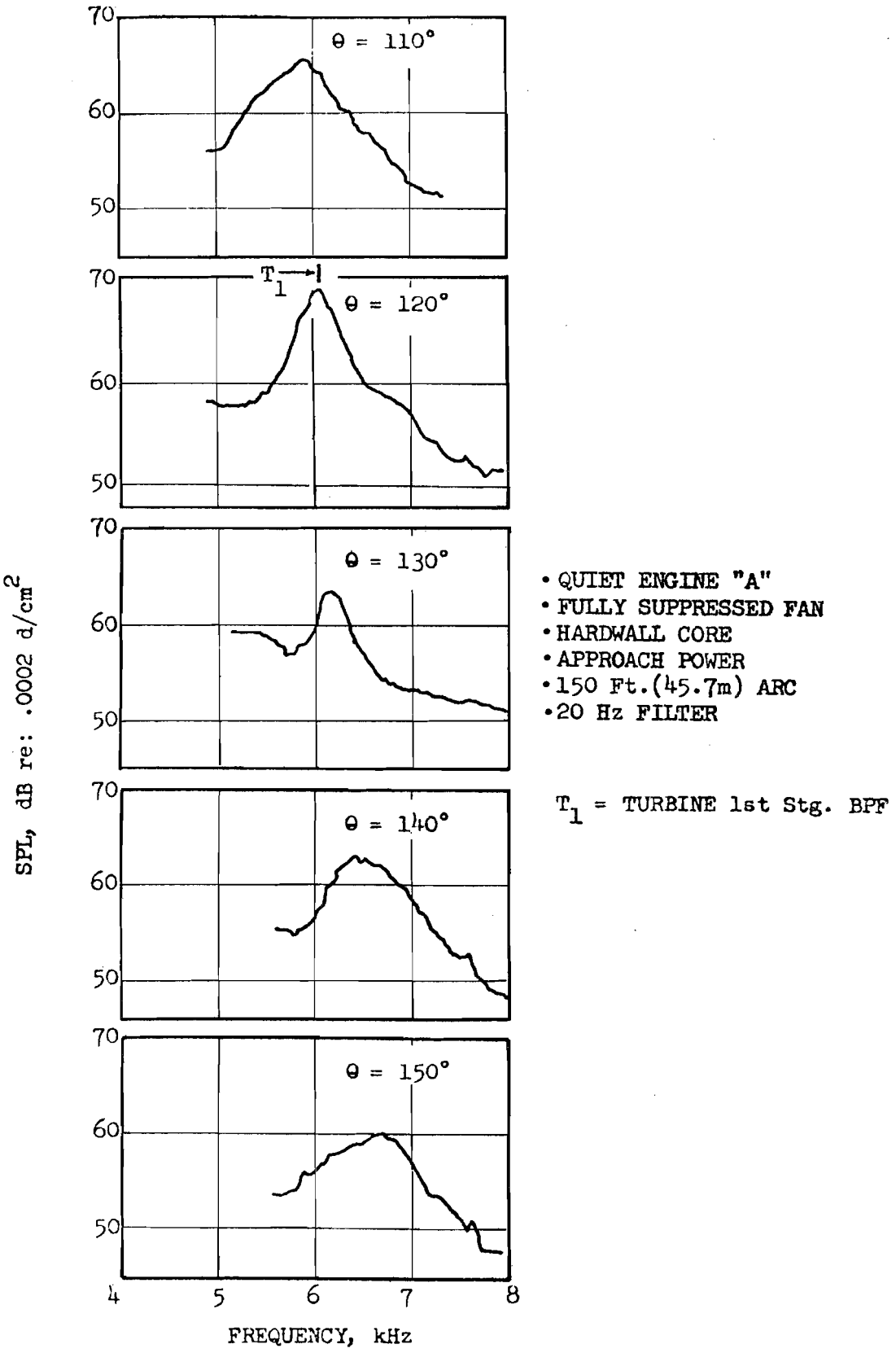

FIGURE 5.3.4-1 HAYSTACK PEAK FREQUENCY SHIFT WITH ANGLE WHEN NO DISCRETE FREQUENCY SPIKE CAN BE DISCERNED.

To summarize the analysis, it has been shown that as a coherent signal propagates through a region of turbulence, part of the incident acoustic energy is redistributed into a scattered wave by the turbulence cells. The change of inhomogeneities in time, as seen by the incident wave, produces a change in the frequency of the scattered wave and results in a broadening of the signal bandwidth. The nature of the broadening can be inferred from the form of the time autocorrelation functions of the amplitude and phase fluctuations. In particular, the frequency spread is determined by the correlation time of the turbulence eddies. The amplitude transformation is a strong function of the correlation length, of the eddies, and the turbulence intensity.

The analysis suggests the following suppression techniques for alleviation of the haystacking phenomenon:

- Removing the source, the turbine tone, e.g., through treatment in the core nozzle.
- Weakening the mixing region where the tone propagates out; for example, by means of a coplanar nozzle configuration (Section 5.4).
- Inducing better jet mixing and reducing the turbulence velocities.
- Breaking up large eddies into smaller ones, that is, reducing the correlation length, of the eddies, or increasing the correlation time.

Reduction of the haystacking may not be desirable. No amplification has been shown to be involved. The only result is a redistribution of the tonal energy into sidebands. In fact, if the haystack resulted in spreading energy into adjoining 1/3 octave bands the PNL would be reduced. This would be particularly helpful in the high penalty zone (below 5000 Hz). Turbine BPF's are typically located at high frequencies for current low and high bypass engines, but could occur in the 2000 to 4000 Hz range for very high bypass engines such as those designed for STOL application.

5.4 EXPERIMENTAL DATA ON TURBULENCE SCATTERING

5.4.1 Literature Survey

Extensive work has been reported in the literature on scattering by turbulence (see, for example, References 5.3.3-1 through 5.3.3-4), particularly for the case of atmospheric turbulence and for underwater acoustics. These investigations however, have mainly concentrated on the case for which the acoustic wavelength (λ) is much smaller than the characteristic dimension (ℓ) of the scatterers and for which ray tracing is applicable. The regime of concern herein is the case where λ is comparable to ℓ and for which diffraction effects must be considered. Some experimental work was performed for this regime under a previous FAA contract and is reported in Reference 5.4.1-1. Recently, Ho and Kovasznay (Reference 5.4.1-2)

reported on the effects of propagation of a coherent acoustic signal through a two dimensional turbulent jet. Other than these two studies, the only available information of interest is provided by the engine data already discussed in Section 5.2 and by a coplanar exhaust configuration of Engine "C" run under the NASA/GE Quiet Engine Program.

5.4.2 Engine "C" Coplanar Configuration Tests

The nominal configuration for Quiet Engine "C" has the fan nozzle exhaust plane about 53 inches (1.35 m.) upstream of the core nozzle exhaust plane (Figure 5.4.2-1). The fan nozzle was extended aft for one test series to provide a coplanar exhaust configuration (Figure 5.4.2-2). A back-to-back comparison of the spectra from the two configurations (which include similar acoustic treatment in the core) provides information on the effect of the relative location of the fan/core nozzle exhaust planes. The data from the two configurations can also be used to form a correlation for interaction effects.

A schematic comparison of the nominal and coplanar configurations is shown in Figure 5.4.2-3 and a comparison of typical acoustic spectra measured in Figure 5.4.2-4 in the form of a narrowband overlay. The corresponding 1/3 octave band spectra are shown in Figure 5.4.2-5.

The narrowband results on first glance appear to indicate that the coplana coplanar exhaust enhances the turbine tones, as the tone spikes are made more prominent by this configuration. The sideband noise is reduced, however, and the net effect on the 1/3 octave band SPL is a very small reduction, ranging from 0 to 2 dB. The "rejuvenation" effect of the coplanar exhaust on the tones is most evident at the higher speeds where the tone is no longer perceptible for the nominal configuration.

What is observed in the narrowband spectra is reduced tone modulation due to the coplanar nozzle: an effect which is predicted by the analytical model which links the modulation directly to the turbulence intensity and volume of the turbulence region at the point of propagation of the tone through the jet mixing regions. Moving the fan nozzle exhaust plane aft closer to the core nozzle exhaust plane results in the turbine tone "seeing" reduced turbulence and a thinner mixing region on passage through the outer mixing zone.

Significant changes cannot be expected in the tone 1/3 octave band SPL, or in the OASPL and PNL at any angle (if the spatial scattering is small), since normally an energy redistribution within one 1/3 octave band is involved. Changes definitely can not be expected for the acoustic PWL, as is shown by Table 5.4.2-1 which shows the above quantities as a function of the power setting.

In the case where the tone energy is spread out into adjacent 1/3 octave bands by the haystacking, the coplanar nozzle should result in increased PNL's. The effect however was found to be minimal as a consquence of the

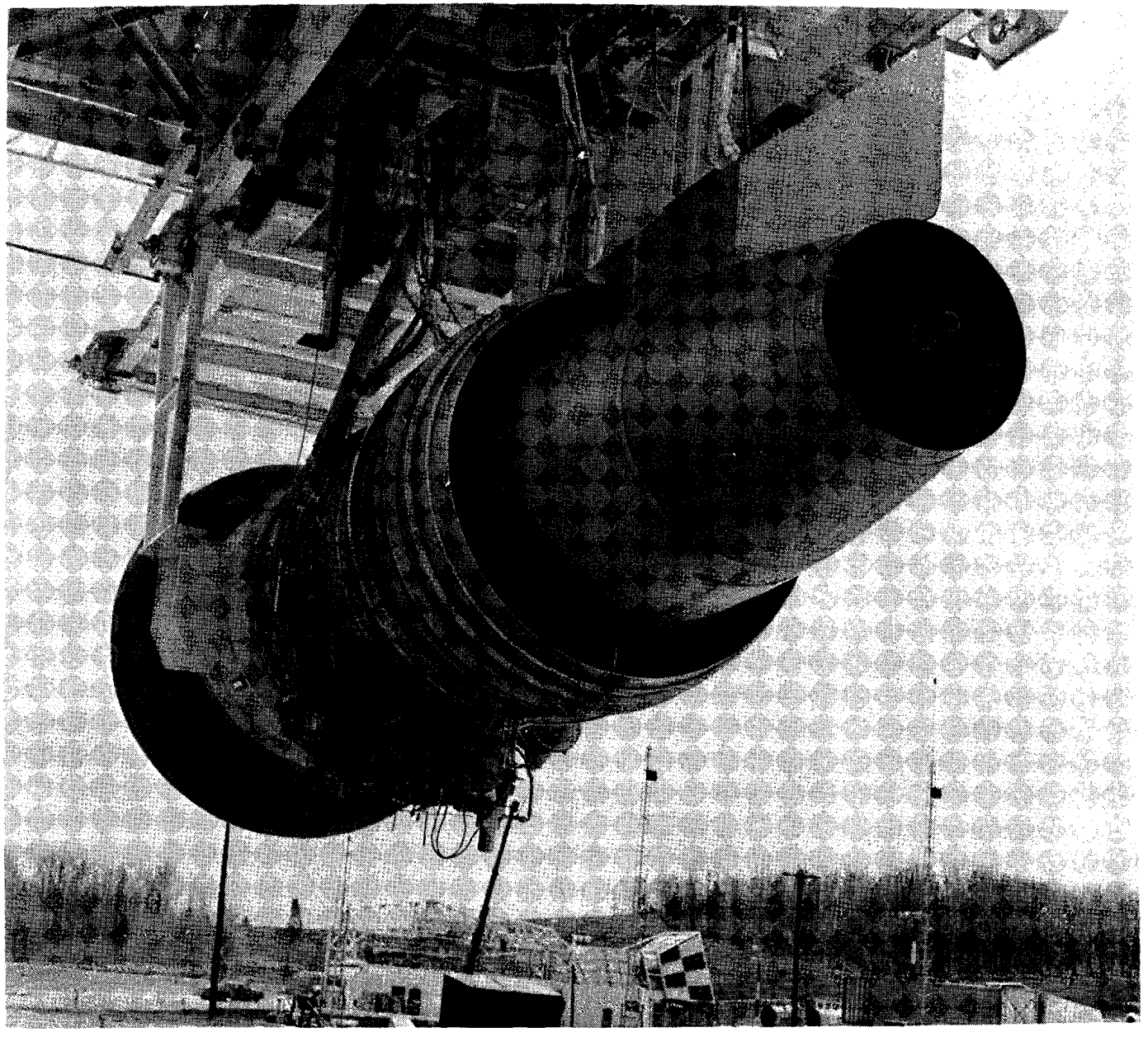

FIGURE 5.4.2-1 NORMAL CONFIGURATION OF QUIET ENGINE "C" WITH STAGGERED FAN AND CORE NOZZLE PLANES

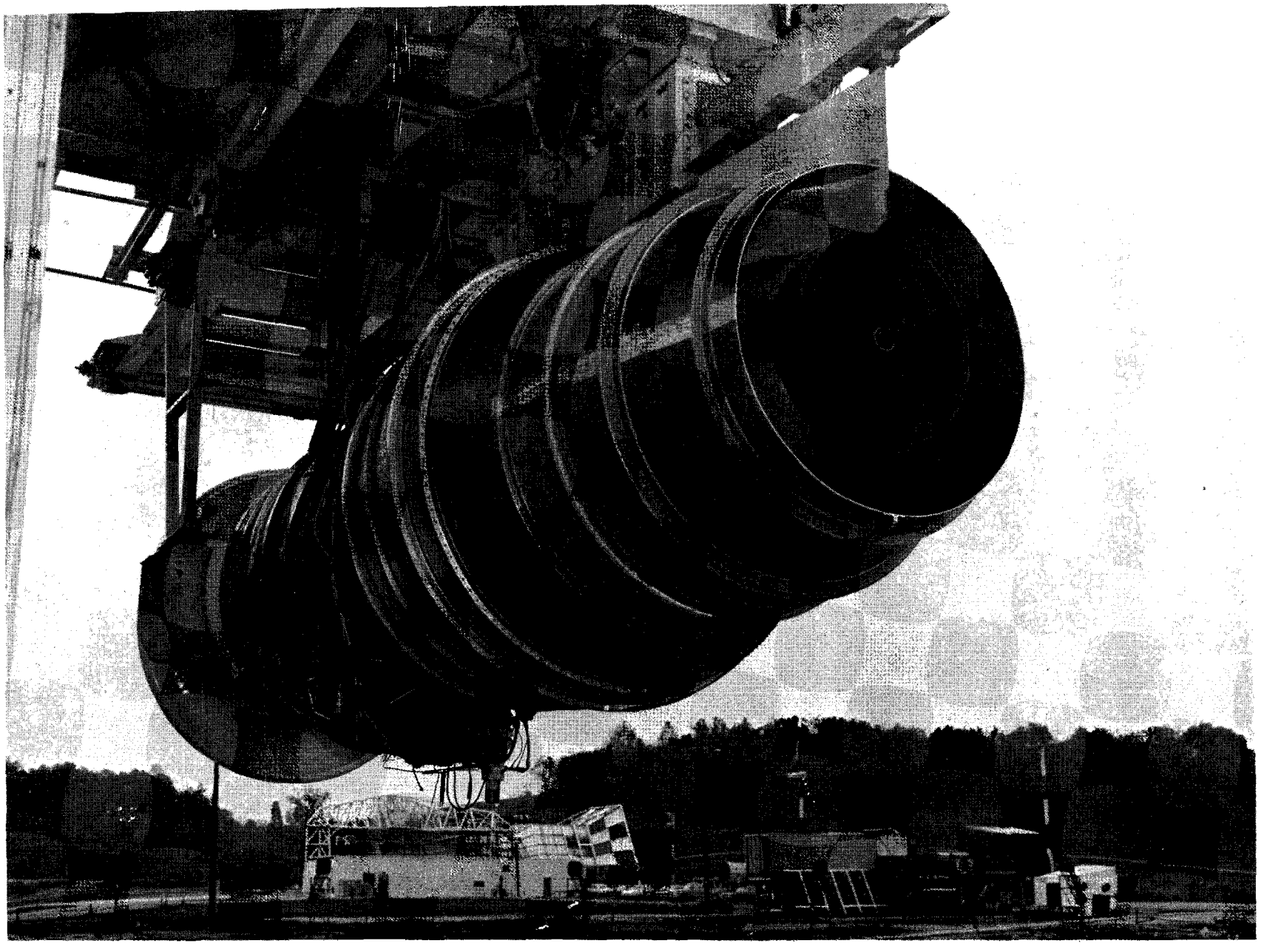

FIGURE 5.4.2-2 COPLANAR CONFIGURATION OF QUIET ENGINE "C"

QUIET ENGINE "C"
COMPARISON OF TWO FAN EXHAUST CONFIGURATIONS

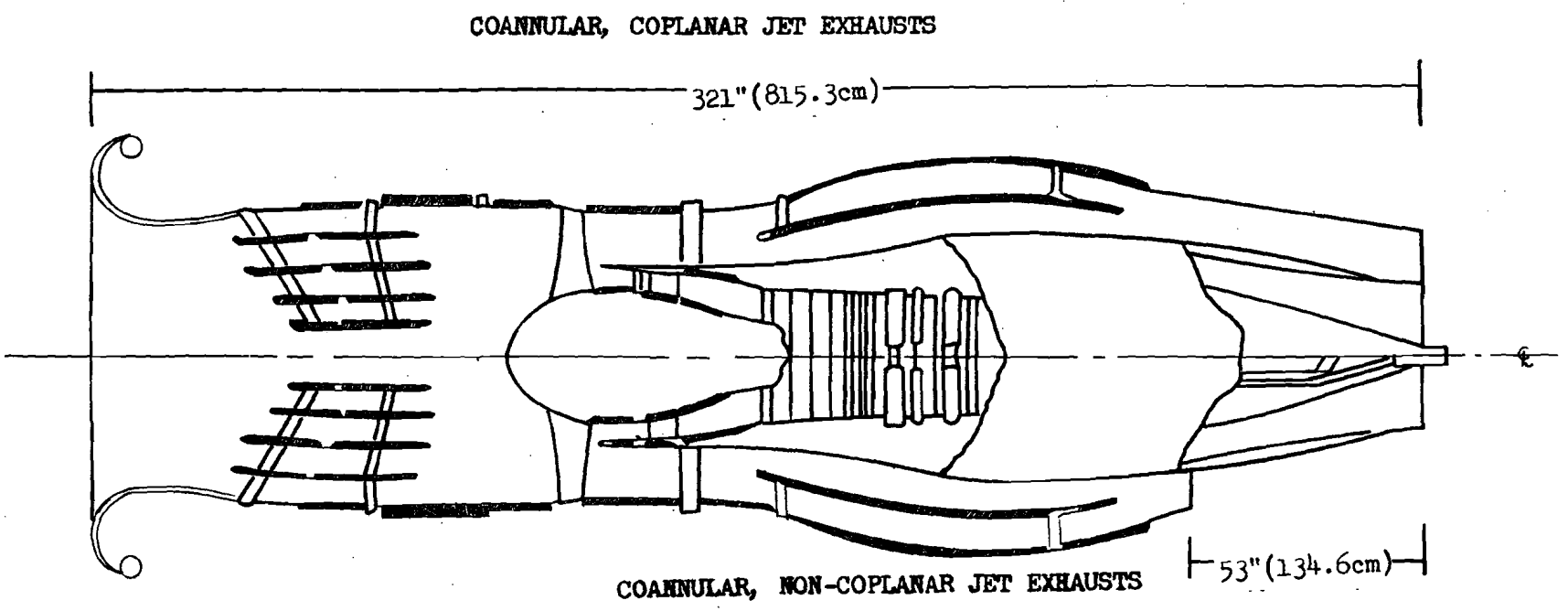

FIGURE 5.4.2-3 QUIET ENGINE "C" COMPARISON OF TWO EXHAUST CONFIGURATIONS.

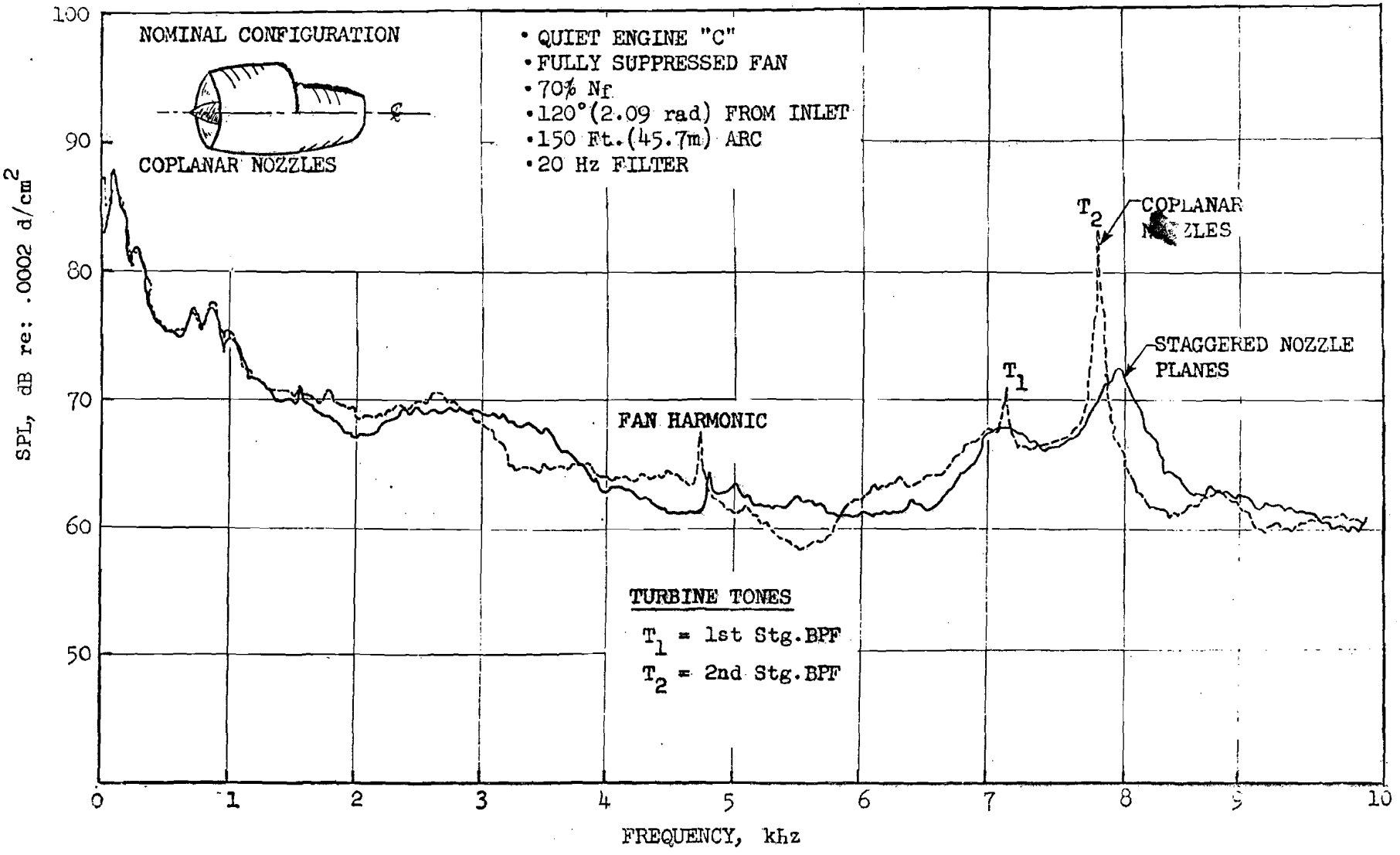

FIGURE 5.4.2-4 REDUCTION OF HAYSTACKING AND ENHANCEMENT OF TURBINE TONES WITH A COPLANAR CONFIGURATION.

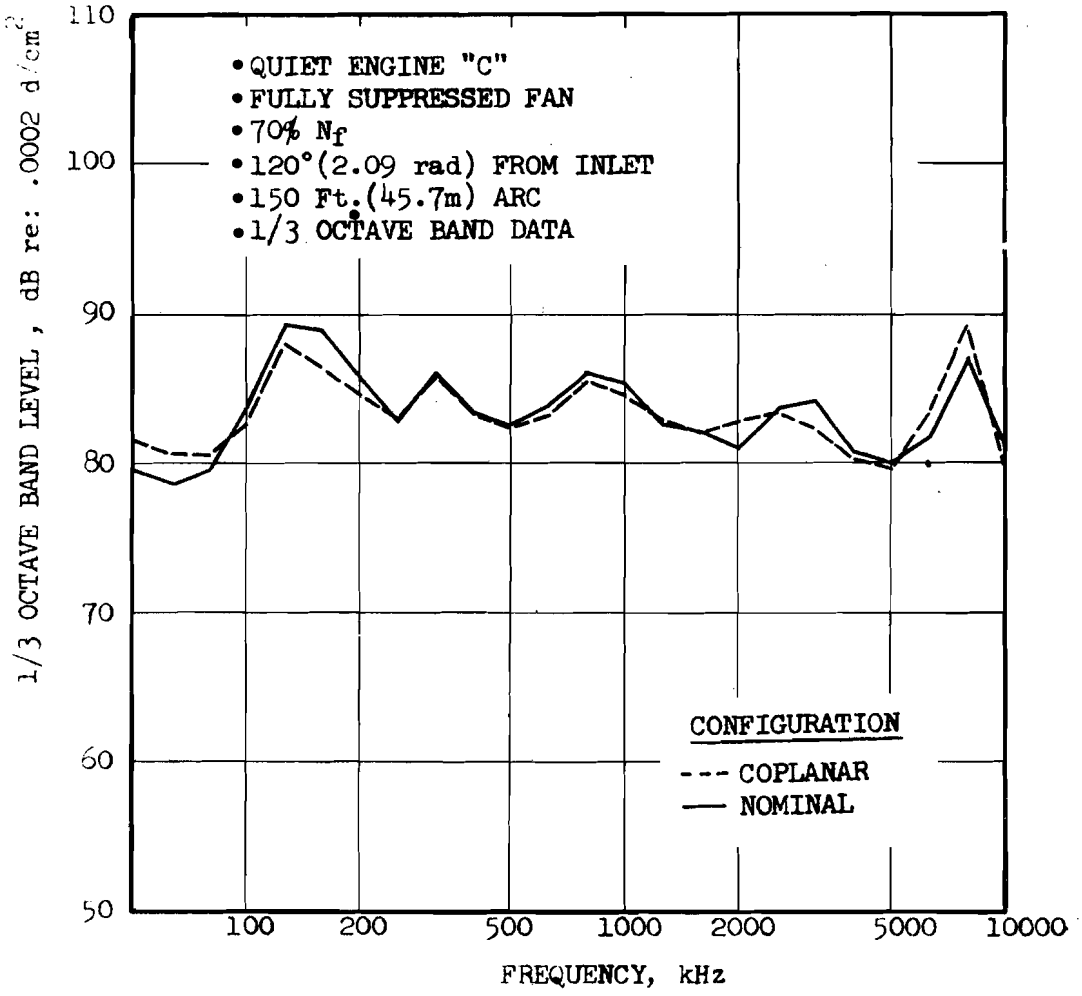

FIGURE 5.4.2-5 COMPARISON OF ENGINE "C" COPLANAR AND NOMINAL NOZZLE DATA.

Table 5.4.2-1. Comparison of Baseline and Coplanar Configurations

Quiet Engine "C"
150' (45.7m.) Arc
Treated Core, Fully Suppressed Fan

Configuration #14 Baseline (Nominal), Staggered Nozzles

#29 Coplanar Nozzles

Config. Number	Speed (% Design)	1/3 O.B. (kHz)	Tones	1/3 O.B. Value at Max Angle (120°) SPL (dB)	OASPL (dB)	PNL (PNdB)	1/3 O.B. PWL (dB)
14	50%	5.0	T_1+T_2	79.4	92.6	104.5	131.7
29	50%	5.0	T_1+T_2	79.9	92.2	104.4	131.6
14	50%	6.3	T_2	79.8	92.6	104.5	134.1
29	50%	6.3	T_2	78.3	92.2	104.4	133.7
14	60%	6.3	T_1+T_2	85.5	94.5	107.1	136.9
29	60%	6.3	T_1+T_2	83.4	93.8	106.0	136.4
14	70%	6.3	T_1	83.9	97.9	109.4	139.2
29	70%	6.3	T_1	82.0	97.9	109.2	138.6
14	70%	8.0	T_1+T_2	89.1	97.9	109.4	139.1
29	70%	8.0	T_1+T_2	86.1	97.9	109.2	139.4
14	80%	8.0	T_1+T_2	86.5	101.2	111.5	139.9
29	80%	8.0	T_1+T_2	85.6	100.9	111.7	140.2
14	80%	10.0	T_2	86.6	101.1	111.5	140.6
29	80%	10.0	T_2	85.4	100.9	111.7	141.3
14	90%	10.0	T_1+T_2	90.2	105.9	115.5	142.0
29	90%	10.0	T_1+T_2	88.1	104.6	114.5	142.7
14	95%	10.0	T_1+T_2	90.9	107.7	117.0	143.4
29	95%	10.0	T_1+T_2	90.0	106.8	116.5	144.0

high noise levels at the lower frequencies (see Figures 5.4.2-4 and 5.4.2-5) and the fact that the penalties were small for the high frequency location of the BPF's.

5.4.3 Refraction Rig Results

Experimental data demonstrating the effect of turbulence modulation was obtained from the Refraction Rig tested under Contract FA68WA-1960 (Reference 5.4.1-1). This siren is illustrated in Figure 5.4.3-1. It includes a siren to inject a high frequency tone into a jet mixing zone similar to that which exists in the core engine exhaust. The inner pipe containing the tone had airflow. The tone level received in the farfield was measured with and without flow in the outer pipe. The pressure ratio for the outer flow was maintained constant at 1.2, but the nozzle temperature was varied, thus providing a velocity change. The nozzle supply temperatures used were 520, 960, 1460 and 1960° R, which would yield flow velocities of 577, 789, 966 and 1119 ft/sec. The results at 90° from the jet axis are shown in Figure 5.4.3-2. These data, representative of the characteristics observed at other angles as discussed in the final report under the previous research work, show that the tone level is reduced and the bandwidth is increased with increasing flow velocity consistent with the results indicated by the analysis of Section 5.3.3 [Equation (5.3.3-17)].

5.4.4 Scattering by a Two Dimensional Jet

The Ho and Kovasznay turbulent jet study (Reference 5.4.1-2), while conducted for a flow environment far from that existing behind an engine, clearly points to the importance of the scattering of periodic acoustic signals by a turbulent jet. A tone was made to impinge normally onto a turbulent jet and considerable amplitude and frequency modulation was recorded. It should be noted that the normal incidence of the acoustic signal in the Ho and Kovasznay study precluded any instability effects, and since the mean velocity was nearly parallel to the wave front, refraction effects were minimized. Turbulence scattering was then responsible for the observed modulation.

The experimental investigation consisted of directing a collimated beam of constant amplitude discrete frequency signal normally across the plane of a turbulent jet. The jet issued from a large aspect ratio (12x400 cm.) orifice and was fully turbulent at the test station which was located 210 cm. downstream of the orifice exit. A schematic of the experimental is given in Figure 5.4.4-1. The centerline jet velocity at the test station was maintained constant at 400 cm/sec except for one data set where it was increased by 20%. The tone frequency was varied from 3 to 90 KHz. Details of the instrumentation and results can be found in Reference 5.4.4-1.

The incident signal was a pure sinusoidal wave and the transmitted signal was found to have the same carrier frequency but was randomly modulated in both amplitude and phase.

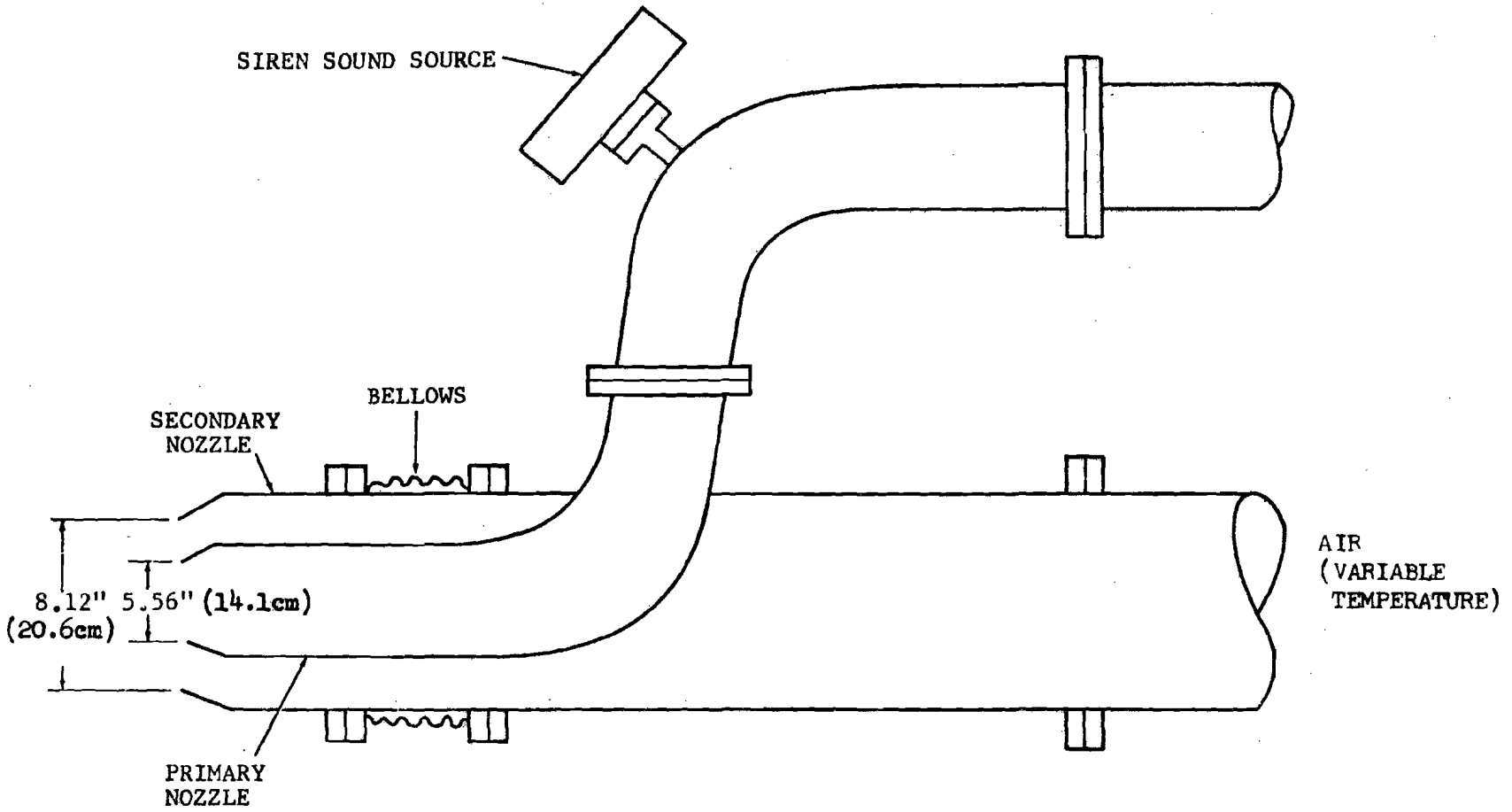

FIGURE 5.4.3-1 REFRACTION TEST RIG.

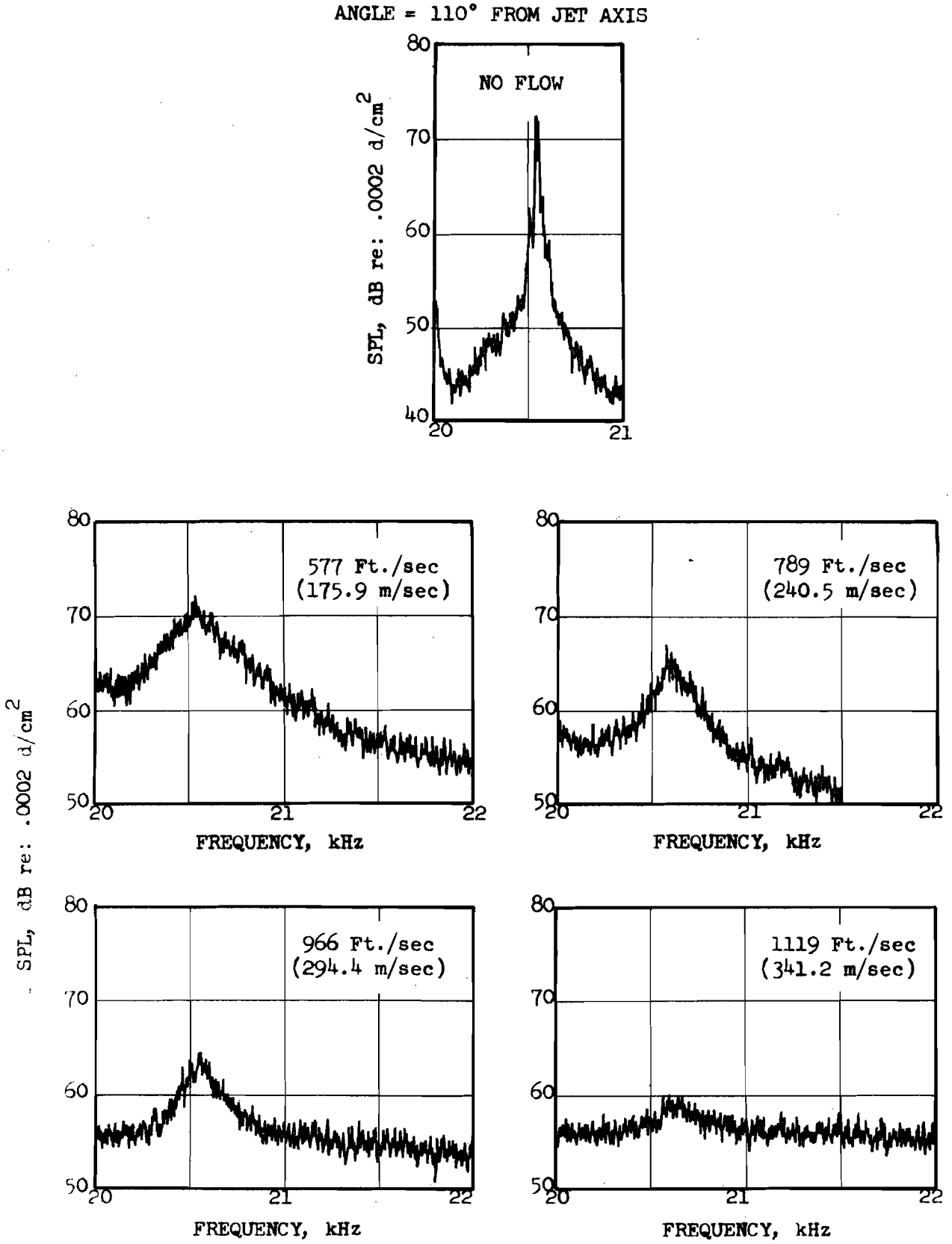

FIGURE 5.4.3-2 REFRACTION RIG RESULTS SHOWING TONE MODULATION BY TURBULENCE.

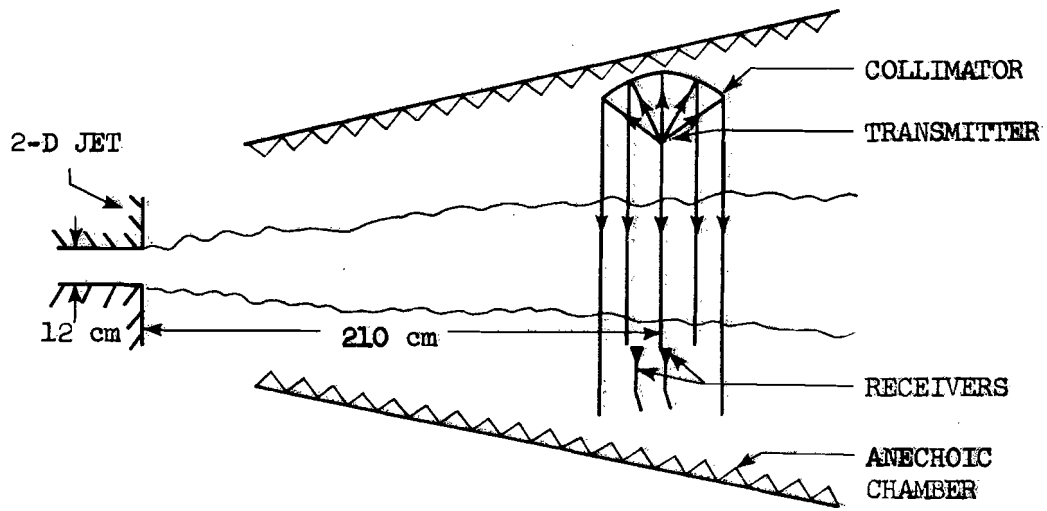

FIGURE 5.4.4-1 SCHEMATIC OF THE EXPERIMENT (Ref. 5.4.1-2)

From dimensional considerations and use of some experimental results, the following functional dependance was derived for the amplitude modulation (reduction) of the transmitted signal over the frequency range where the acoustic wavelength was larger than, or comparable, to the dimensions of the turbulent scatterers:

$$\overline{[\log \frac{A(t)}{A_o}]^2} \propto \kappa_o^2 \text{ b. L. } \frac{\overline{(v')^2}}{c^2} \qquad (5.4.4\text{-}1)$$

where:

A_o = amplitude of the incident wave

$A(t)$ = amplitude of the transmitted wave

k_o = wave number of incident wave, $\frac{2\pi}{g}$

b = distance travelled by acoustic wave through the turbulence zone

L = integral scale of turbulencef turbulence

v' = normal component of turbulence velocity

c = acoustic velocity

The bar denotes mean values.

Comparing Equations (5.4.4-1) and (5.3.3-17), the experimental study and the analysis are seen to provide several common trends; that is, the same dependence on the turbulence Mach number and characteristic length, as well as the effect of the volume of the turbulence region through which the tone propagates. The two-dimensional results do predict a dependance on the frequency of the incident tone which is not obvious from Equation (5.3.3-17). The trends with turbulence Mach number, characteristic length and volume (or path) also coincide with those displayed by engine noise haystacks.

5.5 SUMMARY

Turbine tones have been identified as the source of farfield haystacks and turbulence scattering as the modulation mechanism. For the present and forseeable future engine configurations and turbofan cycles (subsonic core velocity), no amplification is involved. The process by which a pure tone suffers a frequency broadening and consequent reduction in the peak SPL can be described using turbulence scattering.

The analysis and experimental observations indicated that the haystacking could be eliminated or the tone modulation reduced by:

(i) Removal of turbine tones at the source, for example by use of acoustic treatment in the core nozzle.

(ii) Reduction of the turbulence Mach number (i.e. intensity) and the correlation length of the turbulence eddies.

(iii) Moving the fan nozzle exhaust plane aft to a coplanar configuration with the core nozzle exhaust plane. This effect is due to the fact that jet mixing zones increase in turbulence intensity and thickness axially downstream and with the coplanar configuration the turbine tones propagate through the outer mixing zone at a location closer to the start of the zone than is the case for the nominal configuration with staggered fan and core nozzle exhausts.

The last two actions would only serve to reduce the frequency spread, and the total energy content is not affected (the tone appearing as the original sharp spike when the modulation is completely eliminated). This suggests haystacking may be beneficial in that the turbine tone energy may be scattered into adjacent 1/3 octave bands, thus reducing annoyance and possibly tone correction.

REFERENCES

5.2-1 Beranek, L.L., Noise and Vibration Control, Section 5.5, McGraw-Hill, New York, (1971).

5.3.2-1 Miles, John W., "On the Disturbed Motion of a Plane Vortex Sheet," Journal of Fluid Mechanics, Vol. 4, pp. 538-552, 1958.

5.3.2-2 Series of papers by T. Kh. Sedel'nikov in Physics of Aerodynamic Noise, edited by A.V. Rimskiy-Korsakov, translated as NASA TT F-538 (1969).

5.3.2-3 Tam, C.K.W., Journal of Fluid Mechanics, Vol. 46, 4, p. 757 (1971).

5.3.2-4 Crow, S.C. and Champagne, F.H., "Orderly Structure in Jet Turbulence," Journal of Fluid Mechanics, Vol. 48, 3, p. 547 (1971).

5.3.2-5 Liu, J.T.C., "Noise Radiation from Turbulent Shear Layer Instability Waves in Supersonic Jet Exhausts," proceedings of Purdue Noise Control Conference, July 14-16, 1971, Purdue University, West Lafayette, Indiana, pages 450-456.

5.3.2-6 "Papers on Novel Aerodynamic Noise Source Mechanisms at Low Speeds," Aeronautical Research Council Current Papers C.P. No. 1195 (1972).

5.3.2-7 Crighton, D.G., "Radiation Properties of the Semi-Infinite Vortex Sheet," Proceedings of the Royal Society of London, Series A, 330, pp. 185-198 (1972).

5.3.2-8 Gerend, R.P., Kumasaka, H.P. and Roundhill, J.P., "Core Engine Noise," AIAA Paper No. 73-1027, Presented at the AIAA Aero-Acoustic Conference, Seattle, Washington, October 1973.

5.3.2-9 Crow, S.C., "The Predictability of Jet Noise," Lecture at NASA-Langley Res. Center, November 1971.

5.3.3-1 Morse, P.M. and Ingard, K.U.; Theoretical Acoustics, McGraw-Hill, New York (1968).

5.3.3-2 Tatarski, V.I.; Wave Propagation in a Turbulent Medium, transl. from the Russian by R.A. Silverman, Dover Publications, Inc., New York (1967).

5.3.3-3 Chernov, L.A.; Wave Propagation in a Random Medium, transl. from the Russian by R.A. Silverman, Dover Publications, Inc., New York (1967).

REFERENCES (concluded)

5.3.3-4 Lighthill, M.J.; "On the Energy Scattered from the Interaction of Turbulence with Sound and Shock Waves," Proc. of the Cambridge Phil. Soc. 49 (1953).

5.4.1-1 "Fan/Compressor Noise Reduction," Final Report for DOT/FAA Contract FA68WA-1960, Project Number 550-001-01H, General Electric Company, December 1970.

5.4.1-2 Ho, C. and Kovasznay, L.S.G., "Acoustic Wave Propagation Through a Two-Dimensional Turbulent Jet," Interagency Symposium on University Research in Transportation Noise, Vol. I., Stanford University, Stanford, California (March 1973).

5.4.1-3 Kazin, S.B. and Paas, J.E., "NASA/GE Quiet Engine 'C' Test Results," NASA CR-121176 (April 1974).

5.4.4-1 Ho, C.; "Modulation of Acoustic Wave by Turbulent Shear Flow," PhD Thesis, Department of Mechanics and Materials Science, John Hopkins University, Baltimore, Maryland, (1973).

SECTION 6.0

OBSTRUCTION NOISE

6.1 BACKGROUND

In addition to blade rows and vane rows in the jet engine, many other solid obstructions are placed in the flow streams for various reasons. Among these are struts, pylons, flameholders and sensing probes. In general, the noise generated by struts and other such obstructions consists of both a broadband component, and a discrete frequency component, resulting from discrete vortex shedding.

The need for study of obstruction noise was discussed in Section 2.2.5 of Volume I of this report. Narrowband SPL spectra from Engine "A" acoustic tests were presented therein to show the significant reduction in SPL attainable by aerodynamically fairing a rectangular strut. In this volume, results are presented from tests conducted on struts of different shapes and sizes at several flow Mach numbers and at several angles of attack. The results showed that considerable benefit can be achieved by proper selection of dimensions and aerodynamic shaping of struts. Further it was noticed that angle of attack had very little influence on the acoustic output in the 0°-15° range. Based on the data obtained, an empirical method is presented to predict the overall power level and one-third octave band power level spectra for struts in smooth flow in a limited Reynolds number range.

6.2 EXPERIMENTAL WORK

6.2.1 Test Facility

A new duct facility was designed for the specific purpose of conducting the aerodynamic and acoustic measurements. Such a facility, carefully designed for low turbulence and very thin wall boundary layer at the measurement stations was considered desirable for these tests in order to minimize non-uniformity of the flow at the exit plane.

The design of the duct was based on a maximum exit Mach number of 0.54 through a rectangular exit cross-section (cross-section of 5" x 2.4" for weight flow of 3.8 lbs/sec). The facility, shown in Figure 6.2.1-1, consisted of a rectangular plenum followed by a contraction through an ASME nozzle into a straight constant cross-section rectangular duct. The area contraction was chosen to provide an accelerating pressure gradient which thins the boundary layer as it approaches the straight section. This contour also allows the establishment of a uniform flow before Station 6 (axial distance = 6") in Figure 6.2.1-2 which shows an enlarged view of the transition section and the duct.

The air enters the plenum chamber through a quick disconnect valve and a conical diffuser which drops the inlet flow to a Mach number of less than 0.15 at maximum flow. This helped minimize the noise from the inlet and also

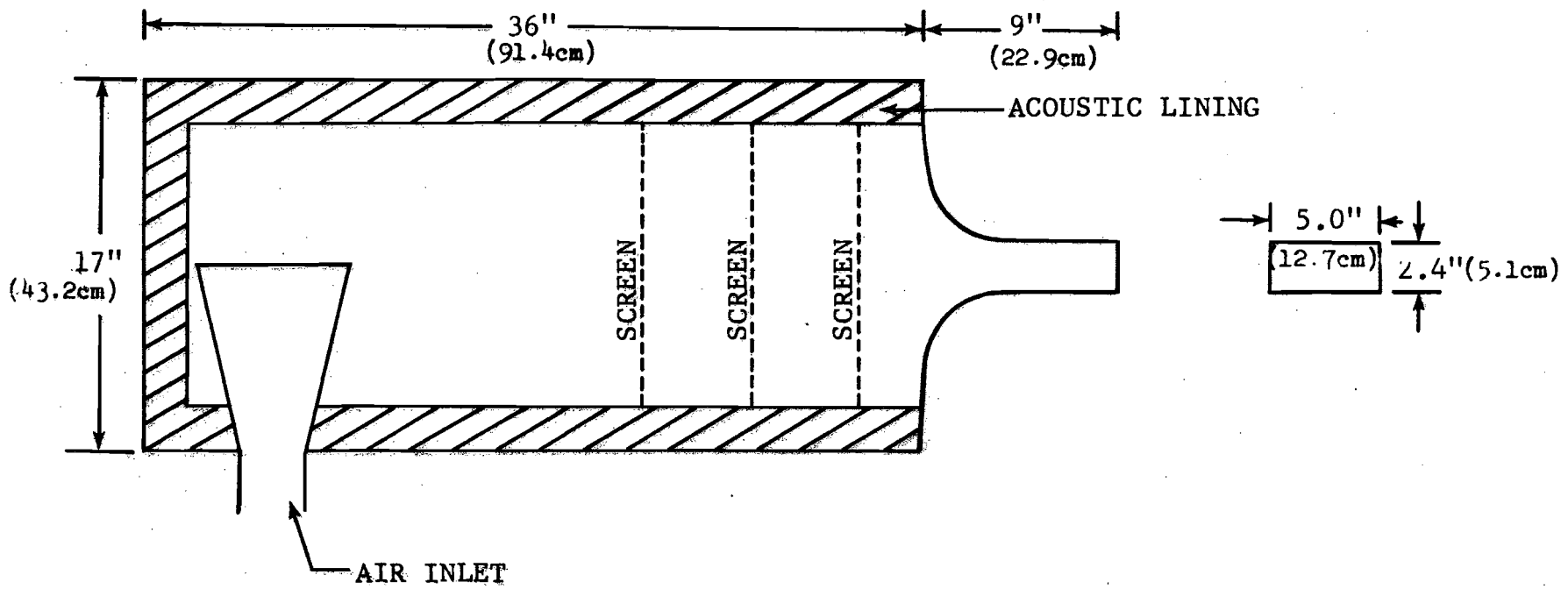

FIGURE 6.2.1-1 ACOUSTIC DUCT FACILITY SCHEMATIC FOR OBSTRUCTION NOISE MEASUREMENTS.

prevent damage to the Scottfelt acoustic lining on the inner walls of the plenum. A series of screens were also provided in the plenum. The plenum and air supply lines were wrapped in lead vinyl for further acoustic isolation.

The duct was located in a semi-reverberant room. The reverberation characteristics of the room were evaluated by measuring the reverberation times (T_{60}) over a frequency range of 125 Hz - 10 KHz. In addition, SPL measurements were taken at 8 different microphone locations in the room for pure jet noise and with the models in the test configuration. The locations were chosen to satisfy the standards recommended by References 6.2.1-1 and 6.2.1-2 . The deviation of the measurements by the different microphones was within 1 dB. The room was thus considered reasonably reverberant below 10 KHz.

6.2.2 Models Tested

Nine models were chosen for the test series. Dimensions of the models are shown in Figure 6.2.2-1 and a photograph of the models is shown in Figure 6.2.2-2. The choice of the models was based on several considerations. Circular cylinder, thick blunt flat plates and double circular arc airfoils are frequently found as obstructions in the form of struts, linkages, levers, etc. Since one of the objectives of the program was to obtain a correlation which would use easily available aerodynamic coefficients, symmetrical and elliptical airfoils were also included in the choice of models. This comprehensive selection of aerodynamic shapes was also expected to point out the direction for progress in noise reduction by aerodynamic shaping. Geometrical parametric variations, like thickness and chord were also included for providing insight towards parametric changes for noise reduction. Table 6.2.2-1 presents the different geometrical comparison series available with the choice of the configuration.

6.2.3 Instrumentation

(a) Aerodynamic

Total pressure measurements were made in the plenum by two Kiel probes located downstream of the screen closest to the exit plane. A traversible total pressure Kiel probe was located at Plane 6.5 (Figure 6.2.1-2) during initial shakedown tests to compare with the plenum measurement. This was subsequently withdrawn due to the aerodynamic and acoustic disturbance caused by the probe. Another traversible Kiel probe was used to measure total pressures downstream of the exit plane. This was mounted on a mechanism (Figure 6.2.3-1) which was capable of traversing in both vertical and horizontal directions in a plane perpendicular to the jet axis. The whole mechanism could also be moved to any axial location downstream of the exit plane. This system was used to conduct the wake survey needed to determine the profile drag coefficient of the various bodies.

Static taps were provided on all the four walls of the rectangular duct at two axial locations near the exit plane. These were used in conjunction with plenum total pressure measurements to set the desired Mach number for the flow.

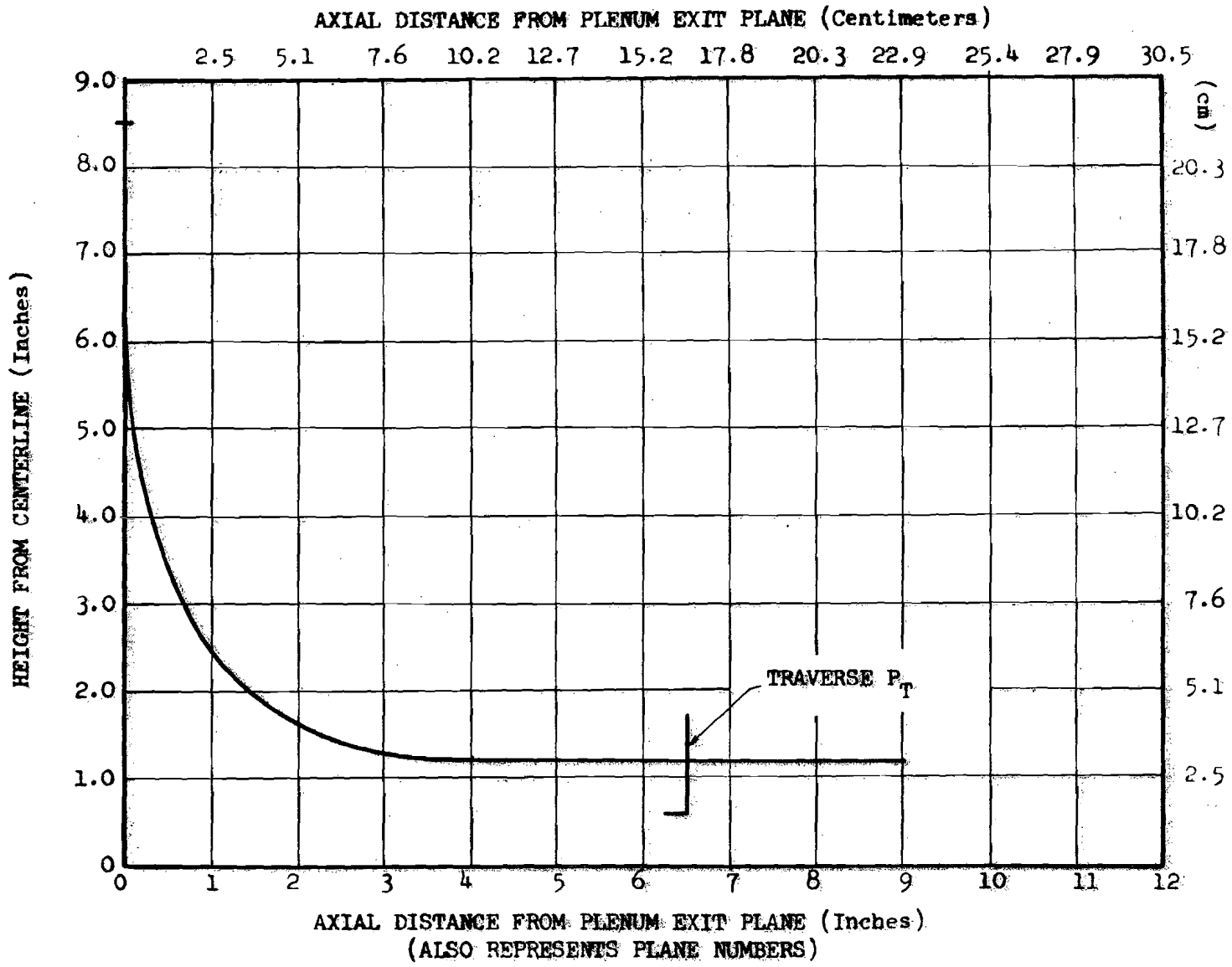

FIGURE 6.2.1-2 VIEW OF THE TRANSITION SECTION OF THE ACOUSTIC DUCT FACILITY.

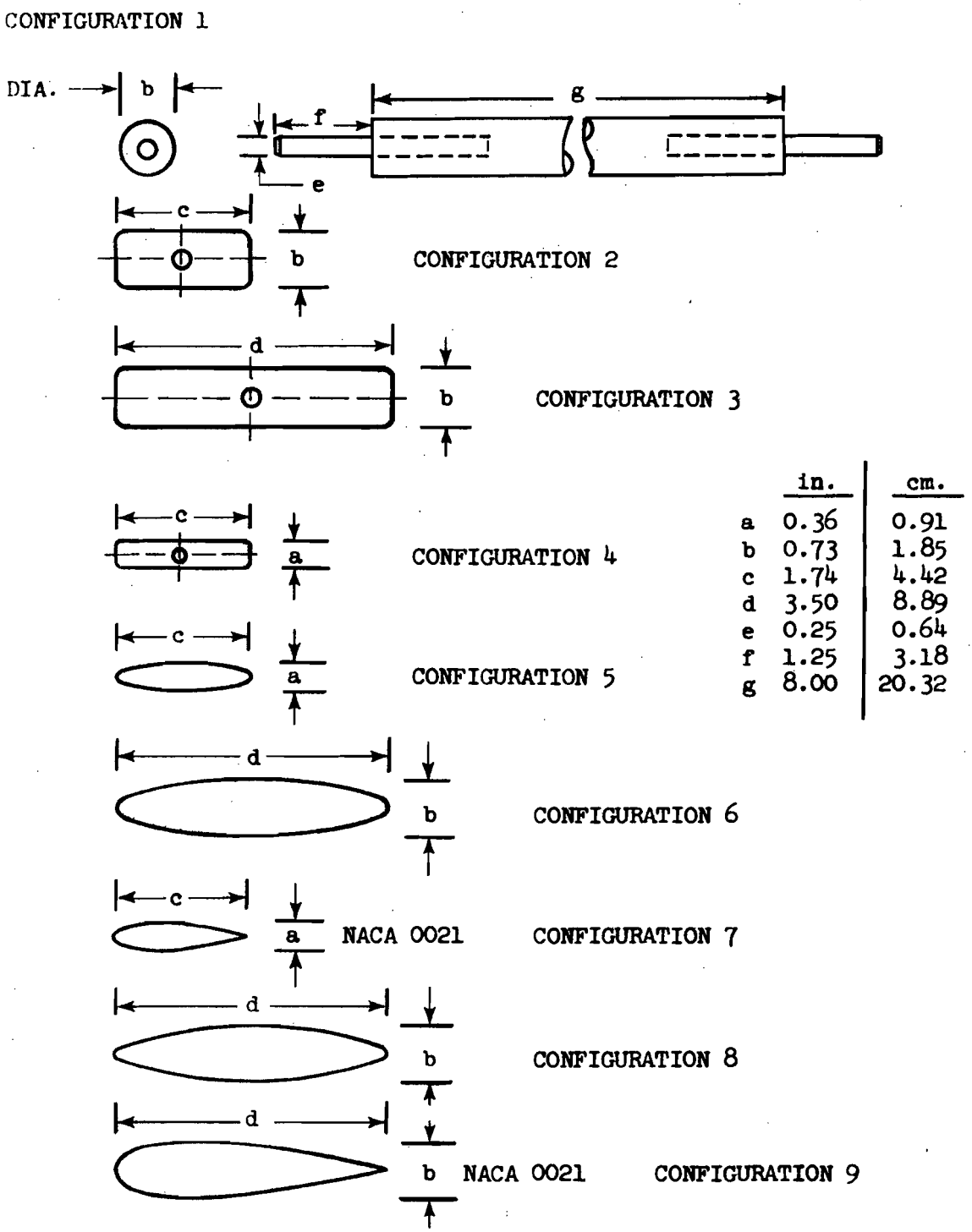

	in.	cm.
a	0.36	0.91
b	0.73	1.85
c	1.74	4.42
d	3.50	8.89
e	0.25	0.64
f	1.25	3.18
g	8.00	20.32

FIGURE 6.2.2-1 CROSS-SECTIONAL VIEW OF CONFIGURATIONS TESTED

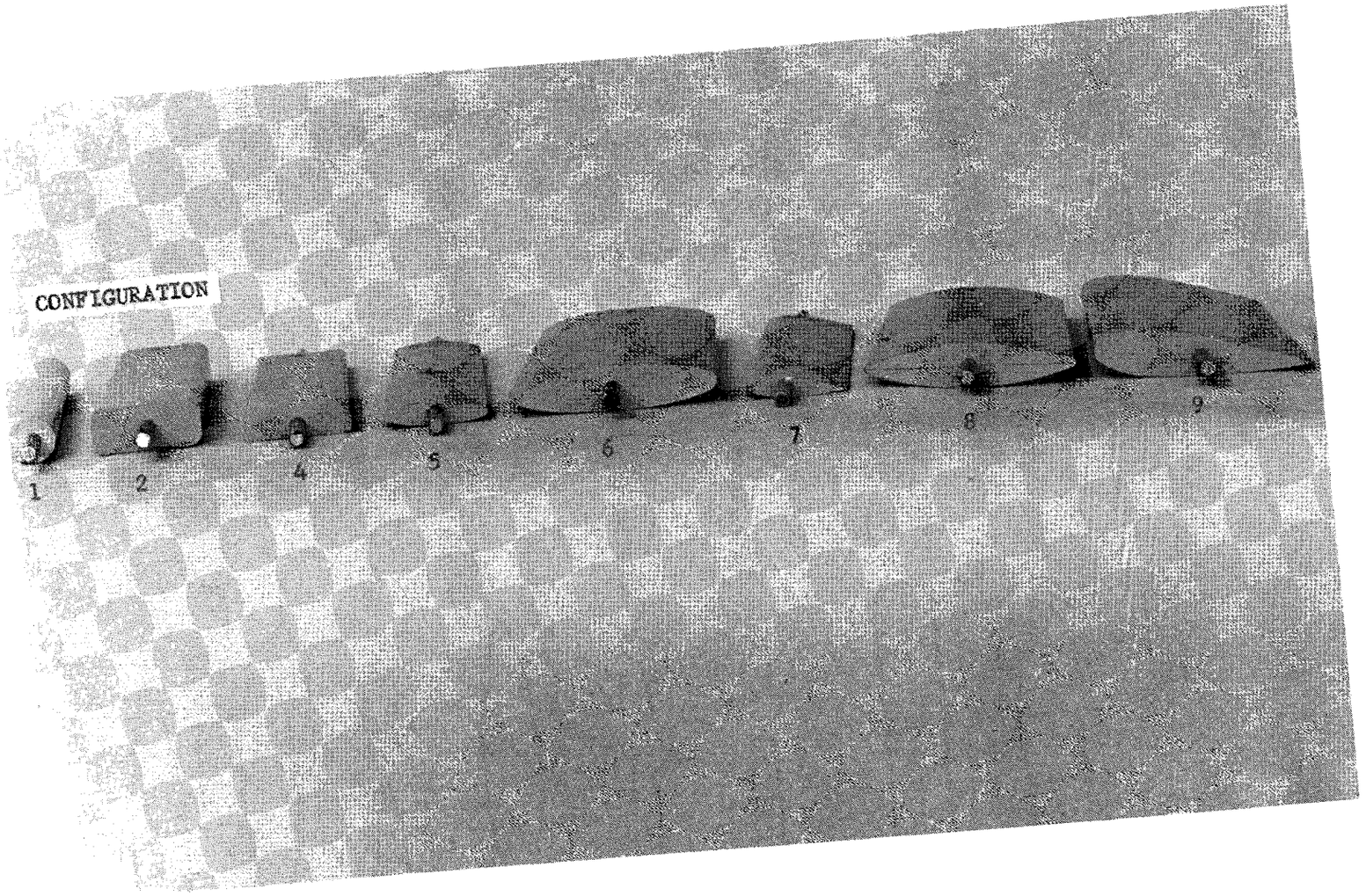

FIGURE 6.2.2-2 CONFIGURATIONS TESTED FOR OBSTRUCTION NOISE. (CONFIGURATIONS 3 IS SHOWN MOUNTED IN FIGURE 6.2.3-1

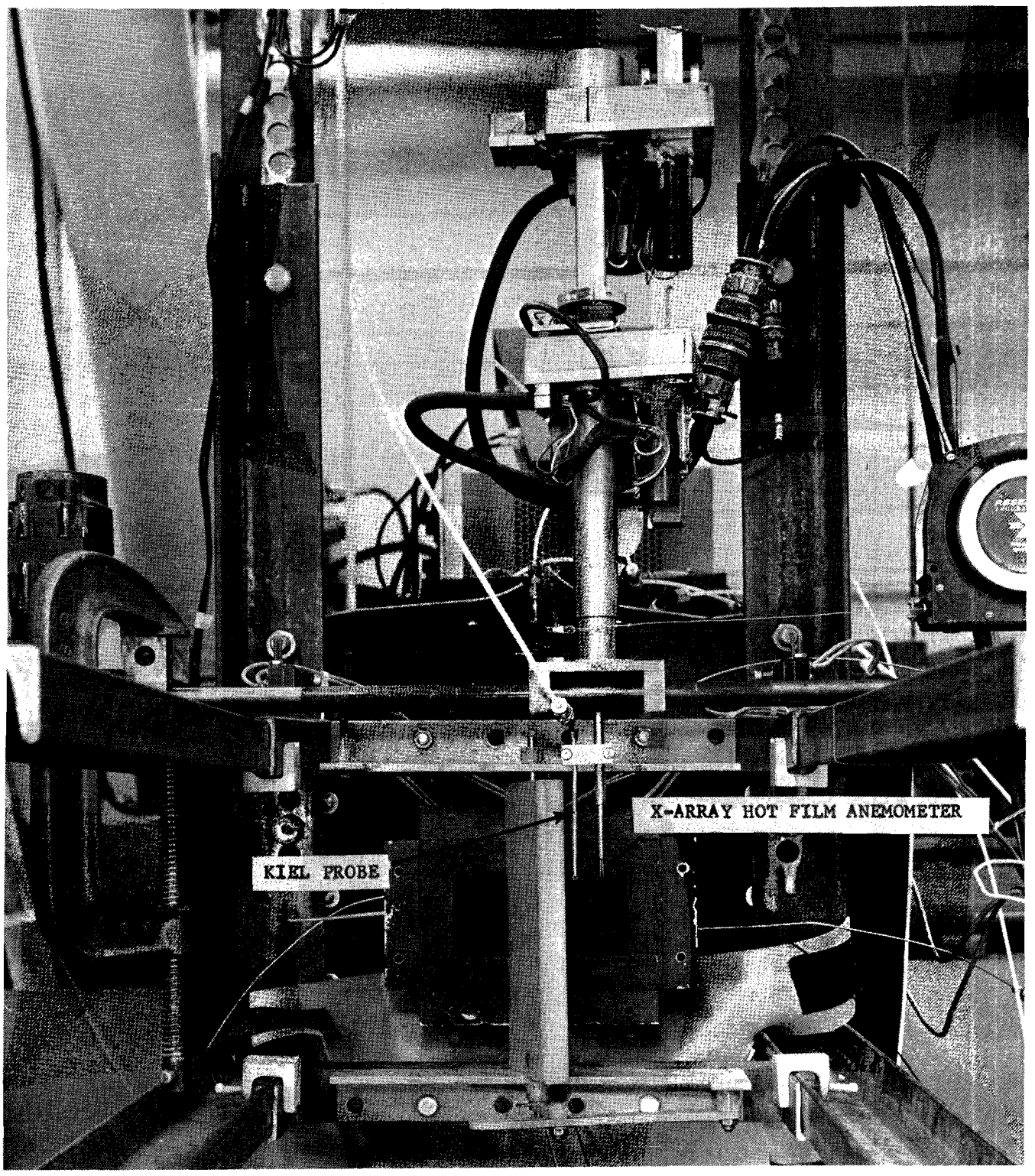

FIGURE 6.2.3-1 END VIEW OF TEST FACILITY WITH CONFIGURATION 3 MOUNTED AT $\alpha° = 15$

TABLE 6.2.2-1 BASIC GEOMETRICAL COMPARISON SERIES

THICK LONG SERIES t = 0.726", C = 3.488"	CONFIG. NUMBER	THIN SHORT SERIES t = 0.36", C = 1.744"	CONFIG. NUMBER	FLAT PLATE SERIES	CONFIG. NUMBER
o FLAT PLATE	3				
o ELLIPSE	6	o FLAT PLATE	4	o THICKNESS VARIATION	2, 4
o DOUBLE CIRCULAR ARC AIRFOIL	8	o ELLIPSE	5		
o SYMMETRICAL (NACA 0021) AIRFOIL	9	o SYMMETRICAL (NACA 0021) AIRFOIL	7	o CHORD VARIATION	2, 3
o CIRCULAR CYLINDAR der (DIA = 0.726")	1				

Direct velocity measurements were made by a traversible X-array hot film anemometer. This probe, mounted on the same system shown in Figure 6.2.3-1 enabled measurement of components of velocity and turbulence along and perpendicular to the axial direction in a horizontal plane. All the pressures and velocities thus measured were recorded by an automatic X-Y-Y strip chart.

(b) Acoustic

SPL measurements were made by B&K microphones located at four (and up to eight during shakedown tests) locations, each more than ten feet away from the nozzle exit plane. The locations were deliberately chosen at random after the checks, referred to earlier, confirmed the reverberant characteristics of the room. The SPL data were recorded on a 4-channel Lockheed 411B tape recorder. On-line narrow band data was also recorded from at least one of the microphones.

6.2.4 Shakedown Tests

Aerodynamic shakedown tests were conducted to investigate the nature of the flow at the exit plane. Minor refinements of the nozzle contours were made during these tests to obtain uniform velocity and pressure profiles and a low turbulence level. For the shakedown tests, horizontal and vertical Kiel and hot film traverses were made in a plane parallel to the exit plane, 3/8" axially downstream of the exit. The lines of traverse are shown in Figure 6.2.4-1.

Profiles of mean velocity $\overline{U}$ (in the axial direction) and the turbulence component u' are shown in Figure 6.2.4-2 for a horizontal traverse at the mid-height plane at a Mach number of 0.21. The profiles are seen to be uniform across the duct except for the regions affected by the boundary layer on the two walls. The turbulence intensity $u'/\overline{U}$ was about 1.1%, away from the wall boundary layers. Figure 6.2.4-3 presents similar data for a Mach number of 0.4. Vertical traverses also showed similar reasonably uniform profiles at all Mach numbers between 0.2 and 0.45. The duct was thus considered aerodynamically clean.

6.2.5 Test Series

The test series was divided into acoustic tests and aerodynamic and wake survey tests. Acoustic tests consisted of acoustic measurements for baseline configuration (no models in the stream) followed by tests with the models placed 1.8" downstream of the duct exit plane, as shown in Figure 6.2.3-1. A complete listing of the Mach number and angle variations for the tests is shown in Table 6.2.5-1. Aerodynamic wake survey data were obtained for all configurations at zero angle of attack. The data consisted of mean velocity, turbulence and total pressure surveys upstream and downstream of the struts at several vertical locations. The traverse probes were withdrawn from the stream while acoustic data were being recorded. Reverberation times were measured at regular intervals during the entire course of the test program.

6.3 DATA ANALYSIS AND RESULTS

6.3.1 Acoustic Data Reduction

Acoustic power spectra are the only significant acoustic parameters

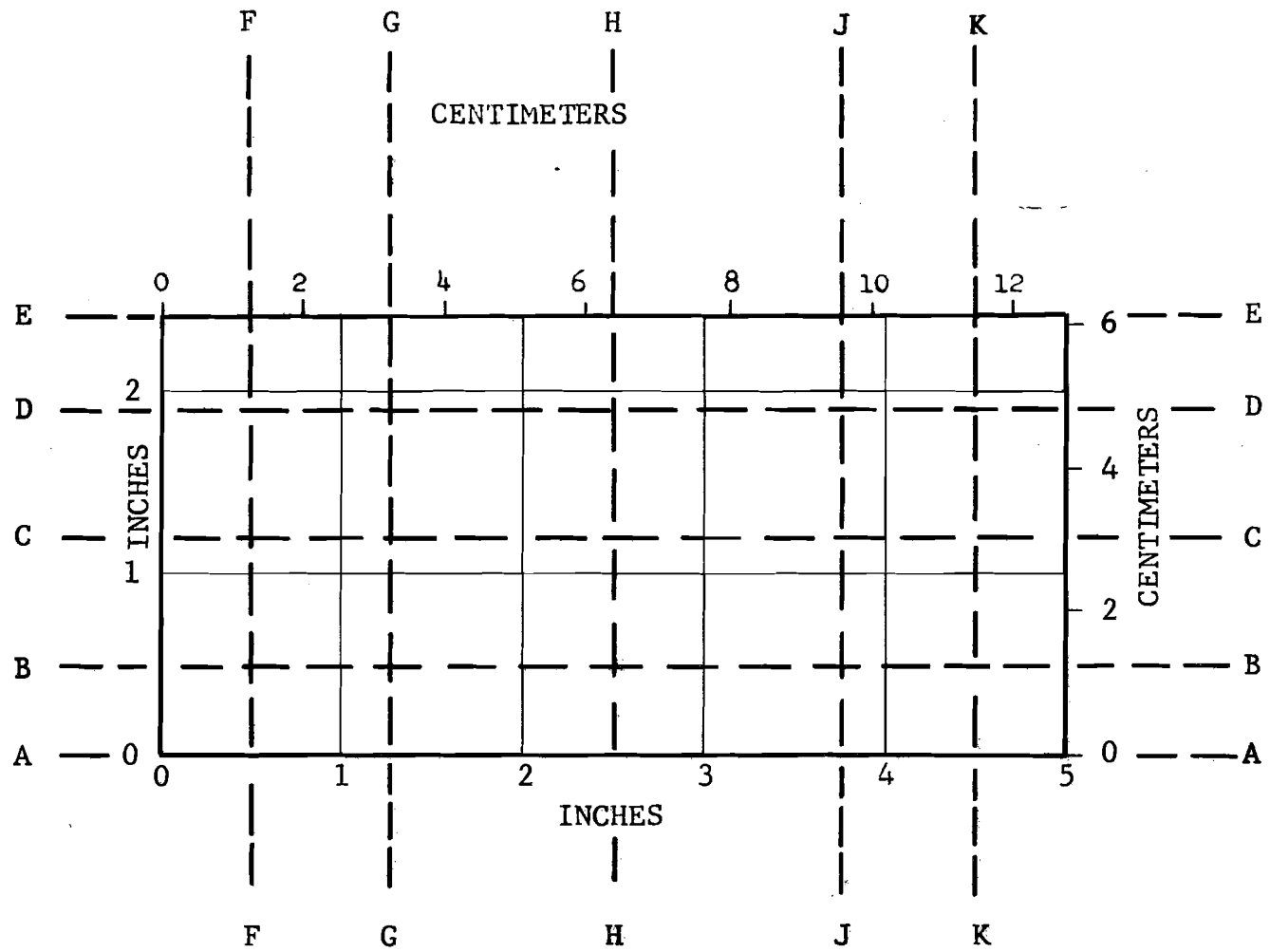

FIGURE 6.2.4-1 LINES OF HORIZONTAL AND VERTICAL HOT FILM ANEMOMETER TRAVERSES FOR SHAKEDOWN TESTS

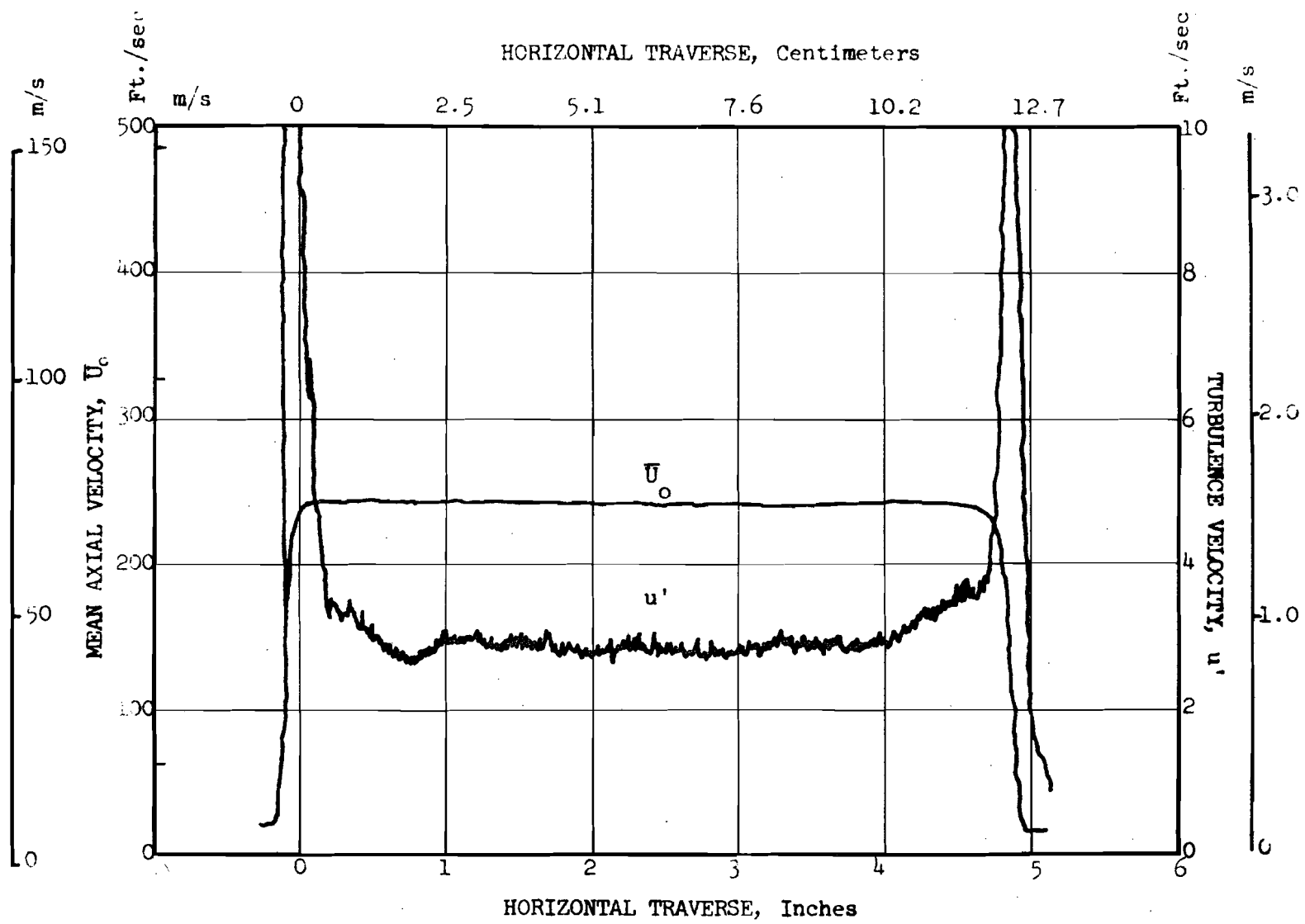

FIGURE 6.2.4-2 PROFILES OF MEAN VELOCITY $\bar{U}_0$ AND TURBULENCE COMPONENT u' ALONG LINE CC 3/8" DOWNSTREAM OF DUCT EXIT PLANE: M = 0.21.

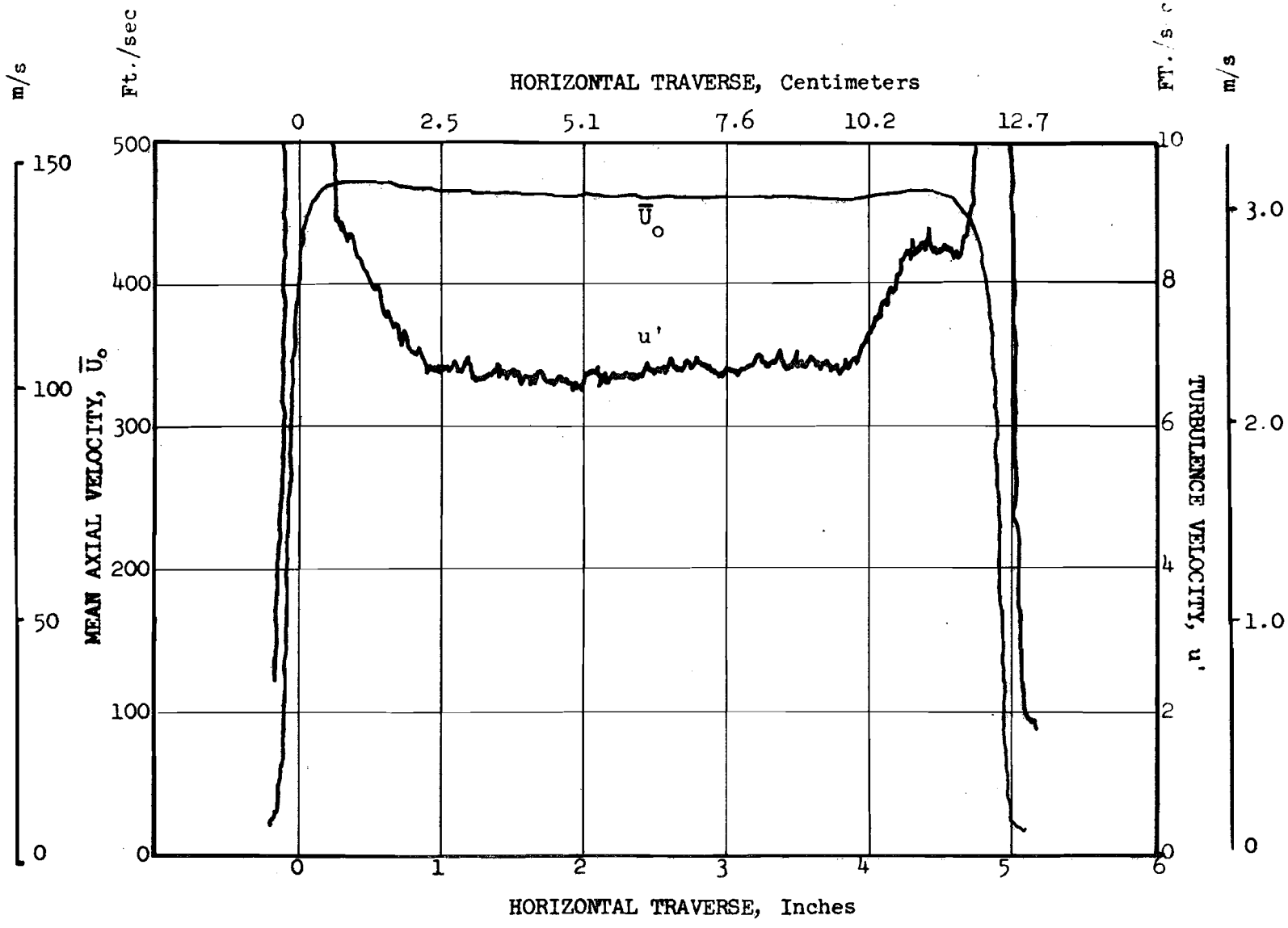

FIGURE 6.2.4-3 PROFILES OF MEAN VELOCITY $\bar{U}_0$ AND TRUBULENCE COMPONENT u' ALONG LINE CC 3/8" DOWNSTREAM OF DUCT EXIT PLANE; $M \approx 0.41$.

TABLE 6.2.5-1 TEST CONDITIONS

	CONFIGURATION	MACH NUMBER, M	ANGLE OF ATTACK
ACOUSTIC TESTS	BASELINE	0.2, 0.3, 0.4, 0.45	—
	1	↓	—
	2		0°, 5°, 10°, 15°
	3		↓
	4		
	5		
	6		
	7		
	8		
	9		
WAKE SURVEYS	BASELINE	0.2, 0.3, 0.4, 0.45	—
	1	↓	—
	2		0°
	3		↓
	4		
	5		
	6		
	7		
	8		
	9		

available when measurements are made in a reverberant room since the energy density is very nearly uniform throughout the room. Directivity information cannot thus, be obtained.

The SPL's from all the microphones were first averaged for each one-third octave band and this average, together with the reverberation time, room volume and barometric pressure was used to obtain the PWL by the following relation (Reference 6.2.1-2).

$$PWL_{1/3\ OB} = (\text{Average } SPL_{1/3\ OB}) + 10 \log_{10} V - 10 \log_{10} T - 29.5 \qquad (6.3.1\text{-}1)$$

$$+ 10 \log_{10} \left[\left(\frac{460+t}{528}\right)^{1/2} \left(\frac{30}{B}\right) \right] \text{ dB} \quad \text{re: } 10^{-13} \text{ watt}$$

where

Average $SPL_{1/3\ OB}$ = average of the SPL (re: 0.0002 microbar) for all the microphones for any designated 1/3 octave band

V = total air volume of the reverberation chamber, ft^3

T = reverberation time of the reverberation chamber for the frequency band with the source in place, seconds

t = air temperature, ° F

B = barometric pressure, inches mercury

6.3.2 Results and Discussion

(1) Acoustic Data $\alpha^o = 0$

(a) Spectra

The one-third octave band power level spectra at the four Mach numbers for the baseline tests are presented in Figure 6.3.2-1. The low frequency jet noise peaks and levels appear to be consistent with predictions.

One-third octave band power level spectra at the four Mach numbers at $\alpha^o = 0$ for all the nine configurations are presented in Figures 6.3.2-2 through 6.3.2-10. The significant observations were that while blunt shapes like the circular cylinder and the thick flat plates exhibited sharp peaks with a consistent velocity dependency of the frequency peaks, streamlined shapes like the elliptical, double-circular-arc and the symmetrical airfoils exhibited only broad-band spectra.

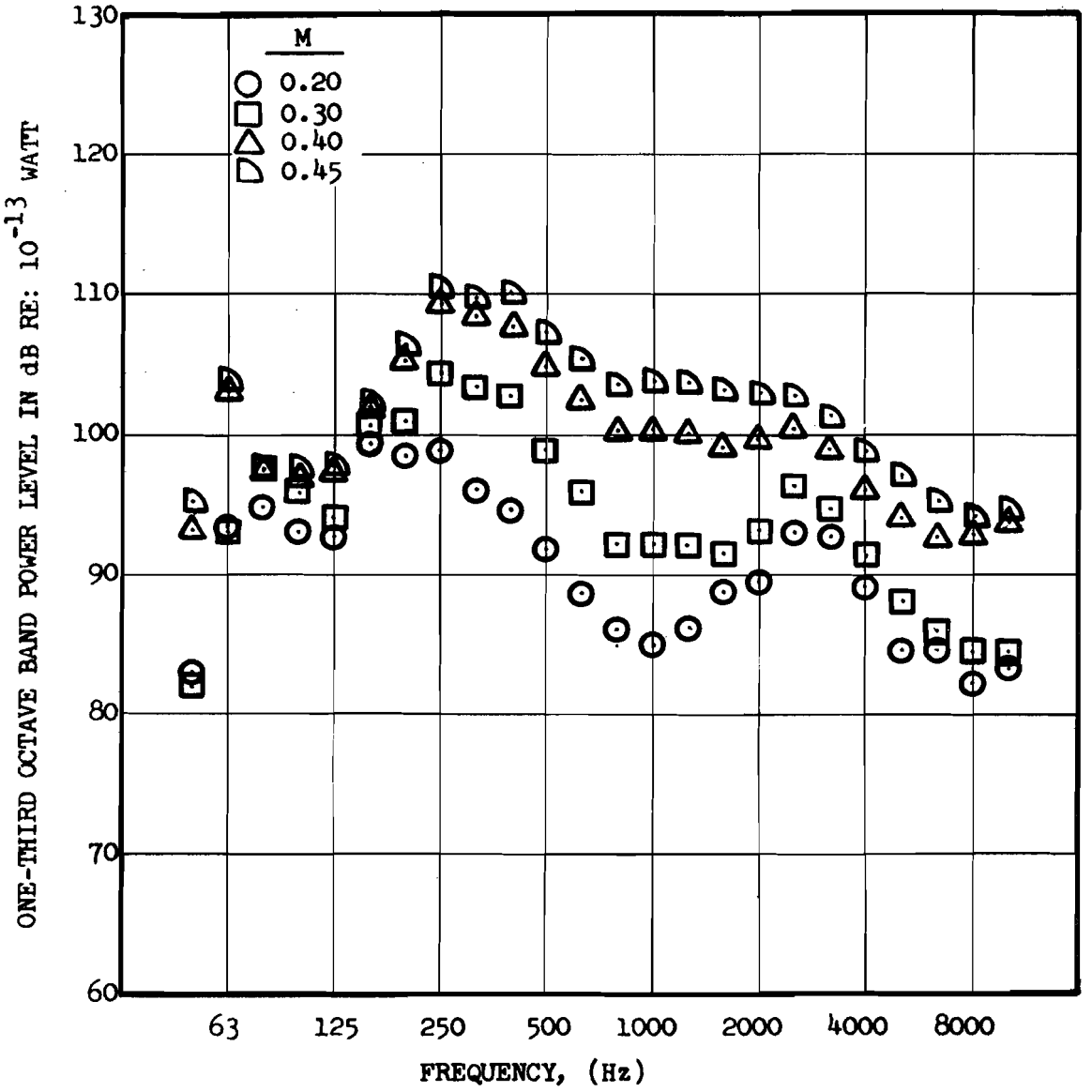

FIGURE 6.3.2-1 VARIATION OF ONE-THIRD OCTAVE BAND POWER LEVEL SPECTRUM WITH FLOW MACH NUMBER; BASELINE

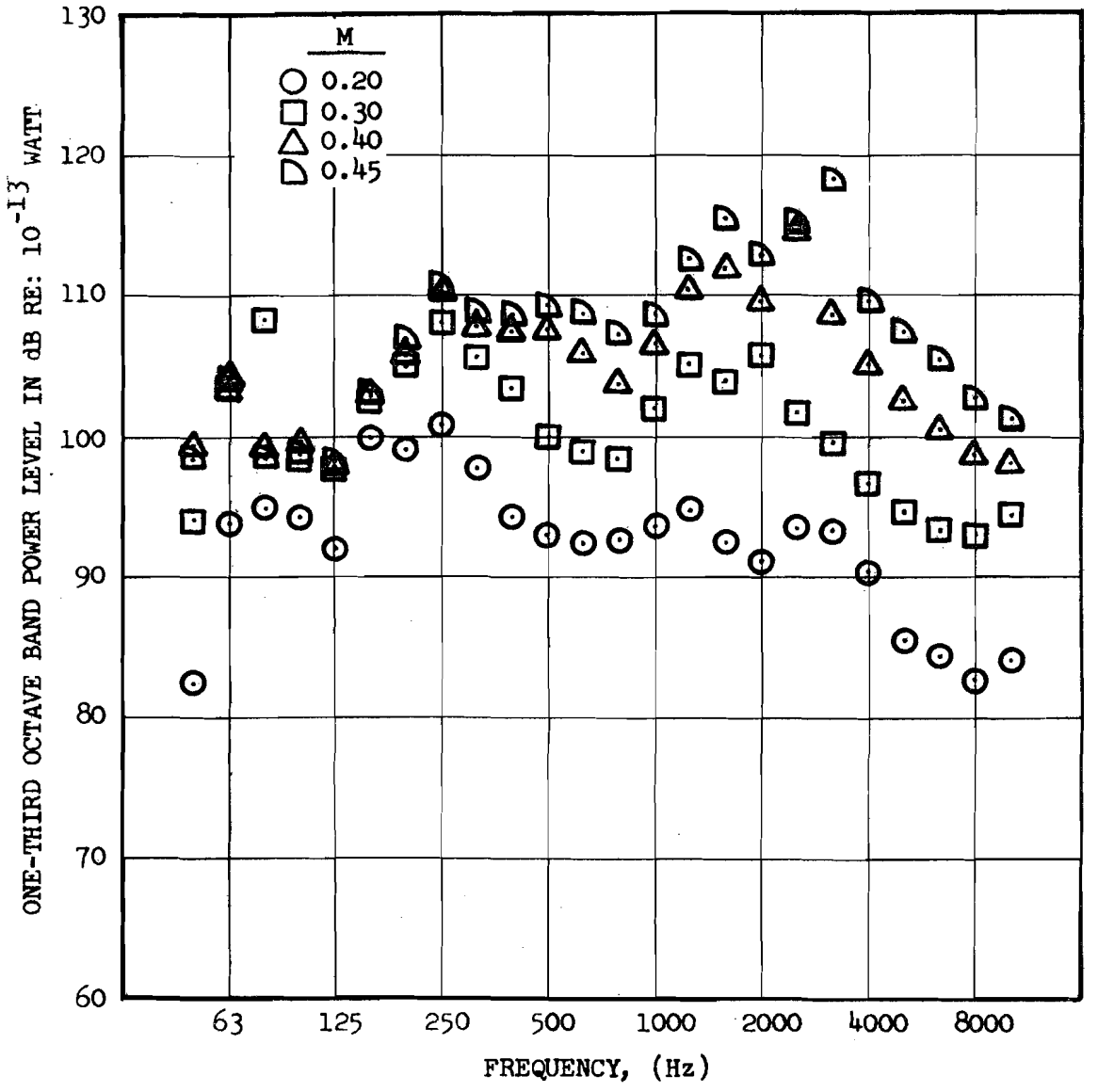

FIGURE 6.3.2-2 VARIATION OF ONE-THIRD OCTAVE BAND POWER LEVEL SPECTRUM WITH FLOW MACH NUMBER; CONFIGURATION 1

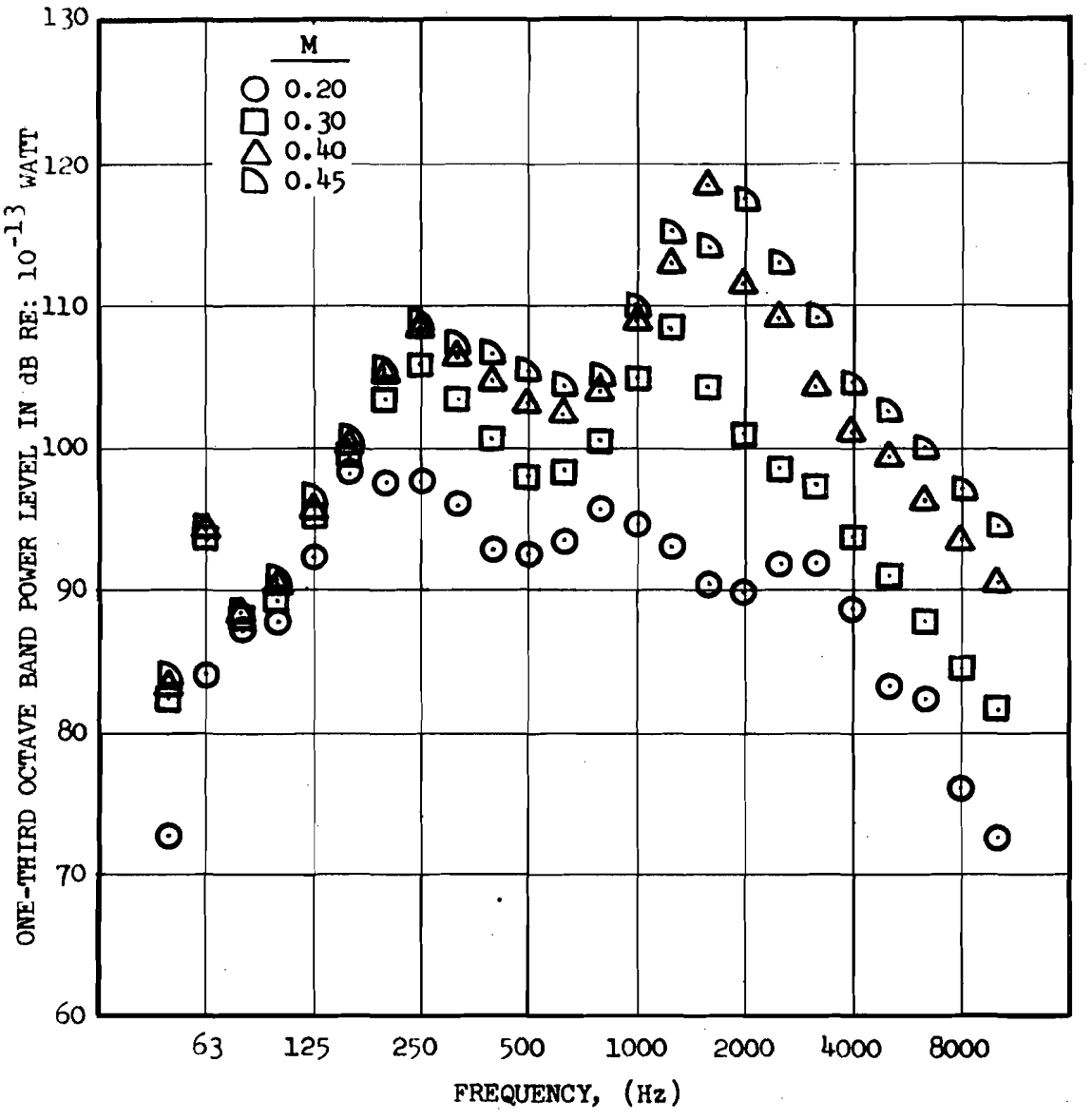

FIGURE 6.3.2-3 VARIATION OF ONE-THIRD OCTAVE BAND POWER LEVEL SPECTRUM WITH FLOW MACH NUMBER; CONFIGURATION 2, $\alpha^{\bullet} = 0$

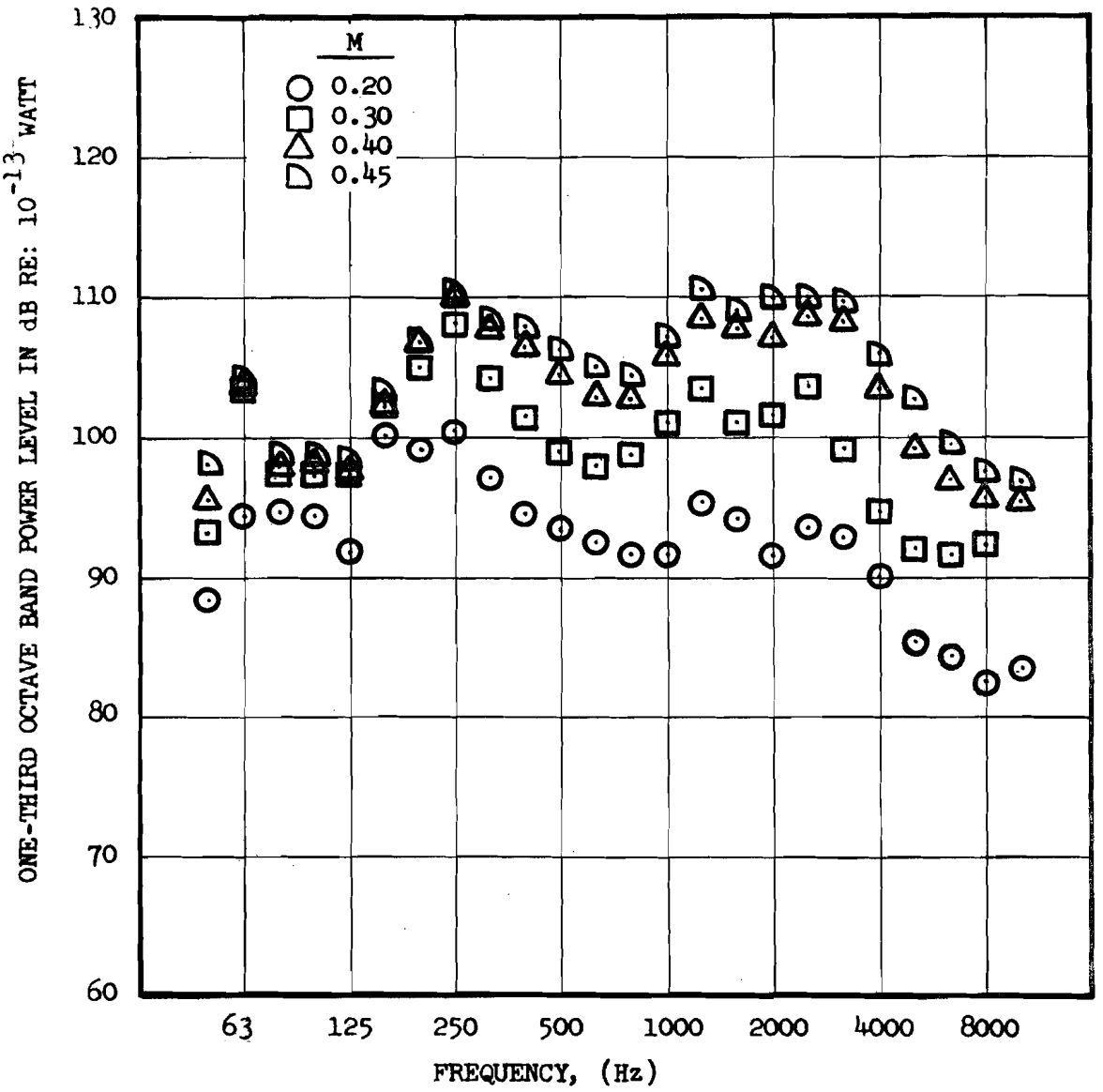

FIGURE 6.3.2-4 VARIATION OF ONE-THIRD OCTAVE BAND POWER LEVEL SPECTRUM WITH FLOW MACH NUMBER; CONFIGURATION 4, $\alpha^{\circ} = 0$

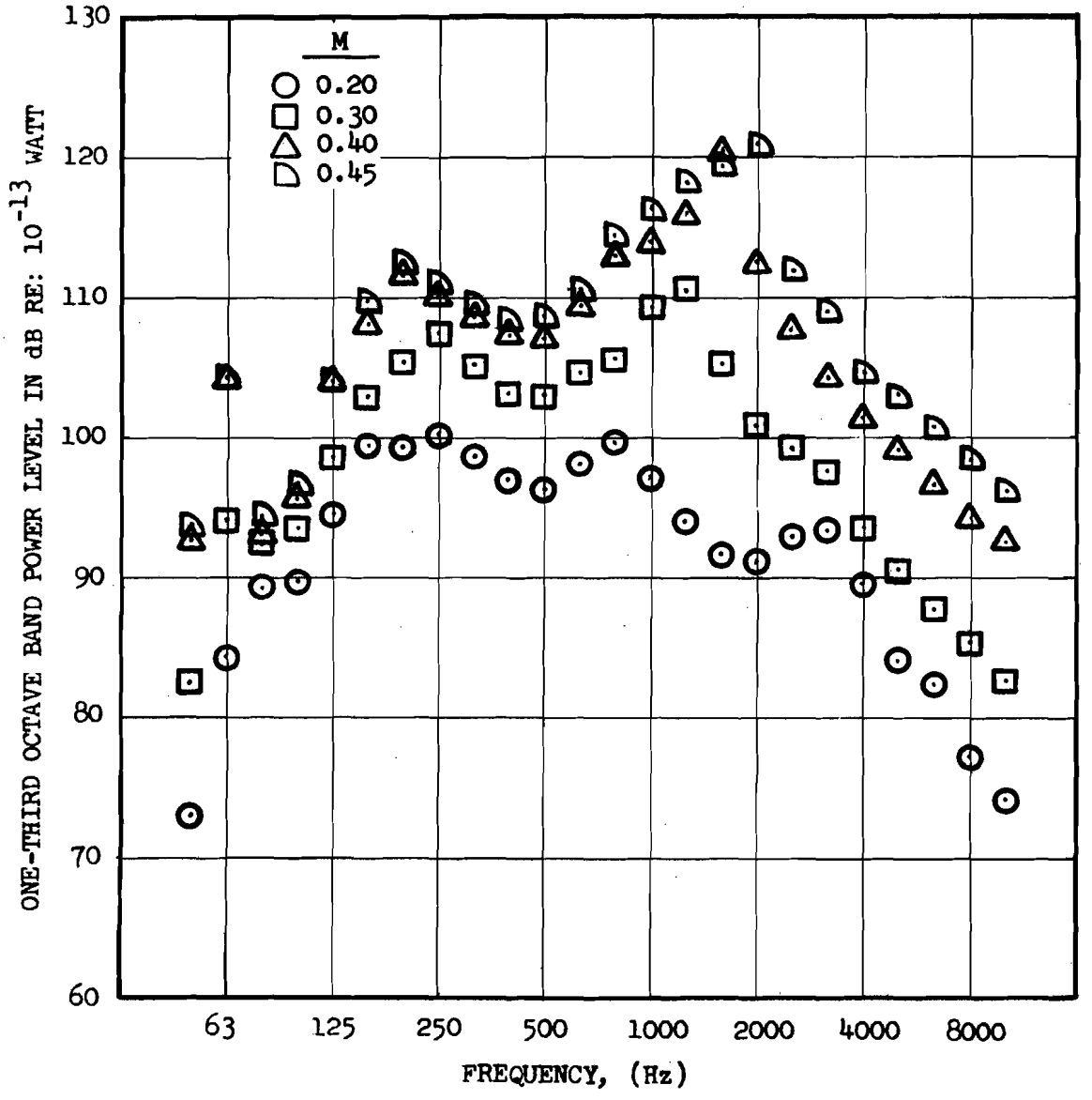

FIGURE 6.3.2-5 VARIATION OF ONE-THIRD OCTAVE BAND POWER LEVEL SPECTRUM WITH FLOW MACH NUMBER, CONFIGURATION 3, $\alpha^{\circ} = 0$

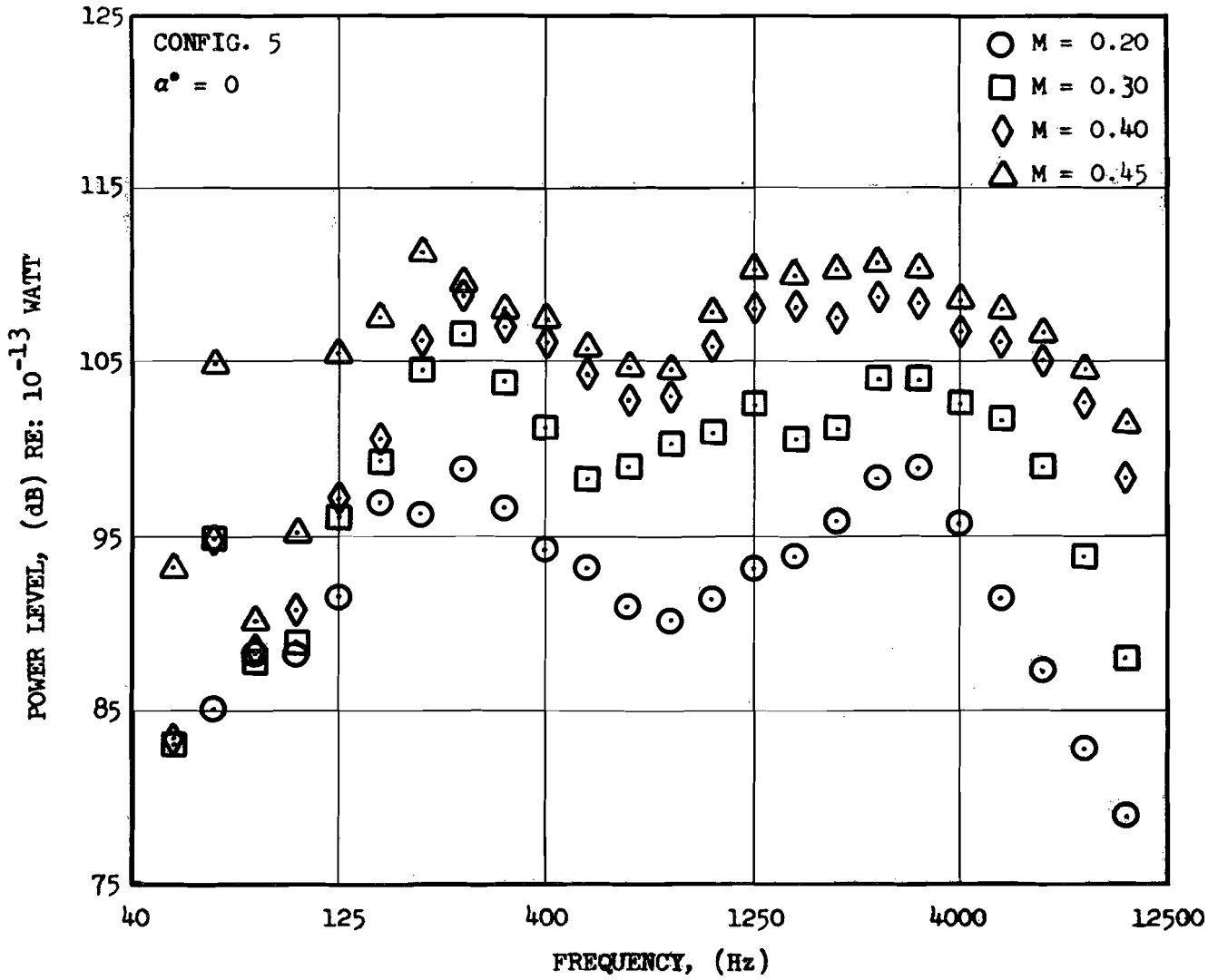

FIGURE 6.3.2-6 VARIATION OF ONE-THIRD OCTAVE BAND POWER LEVEL SPECTRUM WITH FLOW MACH NUMBER; CONFIGURATION 5, $\alpha^{\circ} = 0$.

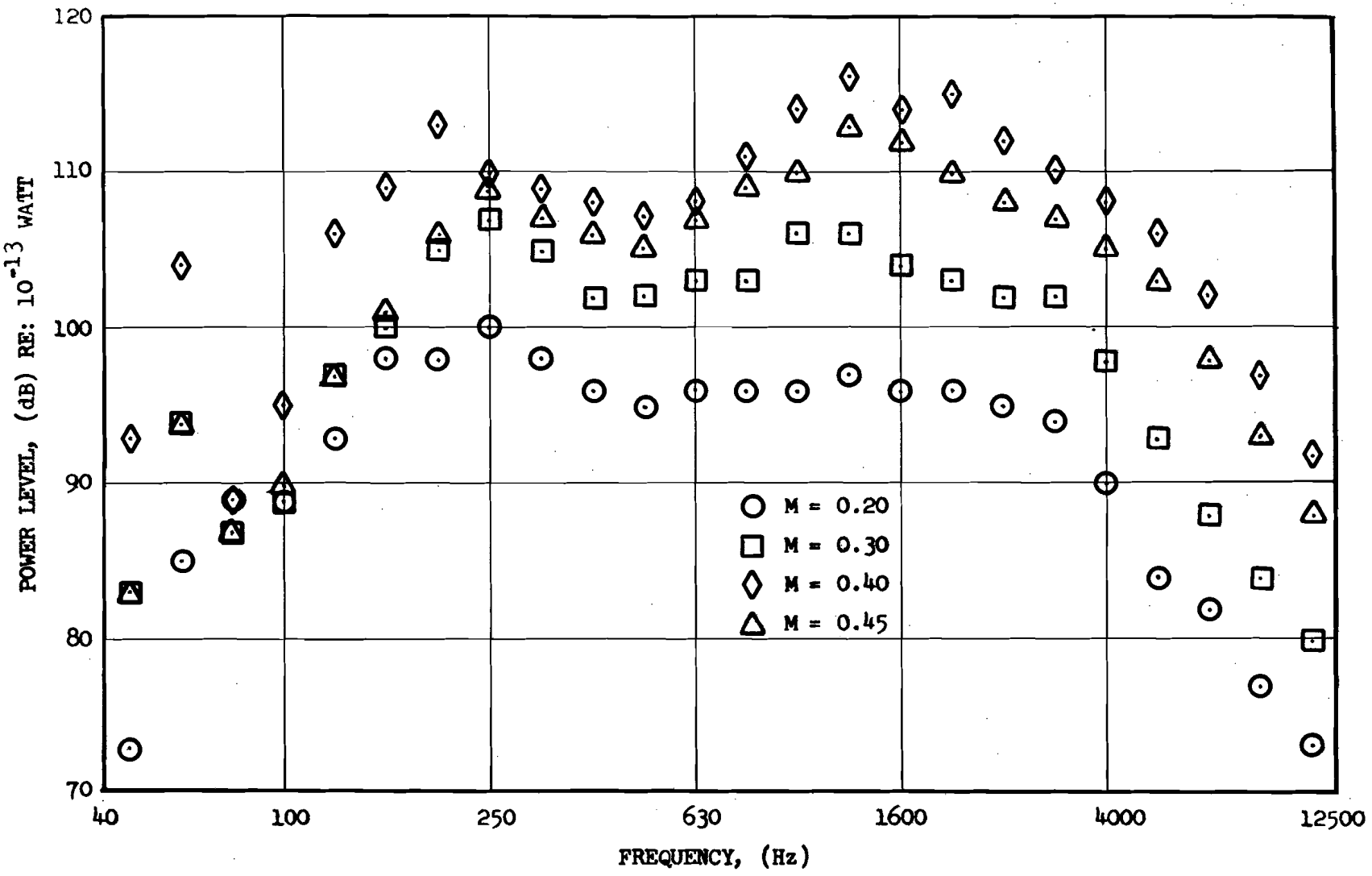

FIGURE 6.3.2-7 VARIATION OF ONE-THIRD OCTAVE BAND POWER LEVEL SPECTRUM WITH FLOW MACH NUMBER; CONFIGURATION 6, $\alpha^{\circ} = 0$.

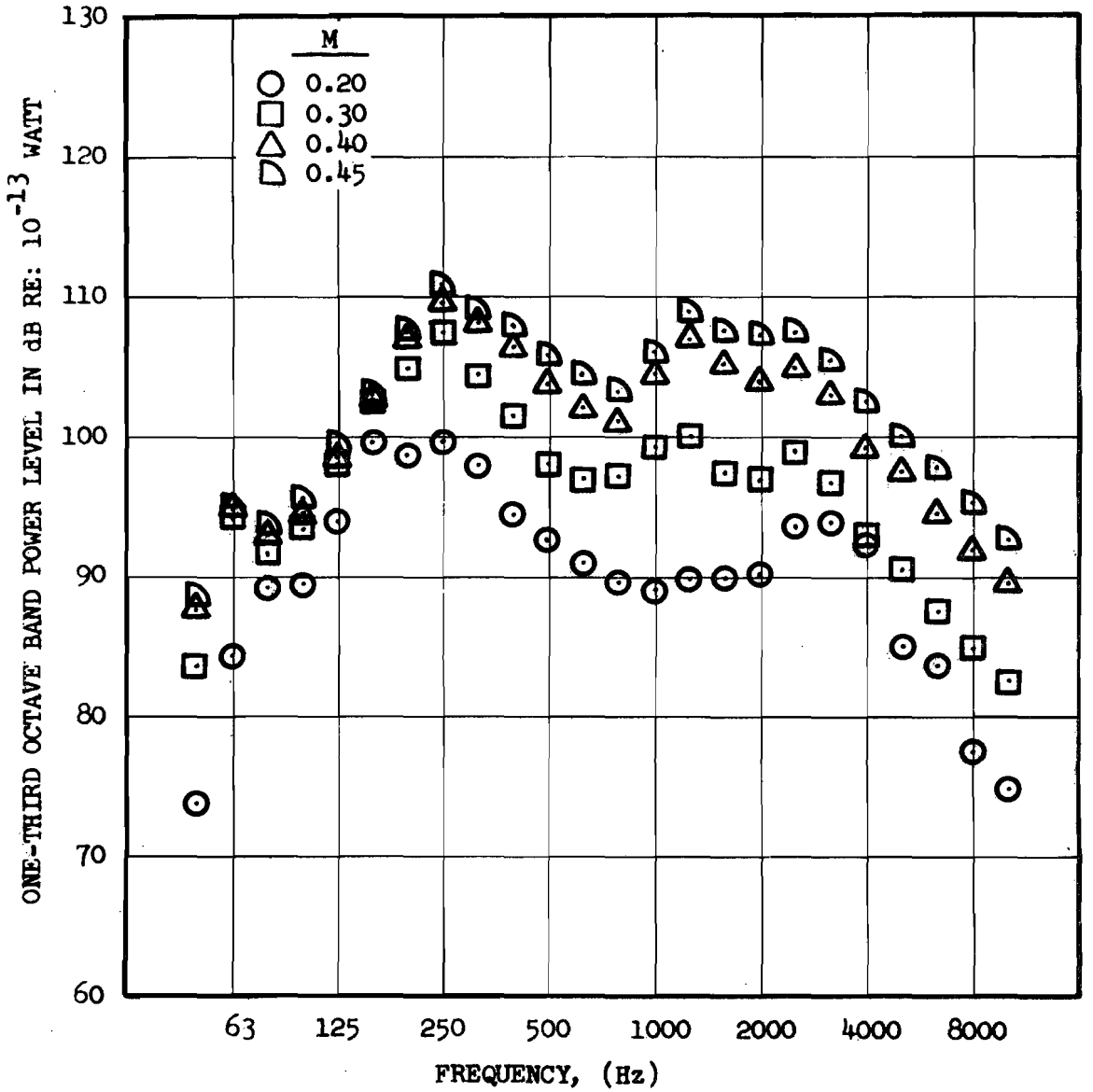

FIGURE 6.3.2-8 VARIATION OF ONE-THIRD OCTAVE BAND POWER LEVEL SPECTRUM WITH FLOW MACH NUMBER; CONFIGURATION 7, $\alpha^{\circ} = 0$

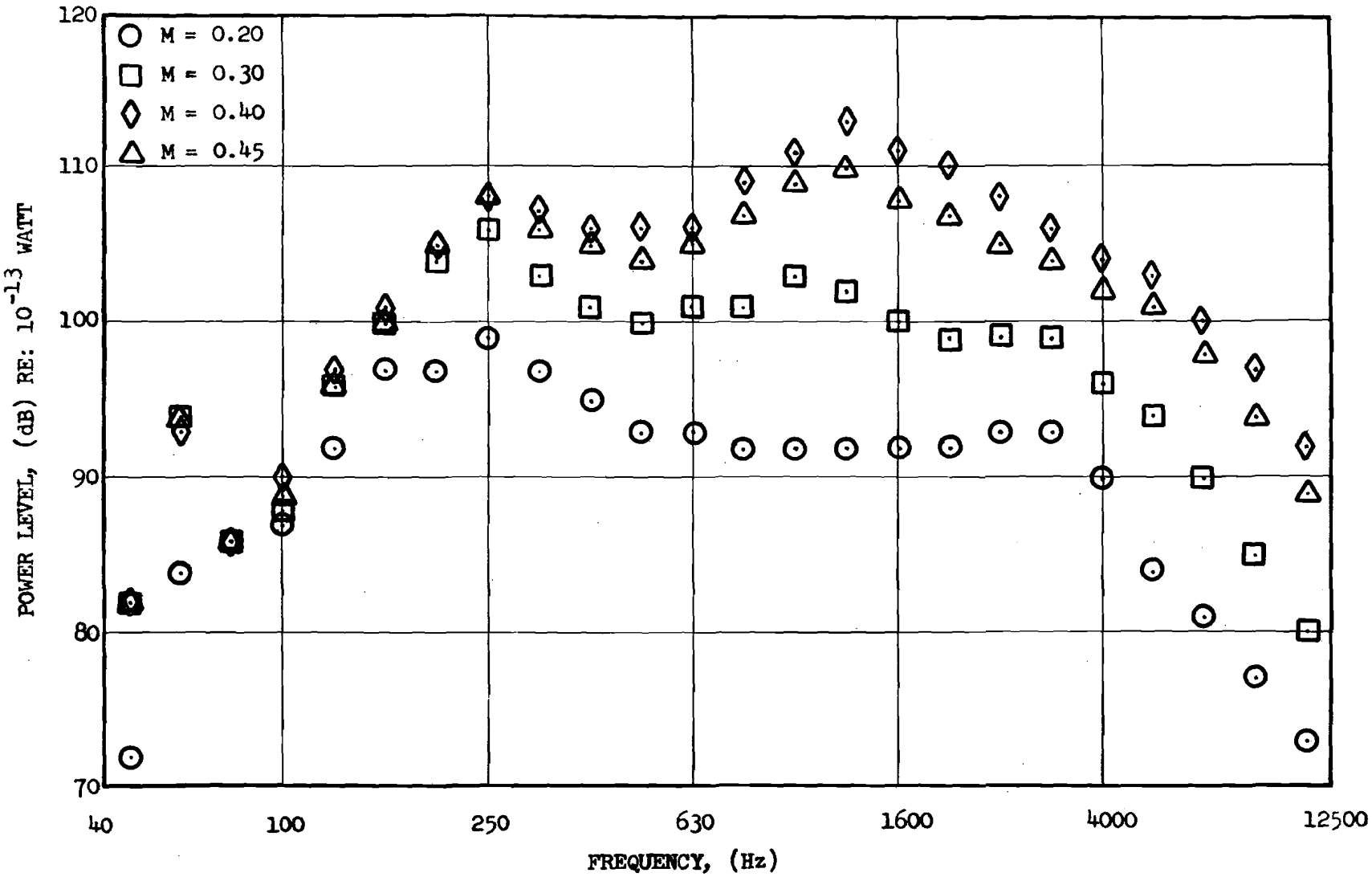

FIGURE 6.3.2-9 VARIATION OF ONE-THIRD OCTAVE BAND POWER LEVEL SPECTRUM WITH FLOW MACH NUMBER; CONFIGURATION 8, $\alpha^{\circ} = 0$.

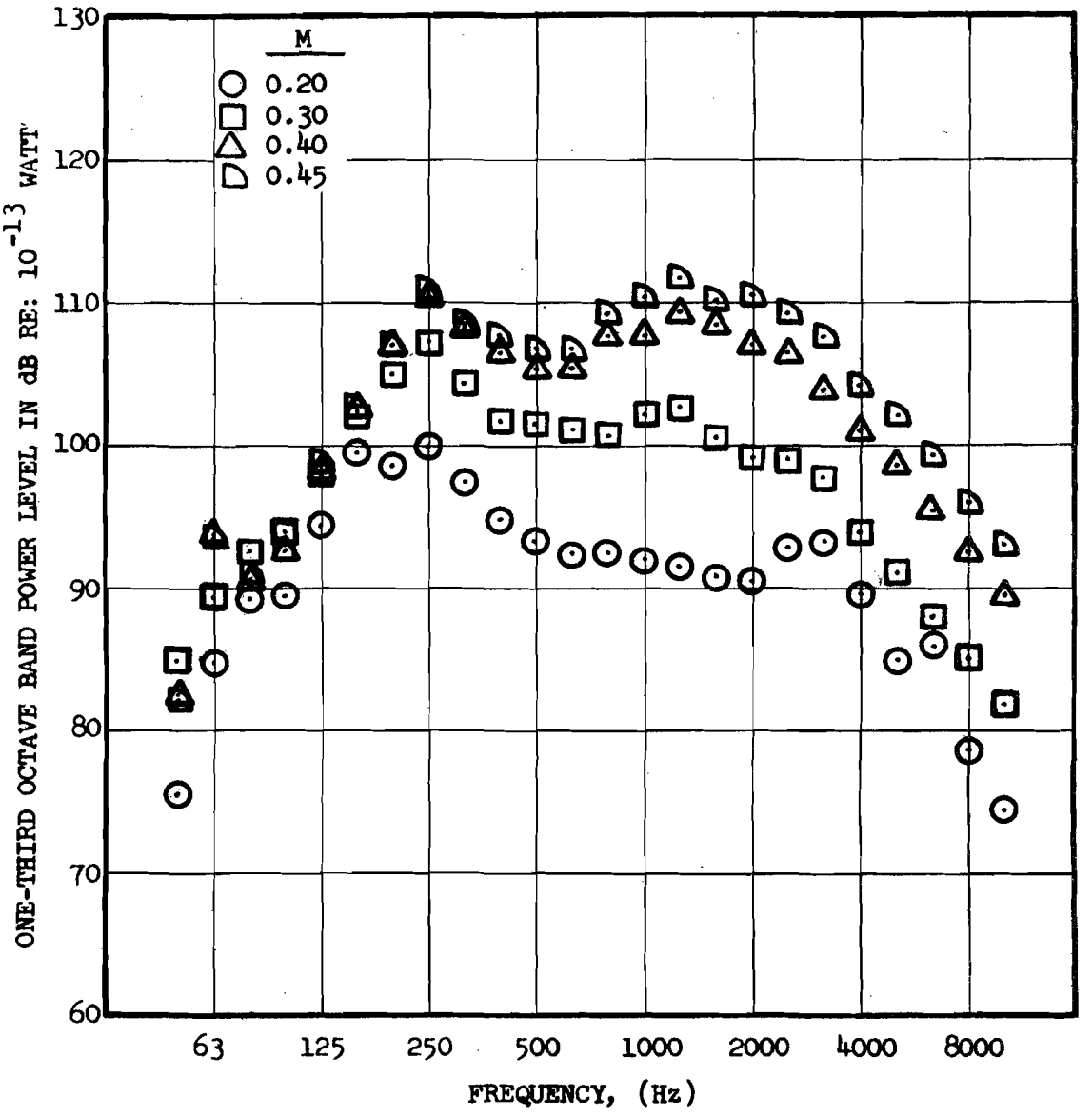

FIGURE 6.3.2-10 VARIATION OF ONE-THIRD OCTAVE BAND POWER LEVEL SPECTRUM WITH FLOW MACH NUMBER; CONFIGURATION 9, $\alpha^{\circ} = 0$

(b) Overall Power Level Comparisons $\alpha^o = 0$

Comparison of the spectra for the different configurations with the baseline tests indicated that the background noise level was so high that at M = 0.2 no significant strut noise could be measured. Hence M = 0.2 runs were dropped from further considerations. At higher Mach numbers, strut noise was clearly discernible above the background noise. Similarly, the spectra below and up to 630 Hz were not influenced by the presence of the strut and were thus not added in calculating overall power levels radiated by the struts alone.

The variation of absolute overall power levels with velocity for the different configurations at $\alpha^o = 0$ is shown in Figure 6.3.2-11. The exact velocities were obtained from the hot-film anemometer traverse data. It is seen that there isga maximum spread of nearly 20 dB between the lowest (Configuration 7 at M ≃ 0.3) and the highest (Configuration 3 at M ≃ 0.45). Further, at the highest velocity, there is a spread of more than 10 dB in the absolute OAPWL between Configurations 3 and 7. However, since jet and background noise changes could obscure the direct contribution by the strut-flow interaction, the baseline OAPWL was subtracted from the absolute data. The Δ OAPWL = $OAPWL_{conf.} - OAPWL_{BL}$ thus obtained is shown plotted in Figure 6.3.2-12 for all the configurations at the different velocities at $\alpha^o = 0$.

Note that Δ OAPWL is defined here as

$$\Delta \text{ OAPWL} = 10 \log_{10} \left(\frac{W_{config} - W_{baseline}}{W_{ref}} \right)$$

For the sake of convenience, these are tabulated also in Table 6.3.2-1. Typically a 5th to 6th power velocity dependence is seen from the data.

Several broad trends are immediately obvious from Table 6.3.2-1.

(i) There is a strong velocity dependency of the OAPWL.

(ii) Chord and thickness have definite contribution to the OAPWL.

(iii) Streamlining the geometry has a distinct benefit. For example, comparing Configurations 3, 6, 8, and 9 (same thickness and same chord), the blunt flat plate is the worst and the double-circular-arc and symmetrical airfoils are the best. The same observation can be made by comparing Configurations 4, 5, and 7 also.

(iv) The double-circular arc airfoil and symmetrical (NACA 0021) airfoil appear to generate the same OAPWL. Their spectra also were similar. Due to greater ease and lower cost of fabrication, the double-circular arc airfoil thus appears to be the most desirable section for struts, linkages, etc. from an acoustic/economic standpoint.

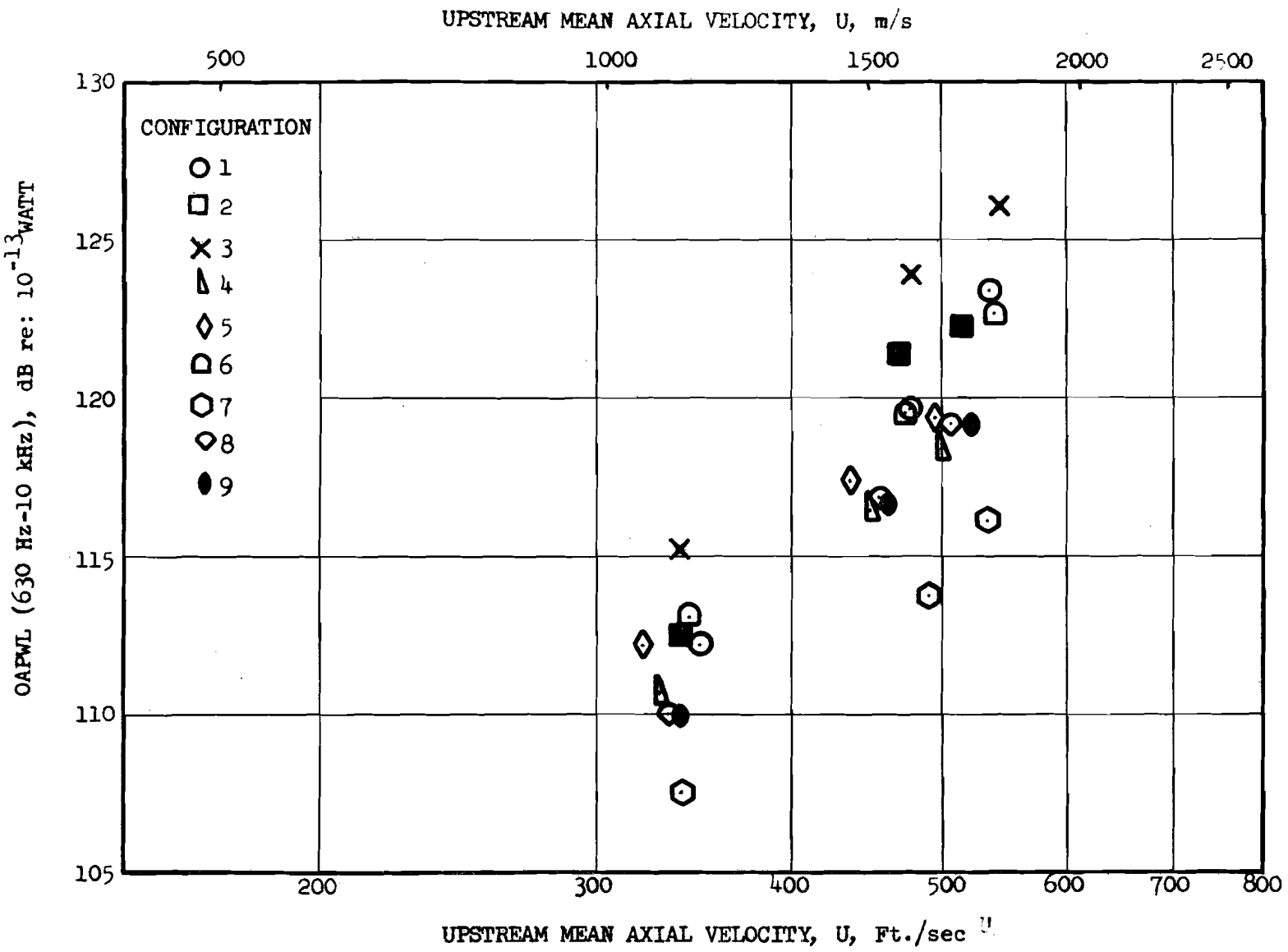

FIGURE 6.3.2-11 VARIATION OF OVERALL POWER LEVEL WITH UPSTREAM MEAN AXIAL VELOCITY AND CONFIGURATION, $\alpha^0 = 0$.

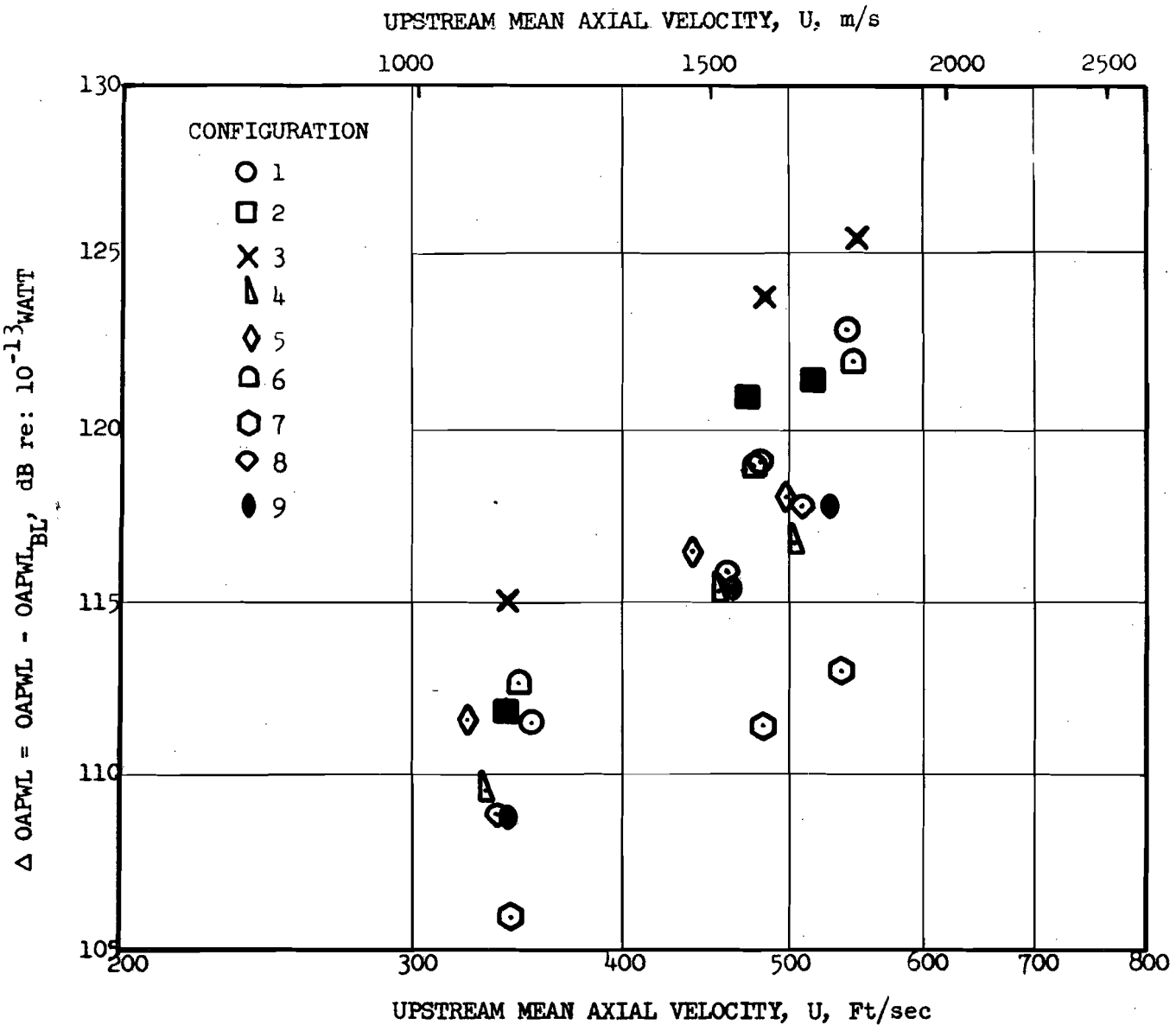

FIGURE 6.3.2-12 Δ OAPWL vs. UPSTREAM MEAN AXIAL VELOCITY, ALL CONFIGURATIONS, $\alpha^0 = 0$.

TABLE 6.3.2-1 TABULATION OF ΔOAPWL FOR ALL CONFIGURATIONS AT $\alpha = 0$

CONFIGURATION NUMBER	SHAPE: (SKETCH APPROXIMATELY TO SCALE)	$\Delta\ OAPWL = OAPWL - OAPWL_{BL} = 10 \log_{10}\left[\frac{W_{conf} - W_{BL}}{W_{ref}}\right]$		
		M		
		.3	.4	.45
1		111.6	119.2	122.9
2		111.8	121.1	121.6
3		115.0	123.8	125.6
4		109.7	115.4	116.8
5		111.6	116.5	118.2
6		112.7	119.0	122.1
7		105.9	111.5	113.2
8		108.9	115.9	117.9
9		108.9	115.6	117.9

(2) Aerodynamic Data $\alpha^o = 0$

The discussions in the previous section indicate a dependency of the OAPWL on the aerodynamic coefficients of the body. Profile drag coefficient C_D was determined for all the configurations at Mach numbers of 0.3, 0.4, and 0.45 at $\alpha^o = 0$ by a wake-survey method. Horizontal traverses were made at several spanwise locations aft of the struts with the total pressure Kiel probe and the X-array hot film anemometer. Analysis of the data was done, using Jones' relation (Reference 6.3.2-1) which was modified to include velocity. The profile drag of a body can be determined from the loss of momentum per unit time that it imposes on the free-stream. Referring to Figure 6.3.2-13, the C_D can be derived in the form

$$C_D = \frac{2}{\ell} \cdot \frac{\overline{U}_2}{\overline{U}_o} \int_{\text{Wake}} \left[1 - \frac{P_2 - P_o + 1/2\ \rho\ \overline{U}_o^2}{1/2\ \rho\ \overline{U}_o^2} \right] \cdot dy \qquad (6.3.2\text{-}1)$$

where $\overline{U}$ and P refer to mean axial velocity and total pressure respectively and subscripts 0 and 2 refer to upstream and downstream conditions respectively. Typical total pressure and velocity wake profiles are shown in Figure 6.3.2-14. These have been adjusted for the relative displacement of the Kiel and hot film probes seen in Figure 6.3.2-1. The analysis of these profiles was carried out by first digitizing through a Bendix Datagrid Digitizer at closely spaced intervals and performing a numerical integration by standard computer techniques.

(3) Acoustic-Aerodynamic-Geometric Coupling

Figure 6.3.2-15 shows a plot of OAPWL versus C_D for all the configurations at approximate Mach numbers of 0.3, 0.4, and 0.45 at $\alpha^o = 0$. The increase in OAPWL with Mach number, C_D and body dimensions indicates the possibility of an empirical correlation which would collapse all the data into a single curve. Based on an analytical modeling, the power level was expressed as

$$\text{OAPWL} = 10 \log_{10} \left[k \cdot \ell \cdot t \cdot h \cdot \overline{U}_o^n \cdot C_D^{\ m} \right] \qquad (6.3.2\text{-}2)$$

where

ℓ = chord, feet

h = span, feet

t_{max} = maximum thickness, feet

$\overline{U}_o$ = upstream mean velocity, feet/sec.

C_D = profile drag coefficient

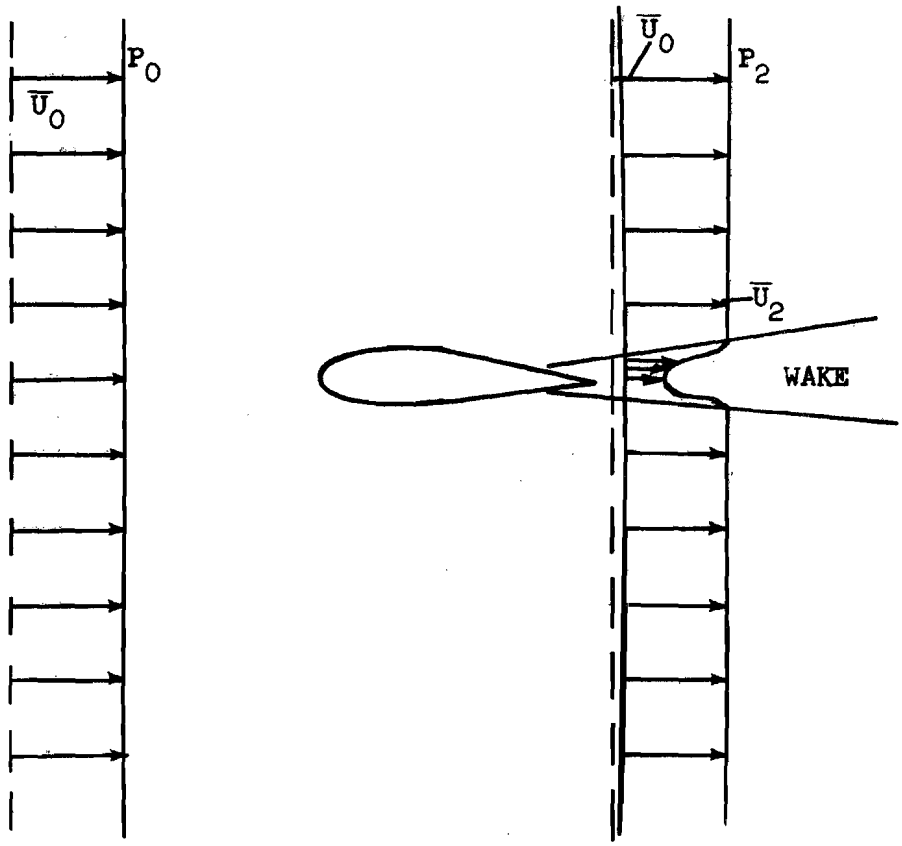

FIGURE 6.3.2-13 DIAGRAM OF AIRFOIL AND WAKE USED IN DRAG COEFFICIENT FORMULATION.

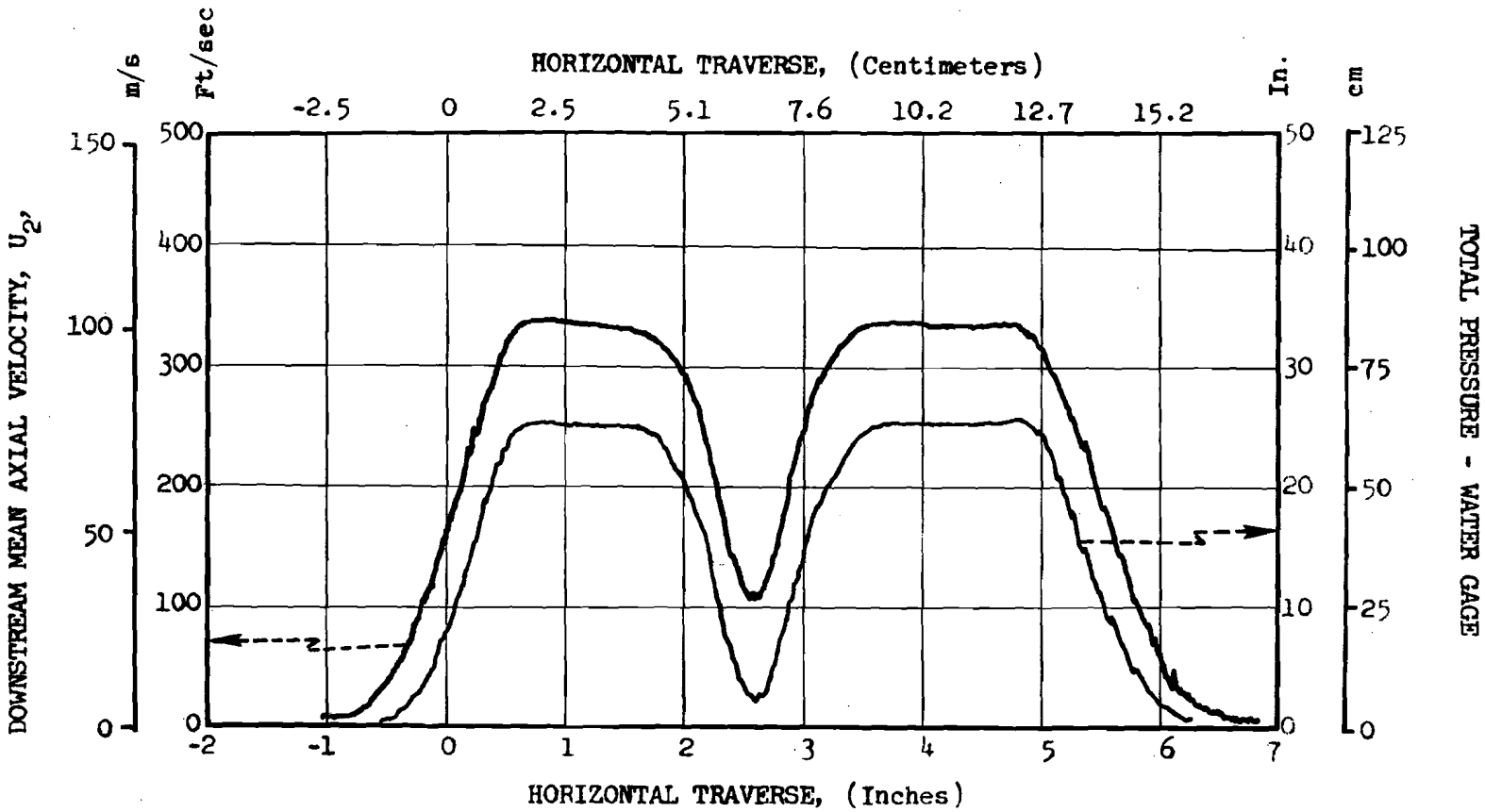

FIGURE 6.3.2-14 TYPICAL VELOCITY AND TOTAL PRESSURE WAKE PROFILE AT MID-HEIGHT LOCATION, CONFIGURATION 3.

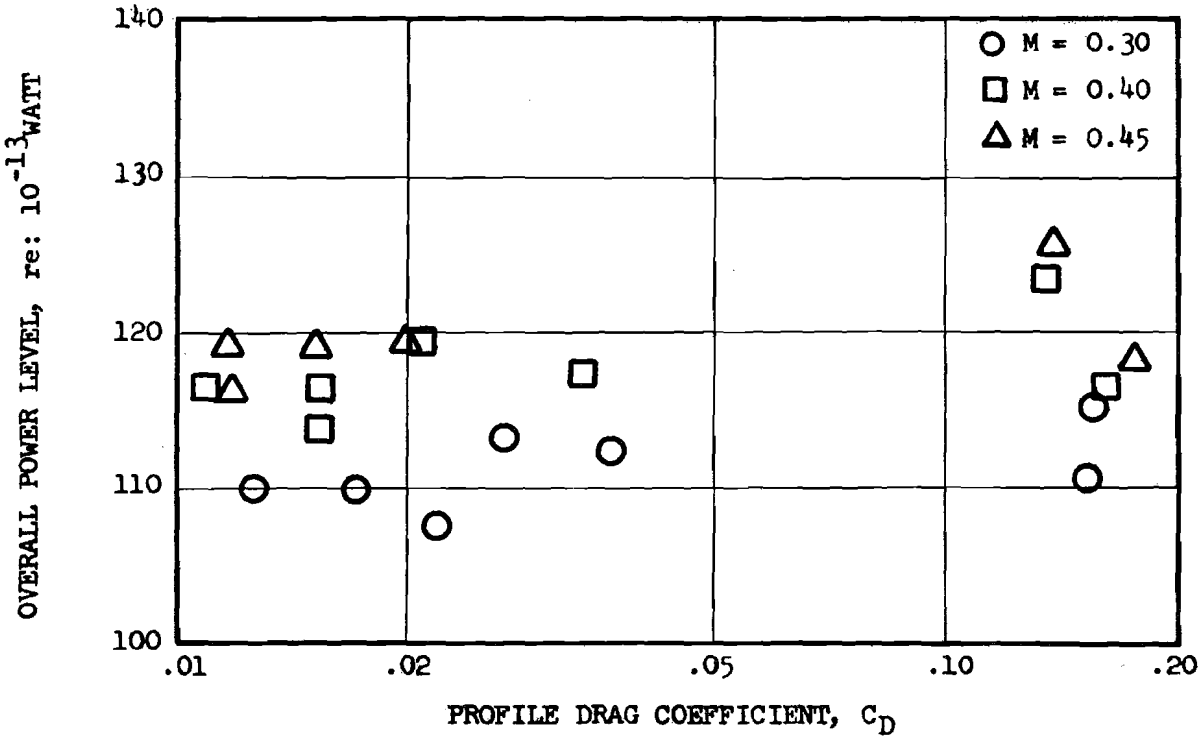

FIGURE 6.3.2-15 VARIATION OF OAPWL WITH PROFILE DRAG COEFFICIENT, ALL CONFIGURATIONS, $\alpha^0 = 0$.

and k, n, m are constants to be empirically determined. Defining a normalized power level by

$$NPWL = OAPWL_{measured} - 10 \cdot \log_{10} \left(\ell \cdot \overline{U}_o^n \quad t \cdot h \right) \qquad (6.3.2\text{-}3)$$

and plotting versus C_D, it was found that the best value for n was 5. A plot of NPWL with a fifth power of velocity (n = 5) versus C_D is shown in Figure 6.3.2-16. The data appears to satisfy the relation

$$NPWL = 16.8 + 10 \log_{10} \left(C_D^{0.4} \right) \qquad (6.3.2\text{-}4)$$

The three flagged points are data from configuration 5 which appear to form a parallel line with a higher value of the constant. This configuration had been accidentally damaged and repaired prior to the test, and the high values are most likely the result of a poor surface finish.

(4) Overall Power Level Correlation

The OAPWL radiated by bodies placed in a low turbulence flow can thus be determined by

$$OAPWL = 16.8 + 10 \log_{10} \left(\ell \cdot t_{max} \quad h \cdot \overline{U}_o^5 \right) + 4 \log C_D, \text{ dB re: } 10^{-13} \text{ Watt} \qquad (6.3.2\text{-}5)$$

where all the symbols carry the meaning and units mentioned in the previous section.

(5) Comparison of the Model with Test Data

The OAPWL calculated by using the correlation of Equation 6.3.2-5 is shown plotted in Figure 6.3.2-17 versus the measured OAPWL for the eight configurations tested at $\alpha^o = 0$ (configuration 5 was dropped from further consideration). It should be emphasized that the correlation was derived from the measured data. The line drawn at 45° to either axis indicates the closeness of the agreement of the formulation with the data.

Data from two other sources was obtained for the purpose of comparison.

(a) Hayden et al., References 6.3.2-2 and 6.3.2-3.

NACA 0012 Airfoil

chord = 6", wetted span = 16", δ = 0.72", $\overline{U}_o$ = 100 fps, C_D = 0.007
$\alpha° = 4°$

Measured OAPWL = 94.7 dB re: 10^{-13} watts.

OAPWL calculated by our model = 94.5 dB re: 10^{-13} watts.

This is plotted as the solid square in Figure 6.3.2-17.

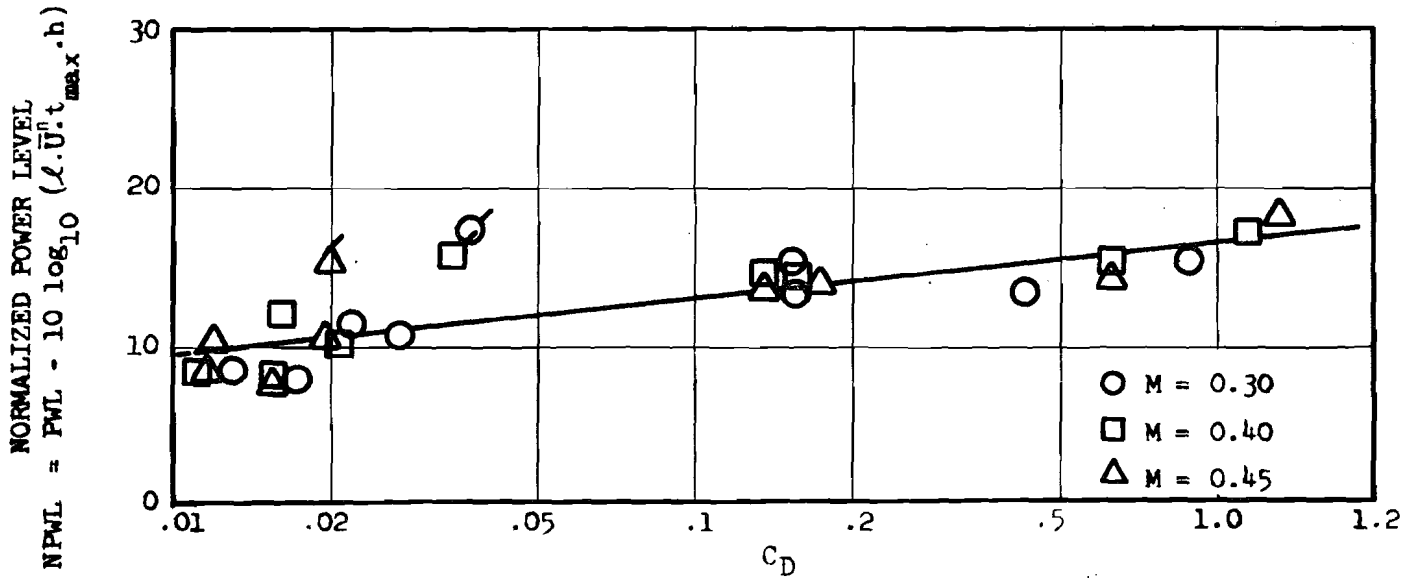

FIGURE 6.3.2-16 PLOT OF NORMALIZED OVERALL POWER LEVEL versus C_D, ALL CONFIGURATIONS, $\alpha^0 = 0$.

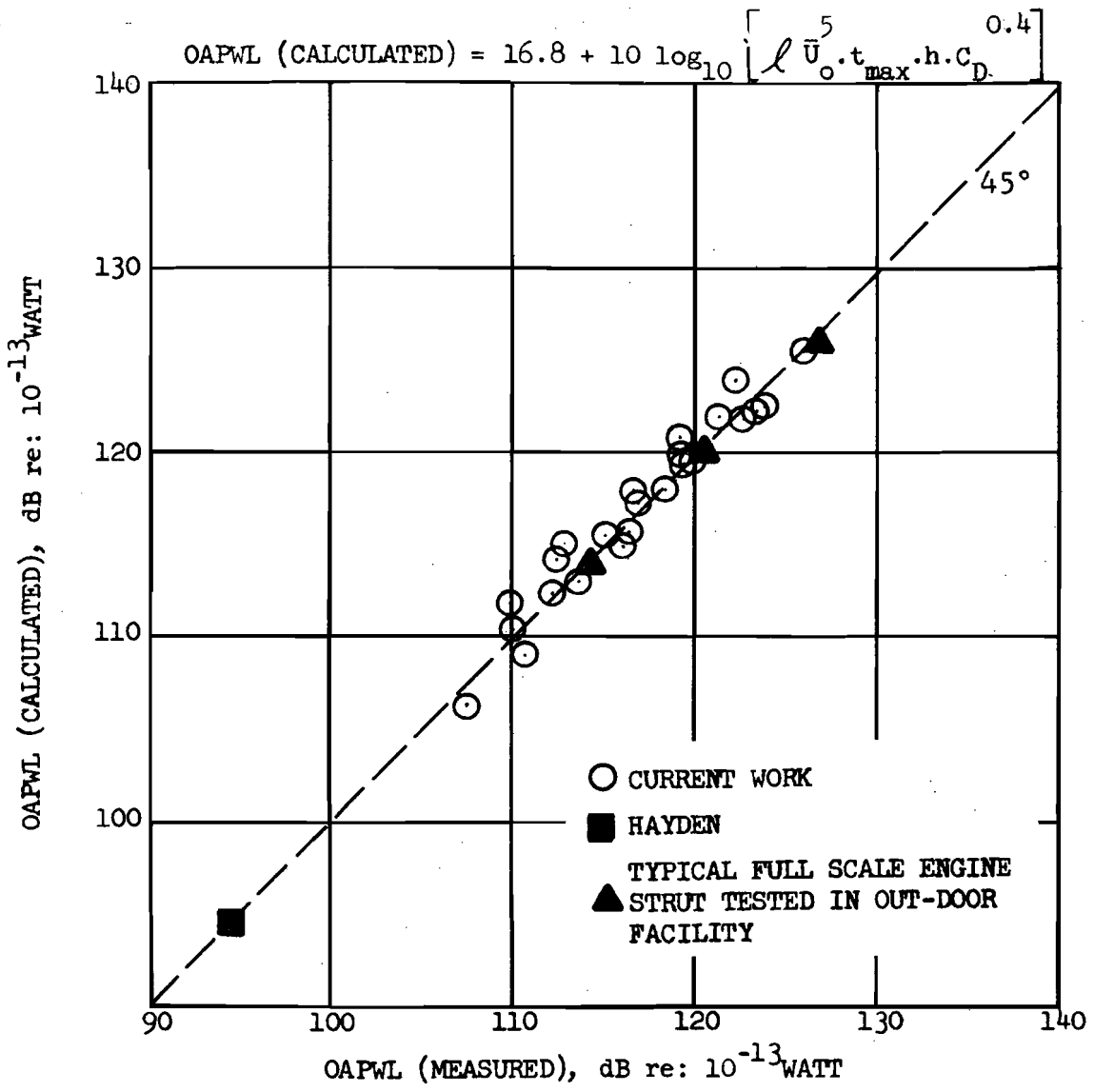

FIGURE 6.3.2-17 COMPARISON BETWEEN CALCULATED AND MEASURED OVERALL POWER LEVELS. $\alpha^0 = 0$, ALL CONFIGURATIONS, M = 0.30, 0.40, 0.45.

(b) Typical Engine Full Scale Strut Noise Test - GE (Reference 6.3.2-4)

Comparison of the calculated OAPWL with data measured from a typical engine full scale strut noise test also indicates excellent agreement. These tests were conducted in a different test facility (outdoor, 306 Acoustic Duct Test Facility) and acoustic measurements were made by means of microphones located on a 25 ft arc at angles of 20°, 30°, 40°, 50°, 60°, 70°, 80°, and 90° relative to the duct exit axis. (The current core engine tests were conducted in a semi-reverberant room). The significant results are listed below: Elliptical Section;

$\delta = 0.73''$, $\ell = 1.74''$, $h = 4''$, $\alpha^o = 0$

$C_D = 0.15$ (Reference 6.3.2-5)

$\overline{U}_o$ fps	OAPWL calculated	OAPWL dB: re 10^{-13} Watts measured
335	114.3	114.5
445	120.2	120.8
588	126.6	126.8

The agreement is strikingly close, and this data is shown in Figure 6.3.2-17 as solid triangles. Figure 6.3.2-17 thus collapses data obtained from three entirely independent sources under different test conditions.

(6) Influence of Angle of Attack

The influence of angle of attack on the radiated acoustic power was examined by tests at angles of attack of 0°, 5°, 10° and 15° at constant Mach numbers. The acoustic contribution of the angle of attack results primarily from its effect on lift and drag forces and on the wake shape and size. The one-third octave band power level spectra at the four angles of attack for a Mach number of 0.4 are shown in Figure 7.3.2-18 for configuration 7, as a typical case.

Similar spectra for all the other configurations were obtained for all the test conditions. In general, it was found that the influence of α^o was small within the 0 - 15 range.

It appears conceivable that the thickness term in equation (6.3.2-5) should be defined as ($t_{max} \cdot \cos \alpha^o + \ell \cdot \sin \alpha^o$) representing the projected frontal thickness of a body when placed at an angle of attack, α^o. This should be an important parameter in the physical wake thickness, and hence the acoustic power level. Overall power levels were calculated assuming $\alpha^o = 0$ (i.e., setting $t_{maxo} \cdot \cos \alpha^o + \ell \cdot \sin \alpha^o = t_{max}$) and were compared with measured OAPWL at $\alpha^o = 0$, 5, 10 and 15. The result shown in Figure 6.3.2-19 indicates that neglecting the influence of α^o in the range of 0° to 15° in the formulation is acceptable. This conclusion is further enhanced by a comparison of OAPWL with the measured data, including the effect of α^o on frontal thickness, shown in Figure 6.3.2-20, indicating calculated values higher than

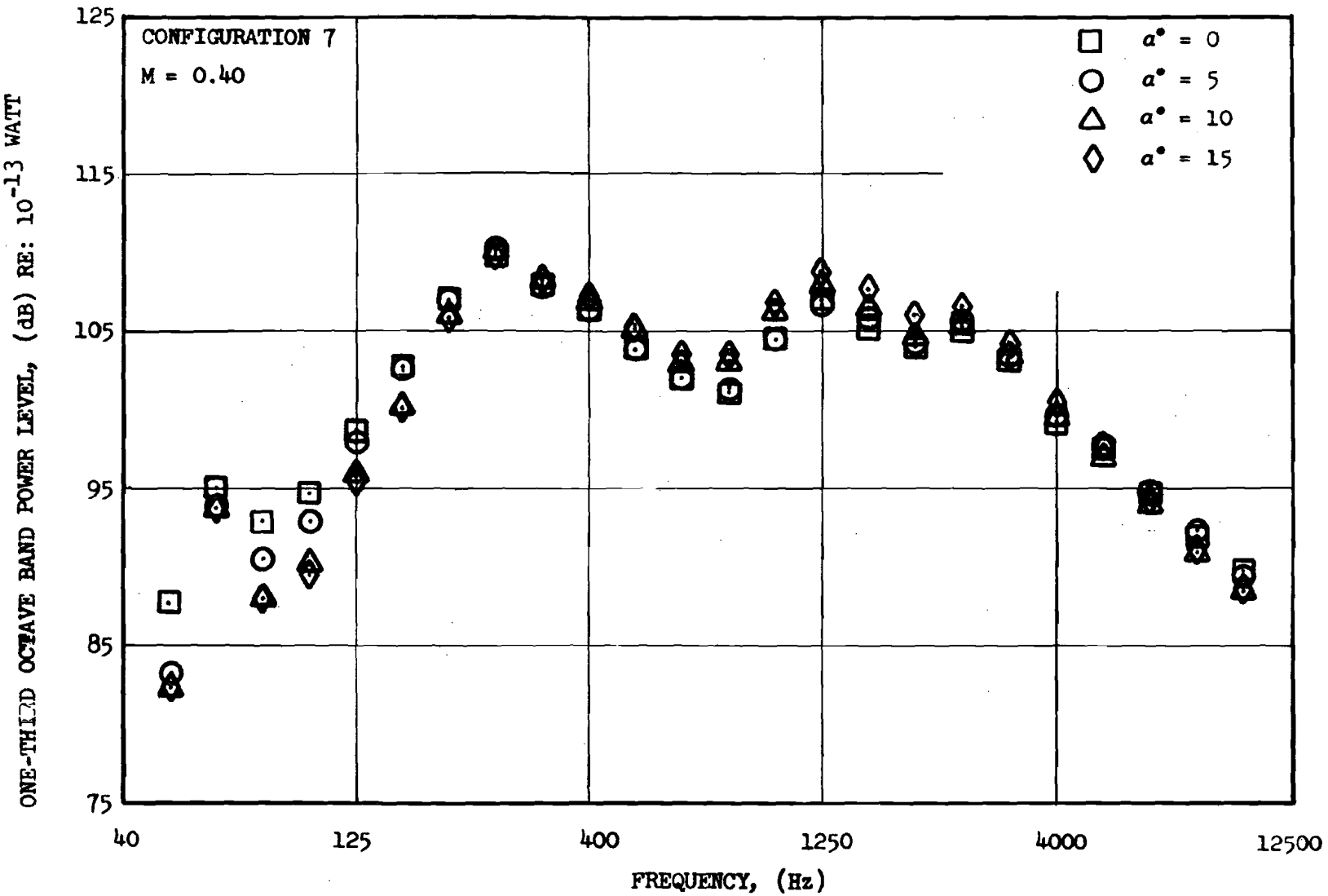

FIGURE 6.3.2-18 VARIATION OF ONE-THIRD OCTAVE BAND POWER LEVEL SPECTRUM WITH ANGLE OF ATTACK; CONFIGURATION 7, M = 0.40 .

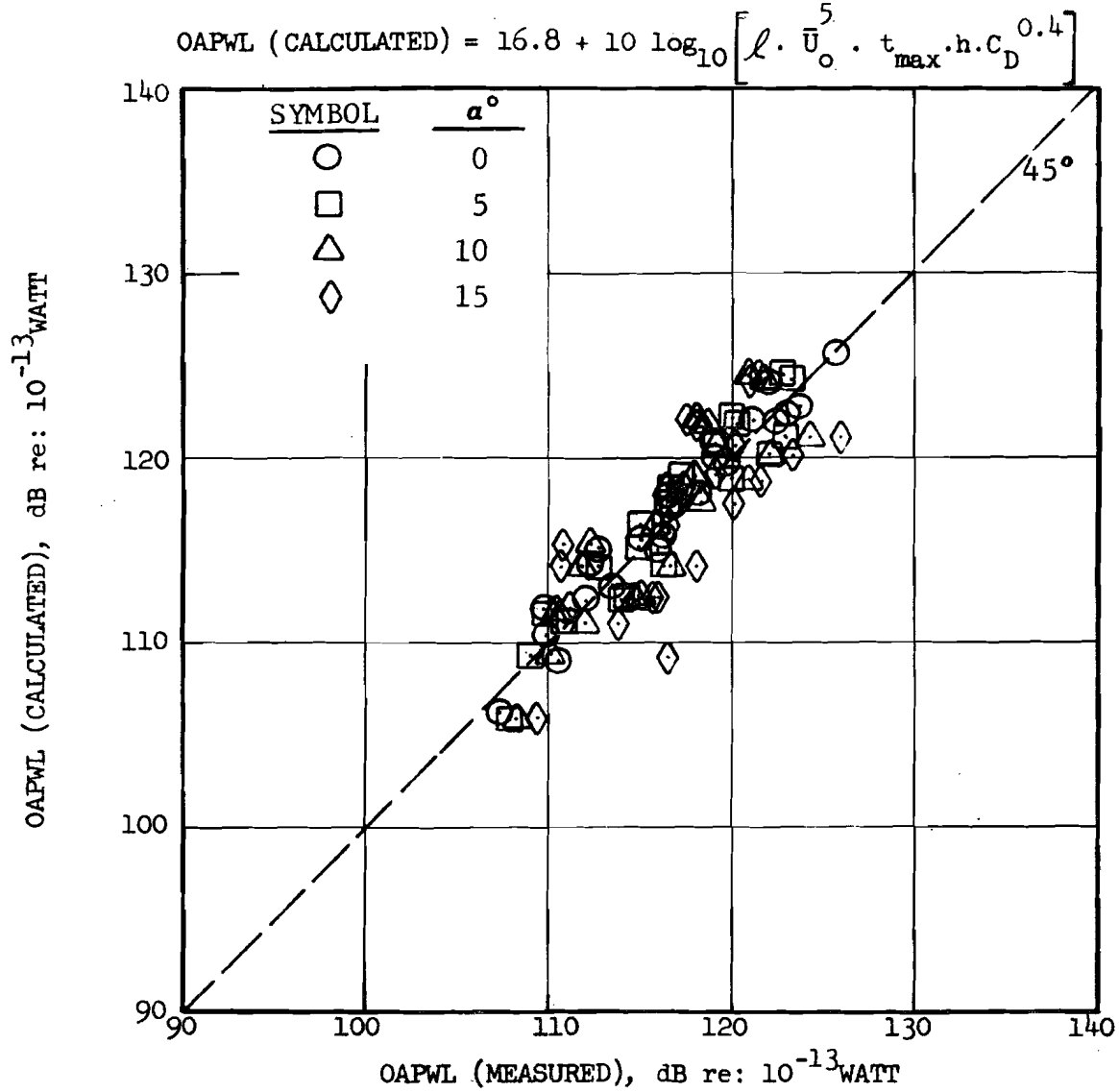

FIGURE 6.3.2-19 COMPARISON BETWEEN CALCULATED AND MEASURED OAPWL. ALL CONFIGURATIONS, M = 0.30, 0.40, 0.45; α° NEGLECTED IN THICKNESS FORMULATION.

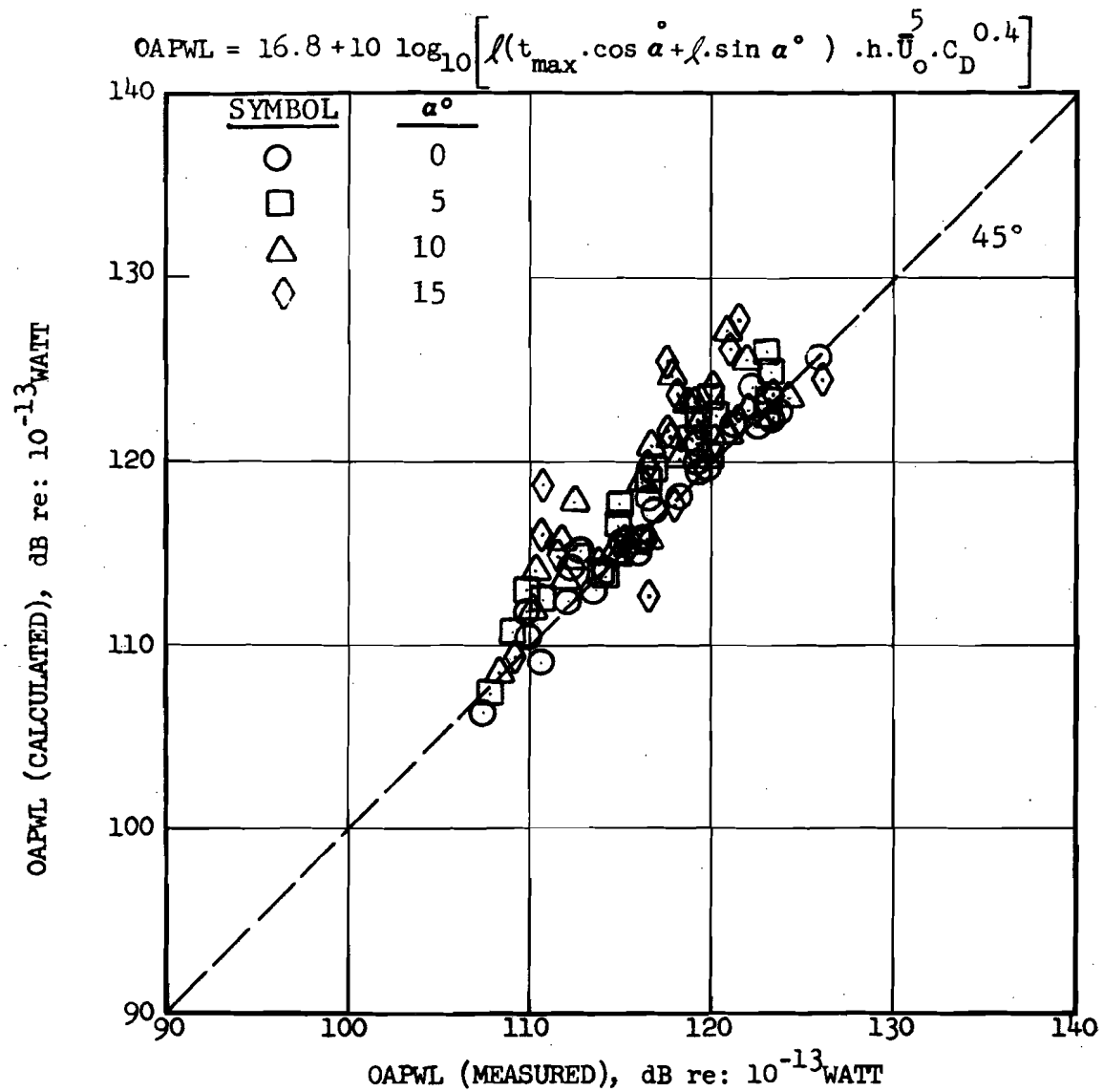

FIGURE 6.3.2-20 COMPARISON BETWEEN CALCULATED AND MEASURED OAPWL. ALL CONFIGURATIONS, M = 0.30, 0.40, 0.45, α^0 INCLUDED IN THICKNESS FORMULATION.

measured values. The C_D value was taken to be the same as that at $\alpha^o = 0$, which is an approximation. Using the higher C_D values applicable at higher angles of attack would tend to close in the band in Figure 6.3.2-19 more and move the band farther away from the 45° line in Figure 6.3.2-20. Hence this approximation is conservative.

(7) Spectral Correlations

The shapes with blunt thick leading edges (Configurations 1-4) exhibited tones with a Strouhal number of ~ 0.2 ($= f\ \delta/\overline{U}_o$) based on maximum thickness, whereas the streamlined shapes (Configurations 5-9) exhibited only broadband spectra. δ represents maximum thickness in inches. A reasonable calculation is still possible however.

Normalization of the one-third octave band power level by defining a normalized power level,

$$PWL_N = PWL_{1/3\ OB} - OAPWL_{calculated}$$

collapsed the spectra (versus frequency) at the three Mach numbers for each configuration individually. Examples of such normalized power level spectra are shown in Figures 6.3.2-21 and 6.3.2-22 for Configurations 6 and 7 respectively. However, such spectra do not account for the changes in the frequency region with geometry and velocity, which are needed to obtain a universal spectrum. Typical normalized spectra obtained by plotting PWL_N versus a Strouhal-type frequency defined by $f^* = f\ \delta/\overline{U}_o$ (where f = frequency, Hz., δ = maximum thickness, inches and $\overline{U}_o$ = mean upstream axial velocity) are shown in Figures 6.3.2-23 and 6.3.2-24 for Configurations 6 and 9 respectively. Normalized spectra like these were obtained for all the configurations. The envelope of such data from all the nine configurations is shown in Figure 6.3.2-25 and an approximate prediction line is drawn to indicate a reasonable model for broadband noise spectral prediction for flow over obstructions. This data is based on tests in the Reynolds number range of 3×10^5 to 1×10^6 based on the chord. Extrapolation to lower Reynolds numbers should be done with caution to account for possible tones from discrete vortex shedding. Blunt shapes (Configurations 1-3) had sharper peaks at the same value of f* as the broadband mean spectrum shown in Figure 6.3.2-25 and the peak value of PWL_N was higher and the spectrum shape narrower.

Comparisons with Hayden's and full scale engine strut noise data show reasonable agreement of the broadband spectrum. However, comparison with the engine strut noise data particularly also showed that a constant multiplier to the f* will allow an extremely close prediction of the broadband spectrum, indicating the desirability of redefining the thickness that should be considered as characteristic.

6.4 SUMMARY

(1) Based on the data obtained in this program, it can be concluded that solid obstructions like struts, pylons, actuators etc. can cause a considerable amount of acoustic radiation when placed in the stream. In the Reynolds

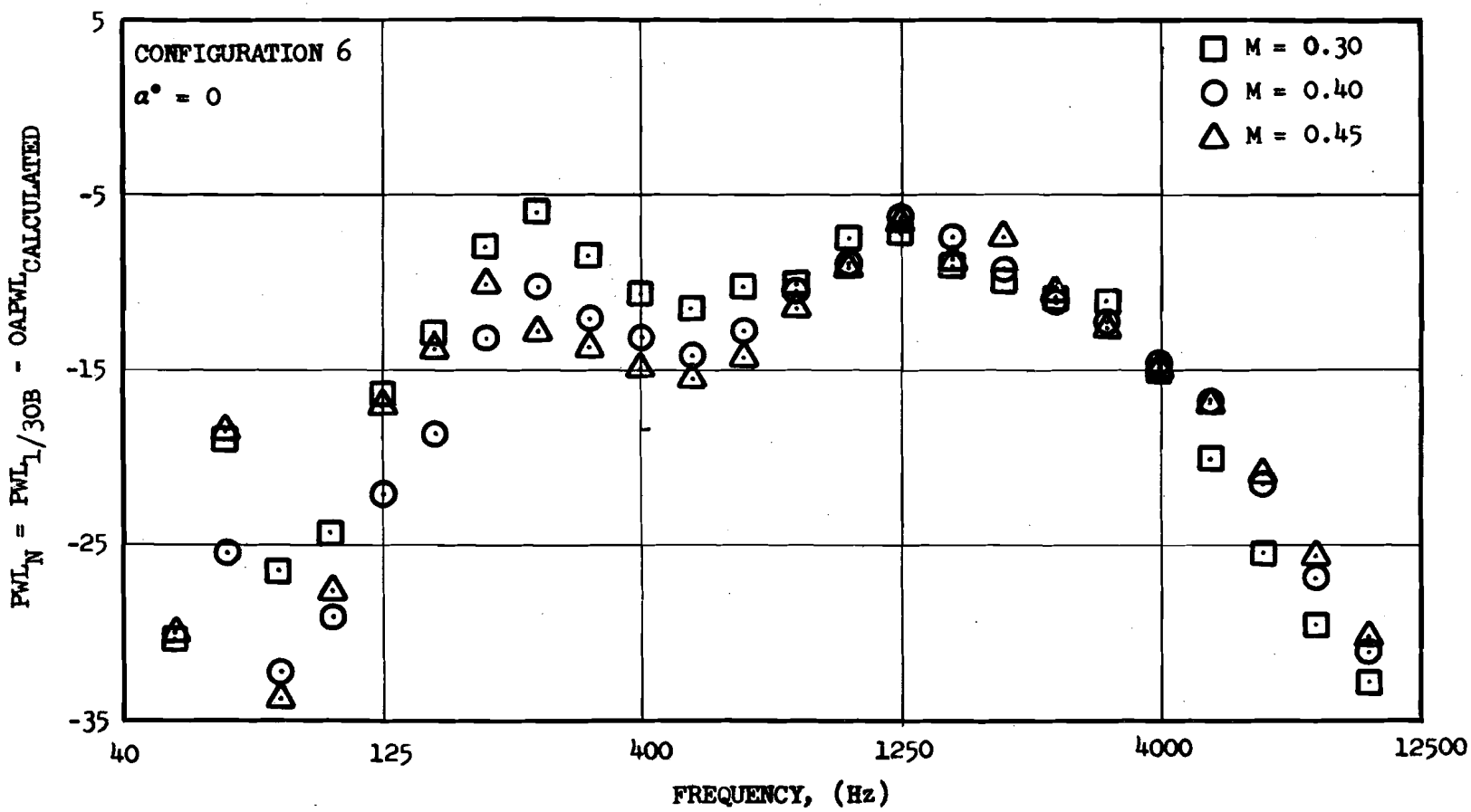

FIGURE 6.3.2-21 NORMALIZED POWER LEVEL vs. FREQUENCY; CONFIGURATION 6, $\alpha^\circ = 0$

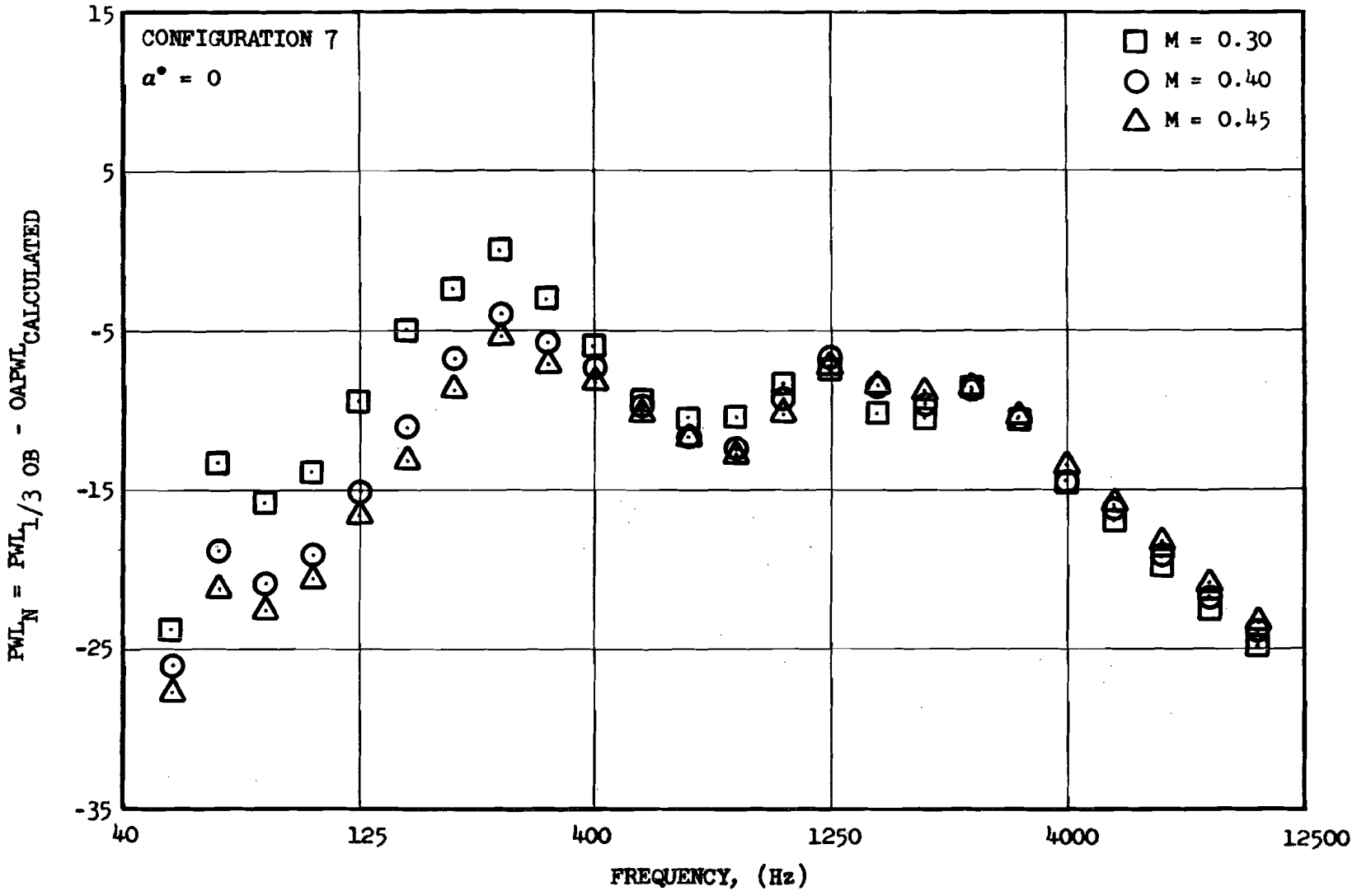

FIGURE 6.3.2-22 NORMALIZED POWER LEVEL vs. FREQUENCY; CONFIGURATION 7, $\alpha^{\circ} = 0$

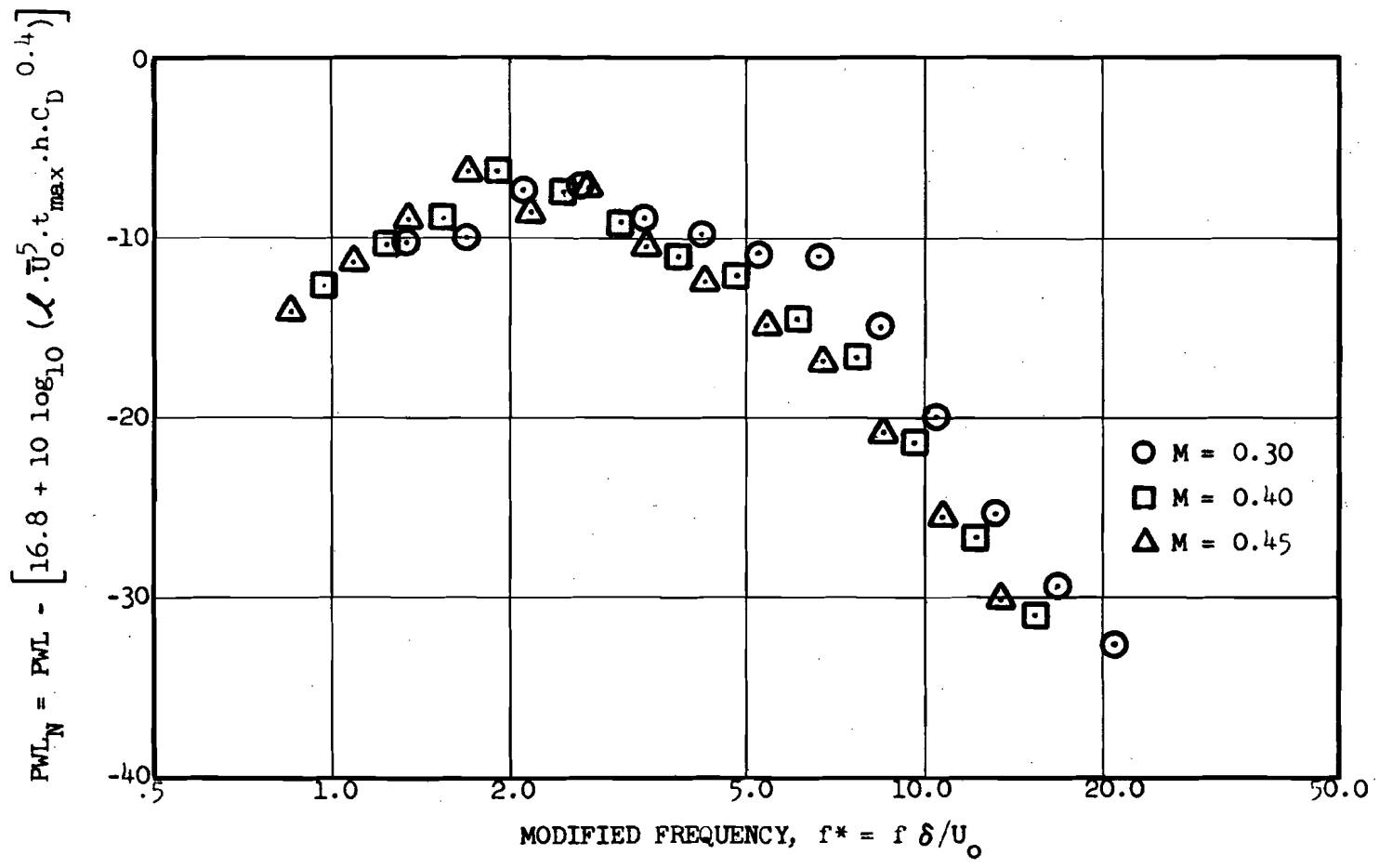

FIGURE 6.3.2-23 NORMALIZED SPECTRUM FOR CONFIGURATION 6, $\alpha^0 = 0$, M = 0.30, M = 0.40, M = 0.45.

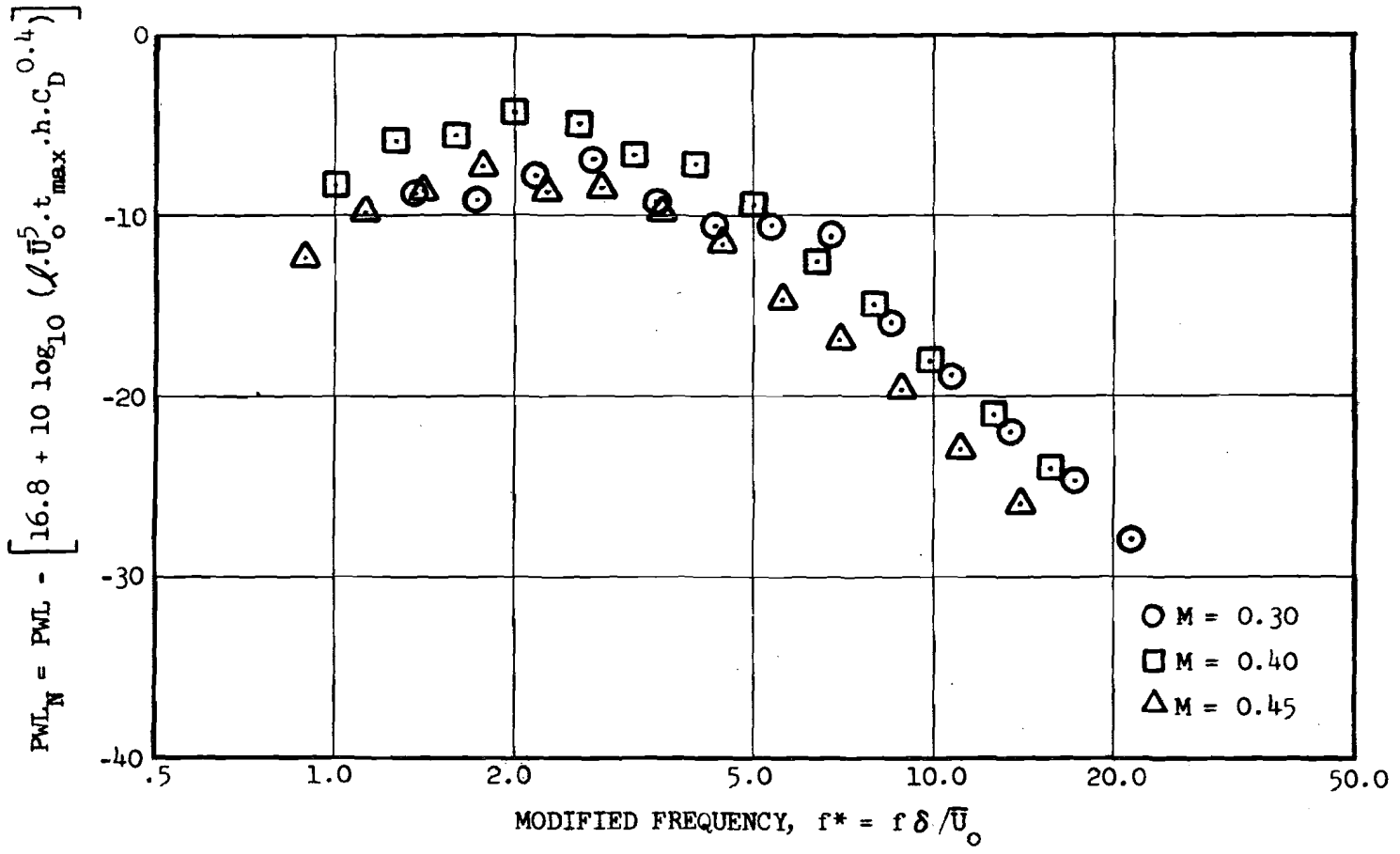

FIGURE 6.3.2-24 NORMALIZED SPECTRUM FOR CONFIGURATION 9, $\alpha^{\circ} = 0$, M = 0.30, M = 0.40, 0.45.

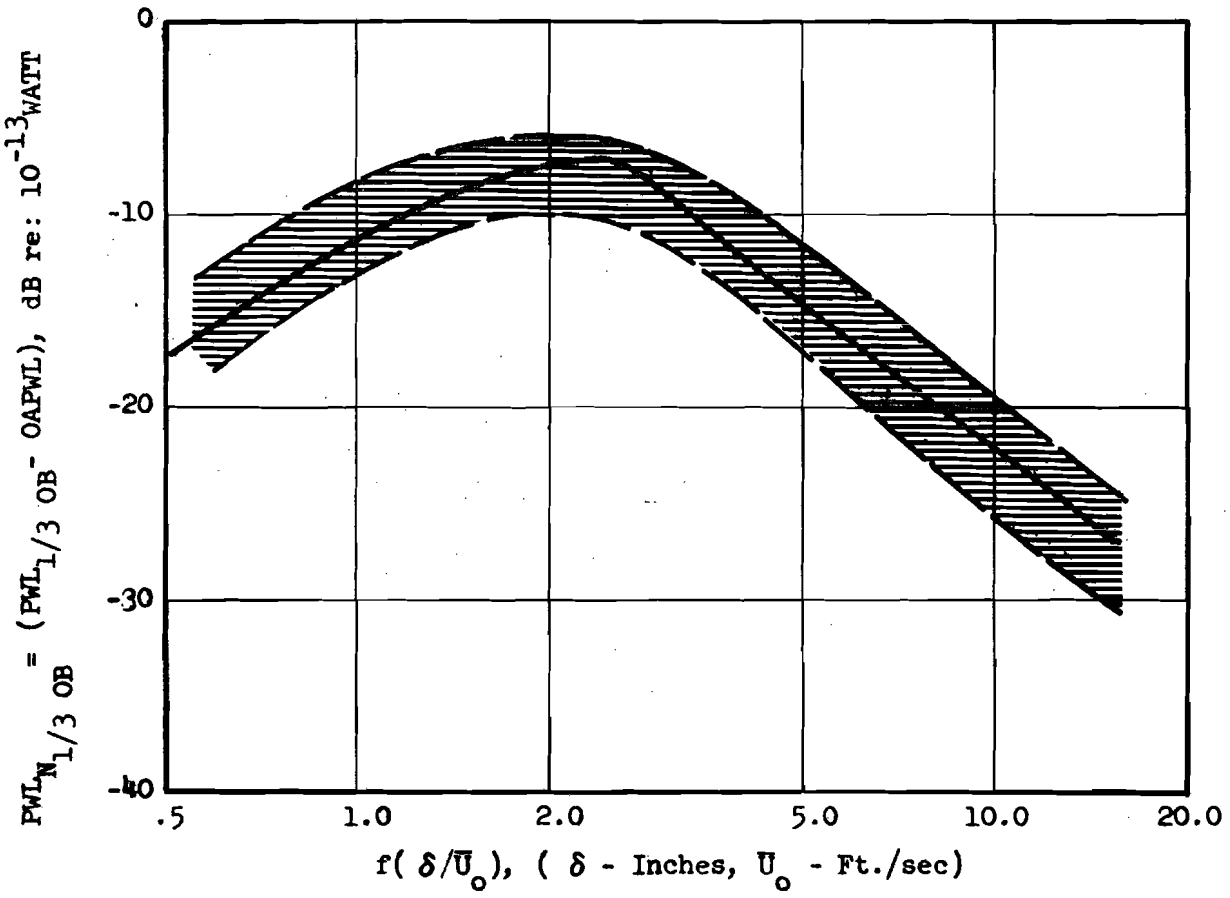

FIGURE 6.3.2-25 NORMALIZED SPECTRUM OF OBSTRUCTION NOISE.

number range investigated (3×10^5 to 1×10^6), blunt bodies produced tones tracking with flow velocity together with considerable broadband radiation around the tone frequency. Streamlining the bodies retaining the same maximum dimensions (i.e. maximum thickness and chord) eliminated the tones.

(2) Broadband acoustic radiation due to flow over obstructions is generally a result of fluctuating forces of random nature acting on the body. The forces are generated by one or more of the following factors: inflow turbulence, turbulent boundary layer and random vortices shed at the trailing edge. When the vortex shedding is discrete, tones are observed at the discrete frequency. The present study indicates that streamlining the body eliminates discrete tones and also reduces accompanying broadband radiation.

(3) Among the configurations tested, both symmetrical NACA airfoils and double circular arc airfoil showed considerable noise reduction compared to elliptical, circular cylinder and blunt flat plates. Since a double-circular arc airfoil section is considerably more economical to fabricate than a symmetrical NACA airfoil section, the double-circular arc airfoil section appears to be the best for flow discontinuities like struts etc. from an acoustic/economic standpoint.

(4) An empirical scheme has been formulated to predict the overall power level and one-third octave band spectra for the acoustic radiation due to smooth (upstream) flow over solid obstructions.

(a) $$\text{OAPWL} = 16.8 + 10 \log_{10} (\ell . t_{max} . h . \overline{U}_o^5) + 4 \log_{10} C_D \quad \text{dB re: } 10^{-13} \text{ Watt}$$

where

ℓ = chord, feet

h = span, feet

t_{max} = maximum thickness, feet

$\overline{U}_o$ = upstream mean axial velocity, feet/sec

C_D = Profile drag coefficient

(b) The normalized spectrum presented in Figure 6.3.2-25 may be used to obtain the 1/3 OB PWL vs frequency spectrum.

(5) Since velocity upstream of the struts is the principal contributor to the radiated acoustic power, noise reduction can be achieved by locating the unavoidable obstructions at low velocity sections of the flowpath whenever feasible.

(6) Noise reduction can be achieved by minimizing the physical dimensions of the obstructions.

(7) The results are based on data obtained in a narrow range of Reynolds number (3×10^5 to 1×10^6). Uniform and low-turbulence flow conditions

prevailed in the tests, with the strut being placed essentially in the potential core region of a free jet. The blockage to the flow was small, and typical of blockage due to flow obstructions in the fan and core regions. The margin of error may be high if the spectral prediction is used in cases where sharp tones are anticipated.

References

6.2.1-1 Beranek, Leo L., Noise and Vibration Control, McGraw Hill, 1971.

6.2.1-2 USA Standard, Method for the Physical Measurement of Sound, USAS S1.2, 1962.

6.3.2-1 Goett, Harry J., "Experimental Investigation of the Momentum Method for Determining Profile Drag", NACA Report No. 660, 1936.

6.3.2-2 Hayden, Richard E., "Noise from Interaction of Flow with Rigid Surfaces: A Review of Current Status of Prediction Techniques", Bolt, Beranek and Newman Report No. 2276.

6.3.2-3 Hersh, Alan S. and Hayden, Richard E., "Aerodynamic Sound Radiation from Lifting Surfaces with and without Leading-Edge Serrations", NASA CR-114370.

6.3.2-4 Private Communication from K.R. Bilwakesh to M.J. Benzakein, dated January 16, 1973.

6.3.2-5 Hoerner, Sighard F., Fluid Dynamic Drag, Published by Author, 1965.

SECTION 7.0

CASING RADIATION

7.1 BACKGROUND

When engine inlet and exhaust noise is sufficiently suppressed, engine noise transmission through the casing may become important. It has been shown, for example, that wrapping an engine casing (fully suppressed NASA Quiet Engine "A") with six-inch thick polyurethane foam will reduce casing radiation by 5 dB (see Volume I, Section 2.2.6). The objectives of the casing radiation investigation were to develop quantitative definitions of the mechanisms of casing noise radiation and suppression.

7.2 CASING RADIATION SOURCES

Casing noise radiation, in general, is due to the following three sources:

1. Compressor
2. Combustor
3. Turbine

Therefore the initial investigation was directed toward the analysis of an extensive set of data taken on a J79-15 engine. The engine was tested with an open core nozzle (to reduce jet noise) and large inlet and exhaust suppressors (see Figure 7.2-1).

Figure 7.2-2 shows the locations of 3 casing microphones [(5 inches (12.7 cm) from the engine)] and 32 nearfield microphones. Casing microphone axial locations were as follows:

#51 Compressor 10th stage
#52 Mid-point of combustor casing
#53 Turbine third stage

The PWL spectra for the casing microphones are shown in Figure 7.2-3. The power calculation is based on the SPL measured by the microphone and a cylindrical area. The area being determined by a radius from the engine centerline and a width of the component (compressor, combustor, or turbine) closest to the individual microphone. Note that the highest PWL comes from microphone #53 (located at turbine third stage). The OAPWL measured at these three microphones were:

Microphone Location	OAPWL
#51	122 dB
#52	133 dB
#53	141 dB

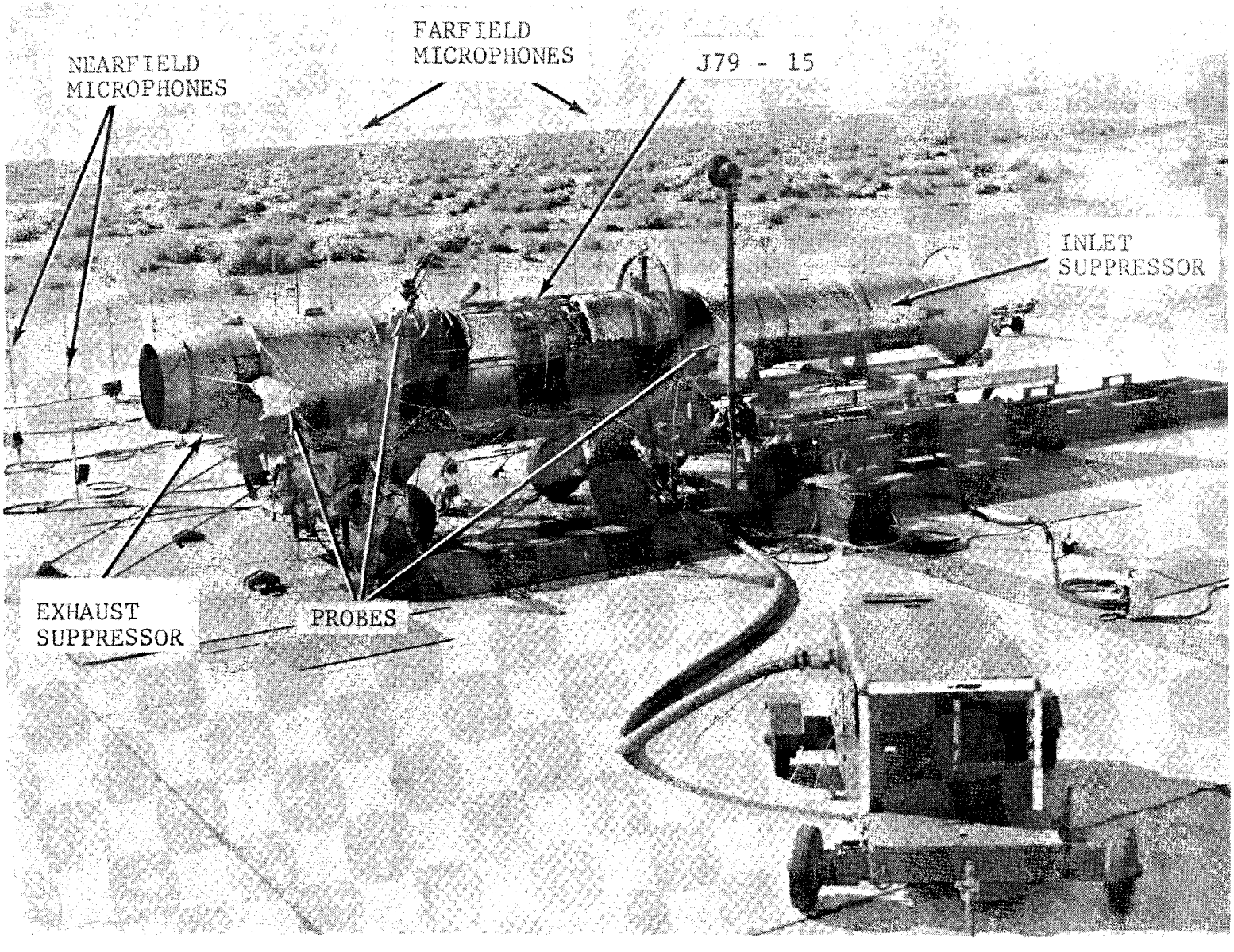

FIGURE 7.2 - 1 J79-15 TURBOMACHINERY NOISE TEST - EDWARDS AFB

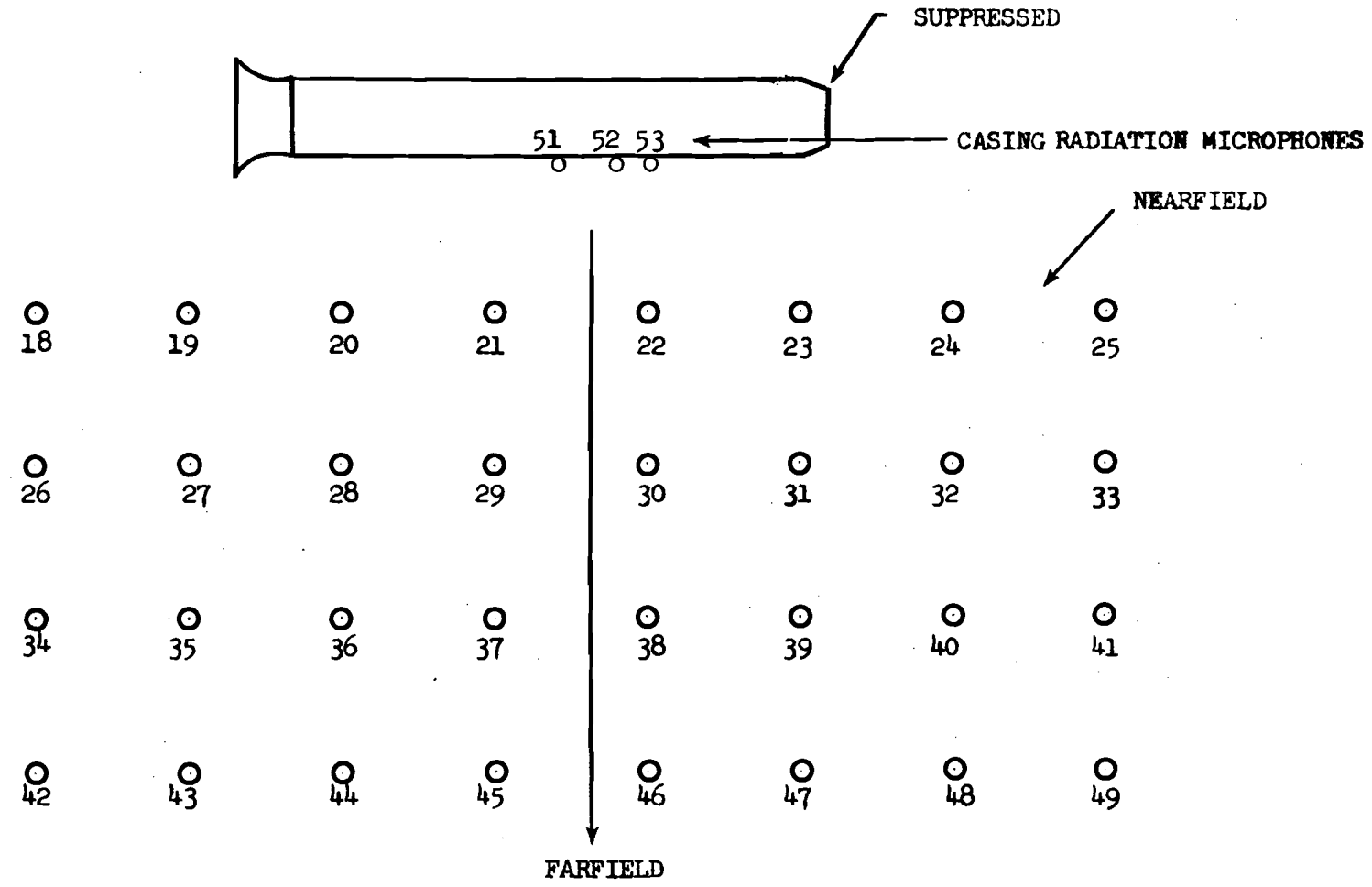

FIGURE 7.2-2 NEARFIELD MICROPHONE ARRANGEMENT FOR J79 TESTS.

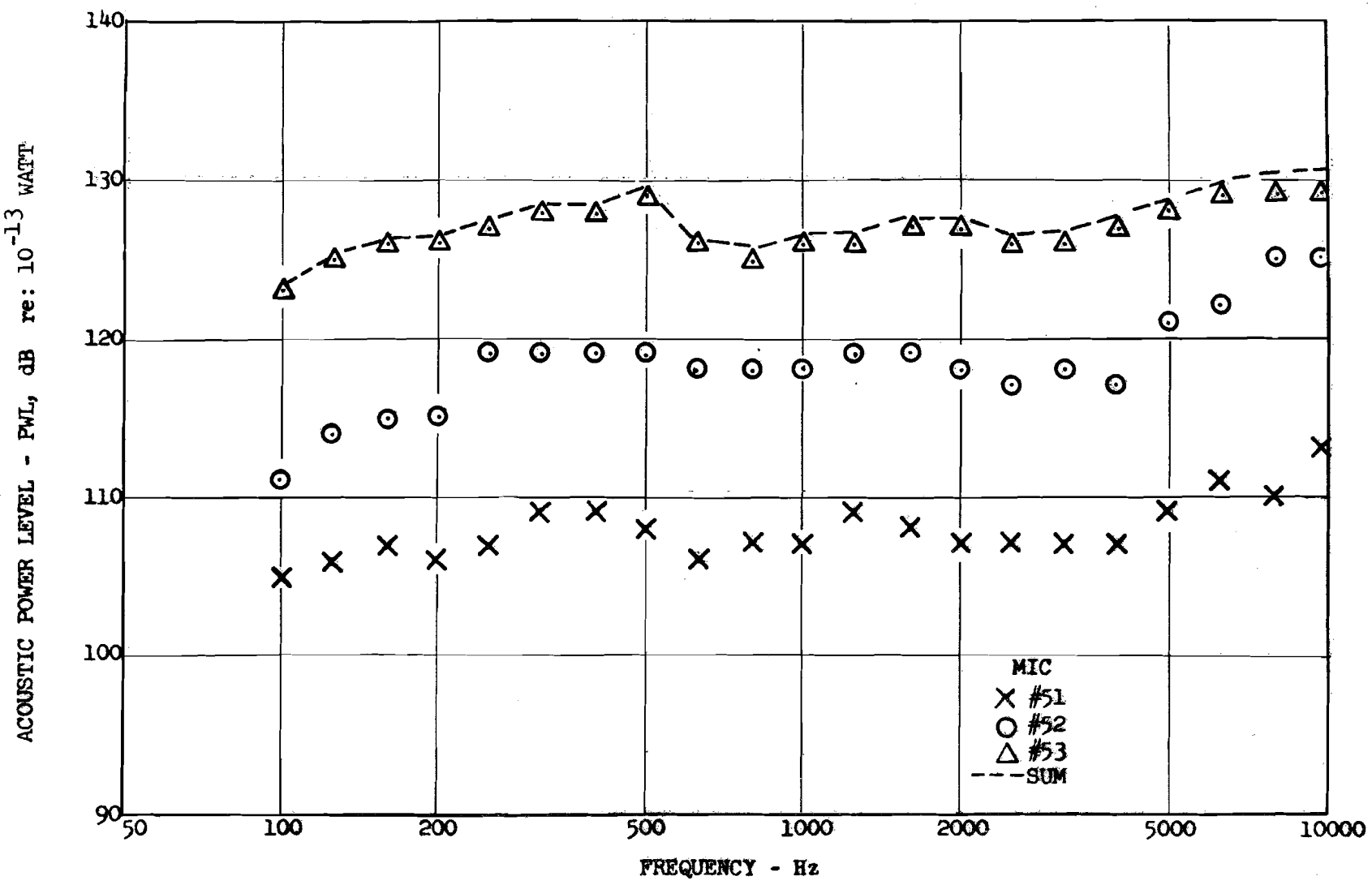

FIGURE 7.2-3 POWER SPECTRAL DISTRIBUTION FOR CASING RADIATION.

The nearfield data was also examined to determine the sources of casing radiation by establishing contours of tone SPL's.

Figure 7.2-4 shows SPL contours for the compressor stage 10 BPF tone. The maximum SPL is emanating from the location #52 (mid-point of combustor), instead of the location #51 (compressor stage 10). Actually, all of the compressor aft stage tones are emanating from the location #52. This may be due to the compressor casing being thicker than the combustor casing.

The origin of turbine noise can be traced in a similar manner. Figure 7.2-5 shows SPL contours of the turbine stage 3 tone. It is emanating from the location #53 (turbine third stage). This confirms that the turbine tone is transmitted through the casing and radiates from the surface. The thickness of the casing is .17 inches and the attenuation at 10 KHz is 71 dB but the tone is still clearly indicated in the farfield.

7.3 REDUCTION OF CASING RADIATED NOISE

There are several classical approaches to reducing noise radiation from vibrating structures, all of which reduce the panel motion amplitude or decrease the spatial correlation. These approaches are applicable to panel radiation produced by structure borne vibration, internal acoustic loads, or aerodynamically induced fluctuating pressures.

Addition of mass and/or stiffness can be used to reduce the panel radiation by changing the modal response patterns of the structure. The analysis of the response of multi-modal structures is complex and the addition of mass/stiffness elements can aggravate a problem rather than reduce it. These methods will be evaluated analytically to scope the potential casing noise reduction. This approach is most useful where a forcing input is centered at one frequency which coincides with one of the normal modes of the structure.

In light of the above, casing radiation reduction and control can be divided into the following five (5) categories :

1. Casing thickness and material
2. Acoustic barrier
3. Critical frequency and its damping
4. Ring frequency effects
5. Adjustment and relocation of struts for structure borne noise.

The noise source PWL control is a separate subject and it is discussed under each noise component (E.G. compressor, combustor and turbine).

1. Casing Thickness and Material

A transmission coefficient, T, may be defined as the ratio of a transmitted acoustic power to the incident acoustic power. For a given angle of plane-wave incidence, it can be shown to be: (Ref 7.3-1)

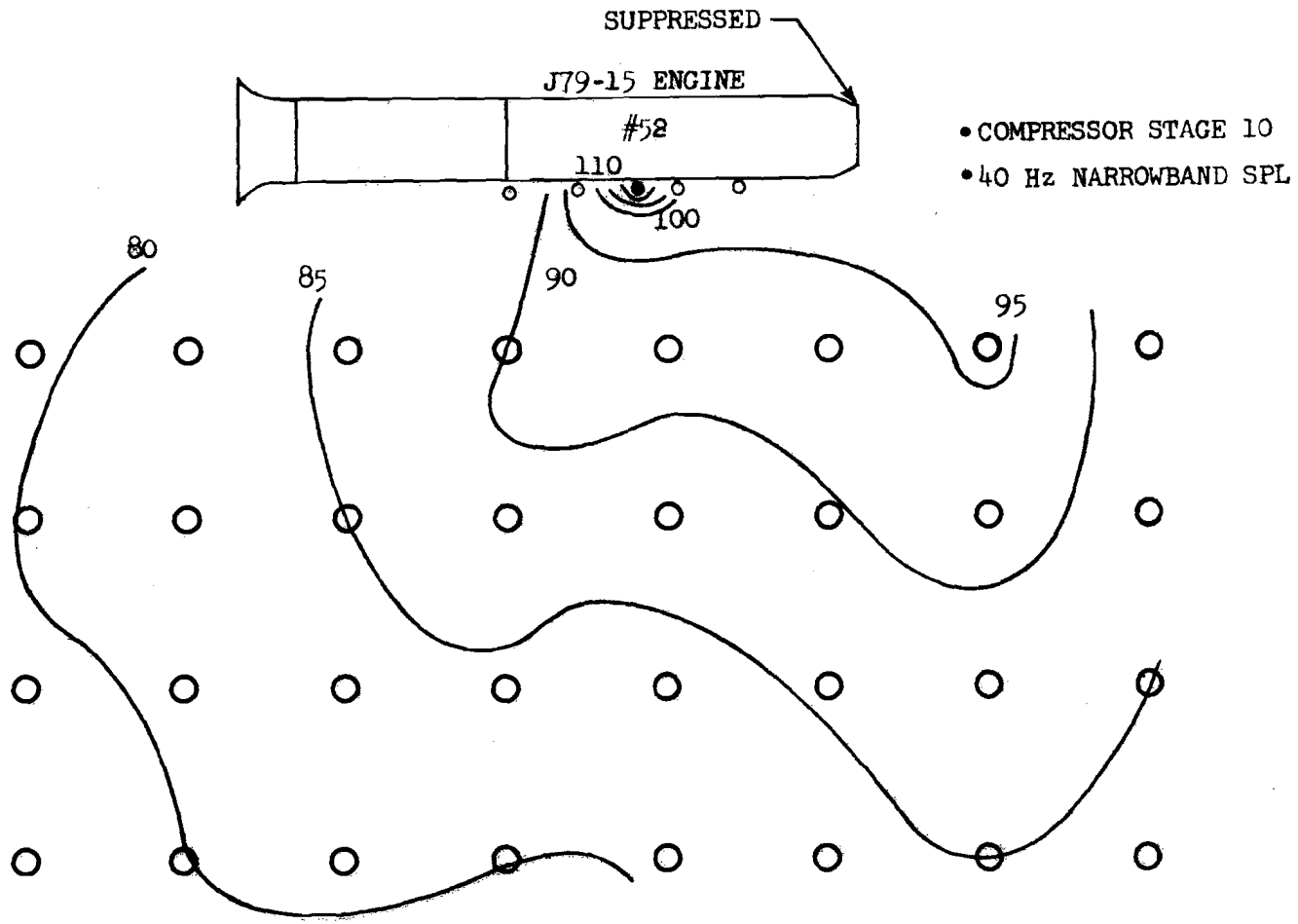

FIGURE 7.2-4 SPL CONTOURS - NEARFIELD ARRAY.

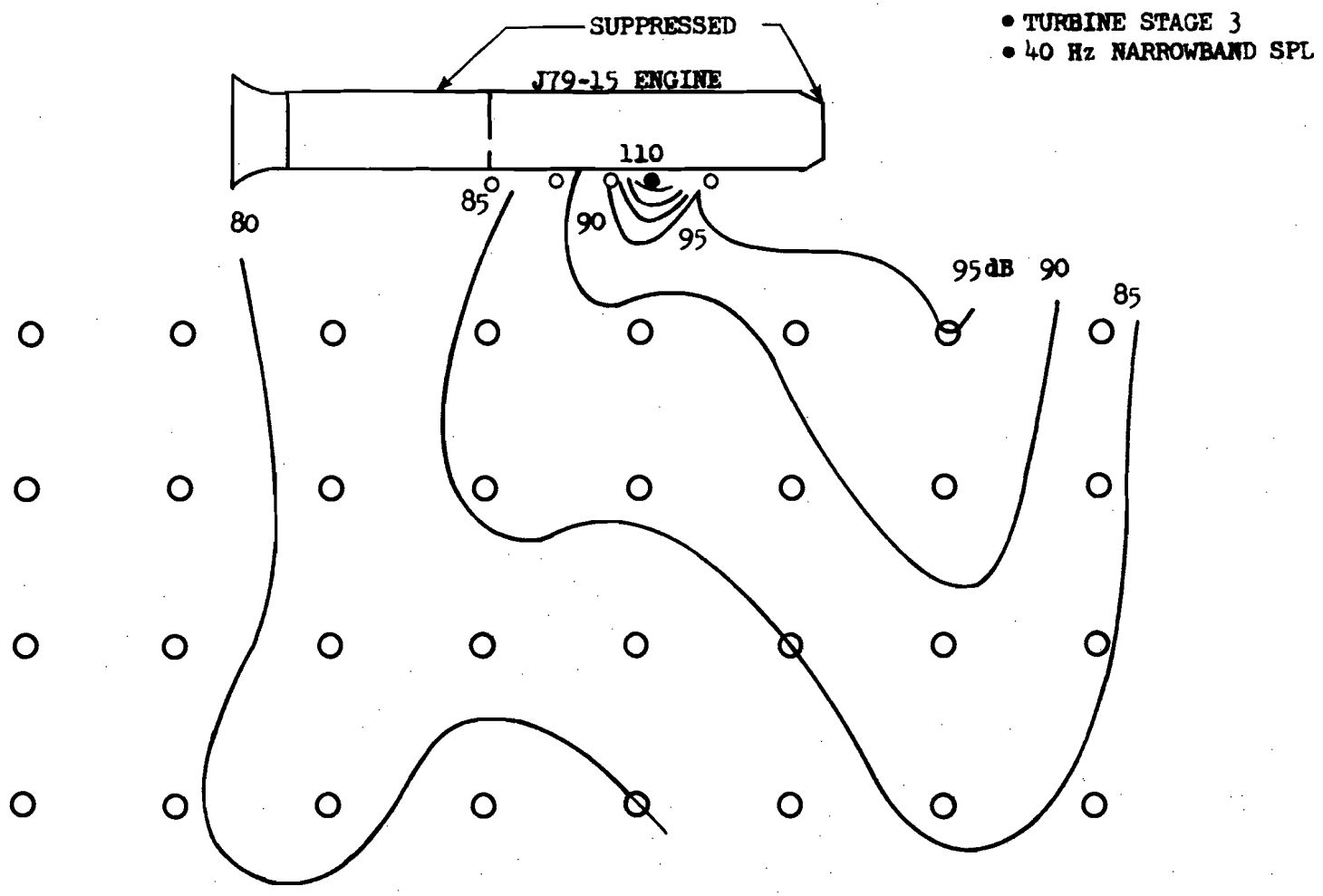

FIGURE 7.2-5 SPL CONTOURS - NEARFIELD ARRAY.

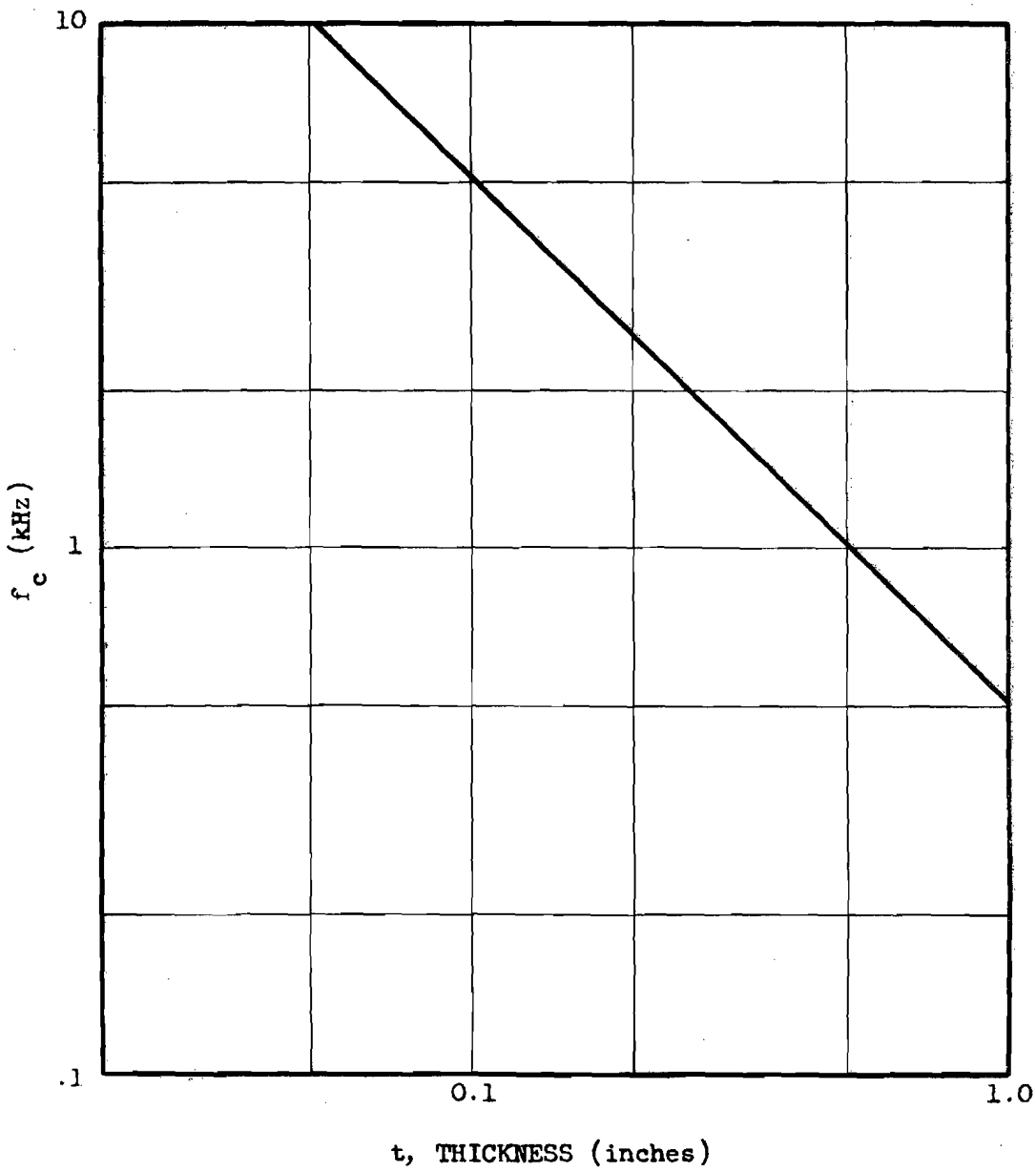

FIGURE 7.3-1 CRITICAL FREQUENCY vs. MATERIAL THICKNESS.

$$T(\theta) = \frac{I_t}{I_i}$$

$$= \left\{ \left[1 + \eta \left(\frac{\omega \rho_s}{2\rho c} \cos \theta \right) \left(\frac{\omega^2 \beta}{c^4 \rho_s} \sin^4 \theta \right) \right]^2 \right.$$

$$\left. + \left[\left(\frac{\omega \rho_s}{2\rho c} \cos \theta \right) \left(1 \right) - \left(\frac{\omega^2 B}{c^4 \rho_s} \sin^4 \theta \right) \right]^2 \right\}^{-1} \qquad (7.3\text{-}1)$$

where

$T(\theta)$ = transmission coefficient

I = sound intensity, Watts/m^2

ω = $2\pi f$

η = composite plate loss factor

ρ_s = ρ_m/t = plate surface density, kg/m^2

ρ_m = density of the plate material kg/m^3

t = thickness of a plate, m

ρ = density of air, kg/m^3

c = speed of sound in air, m/sec

θ = angle between the normal to the plate and the wave

B = plate bending stiffness per unit width, N-m

and the transmission loss R is defined as:

$$R = 10 \text{ LOG } \frac{1}{T} \text{ dB} \qquad (7.3\text{-}2)$$

and

$$R(\theta) \approx 10 \text{ LOG } \left[1 + \left(\frac{\omega \rho_s}{2\rho c} \cos \theta \right)^2 \right] \qquad (7.3\text{-}3)$$

where ω = $2\pi f$

ρ_s = surface density of casing material

2. <u>Acoustic Barrier</u>

The formula (Ref. 7.3-1) for the excess attenuation of a rigid straight nonporous barrier with a large mass, for sound incident from a point source is:

$$TL = 20 \text{ LOG } \frac{\sqrt{2\pi N}}{\tanh \sqrt{2\pi N}} + 5 \text{ dB} \qquad (7.3\text{-}4)$$

N is the Fresnel number:

$$N = \pm \frac{2}{\lambda} (A + B - D) \qquad (7.3\text{-}5)$$

where λ = wavelength of sound, m

D = straight line distance between source and receiver, m

A+B = shortest path length travel over the wall between source and receiver, m

In most cases A+B is almost equal to D, then TL is about 5 to 6 dB.

3. Critical Frequency

At critical frequency, the casing material becomes an efficient transmitter of the sound at that frequency.

The critical frequency f_c is (Ref. 7.3-1)

$$f_c = \frac{c^2}{2\pi}\sqrt{\frac{\rho_s}{B}} = \frac{c^2}{1.8t}\sqrt{\frac{\rho_m}{E}} = \frac{c_2}{1.8\ C_L\ t} \qquad (7.3\text{-}6)$$

where

C_L = longitudinal wave speed, m/sec

Figure 7.3-1 shows critical frequency as a function of material (steel) thickness. A steel plate of .25 inch thickness can transmit a 2 KHZ tone efficiently.

4. Ring Frequency Effect

The radiative properties of a structure consisting of flat or curved panels can be described in terms of the radiation efficiency σ. The overall radiation efficiency $\bar{\sigma}$ of the panel in a frequency band containing several resonant modes is obtained from averages and sums:

$$\bar{\sigma}_i = \sum_j \frac{\sigma_{ij}}{n_i} \qquad (7.3\text{-}7)$$

$$\sigma = \sum_{i=f,s,p} \frac{n_i\ \bar{\sigma}_i}{n_{tot}}$$

where f: acoustically fast mode

s: strip mode

p: piston mode

The existance of f, s and p modes is dependent on the magnitude of bending-wave speed C_b and phase speeds C_x and C_y, of the acoustic wave in the directions of the panel edges. Prevailing conditions for existence of the above modes are:

f mode: $C_b > C$

s mode: C_x or $C_y > C$ $\qquad C_b > C$

p mode: C_x and $C_y < C$

where $$C_b = \frac{\omega^2 B}{\rho_s}^{1/4}$$

and B = bending stiffness, N/m.

The analysis for a cyclindrical shell requires two distinct modifications from that for a flat panel. They are due to:

1. geometry of the cylinder

2. effect of curvature on the structural vibration

Assuming a "equivalent plate" model, the piston modes and axial strip modes almost vanish below the critical frequency and radiate only at a discontinuity, which is non-existent in the case of a cylinder. The radiation efficiency of the equivalent plate may be written as

$$\sigma = \frac{\eta_{cs}\,\bar{\sigma}_{cs}}{\eta_{tot}} \qquad (7.3\text{-}8)$$

where η_{cs}: number of circumferential strip modes

$\bar{\sigma}_{cs}$: average modal radiation efficiency

It has been shown that the curvature tends to increase the flexural-wave speeds (Reference 7.3-2). This increase causes a corresponding increase in resonance frequencies of the cylinder. For the equivalent plate, the resonance frequencies are governed by the equation

$$\nu^2 = \beta^2\,\alpha^4\,k^4 \qquad (7.3\text{-}9)$$

while those of the cylindrical shell are governed by

$$\nu^2 = \beta^2 \alpha^2 k^4 = (1 - \mu^2) \left(\frac{k_y}{k} \right)^4 \qquad (7.3\text{-}10)$$

where

a = radius of the cylinder, m

k = axial wave number, m^{-1}

μ = Poisson's ratio

$\beta = \dfrac{h}{[2(3a)^{1/2}]}$

h = shell plate thickness, m

The curvature effects are seen in the term $(1-\mu^2)\ (k_y/k)^4$ of equation (7.3-10).

Due to the existence of this term, when $f<f_r$ as k_x diminishes k_y diminishes. However, the modal vibration fields of the equivalent plate and the cylindrical shell are approximately the same for $f>f_r$.

Since the radiation efficiency of an acoustically fast mode is usually very much larger than that of the corresponding circumferential-strip mode, a large increase in the radiation efficiency is expected as a result of the curvature.

For the above conditions,

$$\sigma = \frac{\eta_f}{\eta_{tot}}$$

where η_f: number of modes in AFM (acoustically fast)

η_{tot}: total modes

By using equations (7.3-8 and 7.3-11), Figure (7.3-2) was plotted (Reference 7.3-3). This is based on a cylinder with the following dimensions.

D = 36 in

l = 24 in

h = 1/8 in

The decrease in σ at and below 700 Hz occurs because theoretically no radiation modes occur below this frequency.

It is clear from the Figure 7.3-2 that σ increases at f_c (critical frequency) and f_r (ring frequency).

In the following paragraphs, computations of f_r and f_c center frequency for a typical casing material (steel) was made to determine the acoustically transparent region of engine casing.

Figure 7.3-3 was plotted to examine the f_r. Any engine cylindrical section whose radius is between 6 to 14 inches has a f_r between 2 to 5 KHz where NOY weighting is large. It is also noted that the larger engine casing can transmit low frequency noise efficiently.

Ring frequency f_r is:

$$f_r = C_L/2\pi R \approx 1.14 \times 10^6/R$$

where f_r = ring frequency, Hz

C_L = longitudinal wave velocity, m/sec

R = radius of the pipe, m

As an example the above precedures were applied to Quiet Engine "A". The ring frequency is 2.168 kHz. Therefore any noise below this frequency should have excess attenuation of about 10 dB.

The compressor casing has attenuation of 52 dB at kHz. The combustor casing attenuation is 47 dB and the turbine casing attenuation is 54 dB at 1 kHz.

4. <u>Adjustment and Relocation of Struts, etc., for Structure Borne Noise</u>

One of the most effective methods to trace structure borne noise is to use coherence function techniques (Ref. 7.3-4).

Coherence function (γ^2) is:

$$\gamma^2 = \frac{(CSD_{xy})^2}{(PSD_x)(PSD_y)} \qquad (7.3\text{-}13)$$

where PSD_x: power spectral density of input (x)

PSD_y: power spectral density of output (y)

CSD_{xy}: cross spectral density of x and y

In the equation 7.3-13, it should be noted that the value of γ^2 varies

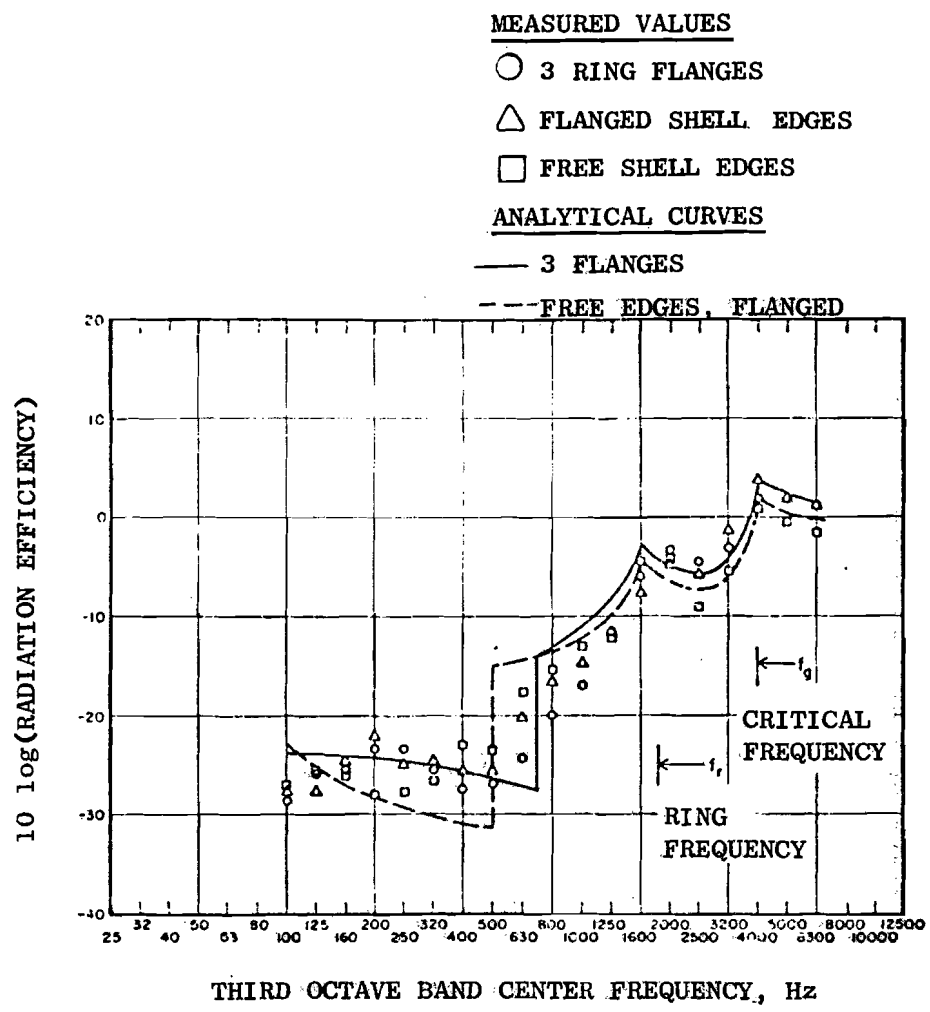

FIGURE 7.3-2 EFFECT OF RING FREQUENCY AND CRITICAL FREQUENCY ON TRANSMISSION LOSS THROUGH CYLINDRICAL SHELLS (REFERENCE 7.3-3).

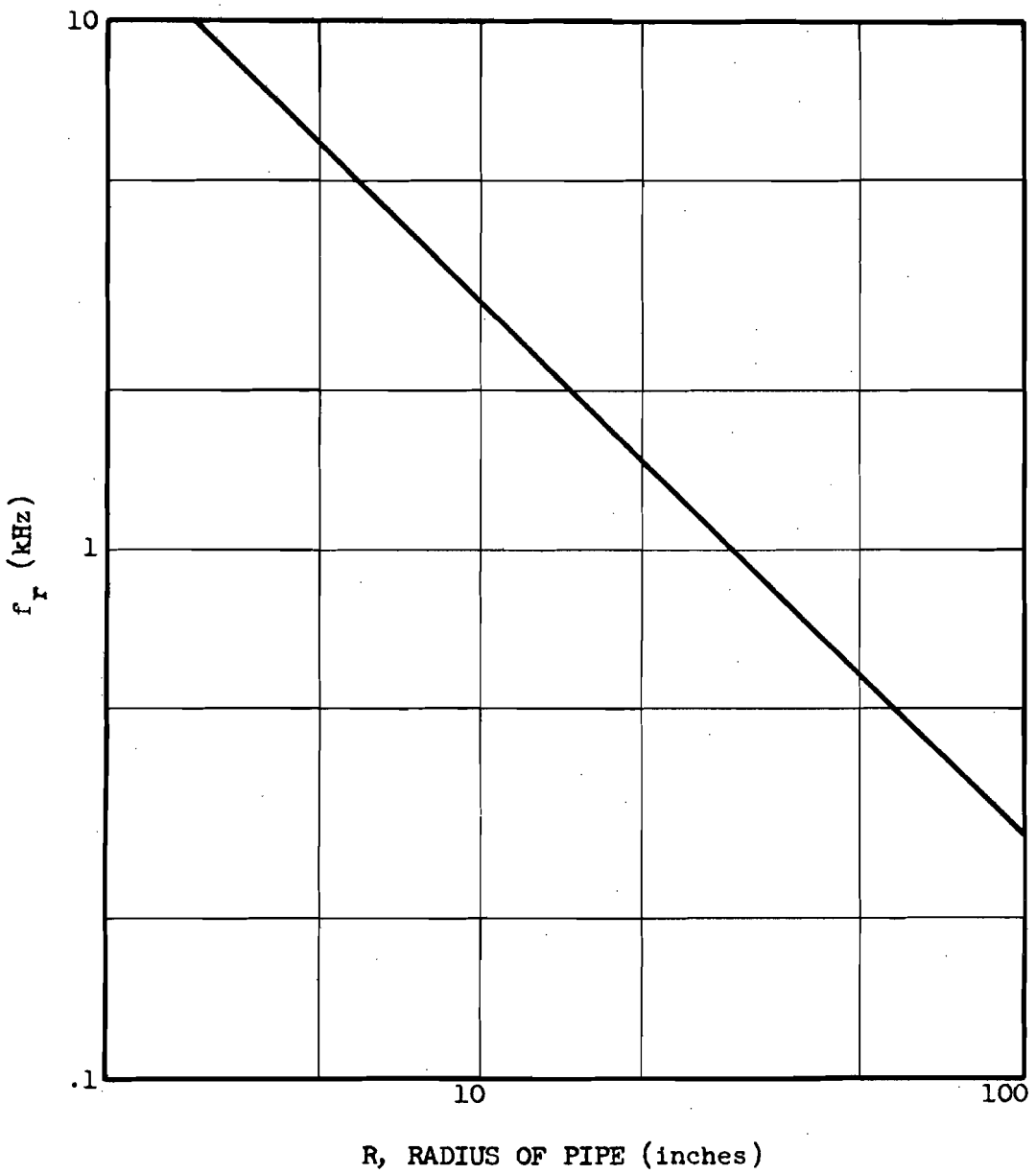

FIGURE 7.3-3 RING FREQUENCY FOR CYLINDRICAL SHELL.

between 0 and 1. When γ^2 is one, the input (x) and the output (y) are 100% coherent, indicating that all the acoustic energy arriving at y is due to the noise generated at x. Thus comparison of the γ^2's between an observer (e.g., farfield microphones) and various source points at a given frequency will give the magnitude of noise contribution from each noise source. An example of such a situation is illustrated in Figure 7.3-4. Ordinary and partial coherence function calculations were used to identify a 147 HX noise on a marine engine test installation.

The notation M at the top of the figure is the microphone in the test room. Numbers 1, 2, 3, and 4 are accelerometers mounted on the following locations.

1. water break base

2. water break floor

3. engine module floor

4. engine module compartment

It is evident from the partial coherence measurements (γ_p^2), a large amount of noise at 147 HZ is transmitted to the engine module floor from the engine module compartment.

From the above observations, it is suggested that the 147 HZ noise is not transmitted to the floor through the water brake base (i.e., γ_p^2 = .0437). Simultaneous high coherence between engine floor (3), engine compartment (4) and the room microphone indicates that the 147 HZ noise is transmitted from the engine compartment to the floor through acoustic absorber (A) and reradiating from the floor to the room microphone.

The fix here was to make the acoustic/vibration absorber (A) resistant to the transmission of 147 HZ vibration.

7.4 SUMMARY

As has been noted, casing radiation is not a noise source in the sense of the other core engine noise sources. However, the salient engine characteristics which effect casing radiation have been identified and methods for determining casing attenuation (or lack of it) presented. In Volume III (Phase IV, Development of Prediction Techniques) this information will be used to develop a core noise casing radiation prediction method.

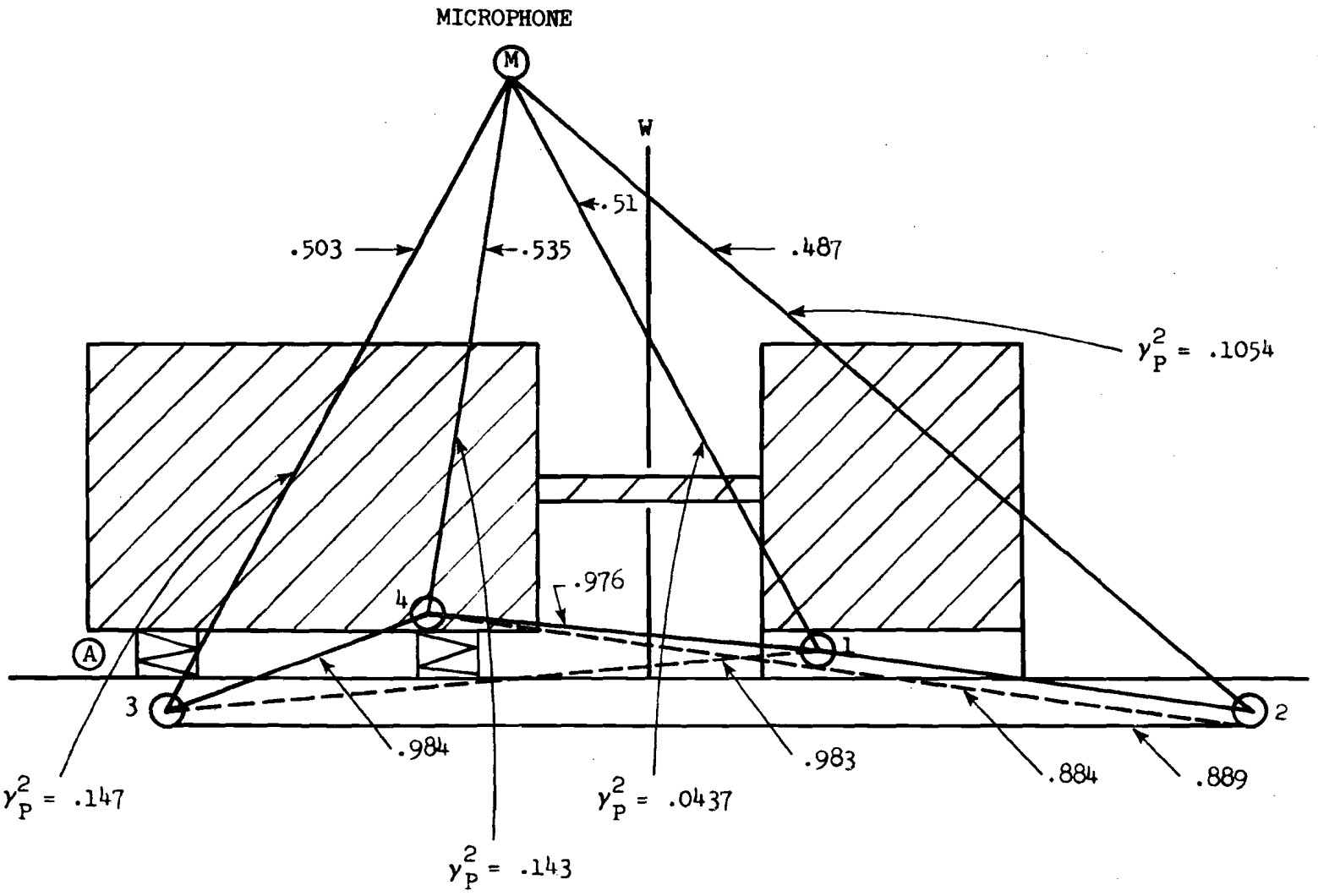

FIGURE 7.3-4 COHERENCE FUNCTION BETWEEN ROOM MICROPHONE (M) AND VARIOUS ACCELEROMETERS (1-4).

References

7.3-1 Ed. L.L. Beranek; Noise and Vibration Control, McGraw-Hill Book Company, New York, 1971.

7.3-2 Smith, P.W., Jr.; "Sound Transmission Through Thin Cylindrical Shell," J. Acoust. Soc. Am. 29, 721-729, 1957, 30, 140-141, 1958.

7.3-3 Manning, J.E. and G. Maidanik,; "Radiation Properties of Cylindrical Shells," J. Acoust. Soc, Am, Vol. 36, No. 9, 1964.

7.3-4 Bendat, J.S. and Piersol, A.G.; Measurement and Analysis of Random Data, John Wiley and Sons, New York, 1966.

SECTION 8.0

COMPRESSOR NOISE

8.1 BACKGROUND

Compressor noise - its generation and an extensive prediction method - was investigated and reported under previous FAA sponsorship (Contract No. DOT FA68WA-1960) in a report entitled "Fan/Compressor Noise Research" (Reference 8.1-1). In the present effort, compressor noise was examined by the methods developed in the previous effort to assess its contribution to the overall engine noise (see Volume I, Section 2.2.8), determine how well acoustic treatment would suppress compressor noise, and to check the prediction against test data obtained since the end of the previous program.

Considerable test data on a turbofan engine with the fan highly suppressed was accumulated during the NASA/GE Quiet Engine Program on Engine "A" (Reference 8.1-2). The engine was run in several configurations with internal measurements as shown in Figure 8.1-1. In addition to the configuration with the three inlet splitters, tests were performed on the engine with "Frame Treatment" and a "Long Treated Inlet" (see Figure 8.1-1). For all of the configurations acoustic treatment was included in the "goose neck" between the fan and compressor inlet. Both internal and external data from these tests were examined to determine the effects of compressor noise in the engine environment.

8.2 ANALYSIS OF COMPRESSOR NOISE PROPAGATION PATHS

As a first step in examining the Engine "A" data for compressor noise content, narrowband analysis of farfield data was examined for a low engine power setting with the engine in the "Fully Suppressed" configuration. Figure 8.2-1 shows the data at 60 degrees and Figure 8.2-2 at 120 degrees to the inlet axis. Even though the fan is highly suppressed and the engine is at a low power setting (i.e. jet velocity is low), compressor tones are still barely visible. It is, of course, likely that the compressor contribution would be considerably higher if the "goose neck" were not treated. Most conventional takeoff and and landing (CTOL) aircraft engines however will have core booster stages which will offer considerable resistance to forward radiated noise. For example, if three such stages are used, Reference 8.2-1 indicates an 18 db reduction in forward radiated noise.

The core inlet is, of course, not the only path for a compressor noise radiation. The casing and core exhaust may also be paths. Figures 8.2-3, and 8.2-4 show, respectively, narrowband analysis of a probe in the core exhaust and the fan exhaust on Engine "A". Neither probe shows any sign of compressor tone noise. The inlet probe data, Figure 8.2-5, however, clearly shows the first and fifth compressor stages. The reason for the fifth stage radiation is believed to be related to the fact that the fifth stage is surrounded by several bleed ports which effectively provide a casing path for radiation. The mechanism by which this noise reaches the inlet (and not the exhaust) is, however, unknown.

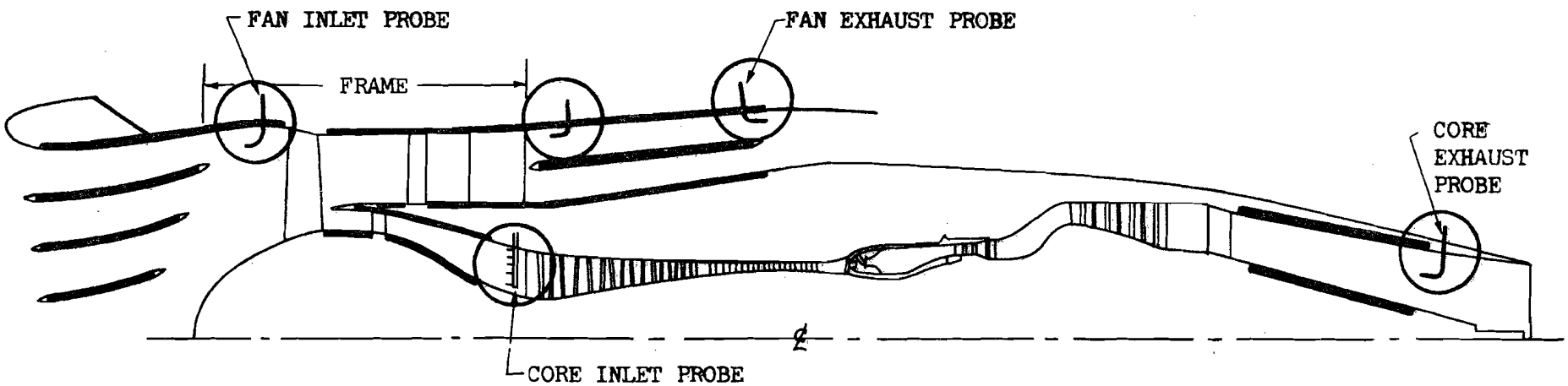

FIGURE 8.1-1 NASA/GE QUIET ENGINE "A" INTERNAL SENSOR LOCATIONS.

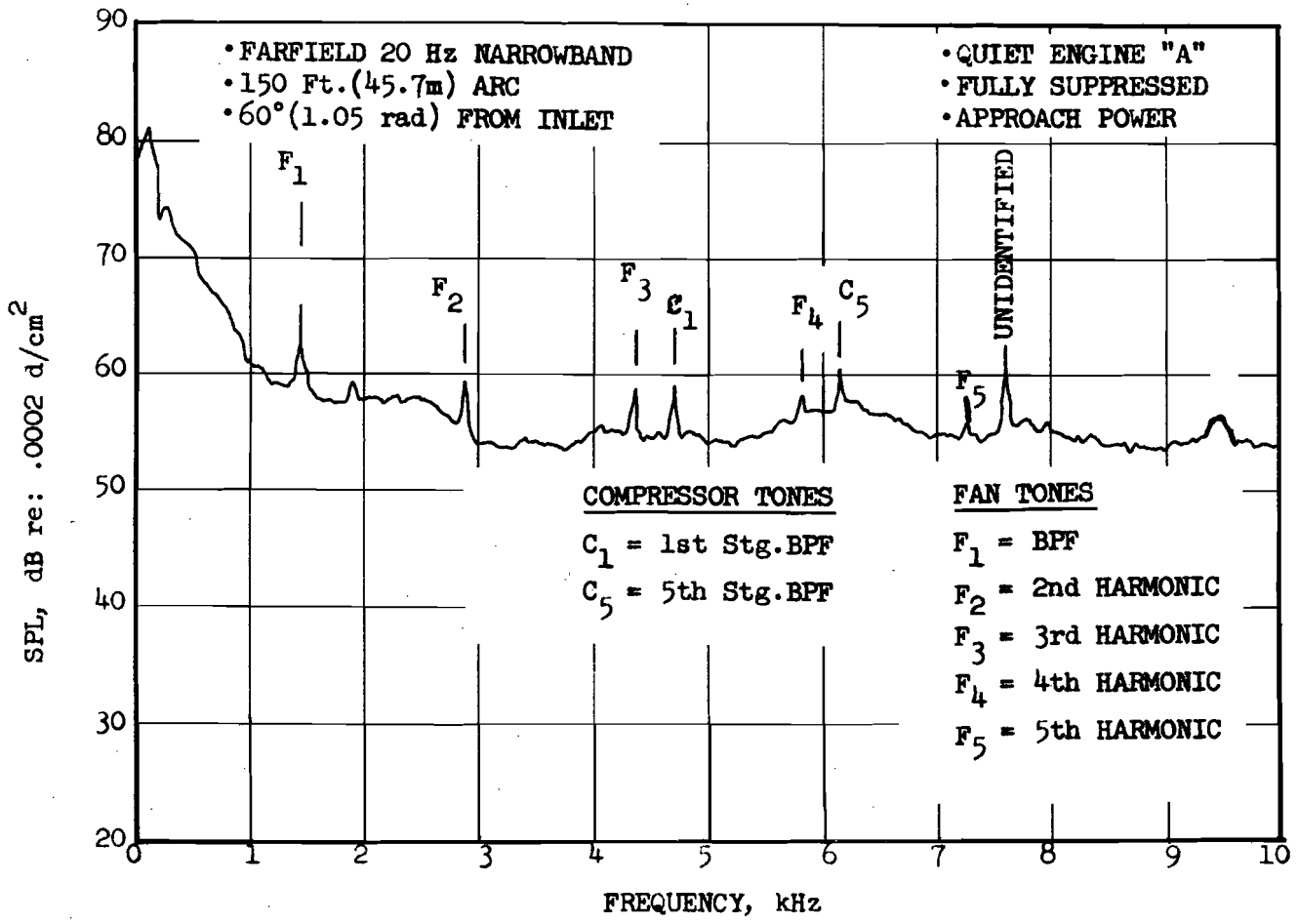

FIGURE 8.2-1 FARFIELD NARROWBAND SPECTRUM SHOWING EXTENT OF COMPRESSOR NOISE AT FRONT MAX ANGLE.

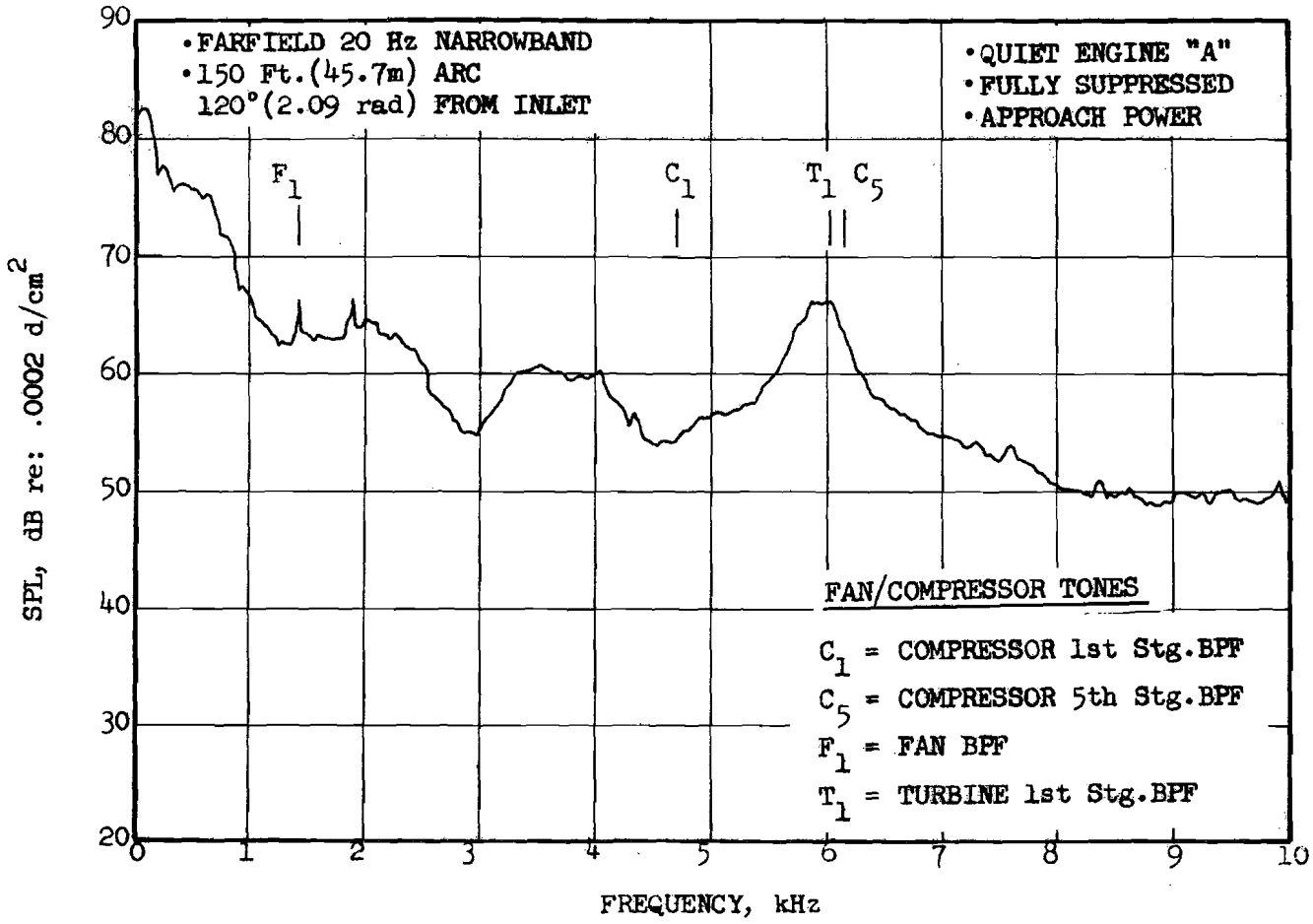

FIGURE 8.2-2 FARFIELD NARROWBAND SPECTRUM SHOWING LACK OF COMPRESSOR NOISE AT MAX AFT ANGLE.

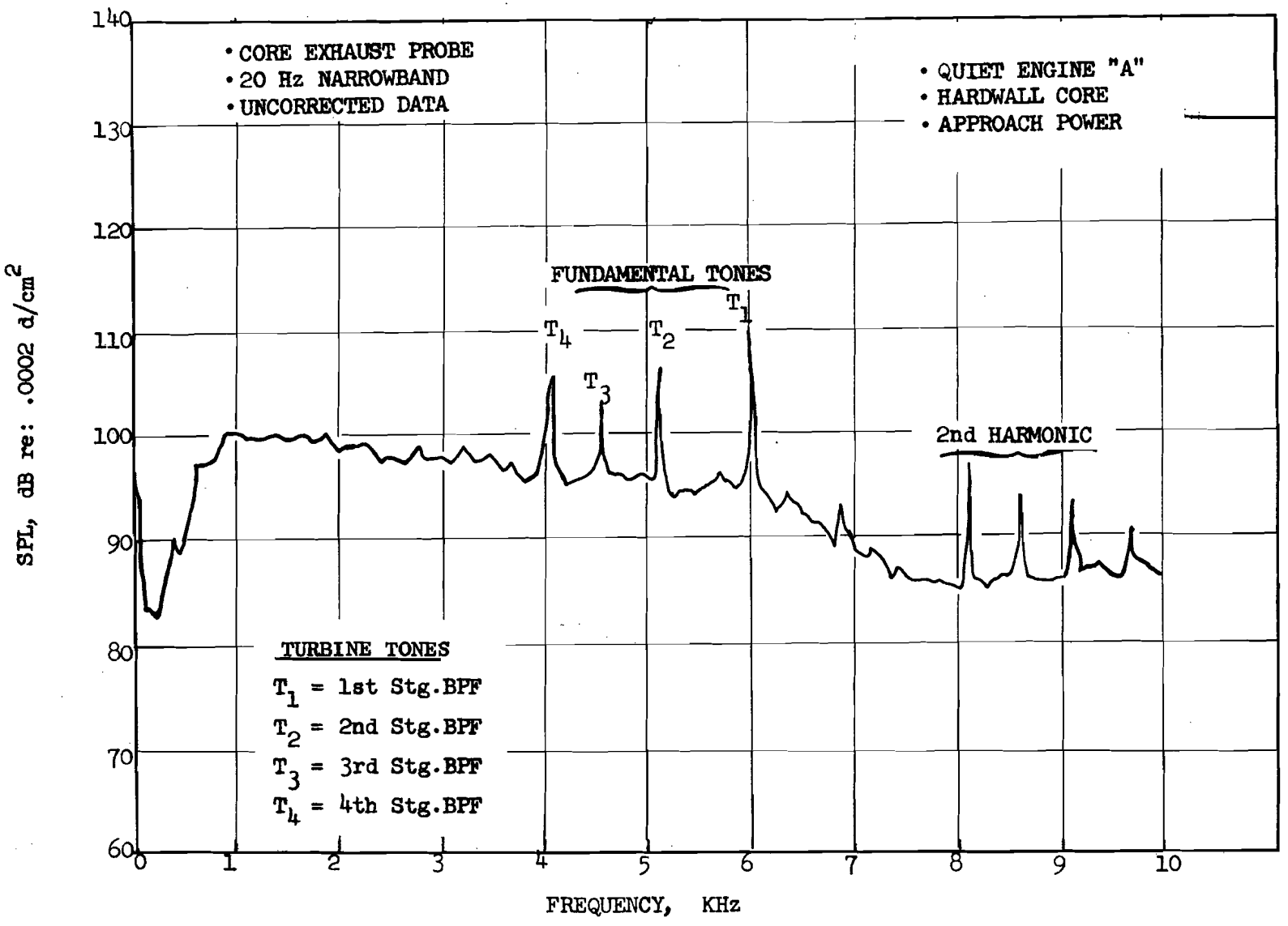

FIGURE 8.2-3 CORE NOZZLE PROBE SPECTRUM WITHOUT DISCERNIBLE COMPRESSOR NOISE.

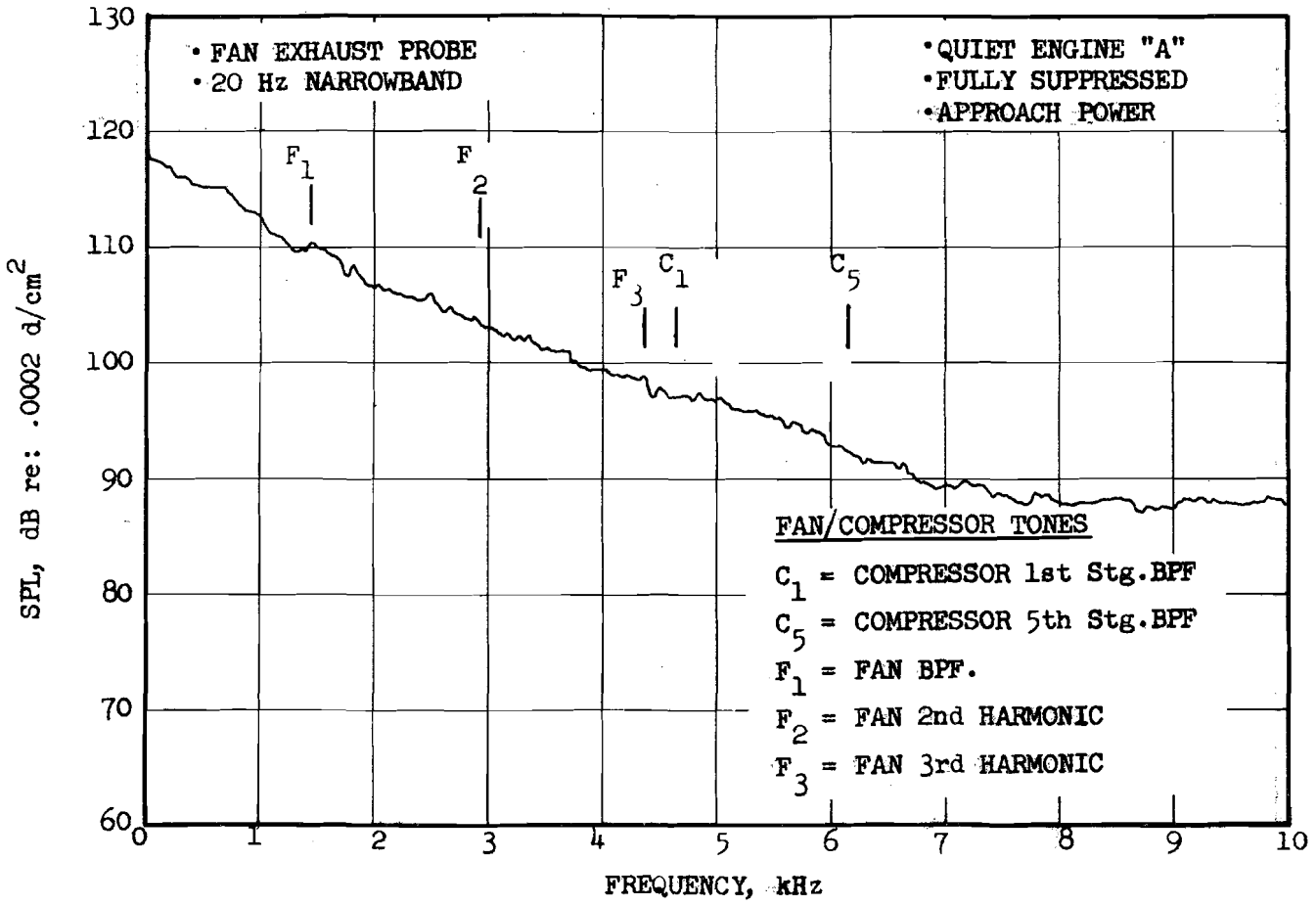

FIGURE 8.2-4 FAN EXHAUST PROBE SPECTRUM WITHOUT DISCERNABLE COMPRESSOR NOISE.

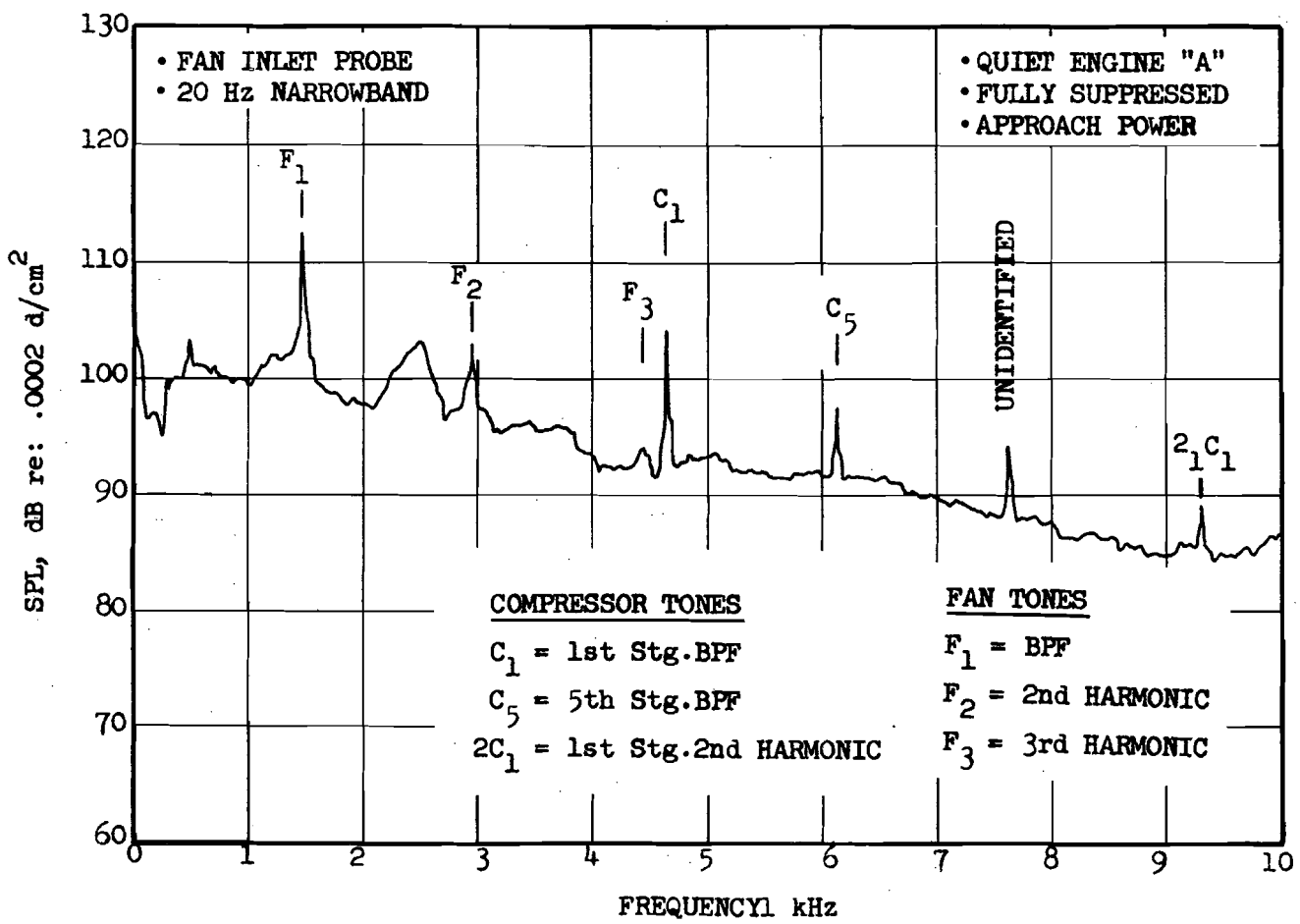

FIGURE 8.2-5 FAN INLET PROBE SPECTRUM SHOWING COMPRESSOR TONES.

Since the principle path of compressor radiation is apparently out the inlet, a probe was incorporated into Engine "A" at the core inlet (see Figure 8.1-1). A narrowband from this probe is shown in Figure 8.2-6 where the first stage tone is again visible.

Examination of narrowband data does not constitute an exclusive method of finding compressor noise. It remains possible that other noise sources are masking the compressor despite the fact that the fan is highly suppressed and the engine is at low power settings. Another method of analyzing internal (probe) and external (farfield) data is by determining the degree of phase coherence which exists between the two signals. Figure 8.2-7 contains such an analysis for the fan inlet and exhaust probes and two farfield positions for each possible compressor tone. Generally a coherence of 30% indicates that a measurable amount of energy arriving at the farfield point has passed the internal point.

Figure 8.2-7 shows the front compressor stages to have a high degree of coherence with the front angle and the rear stages with the aft angle as might be expected. The coherence function does not indicate the level of the noise at the farfield point; but it does indicate the existence of a compressor noise signal, even though it is not visible in the spectrum.

8.3 COMPARISON OF PREDICTED AND MEASURED COMPRESSOR NOISE

In Reference 8.1-1 an analytical prediction method was developed which was based on the aerodynamic and geometric parameters which define a fan or compressor stage. In order to check the validity of the prediction procedure, internal probe and farfield data from Engine "A" in the "Frame Treated" configuration (see Figure 8.3-1) were employed. The internal core inlet probe data (see Figure 8.3-2) indicated that the first compressor stage was generating 153.0 db PWL. Figure 8.3-2 shows the SPL at two different immersions for this core probe which when integrated provides the acoustic power. Using the prediction of Reference 9.1-1 results in a predicted PWL of 152.1 db versus a measured level of 153.0 db. Thus the prediction is valid for the Engine "A" core compressor's first stage.

8.4 METHODS OF SUPPRESSION

One means of suppressing compressor radiated noise is to apply acoustically absorbing materials to the "goose neck" between the compressor inlet and fan inner flowpath OGV as was done in QEP Engine "A" (see Figure 8.3-1). It was predicted that this acoustic treatment would result in a 16 db decrease in the compressor first stage PWL. In order to validate this, the predicted first stage PWL was suppressed by 16 db due to the treatment and 6 db due to the fan rotor and OGV and compared to the farfield measure PWL. The farfield power measured 125.7 db while the predicted level was 130.1 db. The most likely reason for the discrepancy is farfield energy which could not be seen at angles beyond 60 degrees due to the predominance of other noise sources. Figure 8.4-1 indicates that at 70 degrees the 1st stage tone can no longer be seen. Nevertheless, it is clear that a considerable amount of the first stage power which was measured at the compressor inlet did not reach the farfield due to the core treatment.

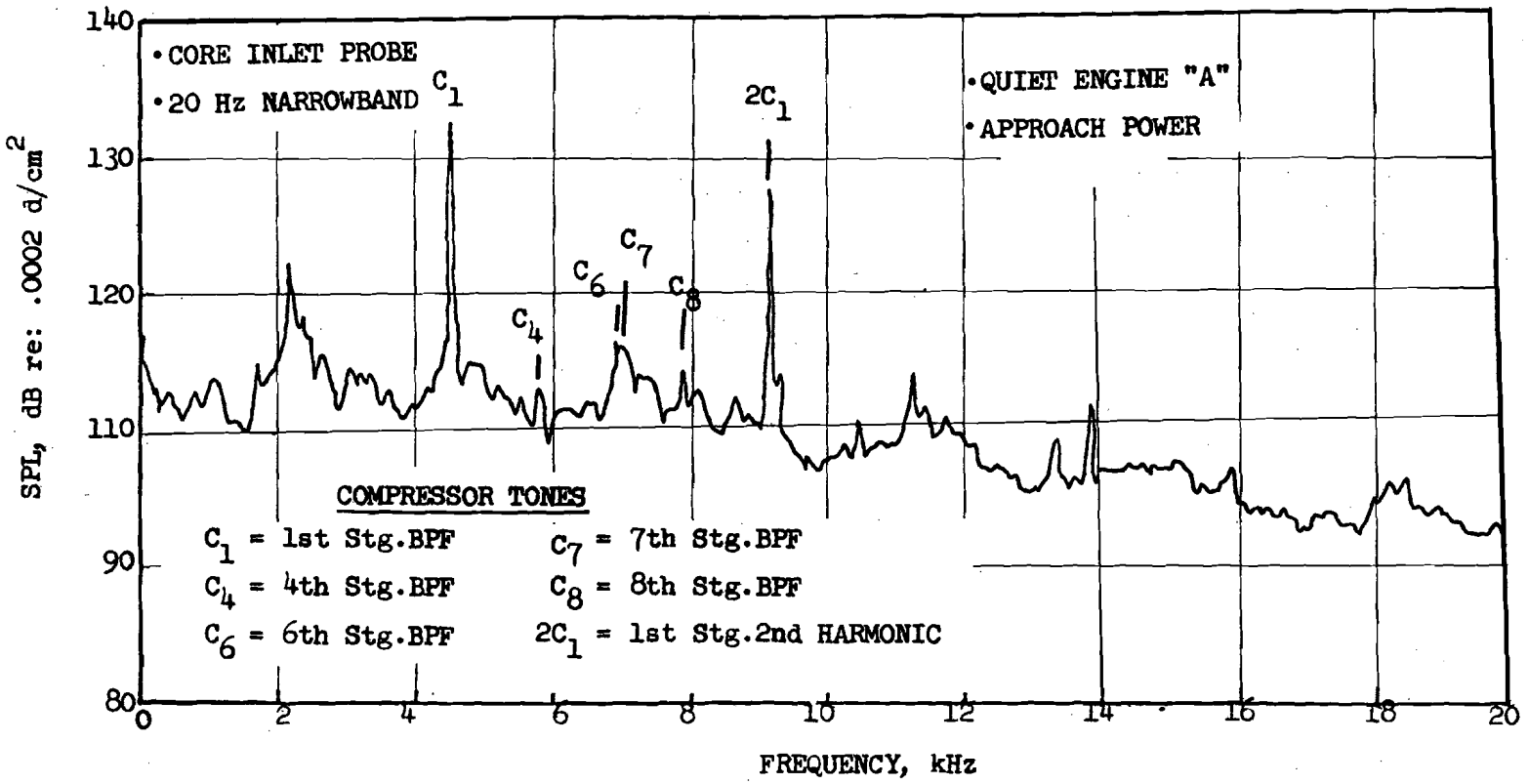

FIGURE 8.2-6 CORE INLET PROBE SPECTRUM SHOWING COMPRESSOR FIRST AND FIFTH STAGE TONES.

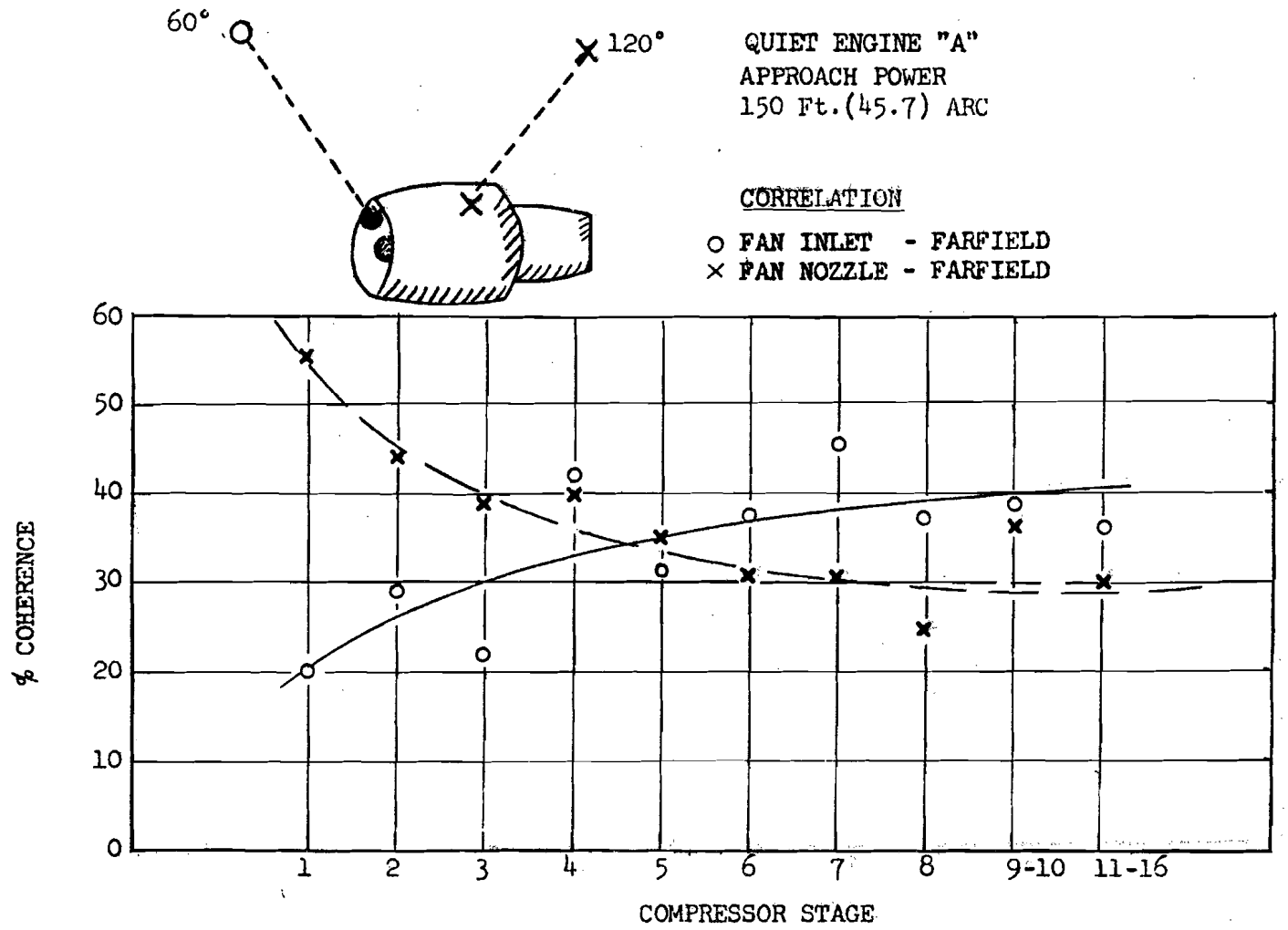

FIGURE 8.2-7 QUIET ENGINE "A" APPROACH POWER SETTING COHERENCE FUNCTION vs. COMPRESSOR STAGES.

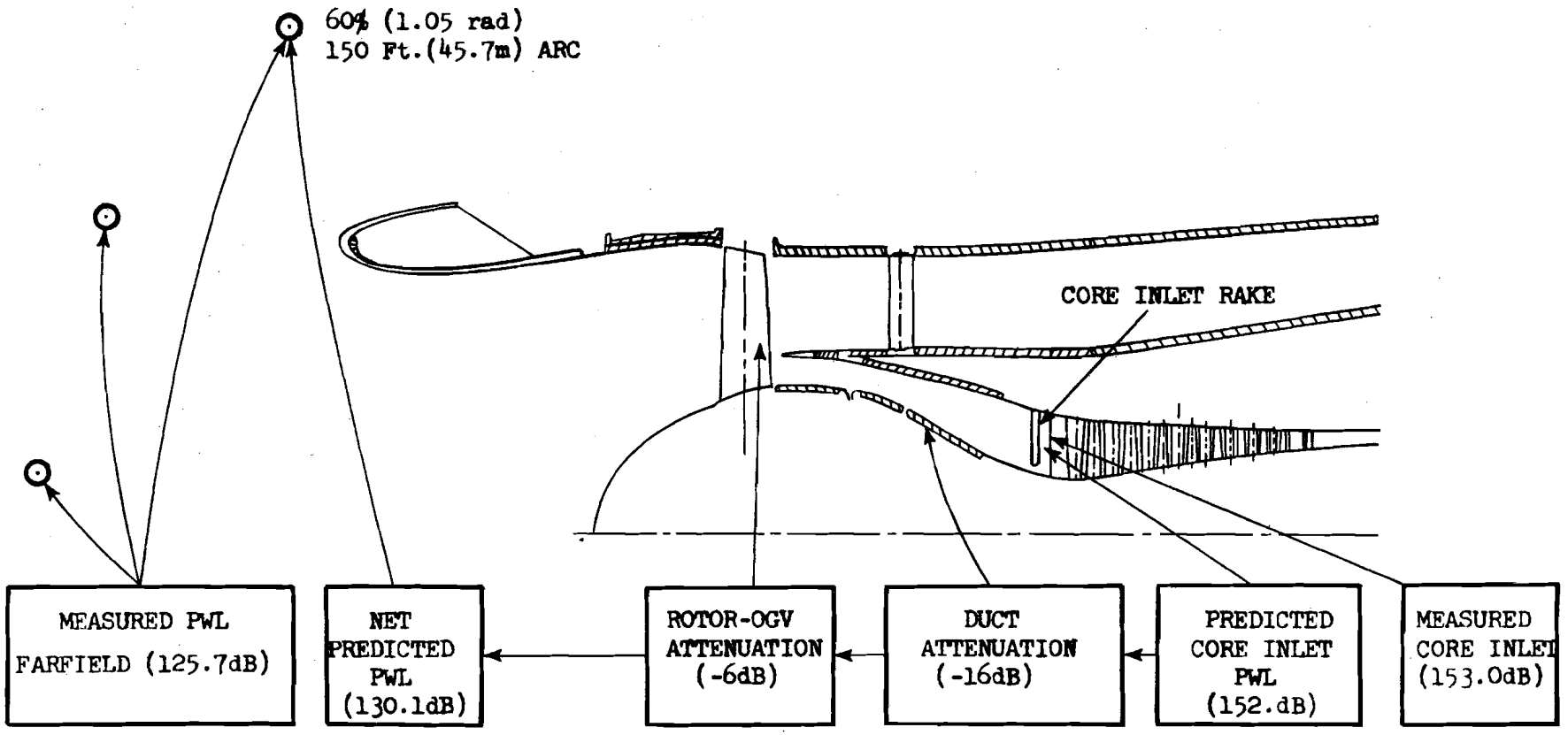

VALUES FOR FRAME TREATMENT, BELLMOUTH INLET, NOMINAL NOZZLE CONFIGURATION.
APPROACH SETTING.

FIGURE 8.3-1 COMPARISON OF PREDICTED AND MEASURED COMPRESSOR NOISE LEVELS FOR ENGINE "A".

• QUIET ENGINE "A"
• CORE INLET PROBE
• APPROACH POWER
• 20 Hz NARROWBAND

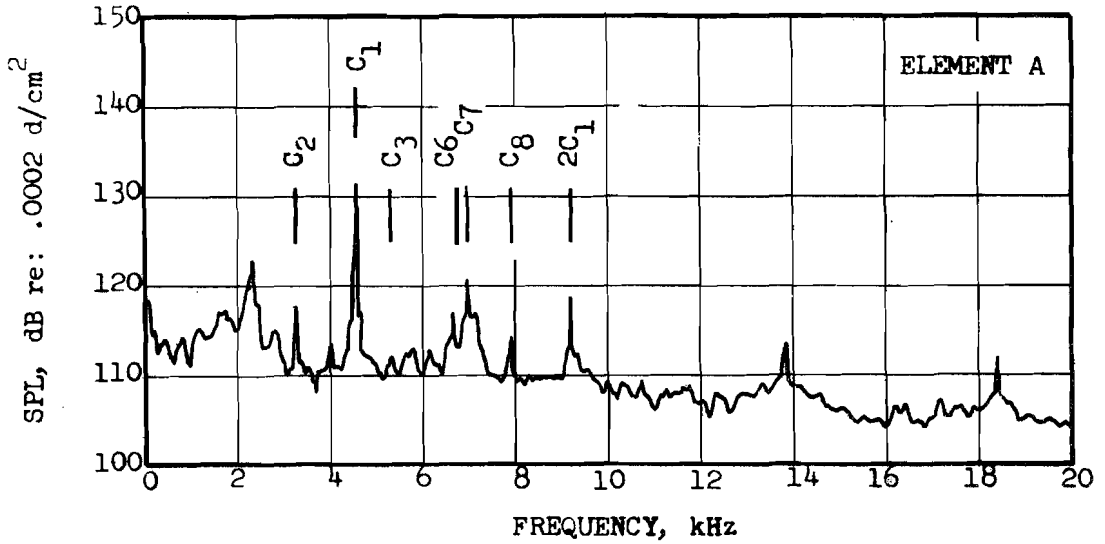

COMPRESSOR TONES

C_1 = 1st Stg.BPF	C_6 = 6th Stg.BPF
C_2 = 2nd Stg.BPF	C_7 = 7th Stg.BPF
C_3 = 3rd Stg.BPF	C_8 = 8th Stg.BPF
C_4 = 4th Stg.BPF	$2C_1$ = 1st Stg.2nd HARMONIC

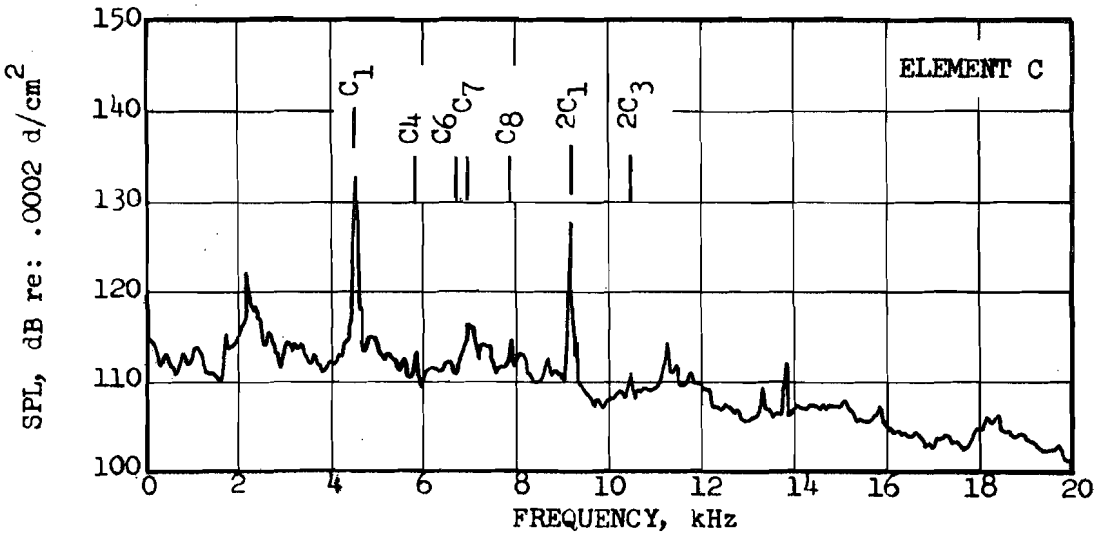

FIGURE 8.3-2 CORE INLET PROBE DATA SHOWING COMPRESSOR TONES.

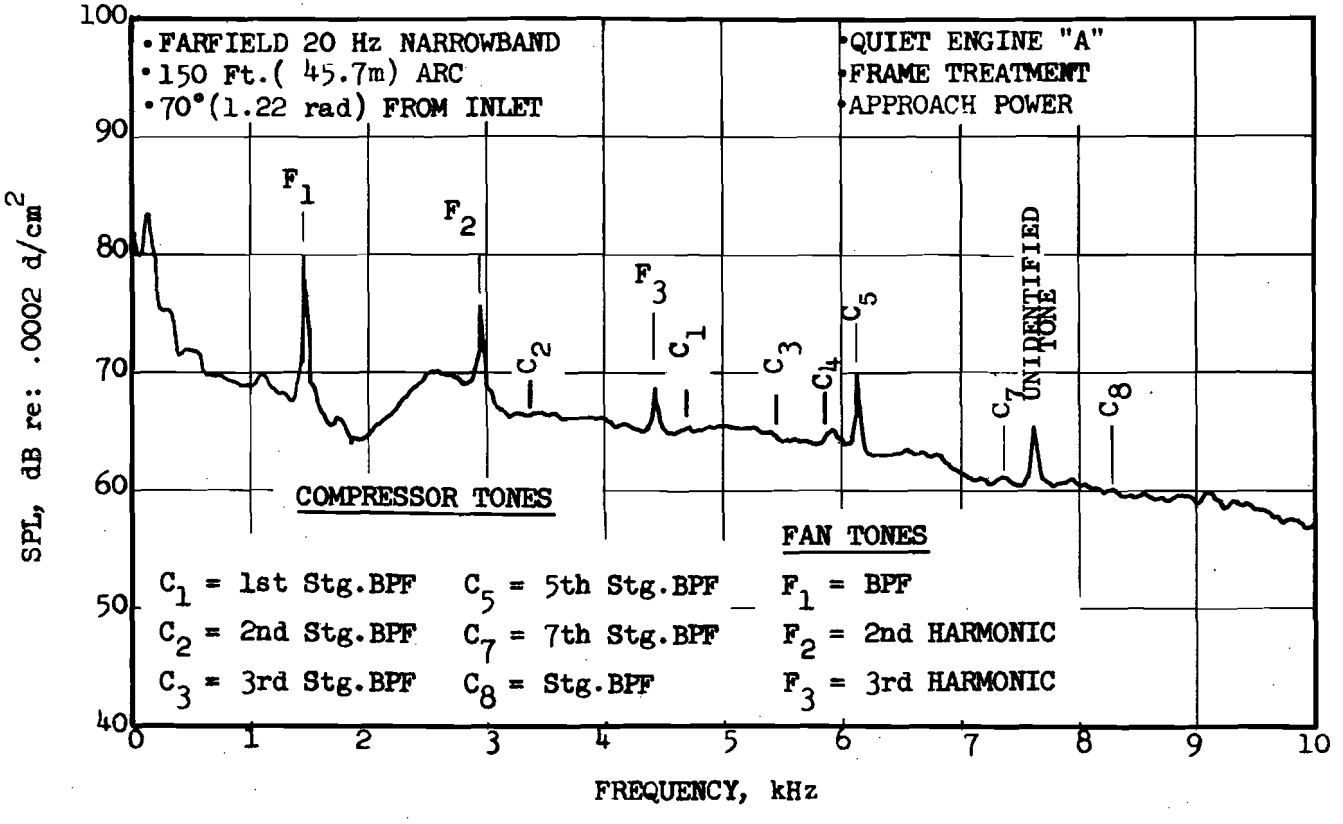

FIGURE 8.4.1 QUIET ENGINE "A" FARFIELD SPECTRUM WITHOUT SIGNIFICANT COMPRESSOR NOISE CONTENT AT 70°(1.22 rad) FROM INLET.

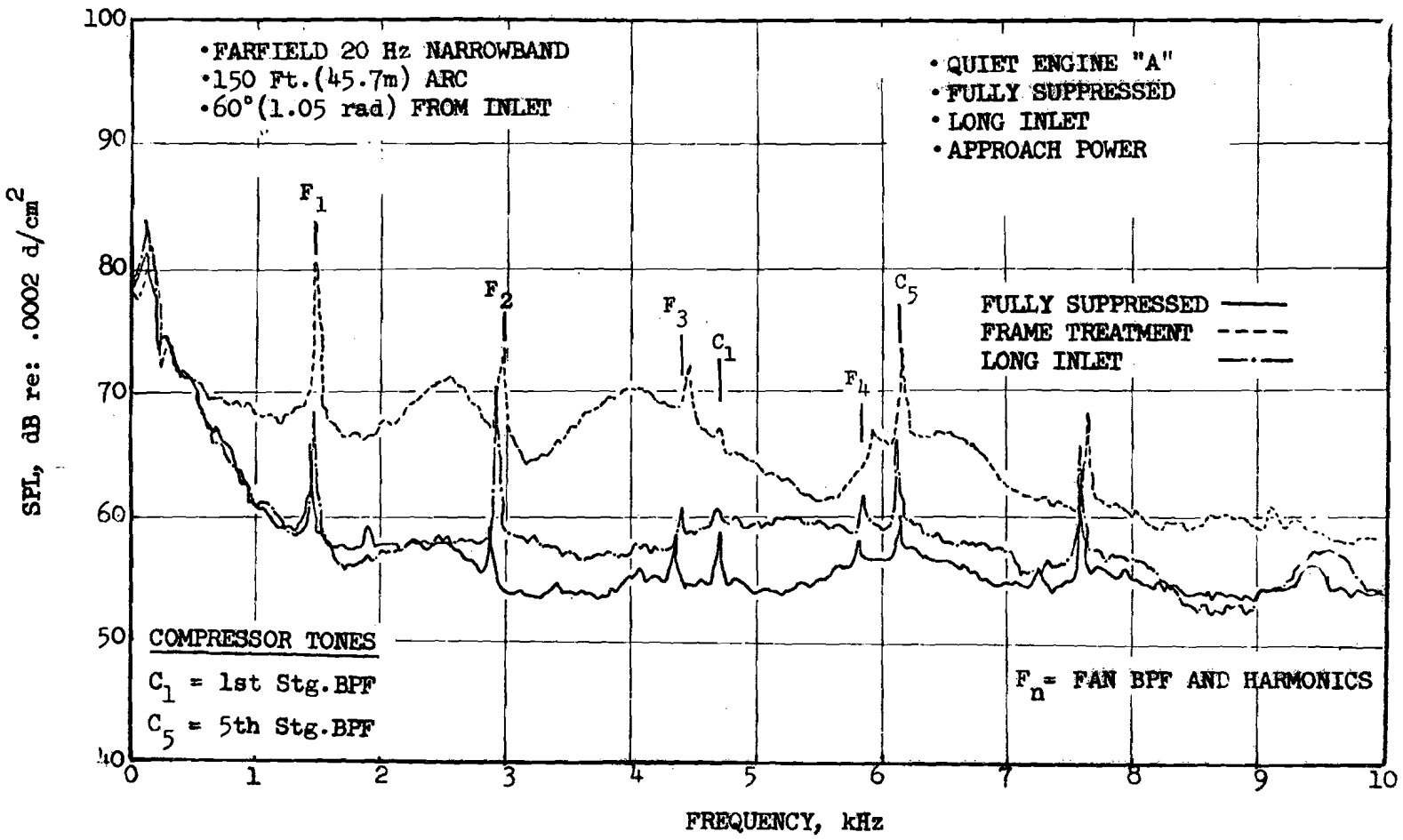

FIGURE 8.4-2 COMPRESSOR NOISE REDUCTION BY FAN INLET ACOUSTIC TREATMENT.

In examining the Engine "A" data another means of suppressing compressor inlet noise was discovered. Figure 8.4-2 shows the result of adding fan inlet acoustic treatment on the compressor noise. The three Engine "A" configuration are indicated in Figure 8.1-1. In general, the inlet suppression techniques - even extended wall acoustic treatment only - have a profound effect on compressor noise.

8.5 SUMMARY

The contribution of compressor noise has been shown to be small in the overall engine environment with the principle path of radiation the engine inlet. Furthermore, the identification of compressor noise in the farfield can be enhanced by use of coherence function analysis.

The analytic prediction method developed in Reference 8.1-1 was also found to be valid for the inlet radiated noise of a core compressor. In addition, it was determined that compressor inlet radiated noise may be suppressed by the addition of acoustic treatment to the "goose neck" and/or the inlet outer cowl wall.

REFERENCES

8.1-1 "Fan/Compressor Noise Research", Volume I, Final Report under DOT/FAA Contract FA68WA-1960, Project Number 550-001-01H, General Electric Company (AEG), December 1970, FAA Report FAA-RD-71-85, December 1971.

8.1-2 Kazin, S.B. and Paas, J.E., "NASA/GE Quiet Engine "A" Acoustic Test Results", NASA CR-121175, October 1973.

8.2-1 Smith, M.J.T. and House, M.E.," Internally Generated Noise From Gas Turbine Engines, Measurement and Prediction", J. Eng. for Power, Trans. ASME, Series A, 89 April 1967.

NOZZLE PERFORMANCE DATA

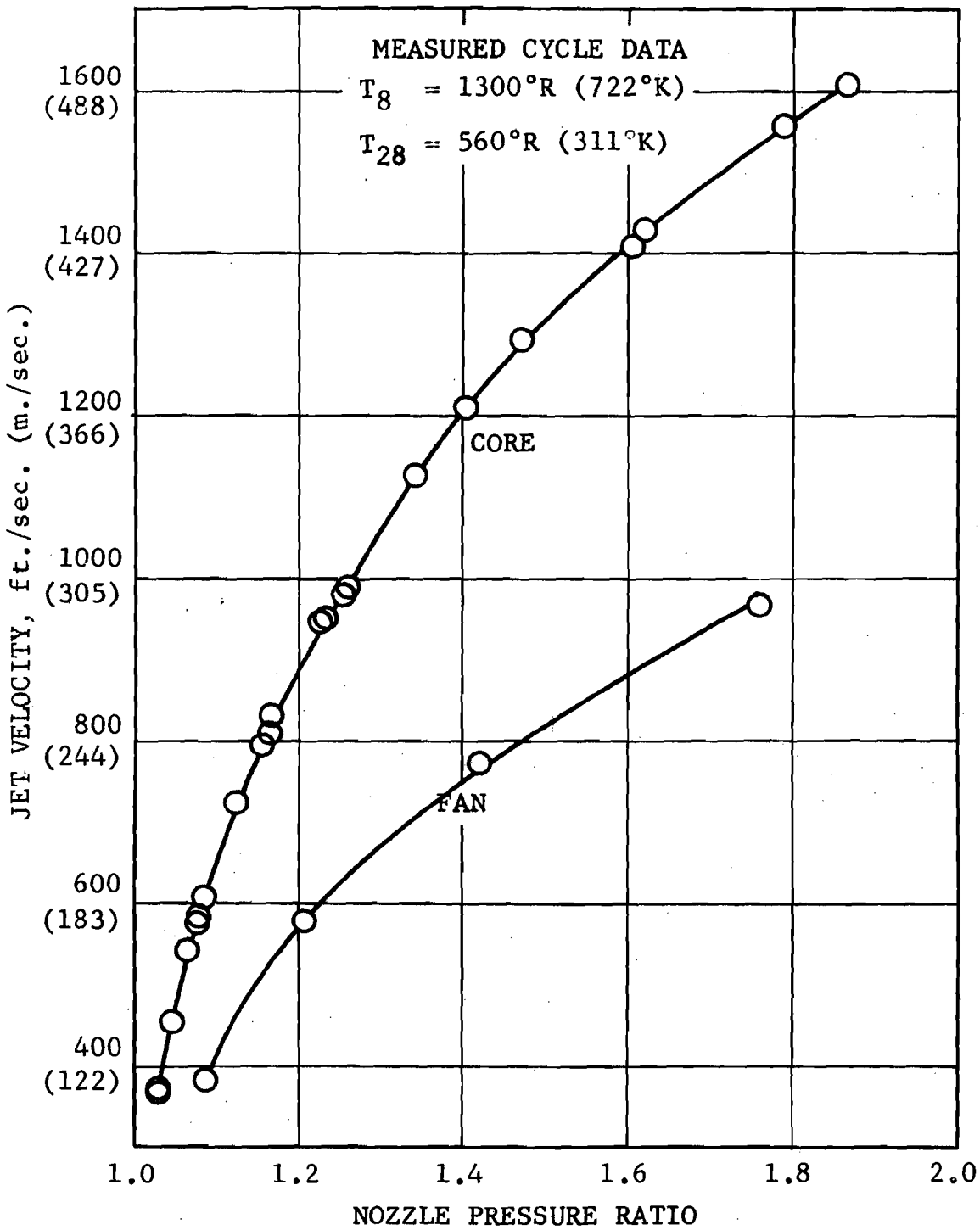

FIGURE A-1 JET VELOCITY vs. NOZZLE PRESSURE RATIO
COANNULAR/COPLANAR NOZZLE AR = 2

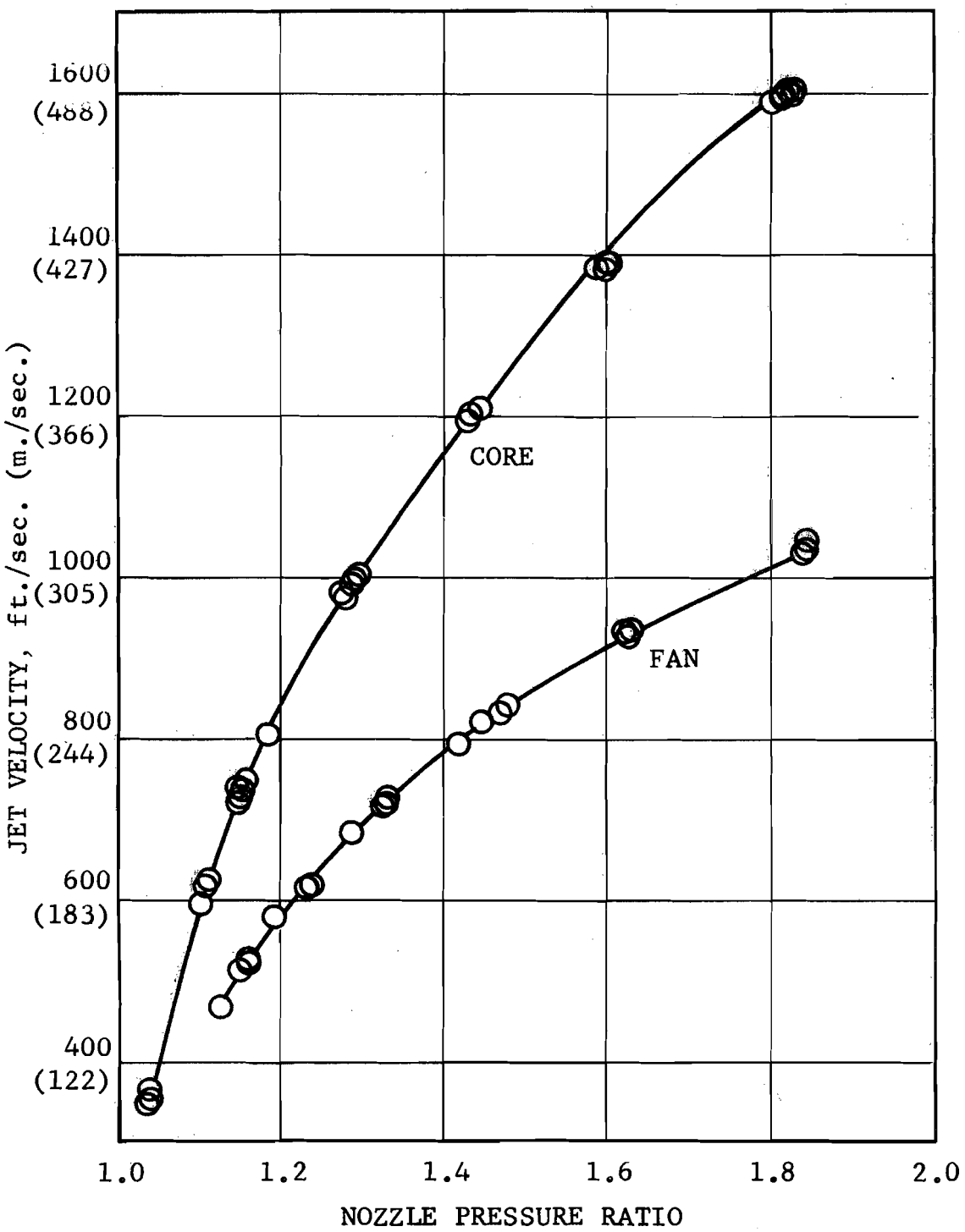

FIGURE A - 2 JET VELOCITY vs. NOZZLE PRESSURE RATIO
COANNULAR/COPLANAR NOZZLE AR = 4

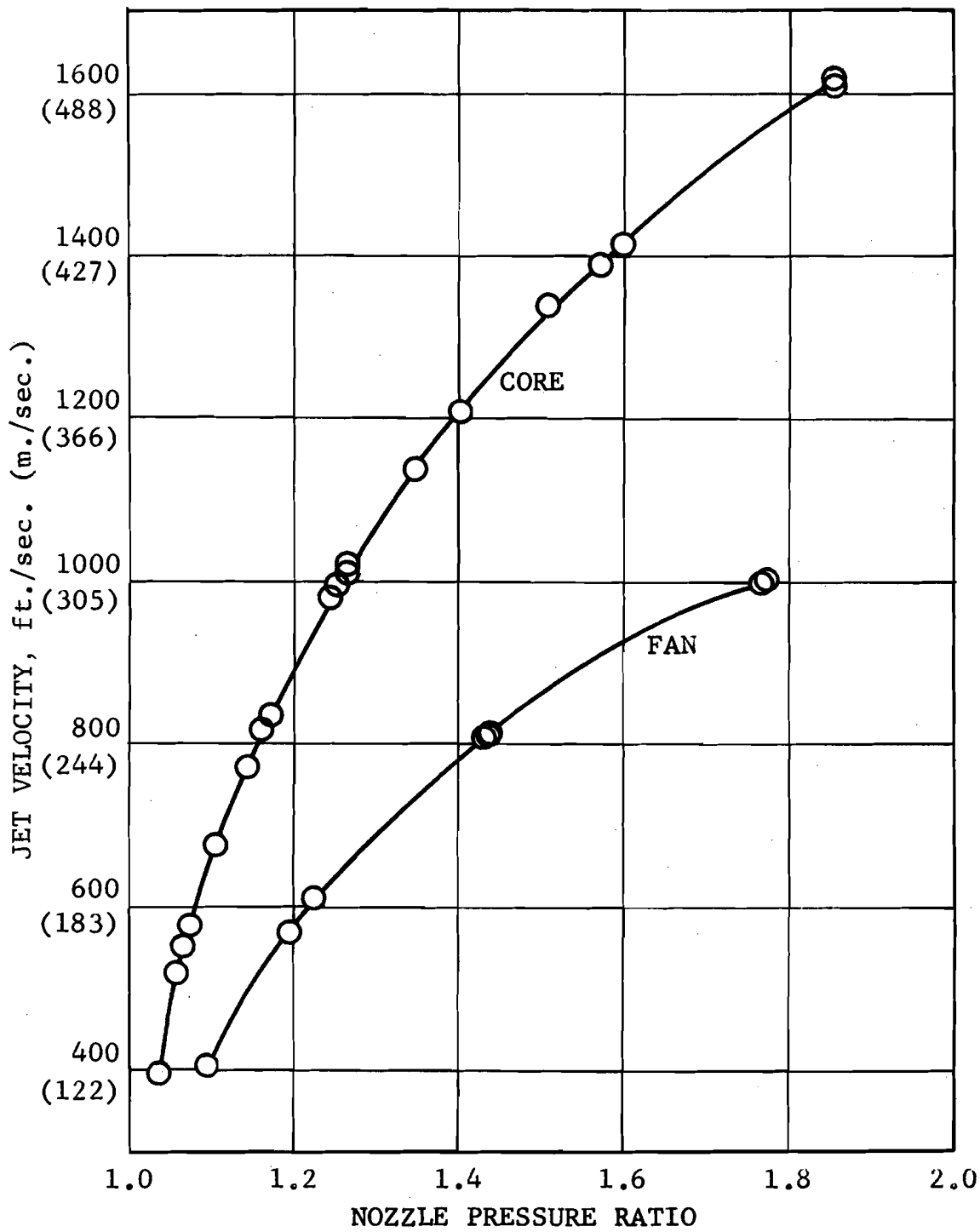

FIGURE A-3 JET VELOCITY vs. NOZZLE PRESSURE RATIO
COANNULAR/COPLANAR NOZZLE AR = 6

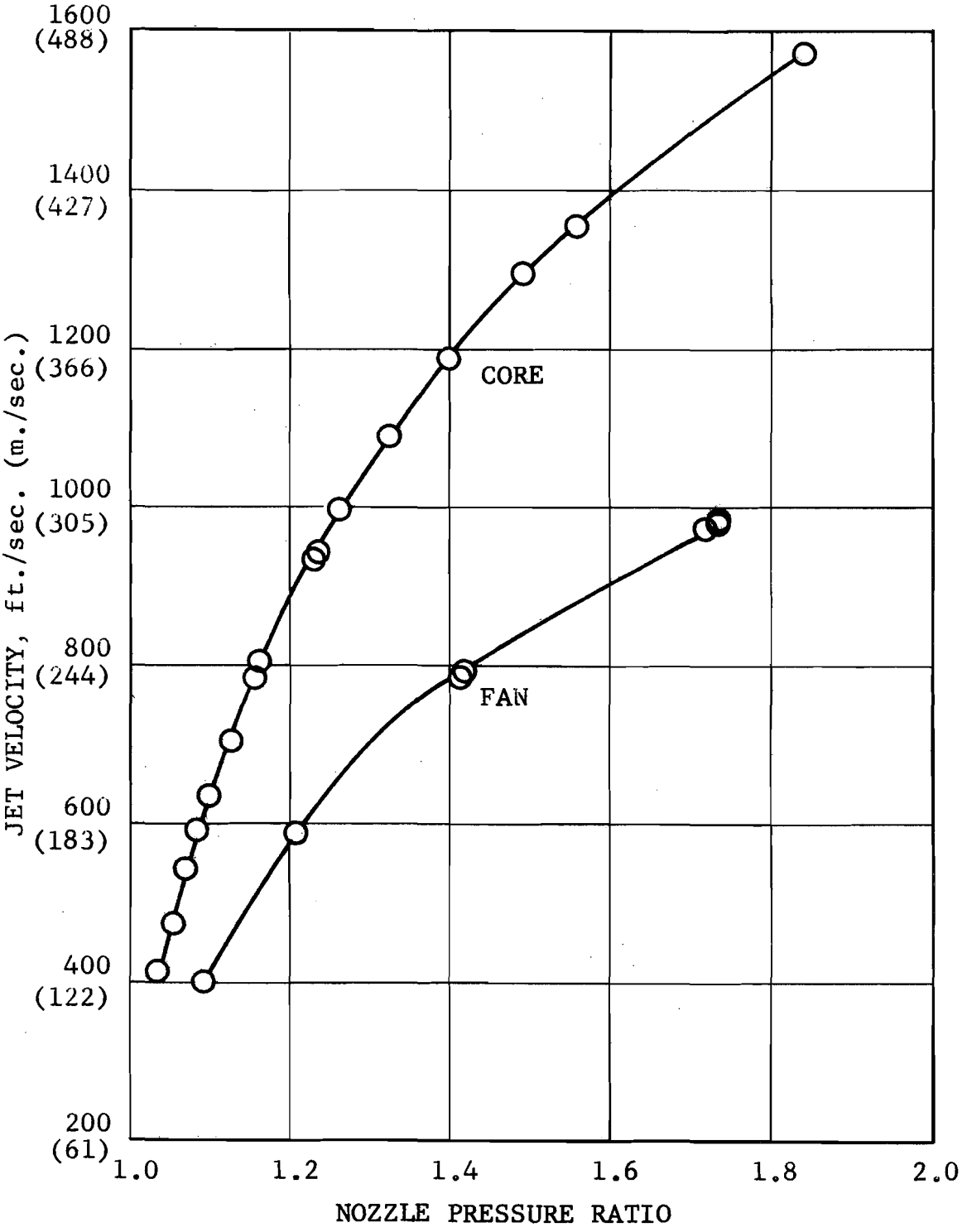

FIGURE A-4 JET VELOCITY vs. NOZZLE PRESSURE RATIO
COANNULAR/COPLANAR NOZZLE AR = 8

APPENDIX B

AERO-ACOUSTIC DATA MODEL

TABLE B-1. AREA RATIO = 2, CORE ONLY

TEST DATE: 10/11/72; RUN NO. 4

A_8 = .069 FT^2 (.00641 m^2);

PT. No.	P_o psia	T_o °R	$\frac{P_{T8}}{P_o}$	$\frac{P_{T28}}{P_o}$	T_{T8} °R	T_{T28} °R	V_8 Ft/Sec	V_{28} Ft/Sec	W_8 Lbs/Sec	W_{28} Lbs/Sec	$\frac{V_{28}}{V_8}$	$\frac{W_{28}}{W_8}$	V_M Ft/Sec	10 LOG ρA	10 LOG $\rho^2 A$	40 FT. ARC: PEAK OASPL	40 FT. ARC: PEAK OASPL ANGLE Degrees	40 FT. ARC: PEAK PNL	40 FT. ARC: PEAK PNL ANGLE Degrees
3	14.66	519	1.158	-	1309	-	804	-	1.64	-	-	-	789	-26.7	-41.7	95.0	140	106.3	140
4	14.66	519	1.247	-	1308	-	982	-	2.04	-	-	-	982	-26.6	-41.5	101.6	150	112.7	140
5	14.66	521	1.396	-	1308	-	1198	-	2.62	-	-	-	1198	-26.4	-41.2	108.9	140	120.1	140
6	14.65	522	1.603	-	1303	-	1409	-	3.21	-	-	-	1409	-26.3	-40.9	115.2	140	126.7	140
7	14.65	522	1.860	-	1316	-	1608	-	3.83	-	-	-	1608	-26.1	-40.6	120.5	140	132.8	140

PT. No.	P_o N/m^2 x 10^4	T_o °K	$\frac{P_{T8}}{P_o}$	$\frac{P_{T28}}{P_o}$	T_{T8} °K	T_{T28} °K	V_8 m/Sec	V_{28} m/Sec	W_8 Kg/Sec	W_{28} Kg/Sec	$\frac{V_{28}}{V_8}$	$\frac{W_{28}}{W_8}$	V_M m/Sec	10 LOG ρA	10 LOG $\rho^2 A$	12.2 m ARC: PEAK OASPL	12.2 m ARC: PEAK OASPL ANGLE Radians	12.2 m ARC: PEAK PNL	12.2 m ARC: PEAK PNL ANGLE Radians
3	10.11	288	1.158	-	727.2	-	245.1	-	.744	-	-	-	240.5	-26.7	-41.7	95.0	2.45	106.3	2.45
4	10.11	288	1.247	-	726.7	-	299.3	-	.925	-	-	-	299.3	-26.6	-41.5	101.6	2.625	112.7	2.45
5	10.11	289	1.396	-	726.7	-	365.2	-	1.188	-	-	-	365.2	-26.4	-41.2	108.9	2.45	120.1	2.45
6	10.10	290	1.603	-	723.9	-	429.5	-	1.456	-	-	-	429.5	-26.3	-40.9	115.2	2.45	126.7	2.45
7	10.10	290	1.860	-	731.1	-	490.1	-	1.737	-	-	-	490.1	-26.1	-40.6	120.5	2.45	132.8	2.45

TABLE B-2. AREA RATIO = 2, CORE ONLY

TEST DATE: 10/20/72; RUN NO. 5

A_8 = .069 FT^2 (.006 m^2);

PT. No.	P_o psia	T_o °R	$\frac{P_{T8}}{P_o}$	$\frac{P_{T28}}{P_o}$	T_{T8} °R	T_{T28} °R	V_8 Ft/Sec	V_{28} Ft/Sec	W_8 Lbs/Sec	W_{28} Lbs/Sec	$\frac{V_{28}}{V_8}$	$\frac{W_{28}}{W_8}$	V_M Ft/Sec	10 LOG ρA	10 LOG $\rho^2 A$	40 FT. ARC PEAK OASPL	PEAK OASPL ANGLE Degrees	PEAK PNL	PEAK PNL ANGLE Degrees
1	14.65	508	1.031	-	1307	-	372	-	.725	-	-	-	372	-26.8	-41.9	77.2	130	84.9	130
2	14.65	512	1.079	-	1306	-	582	-	1.157	-	-	-	582	-26.7	-41.8	86.8	150	96.6	130
3	14.65	513	1.155	-	1312	-	798	-	1.586	-	-	-	798	-26.7	-41.7	95.4	140	106.5	140
4	14.66	511	1.260	-	1297	-	992	-	2.105	-	-	-	992	-26.4	-41.3	103.1	140	114.3	140
5	14.66	509	1.403	-	1311	-	1208	-	2.568	-	-	-	1208	-26.4	-41.2	109.9	140	120.8	140
6	14.66	510	1.620	-	1312	-	1428	-	3.173	-	-	-	1428	-26.3	-40.9	115.9	140	127.1	140
7	14.66	510	1.789	-	1311	-	1558	-	3.783	-	-	-	1558	-26.2	-40.7	121.2	140	132.9	140

PT. No.	P_o N/m^2 x 10^4	T_o °K	$\frac{P_{T8}}{P_o}$	$\frac{P_{T28}}{P_o}$	T_{T8} °K	T_{T28} °K	V_8 m/Sec	V_{28} m/Sec	W_8 Kg/Sec	W_{28} Kg/Sec	$\frac{V_{28}}{V_8}$	$\frac{W_{28}}{W_8}$	V_M m/Sec	10 LOG ρA	10 LOG $\rho^2 A$	12.2 m ARC PEAK OASPL	PEAK OASPL ANGLE Radians	PEAK PNL	PEAK PNL ANGLE Radians
1	10.10	282.2	1.031	-	726.1	-	113.4	-	.3289	-	-	-	113.4	-26.8	-41.9	77.2	2.275	84.9	2.275
2	10.10	284.4	1.079	-	725.6	-	177.4	-	.5248	-	-	-	177.4	-26.7	-41.8	86.8	2.625	96.6	2.275
3	10.10	285.0	1.155	-	728.9	-	243.2	-	.7194	-	-	-	243.2	-26.7	-41.7	95.4	2.45	106.5	2.45
4	10.11	283.9	1.260	-	720.6	-	302.4	-	.9548	-	-	-	302.4	-26.4	-41.3	103.1	2.45	114.3	2.45
5	10.11	282.8	1.403	-	728.3	-	368.2	-	1.165	-	-	-	368.2	-26.4	-41.2	109.9	2.45	120.8	2.45
6	10.11	283.3	1.620	-	728.9	-	435.3	-	1.439	-	-	-	435.3	-26.3	-40.9	115.9	2.45	127.1	2.45
7	10.11	283.3	1.789	-	728.3	-	474.9	-	1.716	-	-	-	474.9	-26.2	-40.7	121.2	2.45	132.9	2.45

TABLE 8-3. AREA RATIO = 2, DUAL FLOW

TEST DATE: 10/20/72; RUN NO. 5

A_8 = .069 FT^2 (.006 m^2); A_{28} = .139 FT^2 (.013 m^2)

PT. No.	P_o psia	T_o °R	P_{T8}/P_o	P_{T28}/P_o	T_{T8} °R	T_{T28} °R	V_8 Ft/Sec	V_{28} Ft/Sec	W_8 Lbs/Sec	W_{28} Lbs/Sec	V_{28}/V_8	W_{28}/W_8	V_M Ft/Sec	10 LOG ρA	10 LOG $\rho^2 A$	40 FT. ARC PEAK OASPL	PEAK OASPL ANGLE Degrees	PEAK PNL	PEAK PNL ANGLE Degrees
8	14.69	505	1.031	1.086	1299	516	368	381	.612	3.89	1.04	6.36	379	N/A	N/A	81.9	160	88.4	150
9	14.69	506	1.047	1.086	1312	515	455	380	.805	3.89	.84	4.83	393			80.0	150	88.8	140
10	14.69	505	1.068	1.086	1304	514	540	379	.985	3.89	.70	3.95	411			82.9	150	91.6	140
11	14.69	509	1.085	1.086	1318	511	604	378	1.121	3.89	.63	3.47	429			86.1	150	93.8	140
12	14.69	503	1.079	1.211	1299	517	578	575	1.01	6.13	.99	6.07	575			90.5	150	101.1	140
13	14.69	502	1.124	1.211	1316	518	722	576	1.34	6.14	.80	4.58	602			94.9	150	103.4	140
14	14.69	506	1.170	1.211	1308	520	832	577	1.6	6.13	.69	3.21	630			NO ACOUSTIC DATA			
15	14.69	511	1.232	1.211	1299	521	951	578	1.91	6.14	.61	3.16	667			99.9	150	109.5	140

PT. No.	P_o M/m^2 x 10^4	T_o °K	P_{T8}/P_o	P_{T28}/P_o	T_{T8} °K	T_{T28} °K	V_8 m/Sec	V_{28} m/Sec	W_8 Kg/Sec	W_{28} Kg/Sec	V_{28}/V_8	W_{28}/W_8	V_M m/Sec	10 LOG ρA	10 LOG $\rho^2 A$	12.2 m ARC PEAK OASPL	PEAK OASPL ANGLE Radians	PEAK PNL	PEAK PNL ANGLE Radians
8	10.13	280.6	1.031	1.086	721.7	286.7	112.2	116.1	.2776	1.764	1.04	6.36	115.5	N/A	N/A	81.9	2.80	88.4	2.625
9	10.13	281.1	1.047	1.086	728.9	286.1	138.7	115.8	.3651	1.764	.84	4.83	119.8			80.0	2.625	88.8	2.45
10	10.13	280.6	1.068	1.086	724.4	285.6	164.6	115.5	.4468	1.764	.70	3.95	125.3			82.9	2.625	91.6	2.45
11	10.13	282.8	1.085	1.086	732.2	283.9	184.1	115.2	.5085	1.764	.63	3.47	130.8			86.1	2.625	93.8	2.45
12	10.13	279.4	1.079	1.211	721.7	287.2	176.2	175.3	.4581	2.781	.99	6.07	175.3			90.5	2.625	101.1	2.45
13	10.13	278.9	1.124	1.211	731.1	287.8	220.1	175.6	.6078	2.785	.80	4.58	183.5			94.9	2.625	103.4	2.45
14	10.13	281.1	1.170	1.211	726.7	288.9	253.6	175.9	.7258	2.781	.69	3.21	192.0			NO ACOUSTIC DATA			
15	10.13	283.9	1.232	1.211	721.7	289.4	289.9	176.2	.8664	2.785	.61	3.16	203.3			99.9	2.625	109.5	2.45

TABLE B-4. AREA RATIO = 2, DUAL FLOW

TEST DATE: 10/20/72; RUN NO. 5

A_8 = .069 FT^2 (.006 m^2); A_{28} = .139 FT^2 (.013 m^2)

PT. No.	P_o psia	T_o °R	P_{T8}/P_o	P_{T28}/P_o	T_{T8} °R	T_{T28} °R	V_8 Ft/Sec	V_{28} Ft/Sec	W_8 Lbs/Sec	W_{28} Lbs/Sec	V_{28}/V_8	W_{28}/W_8	V_M Ft/Sec	10 LOG ρA	10 LOG $\rho^2 A$	40 FT. ARC PEAK OASPL	PEAK OASPL ANGLE Degrees	PEAK PNL	PEAK PNL ANGLE Degrees
16	14.69	506	1.161	1.419	1297	522	806	773	1.47	8.67	.96	5.9	778	N/A	N/A	101.1	150	111.7	140
17	14.69	503	1.229	1.419	1323	522	954	773	1.8	8.67	.81	4.82	804			103.6	150	113.5	140
18	14.69	505	1.343	1.419	1308	522	1129	773	2.32	8.67	.69	3.74	848			106.8	150	116.9	140
19	14.69	506	1.472	1.421	1319	522	1291	774	2.74	8.65	.60	3.16	898			110.4	150	120.6	140
20	14.69	504	1.254	1.759	1302	522	991	967	1.88	11.71	.98	6.23	970			109.3	150	120.1	140
21	14.68	506	1.405	1.760	1317	525	1213	970	2.4	11.64	.80	4.85	1012			112.8	150	122.3	140
22	14.68	508	1.602	1.759	1302	526	1407	971	3.05	11.66	.69	3.82	1061			115.3	150	125.5	140
23	14.66	510	1.864	1.762	1307	528	1605	974	3.77	11.65	.61	3.09	1128			119.3	140	130.6	140

PT. No.	P_o N/m^2 x 10^4	T_o °K	P_{T8}/P_o	P_{T28}/P_o	T_{T8} °K	T_{T28} °K	V_8 m/Sec	V_{28} m/Sec	W_8 Kg/Sec	W_{28} Kg/Sec	V_{28}/V_8	W_{28}/W_8	V_M m/Sec	10 LOG ρA	10 LOG $\rho^2 A$	12.2 m ARC PEAK OASPL	PEAK OASPL ANGLE Radians	PEAK PNL	PEAK PNL ANGLE Radians
16	10.13	281.1	1.161	1.419	720.6	290.0	245.7	235.6	.6668	3.933	.96	5.9	237.1	N/A	N/A	101.1	2.625	111.7	2.45
17	10.13	279.4	1.229	1.419	735.0	290.0	290.8	235.6	.8165	3.933	.81	4.82	245.1			103.6	2.625	113.5	2.45
18	10.13	280.6	1.343	1.419	726.7	290.0	344.1	235.6	1.052	3.933	.69	3.74	258.5			106.8	2.625	116.9	2.45
19	10.13	281.1	1.472	1.421	732.8	290.0	393.5	235.9	1.243	3.924	.60	3.16	273.7			110.4	2.625	120.6	2.45
20	10.13	280.0	1.254	1.759	723.3	290.0	302.1	294.7	.8528	5.312	.98	6.23	295.7			109.3	2.625	120.1	2.45
21	10.12	281.1	1.405	1.760	731.7	291.7	369.7	295.7	1.089	5.280	.80	4.85	308.5			112.8	2.625	122.3	2.45
22	10.12	282.2	1.602	1.759	723.3	292.2	428.9	296.0	1.383	5.289	.69	3.82	323.4			115.3	2.625	125.5	2.45
23	10.11	283.3	1.864	1.762	726.1	293.3	489.2	296.9	1.710	5.284	.61	3.09	343.8			119.3	2.45	130.6	2.45

TABLE B-5. AREA RATIO = 4, FAN ONLY

TEST DATE: 8/22/72; RUN NO. 7

A_{28} = .272 FT^2 (.025 m^2)

PT. No.	P_o psia	T_o °R	$\frac{P_{T8}}{P_o}$	$\frac{P_{T28}}{P_o}$	T_{T8} °R	T_{T28} °R	V_8 Ft/Sec	V_{28} Ft/Sec	W_8 Lbs/Sec	W_{28} Lbs/Sec	$\frac{V_{28}}{V_8}$	$\frac{W_{28}}{W_8}$	V_M Ft/Sec	10 LOG ρA	10 LOG $\rho^2 A$	40 FT. ARC PEAK OASPL	PEAK OASPL ANGLE Degrees	PEAK PNL	PEAK PNL ANGLE Degrees
1	14.39	546	-	1.151	-	553	-	512	-	9.78	-	-	512	-17	-28.4	86.6	130	95.8	130
2	14.39	544	-	1.228	-	551	-	614	-	11.98	-	-	614	-16.9	-28.2	90.0	150	100.8	130
3	14.39	544	-	1.324	-	551	-	714	-	14.18	-	-	714	-16.8	-28.0	INSUFFICIENT DATA			
4	14.39	545	-	1.468	-	549	-	828	-	17.06	-	-	828	-16.7	-27.7	100.9	150	111.9	120
5	14.39	546	-	1.623	-	550	-	924	-	19.52	-	-	924	-16.6	-27.5	105.3	150	116.4	140
6	14.39	546	-	1.839	-	551	-	1029	-	22.67	-	-	1029	-16.4	-27.2	110.8	150	120.8	150

PT. No.	P_o $N/m^2 \times 10^4$	T_o °K	$\frac{P_{T8}}{P_o}$	$\frac{P_{T28}}{P_o}$	T_{T8} °K	T_{T28} °K	V_8 m/Sec	V_{28} m/Sec	W_8 Kg/Sec	W_{28} Kg/Sec	$\frac{V_{28}}{V_8}$	$\frac{W_{28}}{W_8}$	V_M m/Sec	10 LOG ρA	10 LOG $\rho^2 A$	12.2 m ARC PEAK OASPL	PEAK OASPL ANGLE Radians	PEAK PNL	PEAK PNL ANGLE Radians
1	9.92	303.3	-	1.151	-	307.2	-	156.1	-	4.436	-	-	156.1	-17.0	-28.4	86.6	2.275	95.8	2.275
2	9.92	302.2	-	1.228	-	306.1	-	187.1	-	5.434	-	-	187.1	-16.9	-28.2	90.0	2.625	100.8	2.275
3	9.92	302.2	-	1.324	-	306.1	-	217.6	-	6.432	-	-	217.6	-16.8	-28.0	INSUFFICIENT DATA			
4	9.92	302.8	-	1.468	-	305.0	-	252.4	-	7.738	-	-	252.4	-16.7	-27.7	100.9	2.625	111.9	2.10
5	9.92	303.3	-	1.623	-	305.6	-	281.6	-	8.854	-	-	281.6	-16.6	-27.5	105.3	2.625	116.4	2.45
6	9.92	303.3	-	1.839	-	306.1	-	313.6	-	10.283	-	-	313.6	-16.4	-27.2	110.8	2.625	120.8	2.625

TABLE B-6. AREA RATIO = 4, CORE ONLY

TEST DATE: 8/22/72; RUN NO. 7

A_8 = .069 FT^2 (.006 m^2)

PT. No.	P_o psia	T_o °R	$\frac{P_{T8}}{P_o}$	$\frac{P_{T28}}{P_o}$	T_{T8} °R	T_{T28} °R	V_8 Ft/Sec	V_{28} Ft/Sec	W_8 Lbs/Sec	W_{28} Lbs/Sec	$\frac{V_{28}}{V_8}$	$\frac{W_{28}}{W_8}$	V_M Ft/Sec	10 LOG ρA	10 LOG $\rho^2 A$	40 FT. ARC PEAK OASPL	PEAK OASPL ANGLE Degrees	PEAK PNL	PEAK PNL ANGLE Degrees
7	14.38	544	1.035	-	1051	-	352	-	.761	-	-	-	352	-25.9	-40.2				
8	14.38	543	1.102	-	1075	-	595	-	1.39	-	-	-	595	-25.9	-40.2	86.2	150	97.3	130
9	14.38	545	1.184	-	1134	-	802	-	1.82	-	-	-	802	-26.1	-40.5	95.2	150	106.1	130
10	14.38	544	1.287	-	1169	-	990	-	2.28	-	-	-	990	-26.1	-40.6	101.7	150	109.2	150
11	14.37	545	1.442	-	1220	-	1209	-	2.73	-	-	-	1209	-26.2	-40.7	109.2	150	119.9	130
12	14.37	544	1.588	-	1278	-	1382	-	3.09	-	-	-	1382	-26.3	-40.9	113.8	150	124.8	130
13	14.37	543	1.828	-	1343	-	1604	-	3.59	-	-	-	1604	-26.3	-41.0	119.6	150	132.1	150

PT. No.	P_o N/m^2 x 10^4	T_o °K	$\frac{P_{T8}}{P_o}$	$\frac{P_{T28}}{P_o}$	T_{T8} °K	T_{T28} °K	V_8 m/Sec	V_{28} m/Sec	W_8 Kg/Sec	W_{28} Kg/Sec	$\frac{V_{28}}{V_8}$	$\frac{W_{28}}{W_8}$	V_M m/Sec	10 LOG ρA	10 LOG $\rho^2 A$	12.2 m ARC PEAK OASPL	PEAK OASPL ANGLE Radians	PEAK PNL	PEAK PNL ANGLE Radians
7	9.915	302.2	1.035	-	583.9	-	107.3	-	.345	-	-	-	107.3	-25.9	-40.2				
8	9.915	301.7	1.102	-	597.2	-	181.4	-	.630	-	-	-	181.4	-25.9	-40.2	86.2	2.625	97.3	2.275
9	9.915	302.8	1.184	-	630.0	-	244.4	-	.826	-	-	-	244.4	-26.1	-40.5	95.2	2.625	106.1	2.275
10	9.915	302.2	1.287	-	649.4	-	301.8	-	1.034	-	-	-	301.8	-26.1	-40.6	101.7	2.625	109.2	2.625
11	9.908	302.8	1.442	-	677.8	-	368.5	-	1.238	-	-	-	368.5	-26.2	-40.7	109.2	2.625	119.9	2.275
12	9.908	302.2	1.588	-	710.0	-	421.2	-	1.402	-	-	-	421.2	-26.3	-40.9	113.8	2.625	124.8	2.275
13	9.908	301.7	1.828	-	746.1	-	488.9	-	1.628	-	-	-	488.9	-26.3	-41.0	119.6	2.625	132.1	2.625

TABLE B-7. AREA RATIO = 4, DUAL FLOW

TEST DATE: 8/22/72; RUN NO. 7

A_8 = .069 FT^2 (.006 m^2); A_{28} = .272 FT^2 (.025 m^2)

PT. No.	P_o psia	T_o °R	$\frac{P_{T8}}{P_o}$	$\frac{P_{T28}}{P_o}$	T_{T8} °R	T_{T28} °R	V_8 Ft/Sec	V_{28} Ft/Sec	W_8 Lbs/Sec	W_{28} Lbs/Sec	$\frac{V_{28}}{V_8}$	$\frac{W_{28}}{W_8}$	V_M Ft/Sec	10 LOG ρA	10 LOG $\rho^2 A$	40 FT. ARC PEAK OASPL	PEAK OASPL ANGLE Degrees	PEAK PNL	PEAK PNL ANGLE Degrees
14	14.38	543	1.036	1.160	1091	549	363	524	1.139	2.892	1.44	8.68	507	-	-	90.6	150	99.1	150
15	14.38	542	1.034	1.229	1018	549	341	615	.801	11.91	1.8	14.87	598	-	-	90.5	150	100.9	150
16	14.38	542	1.031	1.331	1126	549	343	720	1.082	14.16	2.1	13.08	693	-	-	96.1	150	107.0	130
20	14.38	544	1.108	1.159	1090	553	615	524	1.587	9.77	.85	6.16	537	-	-	91.2	150	99.6	140
21	14.38	544	1.112	1.230	1081	551	623	617	1.426	11.81	.99	8.28	617	-	-	92.7	150	102.8	130
22	14.38	545	1.108	1.332	1092	549	616	721	1.089	14.12	1.17	12.96	713	-	-	97.0	150	107.4	130

PT. No.	P_o N/m^2 x 10^4	T_o °K	$\frac{P_{T8}}{P_o}$	$\frac{P_{T28}}{P_o}$	T_{T8} °K	T_{T28} °K	V_8 m/Sec	V_{28} m/Sec	W_8 Kg/Sec	W_{28} Kg/Sec	$\frac{V_{28}}{V_8}$	$\frac{W_{28}}{W_8}$	V_M m/Sec	10 LOG ρA	10 LOG $\rho^2 A$	12.2 m ARC PEAK OASPL	PEAK OASPL ANGLE Radians	PEAK PNL	PEAK PNL ANGLE Radians
14	9.915	301.7	1.036	1.160	606.1	305.0	110.6	159.7	.517	4.487	1.44	8.68	154.5	-	-	90.6	2.625	99.1	2.625
15	9.915	301.1	1.034	1.229	565.6	306.0	103.9	187.5	.363	5.402	1.8	14.87	182.3	-	-	90.5	2.625	100.9	2.625
16	9.915	301.1	1.031	1.331	625.6	305.0	104.5	219.5	.491	6.423	2.1	13.08	211.2	-	-	96.1	2.625	107.0	2.275
20	9.915	302.2	1.108	1.159	605.6	307.2	187.5	159.7	.720	4.432	.85	6.16	163.7	-	-	91.2	2.625	99.6	2.45
21	9.915	302.2	1.112	1.230	600.6	306.1	189.9	188.1	.647	5.357	.99	8.28	188.1	-	-	92.7	2.625	102.8	2.275
22	9.915	302.8	1.108	1.332	606.7	305.0	187.8	219.8	.494	6.405	1.17	12.96	217.3	-	-	97.0	2.625	107.4	2.275

TABLE B-8. AREA RATIO = 4, DUAL FLOW

TEST DATE: 8/17/72; RUN NO. 5

A_8 = .069 FT^2 (.006 m^2); A_{28} = .272 FT^2 (.025 m^2)

PT. No.	P_o psia	T_o °R	$\frac{P_{T8}}{P_o}$	$\frac{P_{T28}}{P_o}$	T_{T8} °R	T_{T28} °R	V_8 Ft/Sec	V_{28} Ft/Sec	W_8 Lbs/Sec	W_{28} Lbs/Sec	$\frac{V_{28}}{V_8}$	$\frac{W_{28}}{W_8}$	V_M Ft/Sec	10 LOG ρA	10 LOG $\rho^2 A$	40 FT. ARC PEAK OASPL	PEAK OASPL ANGLE Degrees	PEAK PNL	PEAK PNL ANGLE Degrees
17	14.45	547	1.034	1.474	1063	552	349	834	1.03	17.06	2.39	16.62	807	-	-	101.1	150	112.2	140
18	14.45	547	1.023	1.620	1045	555	285	927	.66	19.37	3.25	29.25	906	-	-	105.8	150	116.4	130
19	14.44	547	1.022	1.843	1026	556	277	1035	1.41	22.56	3.74	15.96	990	-	-	110.6	150	121.0	150
23	14.43	550	1.103	1.479	1089	559	602	843	1.78	17.07	1.4	9.61	820	-	-	102.1	150	112.8	130
24	14.43	552	1.107	1.629	1086	558	612	934	1.73	19.49	1.53	11.27	908	-	-	105.7	150	116.7	130
25	14.43	549	1.096	1.841	1102	559	585	1037	1.27	22.39	1.77	17.7	1013	-	-	110.7	150	121.2	140
26	14.43	550	1.159	1.121	1132	561	750	465	2.16	8.49	.62	3.94	523	-	-	94.2	160	98.2	160

PT. No.	P_o N/m^2 x 10^4	T_o °K	$\frac{P_{T8}}{P_o}$	$\frac{P_{T28}}{P_o}$	T_{T8} °K	T_{T28} °K	V_8 m/Sec	V_{28} m/Sec	W_8 Kg/Sec	W_{28} Kg/Sec	$\frac{V_{28}}{V_8}$	$\frac{W_{28}}{W_8}$	V_M m/Sec	10 LOG ρA	10 LOG $\rho^2 A$	12.2 m ARC PEAK OASPL	PEAK OASPL ANGLE Radians	PEAK PNL	PEAK PNL ANGLE Radians
17	9.963	303.9	1.034	1.474	590.6	306.7	106.4	254.2	.467	7.738	2.39	16.62	246.0	-	-	101.1	2.625	112.2	2.45
18	9.963	303.9	1.023	1.620	580.6	308.3	86.9	282.5	.299	8.786	3.25	29.25	276.1	-	-	105.8	2.625	116.4	21275
19	9.956	303.9	1.022	1.843	570.0	308.9	84.4	315.5	.640	10.23	3.74	15.96	301.7	-	-	110.6	2.625	121.0	2.625
23	9.949	305.6	1.103	1.479	605.0	310.6	183.5	256.9	.807	7.743	1.4	9.61	249.9	-	-	102.1	2.625	112.8	2.275
24	9.949	306.7	1.107	1.629	603.3	310.0	186.5	284.7	.785	8.841	1.53	11.27	276.8	-	-	105.7	2.625	116.7	2.275
25	9.949	305.0	1.096	1.841	612.2	310.6	178.3	316.1	.576	10.16	1.77	17.7	308.8	-	-	110.7	2.625	121.2	2.45
26	9.949	305.6	1.159	1.121	628.9	311.7	228.6	141.7	.980	3.851	.62	3.94	159.4	-	-	94.2	2.8	98.2	2.8

TABLE B-9. AREA RATIO = 4, DUAL FLOW

TEST DATE: 8/17/72; RUN NO. 5

A_8 = .069 FT^2 (.006 m^2); A_{28} = .272 FT^2 (.025 m^2)

PT. No.	P_o psia	T_o °R	$\frac{P_{T8}}{P_o}$	$\frac{P_{T28}}{P_o}$	T_{T8} °R	T_{T28} °R	V_8 Ft/Sec	V_{28} Ft/Sec	W_8 Lbs/Sec	W_{28} Lbs/Sec	$\frac{V_{28}}{V_8}$	$\frac{W_{28}}{W_8}$	V_M Ft/Sec	10 LOG A	10 LOG ^2A	40 FT. ARC PEAK OASPL	PEAK OASPL ANGLE Degrees	PEAK PNL	PEAK PNL ANGLE Degrees
27	14.43	548	1.146	1.192	1128	561	720	575	1.80	10.7	.80	5.94	596	-	-	91.1	150	100.1	130
28	14.43	549	1.145	1.287	1153	560	726	684	1.66	13.18	.94	7.95	689	-	-	96.1	150	105.8	130
29	14.43	549	1.148	1.414	1134	559	726	796	1.52	15.78	1.1	10.35	790	-	-	100.7	150	110.9	130
30	14.43	550	1.154	1.620	1127	559	737	930	1.77	19.29	1.26	10.89	914	-	-	106.3	150	116.6	130
31	14.43	551	1.153	1.845	1138	563	739	1042	1.53	22.54	1.41	14.74	1023	-	-	110.9	150	120.9	150
32	14.42	553	1.297	1.152	1173	565	1006	519	2.49	9.48	.52	3.81	620	-	-	98.4	150	106.0	150
55	14.42	552	1.829	1.841	1349	561	1607	1039	3.57	22.30	.65	6.24	1117	-	-	118.6	150	126.7	150

PT. No.	P_o N/m^2 x 10^4	T_o °K	$\frac{P_{T8}}{P_o}$	$\frac{P_{T28}}{P_o}$	T_{T8} °K	T_{T28} °K	V_8 m/Sec	V_{28} m/Sec	W_8 Kg/Sec	W_{28} Kg/Sec	$\frac{V_{28}}{V_8}$	$\frac{W_{28}}{W_8}$	V_M m/Sec	10 LOG ρA	10 LOG $\rho^2 A$	12.2 m ARC PEAK OASPL	PEAK OASPL ANGLE Radians	PEAK PNL	PEAK PNL ANGLE Radians
27	9.949	304.4	1.146	1.192	626.7	311.7	219.5	175.3	.816	4.854	.80	5.94	181.7	-	-	91.1	2.625	100.1	2.275
28	9.949	305.0	1.145	1.287	640.6	311.1	221.3	208.5	.753	5.978	.94	7.95	210.0	-	-	96.1	2.625	105.8	2.275
29	9.949	305.0	1.148	1.414	630.0	310.6	221.3	242.6	.689	7.158	1.1	10.35	240.8	-	-	100.7	2.625	110.9	2.275
30	9.949	305.6	1.154	1.620	626.1	310.6	224.6	283.5	.803	8.750	1.26	10.89	278.6	-	-	106.3	2.625	116.6	2.275
31	9.949	306.1	1.153	1.845	632.2	312.8	225.2	317.6	.694	10.22	1.41	14.74	311.8	-	-	110.9	2.625	120.9	2.625
32	9.943	307.2	1.297	1.152	651.7	313.9	306.6	158.2	1.129	4.30	.52	3.81	189.0	-	-	98.4	2.625	106.0	2.625
55	9.943	306.7	1.829	1.841	749.4	311.7	489.8	316.7	1.619	10.12	.65	6.24	340.5	-	-	118.6	2.625	126.7	2.625

TABLE B-10. AREA RATIO = 4, DUAL FLOW

TEST DATE: 8/21/72; RUN NO. 6

A_8 = .069 FT^2 (.006 m^2); A_{28} = .272 FT^2 (.025 m^2)

PT. No.	P_o psia	T_o °R	P_{T8}/P_o	P_{T28}/P_o	T_{T8} °R	T_{T28} °R	V_8 Ft/Sec	V_{28} Ft/Sec	W_8 Lbs/Sec	W_{28} Lbs/Sec	V_{28}/V_8	W_{28}/W_8	V_M Ft/Sec	10 LOG ρA	10 LOG $\rho^2 A$	40 FT. ARC PEAK OASPL	PEAK OASPL ANGLE Degrees	PEAK PNL	PEAK PNL ANGLE Degrees
33	14.46	532	1.291	1.227	1179	538	1000	606	2.37	11.84	.61	5.0	672	-	-	99.2	150	107.6	140
34	14.46	534	1.276	1.325	1183	541	979	709	2.16	14.19	.72	6.58	745	-	-	101.5	150	110.0	140
35	14.46	537	1.285	1.458	1169	543	987	817	2.14	16.82	.83	7.86	833	-	-	104.9	160	114.2	130
36	14.46	534	1.294	1.615	1172	544	1001	915	2.08	19.37	.91	9.31	924	-	-	108.5	150	118.4	140
37	14.46	537	1.279	1.838	1163	546	975	1024	1.91	22.63	1.05	11.85	1020	-	-	111.8	150	121.7	140
38	14.45	546	1.433	1.148	1224	558	1201	509	2.79	9.64	.42	3.46	664	-	-	104.5	150	112.1	150
39	14.45	542	1.434	1.215	1218	557	1199	602	2.34	11.51	.50	4.92	703	-	-	105.0	160	112.4	140
40	14.46	542	1.434	1.313	1235	553	1207	705	1.99	13.89	.58	6.98	768	-	-	106.1	150	113.9	140
41	14.46	542	1.428	1.449	1233	553	1200	818	1.94	16.60	.68	8.56	858	-	-	108.3	150	116.4	150

PT. No.	P_o $N/m^2 \times 10^4$	T_o °K	P_{T8}/P_o	P_{T28}/P_o	T_{T8} °K	T_{T28} °K	V_8 m/Sec	V_{28} m/Sec	W_8 Kg/Sec	W_{28} Kg/Sec	V_{28}/V_8	W_{28}/W_8	V_M m/Sec	10 LOG ρA	10 LOG $\rho^2 A$	12.2 m ARC PEAK OASPL	PEAK OASPL ANGLE Radians	PEAK PNL	PEAK PNL ANGLE Radians
33	9.97	295.6	1.291	1.227	655.0	298.9	304.8	184.7	1.075	5.371	.61	5.0	204.8	-	-	99.2	2.625	107.6	2.45
34	9.97	296.7	1.276	1.325	657.2	300.6	298.4	216.1	.980	6.437	.72	6.58	227.1	-	-	101.5	2.625	110.0	2.45
35	9.97	298.3	1.285	1.458	649.4	301.7	300.8	249.0	.971	7.629	.83	7.86	253.9	-	-	104.9	2.80	114.2	2.275
36	9.97	296.7	1.294	1.615	651.1	302.2	305.1	278.9	.943	8.786	.91	9.31	281.6	-	-	108.5	2.625	118.4	2.45
37	9.97	298.3	1.279	1.838	646.1	303.3	297.2	312.1	.866	10.265	1.05	11.85	310.9	-	-	111.8	2.625	121.7	2.45
38	9.963	303.3	1.433	1.148	680.0	310.0	366.1	155.1	1.266	4.373	.42	3.46	202.4	-	-	104.5	2.625	112.1	2.625
39	9.963	301.1	1.434	1.215	676.7	309.4	365.5	183.5	1.061	5.221	.50	4.92	214.3	-	-	105.0	2.80	112.4	2.45
40	9.97	301.1	1.434	1.313	686.1	307.2	367.9	214.9	.903	6.300	.58	6.98	234.1	-	-	106.1	2.625	113.9	2.45
41	9.97	301.1	1.428	1.449	685.0	307.2	365.8	249.3	.880	7.530	.68	8.56	261.5	-	-	108.3	2.625	116.4	2.625

TABLE B-11. AREA RATIO = 4, DUAL FLOW

TEST DATE: 8/21/72; RUN NO. 6

A_8 = .069 FT^2 (.006 m^2); A_{28} = .272 FT^2 (.025 m^2)

PT. NO.	P_o psia	T_o °R	P_{T8}/P_o	P_{T28}/P_o	T_{T8} °R	T_{T28} °R	V_8 Ft/Sec	V_{28} Ft/Sec	W_8 Lbs/Sec	W_{28} Lbs/Sec	V_{28}/V_8	W_{28}/W_8	V_M Ft/Sec	10 LOG ρA	10 LOG $\rho^2 A$	40 FT. ARC PEAK OASPL	PEAK OASPL ANGLE Degrees	PEAK PNL	PEAK PNL ANGLE Degrees
42	14.45	542	1.437	1.608	1220	553	1203	919	2.26	19.31	.76	8.54	948	-	-	111.1	150	119.4	150
43	14.45	546	1.426	1.822	1228	554	1195	1024	2.47	22.44	.86	9.09	1041	-	-	114.4	150	122.6	150
44	14.45	544	1.60	1.148	1277	562	1392	511	3.11	9.52	.37	3.06	728	-	-	109.9	150	118.4	150
45	14.45	543	1.595	1.219	1271	562	1384	610	3.09	11.42	.44	3.70	775	-	-	109.8	150	118.2	130
46	14.44	546	1.605	1.315	1268	562	1391	713	3.08	13.85	.51	4.48	837	-	-	110.5	150	118.4	150
47	14.44	546	1.595	1.447	1280	560	1389	821	2.99	16.46	.59	5.51	908	-	-	111.5	150	119.3	130
48	14.44	549	1.594	1.618	1266	559	1381	929	2.96	19.15	.67	6.47	990	-	-	113.7	150	121.5	150
49	14.44	546	1.596	1.834	1274	558	1387	1033	2.90	22.41	.74	7.73	1074	-	-	116.1	150	123.9	150
50	14.44	544	1.819	1.151	1339	563	1595	516	3.51	9.50	.32	2.71	807	-	-	115.4	150	125.9	150

PT. NO.	P_o N/m^2 x 10^4	T_o °K	P_{T8}/P_o	P_{T28}/P_o	T_{T8} °K	T_{T28} °K	V_8 m/Sec	V_{28} m/Sec	W_8 Kg/Sec	W_{28} Kg/Sec	V_{28}/V_8	W_{28}/W_8	V_M m/Sec	10 LOG ρA	10 LOG $\rho^2 A$	12.2 m ARC PEAK OASPL	PEAK OASPL ANGLE Radians	PEAK PNL	PEAK PNL ANGLE Radians
42	9.963	301.1	1.437	1.608	677.8	307.2	366.7	280.1	1.025	8.759	.76	8.54	288.9	-	-	111.1	2.625	119.4	2.625
43	9.963	303.3	1.426	1.822	682.2	307.8	364.2	312.1	1.120	10.179	.86	9.09	317.3	-	-	114.4	2.625	122.6	2.625
44	9.963	302.2	1.60	1.148	709.4	312.2	424.3	155.8	1.411	4.318	.37	3.06	221.9	-	-	109.9	2.625	118.4	2.625
45	9.963	301.7	1.595	1.219	706.1	312.2	421.8	185.9	1.402	5.180	.44	3.70	236.2	-	-	109.8	2.625	118.2	2.275
46	9.956	303.3	1.605	1.315	704.4	312.2	424.0	217.3	1.397	6.282	.51	4.48	255.1	-	-	110.5	2.625	118.4	2.625
47	9.956	303.3	1.595	1.447	711.1	311.1	423.4	250.2	1.356	7.466	.59	5.51	276.8	-	-	111.5	2.625	119.3	2.275
48	9.956	305.0	1.594	1.618	703.3	310.6	420.9	283.2	1.343	8.686	.67	6.47	301.8	-	-	113.7	2.625	121.5	2.625
49	9.956	303.3	1.596	1.834	707.8	310.0	422.8	314.9	1.315	10.165	.74	7.73	327.4	-	-	116.1	2.625	123.9	2.625
50	9.956	302.2	1.819	1.151	743.9	312.8	486.2	157.3	1.592	4.309	.32	2.71	246.0	-	-	115.4	2.625	125.9	2.625

TABLE B-12. AREA RATIO = 4, DUAL FLOW

TEST DATE: 8/21/72; RUN NO. 6

A_8 = .069 FT^2 (.006 m^2); A_{28} = .272 FT^2 (.025 m^2)

PT. No.	P_o psia	T_o °R	$\frac{P_{T8}}{P_o}$	$\frac{P_{T28}}{P_o}$	T_{T8} °R	T_{T28} °R	V_8 Ft/Sec	V_{28} Ft/Sec	W_8 Lbs/Sec	W_{28} Lbs/Sec	$\frac{V_{28}}{V_8}$	$\frac{W_{28}}{W_8}$	V_M Ft/Sec	10 LOG ρA	10 LOG $\rho^2 A$	40 FT. ARC PEAK OASPL	PEAK OASPL ANGLE Degrees	PEAK PNL	PEAK PNL ANGLE Degrees
51	14.44	546	1.817	1.223	1339	562	1594	615	3.51	11.51	.39	3.28	843	-	-	115.1	150	125.0	150
52	14.44	546	1.800	1.323	1345	560	1586	719	3.45	13.84	.45	4.01	892	-	-	114.7	150	124.3	150
53	14.44	546	1.822	1.454	1339	559	1597	826	3.51	16.44	.52	4.68	962	-	-	115.6	150	124.4	150
54	14.44	545	1.823	1.623	1347	558	1603	931	3.51	19.20	.58	5.47	1035	-	-	116.9	150	124.9	140
56	14.43	547	1.189	1.151	1659	556	982	518	1.37	9.51	.53	6.94	576	-	-	97.7	150	105.4	130
57	14.43	549	1.194	1.224	1649	567	991	619	1.41	11.49	.62	8.15	659	-	-	99.5	150	107.5	130
58	14.43	547	1.189	1.321	1662	568	983	723	1.34	13.77	.73	10.30	746	-	-	101.9	150	110.0	130
59	14.43	547	1.191	1.458	1657	567	986	834	1.28	16.31	.85	12.70	845	-	-	105.9	150	114.4	130
60	14.43	550	1.192	1.623	1627	566	980	938	1.28	18.98	.96	14.83	941	-	-	109.1	150	117.9	130

PT. No.	P_o N/m^2 x 10^4	T_o °K	$\frac{P_{T8}}{P_o}$	$\frac{P_{T28}}{P_o}$	T_{T8} °K	T_{T28} °K	V_8 m/Sec	V_{28} m/Sec	W_8 Kg/Sec	W_{28} Kg/Sec	$\frac{V_{28}}{V_8}$	$\frac{W_{28}}{W_8}$	V_M m/Sec	10 LOG ρA	10 LOG $\rho^2 A$	12.2 m ARC PEAK OASPL	PEAK OASPL ANGLE Radians	PEAK PNL	PEAK PNL ANGLE Radians
51	9.956	303.3	1.817	1.223	743.9	312.2	485.9	187.5	1.592	5.221	.39	3.28	256.9	-	-	115.1	2.625	125.0	2.625
52	9.956	303.3	1.800	1.323	747.2	311.1	483.4	219.2	1.565	6.278	.45	4.01	271.9	-	-	114.7	2.625	124.3	2.625
53	9.956	303.3	1.822	1.454	743.9	310.6	486.8	251.8	1.592	7.457	.52	4.68	293.2	-	-	115.6	2.625	124.4	2.625
54	9.956	302.8	1.823	1.623	748.3	310.0	488.6	283.8	1.592	8.709	.58	5.47	315.5	-	-	116.9	2.625	124.9	2.45
56	9.949	303.9	1.189	1.151	921.7	308.9	299.3	157.9	.621	4.314	.53	6.94	175.6	-	-	97.7	2.625	105.4	2.275
57	9.949	305.0	1.194	1.224	916.1	315.0	302.1	188.7	.640	5.212	.62	8.15	200.9	-	-	99.5	2.625	107.5	2.275
58	9.949	303.9	1.189	1.321	923.3	315.6	299.6	220.4	.608	6.246	.73	10.30	227.4	-	-	101.9	2.625	110.0	2.275
59	9.949	303.9	1.191	1.458	920.6	315.0	300.5	254.2	.581	7.398	.85	12.70	257.6	-	-	105.9	2.625	114.4	2.275
60	9.949	305.6	1.192	1.623	903.9	314.4	298.7	285.9	.581	8.609	.96	14.83	286.8	-	-	109.1	2.625	117.9	2.275

TABLE B-13. AREA RATIO = 4, DUAL FLOW

TEST DATE: 8/21/72; RUN NO. 6

A_8 = .069 FT^2 (.006 m^2); A_{28} = .272 FT^2 (.025 m^2)

PT. No.	P_o psia	T_o °R	$\frac{P_{T8}}{P_o}$	$\frac{P_{T28}}{P_o}$	T_{T8} °R	T_{T28} °R	V_8 Ft/Sec	V_{28} Ft/Sec	W_8 Lbs/Sec	W_{28} Lbs/Sec	$\frac{V_{28}}{V_8}$	$\frac{W_{28}}{W_8}$	V_M Ft/Sec	10 LOG ρA	10 LOG $\rho^2 A$	40 FT. ARC PEAK OASPL	PEAK OASPL ANGLE Degrees	PEAK PNL	PEAK PNL ANGLE Degrees
61	14.43	548	1.193	1.838	1652	564	990	1040	1.19	22.28	1.05	18.73	1038	-	-	112.5	150	121.5	130
62	14.41	548	1.385	1.146	916	561	990	507	2.92	9.5	.51	3.25	621	-	-	97.7	150	105.7	130
63	14.42	548	1.381	1.222	912	562	983	613	2.91	11.63	.62	3.99	687	-	-	98.6	150	106.8	140
64	14.42	548	1.379	1.322	911	562	981	720	2.88	13.94	.73	4.84	765	-	-	101.9	160	109.9	130
65	14.42	549	1.388	1.462	917	561	994	833	2.76	16.74	.84	6.07	856	-	-	105.2	150	113.9	130
66	14.42	550	1.384	1.621	910	561	986	932	2.65	19.36	.95	7.31	939	-	-	108.4	160	117.7	130
67	14.42	549	1.383	1.831	906	562	982	1036	2.59	22.28	1.05	8.6	1030	-	-	112.1	160	121.4	150
68	14.41	549	1.412	1.701	1213	562	1172	975	2.43	20.51	.83	8.44	996	-	-	113.6	150	121.9	130
69	14.41	547	1.177	1.397	1161	562	797	784	1.72	15.60	.98	9.07	786	-	-	101.3	150	110.9	130
70	14.41	548	1.088	1.250	1088	562	558	646	1.61	12.40	1.16	7.70	636	-	-	92.7	150	103.6	130

PT. No.	P_o N/m^2 x 10^4	T_o °K	$\frac{P_{T8}}{P_o}$	$\frac{P_{T28}}{P_o}$	T_{T8} °K	T_{T28} °K	V_8 m/Sec	V_{28} m/Sec	W_8 Kg/Sec	W_{28} Kg/Sec	$\frac{V_{28}}{V_8}$	$\frac{W_{28}}{W_8}$	V_M m/Sec	10 LOG ρA	10 LOG $\rho^2 A$	12.2 m ARC PEAK OASPL	PEAK OASPL ANGLE Radians	PEAK PNL	PEAK PNL ANGLE Radians
61	9.949	304.4	1.193	1.838	917.8	313.3	301.8	317.0	.540	10.106	1.05	18.73	316.4	-	-	112.5	2.625	121.5	2.275
62	9.936	304.4	1.385	1.146	508.9	311.7	301.8	154.5	1.325	4.309	.51	3.25	189.3	-	-	97.7	2.625	105.7	2.275
63	9.943	304.4	1.381	1.222	506.7	312.2	299.6	186.8	1.320	5.275	.62	3.99	209.4	-	-	98.6	2.625	106.8	2.45
64	9.943	304.4	1.379	1.322	506.1	312.2	299.0	219.5	1.306	6.323	.73	4.84	233.2	-	-	101.9	2.80	109.9	2.275
65	9.943	305.0	1.388	1.462	509.4	311.7	303.0	253.9	1.252	7.593	.84	6.07	260.9	-	-	105.2	2.625	113.9	2.275
66	9.943	305.6	1.384	1.621	505.6	311.7	300.5	284.1	1.202	8.782	.95	7.31	286.2	-	-	108.4	2.80	117.7	2.275
67	9.943	305.0	1.383	1.831	503.3	312.2	299.3	315.8	1.175	10.106	1.05	8.6	313.9	-	-	112.1	2.80	121.4	2.625
68	9.936	305.0	1.412	1.701	673.9	312.2	357.2	297.2	1.102	9.303	.83	8.44	303.6	-	-	113.6	2.625	121.9	2.275
69	9.936	303.9	1.177	1.397	645.0	312.2	242.9	239.0	.780	7.076	.98	9.07	239.6	-	-	101.3	2.625	110.9	2.275
70	9.936	304.4	1.088	1.250	604.4	312.2	170.1	196.9	.730	5.625	1.16	7.70	193.9	-	-	92.7	2.625	103.6	2.275

TABLE B-14. AREA RATIO = 6

TEST DATE: 10/6/72 & 10/20/72; RUN NO. 3 & 5

A_8 = .069 FT^2 (.006 m^2); A_{28} = .416 FT^2 (.039 m^2)

	PT. No.	P_o psia	T_o °R	P_{T8}/P_o	P_{T28}/P_o	T_{T8} °R	T_{T28} °R	V_8 Ft/Sec	V_{28} Ft/Sec	W_8 Lbs/Sec	W_{28} Lbs/Sec	V_{28}/V_8	W_{28}/W_8	V_M Ft/Sec	10 LOG ρA	10 LOG $\rho^2 A$	40 FT. ARC PEAK OASPL	PEAK OASPL ANGLE Degrees	PEAK PNL	PEAK PNL ANGLE Degrees
RUN NO. 3 10/6/72	4	14.40	524	1.266	-	1312	-	1014	-	2.04	-	-	-	1014	-26.6	-41.6	102.4	150	113.5	130
	5	14.40	527	1.404	-	1316	-	1212	-	2.58	-	-	-	1212	-26.5	-41.4	109.0	150	120.1	130
	6	14.40	524	1.600	-	1326	-	1418	-	3.12	-	-	-	1418	-26.4	-41.2	115.3	150	126.1	140
	7	14.40	525	1.855	-	1343	-	1622	-	3.80	-	-	-	1622	-26.3	-41.0	120.7	150	132.9	150
RUN NO. 5 10/20/72	8	14.64	511	1.036	1.094	1320	534	397	404	.574	11.92	1.02	20.77	404	-	-	83.3	150	91.9	140
	9	14.64	511	1.056	1.095	1323	534	498	406	.799	11.92	.82	14.92	412	-	-	82.0	150	91.9	140
	10	14.64	512	1.076	1.094	1330	534	576	404	.991	11.92	.70	12.03	417	-	-	83.3	150	92.4	140
	11	14.64	513	1.109	1.095	1310	534	676	406	1.15	11.90	.60	10.35	430	-	-	86.3	150	94.2	140
	12	14.63	512	1.069	1.198	1320	532	549	567	.86	17.52	1.03	20.37	566	-	-		NO ACOUSTIC DATA		
RUN NO. 3 10/6/72	13	14.38	530	1.143	1.224	1323	551	772	609	1.23	17.23	.79	14.01	620	-	-	94.8	150	104.3	120

PT. No.	P_o N/m^2 x 10^4	T_o °K	P_{T8}/P_o	P_{T28}/P_o	T_{T8} °K	T_{T28} °K	V_8 m/Sec	V_{28} m/Sec	W_8 Kg/Sec	W_{28} Kg/Sec	V_{28}/V_8	W_{28}/W_8	V_M m/Sec	10 LOG ρA	10 LOG $\rho^2 A$	12.2 m ARC PEAK OASPL	PEAK OASPL ANGLE Radians	PEAK PNL	PEAK PNL ANGLE Radians
4	9.929	291.1	1.266	-	728.9	-	309.1	-	.925	-	-	-	309.1	-26.6	-41.6	102.4	2.625	113.5	2.275
5	9.929	292.8	1.404	-	731.1	-	369.4	-	1.170	-	-	-	369.4	-26.5	-41.4	109.0	2.625	120.1	2.275
6	9.929	291.1	1.600	-	736.7	-	432.2	-	1.415	-	-	-	432.2	-26.4	-41.2	115.3	2.625	126.1	2.45
7	9.929	291.7	1.855	-	746.1	-	494.4	-	1.724	-	-	-	494.4	-26.3	-41.0	120.7	2.625	132.9	2.625
8	10.094	283.9	1.036	1.094	733.3	296.7	121.0	123.1	.260	5.407	1.02	20.77	123.1	-	-	83.3	2.625	91.9	2.45
9	10.094	283.9	1.056	1.095	735.0	296.7	151.8	123.7	.362	5.407	.82	14.92	125.6	-	-	82.0	2.625	91.9	2.45
10	10.094	284.4	1.076	1.094	738.9	296.7	175.6	123.1	.449	5.407	.70	12.03	127.1	-	-	83.3	2.625	92.4	2.45
11	10.094	285.0	1.109	1.095	727.8	296.7	206.0	123.7	.522	5.398	.60	10.35	131.1	-	-	86.3	2.625	94.2	2.45
12	10.087	284.4	1.069	1.198	733.3	295.6	167.3	172.8	.390	7.947	1.03	20.37	172.5	-	-		NO ACOUSTIC DATA		
13	9.915	294.4	1.143	1.224	735.0	306.1	235.3	185.6	.558	7.816	.79	14.01	189.0	-	-	94.8	2.625	104.3	2.10

TABLE B-15. AREA RATIO = 6, DUAL FLOW

TEST DATE: 10/6/72; RUN NO. 3

A_8 = .069 FT^2 (.006 m^2); A_{28} = .416 FT^2 (.039 m^2)

PT. No.	P_o psia	T_o °R	$\frac{P_{T8}}{P_o}$	$\frac{P_{T28}}{P_o}$	T_{T8} °R	T_{T28} °R	V_8 Ft/Sec	V_{28} Ft/Sec	W_8 Lbs/Sec	W_{28} Lbs/Sec	$\frac{V_{28}}{V_8}$	$\frac{W_{28}}{W_8}$	V_M Ft/Sec	10 LOG ρA	10 LOG $\rho^2 A$	40 FT. ARC PEAK OASPL	PEAK OASPL ANGLE Degrees	PEAK PNL	PEAK PNL ANGLE Degrees
14	14.37	529	1.173	1.224	1311	550	839	610	1.44	17.25	.73	11.98	628	-	-	96.1	150	105.0	140
15	14.37	530	1.254	1.225	1320	549	999	610	1.78	17.29	.61	9.71	646	-	-	97.9	150	106.6	140
16	14.38	529	1.163	1.429	1323	553	820	803	1.23	23.54	.98	19.14	804	-	-	104.2	150	114.7	140
17	14.38	529	1.247	1.432	1309	554	982	806	1.66	23.51	.82	14.16	818	-	-	105.6	150	115.2	140
18	14.38	530	1.350	1.434	1308	554	1139	807	2.13	23.48	.71	11.02	835	-	-	107.4	150	115.9	150
19	14.38	531	1.513	1.436	1334	552	1341	807	2.69	23.4	.60	8.70	862	-	-	109.8	150	118.1	140
20	14.39	529	1.267	1.774	1337	551	1026	1000	1.54	31.16	.975	20.23	1001	-	-	113.5	150	123.0	140
21	14.39	531	1.403	1.769	1323	553	1213	1000	2.13	31.06	.824	14.58	1014	-	-	114.6	150	123.2	140
22	14.39	529	1.576	1.769	1313	552	1390	999	2.75	31.03	.719	11.28	1031	-	-	116.1	150	124.4	150
23	14.38	528	1.860	1.775	1326	554	1614	1003	3.56	30.87	.621	8.67	1066	-	-	118.8	150	126.9	140

PT. No.	P_o N/m^2 x 10^4	T_o °K	$\frac{P_{T8}}{P_o}$	$\frac{P_{T28}}{P_o}$	T_{T8} °K	T_{T28} °K	V_8 m/Sec	V_{28} m/Sec	W_8 Kg/Sec	W_{28} Kg/Sec	$\frac{V_{28}}{V_8}$	$\frac{W_{28}}{W_8}$	V_M m/Sec	10 LOG ρA	10 LOG $\rho^2 A$	12.2 m ARC PEAK OASPL	PEAK OASPL ANGLE Radians	PEAK PNL	PEAK PNL ANGLE Radians
14	9.908	293.9	1.173	1.224	728.3	305.6	255.7	185.9	.653	7.825	.73	11.98	191.4	-	-	96.1	2.625	105.0	2.45
15	9.908	294.4	1.254	1.225	733.3	305.0	304.5	185.9	.807	7.843	.61	9.71	196.9	-	-	97.9	2.625	106.6	2.45
16	9.915	293.9	1.163	1.429	735.0	307.2	249.9	244.8	.558	10.678	.98	19.14	245.0	-	-	104.2	2.625	114.7	2.45
17	9.915	293.9	1.247	1.432	727.2	307.8	299.3	245.7	.753	10.664	.82	14.16	249.3	-	-	105.6	2.625	115.2	2.45
18	9.915	294.4	1.350	1.434	726.7	307.8	347.2	246.0	.966	10.650	.71	11.02	254.5	-	-	107.4	2.625	115.9	2.625
19	9.915	295.0	1.513	1.436	741.1	306.7	408.7	246.0	1.220	10.614	.60	8.70	262.7	-	-	109.8	2.625	118.1	2.45
20	9.922	293.9	1.267	1.774	742.8	306.1	312.7	304.8	.698	14.134	.975	20.23	305.1	-	-	113.5	2.625	123.0	2.45
21	9.922	295.0	1.403	1.769	735.0	307.2	369.7	304.8	.966	14.089	.824	14.58	309.1	-	-	114.6	2.625	123.2	2.45
22	9.922	293.9	1.576	1.769	729.4	306.7	423.7	304.5	1.247	14.075	.719	11.28	314.2	-	-	116.1	2.625	124.4	2.625
23	9.915	293.3	1.860	1.775	736.7	307.8	491.9	305.7	1.615	14.003	.621	8.67	324.9	-	-	118.8	2.625	126.9	2.45

TABLE B-16. AREA RATIO = 6, DUAL FLOW

TEST DATE: 10/5/72; RUN NO. 2

A_8 = .069 FT^2 (.006 m^2); A_{28} = .555 FT^2 (.052 m^2)

PT. No.	P_o psia	T_o °R	P_{T8}/P_o	P_{T28}/P_o	T_{T8} °R	T_{T28} °R	V_8 Ft/Sec	V_{28} Ft/Sec	W_8 Lbs/Sec	W_{28} Lbs/Sec	V_{28}/V_8	W_{28}/W_8	V_M Ft/Sec	10 LOG ρA	10 LOG $\rho^2 A$	40 FT. ARC PEAK OASPL	PEAK OASPL ANGLE Degrees	PEAK PNL	PEAK PNL ANGLE Degrees
8	14.47	529	1.038	1.086	1319	548	410	392	-	14.41	.96	-	-	-	-	82.3	150	91.5	140
9	14.47	525	1.054	1.088	1270	551	477	397	.773	14.39	.83	18.62	401	-	-	80.1	140	91.2	140
10	14.47	530	1.07	1.088	1279	554	542	398	.888	14.39	.73	16.21	406	-	-	80.8	140	91.7	140
11	14.47	526	1.099	1.088	1276	555	638	399	1.15	14.38	.625	12.51	417	-	-	82.9	160	93.0	140
12	14.47	526	1.083	1.202	1288	554	591	584	.828	21.79	.988	26.3	584	-	-	91.5	140	103.5	140
13	14.48	525	1.122	1.205	1272	555	704	588	.999	-	.835	-	-	-	-	92.3	140	104.3	140
14	14.48	524	1.163	1.206	1279	555	806	590	1.361	21.83	.732	16.04	603	-	-	94.2	160	104.8	140
15	14.47	527	1.229	1.208	1273	554	937	592	1.75	21.84	.632	12.48	618	-	-	95.5	150	105.7	140

PT. No.	P_o $N/m^2 \times 10^4$	T_o °K	P_{T8}/P_o	P_{T28}/P_o	T_{T8} °K	T_{T28} °K	V_8 m/Sec	V_{28} m/Sec	W_8 Kg/Sec	W_{28} Kg/Sec	V_{28}/V_8	W_{28}/W_8	V_M m/Sec	10 LOG ρA	10 LOG $\rho^2 A$	12.2 m ARC PEAK OASPL	PEAK OASPL ANGLE Radians	PEAK PNL	PEAK PNL ANGLE Radians
8	9.977	293.9	1.038	1.086	732.8	304.4	125.0	119.5	-	6.536	.96	-	-	-	-	82.3	2.625	91.5	2.45
9	9.977	291.7	1.054	1.088	705.6	306.1	145.4	121.0	.351	6.527	.83	18.62	122.2	-	-	80.1	2.45	91.2	2.45
10	9.977	294.4	1.07	1.088	710.6	307.8	165.2	121.3	.403	6.527	.73	16.21	123.7	-	-	80.8	2.45	91.7	2.45
11	9.977	292.2	1.099	1.088	708.9	308.3	194.5	121.6	.522	6.523	.625	12.51	127.1	-	-	82.9	2.80	93.0	2.45
12	9.977	292.2	1.083	1.202	715.6	307.8	180.1	178.0	.376	9.884	.988	26.3	178.0	-	-	91.5	2.45	103.5	2.45
13	9.984	291.7	1.122	1.205	706.7	308.3	214.6	179.2	.453	-	.835	-	-	-	-	92.3	2.45	104.3	2.45
14	9.984	291.1	1.163	1.206	710.6	308.3	245.7	179.8	.617	9.902	.732	16.04	183.8	-	-	94.2	2.80	104.8	2.45
15	9.977	292.8	1.229	1.208	707.2	307.8	285.6	180.4	.794	9.907	.632	12.48	188.4	-	-	95.5	2.625	105.7	2.45

TABLE B-17. AREA RATIO = 8, DUAL FLOW

TEST DATE: 10/5/72; RUN NO. 2

A_8 = .069 FT^2 (.006 m^2); A_{28} = .555 FT^2 (.052 m^2)

PT. No.	P_o psia	T_o °R	$\frac{P_{T8}}{P_o}$	$\frac{P_{T28}}{P_o}$	T_{T8} °R	T_{T28} °R	V_8 Ft/Sec	V_{28} Ft/Sec	W_8 Lbs/Sec	W_{28} Lbs/Sec	$\frac{V_{28}}{V_8}$	$\frac{W_{28}}{W_8}$	V_M Ft/Sec	10 LOG ρA	10 LOG $\rho^2 A$	40 FT. ARC PEAK OASPL	PEAK OASPL ANGLE Degrees	PEAK PNL	PEAK PNL ANGLE Degrees
16	14.48	525	1.153	1.405	1278	553	783	785	1.125	30.18	1.00	26.83	785	-	-	102.2	140	-	-
17	14.48	524	1.233	1.408	1276	553	945	787	1.58	30.2	.833	19.1	795	-	-	103.6	160	-	-
18	14.48	523	1.324	1.410	1275	550	1088	786	2.02	30.41	.722	15.06	805	-	-	104.6	160	-	-
19	14.49	524	1.491	1.418	1293	547	1297	790	2.62	30.59	.609	11.68	830	-	-	107.2	150	-	-
20	14.49	519	1.26	1.729	1269	554	988	982	1.45	40.59	.994	28.0	982	-	-	111.9	160	122.7	140
21	14.50	522	1.398	1.729	1280	552	1187	980	2.13	40.54	.826	19.0	990	-	-	112.9	150	122.8	140
22	14.50	522	1.551	1.733	1297	553	1359	983	2.61	40.55	.723	15.54	1006	-	-	114.3	160	123.5	140
23	14.50	523	1.839	1.717	1279	554	1572	976	3.6	39.66	.621	11.02	1026	-	-	116.5	150	125.3	140

PT. No.	P_o N/m^2 x 10^4	T_o °K	$\frac{P_{T8}}{P_o}$	$\frac{P_{T28}}{P_o}$	T_{T8} °K	T_{T28} °K	V_8 m/Sec	V_{28} m/Sec	W_8 Kg/Sec	W_{28} Kg/Sec	$\frac{V_{28}}{V_8}$	$\frac{W_{28}}{W_8}$	V_M m/Sec	10 LOG ρA	10 LOG $\rho^2 A$	12.2 m ARC PEAK OASPL	PEAK OASPL ANGLE Radians	PEAK PNL	PEAK PNL ANGLE Radians
16	9.984	291.7	1.153	1.405	710.0	307.2	238.7	239.3	.510	13.690	1.00	26.83	239.3	-	-	102.2	2.45	-	-
17	9.984	291.1	1.233	1.408	708.9	307.2	288.0	239.9	.717	13.699	.833	19.1	242.3	-	-	103.6	2.80	-	-
18	9.984	290.6	1.324	1.410	708.3	305.6	331.6	239.6	.916	13.794	.722	15.06	245.4	-	-	104.6	2.80	-	-
19	9.991	291.1	1.491	1.418	718.3	303.9	395.3	240.8	1.188	13.876	.609	11.68	253.0	-	-	107.2	2.625	-	-
20	9.991	288.3	1.260	1.729	705.0	307.8	301.1	299.3	.658	18.412	.994	28.0	299.3	-	-	111.9	2.80	122.7	2.45
21	9.998	290.0	1.398	1.729	711.1	306.7	361.8	298.7	.966	18.389	.826	19.0	301.8	-	-	112.9	2.625	122.8	2.45
22	9.998	290.0	1.551	1.733	720.6	307.2	414.2	299.6	1.184	18.393	.723	15.54	306.6	-	-	114.3	2.80	123.5	2.45
23	9.998	290.6	1.839	1.717	710.6	307.8	479.1	297.5	1.633	17.990	.621	11.02	312.7	-	-	116.5	2.625	125.3	2.45

APPENDIX C

SUPPRESSOR TESTS AERO DATA

TABLE C-1 LOW VELOCITY JET NOISE SUPPRESSOR TEST I

BASELINE I

SCALE FACTOR 7.5

DATA PT	P_T/P_0	P_{T28}/P_0	A_{28}/A_8	V_{28}/V_8	W_8	W_{28}	W_T	F_8	F_{28}	F_T	A_8	A_{28}	$10\log \rho_8 A_8$	$10\log \rho_{28} A_{28}$	$10\log \rho^2 A_8$	$10\log \rho^2 A_{28}$
	COMMON DATA				SCALE MODEL DATA											
					← lbs/sec →			← lbs →			← ft^2 →					
1	1.061	-	-	-	1.68	-	1.68	24.6	-	24.6	.0985	-	-24.5	-	-38.8	-
2	1.116	-	-	-	2.23	-	2.23	45.9	-	45.9	.0985	-	-24.7	-	-39.3	-
3	1.211	-	-	-	2.89	-	2.89	81.	-	81.	.0985	-	-24.9	-	-39.8	-
4	1.403	-	-	-	3.76	-	3.76	146.	-	146.	.0985	-	-25.2	-	-40.3	-
5	1.589	-	-	-	4.37	-	4.37	203	-	203	.0985	-	-25.3	-	-40.6	-
6	1.693	-	-	-	4.65	-	4.65	233	-	233	.0985	-	-25.6	-	-40.7	-
7	-	1.129	-	-	-	10.87	10.87	-	159	159	-	.308	-	-16.3	-	-27.6
8	-	1.214	-	-	-	13.97	13.97	-	257	257	-	.308	-	-16.3	-	-27.4
9	-	1.335	-	-	-	17.39	17.39	-	389	389	-	.308	-	-16.1	-	-27.2
10	-	1.532	-	-	-	21.71	21.71	-	586	586	-	.308	-	-16.0	-	-26.9
	V_8	V_{28}	T_8	T_{28}	FULL SCALE DATA											
	← ft/sec →		← °R →													
1	469	-	1090	-	94.5	-	94.5	1413	-	1413	5.66	-	-6.9	-	-21.2	-
2	658	-	1166	-	128	-	128	2638	-	2638	5.66	-	-7.1	-	-21.7	-
3	897	-	1254	-	166	-	166	4652	-	4652	5.66	-	-7.3	-	-22.2	-
4	1241	-	1385	-	216	-	216	8388	-	8388	5.66	-	-7.6	-	-22.7	-
5	1487	-	1475	-	251	-	251	11657	-	11657	5.66	-	-7.7	-	-23.0	-
6	1599	-	1513	-	267	-	267	13361	-	13361	5.66	-	-8.0	-	-23.1	-
7	-	469	-	537	-	625	625	-	9156	9156	-	17.279	-	1.3	-	-10.0
8	-	589	-	536	-	803	803	-	14788	14788	-	17.279	-	1.3	-	-9.8
9	-	716	-	538	-	1000	1000	-	22338	22338	-	17.279	-	1.5	-	-9.6
10	-	863	-	540	-	1249	1247	-	33647	33647	-	17.279	-	1.6	-	-9.3

TABLE C-2 LOW VELOCITY JET NOISE SUPPRESSOR TEST I

SCALE FACTOR 7.5

BASELINE I

DATA PT	P_T/P_0	P_{T28}/P_0	A_{28}/A_8	V_{28}/V_8	W_8	W_{28}	W_T	F_8	F_{28}	F_T	A_8	A_{28}	$10\log \rho_8 A_8$	$10\log \rho_{28} A_{28}$	$10\log \rho_8^2 A_8$	$10\log \rho_{28}^2 A_{28}$
					lbs/sec			lbs			ft^2					
COMMON DATA					SCALE MODEL DATA											
11	-	1.651	-	-	-	23.93	23.93	-	695	695	-	.308	-	-15.9	-	-26.7
12	-	1.692	-	-	-	24.62	24.62	-	732	732	-	.308	-	-15.9	-	-26.6
13	1.062	1.122	3.13	.97	1.69	10.56	12.25	24.97	151	176	.0985	.308	-24.5	-16.4	-38.9	-27.6
14	1.117	1.212	3.13	.89	2.24	13.87	16.11	46.2	255	301.2	.0985	.308	-24.7	-16.3	-39.3	-27.4
15	1.221	1.333	3.13	.78	2.95	17.29	20.24	84.4	386	470.4	.0985	.308	-24.9	-16.2	-39.7	-27.2
16	1.398	1.527	3.31	.70	3.75	21.6	24.35	144	580	724	.0985	.308	-25.2	-16.0	-40.3	-26.7
17	1.602	1.654	3.13	.62	4.42	23.94	28.36	206	698	904	.0985	.308	-25.3	-15.9	-40.5	-26.7
18	1.699	1.701	3.13	.60	4.65	24.61	29.26	234	740	974	.0985	.308	-25.4	-15.9	-40.7	-26.7
19	1.696	1.439	3.13	.50	4.65	19.66	24.31	233	495	728	.0985	.308	-25.4	-16.1	-40.7	-27.1
20	1.697	1.24	3.13	.39	4.64	14.64	19.28	233	286	519	.0985	.308	-25.4	-16.3	-40.7	-27.5
	V_8	V_{28}	T_8	T_{28}	FULL SCALE DATA											
	ft/sec		°R													
11	-	930	-	539	-	1374	1374	-	39955	39955	-	17.279	-	1.7	-	-9.1
12	-	952	-	540	-	1414	1414	-	42061	42061	-	17.279	-	1.7	-	-9.0
13	473	457	1090	538	97.1	606	703	1434	8673	10108	5.66	17.279	-6.9	1.2	-21.3	-10.0
14	660	588	1163	538	128.7	797	926	2655	14639	17294	5.66	17.279	-7.1	1.3	-21.7	-9.8
15	914	715	1250	539	169	993	1162	4847	22187	27034	5.66	17.279	-7.3	1.4	-22.1	-9.6
16	1232	859	1377	539	215	1241	1456	8285	33350	41635	5.66	17.279	-8.6	1.6	-22.7	-9.3
17	1495	933	1468	541	254	1375	1629	11859	40111	51970	5.66	17.279	-7.7	1.7	-26.9	-9.3
18	1609	962	1521	547	267	1414	1681	13437	42519	55956	5.66	17.279	-7.8	1.7	-23.1	-9.3
19	1605	805	1519	546	267	1130	1397	13390	28426	41816	5.66	17.279	-7.8	1.5	-23.1	-9.5
20	1607	625	1522	545	267	841.	1108	13396	16431	29827	5.66	17.279	-7.8	1.3	-23.1	-9.9

TABLE C-3 LOW VELOCITY JET NOISE SUPPRESSOR TEST I

SCALE FACTOR 7.5

BASELINE I and 18 Lobe Suppression AR=2

	DATA PT	P_{T8}/P_0	P_{T28}/P_0	A_{28}/A_8	V_{28}/V_8	W_8 (lbs/sec)	W_{28} (lbs/sec)	W_T (lbs/sec)	F_8 (lbs)	F_{28} (lbs)	F_T (lbs)	A_8 (ft^2)	A_{28} (ft^2)	$10\log \rho_8 V_8$	$10\log \rho_{28} A_{28}$	$10\log \rho_8^2 A_8$	$10\log \rho_{28}^2 A_8$
	CONTROL DATA					SCALE MODEL DATA											
Baseline 1	21	1.118	1.111	3.13	.66	2.25	10.08	12.33	46.61	138	184.6	.0985	.308	-24.7	-16.4	-39.3	-27.6
	22	1.118	1.062	3.13	.60	2.25	7.55	9.8	46.62	78.3	124.9	.0985	.308	-24.7	-16.4	-39.3	-27.4
18 Lobe AR=2	23	1.064	-	-	-	1.71	-	1.71	25.5	-	25.5	.0985	-	-24.5	-	-38.8	-
	24	1.118	-	-	-	2.23	-	2.23	46.16	-	46.16	.0985	-	-24.7	-	-39.3	-
	25	1.215	-	-	-	2.88	-	2.88	81.5	-	81.5	.0985	-	-24.9	-	-39.8	-
	26	1.391	-	-	-	3.68	-	3.68	140.4	-	140.4	.0985	-	-25.2	-	-40.3	-
	27	1.6	-	-	-	4.35	-	4.35	204	-	204	.0985	-	-25.3	-	-40.6	-
	28	1.684	-	-	-	4.57	-	4.57	227	-	227	.0985	-	-25.6	-	-40.7	-
	29	-	1.118	-	-	-	10.46	10.46	-	145	145	-	.308	-	-16.3	-	-27.4
	30	-	1.205	-	-	-	13.77	13.77	-	245	245	-	.308	-	-16.2	-	-27.2
		V_8 (ft/sec)	V_{28} (ft/sec)	T_8 (°R)	T_{28} (°R)	FULL SCALE DATA											
	21	663	438	1164	538	129	579	708	2678	7919	10597	5.66	17.279	-7.1	1.2	-21.7	-100
	22	662	332	1161	537	129	434	563	2678	4496	7174	5.66	17.279	-7.1	1.2	-21.7	-9.8
	23	479	-	1085	-	98.3	-	98.3	1465	-	1465	5.66	-	-6.6	-	-21.0	-
	24	663	-	1165	-	128	-	128	2652	-	2652	5.66	-	-6.9	-	-21.5	-
	25	905	-	1257	-	165.5		165.5	4683		4683	5.66	-	-7.1	-	-22.0	-
	26	1224	-	1379	-	211		211	8067		8067	5.66	-	-7.3	-	-22.5	-
	27	1498	-	1476	-	250	-	250	11721		11721	5.66	-	-7.5	-	-22.8	-
	28	1593	-	1515	-	263	-	263	13043	-	13043	5.66	-	-7.5	-	-22.9	-
	29	-	443	-	520	-	601	601	-	8331	8331	-	17.279	-	1.3	-	-9.6
	30	-	568	-	518	-	791	791	-	14077	14077	-	17.279	-	1.4	-	-9.6

TABLE C-4 LOW VELOCITY JET NOISE SUPPRESSOR TEST I

18 LOBE SUPPRESSOR AR=2

SCALE FACTOR 7.5

DATA PT	P_T/P_0	P_{T28}/P_0	A_{28}/A_8	V_{28}/V_8	W_8	W_{28}	W_T	F_8	F_{28}	F_T	A_8	A_{28}	$10\log \rho_8 V_8^3$	$10\log \rho_{28} V_{28}^3$	$10\log \rho_8^2 A_8$	$10\log \rho_{28}^2 A_{28}$
					← lbs/sec		→	← lbs		→	← ft²	→				
COMMON DATA					SCALE MODEL DATA											
31	-	1.333	-	-	-	17.49	17.49	-	383	383	-	.308	-	16.0	-	-26.9
32	-	1.529	-	-	-	21.9	21.9	-	577	577	-	.308	-	-15.9	-	-26.6
33	-	1.656	-	-	-	24.26	24.26	-	693	693	-	.308	-	-15.8	-	-26.4
34	-	1.691	-	-	-	24.58	24.58	-	717	717	-	.308	-	-15.8	-	-26.4
35	1.064	1.122	2.93	.94	1.63	10.73	12.36	24.1	150	174	.0985	.308	-24.4	-16.2	-38.8	-27.3
36	1.115	1.202	2.93	.86	2.2	13.71	15.9	45.	241	286	.0985	.308	-24.7	-16.1	-39.3	-27.2
36R	1.117	1.212	2.93	.88	2.22	13.93	16.1	45.8	253	299	.0985	.308	-24.7	-16.2	-39.3	-27.3
37	1.212	1.328	2.93	.77	2.86	17.35	20.2	80.4	377	457	.0985	.308	-24.9	-16.0	-39.8	-27.0
38	1.398	1.523	2.93	.69	3.73	21.72	25.45	143.	571	714	.0985	.308	-25.2	-15.9	-40.3	-26.6
39	1.593	1.656	2.93	.62	4.33	24.17	28.5	202	693	895	.0985	.308	-25.3	-15.8	-40.6	-26.5
	V_8	V_{28}	T_8	T_{28}	FULL SCALE DATA											
	← ft/sec	→	← °R	→												
31	-	700	-	517	-	1005	1005	-	21987	21987	-	17.279	-	1.5	-	-9.4
32	-	843	-	517	-	1259	1259	-	33137	33137	-	17.279	-	1.6	-	-9.1
33	-	914	-	518	-	1394	1394	-	39826	39826	-	17.279	-	1.7	-	-8.9
34	-	933	-	520	-	1412	1412	-	41201	41201	-	17.279	-	1.7	-	-8.9
35	475	446	1070	511	93.7	617	711	1385	8589	9974	5.66	17.279	-6.6	1.3	-21.0	-9.8
36	656	563	1167	515	124	788	912	2586	13847	16433	5.66	17.279	-7.0	1.4	-21.6	-9.7
36R	660	580	1164	524	128	800	928	2632	14536	17168	5.66	17.279	-6.9	1.3	-21.6	-9.8
37	899	696	1255	518	164	997	1161	4621	21661	26282	5.66	17.279	-7.2	1.5	-22.1	-9.5
38	1225	841	1362	520	214	1248	1462	8216	32808	41024	5.66	17.279	-7.4	1.6	-22.5	-9.1
39	1492	918	1477	522	249	1389	1638	11606	39817	51423	5.66	17.279	-7.6	1.7	-22.9	-9.0

TABLE C-5. LOW VELOCITY JET NOISE SUPPRESSOR TEST I

SCALE FACTOR 7.5

18 lobe suppressor AR= 2 and
18 lobe suppressor AR = 4.8

	DATA PT	P_T/P_0	P_{T28}/P_0	A_{28}/A_8	V_{28}/V_8	W_8	W_{28}	W_T	F_8	F_{28}	F_T	A_8	A_{28}	$10\log \rho_8 V_8$	$10\log \rho_{28} A_{28}$	$10\log \rho_8^2 A_8$	$10\log \rho_{28}^2 A_{28}$
						lbs/sec			lbs			ft^2					
	COMMON DATA					SCALE MODEL DATA											
18 Lobe AR = 2	40	1.689	1.691	2.93	.59	4.59	24.71	29.3	228	724	952	.0985	.308	-25.6	-15.8	-40.7	-26.5
	41	1.686	1.432	2.93	.49	4.57	19.68	24.25	228	483	711	.0985	.308	-25.6	-16.0	-40.7	-26.9
	42	1.679	1.23	2.93	.38	4.54	14.46	19.0	226	273	499	.0985	.308	-25.7	-16.2	-40.7	-27.3
	43	1.121	1.109	2.93	.63	2.25	10.12	12.37	47.3	134	181.3	.0985	.308	-24.7	-16.2	-39.3	-27.3
	44	1.122	1.059	2.93	.47	2.26	7.46	9.72	47.7	73.83	121.5	.0985	.308	-24.7	-16.3	-39.3	-27.4
	44R	1.123	1.061	2.93	.48	2.27	7.52	9.79	50	76.28	126	.0985	.308	-24.7	-16.3	-39.3	-27.6
18 Lobe AR = 4.8	45	1.063	-	-	-	1.7	-	1.7	25.2	-	25.2	.0985	.308	-24.5	-	-38.8	-
	46	1.112	-	-	-	2.18	-	2.18	44.0	-	44.0	.0985	.308	-24.7	-	-39.3	-
	47	1.211	-	-	-	2.88	-	2.88	80.2	-	80.2	.0985	.308	-24.9	-	-39.8	-
	48	1.395	-	-	-	3.7	-	3.7	142	-	142	.0985	.308	-25.2	-	-40.3	-
		V_8	V_{28}	T_8	T_{28}												
		ft/sec		°R		FULL SCALE DATA											
	40	1598	938	1516	525	264	1420	1684	13100	41598	54698	5.66	17.279	-7.6	1.7	-23.0	-9.0
	41	1597	786	1520	527	263	1131	1394	13100	27751	40851	5.66	17.279	-7.6	1.5	-23.0	-9.4
	42	1593	603	1523	527	261	831	1092	12985	15686	28671	5.66	17.279	-7.7	1.3	-23.0	-9.8
	43	671	424	1167	514	129	581	710	2718	7699	10417	5.66	17.279	-7.0	1.3	-21.6	-9.8
	44	673	317	1163	513	130	429	559	2741	4242	6983	5.66	17.279	-6.9	1.2	-21.6	-9.9
	44R	676	324	1164	522	130	432	562	2873	4383	7256	5.66	17.279	-6.9	1.2	-21.6	-10.1
	45	475	-	1082	-	977	-	977	1448	-	1448	5.66	17.279	-6.7	-	-21.1	-
	46	646	-	1162	-	125	-	125	2528	-	2528	5.66	17.279	-6.9	-	-21.6	-
	47	890	-	1236	-	165	-	165	4608	-	4608	5.66	17.279	-7.1	-	-21.9	-
	48	1231	-	1383	-	213	-	213	8159	-	8159	5.66	17.279	-7.4	-	-22.6	-

Table C-6. LOW VELOCITY JET NOISE SUPPRESSOR TEST I

SCALE FACTOR 7.5

18 Lobe Core Suppressor
AR=4.8

DATA PT	P_{T8}/P_0	P_{T28}/P_0	A_{28}/A_8	V_{28}/V_8	W_8	W_{28}	W_T	F_8	F_{28}	F_T	A_8	A_{28}	$10\log \rho_8 A_8$	$10\log \rho_{28} A_{28}$	$10\log \rho_8^2 A_8$	$10\log \rho_{28}^2 A_{28}$
					lbs/sec			lbs			ft^2					
COMMON DATA					SCALE MODEL DATA											
49	1.583	-	-	-	4.3	-	4.3	199	-	199	.0985	-	-25.3	-	-40.6	-
50	1.689	-	-	-	4.59	-	4.59	229	-	229	"	-	-25.6	-	-40.7	-
51	-	1.128	-	-	-	10.76	10.76	-	156	156	-	.308	-	-16.3	-	-27.6
52	-	1.215	-	-	-	13.91	13.91	-	255	255	-	.308	-	-16.2	-	-27.4
53	-	1.34	-	-	-	17.42	17.42	-	388	388	-	.308	-	-16.1	-	-27.1
54	-	1.539	-	-	-	21.79	21.79	-	583	583	-	.308	-	-15.9	-	-26.8
55	-	1.665	-	-	-	24.12	24.12	-	697	697	-	.308	-	-15.8	-	-26.6
56	-	1.702	-	-	-	24.78	24.78	-	730	730	-	.308	-	-15.8	-	-26.5
57	1.059	1.126	2.93	.99	1.65	10.81	12.46	23.4	154	177.4	.0985	.308	-24.5	-16.2	-38.8	-27.4
58	1.127	1.214	2.93	.85	2.33	13.98	16.31	49.4	253	302	"	.308	-24.7	-16.2	-39.3	-27.2
	V_8	V_{28}	T_8	T_{28}	FULL SCALE DATA											
	ft/sec		°R													
49	1480	-	1473	-	247	-	247	11434	-	11434	5.66	-	-7.6	-	-22.9	-
50	1598	-	1517	-	264	-	264	13158		13158	"	-	-7.6	-	-23.0	-
51	-	463	-	527	-	618	618	-	8963	8963	-	17.279	-	1.2	-	-10.1
52	-	586	-	527	-	799	799	-	14651	14651	-	17.279	-	1.3	-	-9.9
53	-	713	-	527	-	1001	1001	-	22293	22293	-	17.279	-	1.4	-	-9.6
54	-	856	-	526	-	1252	1252	-	33497	33497	-	17.279	-	1.6	-	-9.3
55	-	925	-	525	-	1386	1386	-	40047	40047	-	17.279	-	1.7	-	-9.1
56	-	942	-	524	-	1424	1424	-	41943	41943	-	17.279	-	1.7	-	-9.0
57	461	455	1090	516	94.8	621	716	1344	8848	10192	5.66	17.279	-6.7	1.3	-21.2	-9.9
58	686	580	1166	520	134	803	937	2838	14582	17420	"	17.279	-6.7	1.3	-21.6	-9.7

TABLE C-7 LOW VELOCITY JET NOISE SUPPRESSOR TEST I

SCALE FACTOR 7.5

18 Lobe Suppressor AR=4.8

18 Lobe AR=4.8

DATA PT	P_{T8}/P_0	P_{T28}/P_0	A_{28}/A_8	V_{28}/V_8
COMMON DATA				
59	1.212	1.341	2.93	.80
60	1.401	1.521	2.93	.69
61	1.591	1.654	2.93	.62
62	1.687	1.687	2.93	.59
63	1.682	1.424	2.93	.50
64	1.683	1.225	2.93	.37
65	1.129	1.12	2.93	.65
66	1.131	1.066	2.93	.48

	V_8	V_{28}	T_8	T_{28}
	ft/sec		°R	
59	899	714	1255	527
60	1238	851	1382	533
61	1489	925	1476	532
62	1595	939	1515	528
63	1591	799	1515	526
64	1593	597	1517	527
65	690	447	1162	522
66	697	337	1167	523

	W_8	W_{28}	W_T	F_8	F_{28}	F_T	A_8	A_{28}	$10\log \rho_8 c_8^3$	$10\log \rho_{28} A_{28} c_{28}^3$	$10\log \rho_8^2 c_8^3$	$10\log \rho_{28}^2 A_{28} c_{28}^3$
	lbs/sec			lbs			ft^2					
SCALE MODEL DATA												
59	2.84	17.44	20.28	80	389	469	.0985	.308	-24.9	-16.1	-39.8	-27.1
60	3.72	21.44	25.16	144	570	714	.0985	.308	-25.2	-16.0	-40.3	-26.9
61	4.34	23.94	28.28	201	692	893	.0985	.308	-25.3	-15.9	-40.6	-26.6
62	4.59	24.6	29.2	228	722	950	.0985	.308	-25.3	-15.8	-40.7	-26.5
63	4.57	19.54	24.1	227	476	703	.0985	.308	-25.3	-16.0	-40.7	-26.9
64	4.57	14.32	18.89	227	267	494	.0985	.308	-25.3	-16.2	-40.7	-27.3
65	2.33	10.48	12.81	50	146.4	196	.0985	.308	-24.6	-16.3	-39.9	-27.5
66	2.33	7.78	10.11	50.8	82.	132.8	.0985	.308	-24.7	-16.4	-39.2	-27.6
FULL SCALE DATA												
59	163	1002	1165	4597	22351	26948	5.66	17.279	-7.2	1.4	-22.1	-9.6
60	214	2232	2446	8274	32750	41024	5.66	17.279	-7.4	1.5	-22.6	-9.4
61	249	1376	1625	11549	39760	51309	5.66	17.279	-7.6	1.6	-22.9	-9.1
62	264	1413	1677	13100	41484	54584	5.66	17.279	-7.6	1.8	-23.0	-9.0
63	263	1123	1386	13043	27349	40392	5.66	17.279	-7.6	1.5	-23.0	-9.4
64	263	827	1090	13043	15341	28384	5.66	17.279	-7.6	1.3	-23.0	-9.8
65	134	602	736	2873	8412	11285	5.66	17.279	-6.9	1.2	-21.6	-10.0
66	134	447	581	2919	4711	7630	5.66	17.279	-7.0	1.1	-21.6	-10.1

TABLE C-8 LOW VELOCITY JET NOISE SUPPRESSOR TEST II

SCALE FACTOR 7.5

18 Capped Lobe Suppressor AR=2

	DATA PT	P_{T8}/P_0	P_{T28}/P_0	A_{28}/A_8	V_{28}/V_8	W_8	W_{28}	W_T	F_8	F_{28}	F_T	A_8	A_{28}	$10\log \rho_8 A_8$	$10\log \rho_{28} A_{28}$	$10\log \rho_8^2 A_8$	$10\log \rho_{28}^2 A_{28}$
						← lbs/sec →			← lbs →			← ft^2 →					
		COMMON DATA				SCALE MODEL DATA											
CORE	1	1.119	-	-	-	2.41	-	2.41	49.9	-	49.9	.106	-	-24.4	-	-39.	-
	2	1.4	-	-	-	4.02	-	4.02	154.	-	154	.106	-	-24.9	-	-40.	-
	3	1.68	-	-	-	4.91	-	4.91	243	-	243	.106	-	-25.1	-	-40.4	-
	4	-	1.11	-	-	-	9.79	9.79	-	135	135	-	.308	-	-16.7	-	-28.
	5	-	1.199	-	-	-	13.09	13.09	-	238	238	-	.308	-	-16.5	-	-27.9
FAN	6	-	1.323	-	-	-	16.61	16.61	-	372	372	-	.308	-	-16.4	-	-27.6
	7	-	1.527	-	-	-	21.12	21.12	-	574	574	-	.308	-	-16.2	-	-27.2
	8	-	1.652	-	-	-	23.46	23.46	-	689	689	-	.308	-	-16.1	-	-27.
	9	-	1.686	-	-	-	24.06	24.06	-	719	719	-	.308	-	-16.	-	-26.9
Dual	10	1.062	1.118	2.92	0.97	1.82	10.2	12.02	26.5	144.5	171	.106	.308	-24.1	-16.5	-38.5	-27.9
		V_8	V_{28}	T_8	T_{28}												
		← ft/sec →		← °R →		FULL SCALE DATA											
	1	665	-	1161	-	139	-	139	2864	-	2864	5.96	-	-6.8	-	-21.4	-
	2	1231	-	1369	-	231	-	231	8826	-	8826	5.96	-	-7.3	-	-22.4	-
	3	1590	-	1516	-	282	-	282	13933	-	13933	5.96	-	-7.5	-	-22.8	-
	4	-	444	-	559	-	563	563	-	7764	7764	-	17.33	-	1.0	-	-10.4
	5	-	584	-	562	-	752	752	-	13653	13653	-	17.33	-	1.1	-	-10.3
	6	-	721	-	562	-	954	954	-	21357	21357	-	17.33	-	1.2	-	-10.
	7	-	875	-	559	-	1214	1214	-	32979	32979	-	17.33	-	1.4	-	-9.6
	8	-	945	-	556	-	1348	1348	-	39561	39561	-	17.33	-	1.5	-	-9.4
	9	-	962	-	555	-	1382	1382	-	41289	41289	-	17.33	-	1.6	-	-9.3
	10	470	458	1076	552	102	574	676	1490	8129	9619	5.96	17.33	-6.6	1.0	-21.	-10.4

TABLE C-9 LOW VELOCITY JET NOISE SUPPRESSOR TEST II

SCALE FACTOR 7.5

18 CAPPED LOBE SUPPRESSOR AR=2

DUAL

DATA PT	P_{T8}/P_0	P_{T28}/P_0	A_{28}/A_8	V_{28}/V_8	W_8	W_{28}	W_T	F_8	F_{28}	F_T	A_8	A_{28}	$10\log \rho_8 A_8$	$10\log \rho_{28} A_{28}$	$10\log \rho_8^2 A_8$	$10\log \rho_{28}^2 A_{28}$
	COMMON DATA				SCALE MODEL DATA											
					← lbs/sec →			← lbs →			← ft^2 →					
11	1.106	1.196	2.92	.915	2.27	13.05	15.32	44.6	234	279	.106	.308	-24.4	-16.5	-39.1	-27.8
12	1.211	1.324	2.92	.80	3.08	16.7	19.78	85.8	372.6	458	.106	.308	-24.6	-16.3	-39.5	-27.6
13	1.381	1.517	2.92	.721	3.93	20.9	24.83	147	564	711	.106	.308	-24.9	-16.2	-40.	-27.3
14	1.587	1.649	2.92	.637	4.64	23.34	27.98	214	686	900	.106	.308	-25.	-16.1	-40.3	-27.
15	1.693	1.683	2.92	.601	4.95	23.93	28.88	246	716	962	.106	.308	-25.1	-16.	-40.4	-27.
16	1.429	1.679	2.92	.721	3.94	23.85	27.79	163	712	875	.106	.308	-25.3	-16.1	-40.8	-27.
17	1.216	1.679	2.92	.962	2.82	23.85	26.67	87.6	712	800	.106	.308	-25.5	-16.1	-41.2	-27.
18	1.106	1.115	2.92	.721	2.28	10.	12.28	44.6	141	186	.106	.308	-24.4	-16.6	-39.1	-28.
19	1.051	1.117	2.92	1.034	1.59	10.06	11.65	21.9	143	165	.106	.308	-24.5	-16.6	-39.2	-28.1
20	1.105	1.076	2.92	.629	2.27	7.72	9.99	44.2	94.4	139	.106	.308	-24.4	-17.1	-39.	-29.
	V_8	V_{28}	T_8	T_{28}	FULL SCALE DATA											
	← ft/sec →		← °R →													
11	632	578	1170	557	128	734	862	2509	13172	15681	5.96	17.33	-6.9	1.0	-21.6	-10.3
12	898	718	1256	557	173	940	1113	4825	20960	25785	5.96	17.33	-7.1	1.2	-22.0	-10.1
13	1206	869	1367	559	221	1177	1398	8274	31744	40018	5.96	17.33	-7.4	1.3	-22.4	-9.8
14	1486	946	1476	559	261	1313	1574	12054	38566	50620	5.96	17.33	-7.5	1.4	-22.8	-9.5
15	1602	963	1518	558	279	1346	1625	13858	40260	54118	5.96	17.33	-7.6	1.5	-22.9	-9.5
16	1334	962	1518	559	222	1341	1563	9184	40062	49246	5.96	17.33	-7.8	1.4	-23.3	-9.5
17	1000	962	1524	559	159	1341	1500	4927	40062	44989	5.96	17.33	-8.	1.4	-23.7	-9.5
18	630	454	1163	560	128	562	690	2509	7931	10440	5.96	17.33	-6.9	0.9	-21.6	-10.5
19	444	459	1160	563	89.3	566	655	1230	9063	9293	5.96	17.33	-7.	0.9	-21.7	-10.6
20	626	394	1156	623	128	434	562	2486	5309	7795	5.96	17.33	-6.9	0.4	-21.5	-11.5

TABLE C-10 LOW VELOCITY JET NOISE SUPPRESSOR TEST II

SCALE FACTOR 7.5

18 CAPPED LOBE SUPPRESSOR AR=2

	DATA PT	P_T/P_0	P_{T28}/P_0	A_{28}/A_8	V_{28}/V_8	W_8	W_{28}	W_T	F_8	F_{28}	F_T	A_8	A_{28}	$10\log \rho_8 A_8$	$10\log \rho_{28} A_{28}$	$10\log \rho_8^2 A_8$	$10\log \rho_{28}^2 A_{28}$
						lbs/sec			lbs			ft^2					
	COMMON DATA					SCALE MODEL DATA											
	21	1.105	1.154	2.92	.884	2.27	10.84	13.11	44.2	186	230	.106	.308	-24.4	-17.8	-39.1	-29.1
	22	1.568	1.506	2.92	.62	4.5	19.3	23.8	208	554	762	.106	.308	-25.2	-16.8	-40.6	-28.5
	23	1.689	1.313	2.92	.486	4.93	14.92	19.85	245	361	606	.106	.308	-25.1	-17.2	-40.5	-29.2
	24	1.691	1.488	2.92	.583	4.95	18.57	23.52	246	537	783	.106	.308	-25.1	-17.	-40.4	-28.9
	25	1.392	1.366	2.92	.682	3.98	16.13	20.11	151	416	567	.106	.308	-24.9	-17.1	-39.9	-29.1
DUAL	26	1.692	1.685	2.92	.672	5.14	22.26	27.4	246	717	963	.106	.308	-24.8	-16.7	-39.8	-28.3
DUAL	27	1.647	1.668	2.92	.655	4.81	22.18	26.99	233	702	935	.106	.308	-25.1	-16.6	-40.4	-28.1
	28	NO DATA															
	29	1.596	1.65	2.92	.678	4.69	21.88	26.57	217	687	904	.106	.308	-25.	-16.6	-40.3	-28.2
	30	1.384	1.525	2.92	.764	3.93	19.85	23.78	148	572	720	.106	.308	-24.9	-16.7	-40.	-28.3
		V_8	V_{28}	T_8	T_{28}												
		ft/sec		°R		FULL SCALE DATA											
	21	627	554	1161	636	128	610	738	2486	10487	12973	5.96	17.33	-6.9	0.4	-21.6	-11.6
	22	1490	924	1522	643	253	1086	1339	11716	31156	42872	5.96	17.33	-7.7	0.7	-23.1	-11.
	23	1602	779	1525	675	277	839	1116	13790	20312	34102	5.96	17.33	-7.6	0.3	-23.	-11.7
	24	1598	931	1514	671	279	1045	1324	13825	30188	44013	5.96	17.33	-7.6	0.5	-22.9	-11.4
	25	1219	831	1366	673	224	907	1131	8487	23398	31885	5.96	17.33	-7.4	0.4	-22.4	-11.6
DUAL	26	1544	1038	1413	647	289	1252	1541	13855	40358	54213	5.96	17.33	-7.3	0.8	-22.3	-10.8
DUAL	27	1557	1020	1507	636	271	1248	1519	13085	39515	52600	5.96	17.33	-7.6	0.9	-22.9	-10.6
	28	NO DATA															
	29	1490	1010	1468	637	264	1231	1495	12212	38616	50828	5.96	17.33	-7.5	0.9	-22.8	-10.7
	30	1214	928	1377	630	221	1117	1338	8332	32169	40501	5.96	17.33	-7.4	0.8	-22.5	-10.8

TABLE C-11 LOW VELOCITY JET NOISE SUPPRESSOR TEST II

SCALE FACTOR 7.5

18 CAPPED LOBE SUPPRESSOR AR=2

	DATA PT	P_T/P_0	P_{s28}/P_0	A_{28}/A_8	V_{28}/V_8	W_8	W_{28}	W_T	F_8	F_{28}	F_T	A_8	A_{28}	$10\log \rho_8 A_8$	$10\log \rho_{28} A_{28}$	$10\log \rho_8^2 A_8$	$10\log \rho_{28}^2 A_{28}$
		COMMON DATA				SCALE MODEL DATA											
						← lbs/sec →			← lbs →			← ft² →					
DUAL FAN	31	1.208	1.326	2.92	.813	3.06	16.66	19.72	84.6	374.7	459	.106	.308	-24.6	-16.4	-39.5	-27.6
	32	1.115	1.206	2.92	.904	2.37	13.31	15.68	48.2	245	293	.106	.308	-24.4	-16.5	-39.1	-27.9
	33	1.049	1.113	2.92	1.071	1.6	9.88	11.48	21.	139	160	.106	.308	-24.2	-16.6	-38.7	-28.1
	34	1.696	1.72	2.92	.679	5.13	32.84	27.97	247.	748	995	.106	.308	-24.8	-16.6	-39.9	-28.2
	35	1.77	1.762	2.92	.651	5.21	23.36	28.57	269.	784	1053	.106	.308	-25.	-16.7	-40.3	-28.2
	36	1.574	1.942	2.92	.725	4.53	27.7	32.23	210	932	1142	.106	.308	-25.2	-15.9	-40.6	-26.7
	37	1.757	1.997	2.92	.669	5.17	28.45	33.62	265	975	1240	.106	.308	-25.	-15.9	-40.3	-26.7
	38	-	1.077	-	-	-	7.48	7.48	-	95.6	95.6	-	.308	-	-17.4	-	-29.7
	39	-	1.153	-	-	-	10.5	10.5	-	185	185	-	.308	-	-17.3	-	-29.6
	40	-	1.499	-	-	-	18.76	18.76	-	547	547	-	.308	-	-17.	-	-28.9
		V_8	V_{28}	T_8	T_{28}	FULL SCALE DATA											
		← ft/sec →		← °R →													
	31	890	724	1249	563	172	937	1109	4761	21077	25838	5.96	17.33	-7.1	1.1	-22.	-10.1
	32	656	593	1167	562	133	749	882	2713	13801	16514	5.96	17.33	-6.9	1.0	-21.6	-10.4
	33	422	452	1093	563	90	556	646	1183	7798	8981	5.96	17.33	-6.7	0.9	-21.2	-10.6
	34	1553	1054	1423	644	289	1285	1574	13921	42075	55996	5.96	17.33	-7.3	0.9	-22.4	-10.7
	35	1661	1081	1513	650	293	1314	1607	15121	44103	59224	5.96	17.33	-7.5	0.8	-22.8	-10.7
	36	1494	1083	1518	565	255	1558	1813	11822	52420	64242	5.96	17.33	-7.7	1.6	-23.1	-9.2
	37	1651	1104	1513	565	291	1600	1891	14911	54851	69762	5.96	17.33	-7.5	1.6	-22.8	-9.2
	38	-	412	-	673	-	430	430	-	5495	5495	-	17.33	-	0.2	-	-12.1
	39	-	568	-	674	-	603	603	-	10650	10650	-	17.33	-	0.3	-	12.
	40	-	639	-	672	-	1078	1078	-	31452	31452	-	17.33	-	0.6	-	-11.3

Table C-12. LOW VELOCITY JET NOISE SUPPRESSOR TEST II

SCALE FACTOR 7.5

18 Capped Lobe Suppressor AR = 2

DATA PT	P_{T8}/P_0	P_{T28}/P_0	A_{28}/A_8	V_{28}/V_8	W_8	W_{28}	W_T	F_8	F_{28}	F_T	A_8	A_{28}	$10\log \rho_8 A_8$	$10\log \rho_{28} A_{28}$	$10\log \rho_8^2 A_8$	$10\log \rho_{28}^2 A_{28}$
	COMMON DATA				SCALE MODEL DATA											
					← lbs/sec →			← lbs →			← ft^2 →					
41	-	1.312	-	-	-	14.92	14.92	-	360	360	-	.308	-	-17.2	-	-29.2
42	-	1.486	-	-	-	19. .	19.	-	535	535	-	.308	-	-16.8	-	-28.5
43	-	1.371	-	-	-	16.63	16.63	-	421	421	-	.308	-	-16.9	-	-28.7
44	-	1.733	-	-	-	23.05	23.05	-	759	759	-	.308	-	-16.6	-	-28.2
45	-	1.768	-	-	-	23.57	23.57	-	789	789	-	.308	-	-16.6	-	-28.1
46	-	1.684	-	-	-	22.3	22.3	-	717	717	-	.308	-	-16.7	-	-28.2
47	-	1.665	-	-	-	22.06	22.06	-	700	700	-	.308	-	-16.7	-	-28.2
	V_8	V_{28}	T_8	T_{28}	FULL SCALE DATA											
	← ft/sec →		← °R →													
41	-	777	-	673	-	857	857	-	20695	20695	-	17.33	-	0.4	-	-11.6
42	-	907	-	639	-	1092	1092	-	30737	30737	-	17.33	-	0.8	-	-10.9
43	-	816	-	642	-	955	955	-	24201	24201	-	17.33	-	0.7	-	-11.1
44	-	1061	-	644	-	1324	1324	-	43638	43638	-	17.33	-	1.0	-	-10.6
45	-	1079	-	644	-	1354	1354	-	45358	45358	-	17.33	-	1.0	-	-10.5
46	-	1035	-	644	-	1281	1281	-	41188	41188	-	17.33	-	0.9	-	-10.6
47	-	1022	-	641	-	1267	1267	-	40225	40225	-	17.33	-	0.9	-	-10.6

FAN

Table C-13. LOW VELOCITY JET NOISE SUPPRESSOR TEST III

SCALE FACTOR 7.5

Baseline II

	DATA PT	P_{T8}/P_0	P_{T28}/P_0	A_{28}/A_8	V_{28}/V_8	W_8	W_{28}	W_T	F_8	F_{28}	F_T	A_8	A_{28}	$10\log \rho_8 A_8$	$10\log \rho_{28} A_{28}$	$10\log \rho_0^2 A_8$	$10\log \rho_{28}^2 A_{28}$
		COMMON DATA				SCALE MODEL DATA											
						lbs/sec			lbs			ft^2					
CORE	1	1.754	-	-	-	5.42	-	5.42	277	-	277	.1097	-	-24.8	-	-40.	-
	2	1.694	-	-	-	5.21	-	5.21	259	-	259	.1097	-	-24.9	-	-40.1	-
	3	1.642	-	-	-	5.05	-	5.05	243	-	243	.1097	-	-24.9	-	-40.1	-
	4	1.576	-	-	-	4.82	-	4.82	221	-	221	.1097	-	-24.9	-	-40.1	-
	5	1.392	-	-	-	4.14	-	4.14	158	-	158	.1097	-	-24.7	-	-39.9	-
	6	1.198	-	-	-	3.13	-	3.13	84.8	-	84.8	.1097	-	-24.5	-	-39.3	-
	7	1.109	-	-	-	2.39	-	2.39	48.1	-	48.1	.1097	-	-24.3	-	-39.	-
FAN	8	-	1.741	-	-	-	23.5	23.5	-	774	774	-	.308	-	-16.6	-	-28.
	9	-	1.684	-	-	-	22.5	22.5	-	724	724	-	.308	-	-16.6	-	-28.1
	10	-	1.669	-	-	-	22.3	22.3	-	710	710	-	.308	-	-16.6	-	-28.2
		V_8	V_{28}	T_8	T_{28}	FULL SCALE DATA											
		ft/sec		°R													
	1	1646	-	1509	-	305	-	305	15595	-	15595	6.17	-	-7.3	-	-22.5	-
	2	1600	-	1512	-	293	-	293	14559	-	14559	6.17	-	-7.4	-	-22.6	-
	3	1548	-	1498	-	284	-	284	13641	-	13641	6.17	-	-7.4	-	-22.6	-
	4	1477	-	1479	-	271	-	271	12445	-	12445	6.17	-	-7.4	-	-22.6	-
	5	1230	-	1390	-	233	-	233	8904	-	8904	6.17	-	-7.2	-	-22.4	-
	6	873	-	1257	-	176	-	176	4770	-	4770	6.17	-	-7.0	-	-21.8	-
	7	647	-	1194	-	135	-	135	2704	-	2704	6.17	-	-6.8	-	-21.5	-
	8	-	1061	-	639	-	1321	1321	-	43514	43514	-	17.33	-	1.0	-	-10.5
	9	-	1035	-	644	-	1266	1266	-	40702	40702	-	17.33	-	0.9	-	-10.6
	10	-	1028	-	645	-	1252	1252	-	39951	39951	-	17.33	-	0.9	-	-10.7

TABLE C-14 LOW VELOCITY JET NOISE SUPPRESSOR TEST III

SCALE FACTOR 7.5

BASELINE II

FAN DUAL

DATA PT	P_{T8}/P_0	P_{T28}/P_0	A_{28}/A_8	V_{28}/V_8	W_8 (lbs/sec)	W_{28} (lbs/sec)	W_T (lbs/sec)	F_8 (lbs)	F_{28} (lbs)	F_T (lbs)	A_8 (ft^2)	A_{28} (ft^2)	$10\log \rho_8 A_8$	$10\log \rho_{28} A_{28}$	$10\log \rho_8^2 A_8$	$10\log \rho_{28}^2 A_{28}$
COMMON DATA					SCALE MODEL DATA											
11	-	1.643	-	-	-	21.9	21.9	-	687	687	-	.308	-	-16.6	-	-28.2
12	-	1.528	-	-	-	20.	20.	-	580	580	-	.308	-	-16.7	-	-28.3
13	-	1.37	-	-	-	17.2	17.2	-	424	424	-	.308	-	-16.6	-	-28.2
14	-	1.23	-	-	-	13.6	13.6	-	275	275	-	.308	-	-16.8	-	-28.4
15	1.758	1.726	2.81	.64	5.43	23.18	28.6	279	761	1040	.1097	.308	-24.8	-16.6	-40.1	-28.1
16	1.679	1.68		.649	5.13	22.39	27.5	254	721	975	.1097	.308	-24.9	-16.7	-40.3	-28.2
17	1.641	1.661		.66	5.04	22.18	27.2	242	704	946	.1097	.308	-24.9	-16.6	-40.1	-28.2
18	1.572	1.648		.668	4.71	22.19	26.9	220	692	912	.1097	.308	-25.	-16.6	-40.5	-28.
19	1.39	1.531		.769	4.14	19.93	24.1	158	584	742	.1097	.308	-24.7	-16.7	-39.8	-28.4
20	1.206	1.397		.897	3.2	17.59	20.8	88.1	434	522	.1097	.308	-24.4	-16.5	-39.2	-28.
	V_8 (ft/sec)	V_{28} (ft/sec)	T_8 (°R)	T_{28} (°R)	FULL SCALE DATA											
11	-	1009	-	641	-	1232	1232	-	38638	38638	-	17.33	-	0.9	-	-10.7
12	-	935	-	638	-	1124	1124	-	32644	32644	-	17.33	-	0.8	-	-10.8
13	-	796	-	613	-	965	965	-	23858	23858	-	17.33	-	0.8	-	-10.7
14	-	648	-	608	-	768	768	-	15446	15446	-	17.33	-	0.7	-	-10.9
15	1652	1057	1513	644	306	1304	1610	15673	42808	58481	6.17	17.33	-7.3	0.9	-22.6	-10.6
16	1597	1036	1530	648	288	1260	1548	14303	40529	54832	6.17	17.33	-7.4	0.8	-22.8	-10.7
17	1547	1021	1499	643	284	1248	1532	13632	39574	53206	6.17	17.33	-7.4	0.9	-22.6	-10.7
18	1504	1004	1541	630	265	1248	1513	12373	38917	51290	6.17	17.33	-7.5	0.9	-23.	-10.5
19	1227	943	1389	645	233	1121	1354	8869	32825	41694	6.17	17.33	-7.2	0.8	-22.3	-10.9
20	885	794	1248	597	180	990	1170	4954	24393	29347	6.17	17.33	-6.9	1.0	-21.7	-10.5

TABLE C-15 LOW VELOCITY JET NOISE SUPPRESSOR TEST III

SCALE FACTOR 7.5

BASELINE II

DATA PT	P_{T8}/P_0	P_{T28}/P_0	A_{28}/A_8	V_{28}/V_8	W_8 (lbs/sec)	W_{28} (lbs/sec)	W_T (lbs/sec)	F_8 (lbs)	F_{28} (lbs)	F_T (lbs)	A_8 (ft^2)	A_{28} (ft^2)	$10\log \rho_8 A_8$	$10\log \rho_{28} A_{28}$	$10\log \rho_8^2 A_8$	$10\log \rho_{28}^2 A_{28}$
COMMON DATA					SCALE MODEL DATA											
21	1.109	1.229	2.81	1.009	2.41	13.6	16.0	48.1	274	322	.1097	.308	-24.3	-16.8	-38.9	-28.4
22	1.657	1.746		.669	4.97	23.4	28.4	247.	778	1025	.1097	.308	-25.1	-16.6	-40.6	-28.1
23	1.545	1.773		.757	4.72	23.66	28.4	211	801	1012	.1097	.308	-24.9	-16.6	-40.1	-28.2
24	1.519	1.795		.778	4.61	24.	28.6	202	820	1022	.1097	.308	-24.9	-16.6	-40.1	-28.1
25	1.455	1.802		.828	4.37	24.15	28.5	181	826	1007	.1097	.308	-24.8	-16.6	-40.1	-28.1
21R	1.115	1.226		.964	2.44	13.5	15.9	50.6	270	321	.1097	.308	-24.4	-16.8	-39.2	-28.5

	V_8 (ft/sec)	V_{28} (ft/sec)	T_8 (°R)	T_{28} (°R)	FULL SCALE DATA											
21	642	648	1176	610	136	765	901	2706	15393	18099	6.17	17.33	-6.8	0.7	-21.4	-10.9
22	1602	1071	1578	648	279	1317	1596	13908	43786	57694	6.17	17.33	-7.6	0.9	-23.1	-10.6
23	1441	1091	1470	656	265	1331	1596	11879	45093	56972	6.17	17.33	-7.3	0.9	-22.6	-10.7
24	1415	1101	1471	655	259	1350	1609	11389	46147	57536	6.71	17.33	-7.4	0.9	-22.6	-10.6
25	1331	1102	1443	652	246	1358	1604	10159	46481	56640	6.17	17.33	-7.4	0.9	-22.6	-10.6
21R	669	645	1213	611	137	760	897	2849	15205	18054	6.17	17.33	-6.9	0.7	-21.7	-11.

DUAL

Table C-16. LOW VELOCITY JET NOISE SUPPRESSOR TEST III

SCALE FACTOR 7.5

24 Hole Suppressor

DATA PT	P_{T8}/P_0	P_{T28}/P_0	A_{28}/A_8	V_{28}/V_8	W_8	W_{28}	W_T	F_8	F_{28}	F_T	A_8	A_{28}	$10\log \rho_8 A_8$	$10\log \rho_{28} A_{28}$	$10\log \rho_8^2 A_8$	$10\log \rho_{28}^2 A_{28}$
					← lbs/sec →			← lbs →			← ft^2 →					
COMMON DATA					SCALE MODEL DATA											
26	1.767	-	-	-	5.46	-	5.46	281	-	281	.1097	-	-24.8	-	-40.	-
27	1.685	-	-	-	5.16	-	5.16	256	-	256	.1097	-	-24.9	-	-40.2	-
28	1.633	-	-	-	5.01	-	5.01	240	-	240	.1097	-	-24.9	-	-40.1	-
29	1.568	-	-	-	4.8	-	4.8	219	-	219	.1097	-	-24.9	-	-40.1	-
30	1.4	-	-	-	4.18	-	4.18	161	-	161	.1097	-	-24.7	-	-39.9	-
31	1.204	-	-	-	3.17	-	3.17	87.2	-	87.2	.1097	-	-24.5	-	-39.3	-
32	1.116	-	-	-	2.48	-	2.48	51.	-	51.	.1097	-	-24.3	-	-39.	-
33	-	1.725	-	-	-	23.1	23.1	-	758	758	-	.308	-	-16.6	-	-28.1
34	-	1.676	-	-	-	22.4	22.4	-	716	716	-	.308	-	-16.6	-	-28.2
35	-	1.659	-	-	-	22.1	22.1	-	701	701	-	.308	-	-16.7	-	-28.2
	V_8	V_{28}	T_8	T_{28}												
	← ft/sec →		← °R →		FULL SCALE DATA											
26	1658	-	1512	-	307	-	307	15815	-	15815	6.17	-	-7.3	-	-22.5	-
27	1598	-	1523	-	290	-	290	14399	-	14399	6.17	-	-7.4	-	-22.7	-
28	1539	-	1498	-	282	-	282	13480	-	13480	6.17	-	-7.4	-	-22.6	-
29	1467	-	1475	-	270	-	270	12298	-	12298	6.17	-	-7.3	-	-22.6	-
30	1241	-	1392	-	235	-	235	9065	-	9065	6.17	-	-7.2	-	-22.3	-
31	885	-	1257	-	179	-	179	4905	-	4905	6.17	-	-6.9	-	-21.8	-
32	663	-	1184	-	139	-	139	2871	-	2871	6.17	-	-6.8	-	-21.5	-
33	-	1058	-	645	-	1298	1298	-	42643	42643	-	17.33	-	0.9	-	-10.6
34	-	1031	-	645	-	1258	1258	-	40302	40302	-	17.33	-	0.9	-	-10.7
35	-	1022	-	645	-	1243	1243	-	39448	39448	-	17.33	-	0.9	-	-10.7

CORE

FAN

Table C-17. LOW VELOCITY JET NOISE SUPPRESSOR TEST III

SCALE FACTOR 7.5

24 Hole Suppressor

DATA PT	P_{T8}/P_0	P_{T28}/P_0	A_{28}/A_8	V_{28}/V_8	W_8	W_{28}	W_T	F_8	F_{28}	F_T	A_8	A_{28}	$10\log \rho_8 A_8$	$10\log \rho_{28} A_{28}$	$10\log \rho_8^2 A_8$	$10\log \rho_{28}^2 A_{28}$
					lbs/sec.			lbs			ft^2					
COMMON DATA					SCALE MODEL DATA											
36	-	1.634	-	-	-	21.7	21.7	-	679	679	-	.308	-	-16.7	-	-28.2
37	-	1.519	-	-	-	20.1	20.1	-	572	572	-	.308	-	-16.6	-	-28.1
38	-	1.37	-	-	-	17.3	17.3	-	424	424	-	.308	-	-16.6	-	-28.1
39	-	1.22	-	-	-	13.6	13.6	-	270	270	-	.308	-	-16.7	-	-28.3
40	1.762	1.727	2.81	.634	5.43	23.3	28.7	279	760	1039	.1097	.308	-24.8	-16.5	-40.1	-28.
41	1.676	1.678		.645	5.12	22.5	27.6	253	717	970	.1097	.308	-24.9	-16.6	-40.2	-28.1
42	1.653	1.668		.663	5.1	22.2	27.3	246	708	954	.1097	.308	-24.8	-16.7	-40.1	-28.2
43	1.594	1.64		.668	4.87	21.9	26.8	227	683	910	.1097	.308	-24.9	-16.6	-40.2	-28.1
44	1.404	1.528		.756	4.21	19.86	24.1	162	580	742	.1097	.308	-24.7	-16.7	-39.8	-28.4
45	1.204	1.373		.902	3.16	17.18	20.3	87.1	426.6	514	.1097	.308	-24.5	-16.7	-39.4	-28.2
	V_8	V_{28}	T_8	T_{28}												
	ft/sec		°R		FULL SCALE DATA											
36	-	1007	-	644	-	1221	1221	-	38180	38180	-	17.33	-	0.8	-	-10.7
37	-	918	-	622	-	1129	1129	-	32161	32161	-	17.33	-	0.9	-	-10.6
38	-	788	-	601	-	974	974	-	23858	23858	-	17.33	-	0.9	-	-10.6
39	-	638	-	599	-	767	767	-	15196	15196	-	17.33	-	0.8	-	-10.8
40	1655	1050	1514	635	306	1311	1617	15708	42769	58477	6.17	17.33	-7.3	0.9	-22.6	-10.5
41	1589	1025	1521	636	288	1267	1555	14221	40345	54566	6.17	17.33	-7.4	0.9	-22.7	-10.6
42	1552	1029	1489	647	287	1247	1534	13819	39846	53665	6.17	17.33	-7.3	0.8	-22.6	-10.7
43	1500	1002	1491	634	274	1235	1509	12756	38431	51187	6.17	17.33	-7.4	0.9	-22.7	-10.6
44	1242	939	1382	643	237	1118	1355	9133	32597	41730	6.17	17.33	-7.2	0.8	-22.3	-10.9
45	887	800	1263	614	178	966	1144	4899	23997	28896	6.17	17.33	-7.	0.8	-21.9	-10.7

FAN DUAL

Table C-18. LOW VELOCITY JET NOISE SUPPRESSOR TEST III

SCALE FACTOR 7.5

24 Hole Suppressor

	DATA PT	P_{T8}/P_0	P_{T28}/P_0	A_{28}/A_8	V_{28}/V_8	W_8 (lbs/sec)	W_{28} (lbs/sec)	W_T (lbs/sec)	F_8 (lbs)	F_{28} (lbs)	F_T (lbs)	A_8 (ft^2)	A_{28} (ft^2)	$10\log \rho_8 A_8$	$10\log \rho_{28} A_{28}$	$10\log \rho_8^2 A_8$	$10\log \rho_{28}^2 A_{28}$
	COMMON DATA					SCALE MODEL DATA											
DUAL	46	1.113	1.229	2.81	.982	2.44	13.65	16.1	49.7	273	323	.1097	.308	-24.3	-16.7	-39.	-28.4
	47	1.663	1.758		.672	4.97	23.4	28.4	249	787	1036	.1097	.308	-25.1	-16.7	-40.6	-28.2
	48	1.557	1.782		.743	4.73	23.94	28.7	215	808	1023	.1097	.308	-24.9	-16.6	-40.2	-28.
												.1097	.308				
												.1097	.308				
Rdg 18	99	1.615	1.778		.726	5.02	23.77	28.8	234	804	1038	.1097	.308	-24.8	-16.6	-39.9	-28.1

		V_8 (ft/sec)	V_{28} (ft/sec)	T_8 (°R)	T_{28} (°R)												
						FULL SCALE DATA											
	46	656	644	1186	603	137	768	905	2795	15361	18156	6.17	17.33	-6.8	0.8	-21.5	-10.9
	47	1610	1082	1583	655	280	1317	1597	13985	44276	58261	6.17	17.33	-7.6	0.8	-23.1	-10.7
	48	1462	1086	1487	645	266	1347	1613	12075	45431	57506	6.17	17.33	-7.4	0.9	-22.7	-10.5
												6.17	17.33				
												6.17	17.33				
Rdg 18	99	1500	1089	1453	651	282	1337	1619	13142	45239	58381	6.17	17.33	-7.3	0.9	-22.4	-10.6

TABLE C-19 LOW VELOCITY JET NOISE SUPPRESSOR TEST III

SCALE FACTOR 7.5

24 SPOKE SUPPRESSOR

DATA PT	P_{T8}/P_0	P_{T28}/P_0	A_{28}/A_8	V_{28}/V_8	W_8 (lbs/sec)	W_{28} (lbs/sec)	W_T (lbs/sec)	F_8 (lbs)	F_{28} (lbs)	F_T (lbs)	A_8 (ft^2)	A_{28} (ft^2)	$10\log \rho_8 A_8$	$10\log \rho_{28} A_{28}$	$10\log \rho_8^2 A_8$	$10\log \rho_{28}^2 A_{28}$
CORE	COMMON DATA				SCALE MODEL DATA											
49	1.76	-	-	-	5.44	-	5.44	279	-	279	.1097	-	-24.8	-	-40.	-
50	1.682	-	-	-	5.14	-	5.14	225	-	255	.1097	-	-24.9	-	-40.2	-
51	1.645	-	-	-	5.05	-	5.05	243	-	243	.1097	-	-24.9	-	-40.2	-
52	1.579	-	-	-	4.82	-	4.82	222	-	222	.1097	-	-24.9	-	-40.2	-
53	1.393	-	-	-	4.16	-	4.16	158	-	158	.1097	-	-24.7	-	-39.8	-
54	1.199	-	-	-	3.12	-	3.12	85.1	-	85.1	.1097	-	-24.5	-	-39.4	-
55	1.124	-	-	-	2.58	-	2.58	54.4	-	54.4	.1097	-	-24.2	-	-38.8	-
FAN																
56	-	1.724	-	-	-	23.1	23.1	-	759	759	-	.308	-	-16.6	-	-28.1
57	-	1.687	-	-	-	22.5	22.5	-	726	726	-	.308	-	-16.6	-	-28.1
58	-	1.655	-	-	-	22.1	22.1	-	698	698	-	.308	-	-16.6	-	-28.2
	V_8 (ft/sec)	V_{28} (ft/sec)	T_8 (°R)	T_{28} (°R)	FULL SCALE DATA											
49	1649	-	1505	-	306	-	306	15576	-	15576	6.17	-	-7.3	-	-22.5	-
50	1595	-	1523	-	289	-	289	14327	-	14327	6.17	-	-7.4	-	-22.7	-
51	1551	-	1500	-	284	-	284	13675	-	13675	6.17	-	-7.4	-	-22.7	-
52	1482	-	1485	-	271	-	271	12482	-	12482	6.17	-	-7.4	-	-22.7	-
53	1227	-	1381	-	234	-	234	8912	-	8912	6.17	-	-7.2	-	-22.3	-
54	877	-	1264	-	176	-	176	4789	-	4789	6.17	-	-7.	-	-21.9	-
55	679	-	1167	-	145	-	145	3059	-	3059	6.17	-	-6.7	-	-21.3	-
56	-	1057	-	645	-	1300	1300	-	42682	42682	-	17.33	-	0.9	-	-10.6
57	-	1037	-	645	-	1268	1268	-	40852	40852	-	17.33	-	0.9	-	-10.6
58	-	1018	-	643	-	1241	1241	-	39246	39246	-	17.33	-	0.9	-	-10.7

TABLE C-20 LOW VELOCITY JET NOISE SUPPRESSOR TEST III

SCALE FACTOR 7.5

24 SPOKE SUPPRESSOR

	DATA PT	P_{T8}/P_0	P_{T28}/P_0	A_{28}/A_8	V_{28}/V_8	W_8 (lbs/sec)	W_{28} (lbs/sec)	W_T (lbs/sec)	F_8 (lbs)	F_{28} (lbs)	F_T (lbs)	A_8 (ft^2)	A_{28} (ft^2)	$10\log \rho_8 A_8$	$10\log \rho_{28} A_{28}$	$10\log \rho_8^2 A_8$	$10\log \rho_{28}^2 A_{28}$
		COMMON DATA				SCALE MODEL DATA											
FAN	59	-	1.64	-	-	-	21.9	21.9	-	684	684	-	.308	-	-16.6	-	-28.1
	60	-	1.526	-	-	-	20.0	20.	-	578	578	-	.308	-	-16.7	-	-28.2
	61	-	1.363	-	-	-	17.1	17.1	-	417	417	-	.308	-	-16.6	-	-28.1
	62	-	1.218	-	-	-	13.1	13.1	-	261	261	-	.308	-	-16.9	-	-28.7
DUAL	63	1.751	1.716	2.81	.636	5.38	23.02	28.4	276	751	1027	.1097	.308	-24.9	-16.6	-40.1	-28.1
	64	1.716	1.689		.644	5.3	22.6	27.9	265	727	992	.1097	.308	-24.8	-16.6	-40.1	-28.1
	65	1.666	1.663		.66	5.15	22.01	27.2	250	704	954	.1097	.308	-24.8	-16.7	-40.	-28.3
	66	1.583	1.647		.693	4.86	21.66	26.5	223	690	913	.1097	.308	-24.8	-16.8	-40.1	-28.4
	67	1.402	1.522		.739	4.17	20.05	24.2	162	574	736	.1097	.308	-24.8	-16.6	-39.9	-28.1
	68	1.206	1.37		.922	3.19	16.68	19.9	87.9	423	511	.1097	.308	-24.4	-16.9	-39.3	-28.7
		V_8 (ft/sec)	V_{28} (ft/sec)	T_8 (°R)	T_{28} (°R)	FULL SCALE DATA											
	59	-	1005	-	637	-	1233	1233	-	38485	38485	-	17.22	-	0.9	-	-10.6
	60	-	931	-	634	-	1125	1125	-	32537	32537	-	17.33	-	0.8	-	-10.7
	61	-	784	-	603	-	964	964	-	23452	23452	-	17.33	-	0.9	-	-10.6
	62	-	642	-	625	-	737	737	-	14694	14694	-	17.33	-	0.6	-	-11.2
	63	1651	1050	1521	641	303	1295	1598	15520	42229	57749	6.17	17.33	-7.4	0.9	-22.6	-10.6
	64	1611	1038	1500	644	298	1269	1567	14922	40893	55815	6.17	17.33	-7.3	0.9	-22.6	-10.6
	65	1561	1030	1485	652	290	1238	1528	14050	39593	53643	6.17	17.33	-7.3	0.8	-22.5	-10.8
	66	1480	1025	1472	658	273	1218	1491	12557	38786	51343	6.17	17.33	-7.3	0.7	-22.6	-10.9
	67	1248	922	1401	625	235	1128	1363	9098	32298	41396	6.17	17.33	-7.3	0.9	-22.4	-10.6
	68	887	818	1254	647	179	938	1117	4947	23840	28787	6.17	17.33	-6.9	0.6	-21.8	-11.2

Table C-21. LOW VELOCITY JET NOISE SUPPRESSOR TEST III

24 Spoke Suppressor

SCALE FACTOR 7.5

	DATA PT	P_{T8}/P_0	P_{T28}/P_0	A_{28}/A_8	V_{28}/V_8	W_8	W_{28}	W_T	F_8	F_{28}	F_T	A_8	A_{28}	$10\log \rho_8 A_8$	$10\log \rho_{28} A_{28}$	$10\log \rho_0^2 A_8$	$10\log \rho_{28}^2 A_{28}$
						← lbs/sec →			← lbs →			← ft^2 →					
	COMMON DATA					SCALE MODEL DATA											
DUAL	69	1.107	1.224	2.81	1.052	2.39	12.89	15.3	47.2	268	315	.1097	.308	-24.2	-17.1	-38.9	-29.1
	70	1.653	1.74		.667	4.96	23.36	28.3	245	772	1017	.1097	.308	-25.1	-16.6	-40.5	-28.1
	71	1.489	1.787		.788	4.45	23.9	28.4	192	812	1004	.1097	.308	-24.9	-16.6	-40.3	-28.1

	V_8	V_{28}	T_8	T_{28}												
	← ft/sec →		← °R →		FULL SCALE DATA											
69	635	668	1172	662	134	726	860	2654	15059	17713	6.17	17.33	-6.7	0.4	-21.4	-11.7
70	1594	1063	1569	643	279	1314	1593	13809	43403	57212	6.17	17.33	-7.6	0.9	-23.	-10.6
71	1389	1094	1485	651	250	1345	1595	10792	45670	56462	6.17	17.33	-7.4	0.9	-22.8	-10.6

Table C-1. LOW VELOCITY JET NOISE SUPPRESSOR TEST I

SCALE FACTOR 7.5

Baseline I SI Units

DATA PT	P_{T8}/P_0	P_{T28}/P_0	A_{28}/A_8	V_{28}/V_8	W_8	W_{28}	W_T	F_8	F_{28}	F_T	A_8	A_{28}	$10\log \rho_8 A_8$	$10\log \rho_{28} A_{28}$	$10\log \rho_8^2 A_8$	$10\log \rho_{28}^2 A_{28}$
					← kg/sec		→	← N		→	← m^2	→				
COMMON DATA					SCALE MODEL DATA											
1	1.061				.762	-	.762	109.4	-	109.4	.00915	-	-22.8	-	-25.0	-
2	1.116				1.012	-	1.012	204.2	-	204.2	.00915	-	-23.0	-	-25.5	-
3	1.211				1.311	-	1.311	360.3	-	360.3	.00915	-	-23.2	-	-26.0	-
4	1.403				1.706	-	1.706	649.4	-	649.4	.00915	-	-23.5	-	-26.5	-
5	1.589				1.982	-	1.982	902.9	-	902.9	.00915	-	-23.6	-	-26.8	-
6	1.693				2.109	-	2.109	1036	-	1036	.00915	-	-23.9	-	-26.9	-
7		1.129			-	4.931	4.931	-	707.2	707.2	-	.0286	-	-14.6	-	-13.8
8		1.214			-	6.337	6.337	-	1143	1143	-	.0286	-	-14.6	-	-13.6
9		1.335			-	7.888	7.888	-	1730	1730	-	.0286	-	-14.4	-	-13.4
10		1.532			-	9.848	9.848	-	2607	2607	-	.0286	-	-14.3	-	-13.1
	V_8	V_{28}	T_8	T_{28}												
	← m/sec	→	← °K	→	FULL SCALE DATA											
1	143	-	606	-	42.87		42.87	6285		6285	.526	-	-5.2	-	-7.4	-
2	201	-	645	-	58.06		58.06	11734		11734	.526	-	-5.4	-	-7.9	-
3	273	-	697	-	75.3		75.3	20692		20692	.526	-	-5.6	-	-8.4	-
4	378	-	769	-	97.98		97.98	37310		37310	.526	-	-5.9	-	-8.9	-
5	453	-	819	-	113.9		113.9	51850		51850	.526	-	-6.0	-	-9.2	-
6	487	-	841	-	121.1		121.1	59430		59430	.526	-	-6.3	-	-9.3	-
7	-	143	-	298		283.5	283.5		40726	40726	-	1.605	-	3.0	-	3.8
8	-	180	-	298		364.2	364.2		65777	65777	-	1.605	-	3.0	-	4.0
9	-	218	-	299		453.6	453.6		99359	99359	-	1.605	-	3.2	-	4.2
10	-	263	-	300		565.6	565.6		149662	149662	-	1.605	-	3.3	-	4.5

Table C-2 LOW VELOCITY JET NOISE SUPPRESSOR TEST I

SCALE FACTOR 7.5

Baseline I SI Units

DATA PT	P_{T8}/P_0	P_{T28}/P_0	A_{28}/A_8	V_{28}/V_8	W_8	W_{28}	W_T	F_8	F_{28}	F_T	A_8	A_{28}	$10\log \rho_8 A_8$	$10\log \rho_{28} A_{28}$	$10\log \rho_0^2 A_8$	$10\log \rho_{28}^2 A_{28}$
					kg/sec			N			m^2					
COMMON DATA					SCALE MODEL DATA											
11		1.651			-	10.85	10.85	-	3091	3091	-	.0286	-	-14.2	-	-12.9
12		1.692			-	11.17	11.17	-	3256	3256	-	.0286	-	-14.2	-	-12.8
13	1.062	1.122	3.13	.97	.767	4.79	5.557	111.1	671.6	782.7	.00915	.0286	-22.8	-14.7	-25.1	-13.8
14	1.117	1.212	3.13	.89	1.016	6.291	7.307	205.5	1134	1340	.00915	.0286	-23.0	-14.6	-25.5	-13.6
15	1.221	1.333	3.13	.78	1.338	7.843	9.181	375.4	1717	2092	.00915	.0286	-23.2	-14.5	-25.9	-13.4
16	1.398	1.527	3.13	.70	1.701	9.798	11.05	640.5	2580	3021	.00915	.0286	-23.5	-14.3	-26.5	-12.9
17	1.602	1.654	3.13	.62	2.005	10.86	12.86	916.3	3105	4021	.00915	.0286	-23.6	-14.2	-26.7	-12.9
18	1.699	1.701	3.13	.60	2.109	11.16	13.27	1041	3292	4333	.00915	.0286	-23.7	-14.2	-26.9	-12.9
19	1.696	1.439	3.13	.50	2.109	8.918	11.03	1036	2202	3238	.00915	.0286	-23.7	-14.4	-26.9	-13.3
20	1.697	1.24	3.13	.39	2.105	6.641	8.745	1036	1272	2308	.00915	.0286	-23.7	-14.6	-26.9	-13.7
	V_8	V_{28}	T_8	T_{28}	FULL SCALE DATA											
	m/sec		°K													
11	-	283	-	299	-	623.2	623.2	-	177720	177720	-	1.605	-	3.4	-	4.7
12	-	290	-	300	-	641.4	641.4	-	187087	187087	-	1.605	-	3.4	-	4.8
13	144	139	606	299	44.04	274.9	318.9	6378	38578	44956	.526	1.605	-5.2	2.9	-7.5	3.8
14	201	179	646	299	58.38	361.5	419.9	11809	65114	76923	.526	1.605	-5.4	3.0	-7.9	4.0
15	279	218	694	299	76.66	450.4	527.1	21559	98688	120247	.526	1.605	-5.6	3.1	-8.3	4.2
16	376	262	765	299	97.52	562.9	660.4	36852	148341	185193	.526	1.605	-6.9	3.3	-8.9	4.5
17	456	284	816	301	115.2	623.7	738.9	52749	178414	231163	.526	1.605	-6.0	3.4	-13.1	4.5
18	490	293	845	304	121.1	641.4	762.5	59768	189125	248893	.526	1.605	-6.1	3.4	-9.3	4.5
19	489	245	844	303	121.1	512.6	633.7	59559	126439	185998	.526	1.605	-6.1	3.2	-9.3	4.5
20	490	191	846	303	121.1	381.5	502.6	59585	73085	132670	.526	1.605	-6.1	3.0	-9.3	3.9

Table C-3. LOW VELOCITY JET NOISE SUPPRESSOR TEST I

SCALE FACTOR 7.5

Baseline I and 18 Lobe Suppressor AR=2 SI Units

	DATA PT	P_{T8}/P_0	P_{T28}/P_0	A_{28}/A_8	V_{28}/V_8	W_8 (kg/sec)	W_{28} (kg/sec)	W_T (kg/sec)	F_8 (N)	F_{28} (N)	F_T (N)	A_8 (m^2)	A_{28} (m^2)	$10\log \rho_8 A_8$	$10\log \rho_{28} A_{28}$	$10\log \rho_8^2 A_8$	$10\log \rho_{28}^2 A_{28}$
	COMMON DATA					SCALE MODEL DATA											
Baseline 1	21	1.118	1.111	3.13	.66	1.021	4.572	5.593	207.3	613.8	821.1	.00915	.0286	-23.0	-14.7	-25.5	-13.8
	22	1.118	1.062	"	.60	1.021	3.425	4.446	207.4	348.3	555.7	.00915	.0286	-23.0	-14.7	-25.5	-13.6
18 Lobe AR=2	23	1.064	-	-		.776	-	.776	113.4	-	113.4	.00915	-	-22.8	-	-25.0	-
	24	1.118	-	-		1.012	-	1.012	205.3	-	205.3	.00915	-	-23.0	-	-25.5	-
	25	1.215	-	-		1.306	-	1.306	362.5	-	362.5	.00915	-	-23.2	-	-26.0	-
	26	1.391	-	-		1.669	-	1.669	624.5	-	624.5	.00915	-	-23.5	-	-26.5	-
	27	1.6	-	-		1.973	-	1.973	907.4	-	907.4	.00915	-	-23.6	-	-26.8	-
	28	1.684	-	-		2.073	-	2.073	1010	-	1010	.00915	-	-23.9	-	-26.9	-
	29	-	1.118	-		-	4.745	4.745	-	645.	645	-	.0286	-	-14.6	-	-13.6
	30	-	1.205	-		-	6.246	6.246	-	1090	1090	-	.0286	-	-14.5	-	-13.4
		V_8 (m/sec)	V_{28} (m/sec)	T_8 (°K)	T_{28} (°K)	FULL SCALE DATA											
	21	202	134	647	299	58.51	262.6	321.1	11912	35224	47136	.526	1.065	-5.4	2.9	-7.9	3.8
	22	202	101	645	298	58.51	196.9	255.4	11912	19998	31910	.526	1.605	-5.4	2.9	-7.9	4.0
	23	146	-	603	-	44.59	-	44.59	6516	-	6516	.526	-	-4.9	-	-7.2	-
	24	202	-	647	-	58.06	-	58.06	11796	-	11796	.526	-	-5.2	-	-7.7	-
	25	276	-	698	-	75.07	-	75.07	20830	-	20830	.526	-	-5.4	-	-8.2	-
	26	373	-	766	-	95.71	-	95.71	35882	-	35882	.526	-	-5.6	-	-8.7	-
	27	457	-	820	-	113.4	-	113.4	52135	-	52135	.526	-	-5.8	-	-9.0	-
	28	486	-	842	-	119.3	-	119.3	58015	-	58015	.526	-	-5.8	-	-9.1	-
	29	-	135	-	289	-	272.6	272.6	-	37056	37056	-	1.605	-	3.0	-	4.0
	30	-	173	-	288	-	358.8	358.8	-	62614	62614	-	1.605	-	3.1	-	4.2

TABLE C-4 LOW VELOCITY JET NOISE SUPPRESSOR TEST I

SCALE FACTOR 7.5

SI UNITS

18 LOBE SUPPRESSOR AR-2

DATA PT	P_{T8}/P_0	P_{T28}/P_0	A_{28}/A_8	V_{28}/V_8	W_8	W_{28}	W_T	F_8	F_{28}	F_T	A_8	A_{28}	$10\log \rho_8 A_8$	$10\log \rho_{28} A_{28}$	$10\log \rho_8^2 A_8$	$10\log \rho_{28}^2 A_{28}$
					kg/sec			N			m^2					
COMMON DATA					SCALE MODEL DATA											
31	-	1.333	-	-	-	7.933	7.933	-	1704	1704	-	.0286	-	-14.3	-	-13.1
32	-	1.529	-	-	-	9.934	9.934	-	2566	2566	-	.0286	-	-14.2	-	-12.8
33	-	1.656	-	-	-	11.0	11.0	-	3082	3082	-	.0286	-	-14.1	-	-12.6
34	-	1.691	-	-	-	11.15	11.15	-	3189	3189	-	.0286	-	-14.1	-	-12.6
35	1.064	1.122	2.93	.94	.739	4.867	5.606	107.2	6672	774	.00915	.0286	-22.7	-14.5	-25.0	-13.5
36	1.115	1.202	2.93	.86	.998	6.219	7.217	200.2	1072	1272	.00915	.0286	-23.0	-14.4	-25.5	-13.4
36R	1.117	1.212	2.93	.88	1.007	6.319	7.326	203.7	1125	1330	.00915	.0286	-23.0	-14.5	-25.5	-13.5
37	1.212	1.328	2.93	.77	1.297	7.87	9.167	357.6	1677	2034	.00915	.0286	-23.2	-14.3	-26.0	-13.2
38	1.398	1.523	2.93	.69	1.692	9.852	11.54	636.1	2540	3167	.00915	.0286	-23.5	-14.2	-26.5	-12.8
39	1.593	1.656	2.93	.62	1.964	10.96	12.93	898.5	3082	3981	.00915	.0286	-23.6	-14.1	-26.8	-12.7
	V_8	V_{28}	T_8	T_{28}												
	m/sec		°K		FULL SCALE DATA											
31	-	213	-	287	-	455.9	455.9	-	97798		-	1.605	-	3.2	-	4.4
32	-	257	-	287	-	571.1	571.1	-	147393		-	1.605	-	3.3	-	4.7
33	-	279	-	288	-	632.3	632.3	-	177146		-	1.605	-	3.4	-	4.9
34	-	284	-	289	-	640.5	640.5	-	183262		-	1.605	-	3.4	-	4.9
35	145	136	594	284	42.5	279.9	322.4	6160	38204	44364	.526	1.605	-4.9	3.0	-7.2	4.0
36	200	172	648	286	56.25	357.4	413.7	11503	61591	73094	.526	1.605	-5.3	3.1	-7.8	4.1
36R	201	177	647	291	58.06	362.9	420.9	11707	64656	76363	.526	1.605	-5.2	3.0	-7.8	4.1
37	274	212	697	288	74.39	452.2	526.6	20554	96348	116902	.526	1.605	-5.5	3.2	-8.3	4.3
38	373	256	757	289	94.07	636.2	636.2	36545	145930	182745	.526	1.605	-5.7	3.3	-8.7	4.7
39	455	280	821	290	112.9	630.1	743.	51623	177106	228729	.526	1.605	-5.9	3.4	-9.1	4.8

Table C-7. LOW VELOCITY JET NOISE SUPPRESSOR TEST I

SCALE FACTOR 7.5

18 Lobe Suppressor AR=4.8 SI UNITS

DATA PT	P_{T8}/P_0	P_{T28}/P_0	A_{28}/A_8	V_{28}/V_8	W_8	W_{28}	W_T	F_8	F_{28}	F_T	A_8	A_{28}	$10\log \rho_8 A_8$	$10\log \rho_{28} A_{28}$	$10\log \rho_8^2 A_8$	$10\log \rho_{28}^2 A_{28}$
					← kg/sec →			← N →			← m^2 →					
COMMON DATA					SCALE MODEL DATA											
59	1.212	1.341	2.93	.80	1.288	7.91	9.2	356	1730	2086	.00915	.0286	-23.2	-14.4	-26.0	-13.3
60	1.401	1.521	2.93	.69	1.687	9.73	11.41	641	2535	3176	.00915	.0286	-23.5	-14.3	-26.5	-13.1
61	1.591	1.654	2.93	.62	1.969	10.86	12.83	894	3078	3972	.00915	.0286	-23.6	-14.2	-26.8	-12.8
62	1.687	1.687	2.93	.59	2.082	11.16	13.25	1014	3211	4225	.00915	.0286	-23.6	-14.1	-26.9	-12.7
63	1.682	1.424	2.93	.50	2.073	8.86	10.93	1010	2117	3127	.00915	.0286	-23.6	-14.3	-26.9	-13.1
64	1.683	1.225	2.93	.37	2.073	6.5	8.57	1010	1188	2197	.00915	.0286	-23.6	-14.5	-26.9	-13.5
65	1.129	1.12	2.93	.65	1.057	4.75	5.81	222	651	872	.00915	.0286	-22.9	-14.6	-26.1	-13.7
66	1.131	1.066	2.93	.48	1.057	3.53	4.59	226	365	591	.00915	.0286	-23.0	-14.7	-25.4	-13.8

	V_8	V_{28}	T_8	T_{28}												
	← m/sec →		← °K →													
					FULL SCALE DATA											
59	274	218	697	293	73.9	455	528	20447	99417	119865	.526	1.605	-5.5	3.1	-8.3	4.2
60	377	259	768	296	97.1	1012	1110	36803	145672	182475	.526	1.605	-5.7	3.2	-8.8	4.4
61	454	282	820	296	113	624	737	51370	176852	228222	.526	1.605	-5.9	3.3	-9.1	4.7
62	486	286	842	293	120	641	761	58269	184521	242790	.526	1.605	-5.9	3.5	-9.2	4.8
63	485	244	842	292	119.	509	629	58015	121648	179664	.526	1.605	-5.9	3.2	-9.2	4.4
64	486	182	843	293	119.	375	494	58015	68237	126252	.526	1.605	-5.9	3.0	-9.2	4.0
65	210	136	646	290	60.8	273	334	12779	37417	50196	.526	1.605	-5.2	2.9	-7.8	3.8
66	212	103	648	291	60.8	203	264.	12984	20955	33938	.526	1.605	-5.3	2.8	-7.8	3.7

Table C-8 LOW VELOCITY JET NOISE SUPPRESSOR TEST II

SCALE FACTOR 7.5

18 Capped Lobe Suppressor AR=2 SI Units

DATA PT	P_{T8}/P_0	P_{T28}/P_0	A_{28}/A_8	V_{28}/V_8	W_8	W_{28}	W_T	F_8	F_{28}	F_T	A_8	A_{28}	$10\log \rho_8 A_8$	$10\log \rho_{28} A_{28}$	$10\log \rho_8^2 A_8$	$10\log \rho_{28}^2 A_{28}$
					← kg/sec →			← N →			← m^2 →					
COMMON DATA					SCALE MODEL DATA											
1	1.114	-	-	-	1.093	-	1.093	222	-	222	.00985	-	-22.7	-	-25.2	-
2	1.4	-	-	-	1.823	-	1.823	685	-	685	.00985	-	-23.2	-	-26.2	-
3	1.68	-	-	-	2.227	-	2.229	1081	-	1081	.00985	-	-23.4	-	-26.6	-
4	-	1.11	-	-	-	4.44	4.44	-	600	600	-	.0286	-	-15.	-	-14.2
5	-	1.199	-	-	-	5.94	5.94	-	1059	1059	-	.0286	-	-14.8	-	-14.1
6	-	1.323	-	-	-	7.53	7.53	-	1655	1655	-	.0286	-	-14.7	-	-13.8
7	-	1.527	-	-	-	9.58	9.58	-	2553	2553	-	.0286	-	-14.5	-	-13.4
8	-	1.652	-	-	-	10.64	10.64	-	3065	3065	-	.0286	-	-14.4	-	-13.2
9	-	1.686	-	-	-	10.91	10.91	-	3198	3198	-	.0286	-	-14.3	-	-13.1
10	1.062	1.118	2.92	0.97	.826	4.627	5.45	118	643	761	.00985	.0286	-22.4	-14.8	-24.7	-14.1
	V_8	V_{28}	T_8	T_{28}	FULL SCALE DATA											
	← m/sec →		← °K →													
1	203	-	645	-	63.1	-	63.1	12739	-	12739	.554	-	-5.1	-	-7.6	-
2	375	-	761	-	105	-	105	39258	-	39258	.554	-	-5.6	-	-8.6	-
3	485	-	842	-	128	-	128	61974	-	61974	.554	-	-5.8	-	-9.0	-
4	-	135	-	311	-	313	313	-	34534	34534	-	1.61	-	2.7	-	3.4
5	-	178	-	312	-	341	341	-	60729	60729	-	1.61	-	2.8	-	3.5
6	-	220	-	312	-	433	433	-	94996	94996	-	1.61	-	2.9	-	3.8
7	-	267	-	311	-	551	551	-	146691	146691	-	1.61	-	3.1	-	4.2
8	-	288	-	309	-	611	611	-	175967	175967	-	1.61	-	3.2	-	4.4
9	-	293	-	308	-	627	627	-	183653	183653	-	1.61	-	3.3	-	4.5
10	143	139	598	307	46.3	260.4	307	6628	36157	42785	.0736	1.61		2.7	-7.2	3.4

Table C-9 LOW VELOCITY JET NOISE SUPPRESSOR TEST

SCALE FACTOR 7.5

18 Capped Lobe Suppressor AR=2 SI Units

DATA PT	P_{T8}/P_0	P_{T28}/P_0	A_{28}/A_8	V_{28}/V_8	W_8	W_{28}	W_T	F_8	F_{28}	F_T	A_8	A_{28}	$10\log \rho_8 A_8$	$10\log \rho_{28} A_{28}$	$10\log \rho_8^2 A_8$	$10\log \rho_{28}^2 A_{28}$
					← kg/sec		→	← N		→	← m^2	→				
COMMON DATA					SCALE MODEL DATA											
11	1.106	1.196	2.92	.915	1.03	5.92	6.95	198	1041	1239	.00985	.0286	-22.7	-14.8	-25.3	-14.
12	1.211	1.324	2.92	.80	1.397	7.575	8.97	382	1657	2039	.00985	.0286	-22.9	-14.6	-25.7	-13.8
13	1.381	1.517	2.92	.721	1.783	9.48	11.26	654	2509	3163	.00985	.0286	-23.2	-14.5	-26.2	-13.5
14	1.587	1.649	2.92	.637	2.105	10.59	12.69	952	3051	4003	.00985	.0286	-23.3	-14.4	-26.5	-13.2
15	1.693	1.683	2.92	.601	2.245	10.85	13.1	1094	3185	4279	.00985	.0286	-23.4	-14.3	-26.6	-13.2
16	1.429	1.679	2.92	.721	1.787	10.82	12.61	725	3167	3892	.00985	.0286	-23.6	-14.4	-27.	-13.2
17	1.216	1.679	2.92	.962	1.279	10.82	12.1	390	3167	3557	.00985	.0286	-23.8	-14.4	-27.4	-13.2
18	1.106	1.115	2.92	.721	1.034	4.54	5.57	198	627	825	.00985	.0286	-22.7	-14.9	-25.3	-14.2
19	1.051	1.117	2.92	1.034	.721	4.56	5.28	97.4	636	733	.00985	.0286	-22.8	-14.9	-25.4	-14.3
20	1.105	1.076	2.92	.627	1.03	3.5	4.53	197	420	617	.00985	.0286	-22.7	-15.4	-25.2	-15.2
	V_8	V_{28}	T_8	T_{28}	FULL SCALE DATA											
	← m/sec	→	← °K	→												
11	193	176	650	309	58.1	333	391	11160	58589	69749	.554	1.61	-5.2	2.7	-7.8	3.5
12	274	219	698	309	79.8	426	505	21462	93230	114692	.554	1.61	-5.4	2.9	-8.2	3.7
13	368	265	760	311	100.	534	634	36803	141197	178000	.554	1.61	-5.7	3.	-8.6	4.
14	453	288	820	311	118	596	714	53616	171541	225157	.554	1.61	-5.8	3.1	-9.	4.3
15	488	294	843	310	127	611	737	61640	179076	240716	.554	1.61	-5.9	3.2	-9.1	4.3
16	407	293	843	311	101	608	709	40850	178196	219046	.554	1.61	-6.1	3.1	-9.5	4.3
17	305	293	847	311	72.1	608	680	21915	178196	200111	.554	1.61	-6.3	3.1	-9.9	4.3
18	192	138	646	311	58.1	255	313	11160	35277	46437	.554	1.61	-5.2	2.6	-7.8	3.3
19	135	140	644	313	40.5	257	297	6471	35864	41335	.554	1.61	-5.3	2.6	-7.9	3.2
20	191	120	642	346	58.1	197	255	11058	23614	34672	.554	1.61	-5.2	2.1	-7.7	2.3

Table C-10. LOW VELOCITY JET NOISE SUPPRESSOR TEST II

18 Capped Lobe
Suppressor AR = 2
SI Units

SCALE FACTOR 7.5

DATA PT	P_{T8}/P_0	P_{T28}/P_0	A_{28}/A_8	V_{28}/V_8	W_8 (kg/sec)	W_{28} (kg/sec)	W_T (kg/sec)	F_8 (N)	F_{28} (N)	F_T (N)	A_8 (m^2)	A_{28} (m^2)	$10\log \rho_8 A_8$	$10\log \rho_{28} A_{28}$	$10\log \rho_8^2 A_8$	$10\log \rho_{28}^2 A_{28}$
COMMON DATA					SCALE MODEL DATA											
21	1.105	1.154	2.92	.884	1.03	4.92	5.95	197	827	1024	.00985	.0286	-22.7	-16.1	-25.3	-15.3
22	1.568	1.506	2.92	.62	2.041	8.755	10.8	925	2464	3389	.00985	.0286	-23.5	-15.1	-26.8	-14.7
23	1.689	1.313	2.92	.486	2.236	6.768	9.0	1090	1606	2696	.00985	.0286	-23.4	-15.5	-26.7	-15.4
24	1.691	1.488	2.92	.583	2.245	8.42	10.67	1094	2389	3483	.00985	.0286	-23.4	-15.3	-26.6	-15.1
25	1.392	1.366	2.92	.682	1.805	7.31	9.12	672	1850	2522	.00985	.0286	-23.2	-15.4	-26.1	-15.3
26	1.692	1.685	2.92	.672	2.332	10.1	12.43	1094	3189	4283	.00985	.0286	-23.1	-15.	-26.	-14.5
27	1.647	1.668	2.92	.655	2.182	10.06	12.24	1036	3122	4158	.00985	.0286	-23.4	-14.9	-26.6	-14.3
28	NO DATA															
29	1.596	1.65	2.92	.678	2.127	9.92	12.05	965	3156	4021	.00985	.0286	-23.3	-14.9	-26.5	-14.4
30	1.384	1.525	2.92	.764	1.783	9.0	10.78	658	2544	3202	.00985	.0286	-23.2	-15.	-26.2	-14.5
	V_8 (m/sec)	V_{28} (m/sec)	T_8 (°K)	T_{28} (°K)	FULL SCALE DATA											
21	191	169	645	353	58.1	277	335	11058	46646	57704	.554	1.61	-5.2	2.1	-7.8	1.8
22	454	282	846	357	115	493	608	42113	138582	190695	.554	1.61	-6.	2.4	-9.3	1.2
23	488	237	847	375	126	381	507	61338	90348	151686	.554	1.61	-5.9	2.	-9.2	1.9
24	487	284	842	373	127	474	601	61494	134276	195770	.554	1.61	-5.9	2.2	-9.1	1.6
25	372	253	759	374	102	411	513	37750	104074	141824	.554	1.61	-5.7	2.1	-8.6	1.8
26	471	316	785	359	131	568	699	61627	179512	241139	.554	1.61	-5.6	2.5	-8.5	3.
27	475	311	837	353	123	566	689	58202	175763	233965	.554	1.61	-5.9	2.6	-9.1	3.2
28	NO DATA															
29	454	309	816	354	120	558	678	54319	171764	226083	.554	1.61	-5.8	2.6	-9.	3.1
30	370	283	765	350	100	507	607	37061	143088	180149	.554	1.61	-5.7	2.5	-8.7	3.0

TABLE C-11. LOW VELOCITY JET NOISE SUPPRESSOR TEST II

18 Capped Lobe
Suppressor AR = 2
SI Units

SCALE FACTOR 7.5

DATA PT	P_{T28}/P_0	P_{T28}/P_0	A_{28}/A_8	V_{28}/V_8	W_8	W_{28}	W_T	F_8	F_{28}	F_T	A_8	A_{28}	$10\log \rho_8 A_8$	$10\log \rho_{28} A_{28}$	$10\log \rho_8^2 A_8$	$10\log \rho_{28}^2 A_{28}$
					kg/sec			N			m^2					
COMMON DATA					SCALE MODEL DATA											
31	1.208	1.326	2.92	.813	1.388	7.56	8.95	376	1667	2043	.00985	.0286	-22.9	-14.7	-25.7	-13.8
32	1.115	1.206	2.92	.904	1.075	6.037	7.11	214	1090	1394	.00985	.0286	-22.7	-14.8	-25.3	-14.1
33	1.049	1.113	2.92	1.071	.726	4.48	5.21	93.4	618	711	.00985	.0286	-22.5	-14.9	-24.9	-14.3
34	1.696	1.72	2.92	.679	2.33	10.36	12.69	1099	3327	4426	.00985	.0286	-23.1	-14.9	-26.1	-14.4
35	1.77	1.762	2.92	.651	2.36	10.6	12.96	1197	3487	4684	.00985	.0286	-23.3	-15.	-26.5	-14.4
36	1.574	1.942	2.92	.725	2.05	12.56	14.61	934	4146	5080	.00985	.0286	-23.5	-14.2	-26.8	-12.9
37	1.757	1.997	2.92	.669	2.35	12.9	15.25	1179	4337	5116	.00985	.0286	-23.3	-14.2	-26.5	-12.9
38	-	1.077	-	-	-	3.39	3.39	-			-	.0286	-	-15.7	-	-15.9
39	-	1.153	-	-	-	4.76	4.76	-			-	.0286	-	-15.6	-	-15.8
40	-	1.499	-	-	-	8.51	8.51	-			-	.0286	-	-15.3	-	-15.1
	V_8	V_{28}	T_8	T_{28}												
	m/sec		°K		FULL SCALE DATA											
31	271	221	694	313	78.	425	503	21167	93750	114917	.554	1.61	-5.4	2.8	-8.2	3.7
32	200	181	648	312	60.3	340	400	12060	61299	73359	.554	1.61	-5.2	2.7	-7.8	3.4
33	129	138	607	313	40.8	252	293	5261	34686	39947	.554	1.61	-5.	2.6	-7.4	3.2
34	473	321	790	358	131	583	714	61920	187150	249070	.554	1.61	-5.6	2.6	-8.6	3.1
35	506	329	841	361	133	596	729	67258	196170	263428	.554	1.61	-5.8	2.5	-9.	3.1
36	455	330	843	314	116	707	823	52584	233164	285748	.554	1.61	-6.	3.3	-9.3	4.6
37	503	336	841	314	132	726	858	66324	243977	610301	.554	1.61	-5.8	3.3	-9.	4.6
38	-	126	-	374	-	195	195	-	24442	24442	-	1.61	-	1.9	-	1.7
39	-	173	-	374	-	274	274	-	47371	47371	-	1.61	-	2.	-	1.8
40	-	195	-	373	-	489	489	-	139898	139898	-	1.61	-	2.3	-	2.5

Table C-12. LOW VELOCITY JET NOISE SUPPRESSOR TEST II

18 Capped Lobe Suppressor
AR=2 SI Units

SCALE FACTOR 7.5

DATA PT	P_{T8}/P_0	P_{T28}/P_0	A_{28}/A_8	V_{28}/V_8	W_8	W_{28}	W_T	F_8	F_{28}	F_T	A_8	A_{28}	$10\log \rho_8 A_8$	$10\log \rho_{28} A_{28}$	$10\log \rho_8^2 A_8$	$10\log \rho_{28}^2 A_{28}$
					kg/sec				N		m^2					
COMMON DATA					SCALE MODEL DATA											
41	-	1.312	-	-	-	6.77	6.77	-	1601	1601	-	.0286	-	-15.5	-	-15.4
42	-	1.486	-	-	-	8.62	8.62	-	2380	2380	-	.0286	-	-15.1	-	-14.7
43	-	1.371	-	-	-	7.54	7.54	-	1873	1873	-	.0286	-	-15.2	-	-14.9
44	-	1.733	-	-	-	10.46	10.46	-	3376	3376	-	.0286	-	-14.9	-	-14.4
45	-	1.768	-	-	-	10.69	10.69	-	3509	3509	-	.0286	-	-14.9	-	-14.3
46	-	1.684	-	-	-	10.12	10.12	-	3189	3189	-	.0286	-	-15.	-	-14.4
47	-	1.665	-	-	-	10.01	10.01	-	3114	3114	-	.0286	-	-15.	-	-14.4
					-											

	V_8	V_{28}	T_8	T_{28}
	m/sec		°K	
41	-	237	-	374
42	-	276	-	355
43	-	249	-	357
44	-	323	-	358
45	-	329	-	358
46	-	315	-	358
47	-	312	-	356

FULL SCALE DATA												
-	389	389	-	92051	92051	-	1.61	-	2.1	-	2.2
-	495	495	-	136718	136718	-	1.61	-	2.5	-	2.9
-	433	433	-	107646	107646	-	1.61	-	2.4	-	2.7
-	601	601	-	194102	194102	-	1.61	-	2.7	-	3.2
-	614	614	-	201752	201752	-	1.61	-	2.7	-	3.3
-	581	581	-	183204	183204	-	1.61	-	2.6	-	3.2
-	575	575	-	178921	178921	-	1.61	-	2.6	-	3.2

Table C-13. LOW VELOCITY JET NOISE SUPPRESSOR TEST III

Baseline II
SI Units

SCALE FACTOR 7.5

DATA PT	P_{T8}/P_0	P_{T28}/P_0	A_{28}/A_8	V_{28}/V_8	W_8 (kg/sec)	W_{28} (kg/sec)	W_T (kg/sec)	F_8 (N)	F_{28} (N)	F_T (N)	A_8 (m^2)	A_{28} (m^2)	$10\log \rho_8 A_8$	$10\log \rho_{28} A_{28}$	$10\log \rho_8^2 A_8$	$10\log \rho_{28}^2 A_{28}$
CONSTANT DATA					SCALE MODEL DATA											
1	1.754	-	-	-	2.46	-	2.46	1232	-	1232	.0102	-	-23.1	-	-26.8	-
2	1.694	-	-	-	2.36	-	2.36	1152	-	1152	.0102	-	-23.2	-	-26.3	-
3	1.642	-	-	-	2.29	-	2.29	1041	-	1041	.0102	-	-23.2	-	-26.3	-
4	1.576	-	-	-	2.19	-	2.19	983	-	983	.0102	-	-23.2	-	-26.3	-
5	1.392	-	-	-	1.88	-	1.88	703	-	703	.0102	-	-23.	-	-26.1	-
6	1.198	-	-	-	1.42	-	1.42	377	-	377	.0102	-	-22.8	-	-25.5	-
7	1.109	-	-	-	1.08	-	1.08	214	-	214	.0102	-	-22.6	-	-25.2	-
8	-	1.741	-	-	-	10.66	10.66	-	3443	3443	-	.0286	-	-14.9	-	-14.2
9	-	1.684	-	-	-	10.21	10.21	-	3220	3220	-	.0286	-	-14.9	-	-14.3
10	-	1.669	-	-	-	10.12	10.12	-	3158	3158	-	.0286	-	-14.9	-	-14.4
	V_8 (m/sec)	V_{28} (m/sec)	T_8 (°K)	T_{28} (°K)	FULL SCALE DATA											
1	502	-	838	-	138	-	138	69367	-	69367	.574	-	-5.6	-	-8.7	-
2	488	-	840	-	133	-	133	64758	-	64758	.574	-	-5.7	-	-8.8	-
3	472	-	832	-	129	-	129	60675	-	60675	.574	-	-5.7	-	-8.8	-
4	450	-	822	-	123	-	123	55355	-	55355	.574	-	-5.7	-	-8.8	-
5	375	-	772	-	106	-	106	39605	-	39605	.574	-	-5.5	-	-8.6	-
6	266	-	698	-	79.8	-	79.8	21217	-	21217	.574	-	-5.3	-	-8.	-
7	197	-	663	-	61.2	-	61.2	12027	-	12027	.574	-	-5.1	-	-7.7	-
8	-	323	-	355	-	599	599	-	193550	193550	-	1.61	-	2.7	-	3.3
9	-	315	-	358	-	574	574	-	181042	181042	-	1.61	-	2.6	-	3.2
10	-	313	-	358	-	568	568	-	177020	177020	-	1.61	-	2.6	-	3.1

Table C-14. LOW VELOCITY JET NOISE SUPPRESSOR TEST III

SCALE FACTOR 7.5

Baseline II
SI Units

DATA PT	P_{T8}/P_0	P_{T28}/P_0	A_{28}/A_8	V_{28}/V_8	W_8	W_{28}	W_T	F_8	F_{28}	F_T	A_8	A_{28}	$10\log \rho_8 A_8$	$10\log \rho_{28} A_{28}$	$10\log \rho_8^2 A_8$	$10\log \rho_{28}^2 A_{28}$
					← kg/sec →			← N →			← m^2 →					
COMMON DATA					SCALE MODEL DATA											
11	-	1.643	-	-	-	9.93	9.93	-	3056	3056	-	.0286	-	-14.9	-	-14.4
12	-	1.528	-	-	-	9.07	9.07	-	2580	2580	-	.0286	-	-15.	-	-14.5
13	-	1.37	-	-	-	7.8	7.8	-	1886	1886	-	.0286	-	-14.9	-	-14.4
14	-	1.23	-	-	-	6.17	6.17	-	1223	1223	-	.0286	-	-15.1		-14.6
15	1.758	1.726	2.81	.64	2.46	10.51	12.97	1241	3385	4626	.0102	.0286	-23.1	-14.9	-26.3	-14.3
16	1.679	1.68	2.81	.649	2.33	10.16	12.49	1130	3207	4337	.0102	.0286	-23.2	-15.	-26.5	-14.4
17	1.641	1.661	2.81	.66	2.29	10.06	12.35	1076	3131	4207	.0102	.0286	-23.2	-14.9	-26.3	-14.4
18	1.572	1.648	2.81	.668	2.14	10.07	12.21	979	3078	4057	.0102	.0286	-23.3	-14.9	-26.7	-14.2
19	1.39	1.531	2.81	.769	1.88	9.04	10.92	703	2598	3301	.0102	.0286	-23.	-15.	-26.	-14.6
20	1.206	1.379	2.81	.897	1.45	7.98	9.43	392	1930	2322	.0102	.0286	-22.7	-14.8	-25.4	-14.2
	V_8	V_{28}	T_8	T_{28}												
	← m/sec →		← °K →		FULL SCALE DATA											
11	-	308	-	356	-	559	559	-	171862	171862	-	1.61	-	2.6	-	3.1
12	-	285	-	354	-	510	510	-	145201	145201	-	1.61	-	2.5	-	3.
13	-	243	-	341	-	438	438	-	106120	106120	-	1.61	-	2.5	-	3.1
14	-	198	-	338	-	348	348	-	68704	68704	-	1.61	-	2.4	-	2.9
15	504	322	841	358	139	591	730	69714	190410	260124	.574	1.61	-5.6	2.6	-8.8	3.2
16	487	316	850	360	131	572	703	63620	180273	243893	.574	1.61	-5.7	2.5	-9.	3.1
17	472	311	833	357	129	566	695	60635	176025	236660	.574	1.61	-5.7	2.6	-8.8	3.1
18	458	306	856	350	120	566	686	55035	173103	228138	.574	1.61	-5.8	2.6	-9.2	3.3
19	374	287	772	358	106	508	614	39449	146006	185455	.574	1.61	-5.5	2.5	-8.5	2.9
20	270	242	693	332	81.6	449	531	22035	108500	130535	.574	1.61	-5.2	2.7	-7.9	3.3

TABLE C-15. LOW VELOCITY JET NOISE SUPPRESSOR TEST III

SCALE FACTOR 7.5

Baseline II

SI Units

DATA PT	P_{T8}/P_0	P_{T28}/P_0	A_{28}/A_8	V_{28}/V_8
COMMON DATA				
21	1.109	1.229	2.81	1.009
22	1.657	1.746	2.81	.669
23	1.545	1.773	2.81	.757
24	1.519	1.795	2.81	.778
25	1.455	1.802	2.81	.828
21R	1.115	1.226	2.81	.964

	V_8	V_{28}	T_8	T_{28}
	m/sec		°K	
21	196	198	653	339
22	488	326	877	360
23	439	333	817	364
24	431	336	817	364
25	406	336	802	362
21R	204	197	674	339

	W_8	W_{28}	W_T	F_8	F_{28}	F_T	A_8	A_{28}	$10\log \rho_8 A_8$	$10\log \rho_{28} A_{28}$	$10\log \rho_8^2 A_8$	$10\log \rho_{28}^2 A_{28}$
	kg/sec			N			m^2					
SCALE MODEL DATA												
21	1.09	6.17	7.26	214	1219	1433	.0102	.0286	-22.6	-15.1	-25.1	-14.6
22	2.25	10.61	12.86	1099	3461	4560	.0102	.0286	-23.4	-14.9	-26.8	-14.3
23	2.14	10.73	12.87	939	3563	4502	.0102	.0286	-23.2	-14.9	-26.3	-14.4
24	2.09	10.89	12.98	898	3647	4545	.0102	.0286	-23.2	-14.9	-26.3	-14.3
25	1.98	10.95	12.93	805	3674	4479	.0102	.0286	-23.1	-14.9	-26.3	-14.3
21R	1.11	6.12	7.23	225	1201	1426	.0102	.0286	-22.7	-15.1	-25.4	-14.7
FULL SCALE DATA												
21	61.7	347	409	12036	68468	80504	.574	1.61	-5.1	2.4	-7.6	2.9
22	127	597	724	61863	194760	256623	.574	1.61	-5.9	2.6	-9.3	3.2
23	120	604	724	52838	200574	253412	.574	1.61	-5.6	2.6	-8.8	3.1
24	117	612	729	50658	205262	255920	.574	1.61	-5.7	2.6	-8.8	3.2
25	112	616	728	45187	206747	251934	.574	1.61	-5.7	2.6	-8.8	3.2
21R	62.1	345	407	12672	67632	80304	.574	1.61	-5.2	2.4	-7.9	2.8

Table C-16. LOW VELOCITY JET NOISE SUPPRESSOR TEST III

SCALE FACTOR 7.5

24 Hole Suppressor
SI Units

DATA PT	P_{T8}/P_0	P_{T28}/P_0	A_{28}/A_8	V_{28}/V_8	W_8	W_{28}	W_T	F_8	F_{28}	F_T	A_8	A_{28}	$10\log \rho_8 A_8$	$10\log \rho_{28} A_{28}$	$10\log \rho_8^2 A_8$	$10\log \rho_{28}^2 A_{28}$
					← kg/sec →			← N →			← m^2 →					
COMMON DATA					SCALE MODEL DATA											
26	1.767	-	-	-	2.45	-	2.45	1250	-	1250	.0102	-	-23.1	-	-26.2	-
27	1.685	-	-	-	2.34	-	2.34	1139	-	1139	.0102	-	-23.2	-	-26.4	-
28	1.633	-	-	-	2.27	-	2.27	1068	-	1068	.0102	-	-23.2	-	-26.3	-
29	1.568	-	-	-	2.18	-	2.18	974	-	974	.0102	-	-23.2	-	-26.3	-
30	1.4	-	-	-	1.9	-	1.9	716	-	716	.0102	-	-23	-	-26.1	-
31	1.204	-	-	-	1.44	-	1.44	388	-	388	.0102	-	-22.8	-	-25.5	-
32	1.116	-	-	-	1.12	-	1.12	227	-	227	.0102	-	-22.6	-	-25.2	-
33	-	1.725	-	-	-	10.48	10.48	-	3372	3372	-	.0286	-	-14.9	-	-14.3
34	-	1.676	-	-	-	10.16	10.16	-	3185	3185	-	.0286	-	-14.9	-	-14.4
35	-	1.659	-	-	-	10.02	10.02	-	3118	3118	-	.0286	-	-15.	-	-14.4
	V_8	V_{28}	T_8	T_{28}	FULL SCALE DATA											
	← m/sec →		← °K →													
26	505	-	840	-	139	-	139	70345	-	70345	.574	-	-5.6	-	-8.7	-
27	487	-	846	-	132	-	132	64047	-	64047	.574	-	-5.7	-	-8.9	-
28	469	-	832	-	128	-	128	59959	-	59959	.574	-	-5.7	-	-8.8	-
29	447	-	820	-	122	-	122	54702	-	54702	.574	-	-5.6	-	-8.8	-
30	378	-	773	-	107	-	107	40321	-	40321	.574	-	-5.5	-	-8.5	-
31	270	-	698	-	81.2	-	81.2	21817	-	21817	.574	-	-5.2	-	-8.	-
32	202	-	658	-	63.1	-	63.1	12770	-	12770	.574	-	-5.1	-	-7.7	-
33	-	322	-	358	-	589	589	-	189676	189676	-	1.61	-	2.6	-	3.2
34	-	314	-	358	-	571	571	-	179263	179263	-	1.61	-	2.6	-	3.1
35	-	312	-	358	-	564	564	-	175465	175465	-	1.61	-	2.6	-	3.1

TABLE C-17. LOW VELOCITY JET NOISE SUPPRESSOR TEST III

SCALE FACTOR 7.5

24 Hole Suppressor
SI Units

DATA PT	P_{T8}/P_0	P_{T28}/P_0	A_{28}/A_8	V_{28}/V_8	W_8	W_{28}	W_T	F_8	F_{28}	F_T	A_8	A_{28}	$10\log \rho_8 A_8$	$10\log \rho_{28} A_{28}$	$10\log \rho_8^2 A_8$	$10\log \rho_{28}^2 A_{28}$
					kg/sec			N			m²					
COMMON DATA					SCALE MODEL DATA											
36	-	1.634	-	-	-	9.84	9.84	-	3020	3020	-	.0286	-	-15.	-	-14.4
37	-	1.519	-	-	-	9.12	9.12	-	2544	2544	-	.0286	-	-14.9	-	-14.3
38	-	1.37	-	-	-	7.85	7.85	-	1886	1886	-	.0286	-	-14.9	-	-14.3
39	-	1.22	-	-	-	6.17	6.17	-	1201	1201	-	.0286	-	-15.	-	-14.5
40	1.762	1.727	2.81	.634	2.46	10.57	13.03	1241	3380	4621	.0102	.0286	-23.1	-14.8	-26.3	-14.2
41	1.676	1.678	2.81	.645	2.32	10.21	12.53	1125	3189	4315	.0102	.0286	-23.2	-14.9	-26.4	-14.3
42	1.653	1.668	2.81	.663	2.31	10.07	12.38	1094	3149	4243	.0102	.0286	-23.1	-15.	-26.3	-14.4
43	1.594	1.64	2.81	.668	2.21	9.93	12.14	1010	3038	4048	.0102	.0286	-23.2	-14.9	-26.4	-14.3
44	1.404	1.528	2.81	.756	1.91	9.01	10.93	721	2580	3301	.0102	.0286	-23.	-15.	-26.	-14.6
45	1.204	1.373	2.81	.902	1.43	7.79	9.22	387	1898	2285	.0102	.0286	-22.8	-15.	-25.6	-14.4
	V_8	V_{28}	T_8	T_{28}												
	m/sec		°K		FULL SCALE DATA											
36	-	307	-	358	-	554	554	-	169825	169825	-	1.61	-	2.5	-	3.1
37	-	280	-	346	-	512	512	-	143052	143052	-	1.61	-	2.6	-	3.2
38	-	240	-	334	-	442	442	-	106120	106120	-	1.61	-	2.6	-	3.2
39	-	194	-	333	-	348	348	-	67592	67592	-	1.61	-	2.5	-	3.
40	504	320	841	353	139	595	734	69869	190237	260106	.574	1.61	-5.6	2.6	-8.8	3.3
41	484	312	845	353	131	575	706	63255	179455	242710	.574	1.61	-5.7	2.6	-8.9	3.2
42	473	314	827	359	130	566	696	61467	177235	238702	.574	1.61	-5.6	2.5	-8.8	3.1
43	457	305	828	352	124	560	684	56739	170941	227680	.574	1.61	-5.7	2.6	-8.9	3.2
44	379	286	768	357	108	507	615	40624	144991	185615	.574	1.61	-5.5	2.5	-8.5	2.9
45	270	244	702	341	80.7	438	519	21791	106739	128530	.574	1.61	-5.3	2.5	-8.1	3.1

Table C-18. LOW VELOCITY JET NOISE SUPPRESSOR TEST III

SCALE FACTOR 7.5

24 Hole Suppressor

SI Units

DATA PT	P_{T8}/P_0	P_{T28}/P_0	A_{28}/A_8	V_{28}/V_8	W_8 (lbs/sec)	W_{28} (lbs/sec)	W_T (lbs/sec)	F_8 (lbs)	F_{28} (lbs)	F_T (lbs)	A_8 (ft^2)	A_{28} (ft^2)	$10\log \rho_8 A_8$	$10\log \rho_{28} A_{28}$	$10\log \rho_8^2 A_8$	$10\log \rho_{28}^2 A_{28}$
COMMON DATA					SCALE MODEL DATA											
46	1.113	1.229	2.81	.982	1.11	6.19	7.3	221	1214	1435	.0102	.0286	-22.6	-15.	-25.2	-14.6
47	1.663	1.758	2.81	.672	2.25	10.61	22.86	1108	3501	4609	.0102	.0286	-23.4	-15.	-26.8	-14.4
48	1.557	1.782	2.81	.743	2.15	10.86	13.01	956	3594	4550	.0102	.0286	-23.2	-14.9	-26.4	-14.2
Rdg. 18 99	1.615	1.778	2.81	.726	2.28	10.78	13.06	1041	3576	4617	.0102	.0286	-23.1	-14.9	-26.1	-14.3

	V_8 (ft/sec)	V_{28} (ft/sec)	T_8 (°R)	T_{28} (°R)	FULL SCALE DATA											
46	200	196	659	335	62.1	348	410	12432	68326	80758	.574	1.61	-5.1	2.5	-7.7	2.9
47	491	330	880	364	127	597	724	62205	196940	259145	.574	1.61	-5.9	2.5	-9.3	3.1
48	446	331	826	358	121	611	732	53710	202077	255787	.574	1.61	-5.7	2.6	-8.9	3.3
Rdg. 18 99	457	332	807	362	128	606	734	58456	201223	259679	.574	1.61	-5.6	2.6	-8.6	3.2

TABLE C-19. LOW VELOCITY JET NOISE SUPPRESSOR TEST III

SCALE FACTOR 7.5

SPOKE SUPPRESSOR
SI Units

DATA PT	P_{T8}/P_0	P_{T28}/P_0	A_{28}/A_8	V_{28}/V_8	W_8	W_{28}	W_T	F_8	F_{28}	F_T	A_8	A_{28}	$10\log \rho_8 A_8$	$10\log \rho_{28} A_{28}$	$10\log \rho_8^2 A_8$	$10\log \rho_{28}^2 A_{28}$
					kg/sec			N			m^2					
COMMON DATA					SCALE MODEL DATA											
49	1.76	-	-	-	2.48	-	2.48	1241	-	1241	.0102	-	-23.1	-	-26.2	-
50	1.682	-	-	-	2.33	-	2.33	1134	-	1134	.0102	-	-23.2	-	-26.4	-
51	1.645	-	-	-	2.29	-	2.29	1081	-	1081	.0102	-	-23.2	-	-26.4	-
52	1.579	-	-	-	2.19	-	2.19	987	-	987	.0102	-	-23.2	-	-26.4	-
53	1.393	-	-	-	1.89	-	1.89	703	-	703	.0102	-	-23.	-	-26.	-
54	1.199	-	-	-	1.42	-	1.42	379	-	379	.0102	-	-22.8	-	-25.6	-
55	1.124	-	-	-	1.17	-	1.17	242	-	242	.0102	-	-22.5	-	-25.	-
56	-	1.724	-	-	-	10.48	10.48	-	3376	3376	-	.0286	-	-14.9	-	-14.3
57	-	1.687	-	-	-	10.21	10.21	-	3229	3229	-	.0286	-	-14.9	-	-14.3
58	-	1.655	-	-	-	10.02	10.02	-	3105	3105	-	.0286	-	-14.9	-	-14.4
	V_8	V_{28}	T_8	T_{28}												
	m/sec		°K		FULL SCALE DATA											
49	503	-	836	-	139	-	139	69282	-	69282	.574	-	-5.6	-	-8.7	-
50	486	-	846	-	131	-	131	63726	-	63726	.574	-	-5.7	-	-8.9	-
51	473	-	833	-	129	-	129	60826	-	60826	.574	-	-5.7	-	-8.9	-
52	452	-	825	-	123	-	123	55520	-	55520	.574	-	-5.7	-	-8.9	-
53	374	-	767	-	106	-	106	39641	-	39641	.574	-	-5.5	-	-8.5	-
54	267	-	702	-	79.8	-	79.8	21301	-	21301	.574	-	-5.3	-	-8.1	-
55	207	-	648	-	65.8	-	65.8	13606	-	13606	.574	-	-5.	-	-7.5	-
56	-	322	-	358	-	590	590	-	189850	189850	-	1.61	-	2.6	-	3.2
57	-	316	-	358	-	575	575	-	181710	181710	-	1.61	-	2.6	-	3.2
58	-	310	-	357	-	563	563	-	174566	174566	-	1.61	-	2.6	-	3.1

Table C-20 LOW VELOCITY JET NOISE SUPPRESSOR TEST III

SCALE FACTOR 7.5

24 Spoke Suppressor
SI Units

DATA PT	P_{T8}/P_0	P_{T28}/P_0	A_{28}/A_8	V_{28}/V_8	W_8	W_{28}	W_T	F_8	F_{28}	F_T	A_8	A_{28}	$10\log \rho_8 A_8$	$10\log \rho_{28} A_{28}$	$10\log \rho_8^2 A_8$	$10\log \rho_{28}^2 A_{28}$
	COMMON DATA				SCALE MODEL DATA											
					← kg/sec →			← N →			← m^2 →					
59	-	1.64	-	-	-	9.93	9.93	-	3042	3042	-	.0286	-	-14.9	-	-14.3
60	-	1.526	-	-	-	9.07	9.07	-	2571	2571	-	.0286	-	-15.	-	-14.4
61	-	1.363	-	-	-	7.76	7.76	-	1855	1855	-	.0286	-	-14.9	-	-14.3
62	-	1.218	-	-	-	5.94	5.94	-	1161	1161	-	.0286	-	-15.2	-	-14.9
63	1.751	1.716	2.81	.636	2.44	10.44	12.88	1228	3340	4568	.0102	.0286	-23.2	-14.9	-26.3	-14.3
64	1.716	1.689	2.81	.644	2.4	10.25	12.65	1179	3234	4413	.0102	.0286	-23.1	-14.9	-26.3	-14.3
65	1.666	1.663	2.81	.66	2.34	9.98	12.32	1112	3131	4243	.0102	.0286	-23.1	-15.	-26.2	-14.5
66	1.583	1.647	2.81	.693	2.18	9.83	12.01	992	3069	4061	.0102	.0286	-23.1	-15.1	-26.3	-14.6
67	1.402	1.522	2.81	.739	1.89	9.09	10.98	721	2553	3274	.0102	.0286	-23.1	-14.9	-26.1	-14.3
68	1.206	1.37	2.81	.922	1.45	7.57	9.02	391	1882	2273	.0102	.0286	-22.7	-15.2	-25.5	-14.9
	V_8	V_{28}	T_8	T_{28}	FULL SCALE DATA											
	← m/sec →		← °K →													
59	-	306	-	354	-	559	559	-	171181	171181	-	1.61	-	2.6	-	3.2
60	-	284	-	352	-	510	510	-	144725	144725	-	1.61	-	2.5	-	3.1
61	-	239	-	335	-	437	437	-	104314	104314	-	1.61	-	2.6	-	3.2
62	-	196	-	347	-	334	334	-	65359	65359	-	1.61	-	2.3	-	2.6
63	503	320	845	356	137	587	724	69033	187835	256868	.574	1.61	-5.7	2.6	-8.8	3.2
64	491	316	833	358	135	576	711	66373	181892	248265	.574	1.61	-5.6	2.6	-8.8	3.2
65	476	314	825	362	132	562	694	62494	176110	238604	.574	1.61	-5.6	2.5	-8.7	3.
66	451	312	818	366	124	552	676	55854	172520	228374	.574	1.61	-5.6	2.4	-8.8	2.9
67	380	281	778	347	107	512	619	40468	143662	184130	.574	1.61	-5.6	2.6	-8.6	3.2
	270	249	697	359	81.2	425	506	22004	106040	128044	.574	1.61	-5.2	2.3	-8.0	2.6

Table C-21. LOW VELOCITY JET NOISE SUPPRESSOR TEST III

SCALE FACTOR 7.5

Spoke Suppressor

SI Units

DATA PT	P_{T8}/P_0	P_{T28}/P_0	A_{28}/A_8	V_{28}/V_8	W_8 (kg/sec)	W_{28} (kg/sec)	W_T (kg/sec)	F_8 (N)	F_{28} (N)	F_T (N)	A_8 (m^2)	A_{28} (m^2)	$10\log \rho_8 A_8$	$10\log \rho_{28} A_{28}$	$10\log \rho_8^2 A_8$	$10\log \rho_{28}^2 A_{28}$
COMMON DATA					SCALE MODEL DATA											
69	1.107	1.224	2.81	1.052	1.08	5.85	6.93	210	1192	1402	.0102	.0286	-22.5	-15.4	-25.1	-15.3
70	1.653	1.74	2.81	.667	2.25	10.6	12.85	1090	3434	4524	.0102	.0286	-23.4	-14.9	-26.7	-14.3
71	1.489	1.787	2.81	.788	2.02	10.84	12.86	854	3612	4466	.0102	.0286	-23.2	-14.9	-26.5	-14.3

	V_8 (m/sec)	V_{28} (m/sec)	T_8 (°K)	T_{28} (°K)												
					FULL SCALE DATA											
69	194	204	651	368	60.8	329	390	11805	66982	78787	.574	1.61	-5.	2.1	-7.6	2.1
70	486	324	872	357	127	596	723	61422	193057	254479	.574	1.61	-5.9	2.6	-9.2	3.2
71	423	333	825	362	113	610	723	48003	203140	251143	.574	1.61	-5.7	2.6		3.2

APPENDIX D

COMBUSTOR TEST POINTS

APPENDIX D - COMBUSTOR TEST POINTS

TEST POINT	OAPWL for 100-2000 Hz dBre 10^{-13} Watt	AIR MASS FLOW (lb/sec)	AIR MASS FLOW (kg/sec)	COMBUSTOR EXIT TEMPERATURE T_4 (°R)	COMBUSTOR EXIT TEMPERATURE T_4 (°K)	COMBUSTOR INLET TEMPERATURE T_3 (°R)	COMBUSTOR INLET TEMPERATURE T_3 (°K)	COMBUSTOR EXIT PRESSURE P_4 (psia)	COMBUSTOR EXIT PRESSURE P_4 (N/m^2)
1	116.2	3.71	1.68	664	369	668	371	14.35	98940
2	123.7	3.78	1.72	1346	748	656	364	14.32	98740
3	126.5	3.79	1.72	1833	1018	653	363	14.33	98810
4	128.5	3.84	1.74	2333	1296	668	371	14.32	98740
5	125.9	7.30	3.31	658	366	659	366	14.32	98740
6	130.5	7.51	3.41	1323	735	656	364	14.23	98120
7	133.7	7.69	3.49	1803	1001	659	366	14.20	97910
8	138.7	7.55	3.43	2319	1288	656	364	14.13	97430
9	135.6	14.26	6.47	663	368	665	369	14.08	97090
10	142.2	14.91	6.76	1312	729	666	370	13.80	95150
11	144.4	14.58	6.13	1866	1037	663	368	13.78	95010
12	146.1	14.76	6.70	2133	1185	665	369	13.67	94260
13	122.2	3.74	1.70	941	523	963	535	14.36	99010
14	126.6	3.75	1.70	1637	909	954	530	14.34	98870
15	129.1	3.78	1.71	2132	1184	963	535	14.29	98530
16	127.6	3.80	1.72	2632	1462	966	537	14.31	98670
17	130.1	7.31	3.16	851	473	856	476	14.32	98740
18	134.7	7.56	3.43	1544	858	852	473	14.22	98050
19	140.1	7.58	3.44	2041	1134	862	479	14.14	97500
20	136.9	7.58	3.44	2533	1407	864	480	14.11	97290
21	138.2	14.46	6.56	810	450	815	453	14.06	96944
22	145.0	14.70	6.67	1625	903	805	447	13.81	95220
23	146.6	14.69	6.66	1982	1101	809	449	13.72	94955
24	145.9	14.60	6.62	2077	1154	805	447	13.70	94462

TABLE D-1 CF6 COMBUSTOR COMPONENT TEST

TEST POINT	OAPWL for 100-2000 Hz dBre 10^{-13} Watt	AIR MASS FLOW (lb/sec)	AIR MASS FLOW (kg/sec)	COMBUSTOR EXIT TEMPERATURE T_4 (°R)	COMBUSTOR EXIT TEMPERATURE T_4 (°K)	COMBUSTOR INLET TEMPERATURE T_3 (°R)	COMBUSTOR INLET TEMPERATURE T_3 (°K)	COMBUSTOR EXIT PRESSURE P_4 (psia)	COMBUSTOR EXIT PRESSURE P_4 (N/m^2)
1	120.1	3.69	1.67	776	431	759	422	14.34	98870
2	129.1	3.84	1.74	1259	699	653	363	14.31	98670
3	133.8	3.81	1.73	1683	935	651	362	14.28	98460
4	141.4	3.89	1.76	2079	1155	646	359	14.30	98600
5	124.3	7.24	3.28	658	366	639	355	14.35	98940
6	139.1	7.52	3.41	1348	749	649	361	14.21	97980
7	144.7	7.59	3.44	1823	1012	651	362	14.27	98390
8	150.9	7.61	3.45	2240	1244	655	364	14.28	98460
9	127.0	10.09	4.58	672	373	658	365	14.03	96740
10	147.7	10.07	4.57	1454	808	659	366	14.16	97630
11	147.4	9.62	4.36	1571	873	658	366	14.27	98390
13	119.5	3.93	1.78	960	533	916	509	14.11	97290
14	128.6	4.00	1.81	1650	917	925	514	14.16	97630
15	136.4	3.93	1.78	2154	1197	921	512	14.27	98390
16	140.9	3.90	1.77	2652	1473	927	515	14.17	97700
17	125.9	7.46	3.38	870	483	835	464	14.03	96740
18	136.7	7.45	3.38	1564	869	835	464	14.16	97630
19	143.2	7.50	3.40	2029	1127	833	463	14.28	98460
20	149.6	7.32	3.32	2565	1425	840	467	14.32	98740
21	130.2	10.02	4.55	820	456	797	443	13.98	96390
22	143.7	10.76	4.88	1514	841	781	434	14.13	97430
24	150.1	10.53	4.78	1818	1010	793	441	14.48	99840

TABLE D-2 A.T. COMBUSTOR COMPONENT TEST

APPENDIX E

FLOW CORRECTIONS FOR PROBE MEASUREMENTS

When acoustic measurements are taken with probes in a duct, corrections are required for the duct flow. The corrections follow from the fact that for a plane wave propagating down a duct with airflow, the pressure recorded by the probe differs from the actual acoustic pressure of the wave as given by:

$$\frac{p}{p_{(measured)}} = [1 - M\cos\theta]\exp\left[\frac{ikrM\cos\theta}{1 - M\cos\theta}\right] \qquad \text{(E-1)}$$

where p = Pressure to be used in computing intensity or power levels

$p_{(measured)}$ = Pressure recorded by the probe

M = Airflow Mach number at probe location

θ = Angle of propagating wave front relative to the incoming airflow direction ($\theta = 0$ at inlet and 180° for exhaust).

$k = \omega/c$

r = Axial distance along the duct (for a plane wave)

Only the amplitude correction need be considered here as the phase correction changes only the wavelength and the frequency remains the same.

In the actual case, the direction of propagation is not usually that of a plane wave traversing axially down a duct, but takes the form of a complex mode fluctuating randomly with time. Thus a mean value of 135° is selected for θ in the case of a downstream probe.

The correction for the duct acoustic impedance must be made as the acoustic power level is computed by summing over the signals recorded by the probes at different immersions as follows:

$$PWL = 10\log_{10}\frac{W}{W_{Ref.}} \qquad \text{(E-2)}$$

where $$W = \int_A \frac{p^2}{\rho c}\, dA = \sum_{n=1}^{N} \left[\frac{p^2}{\rho c} \right]_n \qquad \text{(E-3)}$$

and $$W_{Ref} = \frac{p^2_{Ref}}{(\rho c)_{Ref}} \qquad \text{(E-4)}$$

Here W = acoustic power

p = acoustic pressure - given by equation (F-1).

(ρc) = acoustic impedance

ΔA = probe immersion area

N = number of probes

The subscript Ref denotes reference quantities. Equations (E-2, (E-3) and (F-4) yield:

$$PWL = \sum_{n=1}^{N} \left\{ SPL_n + C_n + 10\log_{10}\frac{(\rho c)_{Ref}}{(\rho c)} + 10\log_{10}(\Delta A)_n + 10\log K \right\} \qquad \text{(E-5)}$$

where SPL_n = acoustic sound pressure level recorded with the n-th probe, dB

C_n = probe frequency response correction, dB

and K = constant to adjust for the units, · 891